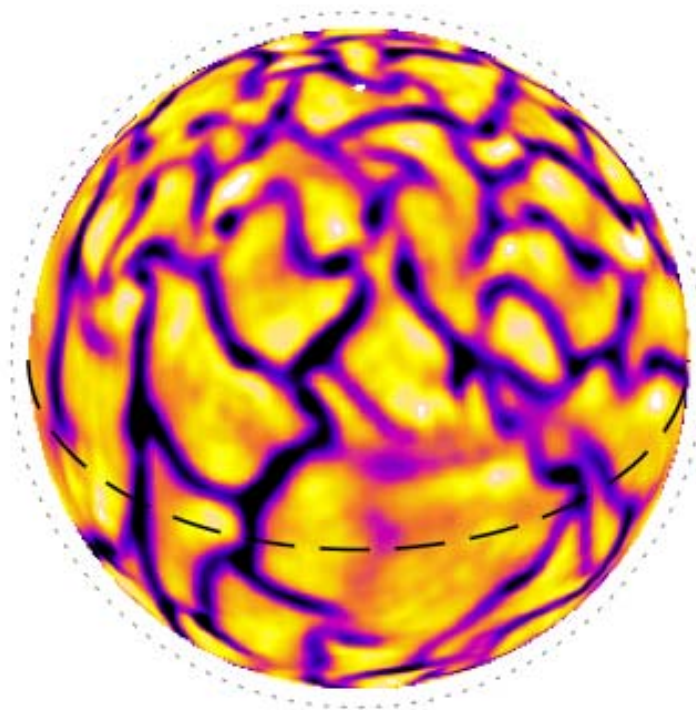


Studying Turbulence Using Numerical Simulation Databases - X

Proceedings of the 2004 Summer Program



Center for Turbulence Research

December 2004

*Dedicated to the memory of William C Reynolds
(1934-2004)*



Preface

The tenth Summer Program of the Center for Turbulence Research was held during the period June 21st – July 16th, 2004. This year, in addition to our traditional seventeen year sponsorship by NASA's aeronautics program, the CTR summer program acknowledges support from NASA's Sun-Earth Connection Program, the AFOSR Turbulence & Rotating Flows program, and the DOE-ASC program. This additional support allowed us to maintain the diversity of the program that we feel is essential for cross-disciplinary fertilization among aerodynamics, turbulent combustion, aeroacoustics, atmospheric physics, geophysics, astrophysics, etc. The program sponsored 50 participants from fourteen countries; they were hosted by 24 participants from Stanford and NASA-Ames.

This Proceedings volume contains 32 papers that span a wide range of topics that reflect the ubiquity of turbulence. The papers have been divided into six groups: Solar Simulations, MHD, LES and Numerical Simulations, RANS Modeling and Simulations, Stability and Acoustics, and Combustion and Multi-Phase Flow. In some cases, a paper could have fitted in more than one group so the classification is somewhat arbitrary. More detailed summaries of the accomplishments of each group can be found in the overviews that precede the grouped papers.

Solar Simulations aim at providing an understanding of the dynamics of the Sun. Solar observations, which provide a wealth of data on the dynamics of the interior of the Sun, are motivating efforts to develop Large-Eddy Simulations that can be verified by comparison with this data; in turn, these LES simulations are used to provide detailed understanding of the observations. Three efforts concerned simulating the near surface region of the Sun's interior, the convection zone of the Sun, and developing a theoretical model for the interaction of convection with the magnetic field. New advances were made in numerical simulation of radiation. These advances will guide parallelization strategies for the simulation of the near surface region. The global simulation effort showed that the boundary conditions in the radial direction play an important role on the global dynamics. The theory effort provided a model for the source of the fine structures observed in sunspots.

Magneto-hydrodynamics plays an important role in astrophysics as well as in engineering applications such as liquid metal processing. New advances were made in our understanding of the interactions between the magnetic field and turbulence. It was found that at low magnetic Reynolds number the velocity field develops strong dimensional anisotropy under the action of Joule dissipation. In a study of the effects of rotation and mean magnetic field on turbulence, it was found that, at sufficiently high magnetic Reynolds numbers, the turbulence kinetic energy will grow even for cases when rotation is expected to suppress the turbulence. High resolution simulations of compressible MHD turbulence of interest in astrophysical studies, showed a flattening of the density spectrum. Of interest to NASA's exploration program is a simulation of Hall thruster plasmas where it was shown that electron transport associated with azimuthal disturbances can be significant.

The development of models and numerical methods for Large Eddy Simulations (**LES**) continues to be at the core of the Summer Program. This summer one finds movement towards a holistic approach to LES where the definition of the resolved field, the modeling and the numerical method are treated together. The wavelet approach used in LES was shown to be competitive with traditional methods. Progress in the evaluation of the VMS (variational multi-scale) approach has shown the definition of a good model is closely tied to the choice of the ideal LES solution. This implies that comparison with experimental data is the most reliable way to evaluate LES methodologies. Progress was also made by evaluating filtering strategies as they impact the fundamental equations, treatment of boundary conditions and commutation errors.

The summer program continues to be a forum where **RANS** (Reynolds-Averaged Navier-Stokes) techniques are developed and evaluated. The rapid time to solution, and limited computational resources required by these methods keep them attractive for applications in industry. Progress was made in modeling the effects on the mean flow, a challenging area in RANS models. Other challenging areas in RANS modeling are cases where the flow is locally unsteady such as in synthetic jets, or where the dynamics (time dependence) is important as in noise predictions. A promising approach for treating synthetic jets as a body force was developed. It was shown that RANS methods are not suitable when predictions of the pressure spectrum is required in computation of noise.

Coupling of analytical tools with numerical solutions were used to provide advances in our understanding of fundamental physics. Theory and simulations were combined to provide an understanding of the coupling between free stream disturbances and the boundary layer dynamics. Multiscale transforms were used to identify the most efficient way to control the wake behind a cylinder. Various formulations for decoupling the compressible flow equations to a noise source and inhomogeneous wave equation were tested using DNS data.

As in previous summer programs, the **Combustion and multi-phase flow** group was the largest of the program; this reflects the strong interest in the subject from three of the four sponsors of the Summer Program. Four areas can be identified: Combustion science & modeling, Two-phase flows, Fires, and Thermoacoustic instabilities and control. New advances were made, with marker field models showing promise at low Damkohler number. A new expression for turbulent burning velocity was tested and showed good agreement with DNS results. Strategies for implementing and parallelizing the filtered-density function (FDF) approach were developed and have shown substantial speed-up compared with direct integration. Other strategies using look-up tables show promise for modeling turbulent diffusion flames. New advances were made in the development of methods for multi-phase simulations. Closely packed droplet models were used to simulate liquid film formation and dense sprays. A mass conserving coupled Volume-of-Fluid/Level-Set method was tested, and it was found that handling cases where surface tension is dominant remains a challenge in spray breakup simulations. New radiation models were developed and tested. As combustion simulation technologies mature, we find increased interest in using them in design and optimization of combustion devices. Modern optimization methods were used to show the potential for control of flame length, temperature and NO_x emission.

This year four review tutorials were given: *Solar Turbulence: order amidst chaos in the deep convection zone* (Juri Toomre), *MHD Turbulence* (Bernard Knaepen), *Wall Turbulence Including Roughness* (Javier Jimenez), and *Computationally efficient implementation of chemistry in turbulent combustion simulations* (Stephen Pope).

The final presentation of research accomplishments on July 16th was attended by a number of colleagues from universities, government agencies, and industry.

Special thanks are due to Millie Chethik for her work on organizing the Program and editing the briefs. Her help in the planning, operation and effective interface with the administrative requirements of Stanford University and NASA Ames Research Center are highly appreciated. Special thanks are also due Dr. Xiaohua Wu for assistance in producing the final briefs.

These Summer Proceedings are dedicated to the memory of William C. Reynolds who passed away in January 2004. His energy, enthusiasm, and genius will reverberate in our hallways forever. He is sorely missed by all of us in the turbulence community.

Parviz Moin
Nagi N. Mansour

This volume is available as a .pdf file on the Web at <http://ctr.stanford.edu>

Solar simulation

Magneto-hydrodynamic activity near the surface of the Sun is the major source of Space weather that impacts space exploration, satellite operations, power grids, communications, and other aspects of modern life. Understanding the changing flow of energy and matter throughout the Sun has been established as one of the objectives in NASA's missions and goals. The three projects in the Solar group are representative of the efforts on developing a better understanding of the dynamics of our closest star, the Sun.

In the first project, Stein *et al.* are interested in the near surface region of the Sun. In this region, accurate simulation of radiation is critical because the domain of interest covers the nearly opaque region below the surface and the transparent solar atmosphere (photosphere). The accuracy of spatial quadrature for integration along a ray is found to be important. The angular quadrature, on the other hand, is found to be less critical. In addition, moment models were applied to compute radiative transfer in the solar atmosphere. They found that these alternative models overestimate absorption in the atmosphere. Finally, high-resolution fields were used to synthesize center-to-limb G-band images to provide a better understanding of the observations.

In the second project, Miesch *et al.* are interested in simulating the convection zone on a global scale (the entire solar sphere) without having to resolve the near surface region or the deep core region. Approximate boundary conditions are used at the inner and outer surface of the simulation domain. The sensitivity of convection simulations to these boundary conditions have been investigated. They found that the flow is surprisingly sensitive to the boundary conditions. In addition to these investigations, acoustic wave simulations on a sphere were initiated. The objective is to simulate acoustic wave propagation through the convection zone and provide essential theoretical support to ongoing observational efforts.

In the third project, Busse developed a theoretical model of thermal convection in a twisted magnetic field. The model aims at providing an interpretation of high resolution observations in the interior of sunspots. A relationship for the dependence of the wavelength of filaments on the strength and twist of the magnetic field has been derived.

Nagi N. Mansour

Page intentionally left blank

Thermal convection in a twisted magnetic field

By F.H. Busse †

The onset of convection in a layer of an electrically conducting fluid heated from below is considered in the case when the layer is permeated by horizontal magnetic field of strength B_0 the orientation of which varies sinusoidally with height. An approximate critical value of the Rayleigh number for the onset of convection is derived. The width δ of the convection rolls, $\delta \sim \sqrt{(h_t/B_0)\sqrt{\rho\mu\lambda\nu}}$ is found to be independent of the height of the layer once the right hand side in this relationship is sufficiently small. Applications to the penumbral filaments of sunspots are briefly discussed.

1. Introduction

Convection driven by thermal buoyancy in the presence of an imposed magnetic field has been studied theoretically and experimentally for several decades. For an early review we refer to the book of Chandrasekhar (1961). Usually the case of an imposed homogeneous vertical magnetic field is treated which exerts a strongly inhibiting influence on convection. A most famous example are sunspots which appear dark because the heat transport by convection in the solar atmosphere is almost completely suppressed at the spot by the emerging radial magnetic field.

Homogeneous horizontal magnetic fields exert a far lesser influence on convection. Two-dimensional convection rolls aligned with the magnetic field do not feel any effect at all and the critical value of the Rayleigh number R for the onset of convection is the same as in the non-magnetic case. Since two-dimensional convection rolls aligned with the magnetic field are subject to three-dimensional instabilities, however, the effect of the horizontal magnetic field is felt by the three-dimensional forms of convection realized at higher values of R (Busse & Clever 1989).

Another situation in which a horizontal magnetic field affects convection in an electrically conducting fluid is that of a twisted magnetic field which changes its direction as function of the vertical coordinate. Such a field is accompanied by a current density. In the following we shall consider the case when the electric current is directed parallel to the magnetic field such that a static “force-free” configuration exists. The onset of convection in such a configuration is the topic of this paper.

It has long been known that magnetic fields of sunspots exhibit a torsion which is equivalent to a twist in the local approximation. In the penumbra of large sunspots where the magnetic field becomes nearly horizontal convection appears to assume the form of thin roll like structures called filaments. The small wavelength of these rolls is usually attributed to the influence of the vertical component of the magnetic field. But the twist of the magnetic field may exert an even stronger effect. This possibility will be explored in the following sections in terms of a simple model which offers the advantage that the boundary conditions in the vertical direction do not seem to be significant.

† Institute of Physics, University of Bayreuth, D-95440, Bayreuth, Germany

2. Mathematical Formulation of the Problem

We consider a layer of height d of an electrically conducting fluid heated from below and cooled from above. The fluid is permeated by a horizontally homogeneous magnetic field of the form

$$\vec{B}_0 = B_0(\vec{i} \cos \gamma z - \vec{j} \sin \gamma z) \quad (2.1)$$

where \vec{i} and \vec{j} denote the unit vectors in the horizontal x - and y -directions of a cartesian system of coordinates. The direction of the z -coordinate is opposite to gravity. Since the field (2.1) is force-free, i.e. $(\nabla \times \vec{B}_0) \times \vec{B}_0 = 0$, a motionless static solution of the problem exists.

Using d as length scale, d^2/ν as time scale where ν denotes the kinematic viscosity of the fluid, and $(T_2 - T_1)P/R$ as scale of the deviation Θ of the temperature from its static distribution we obtain the equations of motion for the dimensionless velocity vector \vec{u} and the heat equation for Θ in the following form

$$(\partial_t + \vec{u} \cdot \nabla) \vec{u} = -\nabla \pi + \vec{k} \Theta + \nabla^2 \vec{u} + \vec{B} \cdot \nabla \vec{B} \ , \quad (2.2)$$

$$0 = \nabla \cdot \vec{u} \ , \quad (2.3)$$

$$P(\partial_t + \vec{u} \cdot \nabla) \Theta = R \vec{k} \cdot \vec{u} + \nabla^2 \Theta \quad (2.4)$$

where \vec{k} is the unit vector in the z -direction and the Prandtl number and the Rayleigh number are defined by

$$P = \frac{\nu}{\kappa}, \quad R = \frac{\alpha(T_2 - T_1)gd^3}{\nu\kappa} \quad (2.5)$$

Here κ and α denote the thermal diffusivity and the coefficient of thermal expansion of the fluid and g is the acceleration of gravity. T_1 and T_2 are the temperatures at the lower and upper boundaries which are positioned at $z = \pm 0.5$. In order to treat the problem in its simplest physically realistic form the Boussinesq approximation has been assumed in which the density ρ is regarded as a constant except in connection with the gravity term where its dependence on the temperature has been taken into account. All terms which can be written as gradients in equation (2.2) have been combined into $\nabla \pi$.

The general representation for solenoidal vector fields in terms of poloidal and toroidal components can be used to write the dimensionless magnetic field in the form

$$\vec{B} = \frac{B_0 d}{\nu \sqrt{\rho \mu}} (\vec{i} \cos \gamma z - \vec{j} \sin \gamma z + \frac{\nu}{\lambda} (\nabla \times (\nabla h \times \vec{k}) + \nabla g \times \vec{k})) \ . \quad (2.6)$$

where λ is the magnetic diffusivity which is defined as the inverse of the product of the electrical conductivity σ and the magnetic permeability μ . By taking the vertical components of the equation of induction,

$$\frac{\lambda}{\nu} \nabla^2 \vec{B} = \partial_t \vec{B} - \nabla \times (\vec{u} \times \vec{B}) \quad (2.7)$$

and of its curl we obtain the equations for h and g

$$\nabla^2 \Delta_2 h = (\vec{i} \cos \gamma z - \vec{j} \sin \gamma z) \cdot \nabla u_z \quad (2.8)$$

$$\nabla^2 \Delta_2 g = (\vec{i} \cos \gamma z - \vec{j} \sin \gamma z) \cdot \nabla (\partial_y u_x - \partial_x u_y - \gamma u_z) \quad (2.9)$$

where all terms multiplied by ν/λ have been neglected since we shall consider only the limit $\nu \ll \lambda$ which is appropriate for liquid metals, but also for solar plasmas. Δ_2 denotes

the horizontal Laplacian, $\Delta_2 = \partial_{xx}^2 + \partial_{yy}^2$. The term $\vec{B} \cdot \nabla \vec{B}$ in equation ((2.2) can now be evaluated,

$$\vec{B} \cdot \nabla \vec{B} = Q[(\vec{i} \cos \gamma z - \vec{j} \sin \gamma z) \cdot \nabla (\nabla \times (\nabla h \times \vec{k}) + \nabla g \times \vec{k}) + \Delta_2 h \gamma (\vec{i} \sin \gamma z + \vec{j} \cos \gamma z)] . \quad (2.10)$$

where Q is the Chandrasekhar number,

$$Q = \frac{B_0^2 d^2}{\nu \rho \mu \lambda} \quad (2.11)$$

In the following we shall restrict the analysis to the linear problem of the onset of steady convection in which case the left hand sides of equations (2.2)-(2.4) can be neglected. Oscillatory onset of convection is possible in the presence of a magnetic field, but not in the limit $\nu \ll \lambda$ when the time derivative in equation (2.7) can be dropped.

By taking the z -component of the double curl of equation (2.2), i. e. by operating with $\vec{k} \cdot \nabla \times (\nabla \times \dots)$ onto it, we find

$$\nabla^4 u_z + \Delta_2 \Theta - Q[(\vec{i} \cos \gamma z - \vec{j} \sin \gamma z) \cdot \nabla (\nabla^2 \Delta_2 h + \gamma^2 \Delta_2 h)] = 0 . \quad (2.12)$$

With the help of equations (2.4) and (2.8) Θ and h can be eliminated from this equation,

$$\begin{aligned} & \nabla^6 u_z - R \Delta_2 u_z - Q[(\vec{i} \cos \gamma z - \vec{j} \sin \gamma z) \cdot \nabla (\nabla^2 - \gamma^2) u_z - \\ & \quad 2\gamma^2 [(\vec{i} \sin \gamma z + \vec{j} \cos \gamma z) \cdot \nabla]^2 u_z + \\ & \quad 4\gamma (\vec{i} \cos \gamma z - \vec{j} \sin \gamma z) \cdot \nabla (\vec{i} \sin \gamma z + \vec{j} \cos \gamma z) \cdot \nabla \partial_z u_z] \\ & = -Q[\gamma^4 (\vec{i} \cos \gamma z - \vec{j} \sin \gamma z) \cdot \nabla \Delta_2 h + 2\gamma^3 (\vec{i} \sin \gamma z + \vec{j} \cos \gamma z) \cdot \nabla \Delta_2 \partial_z h] . \end{aligned} \quad (2.13)$$

On the right hand side terms involving h are still left. We shall neglect these terms by making the assumption that the parameter γ is sufficiently small such that terms multiplied by γ^n with $n \geq 3$ are negligible in comparison with those with a lower power of n .

Equation (2.13) admits solutions of the form

$$u_z = f(z) \exp\{ia(\vec{i} \sin \chi - \vec{j} \cos \chi) \cdot \vec{r}\} \quad (2.14)$$

where χ denotes the angle by which the axis of the convection roll described by (2.14) is turned away from the positive x -axis towards the negative y -axis. The Rayleigh number R for onset of convection will be minimized when convection sets in at a height z_0 such that the angle χ satisfies $\chi = \gamma z_0$. In this case the dominant term multiplied by Q in equation (2.13) vanishes for $z = z_0$. It does not vanish for $z \neq z_0$ and it is appropriate to use a Taylor expansion, $\cos \gamma z = \cos \gamma z_0 - (z - z_0)\gamma \sin \gamma z_0 + \dots$, and likewise for $\sin \gamma z$. Without loosing generality we may assume $\chi = z_0 = 0$ in which case the ordinary differential equation for $f(z)$,

$$[(\frac{d^2}{dz^2} - a^2)^3 + Ra^2 + Q\gamma^2 a^2 (z^2 (\frac{d^2}{dz^2} - a^2) + 2 + 4z \frac{d}{dz})]f(z) = 0 \quad (2.15)$$

is obtained where terms up to the order γ^2 have been taken into account. In the next section an approximate solution of this equation is derived.

3. Derivation of an Approximate Solution

For the solution of equation (2.15) the ansatz

$$f(z) = \sum_{n=0}^{\infty} z^{2n} A_n \exp\{-c^2 z^2\} \quad (3.1)$$

will be made. It will be anticipated that the parameter c can be chosen sufficiently large such that the boundary conditions at $z = \pm 0.5$ will not affect the solution. Since equation (2.15) is linear homogeneous $A_0 = 1$ can be assumed. The solution procedure can be understood most readily when the crudest approximation, $A_n = 0$ for $n \geq 1$, is inspected. Equation (2.15) yields in this case

$$\begin{aligned} & -120\xi^3 - 36\xi^2 - 6\xi - 1 + (R + 2Q\gamma^2)/a^4 \\ & + a^2 z^2 \{720\xi^4 + 144\xi^3 + 12\xi^2 - (1 + 10\xi)\gamma^2 Q/a^2\} + o(z^4) = 0 \end{aligned} \quad (3.2)$$

where the definition $\xi = c^2/a^2$ has been used and where terms of the order z^4 have not been denoted explicitly since we shall neglect them in first approximation. The wavy bracket yields an equation for the determination of c^2 as a function of $\gamma^2 Q$, while the z -independent terms determine R in dependence on a and $\gamma^2 Q$. The onset of convection will occur when R reaches a minimum as a function of a^2 . This minimum is determined by the relationship

$$60\xi^3 - 3\xi - 1 = 0 \quad (3.3)$$

which yields the unique positive root $\xi_c = 0.31961$. The wavy bracket of equation (3.2) then yields

$$c^2 = \sqrt{\gamma^2 Q}/5.600 \quad (3.4)$$

The corresponding critical value R_c of the Rayleigh number is given by $R_c = 71.560c^4$. This relationship shows that the onset of convection does not depend on the external length scale d . For a fixed value of the temperature gradient, $(T_2 - T_1)/d$, a new Raleigh number R^* can be defined with the natural length scale c^{-1} of convection, $R^* = R/c^4$. Its critical value R_c^* is thus given by

$$R_c^* = R_c/c^4 = 31.356R_c/\gamma^2 Q = 71.560 \quad (3.5)$$

corresponding to the critical wavenumber $a_c^* = a_c/c = \xi_c^{-1/2} = 1.768$. The result (3.5) also demonstrates that the assumptions of small γ and large c can be readily satisfied when a sufficiently large value of the Chandrasekhar number is used.

In order to obtain a more accurate solution of equation (2.15) higher order terms in the representation (3.1) must be taken into account. Some preliminary results are shown in table 1.

Table 1						
Truncation	ξ_c	R_c^*	α_c^*	$A_1/\sqrt{\gamma^2 Q}$	$R_c/\gamma^2 Q$	$c^2/\sqrt{\gamma^2 Q}$
$n \geq 1$	0.31961	71.560	1.768	0	2.282	0.4226
$n \geq 2$	0.320	95.68	1.769	-0.5596	1.5617	0.3575

4. Conclusion

Convection rolls in the presence of a twisted magnetic field in sunspots may serve as a model for penumbral filaments. The theory does not strongly depend on the property that the magnetic is horizontal. An extension of the analysis to the case of a moderately inclined magnetic field should yield only minor changes in the results. Since torsions of sunspot fields are known to vary it is tempting to predict a dependence of the wavelength of filaments on the strength of the magnetic field and on its twist. Using the relationship $a_c^* = \xi^{-1/2}$ we obtain for the dimensional width δ (=half wavelength) of filaments

$$\delta = (h_t \pi \sqrt{\rho \mu \lambda \nu} / B_0)^{1/2} 0.632 \quad (4.1)$$

where h_t denotes the height in meters over which the orientation of the magnetic field changes by 180 deg. It will be of interest to look for correlations between the width of filaments and the torsion of the magnetic field in sunspots.

REFERENCES

- BUSSE, F.H. & CLEVER, R.M. 1989 Travelling Wave Convection in the Presence of Horizontal Magnetic Field. *Phys. Rev. A* **40**, 1954-1961.
- CHANDRASEKHAR, S. 1961 Hydrodynamic and Hydromagnetic Stability, Clarendon Press, Oxford.

Page intentionally left blank

Numerical modeling of turbulent convection and acoustic wave propagation in the solar interior

By M. S. Miesch[†], N. N. Mansour AND M. M. Rogers

The advent of helioseismology and the increasing sophistication of numerical models have brought forth a new era in our understanding of solar interior dynamics. High-resolution simulations of turbulent convection have become essential tools in the interpretation of helioseismic data and have provided new insight into the maintenance of large-scale flows and magnetic fields in the solar interior. Still, we can do better. One of the largest uncertainties in current numerical models is the influence of the upper and lower boundary regions which surround the convective envelope and which cannot be fully resolved in a global simulation. In this summer school we began to investigate in more detail the sensitivity of convection simulations to these boundary regions and we found that they have a more significant impact than might be supposed. We also initiated an investigation into the propagation of acoustic waves in the solar interior and their interaction with flow fields, thermal inhomogeneities, and magnetic structures. This project promises to elucidate the *forward problem* of helioseismology, providing essential theoretical support to ongoing observational efforts.

1. Introduction

The sun acts as a resonant cavity. Like a bell with millions of distinct tones, the sun rings with global acoustic oscillations. By studying subtle variations in the frequencies of these oscillations, solar physicists have begun to infer something about the structure and dynamics below the solar photosphere. This is the science of helioseismology, and in the past few decades it has revolutionized the study of solar interior dynamics. This is an exciting time to be a solar physicist.

From a dynamical perspective, the most profound achievement of helioseismology has been the mapping of the internal rotation profile of the sun as a function of latitude and radius. The sun does not rotate as a solid body. Rather, it rotates differentially, with a rotational period of about 25 days near the equator and about 34 days near the poles. The surprise from helioseismology is that this monotonic decrease of angular velocity by about 30% from equator to pole is approximately independent of radius throughout the convection zone (Thompson *et al.* 2003). Below the convection zone, the rotation appears to be uniform within the errors of the helioseismic inversions. The transition from differential to uniform rotation occurs across a narrow region of strong rotational shear located near the base of the convection zone, which has been named the solar tachocline.

Keeping pace with the dramatic progress of helioseismic investigations, dynamical models of the solar interior are becoming increasingly sophisticated. High-resolution numerical simulations have given us new insight into the nature of the solar convection

[†] HAO/NCAR, Boulder, CO 80307-3000 (The National Center for Atmospheric Research is sponsored by the National Science Foundation)

zone, which occupies the outer 30% of the solar interior by radius and which is thought to be highly turbulent, with Reynolds numbers exceeding 10^{12} .

One such numerical model is based on the ASH (Anelastic Spherical Harmonic) code, which was developed at the University of Colorado and JILA (Clune *et al.* 1999). The first scientific results were reported by Miesch *et al.* (2000) and since then, much progress has been made in further developing the model and in exploring different parameter regimes, different geometries, and different physical processes (Miesch 2000; Elliot, Miesch & Toomre 2000; Brun & Toomre 2002; DeRosa, Gilman, & Toomre 2002; Brun, Miesch & Toomre 2004).

Despite the success that the ASH code has enjoyed, further model development is always warranted in a system as complex as the sun. One of the primary questions that is still poorly understood is what effect the convection zone boundary regions have on the global dynamics. At the bottom of the convection zone there is a stiff transition from sub-adiabatic to super-adiabatic stratification, giving rise to a narrow region of convective overshoot. Meanwhile, at the top of the convection zone, there is a complex transition between the envelope where heat is carried outward by convection and the relatively sparse corona where the heat transport is dominated by radiation. Radiative transfer effects, coupled with the steep sub-surface stratification and the ionization of hydrogen, drives vigorous convective motions known as granulation.

The main difficulty with these boundary regions is their relatively small scale. Differential rotation occurs on global scales of ~ 1000 Mm and requires the full spherical geometry to properly address. It is thought to be maintained by large-scale convective motions which are driven by buoyancy on scales of perhaps a few hundred Mm. Granulation, by comparison, occurs on scales of a few Mm, well beyond the resolution of even the most ambitious global-scale model. Furthermore, the overshoot region at the base of the convection zone is no more than 10 Mm thick—less than 1% of the solar radius. Global models cannot accurately capture the complex, small-scale dynamics occurring in these interface regions so some approximations are necessary.

In this summer school we focused on two primary objectives. The first was to investigate in more detail the sensitivity of global solar convection simulations to the upper and lower boundary conditions. We already know that in a global model we cannot explicitly resolve the complex dynamics which occur in the upper and lower transition regions bordering the solar convection zone. What we wish to understand better is: what difference does this make? How sensitive are global features such as the differential rotation to what occurs in the boundary layers?

Our second objective in this summer school was to begin to investigate in greater detail the coupling between large-scale convection and the acoustic waves, known as p-modes, which form the basis of helioseismology. Large-scale convection does not generate p-modes; it's Mach number is too low to be a significant source of acoustic power. Rather, p-modes are generated in the near-surface layers by granulation and propagate downward throughout the convection zone and deep interior.

Although p-modes do not significantly influence the dynamics of large-scale convection, they are the primary diagnostic tool used to probe such motions. Helioseismic inversions rely on p-modes to infer flow fields and structural information about the solar interior. Thus, it is of great practical importance to understand how acoustic waves interact with convective motions and other dynamical phenomena such as zonal jets and magnetic flux tubes.

Since it makes use of the anelastic approximation, the ASH code cannot be used to

	lower boundary	upper boundary
Case A	penetrative	moderate entropy gradient
Case B	non-penetrative	moderate entropy gradient
Case C	non-penetrative	large entropy gradient

TABLE 1. Simulation Summary

follow the propagation of acoustic waves (see §3). Thus, we have developed a separate acoustic solver which will eventually piggyback on the ASH code. However, before we address the acoustic probing of turbulent convection, which is a formidable problem, we will first consider the interaction between a specified acoustic wave field and simple inhomogeneities such as Gaussian temperature perturbations, smooth meridional circulations, and localized zonal jets and magnetic flux tubes.

In the sections that follow, we will say a few more words about each of these projects in turn and where they may be heading.

2. Boundary Sensitivities

The simulations we will describe are carried out using the ASH code, which solves the 3D equations of fluid motion in a rotating spherical shell (Clune *et al.* 1999). The ASH code is based on the anelastic approximation, which is designed for substantially subsonic motions in the presence of a background density stratification. The equations are solved using a pseudo-spectral technique, with spherical harmonic basis functions in the horizontal directions and a stacked Chebyshev expansion in the vertical. Time-stepping is accomplished with an explicit Adams-Bashforth scheme for the nonlinear terms and a semi-implicit Crank-Nicolson scheme for the remaining linear terms. The boundary conditions used here are impenetrable and stress-free, with a fixed entropy gradient. In the applications presented here we neglect magnetic fields.

In order to investigate the sensitivity of global-scale solar convection to the imposed boundary conditions, we have initiated a series of simulations, three of which are summarized in Table 1. Case B can be viewed as the *control* simulation. This case is non-penetrative, meaning that the impenetrable lower boundary of the computational domain is placed at the base of the convection zone, at $r \approx 0.7R_{\odot}$. By contrast, in Case A, the lower boundary of the computational domain is placed well below the base of the convection zone, at $r = 0.55R_{\odot}$. Thus, Case A allows penetration into a stably stratified region below the convective envelope.

The third simulation we describe here, case C, is similar to case B, but we have imposed a larger entropy gradient on the upper boundary, as suggested by some 1D solar structure models (e.g. Christensen-Dalsgaard *et al.* 1996). The difference between the entropy gradient in cases B and C is illustrated in Figure 1a. Each simulation begins with a monotonic decrease in the entropy gradient from its surface value to the lower value imposed at the bottom boundary. However, in all cases, redistribution of entropy by convective motions produces a local minimum in the entropy gradient just below the surface. The entropy gradient in case A is similar to that in case B except that it increases sharply to 10^{-4} below the base of the convection zone at $r = 0.71R_{\odot}$.

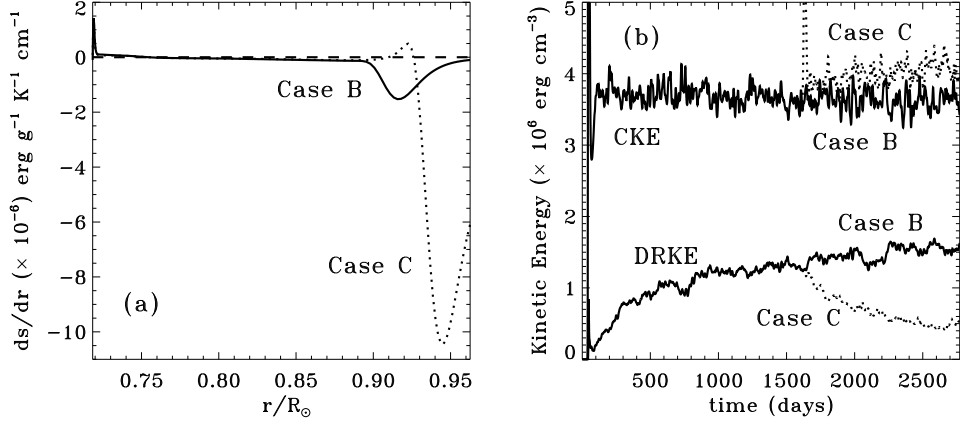


FIGURE 1. Frame (a) shows the horizontally averaged radial entropy gradient in case B (solid line) and case C (dotted line) late in the simulations ($t = 2770$ days and $t = 2860$ days, respectively). In frame (b), the volume-averaged convection kinetic energy (upper curves) and differential rotation kinetic energy (lower curves) are plotted as a function of time for case B (solid lines) and case C (dotted lines).

Cases A and B were initiated from static initial conditions, but case C was restarted from case B after the latter had evolved for about 1600 days. Figure 1b shows the time evolution of the kinetic energy contained in the non-axisymmetric convective motions (CKE) and the kinetic energy contained in the differential rotation (DRKE), both relative to a rotating coordinate system for cases B and C. The convection kinetic energy in case B saturates quickly, reaching a statistically steady state within about 100 days. By contrast, the differential rotation for the same case takes a much longer time to establish and is still growing slowly after about 2000 days.

After the simulation is continued with a different upper boundary condition (case C), the convective kinetic energy increases slightly because of stronger driving in the upper boundary layer. Surprisingly, the change in boundary conditions has also produced a substantial drop in the differential rotation kinetic energy. This decrease is apparent in the differential rotation profiles shown in Figure 2.

Figure 2 indicates that the latitudinal angular velocity variations in cases A and C are both much smaller than in case B. This implies that the presence of an overshoot region and stronger driving near the top of the shell both tend to decrease the differential rotation in the bulk of the convection zone, at least in the parameter regimes studied here. The former conclusion is only tentative, however, because case A has only been evolved for a few hundred days and may not have had time to establish a steady rotation profile. The angular velocity contrast in the sun between the equator and high latitudes is about 30%, somewhat more than that in case B. Thus, the smaller angular velocity gradients in cases A and C are not solar-like.

Despite the divergent rotation profiles in the three simulations, the convection patterns appear similar as shown in Figure 3. The biggest difference occurs with case C, in which the downflow lanes appear relatively narrow and the convection network somewhat more isotropic. This can again be attributed to the stronger buoyancy driving near the surface.

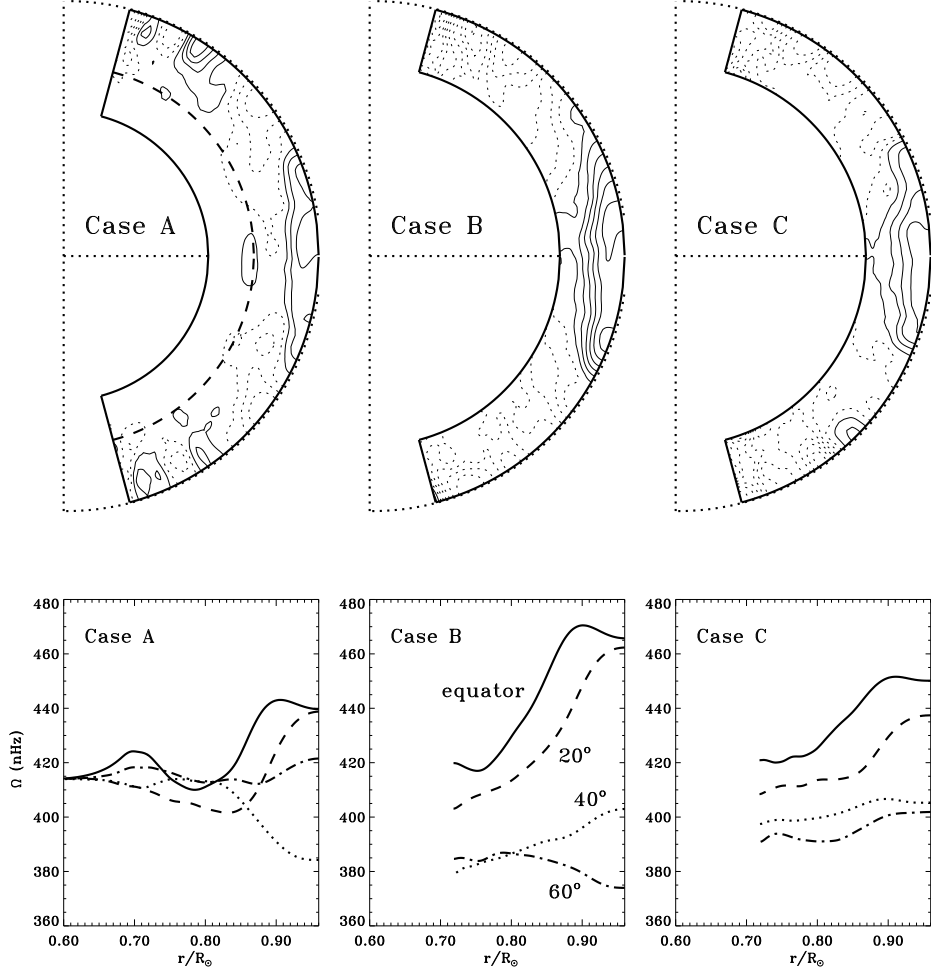


FIGURE 2. The upper frames show the longitudinally averaged angular velocity profile in cases A, B, and C at a time late in the evolution of each simulation. The dashed line in Case A indicates the base of the convection zone. Corresponding radial cuts at chosen latitudes (averaged over both hemispheres) are shown in the lower frames. The polar regions are not shown because there the moment arm, $r \sin \theta$ (θ being the co-latitude) approaches zero and the angular velocity is not well defined.

3. Acoustic Wave Propagation

As mentioned in §1, our primary means of probing solar interior dynamics is through acoustic waves, which are analyzed using the techniques of helioseismology. At the heart of this endeavor lies the so-called *forward problem*; for a given flow or field structure, what acoustic signal will be manifested in the photosphere, where we can observe it?

The influence of flow fields and related structural or magnetic variations on acoustic mode propagation depends on the nature of the modes. For global, resonant oscillations

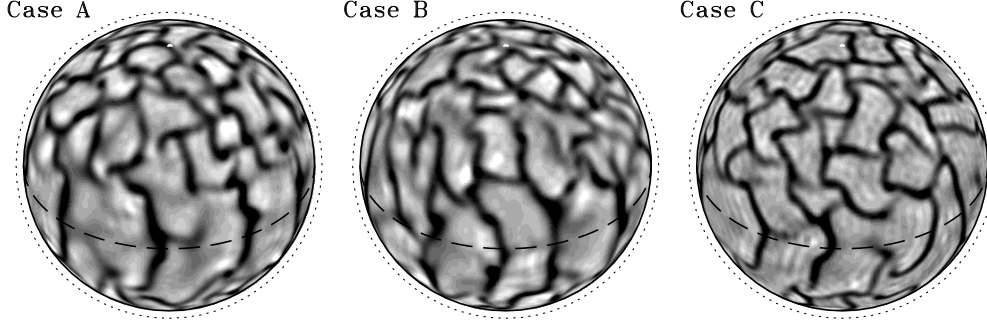


FIGURE 3. Snapshots of the radial velocity field are shown for cases A, B, and C at a horizontal layer near the top of the shell. In these grayscale images, upflows appear bright and downflows appear dark. Each image is an orthographic projection with the north pole tilted 30° toward the observer. The dotted line indicates the outer boundary of the computational domain and the dashed line indicates the equator.

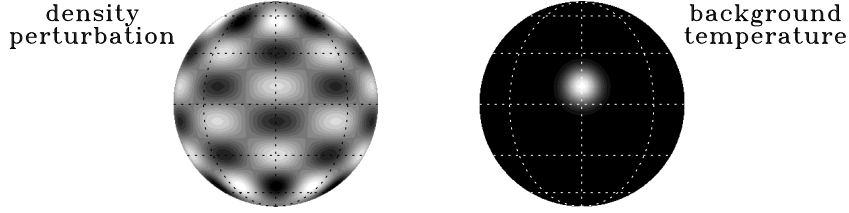


FIGURE 4. Initial conditions for one of our acoustic wave simulations. The density perturbation is chosen to be a spherical harmonic mode with $\ell = 10$, $m = 5$, propagating eastward (toward the right) at a rate equal to the sound speed. The background temperature is uniform except for a Gaussian enhancement (by a factor of two) located at a latitude of 10° N and a longitude of 0° .

of the entire sphere, dynamical variations are manifested as shifts in the oscillation frequencies. Although relatively straightforward to calculate, these shifts can be subtle and difficult to detect. Furthermore, different dynamical processes can give rise to similar frequency shifts, so even if a shift is detected, it may be difficult to interpret. For a local spectrum of high-wavenumber traveling waves the forward problem becomes even more complicated. In both the global and local cases, numerical simulations can potentially provide much new insight.

Over the course of this summer school, we have initiated a project to investigate the interaction between acoustic wave fields and inhomogeneities induced by convective flows or other dynamical processes (e.g. magneto-rotational instabilities in the tachocline). We have developed a numerical model that uses much of the machinery already implemented in the ASH code, such as spherical harmonic transforms and radial derivatives. However, the ASH code is based on the anelastic approximation, which effectively filters out acoustic waves because the time derivative in the mass continuity equation is neglected ($\nabla \cdot (\bar{\rho} \mathbf{v}) = 0$, where $\bar{\rho}$ is the background density). Therefore, we have developed a distinct set of equations designed to follow the propagation of linear, inviscid acoustic waves in a background medium that may in general possess flows and inhomogeneities in the sound speed.

The acoustic equations are derived from the equations of mass and momentum conser-

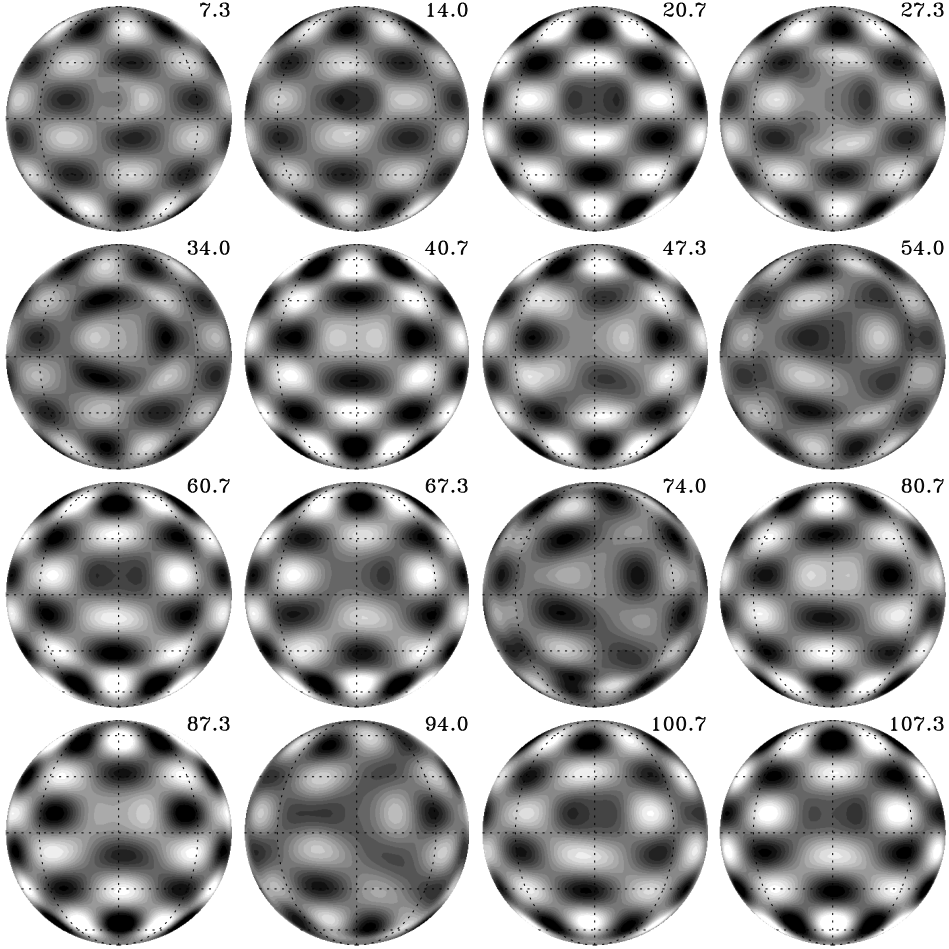


FIGURE 5. The density field is shown as the simulation evolves. As in Figure 4, bright areas denote density enhancements and dark areas rarefactions. The time (in minutes) is indicated to the upper right of each frame. The interval between frames is 400 seconds (6.66 min).

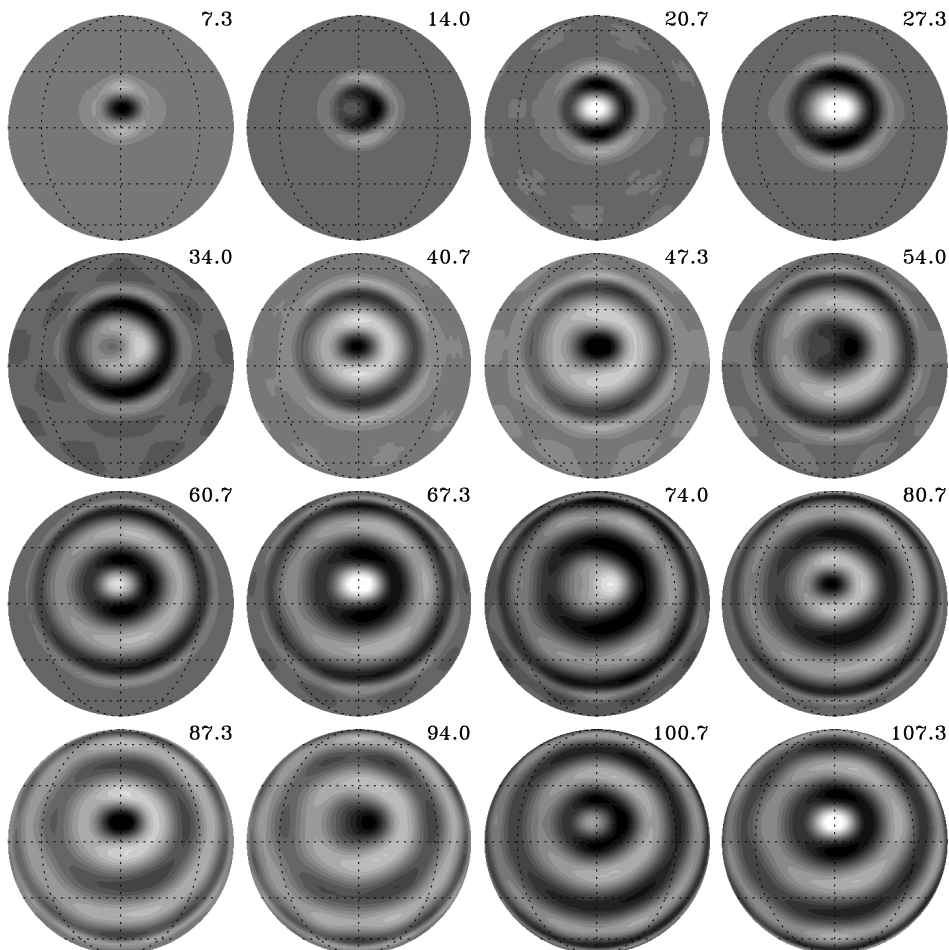
vation for a compressible fluid. As a first approximation we consider adiabatic acoustic waves, but as the project proceeds we will incorporate thermal diffusion, buoyancy, and rotation. With regard to the background state, we will start simple and build up to more complex configurations. Thus, the background state, indicated by an overbar, is for now assumed to be static: $\bar{\mathbf{v}} = 0$. The equations for mass continuity and momentum conservation then reduce to

$$\frac{\partial \rho'}{\partial t} + \nabla^2 \varphi = 0 \quad (3.1)$$

and

$$\frac{\partial}{\partial t} \nabla^2 \varphi + \nabla^2 (c_s^2 \rho') = 0 \quad , \quad (3.2)$$

where ρ' is the perturbation density, c_s is the sound speed, and φ is the velocity potential,

FIGURE 6. Similar to Figure 5 but with the $\ell = 10$, $m = 5$ component subtracted out.

defined in terms of the perturbation mass flux \mathbf{m}' as

$$\mathbf{m}' = \nabla\varphi + \nabla \times \Psi \quad . \quad (3.3)$$

The incompressible component of the velocity field, represented by the vector stream-function Ψ , does not enter into the acoustic equations. For an ideal gas, the sound speed $c_s = \sqrt{C_P(\gamma - 1)\overline{T}}$, where C_p is the specific heat at constant pressure, γ is the ratio of specific heats, and \overline{T} is the background temperature.

We solve equations (3.1)–(3.2) using a pseudo-spectral technique with spherical harmonic basis functions and a leap-frog temporal differencing scheme. One of our first test cases is illustrated in Figures 4–6. As a starting point we consider a 2-D spherical surface and we initialize our system with a specified density perturbation represented by the spherical harmonic mode of degree $\ell = 10$ and order $m = 5$ (Figure 4). The initial velocity potential is given a similar structure but with a phase lag appropriate for an

eastward-propagating wave. Thus, if the background sound speed is homogeneous, the “soccer ball” pattern in the left frame of Figure 4 will simply propagate to the right, maintaining its spatial structure indefinitely.

We now introduce an inhomogeneity. The background temperature field is given a local enhancement centered at a latitude of 10°N and a longitude of 0° as shown in the right frame of Figure 4. The form of the enhancement is Gaussian, with an e-folding length of 10° and a peak value which is twice the background temperature. Thus, the local sound speed is increased by a factor of $\sqrt{2} = 1.4$. This can be regarded as a crude (and exaggerated) first approximation to a sunspot or active region, which are generally associated with localized thermal variations.

The evolution of the simulation is illustrated in Figure 5. The eastward-propagating acoustic wave scatters off the temperature enhancement, sending out a series of circular acoustic pulses. The distortion of the acoustic mode is apparent, but the density field is still dominated by the $\ell = 10$, $m = 5$ mode, which was imposed as the initial condition and which drives the dynamics.

The structure of the acoustic pulses can be seen more clearly if we subtract out the primary driving mode as shown in Figure 6. The temperature enhancement acts as a scattering center, sending off divergent circular waves with a continually varying phase. These waves extract energy from the primary mode, eventually causing it to decay.

4. Conclusions and Outlook

The results presented here are preliminary. Both projects described in sections 2 and 3 are ongoing and there is much work to be done. First, it must be verified that the patterns identified in §3 are robust, particularly with regard to the differential rotation. The existing cases must be evolved for longer durations in order to confirm that the rotation profiles are indeed steady and new cases must be initiated in order to make sure that our conclusions are not limited to the particular parameter regimes chosen here.

Another boundary condition that we plan to investigate was motivated in part by discussions we had with Profs. Nordlund and Stein during the summer school. According to their simulations of granulation in the solar surface layers, motions that possess a non-zero horizontal divergence tend to deform the outer surface rather than turn over upon themselves. Thus, to lowest order, the horizontal divergence is approximately independent of depth, implying a small vertical divergence of the mass flux: $\partial(r^2\bar{\rho}v_r)/\partial r \approx 0$. We have used this result to devise open boundary conditions for the top of our domain that allow flow through the boundary. Since our outer boundary lies within the solar convection zone, this promises to be a more realistic treatment of the upper boundary, provided that it is numerically stable. We implemented this new boundary condition during the summer school but have not yet fully tested it.

With regard to the acoustic wave investigations, the results shown here are only the beginning. Our next step is to add the radial dimension to our acoustic solver and to implement boundary conditions which are realistic and useful from the point of view of helioseismology. We must then incorporate thermal diffusion, buoyancy, and rotation into our formulation. Once these code developments are finished, we will be prepared to investigate the interaction between an acoustic wave field and a series of imposed flows and structural variations of progressively increasing complexity. We will begin by studying the response of an imposed spectrum of acoustic waves to thermal inhomogeneities such as the Gaussian enhancement considered here. The results will be interpreted in

a helioseismic context and applied to practical problems such as far-side imaging. We will then investigate the acoustic signatures of flow variations such as zonal jets and meridional circulations. Eventually we will study these same problems and more in the presence of an evolving, convective, background flow computed with the ASH code.

We thank Juri Toomre and Sacha Brun for taking part in our continuing adventures with the ASH code. We appreciate their insight and support. We also thank Sasha Kosovichev for motivating much of the work initiated here and Aake Nordlund, Bob Stein, and Freidrich Busse for simulating discussions during the summer school. Mausumi Dikpati reviewed this manuscript for NCAR and we thank her for her comments. MSM would also like to thank Parviz Moin, Nagi Mansour, and their colleagues at CTR for an inspiring and productive program.

REFERENCES

- BRUN, A. S., MIESCH, M. S. & TOOMRE, J. 2004 Global-Scale Turbulent Convection and Magnetic Dynamo Action in the Solar Envelope. *Astrophys. J.* (in press)
- BRUN, A. S. & TOOMRE, J. 2002 Turbulent Convection under the Influence of Rotation: Sustaining a Strong Differential Rotation. *Astrophys. J.* **570**, 865-885.
- CHRISTENSEN-DALSGAARD ET AL. 1996 The Current State of Solar Modeling. *Science* **272**, 1286-1291.
- CLUNE, T. C., ELLIOTT, J. R., MIESCH, M. S., TOOMRE, J. & GLATZMAIER, G. A. 1999 Computational Aspects of a Code to Study Rotating Turbulent Convection in Spherical Shells. *Parallel Comput.* **25**, 361-380.
- DEROSA, M. L., GILMAN, P. A. & TOOMRE, J. 2002 Solar Multiscale Convection and Rotation Gradients Studied in Shallow Spherical Shells. *Astrophys. J.* **581**, 1356-1374.
- ELLIOTT, J. R., MIESCH, M. S. & TOOMRE, J. 2000 Turbulent Solar Convection and its Coupling with Rotation: The Effect of Prandtl Number and Thermal Boundary Conditions on the Resulting Differential Rotation. *Astrophys. J.* **533**, 546-556.
- MIESCH, M. S. 2000 The Coupling of Solar Convection and Rotation. *Solar Phys.* **192**, 59-89.
- MIESCH, M. S., ELLIOTT, J. R., TOOMRE, J., CLUNE, T. C., GLATZMAIER, G. A. & GILMAN, P. A. 2000 Three-Dimensional Spherical Simulations of Solar Convection: Differential Rotation and Pattern Evolution Achieved with Laminar and Turbulent States. *Astrophys. J.* **532**, 593-615.
- THOMPSON, M. J., CHRISTENSEN-DALSGAARD, J., MIESCH, M. S. & TOOMRE, J. 2003 The Internal Rotation of the Sun. *Ann. Rev. Astron. Astrophys.* **41**, 599-643.

Solar surface convection

By R. F. Stein [†], Å. Nordlund [‡] J. F. Ripoll AND A. A. Wray

1. Introduction

The dynamics of the solar surface is driven by turbulent convection, magnetic fields and the escape of radiation. Convection transports energy upward through the outer third of the Sun and radiation carries it away to space. Convective motions transport angular momentum and produce differential rotation and the subsurface shear layer (Brummell *et al.* 1998; Miesch *et al.* 2000; Robinson & Chan 2001). Convection builds magnetic fields by dynamo action and transports it downward (Nordlund *et al.* 1992; Tobias *et al.* 1998; Cattaneo 1999; Tobias *et al.* 2001; Emonet & Cattaneo 2001). Magnetic flux tubes which emerge through the surface are shuffled around by the convective motions (Berger & Title 1996; Martinez Pillet *et al.* 1997; Berger *et al.* 1998; Lin & Rimmele 1999; Stolpe & Kneer 2000). This stresses the field whose subsequent relaxation heats the chromosphere and corona and controls their structure (Parker 1988; Galsgaard & Nordlund 1996; Judge *et al.* 1998). Convective motions generate the waves that produce the enhanced emission observed from the chromosphere (Carlsson & Stein 1997; Ulmschneider & Musielak 1998; Skartlien *et al.* 2000; Musielak & Ulmschneider 2001). Convection excites the p-mode oscillations and modifies their eigenfrequencies (Goldreich *et al.* 1994; Rosenthal *et al.* 1999; Stein & Nordlund 2001). Magnetic fields, oscillations and rotational shearing all alter convection itself (Hurlburt *et al.* 1996; Weiss *et al.* 1996; Brummell *et al.* 1998; Steiner *et al.* 1998; Tao *et al.* 1998). The interaction of these various processes controls the flux of radiation received by the Earth.

Convection is inherently three-dimensional, non-linear and non-local. As a result, most progress in understanding convection has come from analyzing numerical simulations. The computational challenge is to compute at high enough Reynolds number to include interactions of very disparate scales of motion. This requires simulations with very large 3D computational grids. We *cannot* hope to model the extremely large dynamic range and high Reynolds number that occur in the Sun. We *can* hope that our limited numerical capabilities will provide insight into what actually occurs in the Sun.

2. Large Scale and High Resolution Simulations

Recent observations with the Swedish 1-meter Solar Telescope have resolution of 70 km on the solar surface and the proposed Advanced Technology Solar Telescope will have a resolution of 30 km. With each new improvement in resolution new phenomena are discovered on the solar surface. The most recent has been the existence of striations in the bright side walls of granules observed toward the limb. To understand these high resolution observations, even higher resolution simulations of the solar surface convection are needed.

Local helioseismology can resolve structures as small as 30 Mm stable over 8 hour time

[†] Michigan State University

[‡] NBIfAFG, University of Copenhagen, DK

intervals. The proper interpretation of such observations requires a simulated testbed on which the inversion techniques can be applied and compared with the actual properties. This requires simulating regions of 50 Mm width by 20 Mm depth to contain the observed short wavelength modes within the computational domain.

The horizontal velocity spectrum at the solar surface is a nearly featureless power law (\propto wavenumber) with a peak at granular scales and a subsequent decline at still smaller scales. Yet the eye picks out “supergranulation” scale structures and there is controversy over their nature. Again this can be clarified by 50 Mm wide by 20 Mm deep simulations.

Such large scale simulations will also reveal the cause of the surface shear layer as well as provide insight into the emergence and dispersal of magnetic flux at the solar surface.

High resolution magneto-convection simulations have very small time steps because of the high Alfvén speed in the upper photosphere and therefore require long simulations to mimic the behavior of the solar surface. Large scale simulations require a long time to relax the thermal structure at large depths and the dynamic structures at the large scales. To undertake both projects therefore requires an MHD code that can run efficiently on very many processors.

3. MHD Code

Our existing magneto-hydrodynamic code was modified to include a tabular equation of state and radiative transfer. Parallelization was implemented using Open MP with parallelization in as large blocks of code as possible, rather than individual loops. This avoids the overhead of repeated creation and destruction of multiple threads.

3.1. Radiation

Radiation from the solar surface produces the low entropy, high density fluid whose buoyancy work drives the convective motions. Observing the radiation from the solar surface provides us with our only information on what is occurring there. In the layer from which photons escape their mean free path is of order unity, so neither the diffusion approximation appropriate at large optical depths nor the optically thin approximation appropriate at very small optical depths is appropriate. To model radiative heating and cooling accurately requires solving the radiation transfer equation. A method is needed accurate enough to determine the radiative heating and cooling and efficient enough to calculate the 3D radiative transport for thousands of time steps on very large meshes. A balance between accuracy and speed is required. One project during the workshop was to test some of the approximations made in the convection simulation code in calculating the radiative transfer.

Radiative heating/cooling is the integral over wavelength of the difference between the opacity \times the angle averaged intensity and the emission, or as it is usually written,

$$Q_{\text{rad}} = 4\pi \int_{\lambda} \kappa_{\lambda} (J_{\lambda} - S_{\lambda}) d\lambda , \quad (3.1)$$

where κ_{λ} is the opacity or inverse of the photon mean free path, J_{λ} is the angle averaged intensity, and S_{λ} , the source function, is the ratio of the emissivity to the opacity. In the solar simulation code, to avoid roundoff errors from taking the difference between two comparable large numbers, we solve directly for the difference $J_{\lambda} - S_{\lambda}$ using the Feautrier method (Feautrier 1964). We assume Local Thermodynamic Equilibrium (LTE), so the source function is the Planck function. Two further approximations are made to greatly speed up the calculation. First, the number of wavelengths for which the transfer equation

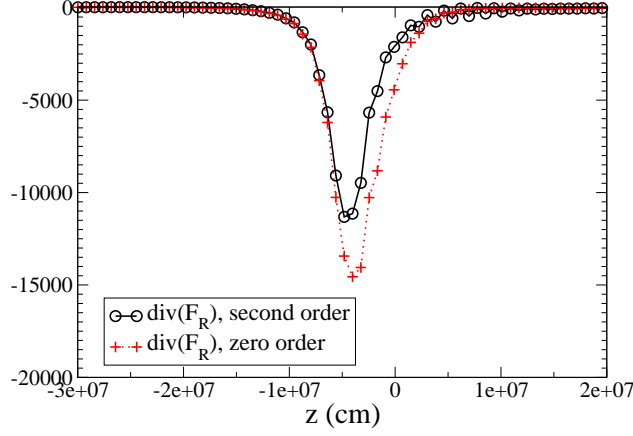


FIGURE 1. Divergence of the radiative flux for a 1D solar atmosphere comparing piecewise constant with second order Taylor expansion approximations for the source function and opacity.

is solved is drastically reduced by binning the opacity at each wavelength into four bins according to its magnitude and binning the source function the same way. Second, the transfer equation is solved along only 5 bi-directional rays – one vertical and four slanted rays through each point on the surface. (For details see Nordlund 1982; Stein & Nordlund 2003.)

Three issues were investigated: the spatial quadrature along a ray, the angular quadrature for the mean intensity, and alternate solution schemes used to solve for the radiation.

First consider the spatial quadrature along a ray. Fig 1 shows the radiative heating and cooling, for a one-dimensional mean solar atmosphere, calculated by the integral method, comparing a piecewise constant approximation with a second-order Taylor expansion for the opacity and source function. A piecewise constant approximation is inadequate unless a large number of depth points is used. In the solar code, both a piecewise linear approximation (trapezoidal rule) and a third order approximation for spatial integrals have been used. Accurate results further require an accurate calculation of the optical depth scale. With a third order integration scheme a spacing of 10 per decade in optical depth, or ~ 15 km near optical depth unity, is needed. Note, in the solar photosphere, the source function is nearly linear in optical depth (Stein & Nordlund 1998, Fig 15).

Next, consider the angular quadrature needed to obtain the net heating/cooling or the mean intensity. Fig 2 shows the horizontally averaged radiative heating in a 3D snapshot from a solar convective simulation for 8 rays (2 polar and 4 azimuthal angles) and 48 rays (4 polar and 12 azimuthal angles) on the left. On the right is shown the horizontal rms of the radiative heating and the difference in the rms for 8 and 48 rays. The difference is less than 3%. Even though the optical depth surface has an rms variation of 35 km, so that hot and cold regions adjoin one another, most of the radiative cooling occurs vertically. However, when magnetic fields are present there is a larger variation (~ 300 km) in the optical depth unity surface and horizontal radiation transfer has a noticeable effect on the emergent intensity. However, even here the temperature at unit optical depth varies only slightly because of the high temperature sensitivity of the dominant

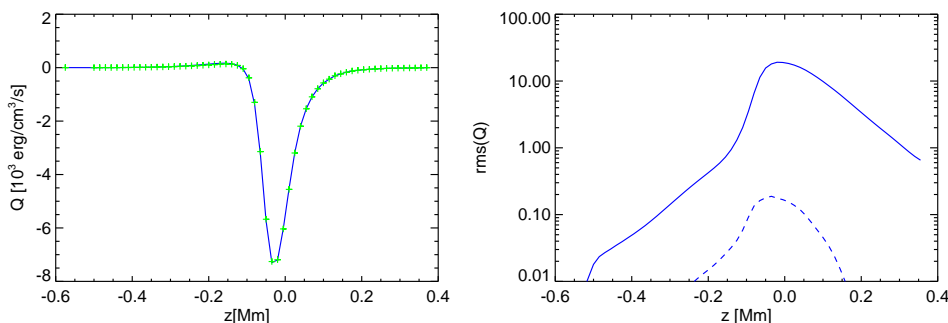


FIGURE 2. Radiative cooling. Left: average heating/cooling for 8 and 48 rays. Right: rms heating/cooling for 48 rays (solid) and difference between 8 and 48 rays (dashed).

opacity source (H^- ions). In the solar simulation code, one vertical and one non-vertical angle with 4 azimuthal angles are used, which provides approximately 1 reason such few angles provides sufficient accuracy in the solar photosphere (more rays are needed in the chromosphere) is the small temperature variation at unit optical depth from which the radiation emerges (see Stein & Nordlund 1998 Fig. 22).

The vertical extent of the photosphere (500 km) is small compared to the radius of the Sun, which therefore appears as an infinite planar source. The radiative anisotropy, is nearly zero below the surface, increases through the photosphere, reaching a maximum of ~ 0.6 at the transition to the chromosphere. Farther away the anisotropy is larger, approaching one as the Sun recedes to a point source.

An alternative method of calculating the radiation is the moment model, in which four conservation equations for the radiation energy density and the three components of the radiative flux vector are solved at every point in the computational domain (Mihalas & Mihalas 1984). To use such a method, the system of moment equations must be closed by relating the radiation stress tensor to the radiation energy density and flux. This is done by means of so called “Eddington factors”, which express the degree of anisotropy and act as a flux limiter (Levermore 1984). If the Eddington factor could be accurately determined analytically, this would be a useful method to obtain the radiative heating/cooling without the necessity of solving the radiative transfer equations. The radiative heating/cooling from several moment models, applied to a one-dimensional, horizontally averaged, solar atmosphere is shown in Fig. 3 (left). Two flux-limited moment models, derived using the maximum entropy closure (Minerbo 1979) the M_1 model (Levermore 1984; Fort 1997)[†] and the M_1^+ model (Ripoll & Wray 2004), are compared to integral RTE solvers. Both models are computed with the second order scheme used in Ripoll *et al.* (2002). They rather accurately capture the cooling near optical depth unity. However, both moment methods overestimate absorption in the atmosphere, for unknown reasons. Equilibrium is approached for $z > 0$ [‡].

The anisotropy and the Eddington closure factor are shown in Fig. 3 (right). It can

[†] see Ripoll (2004) for more references concerning this model, and, Jensen *et al.* in this volume.

[‡] The source term of both moment models has been truncated to zero when the difference between the temperature and the radiative temperature is less than 1 K. This is done in order to avoid numerical wiggles which are generated by the subtraction of two large numbers, the emission and absorption terms, which should almost cancel to give equilibrium.

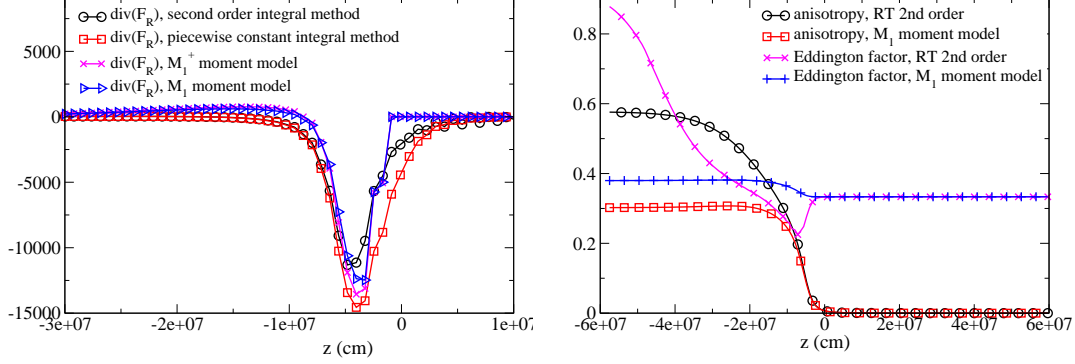


FIGURE 3. Left: radiative cooling computed with 4 different methods. Right: anisotropy and Eddington factor computed by the M_1 model and a RTE solver.

be seen that the anisotropy is below 0.6 ¶, and that the moment methods underestimate this value in the atmosphere. The Eddington factor found by the RTE solver is below 1/3 near the surface, which cannot be reproduced by any existing moment model (for which the lower bound is 1/3, the equilibrium value). The M_1^+ model is only flux-limited for anisotropies larger than 1/2 (to avoid non-physical results and to guarantee numerical stability) and is otherwise equivalent to P_1 ¶. Since $f < 1/2$ everywhere for this particular solar profile, the M_1^+ Eddington factor is simply 1/3 (like P_1), but this may not hold for all solar profiles. It should be noted that the anisotropy is always lower for one-dimensional atmospheres than for three-dimensional ones. In an evolving three-dimensional configuration, different hydrodynamic states may produce larger anisotropies and the flux will need to be limited. The fact that the anisotropy and the Eddington factor from the moment models are not equivalent to the RTE values on the whole domain yet the average radiative cooling/heating is similar, leads to the conclusions that, first, only a small transition region around the surface matters for the escape of radiation, and second, that radiation is primarily determined by its emission and absorption rather than by its direction of propagation, for our one-dimensional atmosphere.

4. High Resolution, Small Scale Simulations

We have simulated a small patch near the surface of the Sun with horizontal size 6×6 Mm and a height range from the temperature minimum at 0.5 Mm above - down to 2.5 Mm below - the visible surface, on a grid of $253 \times 253 \times 163$ zones. Initially we imposed a uniform vertical magnetic field of 250 G on a snapshot of well established hydrodynamic solar convection. The magnetic field is rapidly swept by the granular and mesogranular flows into the mesogranular scale downflow lanes and concentrated to kiloGauss strength.

We have used these simulation results to synthesize center-to-limb G-band images (Fig. 4). Towards the limb the simulations show “hilly” granulation with dark bands on the far side, bright granulation walls and striated faculae, similar to observations. At disk center G-band bright points are flanked by dark lanes. The increased brightness in

¶ for 1D configurations, the upper limit of f is around 1
 ¶ The P_1 closure assumes isotropic propagation and has no flux limiter.

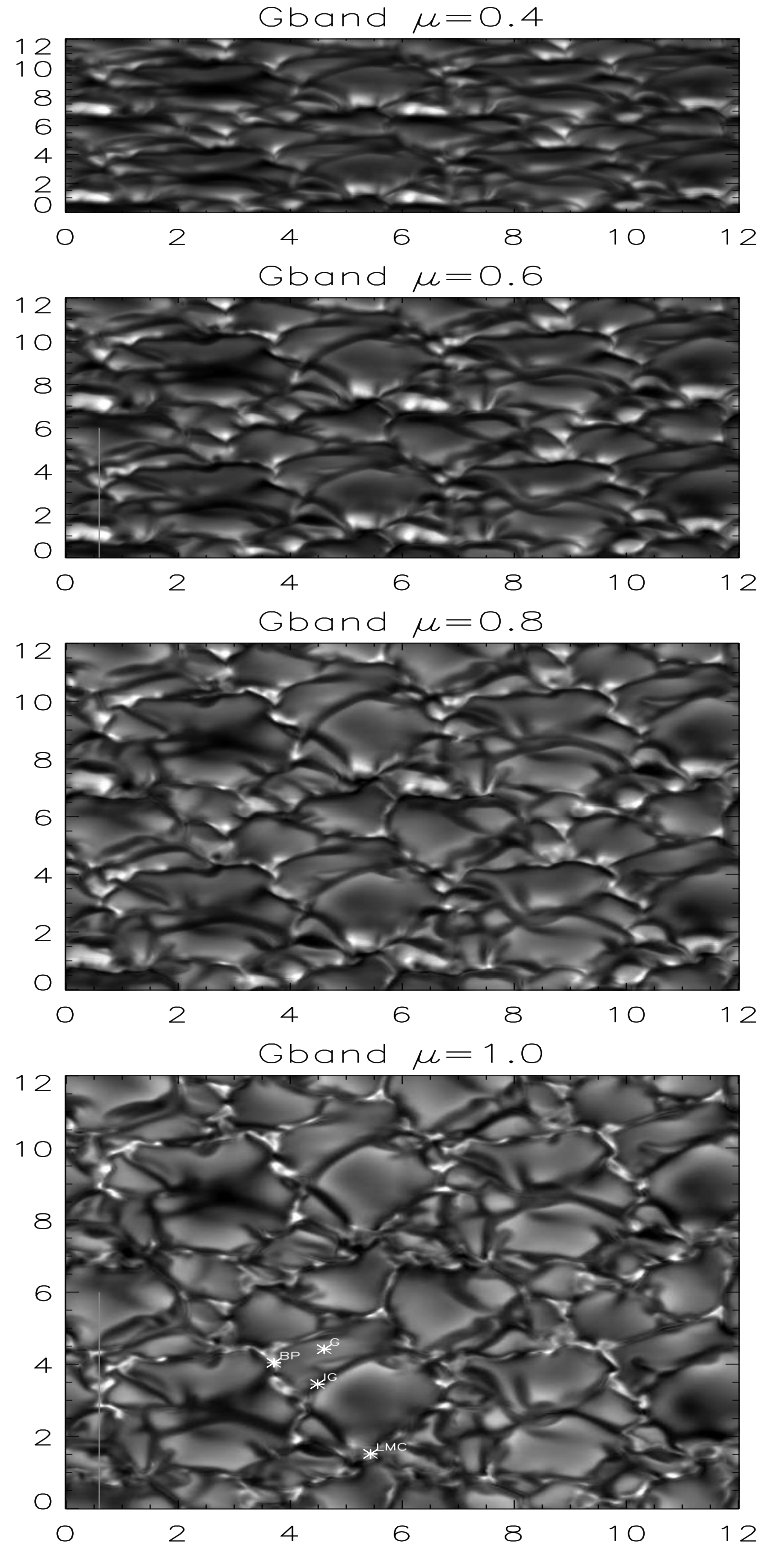


FIGURE 4. G-band images synthesized from magneto-convection simulation. Four images at 30 sec intervals have been combined (UL,LL,UR,LR) to make the patterns more obvious.

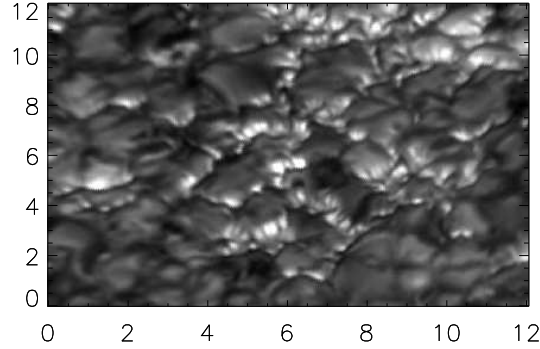


FIGURE 5. Observed G-band intensity at $\mu = 0.63$, from the Swedish 1-m Solar Telescope (June 2003). Data reduction using Multi-Frame-Blind-Deconvolution performed by Luc Rouppe van der Voort. Note “hilly” granulation with dark bands on the far side, bright granulation walls and striated faculae.

magnetic elements is due to their lower density compared with the surrounding inter-granular medium. One thus sees deeper layers where the temperature is higher. At a given geometric height, the magnetic elements are cooler than the surrounding medium. In the G-band, the contrast is further increased by the destruction of CH in the low density magnetic elements. The optical depth unity surface is very corrugated. Bright granules have their continuum optical depth unity 80 km above the mean surface, the magnetic elements 200-300 km below. The horizontal temperature gradient is especially large next to flux concentrations. When viewed at an angle, the deep magnetic elements’ optical surface is hidden by the granules and the bright points are no longer visible, except where the “magnetic valleys” are aligned with the line of sight. Towards the limb, the low density in the strong magnetic elements causes unit line-of-sight optical depth to occur deeper in the granule walls behind, than for rays not going through magnetic elements, and variations in the field strength produce a striated appearance in the bright granule walls (Carlsson *et al.* 2004). An observed G-band image is shown in Fig. 5.

We would now like to perform similar simulations at still higher resolution because we believe that magnetic instabilities will show up at small scales and contribute to the striated appearance of the granule walls, and because the ATS Telescope will provide images of higher resolution than reliably obtainable from our current 25 km horizontal grid size simulations.

5. Large Scale Simulations

Large scale simulations require a long time to develop the large scale dynamical structures because the ratio of velocity to size is small. Large scale simulations require a long time to relax the thermal structure at large depths because the ratio of energy flux to energy density is small. As a first step, we have begun a simulation of $24 \text{ Mm} \times 24 \text{ Mm}$ horizontal size and 9 Mm depth. A time span comparable to a few turnover times of the largest flows in the computational domain is required. This run was started from a 12 Mm wide simulation doubled in each of the periodic horizontal directions with a small perturbation added to break the symmetry (Fig. 6). This relaxation is proceeding. We expect it to develop structure on the computational box (24 Mm). When this domain is relaxed, it will be doubled in size both horizontally and vertically, to reach $48 \text{ Mm} \times 18 \text{ Mm}$ deep.

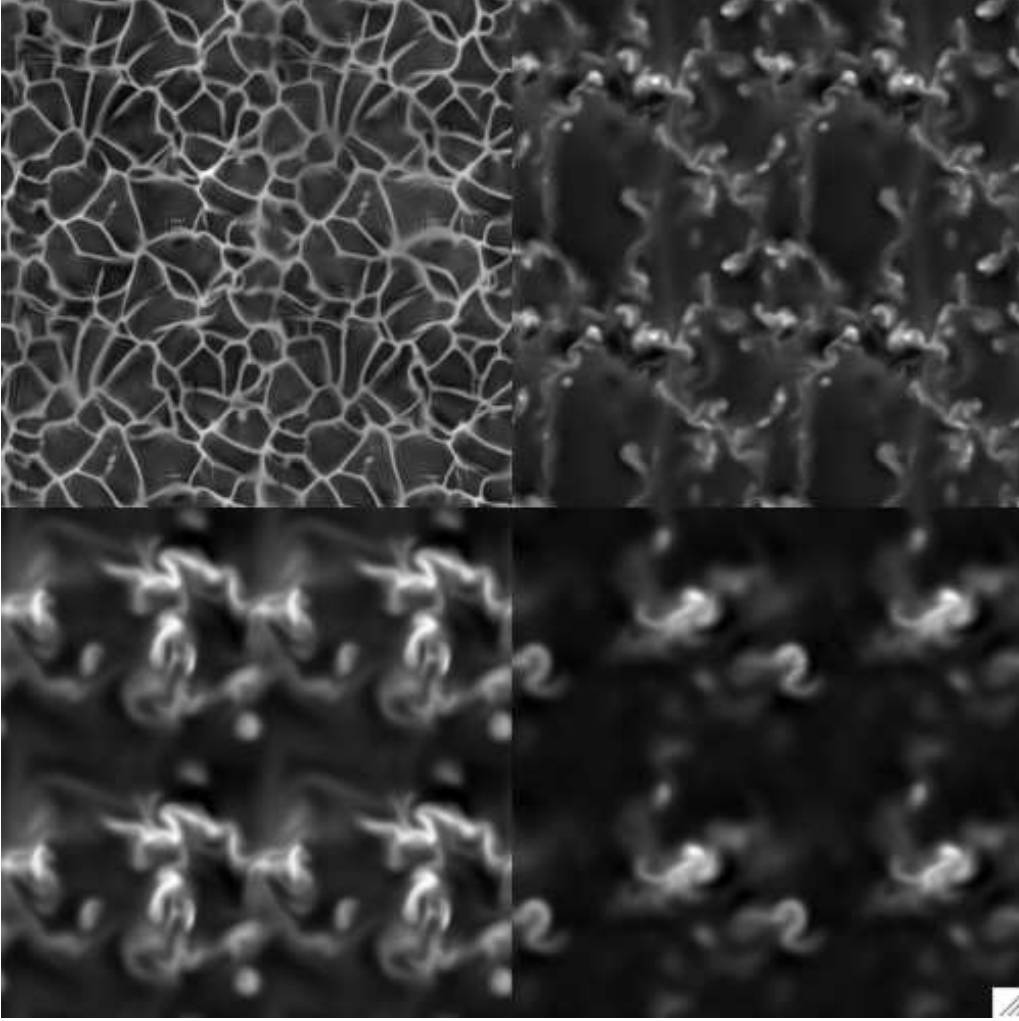


FIGURE 6. Vertical velocity at the surface (UL), 3 Mm (UR), 6 Mm (LL) and 9 Mm (LR) depth. It is clear that the initial structures still need to evolve and larger scale structures need time to develop.

6. Convection Spectrum

The spectrum of solar convection is not separable into spatial and temporal components because the temporal spectrum varies with the spatial wave number. It can be best fit by an analytic expression of the form

$$P_V(\omega, k) = a/(\omega^2 + w^2)^{p(k)}$$

Both the exponent, p , and width, w , increase with increasing spatial wave number (Fig. 7). In the past analytic studies have assumed that the turbulent convective energy spectrum is separable into independent spatial and temporal factors. The more complicated actual situation may explain some of the difficulties that these overly simplified models experience.

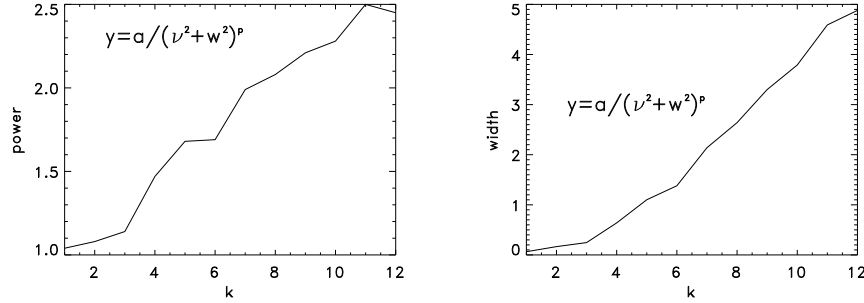


FIGURE 7. Analytic fit to temporal spectrum of vertical velocity in a high resolution convection simulation. Both the exponent of the power law and the width of the low frequency plateau increase with increasing spatial wave number.

REFERENCES

- BERGER, T. E., LOEFDAHL, M. G., SHINE, R. S., AND TITLE, A. M. 1998 Measurements of solar magnetic element motion from high-resolution filtergrams. *ApJ* **495**, 973.
- BERGER, T. E. AND TITLE, A. M. 1996 On the dynamics of small-scale solar magnetic elements. *ApJ* **463**, 365.
- BRUMMELL, N. H., HURLBURT, N. E., AND TOOMRE, J. 1998 Turbulent compressible convection with rotation. II. mean flows and differential rotation. *ApJ* **493**, 955.
- CARLSSON, M. AND STEIN, R. F. 1997 Formation of solar calcium H and K bright grains. *ApJ* **481**, 500.
- CARLSSON, M., STEIN, R. F., NORDLUND, A., SCHARMER, G.B. 2004 Observational manifestations of solar magneto-convection — center-to-limb variation. *ApJ* **610**, L137.
- CATTANEO, F. 1999 On the origin of magnetic fields in the quiet photosphere. *ApJ* **515**, L39–L42.
- EMONET, T. AND CATTANEO, F. 2001 Small-scale photospheric fields: observational evidence and numerical simulations., *ApJ* **560**, L197–L200.
- FEAUTRIER, P. 1964 Sur la resolution numerique de l’equation de transfert. *Comptes Rendus Academie des Sciences Paris* **258**, 3189.
- FORT, J. 1997 Information-theoretical approach to radiative transfer., *Phys. A.*, **243**, 275–303.
- GALSGAARD, K. AND NORDLUND, A. 1996 The heating and activity of the solar corona: I. Boundary shearing of an initially homogeneous magnetic field. *Journal of Geophysical Research* **101(A6)**, 13445–13460.
- GOLDREICH, P., MURRAY, N., AND KUMAR, P. 1994 Excitation of solar p-modes. *ApJ* **424**, 466–479.
- HURLBURT, N. E., MATTHEWS, P. C., AND PROCTOR, M. R. E. 1996 Nonlinear compressible convection in oblique magnetic fields. *ApJ* **457**, 933.
- JUDGE, P. G., HANSTEEN, V., WIKSTOL, O., WILHELM, K., SCHUEHLE, U., AND MORAN, T. 1998 Evidence in support of the “nanoflare” picture of coronal heating from SUMER data. *ApJ* **502**, 981.

- LEVERMORE, D. 1984 Relating Eddington factors to flux limiters., *Jour. Quant. Spectrosc. Radiat. Transfer*, **32(2)**, 149-160.
- LIN, H. AND RIMMELE, T. 1999 The granular magnetic fields of the quiet Sun. *ApJ* **514**, 448-455.
- MARTINEZ PILLET, V., LITES, B. W., AND SKUMANICH, A. 1997 Active region magnetic fields. I. plage fields. *ApJ* **474**, 810.
- MIESCH, M. S., ELLIOTT, J. R., TOOMRE, J., CLUNE, T. L., GLATZMAIER, G. A., AND GILMAN, P. A. 2000 Three-dimensional spherical simulations of solar convection. I. differential rotation and pattern evolution achieved with laminar and turbulent states. *ApJ* **532**, 593-615.
- MIHALAS, D. AND MIHALAS, B.W. 1984 Foundation of radiation hydrodynamics. *Oxford University Press*.
- MINERBO, D. 1984 Maximum entropy Eddington factors, *Jour. Quant. Spectrosc. Radiat. Transfer*, **20**, 541-545.
- MUSIELAK, Z. E. AND ULMSCHNEIDER, P. 2001 Excitation of transverse magnetic tube waves in stellar convection zones. I. Analytical approach. *Astron. Astrophys.* **370**, 541-554.
- NORDLUND, A. 1982 Numerical simulations of the solar granulation. I - basic equations and methods. *Astron. Astrophys.* **107**, 1-10.
- NORDLUND, A., BRANDENBURG, A., JENNINGS, R. L., RIEUTORD, M., ROUKOLAINEN, J., STEIN, R. F., AND TUOMINEN, I. 1992 Dynamo action in stratified convection with overshoot. *ApJ* **392**, 647-652.
- PARKER, E. N. 1988 Nanoflares and the solar x-ray corona. *ApJ* **330**, 474-479.
- RIPOLL, J.-F. 2004 An average formulation of the M_1 radiation model with mean absorption coefficients and presumed probability functions for turbulent flows., *Jour. of Quant. Spectrosc. & Radiat. Transfer.*, **83**, 493-517.
- RIPOLL, J.-F., WRAY, A., A. 2004 A half-moment model for radiative transfer in a 3D gray medium and its reduction to a moment model for hot, opaque sources., *Jour. Quant. Spectrosc. Radiat. Transfer*, in press.
- RIPOLL, J.-F., DUBROCA, B., AUDIT, E. 2002 A factored operator method for solving coupled radiation-hydrodynamics models., *Trans. Theory and Stat. Phys.*, **31(4-6)**, 531-557.
- ROBINSON, F. J. AND CHAN, K. L. 2001 A large-eddy simulation of turbulent compressible convection: differential rotation in the solar convection zone., *MNRAS* **321**, 723-732.
- ROSENTHAL, C. S., CHRISTENSEN-DALSGAARD, J., NORDLUND, A., STEIN, R. F., AND TRAMPEDACH, R. 1999 Convective contributions to the frequencies of solar oscillations. *A&A* **351**, 689-700.
- SKARTLIEN, R., STEIN, R. F., AND NORDLUND, A. 2000 Excitation of chromospheric wave transients by collapsing granules. *ApJ* **541**, 468-488.
- STEIN, R. F. AND NORDLUND, A. 1998 Simulations of solar granulation: I. General properties. *ApJ* **499**, 914-933.
- STEIN, R. F. AND NORDLUND, A. 2001 Solar oscillations and convection. II. excitation of radial oscillations. *ApJ* **546**, 585-603.
- STEIN, R. F. AND NORDLUND, A. 2003 Radiation transfer in 3D numerical simulations. *Stellar Atmosphere Modeling*, eds. I. Hubeny, D. Mihalas, K. Werner, ASP Conf. Ser. **288**, 519-532.

- STEINER, O., GROSSMANN-DOERTH, U., KNOELKER, M., AND SCHUESSLER, M. 1998 Dynamical interaction of solar magnetic elements and granular convection: results of a numerical simulation. *ApJ* **495**, 468.
- STOLPE, F. AND KNEER, F. 2000 On weak magnetic flux structure of the Sun. *Astron. & Astrophys.* **353**, 1094.
- TAO, L., WEISS, N. O., BROWNJOHN, D. P., AND PROCTOR, M. R. E. 1998 Flux separation in stellar magnetoconvection. *ApJ* **496**, L39.
- TOBIAS, S. M., BRUMMELL, N. H., CLUNE, T. L., AND TOOMRE, J. 1998 Pumping of magnetic fields by turbulent penetrative convection. *ApJ* **502**, L177.
- TOBIAS, S. M., BRUMMELL, N. H., CLUNE, T. L., AND TOOMRE, J. 2001 Transport and storage of magnetic field by overshooting turbulent compressible convection. *ApJ* **549**, 1183–1203.
- ULMSCHNEIDER, P. AND MUSIELAK, Z. E. 1998 On the generation of nonlinear magnetic tube waves in the solar atmosphere. II. Longitudinal tube waves., *Astron. Astrophys.* **338**, 311–321.
- WEISS, N. O., BROWNJOHN, D. P., MATTHEWS, P. C., AND PROCTOR, M. R. E. 1996 Photospheric convection in strong magnetic fields *MNRAS* **283**, 1153–1164.

Page intentionally left blank

MHD turbulence

The Summer Program 2004 included a substantial MHD session. It consisted of 6 projects, involving 14 contributors. Furthermore, the solar turbulence group also includes MHD as one of its basic constituents with 4 projects involving 8 contributors. This means that the fundamental coupling between the Navier-Stokes equations and the Maxwell-Ohm equations (themselves often written under the form of the induction equation) has become a significant and quite challenging domain of application for the modeling of turbulent fields.

Among the basic features of MHD turbulence, the most important seems to be that, beside viscous dissipation, a second diffusive mechanism is present. It is related to the Joule dissipation and its efficiency is controlled by the value of the magnetic diffusivity η . Therefore, beside the usual Reynolds number Re , an analogous non-dimensional number, named the *magnetic Reynolds number* and denoted Rm , where the magnetic diffusivity is substituted to the viscosity ν , plays an important role. Clearly, Re is always much larger than unity in turbulence. This is not true of Rm and depending on its value one gets very different classes of turbulent flows. At the laboratory scale, whatever the actual fluid used in the experiments (liquid metal or ionized gas), Rm is always much smaller than unity. This implies that the applied magnetic field B is weakly perturbed ($b \ll B$), although the magnetic field perturbation b ($b \approx RmB$ if $Rm \ll 1$) is large enough to be measured. This asymptotic limit may be characterized by two key effects: i) b obeys a simple linear equation and behaves like a passive quantity, inertia remaining the unique source of non-linear effects, ii) the Alfvén waves, one of the major MHD characteristics, degenerate into a simple diffusion because their damping time is significantly shorter than their transit time. As soon as Rm is in the range $1 - 50$, the former simplicity is not anymore valid and one must consider the full induction equation instead of its linear approximation. This implies that the magnetic field, although still transported by the fluid, does not remain passive (such a transport of a non-passive vector field is still a fully open challenge in turbulence). Furthermore, the Alfvén waves start to be relevant when the applied magnetic field is large enough to yield a Lundquist number Al/η larger than unity, or as soon as the wave transit time l/A is significantly shorter than their damping time l^2/η . Here, $A = B/\sqrt{\mu\rho}$ denotes the Alfvén waves celerity and l a characteristic lengthscale of the flow. This relevance of Alfvén waves may start to be effective even when $Rm \ll 1$.

The domain of very large Rm is quite fascinating, since the Navier-Stokes equation and the induction equation are both highly non-linear. In that regime, the Alfvén waves are of prime importance. And, among the guiding ideas, the analogy between the induction equation and the equation of vorticity in ordinary hydrodynamics suggests that the magnetic field is frozen in the fluid and behaves exactly like fluid particles; this is a consequence of the Alfvén theorem, an MHD equivalent of the Kelvin theorem in ordinary hydrodynamics. One of the noticeable aspects of this class of phenomena is the fact that they cannot be observed in well-controlled laboratory experiments. But they are relevant for the Earth core (except at small scales) and for all astrophysical phenomena, in stars as well as in the interstellar medium. As a consequence, the numerical modeling of that class of phenomena is essential since there is no hope to understand them directly through controlled experiments.

Among the electrically conducting fluids present on Earth at small and moderate scales, one encounters (beside liquid metals) ionized gases, also referred to as plasmas. They are used in different sorts of engineering techniques and thus deserve some particular attention. Very often, they are far from thermodynamic equilibrium and as a consequence, they cannot be modeled as fluids, even multi-phase fluids. This is very much the case for fusion plasmas ($T \approx 10^7 - 10^8 K$) confined by a strong magnetic field and these were not included in the group of projects for the Summer Program 2004. In the Summer Program 2004, the only problem involving plasmas which is investigated is the particular case of Hall thrusters used to propel satellites by producing forces of the order of a few milli-Newtons. It is addressed with the purpose of understanding and modeling the generally observed high transport of electric charges. The key idea is that the high level of observed fluctuations could explain the increase of the apparent electric conductivity.

In spite of the apparent diversity of the MHD phenomena considered during the Summer Program 2004, there is a remarkable unity in the questions being investigated. Among them, the understanding of the anisotropy, due to the privileged direction imposed by the presence of an applied magnetic field, is at the center of the majority of projects. At low Rm , this anisotropy, which seems to be scale independent, yields quasi-two-dimensional structures aligned in the B -direction (however, it is worth noticing that even though the morphology of the turbulent structures is B -dependent, the fluid flow organization within any Q2D structure remains not directly influenced by B). At large Rm , the results obtained by Cho and Lazarian show that the anisotropy is more pronounced in the small scales. As soon as walls perpendicular to the magnetic field are present, as is the case in most of the experiments, some extra effects arise: the velocity component parallel to the applied magnetic field is rapidly suppressed, whereas the perpendicular ones may survive during a much longer time related to the Joule dissipation which takes place within the thin Hartmann layers. The modeling of this influence of the Hartmann walls, which is a necessary step before the development of models capable of computing actual channel flows, is then a significant originality of the Summer Program 2004.

To conclude this brief summary of the most important questions addressed by the participants to the MHD part of the Summer Program 2004, it is important to stress that this international effort seems to be quite timely. Indeed, numerical models should become important tools in the coming years, either to compute industrial MHD flows (e.g. in metals processing or in the design of the blanket of the future nuclear fusion reactor), or to model geophysical and astrophysical flows. In relation to other projects hosted during the Summer Programs 2004, it is worth noting that also in MHD, LES seems to have important advantages over any other modeling techniques, either because the spectral range is so large that DNS is far from being achievable, or because of the presence of an inverse energy cascade when the turbulence becomes Q2D as in liquid metals.

René Moreau

Anisotropy of MHD turbulence at low magnetic Reynolds number

By O. Zikanov and A. Vorobev [†], A. Thess [‡] P. A. Davidson [¶] AND
 B. Knaepen ^{||}

Turbulent fluctuations in MHD flows are known to become dimensionally anisotropic under the action of a sufficiently strong magnetic field. We consider the technologically relevant case of low magnetic Reynolds number and apply the method of DNS of forced flow in a periodic box to generate velocity fields. The analysis based on different anisotropy characteristics shows that the dimensional anisotropy is virtually scale-independent. We also find that, except for the case of very strong magnetic field, the flow is componentally isotropic. Its kinetic energy is practically uniformly distributed among the velocity components.

1. Introduction

Magnetohydrodynamic (MHD) turbulent flows are ubiquitous in the universe, occurring in numerous astrophysical, geophysical, and technological applications. It is known that in the presence of a sufficiently strong magnetic field the turbulent fluctuations become anisotropic, which implies important consequences for the properties of the turbulence and possibly requires modification of numerical models. Specific manifestation of the anisotropy may vary but the principal mechanism is always the elongation of flow structures (turbulent eddies) along the lines of the magnetic field.

The main difference between the kinds of MHD turbulence is due to different values of the magnetic Reynolds number

$$\text{Re}_m \equiv \frac{uL}{\eta}, \quad (1.1)$$

where $\eta = (\sigma\mu_0)^{-1}$ is the magnetic diffusivity, σ and μ_0 being the electric conductivity of the liquid and magnetic permeability, and u , L are the typical velocity and length scales of the flow. If $\text{Re}_m > 1$, there is a two-way coupling between fluctuations of magnetic field and velocity. This happens in astrophysical applications (stars, interstellar medium, etc.), where $\text{Re}_m \gg 1$, and in geophysical applications (Earth dynamo), where Re_m is smaller but still significantly larger than 1. Discussions of anisotropy effects at large magnetic Reynolds number can be found, for example, in the recent review by Cho *et al.* (2002).

The opposite case of $\text{Re}_m \ll 1$ occurs in a majority of technological processes, where a strong steady magnetic field is imposed on an electrically conducting liquid. Examples of such applications include continuous casting of steel and aluminum, growth of semiconductor crystals, and lithium cooling blankets for fusion reactors. In this case, the low- Re_m (so-called quasi-static) approximation can be applied (see, e.g., Moreau 1990 or

[†] University of Michigan - Dearborn

[‡] Ilmenau University of Technology

[¶] University of Cambridge

^{||} Universite Libre de Bruxelles

Davidson 2001). It can be assumed that the fluctuations of the magnetic field \mathbf{b} associated with fluid motions adjust instantaneously to the velocity fluctuations and that their amplitude is negligible in comparison with the amplitude of imposed magnetic field \mathbf{B} . The rotational part of the Lorentz force reduces to the linear functional of the velocity

$$\mathbf{F}[\mathbf{v}] = -\frac{\sigma B^2}{\rho} \Delta^{-1} \frac{\partial^2 \mathbf{v}}{\partial z^2}, \quad (1.2)$$

where ρ and \mathbf{u} are the density and velocity of the fluid, Δ^{-1} is the reciprocal Laplace operator, and we assumed that the imposed magnetic field is uniform and purely vertical $\mathbf{B} = B\mathbf{e}_z$.

The flow transformation under the impact of force (1.2) has been actively studied in analytical (Moffatt 1967, Sommeria & Moreau 1982, Davidson 1997, 1999), experimental (Votsish & Kolesnikov 1976, Alemany *et al.* 1979) and numerical (Schumann 1976, Zikanov & Thess 1998) works. The papers mentioned above represent only a fraction of the literature on the subject, more references being available therein. Far from the walls, the action of the magnetic field was identified as two-fold. First, the induced electric currents result in additional dissipation of kinetic energy, the Joule (magnetic) dissipation. Second, the flow becomes anisotropic, its structures being elongated along the magnetic field lines.

The reason for the anisotropy becomes especially transparent if one assumes that the flow is unbounded and uniform and uses the Fourier representation.[†] The Fourier transform of (1.2) is

$$\hat{\mathbf{F}}[\hat{\mathbf{v}}] = -\frac{\sigma (\mathbf{B} \cdot \mathbf{k})^2}{\rho k^2} \hat{\mathbf{v}}(\mathbf{k}, t) = -\frac{\sigma B^2}{\rho} \hat{\mathbf{v}}(\mathbf{k}, t) \cos^2 \theta, \quad (1.3)$$

where \mathbf{k} is the wavenumber vector and θ is the angle between \mathbf{k} and \mathbf{B} . The rate of Joule dissipation of a Fourier mode with the wavenumber vector \mathbf{k} is

$$\mu(\mathbf{k}) = \frac{\sigma B^2}{\rho} (\hat{\mathbf{v}}(\mathbf{k}, t) \cdot \hat{\mathbf{v}}^*(\mathbf{k}, t)) \cos^2 \theta, \quad (1.4)$$

so the dissipation is anisotropic. It attains maximum for the Fourier modes with $\mathbf{B} \parallel \mathbf{k}$ and zero for modes with $\mathbf{B} \perp \mathbf{k}$, i.e., for modes independent of the z -coordinate. The dissipation tends to eliminate the velocity gradients in the direction of \mathbf{B} and elongate the flow structures in this direction. The limiting case is the two-dimensional state completely independent of the z -coordinate. The Joule dissipation is equal to zero in this state.

This picture of the flow transformation was first given by Moffatt (1967) and later beautifully illustrated by Sommeria & Moreau (1982), who introduced the image of 'Joule cone' in the wavenumber space around the \mathbf{B} -direction, in which the magnetic dissipation takes place. A remarkable feature of the picture is that, according to (1.4), the relative rate of the dissipation $\mu(\mathbf{k})/\hat{\mathbf{u}}^2$ depends on the angle θ but not on the wavenumber k . One can, thus, assume that the anisotropy would develop equally on all length scales of the flow.

The situation, however, looks much more complicated if one takes into account the non-linearity of the Navier-Stokes equations and the resulting energy transfer between the modes and tendency to restoration of isotropy. The ratio between the Lorentz force

[†] The process of development of anisotropy can be viewed from a different angle. In particular, Davidson (1997) proposed a scenario based on the fact that the Lorentz force conserves momentum component parallel to the magnetic field.

and non-linear term is evaluated by the magnetic interaction parameter (Stuart number)

$$N \equiv \frac{\sigma B^2 L}{\rho u}. \quad (1.5)$$

It is clear that the linearized picture of the flow development discussed above is true only in the limit of $N \gg 1$. At finite N , one can expect a more complex scenario, probably with scale-dependent anisotropy. In particular, the analogy with stratified, rotating, or strained turbulence (see, e.g., Smith & Moun 2000) suggests that smaller scales are more isotropic than large scales. Another way to arrive to the suggestion is to notice that, while the Joule damping time $\tau \equiv \rho/\sigma B^2$ is scale-independent, the eddy turnover time $T = L/u$ is not. The magnitude of the scale-related Stuart number $N = T/\tau$ can vary with the scale and so is the flow's anisotropy.

The question of anisotropy at different length scales is particularly important in the view of recent attempts to apply the traditional LES models to the low- Re_m MHD turbulence (Knaepen & Moin 2004). The a-posteriori evaluation of the dynamic model (Germano *et al.* 1991) showed good accuracy for decaying turbulence at moderate hydrodynamic Reynolds number and $N \leq 10$. This result is counter-intuitive since one expects LES models developed in assumption of local isotropy to perform poorly in the case of strongly anisotropic flow. One can not guarantee that equally good results will be obtained at higher Reynolds numbers.

In this paper, we investigate the anisotropy of low- Re_m MHD turbulence using the DNS of forced flow in a box with periodic boundary conditions. The model and the numerical experiments are described in section 2. Various measures of anisotropy are discussed and evaluated in section 3. Possible implications for LES subgrid-scale modeling are discussed in section 4. Finally, summary and concluding remarks are provided in section 5.

2. Model and numerical experiments

We solve MHD equations for viscous, incompressible and electrically-conducting fluid in the quasi-static approximation. The Lorentz force term is given by (1.2). After applying $(\nabla \times) \times$ operation to eliminate pressure and taking Fourier transform, the governing equation become

$$\frac{\partial \hat{\mathbf{v}}}{\partial t}(\mathbf{k}, t) = -\frac{1}{k^2}[\mathbf{k} \times (\mathbf{k} \times \hat{\mathbf{q}})] - \left[\nu \mathbf{k}^2 + \frac{\sigma B_0^2}{\rho} \left(\frac{k_z}{k} \right)^2 \right] \hat{\mathbf{v}}, \quad (2.1)$$

where ν is the kinematic viscosity and $\hat{\mathbf{q}}$ is the Fourier transform of the nonlinear term. The incompressibility condition used in derivation of (2.1) can be applied to recover the modified pressure field. A statistically homogeneous flow is calculated within a rectangular box with periodical boundary conditions. Since we expect axial anisotropy of turbulent flow, and elongation of turbulent vortexes along the z -axis, the elongated box of dimensions $2\pi \times 2\pi \times 4\pi$ is used. The equation (2.1) is solved by the standard pseudo-spectral technique.

In order to generate a statistically steady flow over long period of time, an artificial forcing is applied at large length scales. A constant amount of energy is added at each time-step. When equilibrium is reached the amount of energy added is on average equal to the energy dissipated. The external force

$$\mathbf{H}(\mathbf{k}) = \alpha(\mathbf{k})\hat{\mathbf{v}}(\mathbf{k}) \quad (2.2)$$

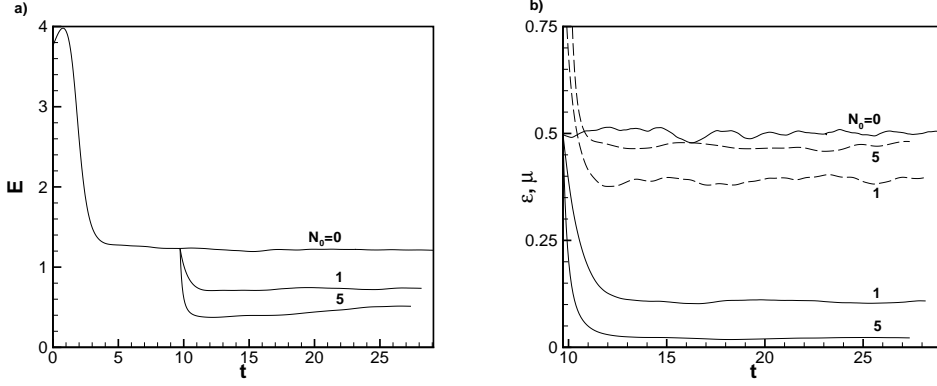


FIGURE 1. (a), Evolution of total energy. (b), Evolution of rates of total viscous (—) and magnetic (---) dissipation.

is applied to modes with $1.5 \leq k \leq 3.1$. The time-dependent coefficients α are determined so that the net work by forcing is equal to the prescribed total (viscous and magnetic) rate of dissipation ϵ_0 and the work is equally divided among the forced modes

$$\alpha(\mathbf{k}) = \frac{\epsilon_0}{N_{forced}(\hat{\mathbf{v}}(\mathbf{k}) \cdot \hat{\mathbf{v}}^*(\mathbf{k}))}, \quad (2.3)$$

where N_{forced} is the number of forced modes and $*$ stands for complex conjugate.

Simulations are performed with numerical resolution $256 \times 256 \times 512$. The parameters $\epsilon_0 = 0.5$ and $\nu = 2.2 \cdot 10^{-3}$ are chosen so as to guarantee the accuracy criterion $k_{max}\eta > 1.5$, where k_{max} is the maximum resolved wavenumber and η is the Kolmogorov dissipation scale. The microscale Reynolds number is $Re_\lambda \approx 94$ in the non-magnetic run.

The numerical experiments are staged as illustrated in figure 1. First, a developed turbulent flow is calculated starting with random, isotropic, and homogeneous field and continuing simulations without magnetic field for sufficiently long period. The completeness of the transitional period is judged by stabilization of the values of the total kinetic energy, viscous and magnetic dissipation rates defined as

$$E = \frac{1}{2} \sum_{\mathbf{k}} (\mathbf{v}(\mathbf{k}) \cdot \mathbf{v}^*(\mathbf{k})), \quad \epsilon = \nu \sum_{\mathbf{k}} k^2 (\mathbf{v}(\mathbf{k}) \cdot \mathbf{v}^*(\mathbf{k})), \quad \mu = \frac{\sigma B_0^2}{\rho} \sum_{\mathbf{k}} \frac{k_z^2}{k^2} (\mathbf{v}(\mathbf{k}) \cdot \mathbf{v}^*(\mathbf{k})). \quad (2.4)$$

The flow field computed at the moment $t_0 = 9.72$ is used as an initial condition for three simulations with different strength of the magnetic field. At $t = t_0$, the integral length scale is $L = 0.73$ and the rms turbulent velocity is $u = 0.71$, which gives the turbulent eddy turnover time of about 1. The strength of magnetic field in each run can be identified by the values of magnetic interaction parameter (1.5) at $t = t_0$. The cases with no magnetic field ($N_0 = 0$), moderate magnetic field ($N_0 = 1$), and strong magnetic field ($N_0 = 5$) are considered†.

A comment must be made regarding the limitations of the traditional DNS approach that can affect the accuracy of our results. First, at moderate Re_λ , the artificial forcing can have some impact on a significant portion of the resolved length scales. Second

† The flow evolution caused by magnetic field leads to significant increase of N during the runs (to about 1.2 in the second case and 10 in the third case).

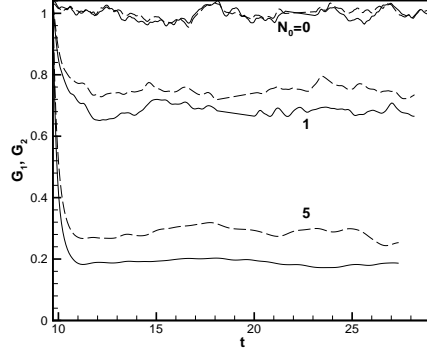


FIGURE 2. Anisotropy coefficients G_1 (—) and G_2 (---) given by (2.6).

(perhaps less important for us here), the integral length scale is relatively large (about $1/5$ of the box size at $t = t_0$). The periodic boundary conditions can, therefore, affect the flow behavior at largest scales.

The evolution of total energy, viscous and magnetic dissipation is shown in figure 1. It can be seen that the period of adjustment after the introduction of magnetic field lasts several turnover times, after which the flow behavior is statistically steady. In the flows with magnetic field, the Joule dissipation is responsible for major part of the total dissipation rate $\epsilon_0 = \epsilon(t) + \mu(t)$.

Zikanov & Thess (2004) proposed using anisotropic Taylor microscales

$$\lambda_i \equiv \left[\frac{\langle v_j^2 \rangle}{(1 + \delta_{ij}) \langle (\partial v_j / \partial x_i)^2 \rangle} \right]^{1/2} \quad (2.5)$$

as global measures of anisotropy of velocity gradients. Here, any velocity component v_i can be used and $\langle \dots \rangle$ stands for volume averaging. For isotropic turbulence, λ_i are all statistically equal to the usual Taylor microscale $\lambda = [15\nu u^2 / \epsilon]^{1/2}$. The ratio $(\lambda_\perp / \lambda_\parallel)^2$ of length scales measured in the directions transverse and parallel to the magnetic field is equal to often used anisotropy coefficients (see, e.g., Schumann 1976 or Zikanov & Thess 1998) shown in figure 2

$$G_1 = \frac{\langle (\partial v_2 / \partial z)^2 \rangle}{2 \langle (\partial v_2 / \partial y)^2 \rangle}, \quad G_2 = 2 \frac{\langle (\partial v_3 / \partial z)^2 \rangle}{\langle (\partial v_3 / \partial y)^2 \rangle}. \quad (2.6)$$

Figure 3 shows skewness and flatness of longitudinal derivatives of the velocity components

$$S_i = - \frac{\langle (\partial v_i / \partial x_i)^3 \rangle}{\langle (\partial v_i / \partial x_i)^2 \rangle^{3/2}}, \quad F_i = \frac{\langle (\partial v_i / \partial x_i)^4 \rangle}{\langle (\partial v_i / \partial x_i)^2 \rangle^2}. \quad (2.7)$$

In the isotropic flow at $N_0 = 0$, all three components of skewness and flatness are approximately equal to $S \approx 0.5$ and $F \approx 5.4$. In the presence of magnetic field, the components measured across and along the magnetic field differ considerably. For skewness, the transverse components remain close to the isotropic value, although some drop can be seen in

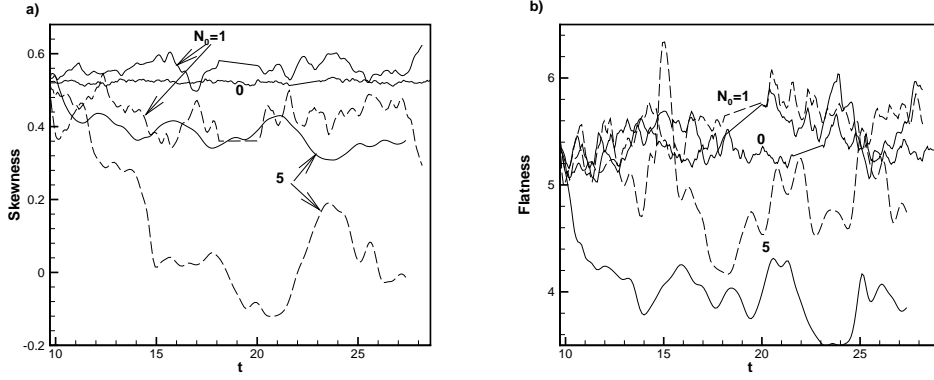


FIGURE 3. Skewness (a) and flatness (b) coefficients (2.7) measured across $((S_1 + S_2)/2$ and $(F_1 + F_2)/2$ shown as —) and along $(S_3$ and F_3 shown as - -) magnetic field. For $N_0 = 0$, solid lines show $(S_1 + S_2 + S_3)/3$ and $(F_1 + F_2 + F_3)/3$.

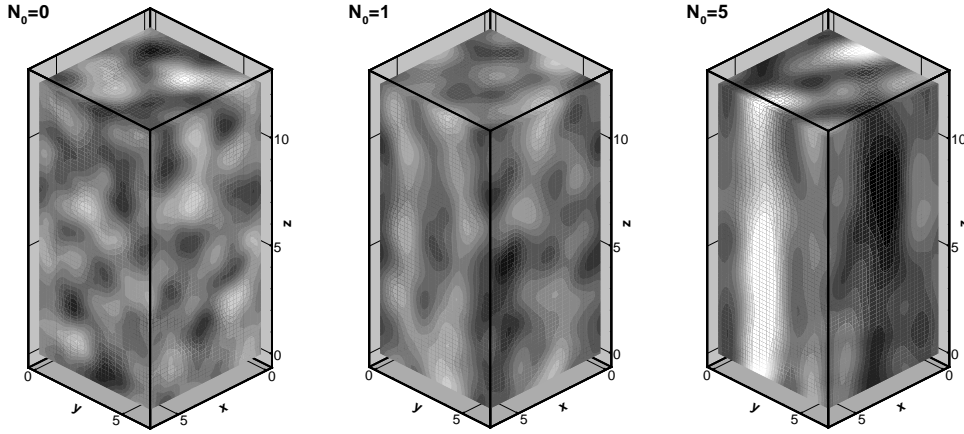


FIGURE 4. Modified pressure fields in developed flows.

the case of $N_0 = 5$. The parallel component decreases significantly at $N_0 = 1$ and even more so at $N_0 = 5$. This clearly indicates suppression of nonlinear energy transfer and dissipation of strong longitudinal velocity gradients by the magnetic field. For flatness, we also observe significant reduction in the case of $N_0 = 5$, more pronounced for the transverse component.

The internal structure of flow field is illustrated in figure 4, where we show snapshots of modified pressure field made in developed flows at different magnetic field. The tendency to anisotropy is clearly seen, although even at $N_0 = 5$ the flow is far from approaching two-dimensional form.

The last issue to be discussed in this section is that of componental anisotropy, which is understood as anisotropy of the Reynolds stress tensor or velocity field (Kassinos *et al.* 2001). As the Joule dissipation directly affects only velocity gradients along the magnetic field lines, the componental anisotropy is a secondary effect, which existence and strength

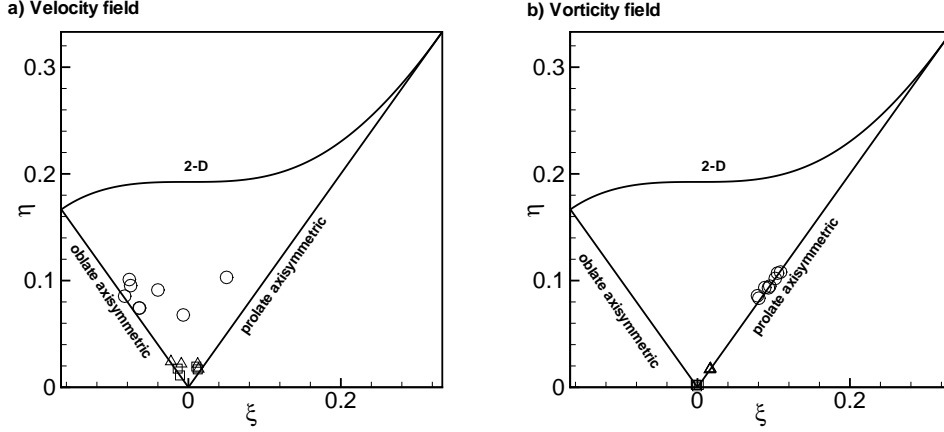


FIGURE 5. Invariant maps for componental anisotropy of velocity (a) and vorticity (b) fields. Squares, triangles, and circles are for $N_0 = 0, 1$, and 5 , correspondingly.

is far from being obvious. The componental anisotropy of field \mathbf{v} is traditionally evaluated with the help of the traceless tensor (Lumley & Newman 1977)

$$b_{ij} = \frac{\langle v_i v_j \rangle}{\langle v_k v_k \rangle} - \frac{1}{3} \delta_{ij}, \quad (2.8)$$

which has two nontrivial invariants $6\eta^2 = b_{ij}b_{ji}$ and $6\xi^3 = b_{ij}b_{jk}b_{ki}$. The magnitude of η represents the degree of anisotropy, with $\eta = 0$ for an isotropic flow, and the upper boundary $\eta = (1/22 + 2\xi^3)^{1/3}$ corresponding to a purely two-component case. The type of the anisotropy is determined by the sign of ξ . If $\xi > 0$, the flow is dominated by the velocity component parallel to the axis of symmetry (so-called prolate axisymmetric flow). Negative values of ξ mean domination of two perpendicular components (oblate axisymmetric flow).

We calculated the invariants at several time moments separated by few eddy turnover times. The results presented on the invariant map in figure 5a show that the velocity fields at $N_0 = 0$ and $N_0 = 1$ are fairly isotropic. The flow with strong magnetic field at $N_0 = 5$ demonstrates a degree of anisotropy. It is interesting that the velocity field migrates from being dominated by two velocity components perpendicular to the magnetic field to being dominated by one parallel component. This behavior can be associated with slow transformation of the large-scale structures of the flow.

We also calculated tensor (2.8) and invariants η and ξ for the vorticity field. The results shown in figure 5b are easy to explain. As the vertical gradients of velocity are eliminated in flows with higher N , the vorticity field becomes dominated by the vertical component.

3. Anisotropy at different length scales

In this section we analyze the calculated flow fields to determine how and whether at all the dimensional anisotropy varies with the length scale. We start with the power spectra shown in figure 6. The steepening of the energy spectrum and accompanying decrease of viscous dissipation are well known phenomena associated with the anisotropy (see, e.g., experiments by Alemany *et al.* 1979 or simulations by Zikanov & Thess 1998).

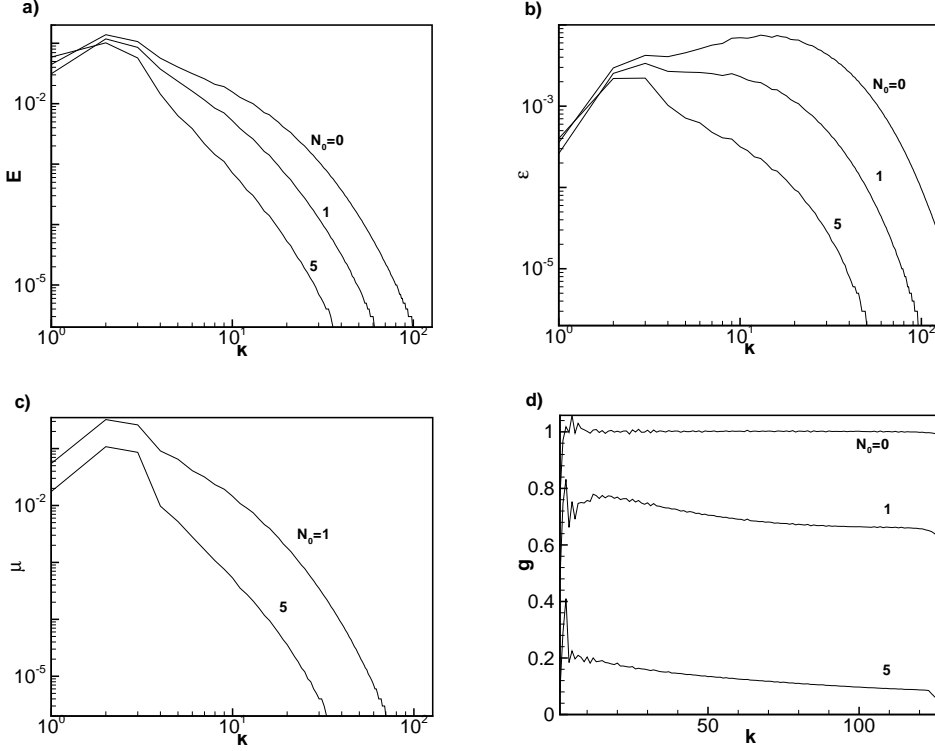


FIGURE 6. Spectra of (a) kinetic energy, (b) rate of viscous and (c) magnetic dissipation, and (d) spectra of anisotropy coefficient (3.1).

More interesting is the fact that the slope of Joule dissipation curves in figure 6c closely follows the slope of kinetic energy curves. This behavior detected earlier by Zikanov & Thess (1998) and confirmed here for larger Reynolds number gives, at least, a partial answer to our question. The ratio

$$g(k) \equiv \frac{3T_J}{2} \frac{\mu(k)}{E(k)} = \frac{3 \sum \frac{k^2}{k^2} \hat{\mathbf{u}} \cdot \hat{\mathbf{u}}^*}{\sum \hat{\mathbf{u}} \cdot \hat{\mathbf{u}}^*} = \frac{3D_{33}(k)}{2E(k)} \quad (3.1)$$

can be considered as a measure of dimensional anisotropy at the wavelength k . In (3.1), the sum is over all wavenumber vectors in the shell $k - 1/2 < |\mathbf{k}| \leq k + 1/2$, $T_J = \rho/\sigma B^2$ is the Joule dissipation time, and D_{33} is the component of the dimensionality tensor considered by Kassinos *et al.* (2001). The scaling factor is chosen so as to provide $g = 1$ in an isotropic flow. It can be seen in figure 6d that, outside of the forced region, $g(k)$ varies only slightly with k both at moderate and strong magnetic field. Even this slight decrease can be attributed to the effect of forcing. The magnitude of $g(k)$ is close to that of the global anisotropy coefficients G_1 and G_2 shown in figure 2.

The use of Fourier wavenumbers is arguably not the best way to consider the length scale decomposition of the flow properties. In the following we concentrate on analyzing the flow anisotropy in the physical space. First, figures 7 and 8 show the two-point velocity correlations along the direction perpendicular and parallel to the magnetic field. For the correlations in figure 7 we assume axial symmetry and calculate, for example,

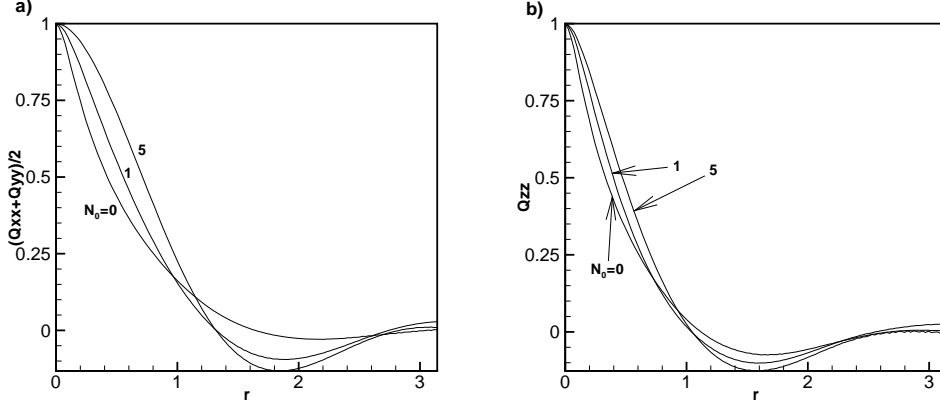


FIGURE 7. Correlations of velocity field in the direction perpendicular to the magnetic field.

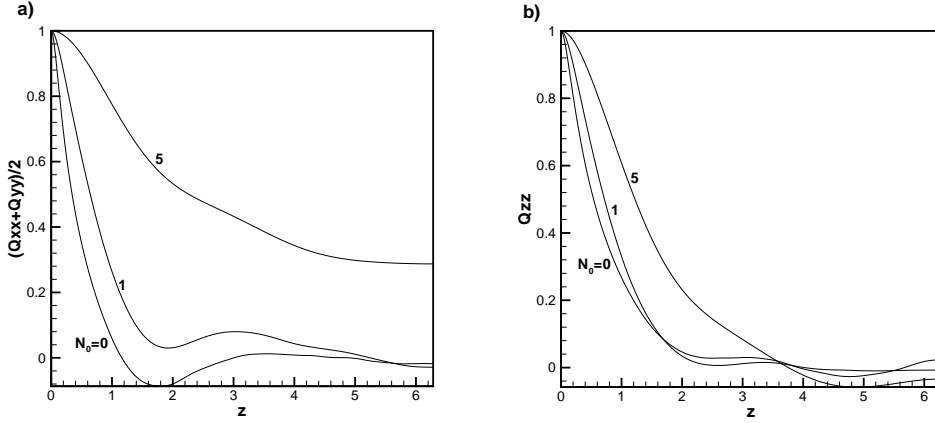


FIGURE 8. Correlations of velocity field in the direction parallel to the magnetic field.

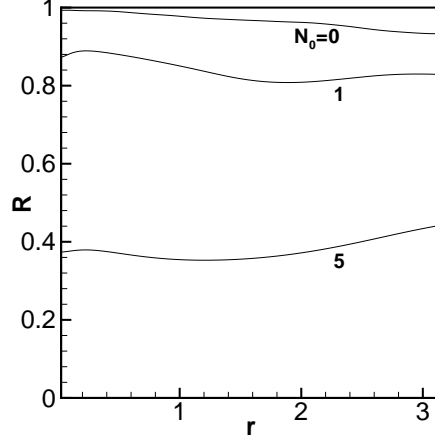
$Q_{xx} = \langle u(\mathbf{x})u(\mathbf{x} + r\mathbf{e}_\perp) \rangle / \langle u^2 \rangle$, where $\langle \dots \rangle$ now stands for space averaging in \mathbf{x} and averaging over all horizontal directions of \mathbf{e}_\perp .

One can see in figures 7 and 8 that imposing a magnetic field leads to growth of correlations not only in parallel but also in perpendicular direction. This is in agreement with the development of larger coherent structures in this case (see figures 4). Interestingly, as can be seen from comparison of plots (a) and (b) in both figures, the vertical velocity component experience much smaller increase than the horizontal components.

Figure 9 can be considered a physical-space analog of figure 6d. We calculate the second-order structure functions $\Upsilon_i(r) \equiv \langle (v_i(\mathbf{x}+r\mathbf{e}_i) - v_i(\mathbf{x}))^2 \rangle$ and evaluate the anisotropy at the physical scale r as the ratio

$$R(r) = \frac{2\Upsilon_3}{\Upsilon_1 + \Upsilon_2}. \quad (3.2)$$

One can see that, again, the anisotropy is virtually scale-independent.

FIGURE 9. Anisotropy coefficient $R(r)$ given by (3.2).

4. Anisotropy of stress and strain tensors

One of the goals of this work is better understanding of properties of MHD flows related to the subgrid-scale turbulence modeling in LES. One can assume that the traditional SGS closures developed under the assumption of local isotropy are not suitable for strongly anisotropic MHD flows at high N . The opposite conclusion was made by Knaepen & Moin (2004) who performed LES of decaying turbulence at moderate Re and N up to 10. They found that the dynamic Smagorinsky model (Germano *et al.* 1991) is not less accurate for the MHD flows than for isotropic flows without magnetic field. Whether such a good performance is specific to the dynamic model and whether it is related to the scale-independence of anisotropy discussed above requires further investigation. So far, we have analyzed the computed data by calculating root-mean-squares of components of the Reynolds stress and rate of strain tensors of filtered velocity field

$$\tau_{ij} = \frac{\delta_{ij}}{3} \tau_{kk}, \text{ where } \tau_{ij} = \widehat{v_i v_j} - \widehat{v_i} \widehat{v_j} \quad (4.1)$$

and

$$S_{ij} = \frac{1}{2} \left(\frac{\partial \widehat{v_i}}{\partial x_j} + \frac{\partial \widehat{v_j}}{\partial x_i} \right). \quad (4.2)$$

Here, the $\widehat{\cdot}$ stands for Fourier cut-off filtering at a wavenumber k . The results are presented as functions of k in figure 10. We assume the axial symmetry and take the averages of statistically equal quantities. It can be seen that the rate of strain tensor becomes increasingly anisotropic with growing N . There is a significant and consistent difference between the amplitudes of, say, S_{12} and S_{13} . On the other hand, the components of the Reynolds stress tensor are virtually indistinguishable for any N and for any filter cut-off k .

5. Conclusions

We performed simulations of forced homogeneous turbulence in a low- Re_m MHD flow. Three numerical experiments with equal constant energy input but different strength of

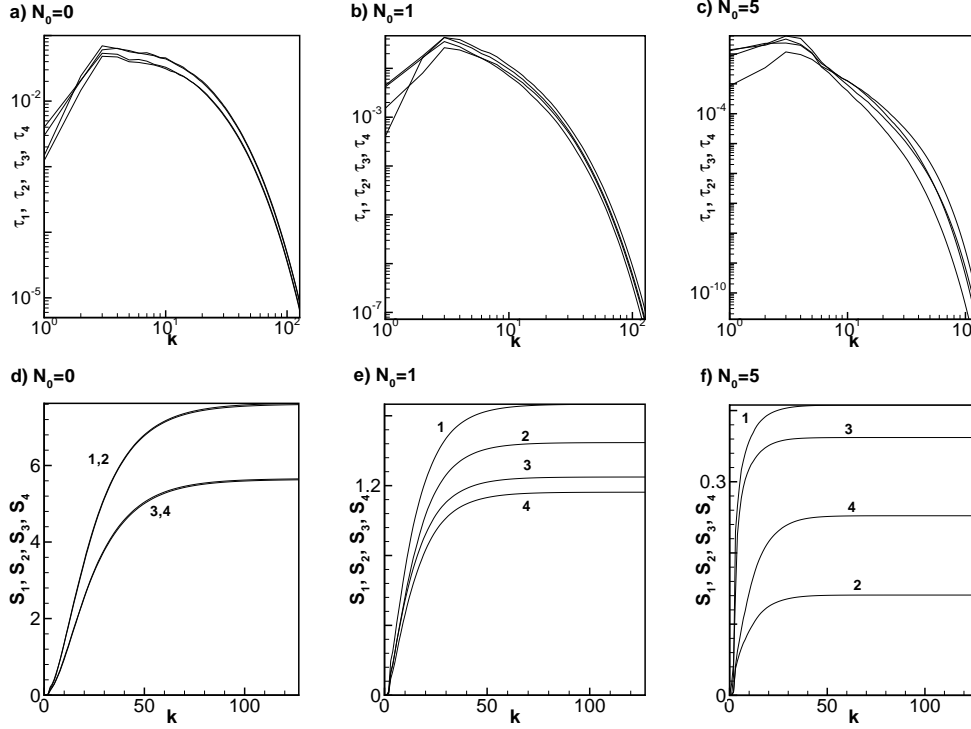


FIGURE 10. Spectra of root-mean squares of components of stress (top) and rate-of-strain (bottom) tensors of filtered velocity field as function of the filter cut-off k . Here $\tau_1 = \langle \tau_{11}^2 + \tau_{22}^2 \rangle / 2$, $\tau_2 = \langle \tau_{33}^2 \rangle$, $\tau_3 = \langle \tau_{12}^2 + \tau_{21}^2 \rangle / 2$, $\tau_4 = \langle \tau_{13}^2 + \tau_{31}^2 + \tau_{23}^2 + \tau_{32}^2 \rangle / 4$. Similar notations used for rate-of-strain tensor. For $N_0 = 0$, τ_1 and τ_2 curves coalesce, as well as τ_3 and τ_4 .

applied magnetic field were performed. The dimensional and componental anisotropy of the flow was analyzed both in the global sense and as a function of length scale. The main conclusions are as follows.

- While the flow develops strong dimensional anisotropy under the action of the Joule dissipation, its componental anisotropy remains insignificant. The kinetic energy remains approximately equally distributed over the velocity components.
- The analysis performed both in spectral and physical space showed that the dimensional anisotropy is virtually scale-independent. We can not exclude the possibility that different behavior can be observed at small scales of flows with much higher Reynolds numbers. On the other hand, the extent of the range of constant anisotropy was found to be quite significant in our simulations (about 2 orders of magnitude). We can consider the constancy a robust feature of low- Re_m MHD turbulence.

Part of this work was performed during the 2004 Summer Program at the Center for Turbulence Research with financial support from Stanford University and NASA Ames Research Center. The authors would like to thank P. Moin and N. Mansour for their hospitality during the stay. The authors have benefited from numerous fruitful discussions with R. Moreau, S. Kassinos, and D. Carati. AV's and OZ's work was supported by the grant DE FG02 03 ER46062 from the US Department of Energy. AT's work is

partially supported by the Deutsche Forschungsgemeinschaft in frame of the "Forscherguppe Magnetofluidodynamik" at Ilmenau University of Technology. OZ, AV and AT are grateful to the Deutscher Akademischer Austauschdienst and the National Science Science Foundation for financial support of their collaboration. The computations were performed on the NASA Ames parallel computers and on the parallel computer cluster at the University of Michigan - Dearborn acquired with the support of the grant CTS 0320621 from the MRI program of the National Science Foundation.

REFERENCES

- ALEMANY A., MOREAU R., SULEM P.L, FRISCH U. 1979 Influence of external magnetic field on homogeneous MHD turbulence. *J. de Mecanique* **18**, 280–313.
- CHO, J., LAZARIAN, A, VISHNIAC, E. T. 2002 MHD turbulence: Scaling laws and Astrophysical applications. *Astro-ph/0205286*.
- DAVIDSON P.A. 1997 The role of angular momentum in the magnetic damping of turbulence. *J. Fluid Mech.* **336**, 123–150.
- DAVIDSON P.A. 1999 Magnetohydrodynamics in Materials Processing. *Annu. Rev. Fluid Mech.* **31**, 273–300.
- DAVIDSON P.A. 2001 An Introduction to Magnetohydrodynamics, *Cambridge University Press*, Cambridge.
- GERMANO, M., PIOMELLI, U., MOIN, P., CABOT, W. H. 1991 A dynamic subgrid-scale eddy viscosity model. *Phys. Fluids A* **3**, 1760–1765.
- KASSINOS, S. C., REYNOLDS, W. C., ROGERS, M. M. 2001 One-point turbulence structure tensors. *J. Fluid Mech.* **428**, 213–248.
- KNAEPEN B., MOIN 2004 Large-eddy simulation of conductive flows at low magnetic Reynolds number. *Phys. Fluids* **16**, 1255–1261.
- LUMLEY, J. L., NEWMAN, G. R. 1977 The return to anisotropy of homogeneous turbulence. *J. Fluid Mech.* **82**, 161–178.
- MOFFATT H.K. 1967 On the suppression of turbulence by a uniform magnetic field. *J. Fluid Mech.* **28**, 571–592.
- MOREAU R. 1990 Magnetohydrodynamics, *Kluwer Academic Publishers*, Dordrecht.
- SCHUMANN U. 1976 Numerical simulation of the transition from three- to two-dimensional turbulence under a uniform magnetic field. *J. Fluid Mech.* **74**, 31–58.
- SMITH, W. D. & MOUM, J. M. 2000 Anisotropy of turbulence in stably stratified mixing layers. *Phys. Fluids* **12**, 6, 1343–1362.
- SOMMERIA J., MOREAU R. 1982 Why, how, and when, MHD turbulence becomes two-dimensional. *J. Fluid Mech.* **118**, 507–518.
- VOTSISH, A. D. AND KOLESNIKOV, YU. B. 1976 Investigation of transition from three-dimensional turbulence to two-dimensional under a magnetic field. *Magn. Hydrodyn.* **3**, 141–142.
- ZIKANOV O., A. THESS 1998 Direct numerical simulation of forced MHD turbulence at low magnetic Reynolds number. *J. Fluid Mech.* **358**, 299–333.
- ZIKANOV O., A. THESS 2004 Direct numerical simulation as a tool for understanding MHD liquid metal turbulence. *Appl. Math. Mod.* **28**, 1–13.

MHD turbulence sheared in fixed and rotating frames

By S. C. Kassinos[†], B. Knaepen[‡] AND A. Wray

We consider homogeneous turbulence in a conducting fluid that is exposed to a uniform external magnetic field while being sheared in fixed and rotating frames. We take both the frame-rotation axis and the applied magnetic field to be aligned in the direction normal to the plane of the mean shear. Here a systematic parametric study is carried out in a series of Direct Numerical Simulations (DNS) in order to clarify the main effects determining the structural anisotropy and stability of the flow. When the time scale of the mean shear is short compared to the Joule time ($\tau_{\text{shear}} \ll \tau_m$), we find that the turbulence structures tend to align preferentially with the streamwise direction irrespective of the magnetic Reynolds number, R_m . When $\tau_{\text{shear}} \gg \tau_m$, we find that at low R_m the turbulent eddies become elongated and aligned with the magnetic field, but at moderately high R_m , there is partial streamwise alignment of the eddies. When $\tau_{\text{shear}} \approx \tau_m$, we find that competing mechanisms tend to produce different structural anisotropies and small variations in dimensionless parameters can have a strong effect on the structure of the evolving flow. For example, for very low R_m , a preferential alignment of structures in the direction of the magnetic field emerges as the flow evolves, consistent with the predictions of the quasi-static approach. For $R_m \sim 1$, the structures are found to be equally aligned in the streamwise and spanwise direction at large times. However, when R_m is moderately high ($10 \lesssim R_m \lesssim 50$) this strong spanwise alignment is replaced by a preferential alignment of structures in the streamwise direction. Counter to intuition, we found evidence that strong rotation in combination with a spanwise magnetic field tends to promote a streamwise alignment of the eddies, at least when $\tau_{\text{shear}} \approx \tau_m$. In some cases with frame counter-rotation, we have observed a bifurcation that leads to 2D turbulence consisting of vertical slabs parallel to the plane of the mean shear. For sufficiently high magnetic Reynolds numbers ($R_m \sim 50$) and strong frame counter-rotation, we find that the magnetic energy exceeds the turbulent kinetic energy. In this regime the ratio of production to dissipation exceeds unity ($P/\epsilon > 1$) even when the ratio of the frame rotation rate to the shear rate is such that in the hydrodynamic case suppression of the turbulence ($P/\epsilon < 1$) is observed. Finally, we also examine the range of validity of the Quasi-Linear approximation by comparing its predictions to those of ideal MHD. The QL approximation is found to be in excellent agreement with full MHD for the entire range of magnetic Reynolds numbers (R_m) that was examined ($R_m \leq 50$).

1. Introduction

1.1. Motivation and objectives

The combined effects of mean shear, frame rotation and an externally-applied magnetic field on turbulence in a conducting fluid are relevant to the accretion of Keplerian disks,

[†] Mechanical and Manufacturing Engineering, University of Cyprus and CTR NASA/Ames

[‡] Université Libre de Bruxelles, Belgium and CTR NASA/Ames

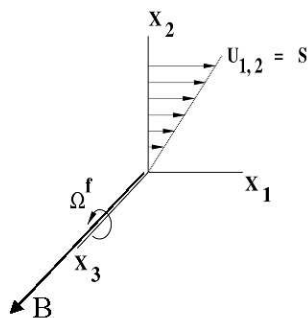


FIGURE 1. Configuration for shear in a rotating frame. Here B denotes the external magnetic field (when applicable), Ω^f the frame rotation rate, and S the shear rate.

to magnetic stirring, fusion plasma, and to Magnetogasdynamic (MGD) applications, involving advanced flow-control and propulsion schemes for hypersonic vehicles.

CFD codes used for the prediction of MHD and MGD flows rely on simple turbulence models, like k - ϵ models, with additional *ad hoc* modifications to account for the effects of the magnetic field. Such closures neglect the important dynamical role that the structure of the turbulence plays in the interaction between the turbulence and the applied magnetic field. As a result, they tend to be of limited applicability.

Structure-Based Models (SBM) are by construction able to account for the dynamical effects of the energy-containing turbulence structure. Preliminary work in the case of homogeneous unstrained MHD turbulence (Kassinos & Reynolds 1999), has shown that SBM are well suited for use in the prediction of MHD and MGD applications. The task of developing turbulence SBM or other closures for MHD and MGD applications can be simplified by taking advantage of approximations to the governing equations that are valid in flow regimes typically encountered in technological applications. In order to proceed further towards the development of SBM for MHD turbulence it is important to understand the combined effects of mean shear and frame rotation on MHD turbulence.

In the purely hydrodynamic case, frame rotation can act to either stabilize or destabilize homogeneous shear flow. For example, in these flows the equilibrium state depends on the ratio of the frame rotation rate $\Omega^f \equiv \Omega_{12}^f$ to the shear rate $S \equiv U_{1,2}$ (see Fig. 1). A limited range of values of $\lambda = \Omega^f/S$ is marked by exponential growth of both the turbulent kinetic energy, k , and the dissipation rate, ϵ . This has been known for a while, but details of the equilibrium state of the turbulence, such as the behavior of the ratio of the turbulent kinetic energy production and dissipation rates, P/ϵ , remained unclear. Virtually all algebraic stress and Reynolds stress transport models using the standard ϵ equation predict that, within this range, equilibrium turbulence is marked by P/ϵ being constant and independent of λ . This behavior has been reported in the literature and, in the absence of DNS data that would have helped evaluate it, has been accepted as reflecting the correct physics. Preliminary results from a DNS by Kassinos, Reynolds, and Wray (see for example Kassinos & Reynolds (2003)) show that in fact the equilibrium value of P/ϵ is a function of λ , as shown in Figure 2. When $\lambda = \Omega^f/S$ is close to $1/4$ the turbulent kinetic energy grows exponentially, and the energy-containing structures tend to quickly fill the computational box and the simulation has to be terminated. Thus obtaining reliable equilibrium values for P/ϵ when $\lambda = \Omega^f/S \sim 1/4$ is challenging. However, in the neighborhood of $\lambda \approx 0.55$, the structures grow relatively slowly and

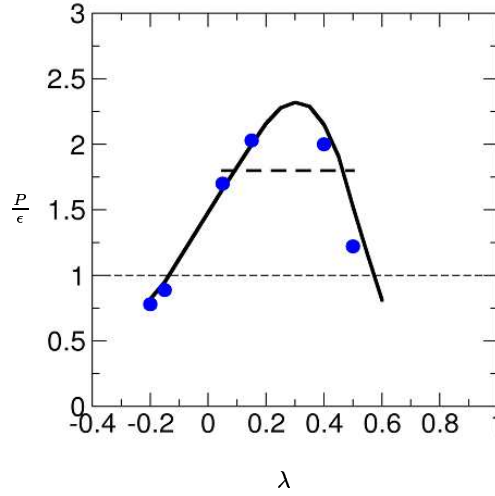


FIGURE 2. The variation of the ratio of production to dissipation (P/ϵ) of the turbulent kinetic energy with the ratio of frame rotation to shear rate η . Positive values of λ correspond to a frame counter-rotating relative to the intrinsic shear rotation sense: • , DNS (Kassinis & Reynolds, 2002); — Structure-based model; ---- model using standard

they are well contained within the computational box as equilibrium is approached. For this reason, it is clear from these simulations that the turbulence is suppressed when the frame counter-rotates at a rate of $\lambda \approx 0.55$ or higher.

For vanishingly small magnetic Reynolds numbers ($R_m \ll 1$), the induced magnetic fluctuations are much weaker than the applied field and their characteristic time scale, based on their diffusion, is much shorter than the eddy turnover time. A classical approximation for decaying MHD turbulence at low R_m is the Quasi-Static (QS) approximation. In this approximation, the induced magnetic field fluctuations become a linear function of the velocity field. Kassinis, Knaepen & Carati (2002) and Knaepen, Kassinis & Carati (2004) considered the case of initially isotropic decaying MHD turbulence, and concluded that the QS approximation was reasonably accurate for $R_m \lesssim 1$. For higher R_m , where the QS approximation fails, they proposed the use of the Quasi-Linear (QL) approximation, which amounts to retaining the unsteady term in the magnetic induction equation, retaining the non-linear hydrodynamic terms in the fluctuating momentum equation, but dropping all the nonlinear terms involving the magnetic fluctuations. They carried out a series of DNS and concluded that in unstrained MHD turbulence the QL approximation was valid for the entire range of magnetic Reynolds numbers they examined ($R_m \lesssim 30$).

Surprisingly, little work has been done to explore the structure of homogeneous MHD turbulence under the influence of mean shear and frame rotation. The objective of this work is to use DNS to probe the fundamental physics in sheared MHD turbulence. Primarily, we are interested in understanding the effects of shear and rotation on the dynamics of MHD turbulence, including the structural morphology and stability of these flows. For example, it is important to establish how the bifurcation diagram of Fig. 2 is modified in the MHD case. Stability modifications due to the presence of the magnetic field can potentially have implications for the evolution of stellar accretion disks and is an important element that must be built into a successful model for MHD turbulence.

We start by discussing the relevant dimensionless parameters that characterize MHD

and MGD flows in the presence of mean shear and frame rotation. In section 3 we introduce the governing equations for ideal MHD and the simplifications associated with the QL approximation as introduced by Kassinos *et al.* (2002) and Kneapen *et al.* (2004). The numerical code and associated initial conditions are described in section 4, while section 5 is devoted to a discussion of the most important results. A concluding summary is given in section 6.

2. Dimensionless parameters

The effects of a uniform magnetic field applied to unstrained homogeneous turbulence in an electrically conductive fluid are characterized by three dimensionless parameters. The first of these is the magnetic Reynolds number

$$R_m = \frac{vL}{\eta} = \left(\frac{v}{L}\right)\left(\frac{L^2}{\eta}\right), \quad (2.1)$$

where L is the integral length scale and v is the r.m.s. fluctuating velocity

$$v = \sqrt{R_{ii}/3}, \quad R_{ij} = \overline{u_i u_j}. \quad (2.2)$$

Here u_i is the fluctuating velocity, and η is the magnetic diffusivity

$$\eta = 1/(\sigma\mu^*) \quad (2.3)$$

where σ is the electric conductivity of the fluid, and μ^* is the fluid magnetic permeability (here we use μ^* for the magnetic permeability and reserve μ for the dynamic viscosity). Thus the magnetic Reynolds number represents the ratio of the characteristic time scale for diffusion of the magnetic field to the time scale of the turbulence. In the case of vanishingly small R_m , the distortion of the magnetic field lines by the fluid turbulence is sufficiently small that the induced magnetic fluctuations \mathbf{b} around the mean (imposed) magnetic field \mathbf{B} are also small.

The second parameter is the magnetic Prandtl number representing the ratio of R_m to the hydrodynamic Reynolds number Re_L

$$P_m \equiv \frac{\nu}{\eta} = \frac{R_m}{Re_L}, \quad Re_L = \frac{vL}{\nu}. \quad (2.4)$$

The magnetic-interaction number (or Stuart number) is

$$N \equiv \frac{\sigma B^2 L}{\rho v} = \frac{(B^{\text{ext}})^2}{\eta} \frac{L}{v} = \frac{\tau}{\tau_m}, \quad (2.5)$$

where B is the magnitude of the magnetic field, $B^{\text{ext}} = B/\sqrt{\mu^*\rho}$ is the magnetic field expressed in Alfvén units, and ρ is the fluid density. N represents the ratio of the large-eddy turnover time τ to the Joule time τ_m , i.e. the characteristic time scale for dissipation of turbulent kinetic energy by the action of the Lorentz force. N parametrizes the ability of an imposed magnetic field to drive the turbulence to a two-dimensional three-component state. In the absence of mean shear and frame rotation, the continuous action of the Lorentz force tends to concentrate energy in modes independent of the coordinate direction aligned with \mathbf{B} . As a two-dimensional state is approached, Joule dissipation decreases because fewer and fewer modes with gradients in the direction of \mathbf{B} are left available.

In addition, the tendency towards two-dimensionality and anisotropy is continuously opposed by non-linear angular energy transfer from modes perpendicular to \mathbf{B} to other modes, which tends to restore isotropy. If N is larger than some critical value N_c , the Lorentz force is able to drive the turbulence to a state of complete two-dimensionality. For smaller N , the Joule dissipation is balanced by non-linear transfer before a complete two-dimensionality is reached. For very small N ($N \leq 1$), the anisotropy induced by the Joule dissipation is negligible. Here we consider N in the range 1 – 20.

In the presence of mean shear and frame rotation, two additional parameters become important. The first of these is the ratio of the time scale of the mean shear to the Joule time τ_m ,

$$M \equiv \frac{(B^{\text{ext}})^2}{\eta S} = \frac{\tau_{\text{shear}}}{\tau_m} \quad (2.6)$$

where S is the mean shear rate. The second is the ratio of the frame rotation rate Ω^f to shear rate S ,

$$\lambda \equiv \frac{\Omega^f}{S} \quad (2.7)$$

where $\Omega^f = -\Omega_{12}^f$ so that positive values of λ correspond to a frame counter-rotating relative to the sense of rotation associated with the mean shear.

3. Governing Equations

Transport in homogeneous MHD shear flow is described by the incompressible MHD equations

$$\tilde{u}_{i,i} = 0 \quad \tilde{b}_{i,i} = 0 \quad (3.1)$$

$$\partial_t \tilde{u}_i + \tilde{u}_s \tilde{u}_{i,s} = -\frac{1}{\rho} P_{,i}^* + \tilde{b}_{i,m} \tilde{b}_m + \nu \tilde{u}_{i,ss} \quad (3.2)$$

$$\partial_t \tilde{b}_i + \tilde{u}_s \tilde{b}_{i,s} = \tilde{b}_s \tilde{u}_{i,s} + \eta \tilde{b}_{i,ss} \quad (3.3)$$

where P^* is the total pressure including magnetic contributions, \tilde{b}_i is the magnetic field in Alfvén units, and \tilde{u}_i are the velocity components. Next, the flow variables are transformed into a rotating frame, where they are explicitly decomposed into a mean and a fluctuating part. We solve the resulting governing equations for the fluctuation fields in a coordinate system that deforms with the mean flow so that Fourier decomposition methods can be employed. In this deforming coordinate system, the transformed equations become

$$\begin{aligned} \partial_t v_i + G_{ik} v_k + \frac{\partial v_i}{\partial x_m} v_k A_{mk} + 2\Omega_{ik}^f v_k = & -\frac{1}{\rho} \frac{\partial p}{\partial x_m} A_{mi} \\ + \frac{\partial B_i^{\text{ext}}}{\partial x_m} b_k A_{mk} + \frac{\partial b_i}{\partial x_m} B_k^{\text{ext}} A_{mk} + \frac{\partial b_i}{\partial x_m} b_k A_{mk} + \nu \frac{\partial^2 v_i}{\partial x_k \partial x_z} A_{zp} A_{kp} \end{aligned} \quad (3.4)$$

and

$$\begin{aligned} \partial_t b_i - G_{ik} b_k = & -v_k \frac{\partial B_i^{\text{ext}}}{\partial x_m} A_{mk} - v_k \frac{\partial b_i}{\partial x_m} A_{mk} \\ & + B_k^{\text{ext}} \frac{\partial v_i}{\partial x_m} A_{mk} + b_k \frac{\partial v_i}{\partial x_m} A_{mk} + \eta \frac{\partial^2 b_i}{\partial x_k \partial x_z} A_{zp} A_{kp}. \end{aligned} \quad (3.5)$$

Here, v_i and b_i are the components of velocity and magnetic fluctuation fields transformed in the rotating frame, x_i are deforming coordinates, $G_{ij} = U_{i,j}$ is the mean velocity gradient tensor, and A_{ij} is the (Rogallo) transformation matrix satisfying

$$\dot{A}_{iz} + A_{ij} G_{jz} = 0. \quad (3.6)$$

In the hydrodynamic case, one can impose any mean strain tensor, but once the mean strain is specified, the homogeneity requirement imposes constraints on the evolution of the mean rotation tensor. In the MHD case, these constraints involve gradients of the mean magnetic field as well. However, when the frame rotation axis and the uniform mean magnetic field vector are perpendicular to the plane of shear, these constraints leave the mean rotation unmodified and need not be considered.

3.1. The Quasi-Linear (QL) approximation

The Quasi-Linear (QL) approximation was introduced by Kassinos, Knaepen & Carati (2002) and Knaepen, Kassinos & Carati (2004) as a moderate- R_m replacement to the classical Quasi-Static approximation Roberts (1967). The QL approximation amounts to neglecting the nonlinear terms involving the fluctuating magnetic field in (3.4) and (3.5),

$$\begin{aligned} \partial_t v_i + G_{ik} v_k + \frac{\partial v_i}{\partial x_m} v_k A_{mk} + 2\Omega_{ik}^f v_k = & -\frac{1}{\rho} \frac{\partial p}{\partial x_m} A_{mi} \\ & + \frac{\partial B_i^{\text{ext}}}{\partial x_m} b_k A_{mk} + \frac{\partial b_i}{\partial x_m} B_k^{\text{ext}} A_{mk} + \nu \frac{\partial^2 v_i}{\partial x_k \partial x_z} A_{zp} A_{kp} \end{aligned} \quad (3.7)$$

and

$$\partial_t b_i - G_{ik} b_k = -v_k \frac{\partial B_i^{\text{ext}}}{\partial x_m} A_{mk} + B_k^{\text{ext}} \frac{\partial v_i}{\partial x_m} A_{mk} + \eta \frac{\partial^2 b_i}{\partial x_k \partial x_z} A_{zp} A_{kp}. \quad (3.8)$$

Note that the nonlinear convective term in the fluctuating momentum equation and the unsteady term $\partial_t b_i$ in the fluctuating induction equation are both retained. Of course, if the latter is also neglected one recovers the QS approximation.

4. Numerical code and initial conditions

We have used a pseudo-spectral code with the ability to simulate either the full MHD equations (3.4) and (3.5), or the reduced QL equations (3.7) and (3.8). The numerical method used to solve the governing equations for homogeneous shear flows is similar to that introduced by Rogallo (1981). The governing equations are transformed to a set of coordinates which deform with the mean flow. This allows Fourier pseudo-spectral methods, with periodic boundary conditions, to be used for the representation of the spatial variation of the flow variables. Time advance is accomplished by a third-order Runge-Kutta method. Since the mean imposed shear skews the computational grid with time, periodic remeshing of the grid is needed in order to allow the simulation to progress to large total shear, where a self-preserving regime might be expected to prevail. The periodic remeshing introduces aliasing errors that are removed by a de-aliasing procedure

Resolution	256 ³
Box size ($\ell_x \times \ell_y \times \ell_z$)	$2\pi \times 2\pi \times 2\pi$
Rms velocity (v)	3.099
Viscosity	0.006
Integral length-scale ($3\pi/4 \times (\int k^{-1} E(k) dk / \int E(k) dk)$)	0.322
$Re = uL/v$	166
Dissipation (ϵ)	47.876
Dissipation scale ($\gamma = (\nu^3/\epsilon)^{(1/4)}$)	0.0082
$k_{\max}\gamma$	1.82
Microscale Reynolds number ($Re_\lambda = \sqrt{15/(\nu\epsilon)}u^2$)	69.40
Eddy turnover time ($\tau = (3/2)u/\epsilon$)	0.097

TABLE 1. Turbulence characteristics of the initial velocity field. All quantities are in MKS units.

included in the code. An MPI based version of the code has been implemented in the Vectoral language and tested individually for accuracy, grid independence, and scalability.

All the runs presented here have a resolution of 256³ Fourier modes in a $(2\pi)^3$ computational domain. The initial conditions for the velocity were common to all cases. They were created starting with a pulse of energy at low wave numbers in Fourier space and a random distribution of phases for the Fourier modes. In order to let the higher-order statistics develop, the flow was evolved in the absence of mean shear or frame rotation and without a mean magnetic field, while forcing was being applied to the low wave number region of the spectrum. This initial phase was continued until an equilibrium state was reached and the skewness acquired its peak value. At that time, hereafter referred to as t_0 , the external magnetic field, mean shear and frame rotation were switched on while the artificial forcing was eliminated. The characteristics of the initial field at time t_0 are summarized in Table 1.

In the MHD runs, an initial condition for b_i has to be chosen at $t = t_0$. Here we have made the choice $b_i(t_0) = 0$. In other words, our simulations describe the response of an initially non-magnetized turbulent conductive fluid to the application of a mean magnetic field. The corresponding completely-linearized problem in the absence of mean shear and frame rotation has been described in detail in Moffatt (1967).

4.1. Parameters

In order to distinguish between our numerical runs, we will vary the magnetic Reynolds number R_m , the magnetic interaction number N , the ratio of the timescale of the mean shear to that for magnetic diffusion M , and the ratio of the frame rotation rate to the mean shear rate λ . Specification of R_m and N completely determines η and B^{ext} according to:

$$B^{\text{ext}} = \frac{Nv^2}{R_m}, \quad \eta = \frac{vL}{R_m}. \quad (4.1)$$

The values of these parameters for the different runs considered are summarized in Table 2. The entries in Table 2 are grouped first according to the initial value of M , then according to the value of the Magnetic Stuart number N , and last according to the magnetic Reynolds number R_m . Thus, the identification number of run CX.Y.Z can be

#	Case	η	B^{ext}	$N(t_0)$	$R_m(t_0)$	M	λ
1	C1.1.1	207.75	3.11	1	0.1	0.1	0.0, 0.25
2	C1.1.5	.387	.696	1	2.0	0.1	0.0, 0.25
3	C1.1.10	.258	.568	1	3.0	0.1	0.0, 0.25
4	C1.1.20	.155	.440	1	5.0	0.1	0.0, 0.25
5	C1.1.50	.0775	.311	1	10.0	0.1	0.0, 0.25
6	C1.2.1	7.75	9.84	10	0.1	0.1	0.0, 0.25
7	C1.2.5	.387	2.20	10	2.0	0.1	0.0, 0.25
8	C1.2.10	.258	1.80	10	3.0	0.1	0.0, 0.25
9	C1.2.20	.155	1.39	10	5.0	0.1	0.0, 0.25
10	C1.2.50	.0775	.984	10	10.0	0.1	0.0, 0.25
11	C2.1.1	7.75	22.0	50	0.1	2	0.0,0.25,0.5,0.75,1.0
12	C2.1.5	.387	4.92	50	2.0	2	0.0,0.25,0.5,0.75,1.0
13	C2.1.10	.258	4.02	50	3.0	2	0.0,0.25,0.5,0.75,1.0
14	C2.1.20	.155	3.11	50	5.0	2	0.0,0.25,0.5,0.75,1.0
15	C2.1.50	.0775	2.20	50	10.0	2	0.0,0.25,0.5,0.75,1.0
16	C2.2.1	7.75	22.0	50	0.1	2	0.0,0.25,0.5,0.75,1.0
17	C2.2.5	.387	4.92	50	2.0	2	0.0,0.25,0.5,0.75,1.0
18	C2.2.10	.258	4.02	50	3.0	2	0.0,0.25,0.5,0.75,1.0
19	C2.2.20	.155	3.11	50	5.0	2	0.0,0.25,0.5,0.75,1.0
20	C2.2.50	.0775	2.20	50	10.0	2	0.0,0.25,0.5,0.75,1.0
21	C3.1.1	7.75	22.0	50	0.1	20	0.0,0.25
22	C3.1.5	.387	4.92	50	2.0	20	0.0,0.25
23	C3.1.10	.258	4.02	50	3.0	20	0.0,0.25
24	C3.1.20	.155	3.11	50	5.0	20	0.0,0.25
25	C3.1.50	.0775	2.20	50	10.0	20	0.0,0.25
26	C3.2.1	7.75	22.0	50	0.1	20	0.0,0.25
27	C3.2.5	.387	4.92	50	2.0	20	0.0,0.25
28	C3.2.10	.258	4.02	50	3.0	20	0.0,0.25
29	C3.2.20	.155	3.11	50	5.0	20	0.0,0.25
30	C3.2.50	.0775	2.20	50	10.0	20	0.0,0.25

TABLE 2. Summary of the parameters for the different runs performed

interpreted as follows:

$$\begin{aligned}
X = 1 &\Rightarrow M(t_0) = 0.1 & X = 2 &\Rightarrow M(t_0) = 2 & X = 3 &\Rightarrow M(t_0) = 20 \\
Y = 1 &\Rightarrow N(t_0) = 1 & Y = 2 &\Rightarrow N(t_0) = 10
\end{aligned}
\tag{4.2}$$

and where Z is such that $R_m = Z$. Thus, for the first ten runs we have $M = 0.1$; for the next ten $M = 2$ and finally, for runs 21-30 we have $M = 20$.

5. Results

In this section we discuss some of the more important results obtained by carrying out the simulations described in the previous sections.

5.1. Eddy alignment

The effects of mean shear, frame rotation, and external magnetic fields on the turbulence structure are well understood whenever these act independently. Mean shear tends to

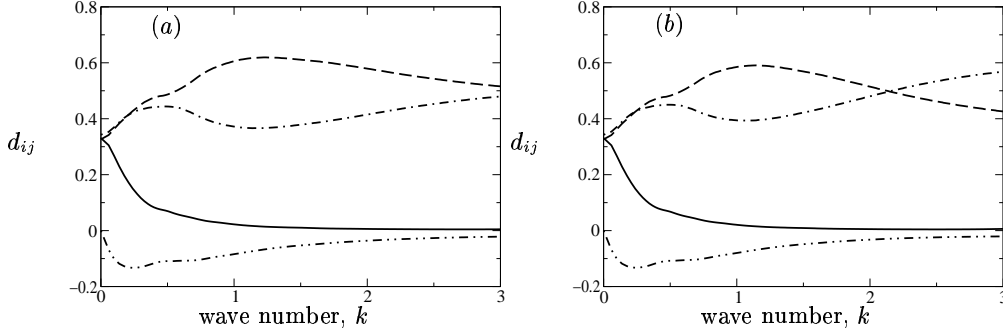


FIGURE 3. Structure anisotropy as measured by d_{ij} (see 5.1) in homogeneous MHD turbulence being sheared in a fixed frame ($\lambda = 0$) for the case with $M = \tau_{\text{shear}}/\tau_m = 0.1$: — d_{11} ; --- d_{22} ; —·— d_{33} ; ··· d_{12} . (a) Case C121 with $R_m = 1$, $N = 10$; (b) Case C1230 with $R_m = 30$, $N = 10$. The induced structural anisotropy is completely determined by the mean shear and is independent of the magnetic Reynolds.

stretch and align the turbulent eddies in the streamwise direction, strong rotation tends to induce columnar structures aligned with the rotation axis, while the action of the Lorentz force tends, through Joule dissipation, to promote long structures aligned with the mean magnetic field. Here, we examine eddy alignment under the combined action of S , Ω and B^{ext} . We first looked at a series of simulations in a fixed frame (zero frame rotation) in an effort to establish the effects of the simultaneous action of the mean shear and the spanwise magnetic field on the turbulence structure. Then we look at these effects in a spanwise rotating frame.

The diagnostic tool used to determine eddy alignment is the structure dimensionality tensor (Kassinis, Reynolds & Rogers, 2001), which for homogeneous turbulence is defined by

$$D_{ij} = \int E(k) \frac{k_i k_j}{k^2} d^3 \mathbf{k} \quad d_{ij} = D_{ij}/D_{kk} \quad D_{kk} = q^2 = 2k. \quad (5.1)$$

Note that each diagonal component of d_{ij} can attain values only between 0 and 1, and that for turbulence in which the energy-containing structures are elongated in the x_α direction, $d_{\alpha\alpha} \rightarrow 0$. On the other hand $d_{\alpha\alpha} \rightarrow 1$ corresponds to structures that are narrow and have strong gradients in the x_α direction.

Figure 3 shows the evolution of the structure dimensionality when $M = \tau_{\text{shear}}/t_m = 0.1$. Two different values of the magnetic Reynolds number ($R_m = 1$ and $R_m = 30$) are considered. In both cases, the magnetic interaction number is $N = 10$. The evolution of the dimensionality anisotropy is dominated by the mean shear and is independent of the R_m . At large times, $d_{11} \approx 0$, indicating a predominance of long streamwise eddies.

The evolution of the dimensionality anisotropy for $M = 20$ is shown in Figure 4. As expected, in this case the external spanwise magnetic field has a strong influence on the development of structure anisotropy. In the case when $R_m = 1$, the turbulence is driven towards a two-dimensional (2D) state corresponding to almost axisymmetric structures aligned with the direction of the magnetic field. Note however that when $R_m = 30$, the magnetic field is less effective in imposing the spanwise eddy alignment. In

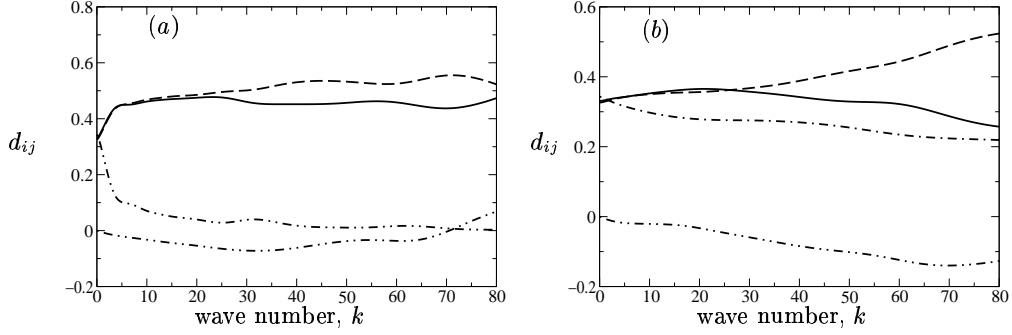


FIGURE 4. Evolution of the normalized dimensionality tensor in homogeneous MHD turbulence being sheared in a fixed frame ($\lambda = 0$) with $M = \tau_{\text{shear}}/\tau_m = 20$: — d_{11} ; ---- d_{22} ; -.- d_{33} ; d_{12} . (a) Case C321 with $R_m = 1$, $N = 10$; (b) Case C3230 with $R_m = 30$, $N = 10$. At low magnetic Reynolds numbers (on the left) the eddies are aligned with the external magnetic field in the spanwise direction. However, at moderately high magnetic Reynolds numbers (on the right) the mean shear is able to induce partial streamwise alignment.

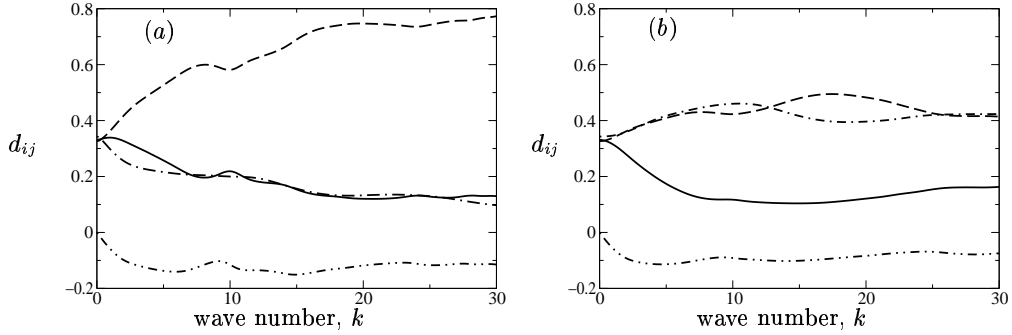


FIGURE 5. Evolution of the normalized dimensionality tensor in homogeneous MHD turbulence being sheared in a fixed frame ($\lambda = 0$) with $M = \tau_{\text{shear}}/t_m = 2$: — d_{11} ; ---- d_{22} ; -.- d_{33} ; d_{12} . (a) Case C221 with $R_m = 1$, $N = 10$ (b) Case C2230 with $R_m = 30$, $N = 10$. At low R_m (on the left) the turbulence structure is characterized by equal elongation in the streamwise and spanwise direction (corresponding to the horizontal sheets of Figure 7a). Thus the magnetic field and the mean shear are equally effective in inducing structural anisotropy. When $R_m = 30$ (on the right), the mean shear dominates and the turbulence is characterized by long streamwise eddies.

fact, at this moderately high R_m the overall dimensionality anisotropy is suppressed as compared to the $R_m = 1$ case. There is also evidence that at large times the mean shear is contributing more effectively in the anisotropy development, and as a result d_{11} and d_{33} seem to decrease at the approximately the same rate. This suggests that initially the structures become elongated in the spanwise direction under the action of the magnetic field. However, as the structures elongate the Joule dissipation becomes less effective, and this allows the shear to induce a streamwise elongation.

A more interesting anisotropy evolution is obtained in the case when $M = 2$, that is when the mean shear time scale is comparable to the Joule time. Figure 5a shows the

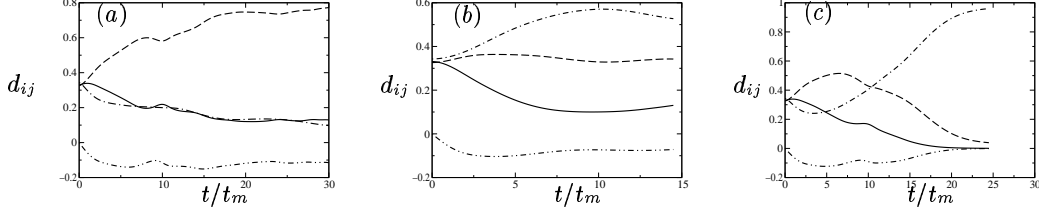


FIGURE 6. Evolution of the normalized dimensionality tensor in homogeneous MHD turbulence being sheared in a rotating frame with $M = \tau_{\text{shear}}/t_m = 2$: — d_{11} ; ---- d_{22} ; -.- d_{33} ; d_{12} . (a) Case C221 with $R_m = 1$, $N = 10$, and $\lambda = 0$ (no rotation); (b) Case C221 with $B = 0$ and $\lambda = 0.25$ (hydrodynamic case); (c) Case C221 with $R_m = 1$, $N = 10$, and $\lambda = 0.25$. In a fixed frame and at low R_m (on the left) the turbulence structure is equally elongated in the streamwise and spanwise direction (corresponding to the horizontal sheets of Figure 7a). In the case of hydrodynamic ($B = 0$) shear in a rotating frame (in the middle) there is preferential alignment of the turbulence eddies with the streamwise direction. When the magnetic field and the frame rotation act simultaneously (on the right), a bifurcation is observed where the structure transitions from a tendency towards horizontal sheets at short times, to vertical sheets at large times (see Figure 7c).

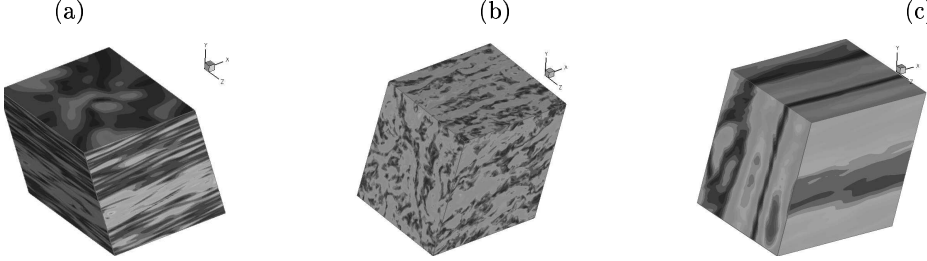


FIGURE 7. Velocity magnitude contours showing the structural anisotropy induced at large times by the combined action of spanwise frame rotation and spanwise mean magnetic field: (a) Case C221 ($M = 2$, $N = 10$, $R_m = 1$) with zero frame rotation. The structure is characterized by horizontal slabs (equal elongation in the streamwise and spanwise direction); (b) Case C221 with frame rotation rate $\lambda = 0.25$ and zero magnetic field (hydrodynamic case). Structures are mostly elongated and aligned with the streamwise direction. Some elongation is observed in the flow normal direction within the plane of the mean shear; (c) Case C221 with both the frame rotation ($\lambda = 0.25$) and the magnetic field being active. The structure is characterized by vertical slabs.

evolution of the dimensionality anisotropy when $R_m = 1$. In this case, $d_{11} \approx d_{33} \rightarrow 0$ suggesting that the mean shear and the external field are equally effective in inducing structural anisotropy. As result, at large times the turbulence is characterized by thin ($d_{22} \rightarrow 1$) horizontal sheets. However, when $R_m = 30$ (Fig. 5b) the mean shear dominates, inducing long, roughly axisymmetric, eddies aligned with the streamwise direction ($d_{11} \rightarrow 0$).

So far we have considered the evolution of structure anisotropy in a fixed frame. Figure 6 shows the development of the normalized dimensionality tensor in the rotating frame for the case $M = 2$, $N = 10$, and at $R_m = 1$. Figure 6a corresponds to 5a and shows that in the fixed frame, the magnetic field and the mean shear are equally effective in inducing two-dimensionality, and as a result the structure evolves towards a

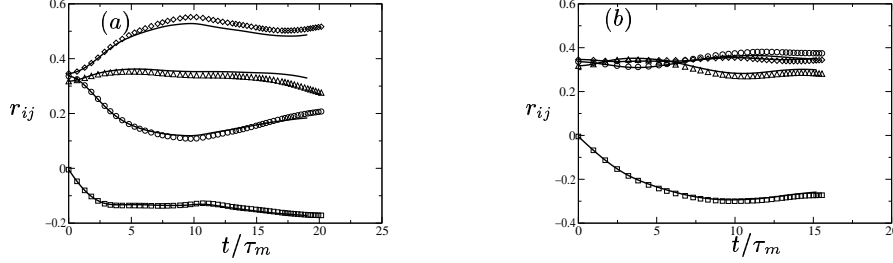


FIGURE 8. Comparison of the predictions of the Quasi-Linear approximation with those of full MHD for the evolution of the Reynolds stress components normalized by the tensor trace. Solid lines are the predictions of the DNS using the QL approximation, and symbols are DNS results for full MHD; \circ r_{11} , \square r_{12} , \diamond r_{22} , \triangle r_{33} . (a) $R_m = 50, N = 10, M = 2, \lambda = 0.75$ and (b) $R_m = 50, N = 10, M = 2, \lambda = 0.25$

state characterized by horizontal sheets (see also Fig. 7a). In a frame rotating about the spanwise axis at a rate $\lambda = 0.25$, and in the absence of an external magnetic field (hydrodynamic case), the structure evolves towards a state characterized by elongated streamwise eddies ($d_{11} \rightarrow 0$), as shown in Fig. 6. Note however, that these eddies tend to be somewhat elongated in the x_2 direction, that is in the flow-normal direction within the frame of the mean shear ($d_{22} < d_{33}$). This flattening of the eddies is also evident in the structure visualization of Fig. 7b. An interesting bifurcation seems to take place in the case when the frame rotation and the external magnetic field act concurrently (Fig. 6c). At short times, the evolution of the normalized dimensionality tensor is similar to the one obtained in the non-rotating case, and reveals a balance between the effects of the mean shear and the external magnetic field. At larger times, however ($\tau/\tau_m \gtrsim 5$) a sudden transition takes place leading eventually to a state characterized by vertical slabs ($d_{11} \approx d_{22} \rightarrow 0$ and $d_{33} \rightarrow 1$). This effect has also been observed in cases C225 and C2210.

5.2. Validity of the Quasi-Linear Approximation

One of the questions that we wanted to answer concerns the range of validity of the Quasi-Linear (QL) approximation (3.7) and (3.8) in the presence of frame rotation and mean shear. Here, we recall that the QL approximation was originally proposed in the context of initially isotropic MHD turbulence (no mean deformation).

We have found that the QL approximation remains in excellent agreement with the full MHD predictions for all the magnetic Reynolds numbers that we have considered, which cover the range $1 \leq R_M \leq 50$. For example, Figure 5.2 shows the evolution of the components of the Reynolds stress tensor normalized by the tensor trace. The predictions of the QL approximation are shown as solid lines and those of the full MHD are shown as symbols. Two different values of λ are considered, and in both cases the QL and the full MHD predictions are in excellent agreement even though the magnetic Reynolds number is relatively high ($R_m = 50$).

5.3. Augmentation of Turbulence in the Counter-Rotating Case

One of the main aims of this work was to establish the effect that the combined action of an external magnetic field, mean shear, and frame rotation can have on the stability of MHD turbulence.

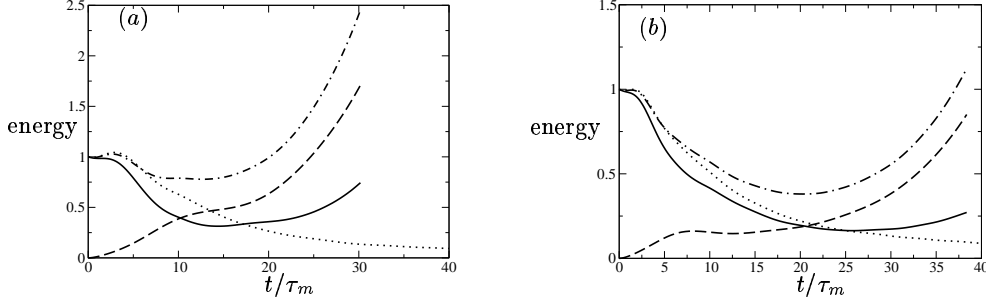


FIGURE 9. Augmentation of shear turbulence in a rotating frame by the imposition of a spanwise magnetic field for the case $R_m = 50$, $N = 10$, $M = 2$: ——— turbulent kinetic energy normalized by its initial value k/k_0 ; ---- magnetic energy normalized by initial turbulent kinetic energy E_b/k_0 ; -·-·- total energy normalized by initial turbulent kinetic energy $(k + E_b)/k_0$; turbulent kinetic energy for the hydrodynamic ($B = 0$) case. (a) $\lambda = 0.75$, and (b) $\lambda = 1.0$.

For the hydrodynamic case, it is well known that frame rotation can act to either suppress or augment turbulence. The parameter that determines which of the two happens is the ratio of the frame rotation rate to the mean shear rate $\lambda = \Omega^f/S$ (see Figure 2). For moderate counter-rotation of the frame relative to the intrinsic shear rotation, ($-0.1 \lesssim \lambda \lesssim 0.51$), the turbulence is augmented as a result of the frame rotation. This is often referred to as the “unstable” regime.

Even though we are still analyzing some of the cases that were simulated during the summer program, we have identified several cases where the presence of the external magnetic field, combined with the rotation of the frame and the mean shear, leads to expansion of the “unstable” regime. We have also identified conditions under which the magnetic fields seems to have little if any effect on the stability of the rotating shear flow.

All the cases where the magnetic field was found to lead to augmentation of the turbulence lie on the left of the bifurcation envelope. That is they correspond to cases where the frame counter rotates at a rate that is equal or larger than the rotation rate associated with the mean shear (see Figure 2). In all cases the external magnetic field was in the spanwise direction. On the contrary, preliminary results of cases involving a streamwise external magnetic field and spanwise frame rotation failed to show a strong effect on the stability of turbulent shear flow.

The effect of an imposed spawise magnetic field on the time histories of the turbulent magnetic and kinetic energies is shown in Figure 9 for two different values of λ . Both values of λ are high enough, that in the hydrodynamic case a suppression of the turbulence is observed as evidenced both by the decay of k in time, and also by the fact that $P/\epsilon < 1$. In the magnetohydrodynamic cases, after an initial transient, both the turbulent kinetic energy k and the turbulent magnetic energy E_b grow exponentially in time. In fact, at larger times, the magnetic energy exceeds the kinetic energy: $E_b > k$.

The evolution of the ratio of the production of the turbulent kinetic energy to its dissipation rate is shown in Figure 10. In the hydrodynamic case, $P/\epsilon < 1$ at large times indicating that the turbulence is suppressed a result of the strong counter-rotation of the frame. However, when the spanwise magnetic field is present, $P/\epsilon > 1$ at large times, indicating that the turbulent kinetic energy is augmented as a result of the combined effects of the Ω^f and B .

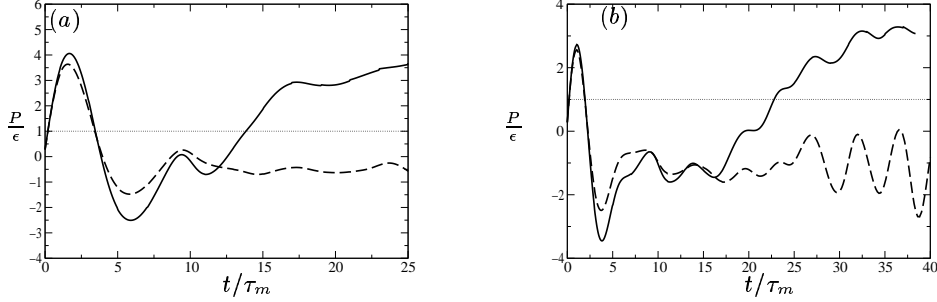


FIGURE 10. Augmentation of shear turbulence in a rotating frame by the imposition of a spanwise magnetic field for the case $R_m = 50, N = 10, M = 2$: — production over dissipation (P/ϵ) for the MHD case; ---- production over dissipation (P/ϵ) for the hydrodynamic ($B = 0$) case; (a) $\lambda = 0.75$, and (b) $\lambda = 1.0$.

5.4. Scale Dependence of Anisotropy

The scale dependence of anisotropy in incompressible MHD turbulence at moderate magnetic Reynolds numbers remains an open question. For compressible turbulence at high magnetic Reynolds numbers, Cho and Lazarian (2003) have found that Alfvén mode velocity fluctuations show a strong scale dependence, with the small scales being more anisotropic than the larger ones.

We have attempted to obtain a scale dependent measure of anisotropy using the spectra of the turbulence structure dimensionality tensor (Kassinos, Reynolds & Rogers, 2001). Thus we define

$$d_{ij}(k) = \sum_{\text{shell}} E(k) \frac{k_i k_j}{k^2} / \sum_{\text{shell}} E(k) \quad d_{ii}(k) = 1, \quad (5.2)$$

where the summation in (5.2) is over shells in Fourier space. For turbulence that is isotropic at the scale set by k we have $d_{ij}(k) = \delta_{ij}/3$. For turbulence that it is two-dimensional (2D) independent of direction x_α , $d_{\alpha\alpha}(k) = 0$.

Figure 11 shows the anisotropy levels obtained for two cases with frame rotation (C2250 with $\lambda = 0.75$ and C2250 with $\lambda = 1.0$). Variations at very low wavenumbers are spurious and attributed to limited sample. On the other end of the spectrum, variations beyond $k \approx 128$ are again contaminated by the progressive loss of modes that extend beyond the limits of the computational box (for these 256^3 simulations). In the intermediate range that lies between these limits, anisotropy as measured by $d_{ij}(k)$ seems to exhibit a weak increase with wave number, especially in the flow-normal directions. This trend is suggestive of the observations of Cho and Lazarian (2003) in compressible MHD turbulence at high R_m . Cases with low R_m did not seem to exhibit this increase of anisotropy with decreasing scale, but a more careful analysis for our results is needed in order to establish a possible Reynolds number dependence. Both cases correspond to $M = 2$, that is the time scale associated with the mean shear is twice as large as the time scale associated with the diffusion of the magnetic field. Yet, in both cases, $d_{11}(k) \approx 0$ for the entire range of wave numbers over which results are meaningful. Thus at these relatively high R_m , the mean shear seems to determine the overall structural anisotropy when the two time scales are comparable. Because of the limited size of the computational box, we were unable to adequately answer the question of anisotropy at small scales. We plan to carry

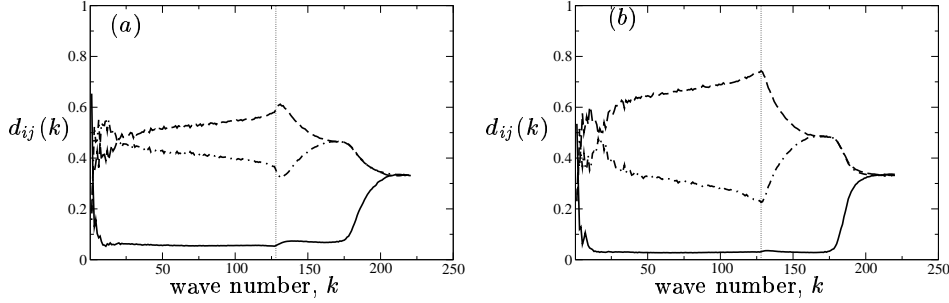


FIGURE 11. Scale dependence of anisotropy as measured by $d_{ij}(k)$ (see 5.2) in homogeneous MHD turbulence being sheared in a rotating frame: — $d_{11}(k)$; --- $d_{22}(k)$; -.- $d_{33}(k)$. (a) Case C2250 ($R_m = 50$, $N = 10$, $M = 2$) with $\lambda = 0.75$ and $t/t_m = 31.7$, and (b) Case C2250 ($R_m = 50$, $N = 10$, $M = 2$) with $\lambda = 1.0$ and $t/t_m = 38.0$.

a series of 512³ simulations in order to address that question more thoroughly. We also hope that these higher-resolution simulations will allow us to clarify the slight increase of anisotropy that was observed in the cases discussed above.

6. Conclusions and future plans

We have used direct numerical simulations to examine the dynamics of homogeneous MHD turbulence subjected to mean shear in fixed and rotating frames. We have found that the most interesting dynamics is observed when the time scale of the mean shear is comparable to that of the applied magnetic field. In this regime, the magnetic field and the mean shear exert competing influences on the structure of the turbulence and relatively small variations in the governing parameters seem to lead to markedly different evolving states.

One particularly significant result concerns the combined effects of the mean magnetic field and the frame rotation on the evolution of the turbulent kinetic energy. We have found that at sufficiently high magnetic Reynolds numbers, $R_m \gtrsim 40$, the application of a spanwise magnetic field leads to augmentation of the turbulence even for cases where in absence of the magnetic field the turbulence is suppressed as a result of the frame rotation. We have observed this effect for cases where the frame is counter-rotating relative to the intrinsic rotation associated with the shear, and for values of the ratio of the frame rotation rate to the shear rate beyond $\eta \approx 0.51$, the limit which marks the onset of suppression of the turbulence as η is increased. In these flows, it was found that the magnetic field energy, which initially is zero, grows and quickly surpasses the turbulent kinetic energy. No such augmentation of the turbulence was observed for cases where the frame is co-rotating with the shear. Preliminary runs where the magnetic field was aligned with the streamwise direction also failed to exhibit such a strong augmentation of the turbulence as a result of the presence of the field.

We have also examined the range of validity of the Quasi-Linear (QL) approximation that was introduced by Kassinos *et al.* in the 2002 CTR Summer Program. The QL approximation was originally evaluated only in the absence of mean deformation. We have found that the predictions of the QL approximation were in excellent agreement with those of the full MHD, for all the magnetic Reynolds numbers we have considered

(up to $R_m = 50$). Other dimensionless parameters, such as the ratio of the shear time scale to the time scale for magnetic diffusion, seem to have little effect on the validity of the approximation.

During the summer program we have generated a substantial amount of data. In the coming months, we plan to analyze this more carefully in order to identify mechanisms and effects that we want to examine more closely. To understand such effects we plan a series of higher resolution runs. We hope this work will lead to an improved fundamental understanding of the combined effects of mean shear, frame rotation and magnetic fields on MHD turbulence. We plan to use this understanding for the development of improved structure-based models of MHD shear turbulence. A deeper understanding of the mechanisms that lead to instability and anisotropy in these flows is also important in the study of accretion in stellar disks and in engineering applications such as magnetogasdynamics.

REFERENCES

- CHO, J. & LAZARIAN, A. 2003 Compressible magnetohydrodynamic turbulence: mode coupling scaling relations, anisotropy, viscosity-damped regime and astrophysical implications. *Monthly Not. Royal Astron. Soc.*, **345**, 325-339.
- KASSINOS, S. C. & REYNOLDS, W. C. 1999 Structure-based modeling for homogeneous MHD turbulence. *Annual Research Briefs*, Center for Turbulence Research, NASA Ames/Stanford Univ., 301-315.
- KASSINOS, S. C., KNAEPEN, B. & CARATI, D. MHD turbulence at moderate magnetic Reynolds number. *Proceedings for the 2002 Summer Program*, Center of Turbulence Research, Stanford/NASA Ames.
- KASSINOS, S.C. REYNOLDS, W.C. & M. M. ROGERS 2001 One-point turbulence structure tensors. *J. Fluid Mech.*, 428, 213-248.
- KASSINOS, S. C. & REYNOLDS, W. C. DNS and Structure-Based Modeling of Rotated Homogeneous Shear Flows. *Proceedings of the Third International Symposium on Turbulence and Shear Flow Phenomena*, Sandai, Japan, June 2003.
- KNAEPEN, B., KASSINOS, S.C., & CARATI, D. 2004 MHD turbulence at moderate magnetic Reynolds number. *J. Fluid Mech.*, (in press).
- MOFFATT, H.K. 1967 On the suppression of turbulence by a uniform magnetic field. *J. Fluid Mech.* **28**, 571-592.
- ROBERTS, P. H. 1967 *An Introduction to Magnetohydrodynamics*. Elsevier, New York.
- ROGALLO, R.S. 1981 Numerical experiments in homogeneous turbulence.

On the transition from two-dimensional to three-dimensional MHD turbulence

By A. Thess [†] and Oleg Zikanov [‡]

We report a theoretical investigation of the robustness of two-dimensional inviscid MHD flows at low magnetic Reynolds numbers with respect to three-dimensional perturbations. We analyze three model problems, namely the flow in the interior of a triaxial ellipsoid, an unbounded vortex with elliptical streamlines, and a vortex sheet parallel to the magnetic field. We demonstrate that motion perpendicular to the magnetic field with elliptical streamlines becomes unstable with respect to the elliptical instability once the velocity has reached a critical magnitude whose value tends to zero as the eccentricity of the streamlines becomes large. Furthermore, vortex sheets parallel to the magnetic field, which are unstable for any velocity and any magnetic field, are found to emit eddies with vorticity perpendicular to the magnetic field and with an aspect ratio proportional to $N^{1/2}$. The results suggest that purely two-dimensional motion without Joule energy dissipation is a singular type of flow which does not represent the asymptotic behavior of three-dimensional MHD turbulence in the limit of infinitely strong magnetic fields.

1. Introduction

Turbulent flows of liquid metals influenced by magnetic fields occur under a wide range of circumstances, ranging from metallurgy (Davidson 1999) and fundamental turbulence research (Tsinober 2001; Moresco & Alboussiere 2004) to the movement of the Earth's inner core (Moffatt 1978). It is widely believed that when the magnetic Reynolds number $Rm = \mu_0 \sigma U L$ is small, and the magnetic field is sufficiently strong, homogeneous MHD-turbulence becomes purely two-dimensional and the electromagnetic dissipation of kinetic energy vanishes. The purpose of the present work is to demonstrate that this belief often contradicts to reality, and that homogeneous MHD-turbulence may differ strongly from purely two-dimensional turbulence even when the magnetic field tends to infinity.

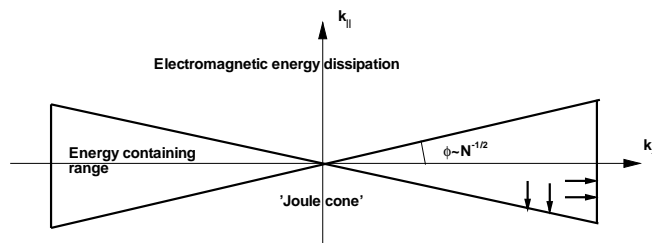
When an incompressible fluid with density ρ , kinematic viscosity ν , electrical conductivity σ , and permeability μ_0 moves with velocity U and characteristic length scale L in a uniform magnetic field B , and when $Rm \ll 1$, the state of the flow is characterized by the Reynolds number and the electromagnetic interaction parameter defined as

$$Re = \frac{UL}{\nu}, \quad N = \frac{\sigma B^2 L}{\rho U}. \quad (1.1)$$

We are interested in fully developed turbulence ($Re \rightarrow \infty$) far away from walls under a strong magnetic field $N \gg 1$. It has been established by Moffatt (1967) (see also Davidson 1997) and confirmed experimentally by Alemany *et al* (1979) and numerically by Schumann (1976), Zikanov & Thess (1998), Knaepen & Moin (2004) that the turbulent flow tends to become two-dimensional so as to avoid electromagnetic (Joule) dissipation. Sommeria & Moreau (1982), who identified the importance of walls perpendicular to the

[†] Ilmenau University of Technology

[‡] University of Michigan - Dearborn

FIGURE 1. Wavenumber distribution of kinetic energy at $N \gg 1$.

magnetic field, have aptly summarized our conceptual understanding of MHD turbulence at $N \gg 1$ by characterizing the distribution of kinetic energy among the wavenumbers k_{\perp} and k_{\parallel} perpendicular and parallel to the magnetic field, respectively. This distribution of kinetic energy in the state of so called “quasi-two-dimensional turbulence” is sketched in figure 1. For $N \gg 1$ the kinetic energy of the flow is confined to a narrow region in the wavenumber space, outside the “Joule cone” in which electromagnetic energy dissipation takes place and below those wavenumbers k_{\perp} for which viscous dissipation dominates. The angle $\varphi \sim N^{-1/2}$ of the energy containing region shrinks to zero as $N \rightarrow \infty$. This picture has tempted researchers to assume that for sufficiently strong magnetic field quasi-two-dimensional MHD turbulence becomes purely two-dimensional and the Joule energy dissipation vanishes.

However, there have been strong experimental and numerical indications which suggest that this hypothesis is unlikely to be correct. In their experiments on freely decaying homogeneous MHD turbulence in mercury Alemany *et al.* (1979) and Caperan & Alemany (1985) found that velocity fluctuations parallel to the applied magnetic field and strong Joule dissipation persisted even at high interaction parameters. Disagreements between drag measurements of MHD flows in channels with very large aspect ratios (low influence of Hartmann walls) (Tsinober 1990) and purely two-dimensional numerical simulations of turbulent channel flow by Jimenez (1990) further support the view that quasi-two-dimensional turbulence may never become purely-two-dimensional. Direct numerical simulations of forced MHD turbulence by Zikanov & Thess (1998) indicated that two-dimensional vortices, once they have formed, may undergo violent three-dimensional instabilities resulting in an intermittent behavior. Finally, numerical simulations of MHD turbulence subject to a two-dimensional forcing, which have been carried out by Nakauchi *et al.* (1992) using an EDQNM model, have provided evidence that even for very high values of the interaction parameter and strong non-isotropy of the flow, the Joule energy dissipation of the flow tends to a nonzero finite value.

The foregoing observations lead us to the conclusion that purely two-dimensional turbulence with zero Joule dissipation is a singular state which may never be reached in MHD, similarly as ordinary hydrodynamic turbulence in the limit of vanishing viscosity will never come close to a state of zero viscous dissipation. We may formulate the following hypothesis: When an electrically conducting fluid is in the state of fully developed turbulence ($\nu \rightarrow 0$) the Joule dissipation of kinetic energy will remain finite as $B \rightarrow \infty$.

In this paper we investigate the singular character of purely two-dimensional turbulence using stability analysis of model problems. We shall demonstrate that for arbitrarily strong magnetic fields a two-dimensional inviscid flow has always access to a sufficient number of unstable degrees of freedom to escape from purely two-dimensional behavior.

2. A didactical model for the instability of purely two-dimensional MHD flow

2.1. An exact solution for inviscid MHD flow in a triaxial ellipsoid

Consider an inviscid electrically conducting incompressible fluid which is confined to the interior of the triaxial ellipsoid

$$\frac{x^2}{a^2} + \frac{y^2}{b^2} + \frac{z^2}{c^2} = 1 \quad (2.1)$$

and subjected to the influence of a homogeneous magnetic field $\mathbf{B} = B\mathbf{e}_z$. If the magnetic Reynolds number is small, the dynamics of the flow is governed by the equations

$$\frac{\partial \mathbf{v}}{\partial t} + (\mathbf{v} \cdot \nabla) \mathbf{v} = -\frac{1}{\rho} \nabla p + \frac{1}{\rho} \mathbf{J} \times \mathbf{B}, \quad \nabla \cdot \mathbf{v} = 0 \quad (2.2)$$

$$\mathbf{J} = \sigma(-\nabla \phi + \mathbf{v} \times \mathbf{B}), \quad \nabla \cdot \mathbf{J} = 0 \quad (2.3)$$

where \mathbf{J} is the electric current density and ϕ the electric potential (Roberts 1967; Moreau 1990; Davidson 2001). The equations are supplemented by the boundary conditions at impermeable electrically insulating walls of the ellipsoid

$$\mathbf{v} \cdot \mathbf{n} = \mathbf{J} \cdot \mathbf{n} = 0. \quad (2.4)$$

If there is no magnetic field, there exists a family of three-dimensional time-dependent exact solutions of the Euler equations

$$\mathbf{v}(x, y, z, t) = U(t) \left[y \frac{c}{b} \mathbf{e}_z - z \frac{b}{c} \mathbf{e}_y \right] + V(t) \left[z \frac{a}{c} \mathbf{e}_x - x \frac{c}{a} \mathbf{e}_z \right] + W(t) \left[x \frac{b}{a} \mathbf{e}_y - y \frac{a}{b} \mathbf{e}_x \right], \quad (2.5)$$

where (U, V, W) satisfy the nonlinear ordinary differential equations, which are mathematically identical to the equations describing the free rotation of a solid body (Kerswell 2002). The velocity field described by (2.5) automatically satisfies the incompressibility constraint, the free-slip condition, and is a superposition of three basic two-dimensional flows. Each of them has elliptical streamlines and a spatially uniform vorticity directed along the axis of the ellipsoid which is perpendicular to the plane of motion.

We extend the existing theory to the case when a magnetic field is present by expressing the electric current density in the form

$$\mathbf{J}(x, y, z, t) = I(t) \left[y \frac{c}{b} \mathbf{e}_z - z \frac{b}{c} \mathbf{e}_y \right] + J(t) \left[z \frac{a}{c} \mathbf{e}_x - x \frac{c}{a} \mathbf{e}_z \right] + K(t) \left[x \frac{b}{a} \mathbf{e}_y - y \frac{a}{b} \mathbf{e}_x \right] \quad (2.6)$$

which satisfies the condition $\nabla \cdot \mathbf{J} = 0$ as well as the boundary condition. The coefficients I, J, K describe the strength of eddy currents induced by the movement of the fluid in the magnetic field. Taking the curl of Ohm's law (2.3) we obtain, after some algebra, $I = \sigma B V a b / (b^2 + c^2)$, $J = -\sigma B U a b / (a^2 + c^2)$, $K = 0$. The vorticity $\boldsymbol{\Omega} = \nabla \times \mathbf{v}$ corresponding to the velocity field (2.5)

$$\boldsymbol{\Omega} = U(t) \left(\frac{b}{c} + \frac{c}{b} \right) \mathbf{e}_x + V(t) \left(\frac{a}{c} + \frac{c}{a} \right) \mathbf{e}_y + W(t) \left(\frac{a}{b} + \frac{b}{a} \right) \mathbf{e}_z \quad (2.7)$$

satisfies exactly the vorticity equation

$$\frac{\partial \boldsymbol{\Omega}}{\partial t} = (\boldsymbol{\Omega} \cdot \nabla) \mathbf{v} + \frac{1}{\rho} \nabla \times (\mathbf{J} \times \mathbf{B}), \quad (2.8)$$

provided that the coefficients U, V, W obey the equations

$$(b^2 + c^2)\dot{U} = (b^2 - c^2)VW - \frac{\sigma B^2}{\rho} \left(\frac{a^2 b^2}{a^2 + c^2} \right) U \quad (2.9)$$

$$(c^2 + a^2)\dot{V} = (c^2 - a^2)UW - \frac{\sigma B^2}{\rho} \left(\frac{a^2 b^2}{b^2 + c^2} \right) V \quad (2.10)$$

$$(a^2 + b^2)\dot{W} = (a^2 - b^2)UV \quad (2.11)$$

It should be emphasized that the derivation of this system from the governing equations (2.2) and (2.3) did not involve any approximation.

The system (2.9)-(2.11) can be made nondimensional by introducing dimensionless variables according to $(U, V, W) = \alpha(U_*, V_*, W_*)$ and $t = t_*/\alpha$ where $\alpha = (\sigma B^2/\rho)a^2 b^2/[(a^2 + c^2)(b^2 + c^2)]$ is the inverse of the Joule decay time. Using the abbreviations $A = a/c$ and $B = b/c$ and dropping the asterisk the equations become

$$\dot{U} = \frac{B^2 - 1}{B^2 + 1} VW - U \quad (2.12)$$

$$\dot{V} = \frac{1 - A^2}{1 + A^2} UW - V \quad (2.13)$$

$$\dot{W} = \frac{A^2 - B^2}{A^2 + B^2} UV \quad (2.14)$$

This nonlinear system has a number of remarkable properties. The nonlinear terms conserve the total kinetic energy and the total angular momentum

$$E = \frac{1}{2} [(1 + B^2)U^2 + (1 + A^2)V^2 + (A^2 + B^2)W^2] \quad (2.15)$$

$$L = (1 + B^2)^2 U^2 + (1 + A^2)^2 V^2 + (A^2 + B^2)^2 W^2 \quad (2.16)$$

The magnetic field gives rise to an anisotropic damping, embodied in the linear dissipative terms on the right-hand-side of equations (2.12) and (2.13). The total kinetic energy obeys

$$\frac{dE}{dt} = -\epsilon \quad (2.17)$$

where $\epsilon = (1 + B^2)U^2 + (1 + A^2)V^2$ is the rate of Joule dissipation. As a result, the kinetic energy of the flow will always decay unless it is in a purely two-dimensional motion perpendicular to the magnetic field ($U = V = 0, W \neq 0$). Observe that the electromagnetic interaction parameter N (cf. equation (1.1)) does not appear in the system because we have used the Joule timescale α^{-1} to nondimensionalize the velocity. Instead, the values of U, V , and W represent the order of magnitude of N .

2.2. Linear stability of steady states

Equations (2.12)-(2.14) admit a steady solution $(U, V, W) = (0, 0, W_0)$ describing two-dimensional motion perpendicular to the magnetic field. We analyze the linear stability of this solution by solving the equations for infinitesimal perturbations (ξ, η, ζ)

$$\dot{\xi} = -\xi + \left(\frac{B^2 - 1}{B^2 + 1} W_0 \right) \eta \quad (2.18)$$

$$\dot{\eta} = \left(\frac{1 - A^2}{1 + A^2} W_0 \right) \xi - \eta \quad (2.19)$$

$$\dot{\zeta} = 0. \quad (2.20)$$

The solvability condition yields the growth rates λ in the form

$$\lambda_{1/2} = \pm W_0 \sqrt{\frac{(A^2 - 1)(1 - B^2)}{(A^2 + 1)(1 + B^2)}} - 1, \quad \lambda_3 = 0 \quad (2.21)$$

Instability occurs when $A > 1, B < 1$ or $A < 1, B > 1$, i.e. when the magnetic field is parallel to the middle axis of the ellipsoid and the W -component exceeds the critical value

$$W_c = \sqrt{\frac{(A^2 + 1)(1 + B^2)}{(A^2 - 1)(1 - B^2)}} \text{ or, in dimensional form, } W_c^{dim} = \frac{\sigma B^2}{\rho} \sqrt{\frac{(a^2 + c^2)(c^2 + b^2)}{(a^2 - c^2)(c^2 - b^2)}} \quad (2.22)$$

When $a \rightarrow \infty$ and $b \rightarrow 0$ we have $W_c \rightarrow 1$ and $W_c^{dim} \rightarrow \sigma B^2 / \rho$ which implies that a very elongated sheet-like structure becomes unstable when the interaction parameter defined as $N = \sigma B^2 / \rho W$ is smaller than $N_c = 1$.

The instability that we have identified in this particular MHD problem is the elliptical instability, widely known in ordinary hydrodynamics as a fundamental mechanism for the transition to turbulence (see, e.g., Kerswell 2002). It is generated by parametric resonance between Kelvin waves, coming from the homogeneously rotating part of the velocity field, and the strain field, being a result of the elliptical shape of the streamlines. We have just shown that a magnetic field can damp but not completely suppress this instability.

2.3. Nonlinear dynamics and the singular character of purely two-dimensional motion

We now analyze the nonlinear evolution of the system focusing the attention on the case where the initial state is an almost two-dimensional flow characterized by $U(0) \ll W(0)$ and $V(0) \ll W(0)$. Solution of (2.12)-(2.14) for $A = 2$ and $B = 0.5$ shows that as long as $W(0) < W_c = 5/3$, the system always relaxes to a purely two-dimensional state ($U = 0, V = 0, W < W_c$). Figure 2 shows that the evolution from an initial condition with $W(0) > W_c$ proceeds in a quite different way. Although the system finally settles at a purely two-dimensional state, the evolution towards this state is characterized by long periods of nearly two-dimensional motion, occasionally interrupted by violent three-dimensional transients. During these transients kinetic energy is fed from the nondissipative two-dimensional mode W to the three-dimensional modes U and V as can be seen in figure 2c. The transients lead to significant Joule dissipation of kinetic energy as illustrated in figures 2b and 2d. Decay of initially almost two-dimensional MHD flow is accompanied by strong divergence from two-dimensionality due to the action of the elliptical instability.

The singular character of purely two-dimensional evolution is further illustrated by extending our model so as to include a phenomenological forcing term, which corresponds to application of an external torque in the z -direction. Equation (2.14) is replaced by

$$\dot{W} = \frac{A^2 - B^2}{A^2 + B^2} UV + 1 \quad (2.23)$$

The new model admits an exact two-dimensional solution

$$U = 0, \quad V = 0, \quad W = t \quad (2.24)$$

whose kinetic energy grows monotonically with time and whose Joule dissipation is zero. However, the numerical solution computed from a weakly three-dimensional initial condition shows a completely different behavior. The flow corresponding to the numerical

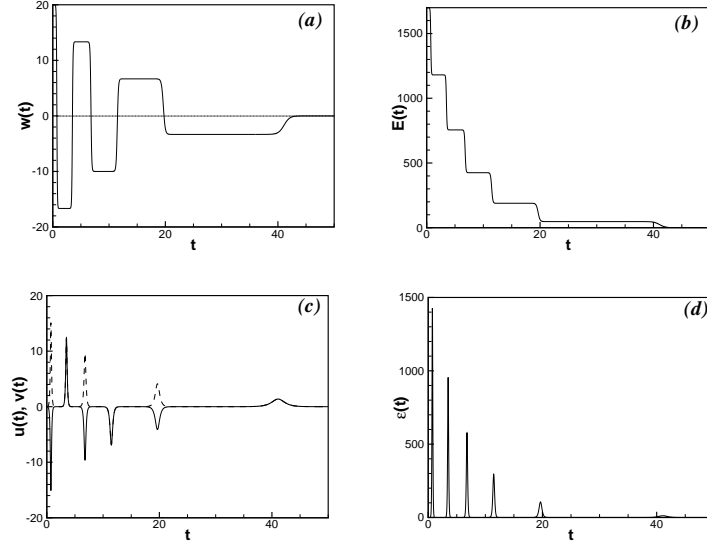


FIGURE 2. Decaying solution of (2.12-2.14). (a), Two-dimensional component $W(t)$. (b), Total kinetic energy (2.15). (c), Three-dimensional components $U(t)$ (solid line) and $V(t)$ (dashed line). (d), Rate of Joule dissipation ϵ .

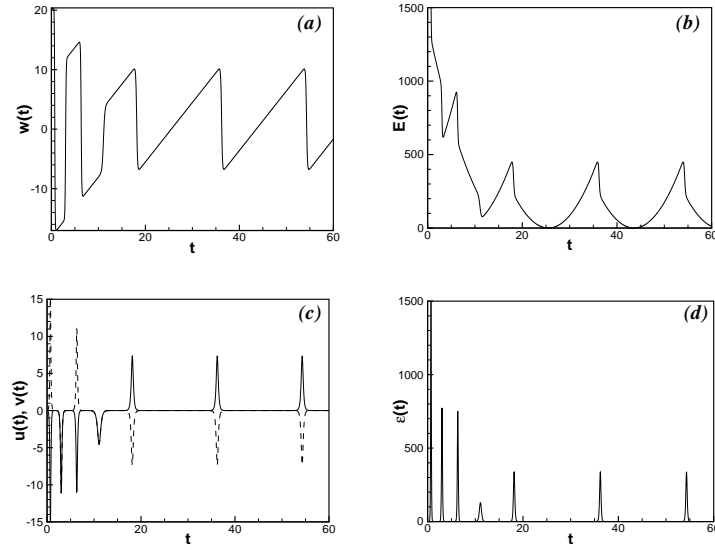


FIGURE 3. As in Figure 2 but for forced system (2.12, 2.13, 2.23).

solution shown in figure 3 is periodic in time and involves long lasting periods of two-dimensional motion interrupted by short three-dimensional excursions. Most importantly, the flow is "statistically" steady in that the time-averaged kinetic energy does not change and the mean Joule dissipation is finite. The flow is therefore neither mathematically nor physically close to the two-dimensional behavior suggested by the exact solution (2.24).

Although our simple model is only a caricature of the behaviour of real MHD turbulence, it allows us to draw a number of conclusions which serve as a guideline for the investigation of the full problem. In particular, we have learned

- that a purely two-dimensional MHD flow is prone to the elliptical instability,
- that the nonlinear three-dimensional evolution of the elliptical instability effectively extracts kinetic energy from the system on account of Joule dissipation,
- that an initially nearly two-dimensional flow does not necessarily stay close to purely two-dimensional evolution.

3. Instability in two-dimensional turbulence in a strong magnetic field

For further analysis it is convenient to rewrite (2.2) and (2.3) as (Roberts 1967)

$$\frac{\partial \mathbf{v}}{\partial t} + (\mathbf{v} \cdot \nabla) \mathbf{v} = -\frac{1}{\rho} \nabla p - \frac{\sigma B^2}{\rho} \Delta^{-1} \frac{\partial^2 \mathbf{v}}{\partial z^2}, \quad \nabla \cdot \mathbf{v} = 0. \quad (3.1)$$

We are interested in the stability of two-dimensional flows for which the Joule dissipation vanishes. The most general flow of this type is of the form

$$\mathbf{v}(x, y, t) = \mathbf{U}(x, y, t) + W(x, y, t) \mathbf{e}_z \quad (3.2)$$

where \mathbf{U} has the properties $\mathbf{U} \cdot \mathbf{e}_z = 0$, $\nabla \cdot \mathbf{U} = 0$ and \mathbf{U} and W are solutions of

$$\frac{\partial \mathbf{U}}{\partial t} + (\mathbf{U} \cdot \nabla) \mathbf{U} = -\frac{1}{\rho} \nabla P, \quad \frac{\partial W}{\partial t} + (\mathbf{U} \cdot \nabla) W = 0 \quad (3.3)$$

The two terms in (3.2) describe the superposition of a two-dimensional motion perpendicular to the magnetic field with a motion parallel to the magnetic field.

Our hypothesis formulated in section 1 implies that the solution (3.2) of equation (3.1) is always unstable in the sense that for any initial condition containing a weak three-dimensional perturbation the solution will diverge from the two-dimensional one and evolve towards a solution with nonzero mean Joule dissipation no matter how strong the magnetic field is. A rigorous proof of this assertion is a formidable task, as it would require consideration of the initial value problem (3.1) for all admissible fields \mathbf{U} and \mathbf{V} . We shall simplify the task considerably by considering two families of structures which we believe are representative of the solutions to (3.3) namely, columnar vortices with elliptical streamlines and vortex sheets whose velocity is parallel to the direction of the magnetic field.

3.1. Instability of motion perpendicular to the magnetic field

We consider an unbounded strained vortex described by

$$\mathbf{U}(x, y) = -\Omega E y \mathbf{e}_x + \Omega E^{-1} x \mathbf{e}_y \quad (3.4)$$

When the eccentricity $E = 1$, the flow is a solid body rotation around the axis of the magnetic field with vorticity 2Ω . When $E > 1$, the flow has a uniform strain and its streamlines are ellipses with semi-axes $a = \sqrt{E}$ and $b = 1/\sqrt{E}$. We extend the analysis of Bayly (1986) and Waleffe (1990) to the magnetic case by perturbing the basic flow (3.4) according to $\mathbf{v} = \mathbf{U} + \mathbf{u}$. Linearizing (3.1) with respect to the perturbation we obtain

$$\frac{\partial \mathbf{u}}{\partial t} + (\mathbf{U} \cdot \nabla) \mathbf{u} + (\mathbf{u} \cdot \nabla) \mathbf{U} = -\frac{1}{\rho} \nabla p - \alpha \Delta^{-1} \frac{\partial^2 \mathbf{u}}{\partial z^2}, \quad \nabla \cdot \mathbf{u} = 0. \quad (3.5)$$

where $\alpha = \sigma B^2 / \rho$. This system admits solutions of the form

$$\{\mathbf{u}, p\} = \{\hat{\mathbf{u}}, \hat{p}\}(t) \cdot \exp \left[i\mathbf{k}(t) \cdot \mathbf{x} - \alpha \int_{t_0}^t \frac{k_z^2(t')}{k^2(t')} dt' \right] \quad (3.6)$$

Inserting (3.6) into (3.5) we obtain equations identical to those for the nonmagnetic problem solved by Bayly (1986) and Waleffe (1990).

$$\dot{\hat{u}}_j + i\hat{k}_l x_l \hat{u}_j + i\hat{k}_m A_{ml} x_l \hat{u}_j + A_{jl} \hat{u}_l = -i\hat{k}_j \hat{p}, \quad k_j \hat{u}_j = 0, \quad (3.7)$$

where $A_{12} = -\Omega E$, $A_{21} = \Omega/E$ and $A_{ij} = 0$ otherwise. The solution includes the wavenumber vector \mathbf{k} rotating around the axis of the vortex as

$$\mathbf{k}(t) = k_0 [\sin \theta \cos \phi(t), E \sin \theta \sin \phi(t), \cos \theta] \quad (3.8)$$

where $\phi(t) = \Omega(t - t_0)$, and the Floquet solution $\hat{\mathbf{u}}(t) = e^{\lambda t} \mathbf{w}[\phi(t)]$, where \mathbf{w} is a 2π -periodic function and the growth rate is

$$\lambda(\Omega, E, \theta) = \frac{\Omega}{2\pi} \ln[\mu(E, \theta)]. \quad (3.9)$$

Here, μ are eigenvalues of an auxiliary eigenvalue problem. The amplitude of perturbations is

$$|\mathbf{u}(t)| = |\mathbf{w}(t)| \cdot \exp[F(t)] \quad (3.10)$$

with

$$F(t) = \lambda(E, \theta, \Omega)t - \alpha \int_{t_0}^t \frac{\cos^2 \theta dt'}{\sin^2 \theta \cos^2 \Omega(t' - t'_0) + E \sin^2 \theta \cos^2 \Omega(t' - t'_0) + \cos^2 \theta}. \quad (3.11)$$

The second term in the right-hand-side is the only correction to the non-magnetic solution. Reverting to dimensionless time $\phi = \Omega(t - t_0)$ and using a magnetic interaction parameter defined by

$$N = \alpha / \Omega = \sigma B^2 / \rho \Omega \quad (3.12)$$

we can express F as

$$F(\phi) = \frac{\phi}{2\pi} \ln[\mu(E, \theta)] - N \int_0^\phi \frac{d\phi'}{1 + \tan^2 \theta [\cos^2 \phi' + E \sin^2 \phi']}. \quad (3.13)$$

The system is unstable if F increases over one period, i.e. $F(2\pi) - F(0) > 0$, it is stable if $F(2\pi) - F(0) < 0$ and the condition for neutral stability is therefore $F(2\pi) - F(0) = 0$. From the last condition we obtain the desired expression for the neutral surface as

$$N(E, \theta) = \ln[\mu(E, \theta)] \cdot \left\{ \int_0^{2\pi} \frac{d\phi}{1 + \tan^2 \theta [\cos^2 \phi + E \sin^2 \phi]} \right\}^{-1} \quad (3.14)$$

Figure 4a shows the numerically computed values of (3.14). For $E = 1$ we have $N = 0$ indicating that a vortex with circular stream lines is always stable. The modes take the form of Kelvin waves which rotate about the magnetic field with a frequency $2\Omega \cos \theta$ (see e.g. Greenspan 1968). At $E > 1$, the flow becomes unstable with respect to perturbations located within a band $\theta_-(E) \leq \theta \leq \theta_+(E)$. Notice that the location of this unstable band is the same as in the nonmagnetic problem since it is determined by the zeros of $\ln[\mu(E, \theta)]$. In particular, this band originates at $\theta = \pi/3$ (Bayly 1986). For a given value of $E > 1$ the maximum of $N(E, \theta)$ over all θ in the unstable band defines the critical magnetic interaction parameter $N_c(E)$ and a critical angle $\theta_c(E)$. These quantities are

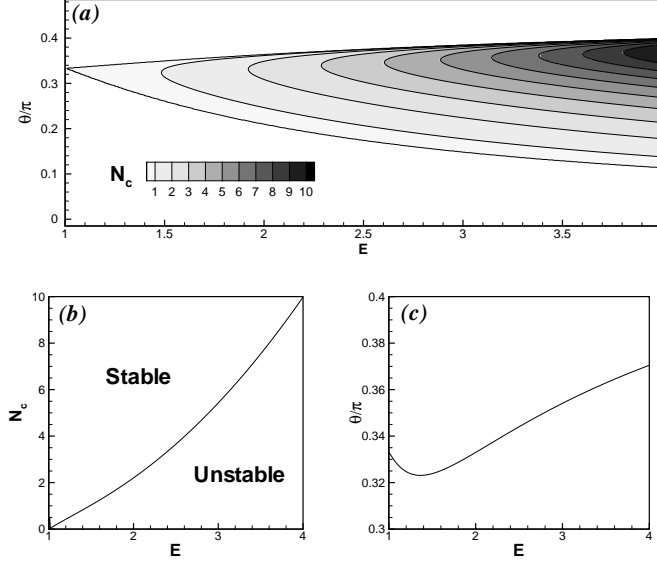


FIGURE 4. Stability of an unbounded strained vortex. (a), Neutral magnetic interaction parameter (3.14) as a function of eccentricity E and angle θ between the wavenumber vector \mathbf{k} of the perturbations and the axis of the vortex. (b) and (c), critical interaction parameter N_c and θ_c as functions of E .

plotted in figure 4b and c. Figure 4b shows that N_c increases rapidly with increasing eccentricity while the critical angle θ_c stays in the vicinity of $\pi/3$. The monotonic increase of the critical interaction parameter implies that strongly elliptical (almost sheet-like) structures are particularly prone to instability. Having in mind that the nonlinear evolution of initially circular vortices governed by the two-dimensional Euler equation (3.2) always leads to the generation of strongly elongated vortex sheets, we can conclude that the two-dimensional evolution proceeds in a way as to make the system more susceptible to the elliptical instability. The fact that $\theta_c \sim \pi/3$ may seem counterintuitive, as one usually expects in MHD that unstable structures have a tendency to align with the magnetic field ($\theta \rightarrow \pi/2$). However, it should be noticed that θ_c is monotonically increasing and probably asymptotes towards $\pi/2$.

Our stability result can be also viewed from another perspective. In a given magnetic field any forced two-dimensional flow will eventually become unstable, once the vorticity amplitude has reached a sufficiently high level Ω such that N falls below its critical value and the system becomes three-dimensionally unstable.

3.2. Instability of motion parallel to the magnetic field

In purely two-dimensional flow the velocity component parallel to the magnetic field behaves like a passive scalar, transported by the velocity $\mathbf{U}(x, y, t)$, cf. equation (3.2). Such evolution is known to produce steep gradients of $W(x, y, t)$ [see e.g. Kraichnan & Montgomery (1980), Lesieur (1990)]. Since the archetype of such structures is a single vortex sheet, which is known to undergo a Kelvin-Helmholtz instability, we will discuss the stability of the flow

$$W(x) = U_0 \frac{x}{|x|} \quad (3.15)$$

under the influence of the magnetic field. This problem, along with more general unidirectional velocity fields, was originally considered by Drazin (1960). However, the spatial structure of the unstable modes were not investigated there and is therefore the central focus of the discussion given below. Infinitesimal perturbations \mathbf{u} superimposed upon the basic flow (3.15) are governed by the linearized equation

$$\frac{\partial \mathbf{u}}{\partial t} + W \frac{\partial \mathbf{u}}{\partial z} + u_x \frac{dW}{dx} \mathbf{e}_z = -\frac{1}{\rho} \nabla p - \alpha \Delta^{-1} \frac{\partial^2 \mathbf{u}}{\partial z^2}, \quad \nabla \cdot \mathbf{u} = 0. \quad (3.16)$$

Squire's theorem, which holds for flow in a parallel magnetic field (Michael 1953; Stuart 1954), permits one to reduce the analysis to two-dimensional perturbations of the form $\mathbf{u} = (u, 0, w)$. They can be decomposed into normal modes according to

$$u(x, z, t) = \hat{u}(x) \cdot \exp[ik(z - ct)], \dots \quad (3.17)$$

After introducing a stream function $\hat{\psi}$ via $\hat{u} = ik\hat{\psi}$ and $\hat{w} = -d\hat{\psi}/dx$, nondimensional variables via $U = U_0 U_*$, $x = x_*/k$, $c = U_0 c_*$, $t = t' * /U_0 k$, an interaction parameter $N = \sigma B^2 / \rho U_0 k$, and dropping the asterisk, it can be shown (Drazin 1960) that the complex wave velocity c is determined by the third-order polynomial equation

$$-ic(1 + c^2) + \frac{N}{4}(1 + 3c^2) = 0. \quad (3.18)$$

The normal mode for $x > 0$ is given by

$$\hat{\psi}(x) = \exp \left(-x \sqrt{1 - i \frac{N}{c - 1}} \right) \quad (3.19)$$

where it is assumed that the square root with the positive real part has been taken.

Drazin (1960) has demonstrated that all three roots of equation (3.18) are purely imaginary and that one of the solutions has always positive imaginary part, but he did not explicitly calculate $c(N)$ and $\psi(x)$. Figure 5a shows the imaginary parts of the three roots. The wavenumber k does not explicitly appear in the solution because it represents the only characteristic length scale of the problem and has therefore been used to nondimensionalize the equations. However, the wavenumber enters the definition of N .

For each value of N there are two stable and one unstable solutions. When $N=0$ we recover the classical Kelvin-Helmholtz instability with $c = i$. For $N > 0$ the imaginary part of the solution originating from $c = i$ always remains positive which implies that the vortex sheet is unstable for arbitrarily strong magnetic fields. The modes with small N , which correspond to small perturbation wavelengths and small magnetic fields are growing fastest, while the modes with large N , corresponding to large scales and strong magnetic fields grow slowest. The asymptotic behavior of the wave velocity for the unstable mode is $c = i(1 - N/4)$ for $N \ll 1$ and $c = i/\sqrt{3}$ for $N \gg 1$. The spatial structure of the unstable modes is best revealed by the stream function $\psi(x, z, t) = \text{Re}\{\hat{\psi}(x) \cdot \exp[i(z - ct)]\}$ (nondimensional variables) which, for $t = 0$, is (see figures 5b and 5c)

$$\psi(x, z) = \exp \left[- \left(1 + \frac{N}{4} \right) x \right] \cos \left[-\frac{N}{4} x + z \right] \quad \text{for } N \ll 1 \quad (3.20)$$

$$\psi(x, z) = \exp \left[-3^{1/4} \left(\frac{N}{8} \right)^{1/2} x \right] \cos \left[-3^{3/4} \left(\frac{N}{8} \right)^{1/2} x + z \right] \quad \text{for } N \gg 1 \quad (3.21)$$

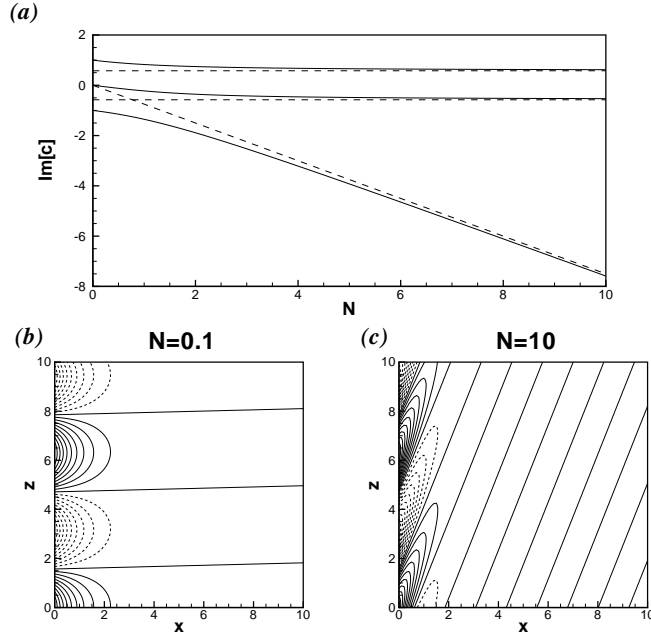


FIGURE 5. Instability of a vortex sheet. (a), Solid lines - roots of the dispersion equation (3.18). Dashed lines - asymptotic limits $\pm 1/3^{1/2}$, $-3N/4$. (b), Streamfunction of the unstable mode at $N \ll 1$ (3.20). (c), Streamfunction of the unstable mode at $N \gg 1$ (3.21).

The unstable modes for large N have an aspect ratio $z/x \sim N^{1/2}$ as is characteristic of MHD flows in strong magnetic fields.

This work was performed during the 2004 Summer Program at the Center for Turbulence Research with financial support from Stanford University and NASA Ames Research Center. The authors would like to thank P. Moin and N. Mansour for their hospitality during the stay. The authors have benefitted from numerous fruitful discussions with A. Tsinober, R. Moreau, B. Knaepen, S. Kassinos, D. Carati, F. Busse, Y. Kolesnikov, P. Davidson, and F. Dolzhansky. AT's work is partially supported by the Deutsche Forschungsgemeinschaft (DFG) in frame of the "Forschergruppe Magnetofluid-dynamik" at Ilmenau University of Technology. OZ's work is supported by the grant DE FG02 03 ER46062 from the US Department of Energy. AT and OZ are grateful to the Deutscher Akademischer Austauschdienst and the National Science Foundation for financial support of their collaboration.

REFERENCES

- ALEMANY A., MOREAU R., SULEM P.L, FRISCH U. 1979 Influence of external magnetic field on homogeneous MHD turbulence. *J. de Mecanique* **18**, 280–313.
- BAYLY B.J. 1986 Three-dimensional instability of elliptical flow. *Phys. Rev. Lett.* **57**, 2160–2163.
- CAPERAN P., ALEMANY A. 1985 Homogeneous low-magnetic-Reynolds-number MHD turbulence - Study of the transition to the quasi-two-dimensional phase and characterization of its anisotropy. *J. de Mecanique* **4**, 175–200.

- DAVIDSON P.A. 1997 Magnetic damping of jets and vortices. *J. Fluid Mech.* **336**, 123–150.
- DAVIDSON P.A. 1999 Magnetohydrodynamics in Materials Processing. *Annu. Rev. Fluid Mech.* **31**, 273–300.
- DAVIDSON P.A. 2001 *An Introduction to Magnetohydrodynamics*, Cambridge University Press, Cambridge.
- DRAZIN P.G. 1960 Stability of parallel flow in a magnetic field at small magnetic Reynolds number. *J. Fluid Mech.* **8**, 130–142.
- GREENSPAN H.P. 1968 *The theory of rotating fluids*, Breukelen Press, Brookline.
- JIMENEZ J. 1990 Transition to turbulence in two-dimensional Poiseuille flow. *J. Fluid Mech.* **281**, 295–297.
- KERSWELL R.R. 2002 Elliptical instability. *Annu. Rev. Fluid Mech.* **33**, 81–113.
- KNAEPEN B., MOIN 2004 Large-eddy simulation of conductive flows at low magnetic Reynolds number. *Phys. Fluids* **16**, 1255–1261.
- KRAICHNAN R.H., MONTGOMERY D. 1980 Two-dimensional turbulence. *Rep. Progr. Phys.* **43**, 547–619.
- LESIEUR M. 1990 *Turbulence in fluids*, Kluwer, Dordrecht.
- MICHAEL D.H. 1953 *Proc. Camb. Phil. Soc.* **49**, 166.
- MOFFATT K. H. 1967 On the suppression of turbulence by a uniform magnetic field. *J. Fluid Mech.* **28**, 571–592.
- MOFFATT K. H. 1978 *Magnetic field generation in electrically conducting fluids*, Cambridge University Press, Cambridge.
- MOREAU R. 1990 *Magnetohydrodynamics*, Kluwer Academic Publishers, Dordrecht.
- MORESCO P., T. ALBOUSSIÈRE 2004 Experimental study of the instability of the Hartmann layer. *J. Fluid Mech.* **504**, 167–181.
- NAKAUCHI N., OSHIMA H., SAITO Y. 1992 Two-dimensionality in low-magnetic Reynolds number magnetohydrodynamic turbulence subjected to a uniform external magnetic field and randomly stirred two-dimensional force. *Phys. Fluids* **4**, 2906–2914.
- ROBERTS P.H. 1967 *An introduction to magnetohydrodynamics*, Elsevier New York.
- SCHUMANN U. 1976 Numerical simulation of the transition from three- to two-dimensional turbulence under a uniform magnetic field. *J. Fluid Mech.* **74**, 31–58.
- SOMMERIA J., MOREAU R. 1982 Why, how, and when, MHD turbulence becomes two-dimensional. *J. Fluid Mech.* **118**, 507–518.
- STUART J.T. 1954 On the stability of viscous flow between parallel planes in the presence of a co-planar magnetic field. *Proc. Roy. Soc. A* **221**, 189.
- TSINOBER A. 1990 MHD flow drag reduction, in: D.M. Bushnell and J.N. Hefner editors, *Viscous drag reduction in boundary layers*, 327–349.
- TSINOBER A. 2001 *An informal introduction to turbulence*, Kluwer Academic Publishers, Dordrecht.
- WALEFFE F.A. 1990 On the three-dimensional instability of strained vortices. *Phys. Fluids* **2**, 76–80.
- ZIKANOV O., A. THESS 1998 Direct numerical simulation of forced MHD turbulence at low magnetic Reynolds number. *J. Fluid Mech.* **358**, 299–333.

Magnetic turbulence in compressible fluids

By J. Cho [†] and A. Lazarian [‡]

We present high resolution numerical simulations of compressible magnetohydrodynamic (MHD) turbulence. We concentrate on studies of spectra and anisotropy of velocity and density. We describe a technique of separating different magnetohydrodynamic (MHD) modes (slow, fast and Alfvén) and apply it to our simulations. For the mildly supersonic case, velocity and density show anisotropy. However, for the highly supersonic case, we observe steepening of the slow mode velocity spectrum and isotropization of density. Our present studies show that the spectrum of density gets substantially *flatter* than the Kolmogorov one.

1. Introduction

Most astrophysical systems, e.g. accretion disks, stellar winds, the interstellar medium (ISM) and intercluster medium are turbulent with an embedded magnetic field that influences almost all of their properties. This turbulence which spans from km to many kpc (see discussion in Armstrong, Rickett, & Spangler 1995) holds the key to many astrophysical processes (e.g., transport of mass and angular momentum, star formation, fragmentation of molecular clouds, heat and cosmic ray transport, magnetic reconnection). Statistics of turbulence is also essential for the cosmic microwave background (CMB) radiation foreground studies (Lazarian & Prunet 2002). In this brief, using high resolution simulations, we discuss statistics of 3D MHD turbulence and present new results on density fluctuations.

Why do we expect astrophysical fluids to be turbulent? A fluid of viscosity ν becomes turbulent when the rate of viscous dissipation, which is $\sim \nu/L^2$ at the energy injection scale L , is much smaller than the energy transfer rate $\sim V_L/L$, where V_L is the velocity dispersion at the scale L . The ratio of the two rates is the Reynolds number $Re = V_L L/\nu$. In general, when Re is larger than 10 – 100 the system becomes turbulent. Chaotic structures develop gradually as Re increases, and those with $Re \sim 10^3$ are appreciably less chaotic than those with $Re \sim 10^8$. Observed features such as star forming clouds are very chaotic for $Re > 10^8$. This makes it difficult to simulate realistic turbulence. The currently available 3D simulations containing 512 grid cells along each side can have Re up to $\sim O(10^3)$ and are limited by their grid sizes. Therefore, it is essential to find “*scaling laws*” in order to extrapolate numerical calculations ($Re \sim O(10^3)$) to real astrophysical fluids ($Re > 10^8$). We show below that even with its limited resolution, numerics is a great tool for *testing* scaling laws.

Kolmogorov theory provides a scaling law for *incompressible non-magnetized* hydrodynamic turbulence. This law provides a statistical relation between the relative velocity v_l of fluid elements and their separation l , namely, $v_l \sim l^{1/3}$. An equivalent description is to express spectrum $E(k)$ as a function of wave number k ($\sim 1/l$). The two descriptions are related by $kE(k) \sim v_l^2$. The famous Kolmogorov spectrum is $E(k) \sim k^{-5/3}$. The

[†] Chungnam National University, Korea

[‡] University of Wisconsin, USA

applications of Kolmogorov theory range from engineering research to meteorology (see Monin & Yaglom 1975) but its astrophysical applications are poorly justified and the application of the Kolmogorov theory can lead to erroneous conclusions (see reviews by Lazarian *et al.* 2003; Lazarian & Yan 2003)

Let us consider *incompressible* MHD turbulence first. There have long been an understanding that the MHD turbulence is anisotropic (e.g. Shebalin *et al.* 1983). Substantial progress has been achieved recently by Goldreich & Sridhar (1995; hereafter GS95), who made an ingenious prediction regarding relative motions parallel and perpendicular to magnetic field \mathbf{B} for incompressible MHD turbulence. An important observation that leads to understanding of the GS95 scaling is that magnetic field cannot prevent mixing motions of magnetic field lines if the motions are perpendicular to the magnetic field. Those motions will cause, however, waves that will propagate along magnetic field lines. If that is the case, the time scale of the wave-like motions along the field, i.e. $\sim l_{\parallel}/V_A$, (l_{\parallel} is the characteristic size of the perturbation along the magnetic field and $V_A = B/\sqrt{4\pi\rho}$ is the local Alfvén speed) will be equal to the hydrodynamic time-scale, l_{\perp}/v_l , where l_{\perp} is the characteristic size of the perturbation perpendicular to the magnetic field. The mixing motions are hydrodynamic-like†. They obey Kolmogorov scaling, $v_l \propto l_{\perp}^{1/3}$, because incompressible turbulence is assumed. Combining the two relations above we can get the GS95 anisotropy, $l_{\parallel} \propto l_{\perp}^{2/3}$ (or $k_{\parallel} \propto k_{\perp}^{2/3}$ in terms of wave-numbers). If we interpret l_{\parallel} as the eddy size in the direction of the local magnetic field and l_{\perp} as that in the perpendicular directions, the relation implies that smaller eddies are more elongated.

GS95 predictions have been confirmed numerically (Cho & Vishniac 2000; Maron & Goldreich 2001; Cho, Lazarian & Vishniac 2002a, hereafter CLV02a; see also CLV03); they are in good agreement with observed and inferred astrophysical spectra (see CLV03). However, the GS95 model considered incompressible MHD, but the media in molecular clouds is *highly compressible*. Does any part of GS95 model survives? Literature on the properties of compressible MHD is very rich (see reviews by Pouquet 1999; Cho & Lazarian 2004 and references therein). Higdon (1984) theoretically studied density fluctuations in the interstellar MHD turbulence. Matthaeus & Brown (1988) studied nearly incompressible MHD at low Mach number and Zank & Matthaeus (1993) extended it. In an important paper Matthaeus *et al.* (1996) numerically explored anisotropy of compressible MHD turbulence. However, those papers do not provide universal scalings of the GS95 type. After the GS95 model, Lithwick & Goldreich studied scaling relations for high- β plasmas and Cho & Lazarian (2002; hereafter CL02) for low- β plasmas.

The complexity of the compressible magnetized turbulence with magnetic field made some researchers believe that the phenomenon is too complex to expect any universal scalings for molecular cloud research. High coupling of compressible and incompressible motions is often quoted to justify this point of view.

Below we shall provide arguments that are suggestive that the fundamentals of compressible MHD can be understood and successfully applied to astrophysical fluids. In many astrophysical fluids the regular (or *uniform*) magnetic field is comparable with the fluctuating one. Therefore for most part of our discussion, we shall discuss results obtained for $\delta V \sim \delta B/\sqrt{4\pi\rho} \sim B_0/\sqrt{4\pi\rho}$, where δB is the r.m.s. strength of the random magnetic field.

Our work done during the summer program at CTR that we report here was an attempt to get a better insight into the physics of MHD turbulence using high resolution

† Recent simulations (Cho *et al.* 2003) suggest that perpendicular mixing is indeed efficient for mean magnetic fields of up to the equipartition value.

simulations (i.e. simulations within a 512^3 box). In what follows we discuss our numerical approach (sect. 2), our results obtained for the velocity and magnetic field statistics (sect. 3) and the density statistics (sect. 4). We concentrate on studies of spectra and turbulence anisotropy.

2. Numerical approach

We use a third-order accurate hybrid essentially non-oscillatory (ENO) scheme (see CL02) to solve the ideal isothermal MHD equations in a periodic box:

$$\partial\rho/\partial t + \nabla \cdot (\rho\mathbf{v}) = 0, \quad (2.1)$$

$$\partial\mathbf{v}/\partial t + \mathbf{v} \cdot \nabla \mathbf{v} + \rho^{-1} \nabla(a^2\rho) - (\nabla \times \mathbf{B}) \times \mathbf{B}/4\pi\rho = \mathbf{f}, \quad (2.2)$$

$$\partial\mathbf{B}/\partial t - \nabla \times (\mathbf{v} \times \mathbf{B}) = 0, \quad (2.3)$$

with $\nabla \cdot \mathbf{B} = 0$ and an isothermal equation of state. Here \mathbf{f} is a random large-scale driving force, ρ is density, \mathbf{v} is the velocity, and \mathbf{B} is magnetic field. The rms velocity δV is maintained to be approximately unity, so that \mathbf{v} can be viewed as the velocity measured in units of the r.m.s. velocity of the system and $\mathbf{B}/\sqrt{4\pi\rho}$ as the Alfvén velocity in the same units. The time t is in units of the large eddy turnover time ($\sim L/\delta V$) and the length in units of L , the scale of the energy injection. The magnetic field consists of the uniform background field and a fluctuating field: $\mathbf{B} = \mathbf{B}_0 + \mathbf{b}$.

We drive turbulence solenoidally in Fourier space and use 512^3 points, $V_A = B_0/\sqrt{4\pi\rho} = 1$, and $\rho_0 = 1$. The average rms velocity in statistically stationary state, δV , is around 1.

For our calculations we assume that $B_0/\sqrt{4\pi\rho} \sim \delta B/\sqrt{4\pi\rho} \sim \delta V$. In this case, the sound speed is the controlling parameter and basically two regimes can exist: supersonic and subsonic. Note that supersonic means low-beta and subsonic means high-beta. When supersonic, we consider mildly supersonic (or, mildly low- β) and highly supersonic (or, very low- β)†.

2.1. Separation of MHD modes

Three types of waves exist (Alfvén, slow and fast) in compressible magnetized plasma. The slow, fast, and Alfvén bases that denote the direction of displacement vectors for each mode are given by

$$\hat{\xi}_s \propto (-1 + \alpha - \sqrt{D})k_{\parallel}\hat{\mathbf{k}}_{\parallel} + (1 + \alpha - \sqrt{D})k_{\perp}\hat{\mathbf{k}}_{\perp}, \quad (2.4)$$

$$\hat{\xi}_f \propto (-1 + \alpha + \sqrt{D})k_{\parallel}\hat{\mathbf{k}}_{\parallel} + (1 + \alpha + \sqrt{D})k_{\perp}\hat{\mathbf{k}}_{\perp}, \quad (2.5)$$

$$\hat{\xi}_A = -\hat{\varphi} = \hat{\mathbf{k}}_{\perp} \times \hat{\mathbf{k}}_{\parallel}, \quad (2.6)$$

where $D = (1 + \alpha)^2 - 4\alpha \cos \theta$, $\alpha = a^2/V_A^2 = \beta(\gamma/2)$, θ is the angle between \mathbf{k} and \mathbf{B}_0 , and $\hat{\varphi}$ is the azimuthal basis in the spherical polar coordinate system. These are equivalent to the expression in CL02:

$$\hat{\xi}_s \propto k_{\parallel}\hat{\mathbf{k}}_{\parallel} + \frac{1 - \sqrt{D} - \beta/2}{1 + \sqrt{D} + \beta/2} \left[\frac{k_{\parallel}}{k_{\perp}} \right]^2 k_{\perp}\hat{\mathbf{k}}_{\perp}, \quad (2.7)$$

† The terms “mildly” and “highly” are somewhat arbitrary terms. We consider these two supersonic cases to cover a broad range of parameter space. Note that Boldyrev, Nordlund, & Padoan (2002) recently provided a Mach number dependence study of the compressible MHD turbulence statistics where only two regimes are manifest: essentially incompressible and essentially compressible shock-dominated (with smooth transition at some M_s of order unity).

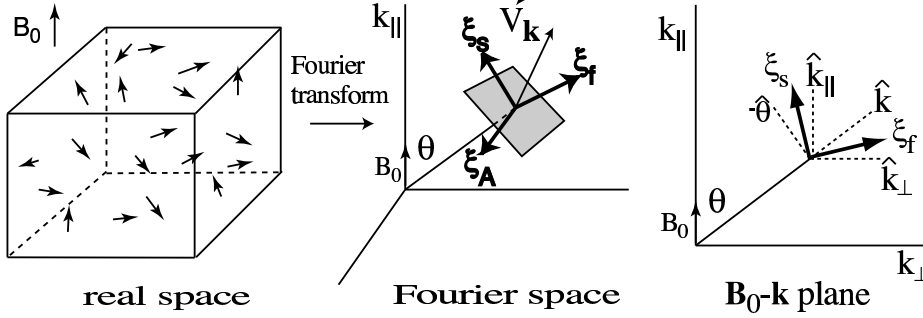


FIGURE 1. Separation method. We separate Alfvén, slow, and fast modes in Fourier space by projecting the velocity Fourier component $\mathbf{v}_{\mathbf{k}}$ onto bases ξ_A , ξ_s , and ξ_f , respectively. Note that $\xi_A = -\hat{\varphi}$. Slow basis ξ_s and fast basis ξ_f lie in the plane defined by \mathbf{B}_0 and \mathbf{k} . Slow basis ξ_s lies between $-\hat{\theta}$ and $\hat{\mathbf{k}}_{\parallel}$. Fast basis ξ_f lies between $\hat{\mathbf{k}}$ and $\hat{\mathbf{k}}_{\perp}$. From Cho & Lazarian (2003).

$$\hat{\xi}_f \propto \frac{1 - \sqrt{D} + \beta/2}{1 + \sqrt{D} - \beta/2} \left[\frac{k_{\perp}}{k_{\parallel}} \right]^2 k_{\parallel} \hat{\mathbf{k}}_{\parallel} + k_{\perp} \hat{\mathbf{k}}_{\perp}. \quad (2.8)$$

(Note that $\gamma = 1$ for isothermal case.)

Slow and fast velocity components can be obtained by projecting velocity Fourier component $\mathbf{v}_{\mathbf{k}}$ onto $\hat{\xi}_s$ and $\hat{\xi}_f$, respectively. See Cho & Lazarian (2003; hereinafter CL03) for discussion regarding how to separate slow and fast magnetic modes. We obtain energy spectra using this projection method. When we calculate the structure functions (e.g. for Alfvén modes) in real space, we first obtain the Fourier components using the projection and, then, we obtain the real space values by performing Fourier transform.

We tested our technique of separation in CL03 for a case when the separation is possible in real space and got essentially identical results with our *statistical* technique. Therefore we believe that our separation procedure works reliably.

3. Velocity and magnetic field spectra

We show in Fig. 2 new results from high resolution simulation of highly supersonic magnetically dominated media. The sonic Mach number, M_s , is ~ 10 . Fig. 2 shows that most of the scaling relations we previously found in the low resolution simulations are still valid in the high resolution simulation. Especially anisotropy of Alfvén, slow, and fast modes is almost identical to the one in the previous studies. However, the power spectra for slow modes do not show the Kolmogorov slope. The slope is close to -2 , which is suggestive of shock formation. At this moment, it is not clear whether or not the -2 slope is the true slope. In other words, the observed -2 slope might be due to the limited numerical resolution. Runs with higher numerical resolution should give the definite answer.

Formation of shocks is expected as within slow modes for sufficiently high Mach numbers the turbulence gets superAlfvénic. However, it is interesting that the turbulence anisotropy is definitely affected by magnetic field.

Alfvén modes follow the GS95 scaling as in the incompressible MHD turbulence. Alfvén perturbations cascade to small scales over just one wave period, while the other non-linear interactions require more time. Therefore we expect that the non-linear interactions with other types of waves should affect Alfvénic cascade only marginally. Moreover, as the

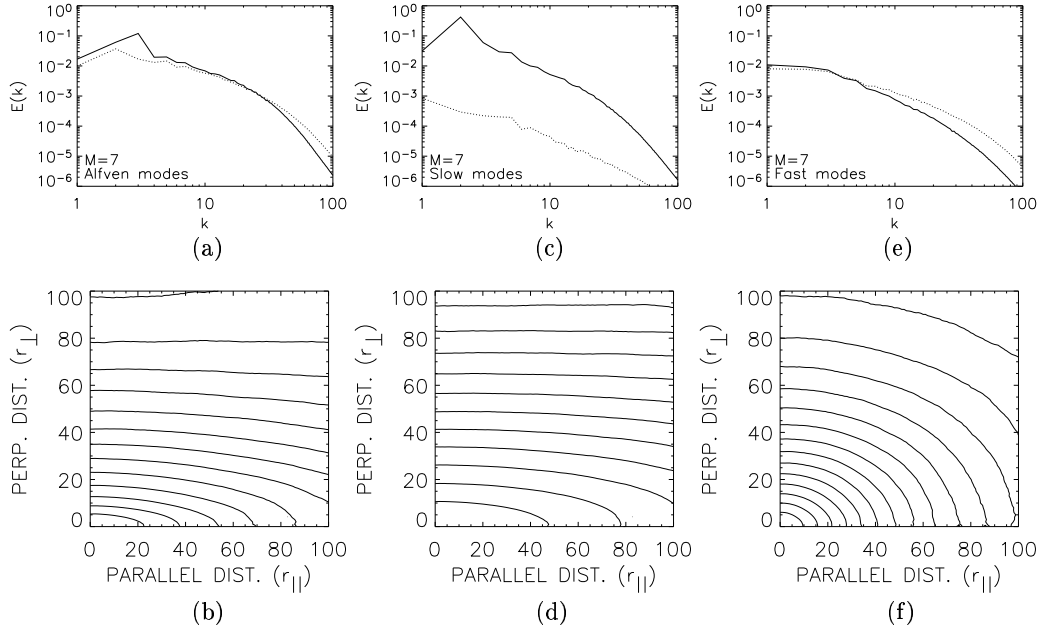


FIGURE 2. $M_s \sim 10$, $M_A \sim 0.5$, $\beta \sim 0.01$, and 512^3 grid points. Solid lines are for velocity spectra and dotted for magnetic field. (a) Spectra of Alfvén modes follow a Kolmogorov-like power law. (b) Eddy shapes (contours of same second-order structure function, SF_2) for velocity of Alfvén modes shows anisotropy similar to the GS95. ($r_{\parallel} \propto r_{\perp}^{2/3}$ or $k_{\parallel} \propto k_{\perp}^{2/3}$). The structure functions are measured in directions perpendicular or parallel to the local mean magnetic field in real space. We obtain real-space velocity and magnetic fields by inverse Fourier transform of the projected fields. (c) Spectra of slow modes are a bit steeper than the Kolmogorov-like power law. They closer to k^{-2} . (d) Slow mode velocity shows anisotropy similar to the GS95. We obtain contours of equal SF_2 directly in real space without going through the projection method, assuming slow mode velocity is nearly parallel to local mean magnetic field in low β plasmas. (e) Spectra of fast modes show a possible departure from the Kolmogorov spectrum or the IK spectrum. (f) The magnetic SF_2 of fast modes shows isotropy.

Alfvén waves are incompressible, the properties of the corresponding cascade do not depend on the sonic Mach number.

4. Density statistics

Density at low Mach numbers follow the GS95 scaling when the driving is incompressible (CL03). However, CL03 showed that this scaling substantially changes for high Mach numbers. Our high resolution results in Fig. 3 confirm the CL03 finding that at high Mach numbers density fluctuations get isotropic. Moreover, our present studies show that the spectrum of density gets substantially *flatter* than the GS95 one (see Fig. 4). Note, that a model of random shocks would produce a spectrum *steeper* than the GS95 one. A possible origin of the flat spectrum is the superAlfvénic perturbations created by fast modes within density perturbations originated from slow modes. This particular regime is clearly identified in a review by CLV03 (see Fig. 9 therein). It may also be related to the regime of superAlfvénic turbulence which is discussed in Norlund & Podoan (2003). However, alternative explanations of the shallow density fluctuations exist and

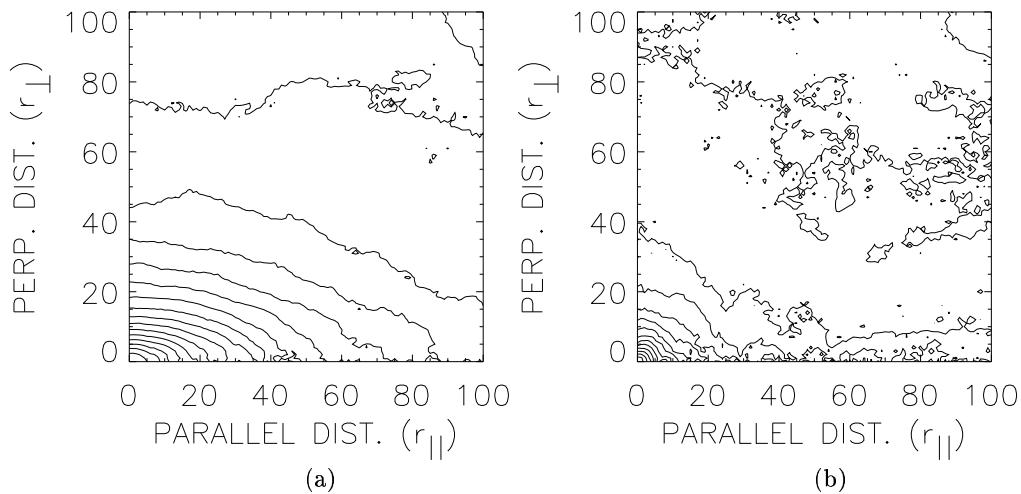


FIGURE 3. (a) Density structures for $M_s \sim 3$. (b) Density structures for $M_s \sim 10$. Density gets isotropic as the Mach number, M_s , increases.

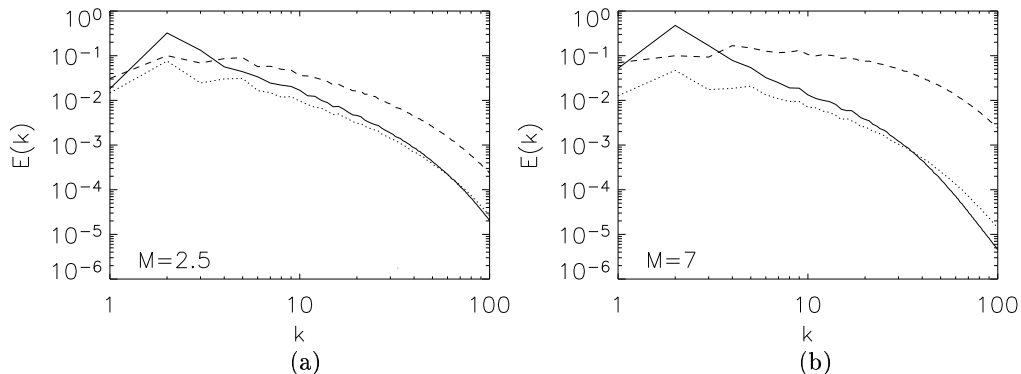


FIGURE 4. (a) Spectra for $M_s \sim 3$ at $t=3.7$. (b) Spectra for $M_s \sim 10$ at $t=6.0$. Dashed lines=density; solid=velocity; dotted=magnetic field. Density spectrum gets flatter as the Mach number, M_s , increases.

our ongoing work should clarify which process is actually responsible for the unusual density scaling that we observe.

The flat spectrum of density perturbations in high Mach number turbulence is definitely a very interesting phenomenon. It does affect the properties of interstellar medium, including the origin of the small scale clumps that are ubiquitous in the diffuse cold gas. This flat density spectrum should affect the star formation processes. A study in Boldyrev *et al.* (2002) indeed testifies that the density spectrum is flat in molecular clouds. However, a more systematic study is necessary.

5. Discussion

In the paper above we have studied scaling relations for Alfvén, fast and slow modes. First question that comes to mind is how good is to speak about different modes in strong MHD turbulence. It is well known, for instance, that for strong perturbations various linear modes are coupled. Well, our work shows that the coupling is indeed a

very important phenomenon at the large scales where the *total* Mach number M_{tot} , which normalizes the velocity perturbations by the sum of Alfvénic and sound velocities, is of the order of unity. At smaller scales when M_{tot} becomes less than unity the perturbations that we identify through our separation of mode procedure develop without much interaction between fast and Alfvén modes. This can be understood if we take into account that Alfvén modes cascade just over one eddy turnover time. Therefore there is not enough time for the non-linear interaction between fast and Alfvén modes to take place. At the same time, the shearing of slow modes by Alfvénic turbulence does take place over a turnover time. Therefore the slow modes mimic Alfvén mode anisotropy. A new effect that we start observing at high resolution is steepening of the slow mode spectrum. This is indicative that while shearing the Alfvén modes create shocks within the gas associated with slow modes. This is not so surprising as the Alfvén velocity is smaller within the slow modes in low beta medium.

We have not studied here a case of turbulence that is globally superAlfvénic. This is motivated by our belief that unless magnetic field is dynamically important the turbulence will behave like ordinary hydro turbulence. At the scale when the Alfvén velocity gets of the order of the perturbation velocity, we should encounter turbulence that is studied here.

Why would we care about those scalings? How wrong is it to use Kolmogorov scalings instead? Dynamics, chemistry and physics of molecular clouds (see Falgarone 1999) presents a complex of problems for which the exact scalings may be required to a different degree. If we talk about dynamics of interstellar dust or propagation of cosmic rays, one *must* account for the actual scalings and couplings of different modes (see reviews by Lazarian & Yan 2003, Lazarian *et al.* 2003). There are other problems, e.g. turbulent heat transport where the exact scaling of modes seems to be less important (Cho *et al.* 2003).

6. Conclusion

In the brief, we have studied statistics of compressible MHD turbulence with high resolution numerical simulation for highly ($M_s \sim 10$) supersonic low- β case. We provided the decomposition of turbulence into Alfvén, slow and fast modes. We have found that GS95 scaling is valid for *Alfvén modes*:

$$\text{Alfvén: } E^A(k) \propto k^{-5/3}, \quad k_{\parallel} \propto k_{\perp}^{2/3}.$$

Slow modes also follows the GS95 anisotropy for highly supersonic low- β case:

$$\text{Slow: } k_{\parallel} \propto k_{\perp}^{2/3}.$$

The velocity spectrum of slow modes tends to be steeper, which may be related to the formation of shocks.

Density shows anisotropy for the mildly supersonic case. But, for the highly supersonic case, density shows more or less isotropic structures. We suspect that shock formation is responsible for the isotropization of density. Our present studies show that the spectrum of density gets substantially *flatter* than the GS95 one (see Fig. 4).

7. Acknowledgments

The authors are grateful to CTR for hospitality. AL acknowledge a support by the NSF Center for Magnetic Self-Organization in the Laboratory and Astrophysical Plasmas.

REFERENCES

- Armstrong, J.W., Rickett, B.J., & Spangler, S.R., 1995, Electron density power spectrum in the local interstellar medium, *Astrophysical J.*, 443, 209-221
- Boldyrev, S., Nordlund, Å., & Padoan P. 2002, Supersonic Turbulence and Structure of Interstellar Molecular Clouds, *Phys. Rev. Lett.* 89, 031102
- Cho, J., Lazarian, A. 2002, Compressible Sub-Alfvénic MHD Turbulence in Low- β Plasmas, *Phys. Rev. Lett.*, 88, 245001 (CL02)
- Cho, J., Lazarian, A. 2003, Compressible magnetohydrodynamic turbulence: mode coupling, scaling relations, anisotropy, viscosity-damped regime and astrophysical implications, *MNRAS*, 345, 325-339 (CL03)
- Cho, J., Lazarian, A. 2004, Generation of Compressible Modes in MHD Turbulence, *Theo. Comp. Fluid Dyn.*, accepted (<http://xxx.lanl.gov/abs/astro-ph/0301462>)
- Cho, J., Lazarian, A., Honein, A., Knaepen, B., Kassinos, S., & Moin, P. 2003, Thermal Conduction in Magnetized Turbulent Gas, *ApJ*, 589, L77-L80
- Cho, J., Lazarian, A., & Vishniac, E. 2002a, Simulations of Magnetohydrodynamic Turbulence in a Strongly Magnetized Medium, *ApJ*, 564, 291-301 (CLV02a)
- Cho, J., Lazarian, A., & Vishniac, E. 2003, in *Turbulence and Magnetic Fields in Astrophysics*, eds. E. Falgarone & T. Passot (Springer LNP), p56-98 (astro-ph/0205286) (CLV03)
- Cho, J. & Vishniac, E. 2000, The Anisotropy of Magnetohydrodynamic Alfvénic Turbulence, *ApJ*, 539, 273-282
- Falgarone, E. 1999, The Intermittent Dissipation of Turbulence: is it Observed in the Interstellar Medium?, in *Interstellar Turbulence*, ed. by J. Franco, A. Carraminana, CUP, p.132
- Goldreich, P. & Sridhar, S. 1995, Toward a theory of interstellar turbulence. 2: Strong alfvénic turbulence, *ApJ*, 438, 763-775 (GS95)
- Higdon, J. C. 1984, Density fluctuations in the interstellar medium: Evidence for anisotropic magnetogasdynamic turbulence. I - Model and astrophysical sites, *ApJ*, 285, 109-123
- Lazarian, A., Petrosian, V., Yan, H., & Cho, J. 2003, preprint (astro-ph/0301181)
- Lazarian, A. & Prunet, S. 2002, Polarized microwave emission from dust, in *Astrophysical Polarized Backgrounds*, ed. by S. Cecchini, S. Cortiglioni, R. Sault, C. Sbarra, (Melville, NY; AIP, Vol. 109) pp.32-43 (astro-ph/0111214)
- Lazarian, A. & Yan, H. 2003, Translational Velocities and Rotational Rates of Interstellar Dust Grains, in “Astrophysical Dust” eds. A. Witt & B. Draine, APS, in press (astro-ph/0311370)
- Lithwick, Y. & Goldreich, P. 2001, Compressible Magnetohydrodynamic Turbulence in Interstellar Plasmas, *ApJ*, 562, 279-296
- Maron, J. & Goldreich, P. 2001, Simulations of Incompressible Magnetohydrodynamic Turbulence, *ApJ*, 554, 1175-1196
- Matthaeus, W. H. & Brown, M. R. 1988, Nearly incompressible magnetohydrodynamics at low Mach number, *Phys. Fluids*, 31(12), 3634-3644
- Matthaeus, W. H., Ghosh, S., Oughton, S., & Roberts, D. A. 1996, Anisotropic three-dimensional MHD turbulence, *J. Geophysical Res.*, 101(A4), 7619-7630
- Monin, A.S., & Yaglom, A.M. 1975, *Statistical Fluid Mechanics: Mechanics of Turbulence*, vol. 2, The MIT Press

- Norlund, A., Padoan, P. 2003, Star Formation and the Initial Mass Function, in *Turbulence and Magnetic Fields in Astrophysics*, eds. E. Falgarone & T. Passot (Springer LNP), p.271-298
- Pouquet, A. 1999, An Introduction to Compressible MHD Turbulence, in *Interstellar Turbulence*, p.87
- Shebalin, J. V., Matthaeus, W. H., & Montgomery, D. C. 1983, Anisotropy in MHD turbulence due to a mean magnetic field, *J. Plasma Phys.*, 29, 525-547
- Zank, G. P. & Matthaeus, W. H. 1993, Nearly incompressible fluids. II - Magnetohydrodynamics, turbulence, and waves, *Phys. Fluids A*, 5(1), 257-273

Page intentionally left blank

Modeling anomalous electron transport in Hall thrusters

By E. Fernandez [†], M. Cappelli [‡] N. Gascon [‡] AND M. Allis [‡]

We examine the issue of electron mobility in Hall thruster plasmas using two hybrid models, one in the radial and axial coordinates ($r - z$ model), and the other in the azimuthal and axial coordinates ($z - \theta$ model). Unlike most $r - z$ simulation efforts, which model the electron transport via an *ad hoc* Bohm parameter, the $r - z$ model presented here uses a transport parameter based on a recent experimental measurement (Meezan, Hargus & Cappelli 2001). An examination of equilibrium profiles as well as $I - V$ curves reveal marked improvement over the simpler Bohm scaling results. Motivated by these results and the need to incorporate azimuthal effects, we formulate a new $z - \theta$ model. It is presented here as the simplest description of Hall thruster plasmas able to capture the azimuthal drifts absent in $r - z$ formulations. Preliminary results show that transport arising from azimuthal disturbances can be significant.

1. Introduction

1.1. Motivation and objectives

Hall thrusters represent an electric propulsion technology that has attracted considerable interest concomitant with the increased number of government and commercial satellites in orbit (Gulczynski & Spores 1996). The main use of these small, high specific impulse rockets lies in low thrust applications like orbit transfer and orbit station keeping. In Hall thruster plasmas, electrons emanating from a cathode ionize xenon neutrals upon collision. The resulting ions are accelerated out of the device by the electric potential drop between the cathode and the anode, typically a few hundred volts. Such potential drop is localized near the exit of the device by an external radial magnetic field set up by an electromagnet. While the overall operation of these thrusters is understood, key physics issues remain open for investigation. Of particular interest is the study of electron transport in these engines. It is well known that the electron conductivity in the Hall thruster is much larger than can be inferred from classical collisions alone (Morozov, Esinchuk, Tilinin, Trofimov, Sharov & Shchepkin 1972). Turbulent fluctuations and wall effects are believed to have a major effect on the enhanced conductivity, which, in turn, affects the electric field, ionization, thrust, and overall discharge behavior. A good understanding of the processes involved in determining this anomalous transport remains the subject of important research, not only in regard to Hall thruster plasmas but fusion and astrophysical plasmas as well.

With the exception of the works by Hirakawa (Hirakawa & Arakawa 1996) and Adams (Adams, Heron & Laval 2004), prior computational work on Hall thrusters has been in one dimension (1D) in the axial direction or two dimensions (2D) in the axial and radial directions. These works have had reasonable success in describing the overall behavior of

[†] Eckerd College

[‡] Mechanical Engineering Department, Stanford University

the plasma discharge. Most notably, they have recovered the dominant instability in these devices - the so-called “breathing mode” instability. However, a key element is missing in these descriptions: azimuthal dynamics. Besides drifting axially opposite to the electric field, electrons in the thruster drift azimuthally as a result of the imposed electric and magnetic fields. Azimuthal perturbations arise from the established equilibrium and, if properly correlated, result in a net axial transport of electrons (Janes & Lowder 1966). This effect is not captured in $r - z$ descriptions and needs to be modeled.

Most 2D works have used a Bohm mobility given by

$$\mu = \frac{1}{16B} \quad (1.1)$$

as a model for the enhanced conductivity (Fernandez, Cappelli & Mahesh 1998). Recently, some works have used a Bohm scaling for the mobility with a constant other than $\frac{1}{16}$ in order to better fit experiments (Bareilles, Hagelaar, Garrigues, Boniface, Boeuf & Gascon 2004). Nonetheless, many plasma transport experiments (outside of Hall thrusters) have demonstrated that electron transport can vary greatly and does not always conform to a Bohm scaling. More importantly, a recent, first direct measurement of electron mobility in Hall thrusters has revealed that such transport is a complicated function of axial location as well as operating parameters (Meezan, Hargus & Cappelli 2001). In particular, at high voltage, Bohm transport seems to fare well in the middle of the channel while at the channel exit the transport is reduced to near its classical value. The experiment, in fact, suggests that a single model does not properly describe the full plasma region from the anode to the near plume. With this experimental observation as our main motivation, our objectives for this paper are a) modify the $r - z$ model by incorporating an *experimentally-based* mobility, and b) construct a $z - \theta$ model which self-consistently evolves the azimuthal drifts and makes no use of transport parameters.

This rest of this paper is organized as follows. Section II describes the $r - z$ model and compares results using Bohm mobility and experimentally based mobility. Section III describes the $z - \theta$ model and the preliminary results from such simulations. Finally, section IV concludes the paper with the conclusions and future work.

2. $r - z$ model

2.1. Overview

A detailed description of the $r - z$ model is given elsewhere (Allis, Gascon, Vialard-Goudou, Cappelli & Fernandez 2004). Here we just present a summary. The radial and axial description of the Hall thruster plasma is based on the model by Fife at MIT (Fife 1995). Electrons, single-ionized xenon ions and xenon neutrals are time-advanced in a geometry that extends from the anode to the inner plume. We assume no azimuthal variation in the plasma quantities; the simulation effectively represents a slab of plasma in the radial and axial directions at an arbitrary azimuthal angle. The model assumes a constant external magnetic field (produced by the electromagnet) and neglects the much smaller magnetic field created by the plasma.

The heavy particle species - ions and neutrals - are fairly collisionless and are described via the particle-in-cell (PIC) method. Neutral superparticles are injected into the domain at the anode position at a prescribed rate. They are, in turn, ionized by electron-impact ionization collisions. The ions born in the ionization process, due to their large inertia, are effectively unmagnetized and respond only to the electric field. Upon colliding with the thruster walls, ions recombine to form neutrals which are then injected into the domain.

The neutrals, not being affected by electromagnetic forces, only modify their velocities if they collide with the walls of the thruster. Elastic collisions among ions and neutrals are assumed small and thus neglected (however, some effects like charge-exchange have recently been considered (Allis, Gascon, Vialard-Goudou, Cappelli & Fernandez 2004)).

The electrons, unlike the heavy xenon ions, are strongly magnetized and are treated as a fluid. The fluid equations that are used are current conservation, parallel and perpendicular (with respect to the magnetic field) momentum, and electron energy. The system is closed by specifying the electric field and imposing quasineutrality. The set of equations is given by:

$$I_a = \int_A (n_i u_{i\hat{n}} - n_e u_{e\hat{n}}) dS \quad (2.1)$$

$$\phi = \frac{kT_e}{e} \ln n_e + \phi^* \quad (2.2)$$

$$\mathbf{E} = -\nabla\phi \quad (2.3)$$

$$u_{e\hat{n}} = -\mu \left(E_{\hat{n}} + \frac{kT_e}{en_e} \frac{\partial n_e}{\partial \hat{n}} + \frac{k}{e} \frac{\partial T_e}{\partial \hat{n}} \right) \quad (2.4)$$

$$\frac{\partial}{\partial t} \left(\frac{3}{2} n_e k T_e \right) + \frac{\partial}{\partial \hat{n}} \left(\frac{5}{2} n_e u_{e\hat{n}} k T_e - K \frac{\partial T_e}{\partial \hat{n}} \right) = -n_e \varphi(T_e) E_i - \alpha T_e^{3/2} + j_{e\hat{n}} E_{\hat{n}} \quad (2.5)$$

$$n_i = n_e \quad (2.6)$$

where the \hat{n} symbol means perpendicular to the magnetic field. The symbols I_a , n_i , n_e , $u_{i\hat{n}}$, $u_{e\hat{n}}$, ϕ , k , T_e , e , ϕ^* , \mathbf{E} , μ , K , \hat{n}_e , $\varphi(T_e)$, E_i , α , $j_{e\hat{n}}$, stand for the discharge current, ion density, electron density, ion velocity, electron velocity, electrostatic potential, Boltzmann constant, electron temperature, electron charge, magnetic field contour constant, electric field, electron mobility, thermal diffusivity, ionization rate, ion production cost, ionization potential, wall loss coefficient and electron current density respectively.

The current conservation equation (eqn. 2.1) says that the total (ion plus electron) electric current cutting each magnetic field contour is constant and equal to the discharge current collected at the anode. It also assumes that no current is lost parallel to the magnetic field. Equation 2.2 is known as Boltzmann relation, and it follows from a balance of electric and pressure forces. The field equation (eqn. 2.3) says that the electric field is purely electrostatic, as magnetic perturbations are small and neglected. The perpendicular momentum equation (eqn. 2.4) is set by electric, pressure and collisional drag forces. However, inertial terms as well as important azimuthal drifts have been neglected. These, and presumably other effects like wall-induced conductivity, are *effectively* captured by using an enhanced mobility μ . The mobility can be given by its Bohm value (eqn. 1.1), or, as seen later, by an experimentally motivated form. In the electron energy equation (eqn. 2.5), the three terms on the right hand side represent ionization losses, wall losses, and joule heating respectively (Fife 1995). We note that the wall-loss term in the temperature equation assumes a constant secondary electron emission coefficient equal to .6 in the present model (Lentz 1990). A more realistic wall-loss term, which takes into account the temperature dependence of the secondary electron emission coefficient as well as sheath saturation effects, will be the subject of future work.

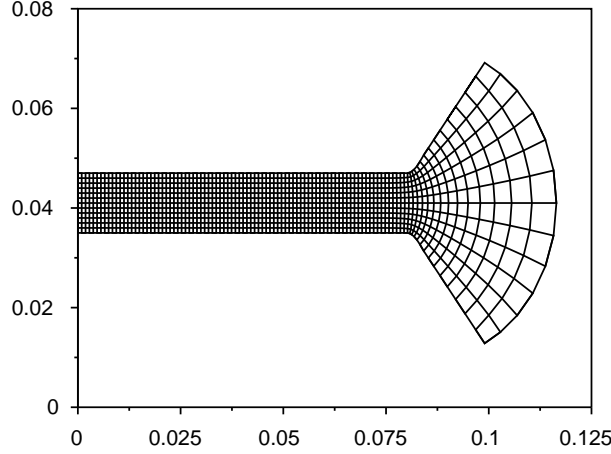


FIGURE 1. Grid for Stanford Hall thruster. The vertical and horizontal axes represent the radial and axial distance respectively. Both distances are in meters.

2.2. Numerical method

2.2.1. Geometry, grid and magnetic field

Stationary Plasma Thruster (SPT 100) and Stanford Hall Thruster (SHT) geometries are considered, but the results presented here use the SHT geometry. Given the geometry, a nonuniform orthogonal grid of 101 by 13 grid points in the axial and radial directions is constructed. The grid, covering the full channel region and inner plume is shown in Figure 1. Once the grid is obtained, the constant external magnetic field is computed using Laplace's equation. Alternatively, the full 2D the magnetic field profile can be obtained from experimental data. The peak of the external magnetic field is on the order of a hundred gauss, mostly in the radial direction, and located just inside the channel exit.

2.2.2. PIC method

The heavy species are described with a PIC method. The standard leap-frog scheme is used to advance the positions and velocities of the particles. Their densities are then obtained at each grid point via bilinear interpolation. Since the time scale of these particles is much slower than that of the electrons, both ions and neutrals are advanced every so many electron-fluid time steps. As is typical of PIC codes, the particles themselves are superparticles, representing a conglomeration of unit particles. In addition, in this code the superparticles are of variable mass. This allows for the efficient handling of regions in the channel with high density and regions with very low density. The ionization of neutrals is done with a Monte Carlo technique. By allowing the ion superparticles to have variable mass, one can dictate the number of ions born in a given cell per timestep, and avoid having cells with too many or too few superparticles. The number of superparticles in the simulation eventually reaches an equilibrium, where the number of neutrals leaving the domain at the downstream boundary, plus those lost through ionization, balance the number of neutrals injected at the anode and those born through ion-recombination at the channel walls. Similarly, the ions lost by wall collisions and those lost by leaving the downstream boundary are balanced by the ions born through ionization events. However,

this equilibrium is not steady and strong oscillations take place (Fernandez, Cappelli & Mahesh 1998). The PIC method couples to the electron fluid method through quasineutrality: the electron density is obtained from the ion density.

2.2.3. Fluid method

Owing to the large parallel electron thermal conductivity, the electron temperature in the thruster can be considered constant along each magnetic contour. Thus, the temperature is solved for each contour λ rather than for each grid point. Specifically, this is done by substituting equations 2.2-2.4 into 2.5, and projecting along λ . The equation that follows is then discretized using a finite difference scheme for the spatial terms, and the resulting system of equations is solved with a fourth-order Runge-Kutta scheme. Two hundred λ contours are used in order to resolve the sharp gradients near the channel exit. The boundary conditions for the temperature are Neumann for the first contour and Dirichlet for the last contour (the first contour is that which just touches the anode and the last contour is that which just touches the cathode). Having obtained the temperature, the electric potential is obtained. Then the algorithm checks if the resulting anode potential is close to the prescribed boundary condition anode potential. If it is, then algorithm proceeds to the next time step. If the potential boundary condition is not met, then a Newton's method on the discharge current I_a is used until the condition is satisfied. The electron fluid algorithm thus solves for the electron temperature, discharge current and electric potential. The field equation (eqn. 2.3) then gives the electric field which is used to advance the particles, and the whole process is repeated until an equilibrium in plasma quantities is established.

2.3. Results

It is important to mention that our objective in this section is to investigate the *qualitative* effect of using various mobility models on simulation results. A more thorough examination that looks at charge-exchange collisions, specular versus diffuse wall scattering, reverse ion flow, inflow of background neutrals, and refined inputs for the ionization rate and experimental mobility, has been done by Allis (Allis, Gascon, Vialard-Goudou, Cappelli & Fernandez 2004). Similarly, $r - z$ model studies that look at breathing-mode and transit-time oscillations are taken up elsewhere (Gascon, Allis, Thomas, Cappelli & Fernandez 2004).

Experimental data indicates that the transport in the SHT is Bohm-like except near the anode and channel exit (Meezan, Hargus & Cappelli 2001). In the latter region, the mobility decreases and comes up again within two centimeters (goes through a dip). At its minimum value, the mobility approaches the "classical value". Interestingly, this region of transport suppression corresponds to a highly sheared electron flow region, and is reminiscent of fusion plasmas where transport has been successfully lowered to classical levels by inducing a sheared flow. Whether the shear suppression mechanism of fusion plasmas is indeed responsible for the dip in the Hall thruster mobility is an open question. Regardless of the mechanism, we can construct an experimentally-motivated expression for the mobility for use in simulations as follows:

$$\mu = \frac{1}{\alpha + \beta \left(\frac{\sin 300(z-.077)}{300(z-.077)} \right)^2} \frac{1}{B} \quad (2.7)$$

where α and β are parameters representing the base line transport level and depth of the dip respectively. The value of .077 corresponds to the location of the dip, which is

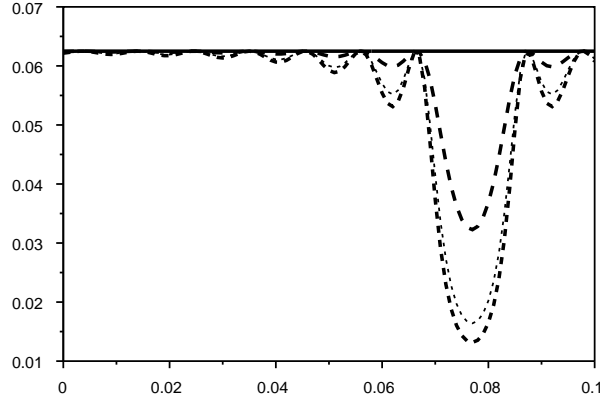


FIGURE 2. Experimentally based mobility model. The vertical axis is dimensionless. The horizontal axis represents axial distance (the channel exit corresponds to .08). The solid trace corresponds to Bohm transport. The bold dotted trace, the dotted trace and the bold dashed trace correspond to the experimentally based mobility for 200, 160 and 120 volts respectively.

centered around the peak of the magnetic field. The factor of 300 in the formula above is used to confine the dip to about 2cm in width. Simple Bohm transport corresponds to $\alpha = 16$ and $\beta = 0$. Experiment shows that the dip gets deeper as the voltage increases, and β is chosen to reflect this trend. Figure 2 shows the mobility for various values of β . We point out that the transport reflected by equation 2.7 goes into the expression we use for the thermal conductivity in the energy equation (eqn. 2.5). Thus, the mobility model affects not only the momentum equation, but also the energy equation through convection *and* thermal conduction effects. Finally, we note that the actual form of equation 2.7 is not what is important here – all we are after is an expression that captures the trends in the experimental data.

In order to assess the effect of the transport coefficient μ on the simulation we present, in Figure 3, $I - V$ curves from three sets of simulations at flow rates of 3mg/s, and experimental data at 2mg/s. In comparing the experimental and simulation $I - V$ curves one should increase the experimental curve values by about 50% to compensate for the two different mass flow rates. It is clear that the experimentally-based mobility does better than the Bohm mobility. The most significant disagreement takes place at low voltage: in the experiment the current drops to zero at about 60 volts whereas in the simulation this happens at 90 volts. In addition, the simulation does not recover the inflection point at about 120 volts - a robust feature in these discharges that lacks explanation at the present time.

More striking is the effect of the mobility on equilibrium profiles, as shown in Figures 4 and 5 (bold, dotted and solid traces represent the experimental, Bohm simulation, and experimentally-based simulation profiles respectively in each figure). Figure 4 shows the electron temperature peaking outside the channel for the Bohm mobility case, something not seen experimentally. In addition, the sharp gradient near the channel exit is not realized. The simulation using the experimentally based mobility clearly does better. It is interesting to note the high temperature near the anode in the experimental curve – something which is seen only at high voltage. Neither model recovers this; a closer examination of this region is the subject of future work. In Figure 5, most of the electric

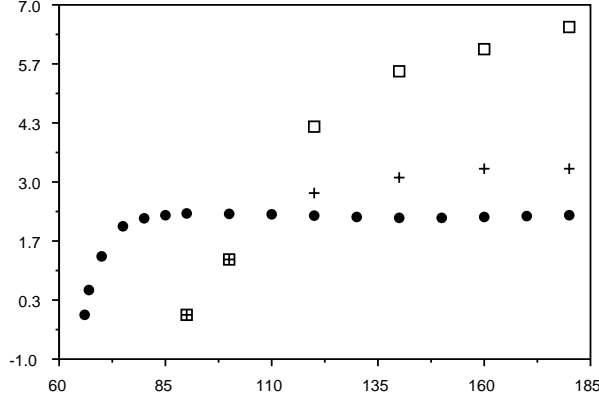


FIGURE 3. $I - V$ curves from simulation and experiment. The solid circles, open squares and crosses represent the experimental data, Bohm simulation and experimentally-based mobility simulation respectively

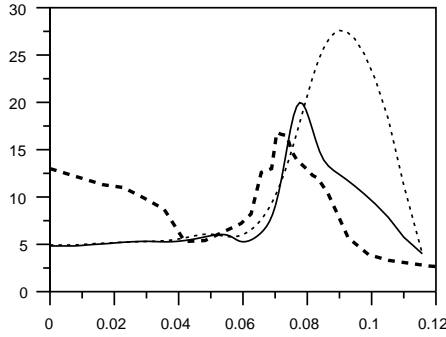


FIGURE 4. Temperature profile.

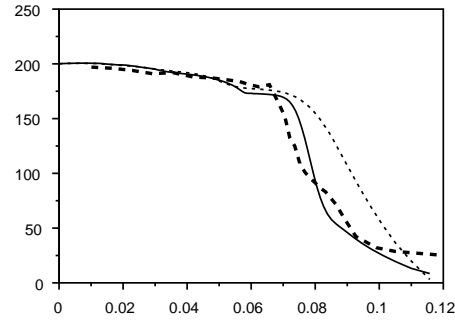


FIGURE 5. Potential profile.

potential drop takes place outside the channel in the Bohm simulation. On the contrary, experiment indicates that most of the potential drop and resulting ion acceleration happen just inside the channel exit. The experimentally-based mobility simulation captures this quite well, as Figure 5 shows. Other plasma profiles as well as simulations using the SPT geometry (not shown) convey a similar conclusion.

The main lesson from the simulations in the $r - z$ model is that a) a simple Bohm model for the mobility is inadequate in reproducing $I - V$ curves and equilibrium profiles, and b) in the absence of sound electron transport theory-based models, experimentally-based approaches for the mobility appear rather necessary in $r - z$ codes.

3. $z - \theta$ model

3.1. Overview

While the use of an experimentally-based expression for the mobility in the $r - z$ model gave improved the results, it is still limiting for a model to depend so critically on an *ad hoc* transport parameter. Motivated by this fact, we formulate a new model for Hall

thruster plasmas. First, we construct the simplest description able to treat electron transport self-consistently. In particular, the new description must resolve the inhomogeneous Hall current and the associated azimuthal fluctuations. Azimuthal waves have been seen experimentally in a number of Hall thrusters. Their amplitude is large and their power spectrum complex, with coherent structures among random, broadband turbulence. Linear stability analysis have predicted azimuthal unstable waves at low frequency (a few hundred kilohertz) and at high frequency (megahertz), driven unstable by resistivity and equilibrium gradients in plasma density and magnetic field (Choueiri 2001). Azimuthal fluctuations in the electric potential, if properly correlated with density fluctuations, can then result in a net axial electron transport. A nonlinear theory describing this process is presently absent, except under simplifying assumptions. An example is the theory of Yoshikawa and Rose (Yoshikawa & Rose 1962), which predicts a Bohm scaling for the electron transport with a coefficient proportional to the relative electron density fluctuation power. An objective of the model presented in this paper is to gain understanding about the azimuthal fluctuations and their associated transport.

The $z - \theta$ model draws from our experience with the $r - z$ model. It is 2D (in the axial and azimuthal directions), and hybrid in nature: the neutrals and ions are described as particles and the electrons are described as a fluid. The treatment of the ions and the neutrals follows that of the $r - z$ model. Particle injection is done by inverting a Maxwellian flux distribution function (Birdsall & Langdon 1991). The nonlinear ionization rate is given by a fit to experiment according to the following formula (Ahedo, Martinez-Cerezo & Martinez-Sanchez 2001):

$$n_e = n_e n_n 5 \times 10^{-20} \sqrt{\frac{8T_e}{\pi m_e}} \left(1 + \frac{T_e E_i}{(T_e + E_i)^2} \right) \exp -E_i/T_e \quad (3.1)$$

The main differences in the $z - \theta$ model come from the electron fluid description. The equations governing the electron fluid are current continuity, perpendicular momentum balance, and parallel momentum balance. The system is closed with an equation for the electric field and quasineutrality. We make two assumptions: a) The magnetic field is purely in the radial direction and only a function of axial position and b) the electron temperature is only a function of axial position and it is assumed constant. The last assumption is particularly severe: we make it at this point in order to simplify the system. As we begin to get results and understand the model, a time-dependent temperature equation with all the necessary physics like ionization, joule heating, wall damping including sheath saturation effects (Barral, Makowski, Peradzynski, Gascon & Dudeck 2003), and conductive and convective fluxes will be implemented. In time, the first assumption will be relaxed as well. In fact, it has been noted that the azimuthal asymmetry in the external magnetic field arising from the magnetic configuration is associated with mode-locking (Cappelli 2004). With these assumptions the electron equations become:

$$0 = \nabla \cdot (n_e \mathbf{v}_e - n_i \mathbf{v}_i) \quad (3.2)$$

$$u_{ez} = -\mu_{\perp} E_z - \frac{D_{\perp}}{n_e} \frac{\partial n_e}{\partial z} - \frac{1}{1 + (\nu/\omega_c)^2} \frac{E_{\theta}}{B} - \frac{1}{1 + (\nu/\omega_c)^2} \frac{kT_e}{en_e B r} \frac{\partial n_e}{\partial \theta} \quad (3.3)$$

$$u_{e\theta} = -\mu_{\perp} E_{\theta} - \frac{D_{\perp}}{n_e r} \frac{\partial n_e}{\partial \theta} + \frac{1}{1 + (\nu/\omega_c)^2} \frac{E_z}{B} + \frac{1}{1 + (\nu/\omega_c)^2} \frac{kT_e}{en_e B} \frac{\partial n_e}{\partial z} \quad (3.4)$$

$$\phi = \frac{kT_e}{e} \ln n_e + \phi^* \quad (3.5)$$

$$\mathbf{E} = -\nabla\phi \quad (3.6)$$

$$n_i = n_e \quad (3.7)$$

where u_{ez} is the axial electron velocity, $u_{e\theta}$ is the azimuthal electron velocity, μ_{\perp} is the classical perpendicular mobility, ν is the electron-neutral collision frequency, ω_c is the electron gyro-frequency, and D_{\perp} is the classical diffusion coefficient arising from electron-neutral collisions. The last four quantities are given by:

$$\mu_{\perp} = \frac{\frac{e}{m_e\nu}}{1 + (\omega_c/\nu)^2} \quad (3.8)$$

$$\nu = n_n \sigma_{en} \bar{c}_e \quad (3.9)$$

$$\omega_c = \frac{eB}{m_e} \quad (3.10)$$

$$D_{\perp} = \frac{\frac{kT_e}{m_e\nu}}{1 + (\omega_c/\nu)^2} \quad (3.11)$$

Finally, $\sigma_{en} = 27 \times 10^{-20} m^2$ is the approximate electron-neutral elastic collision cross section in the range of interest, $\bar{c}_e = \sqrt{\frac{8T_e}{\pi m_e}}$ is the electron thermal velocity, and m_e is the electron mass. The rest of the symbols have the same meaning as in the $r - z$ model.

We note that the axial electron velocity (eqn. 3.3) now has components proportional to E_{θ} and $\frac{\partial n_e}{\partial \theta}$. These terms are proportional to $\frac{1}{1 + (\nu/\omega_c)^2}$, and thus they are important at low neutral densities and high magnetic fields. We expect these terms to dominate for most of the channel, but especially at the exit, where ionization depletes the neutral concentration and the magnetic field is strongest. In the opposite limit – at high neutral densities and low magnetic fields characteristic of the anode region – these terms are small. Indeed, the electron transport seen in the experiment around the anode appears to be classical. The azimuthal electron fluid velocity, $u_{e\theta}$, is given by equation 3.4. The physics associated with this equation was absent in the $r - z$ model and it is an integral part of the current model. In high magnetic field and low neutral density regions, $u_{e\theta}$ is dominated by $E \times B$ and diamagnetic drifts, the third and fourth terms of equation 3.5, respectively. As before, the electric field (eq. 3.6) is purely electrostatic and the parallel momentum equation results in a Boltzmann relation (eq. 3.5). Quasineutrality (eq. 3.7) closes the system, with n_i obtained from the ion particles via the PIC method.

The solution of the equations above yields the electric field and electron fluid velocities. Bilinear interpolation of ion particle positions gives, by quasineutrality, the plasma density. The axial electron current $n_e u_{ez}$ is then obtained as well as an effective mobility. This mobility can be compared with the “classical” value and an assessment of fluctuation-induced transport can be made.

3.2. Numerical method

The SHT geometry is used in the simulations: the axial coordinate extends from $z = 0$ to $z = .12$ (from the anode to 4 cms past the channel exit). The azimuthal coordinate is periodic. For simplicity, a uniform rectangular grid in z and θ is used with 51×50 grid points. The constant external magnetic field, assumed to be purely in the radial direction, is obtained from experiment. The electron temperature, assumed constant and only a function of axial position, is also obtained from experiment. In testing the code, uniform and gaussian profiles for the magnetic field and electron temperature are used as well.

The PIC portion of the $z - \theta$ code follows that of the $r - z$ code and has already been discussed above. We now discuss the solution of the electron fluid equations. In the present geometry, current conservation (eqn. 3.2) and quasineutrality (eqn. 3.7) can be combined to give:

$$\frac{1}{r} \frac{\partial(n_e u_{i\theta})}{\partial \theta} + \frac{\partial(n_e u_{iz})}{\partial z} - \frac{1}{r} \frac{\partial(n_e u_{e\theta})}{\partial \theta} - \frac{\partial(n_e u_{ez})}{\partial z} = 0 \quad (3.12)$$

Expressions for the azimuthal and axial components of the electric field can be obtained from equations 3.5 and 3.6 as follows:

$$E_\theta = -\frac{1}{r} \left(\frac{\partial \phi^*}{\partial \theta} + \frac{kT_e}{en_e} \frac{\partial n_e}{\partial \theta} \right) \quad (3.13)$$

$$E_z = -\frac{\partial \phi^*}{\partial z} - \frac{k \ln n_e}{e} \frac{\partial T_e}{\partial z} + \frac{kT_e}{en_e} \frac{\partial n_e}{\partial z} \quad (3.14)$$

Substituting equations 3.13 and 3.14 into 3.3 and 3.4, and substituting the resulting equations into 3.12, yields the following equation in ϕ^* :

$$a_1 \frac{\partial^2 \phi^*}{\partial \theta^2} + a_2 \frac{\partial \phi^*}{\partial \theta} + a_3 \frac{\partial^2 \phi^*}{\partial z^2} + a_4 \frac{\partial \phi^*}{\partial z} + a_5 = 0 \quad (3.15)$$

where the coefficients a_1 , a_2 , a_3 , a_4 and a_5 are given by:

$$a_1 = -\frac{n_e}{r^2} \mu_\perp \quad (3.16)$$

$$a_2 = -\frac{\mu_\perp}{r^2} \frac{\partial n_e}{\partial \theta} - \frac{n_e}{rB} \frac{\partial}{\partial z} \left(\frac{1}{1 + (\nu/\omega_c)^2} \right) - \left(\frac{1}{1 + (\nu/\omega_c)^2} \right) \left(\frac{1}{rB} \frac{\partial n_e}{\partial z} + \frac{n_e}{rB^2} \frac{\partial B}{\partial z} \right) - \frac{n_e}{r^2} \frac{\partial \mu_\perp}{\partial \theta} \quad (3.17)$$

$$a_3 = -n_e \mu_\perp \quad (3.18)$$

$$a_4 = -n_e \frac{\partial \mu_\perp}{\partial z} + \frac{1}{1 + (\nu/\omega_c)^2} \frac{1}{rB} \frac{\partial n_e}{\partial \theta} - \mu_\perp \frac{\partial n_e}{\partial z} + \frac{n_e}{rB} \frac{\partial}{\partial \theta} \left(\frac{1}{1 + (\nu/\omega_c)^2} \right) \quad (3.19)$$

$$a_5 = \frac{1 + \ln n_e}{1 + (\nu/\omega_c)^2} \frac{k}{erB} \frac{\partial T_e}{\partial z} \frac{\partial n_e}{\partial \theta} - \frac{k \ln n_e}{e} \frac{\partial T_e}{\partial z} \left(\mu_\perp \frac{\partial n_e}{\partial z} + n_e \frac{\partial \mu_\perp}{\partial z} \right) - \frac{kn_e \mu_\perp \ln n_e}{e} \frac{\partial^2 T_e}{\partial z^2} - \frac{k \mu_\perp}{e} \frac{\partial T_e}{\partial z} \frac{\partial n_e}{\partial z} + \frac{kn_e \ln n_e}{erB} \frac{\partial T_e}{\partial z} \frac{\partial}{\partial \theta} \left(\frac{1}{1 + (\nu/\omega_c)^2} \right) + \frac{n_e}{r} \frac{\partial u_{i\theta}}{\partial \theta} + \frac{u_{i\theta}}{r} \frac{\partial n_e}{\partial \theta} + n_e \frac{\partial u_{iz}}{\partial z} + u_{iz} \frac{\partial n_e}{\partial z} \quad (3.20)$$

Equations 3.15-3.20 above are discretized in the θ and z directions using finite differences. The boundary conditions for the electric potential in the axial coordinate are Dirichlet at the anode ($\phi_{anode} = \phi_{discharge}$), and Dirichlet at the downstream boundary ($\phi_{exit} = 0$). In the azimuthal direction the boundary condition is periodic. Upon discretization using standard central difference formulas for the derivatives, along with the boundary conditions, the resulting system becomes block-tridiagonal. The solution is found via a direct-solve method. The electric potential and electric field components then follow from equations 3.5 and 3.13-3.14. Once the electric field is obtained, the particles are advanced, neutrals are ionized via Monte Carlo, neutrals are injected at the anode according to the given mass flow rate, and new particle densities obtained with the PIC method. The electric potential is then found again and the cycle begins again.

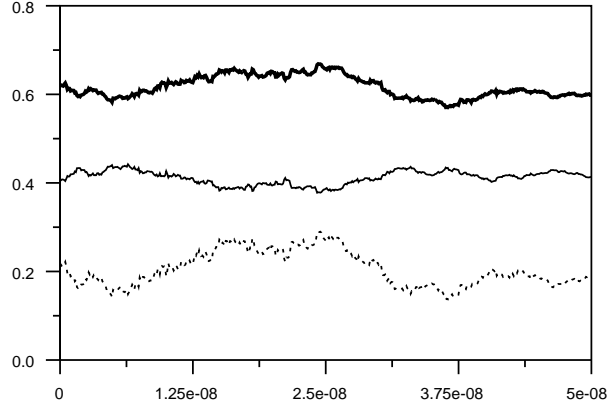


FIGURE 6. Electron current (amps) as a function of time (secs). The bold trace, solid trace and dashed trace represent the total current, the classical contribution, and the azimuthal-fluctuation induced contribution respectively.

A typical simulation is initialized with a background of ions and neutrals placed uniformly in the domain. Their velocities are obtained by inverting a Maxwellian distribution function. A key parameter in the simulation is the value of the Hall parameter, ω_c/ν . If this parameter has a small initial value (due, for instance, to a large value of n_n), the electron transport is found to be classical and azimuthal disturbances negligible. The electric field is localized axially to the region where the magnetic field is strongest and the azimuthal electric field is very small. Simulations that use uniform profiles for the magnetic field and electron temperature yield a uniform profile for the axial electric field, as expected.

However, a simulation started with a small value of the Hall parameter does not remain with that small value (except near the anode where the magnetic field is low and the neutral density is high). This is due to ionization. Ionization eventually depletes the large initial neutral density and brings up the value of the Hall parameter. Azimuthal fluctuations then emerge, along with their associated transport. Figure 6 shows the classical and anomalous contributions to electron transport, where here anomalous is taken to be the transport associated with the last two (azimuthal) terms of Equation 3.3. As shown in Figure 6, the azimuthal contributions are important. Unfortunately, numerical instability prevents us from giving further results at the present time. In fact, ionization drives strong fluctuations and eventually drives our algorithm numerically unstable.

4. Conclusions and further work

We have investigated electron transport in Hall thrusters via numerical simulation using two hybrid models, one in the radial and axial coordinates, one in the azimuthal and axial coordinates. In the $r - z$ model, the electron mobility is modeled with an *ad hoc* parameter which enhances the mobility over the classical prediction. Unlike other simulation efforts, this work uses a parameter motivated by an experimental measurement of the mobility in the Stanford Hall Thruster over a range of discharge voltages. Comparison of simulated and experimental $I - V$ curves and equilibrium profiles indicates that the experimentally-based model is superior to the simple Bohm model. This paper

concludes that, in the absence of a comprehensive nonlinear theory of electron transport, use of experimentally-based models for the mobility in $r - z$ descriptions is critical to the usefulness of such descriptions.

Motivated by the $r - z$ results, a model in the azimuthal and axial coordinates has been formulated. It represents a simplified description of Hall thruster plasmas able to capture azimuthal flows, fluctuations, and their associated transport. Preliminary results indicate that for the typical large experimental values of ω_e/ν found in these engines, the electron transport associated with azimuthal disturbances is significant. However, numerical stability has prevented us from running the model to long time scales.

Our future work with the $r - z$ model lies in a) implementing a realistic wall-damping model for the electron temperature that includes the physics of temperature-dependent secondary electron emission as well as sheath saturation effects, and b) improving the PIC portion of the code by adding more collisional effects, important for the investigation of erosion patterns in these devices. Future work with the $z - \theta$ model involves a) improving the numerical stability of the method of solution, b) examining the azimuthal fluctuations and transport in detail, and c) incorporating a temperature equation with a realistic wall-damping model.

REFERENCES

- ADAMS, J. C., HERON, A. & LAVAL, G. 2004 Study of stationary plasma thrusters using two-dimensional fully kinetic simulations. *Phys. Plasmas* **11**, 295-305.
- AHEDO, E., MARTINEZ-CEREZO, P. & MARTINEZ-SANCHEZ, M. 2001 One-dimensional model of the plasma flow in a Hall thruster. *Phys. Plasmas* **8**, 3058-3068.
- ALLIS, M. K., GASCON, N., VIALARD-GOUDOU, C., CAPPELLI, M. A. & FERNANDEZ, E. 2004 A comparison of 2D hybrid Hall thruster model to experimental measurements AIAA-2004-3951, 40th AIAA/ASME/SAE/ASEE Joint Propulsion Conference, Ft. Lauderdale, FL.
- BARRAL, S., MAKOWSKI, K., PERADZYNSKI, Z., GASCON, N. & DUDECK, M. 2003 Wall material effects in stationary plasma thrusters: near-wall and in-wall conductivity *Phys. Plasmas* **10**, 4137-4152.
- BAREILLES, J., HAGELAAR, G. J. M., GARRIGUES, L., BONIFACE, C., BOEUF, J. P. & GASCON, N. 2004 Critical assessment of a two-dimensional hybrid Hall thruster model: Comparisons with experiments *Phys. Plasmas* **11**, 3035-3046.
- BIRDSALL, C. K. & LANGDON, A. B. 1991 *Plasma Physics via Computer Simulation*. IOP Publishing Ltd.
- CAPPELLI, M. A. 2004 *Private communication*.
- CHOUERI, Y. E. 2001 Plasma oscillations in Hall thrusters. *Phys. Plasmas* **8**, 1411-1426.
- FERNANDEZ, E., CAPPELLI, M. A. & MAHESH, K. 1998 2D simulations of of Hall thrusters. *CTR Annual Research Briefs*, 81-91.
- FIFE, J. M. 1995 Two-dimensional hybrid particle-in-cell modeling of Hall thrusters. S.M. thesis, MIT.
- FIFE, J. M., MARTINEZ-SANCHEZ, M. & SZABO, J. 1997 A numerical study of low-frequency discharge oscillations in Hall thrusters. AIAA-97-3052, 33rd AIAA/ASME/SAE/ASEE Joint Propulsion Conference, Seattle, WA.
- GASCON, N., ALLIS, M. K., THOMAS, C. A., CAPPELLI, M. A. & FERNANDEZ, E. 2004 A closer look at longitudinal oscillations inside a Hall thruster. AIAA-2004-

- 3780, 40th AIAA/ASME/SAE/ASEE Joint Propulsion Conference, Ft. Lauderdale, FL.
- GULCZINSKI, P. & SPORES, R. 1996 Analysis of Hall-Effect Thrusters and Ion Engines for Orbit Transfer Missions. AIAA-96-2973, 32nd AIAA/ASME/SAE/ASEE Joint Propulsion Conference, Lake Buena Vista, FL.
- HIRAKAWA, M. & ARAKAWA, Y. 1996 Numerical Simulation of Plasma Particle Behavior in a Hall Thruster. AIAA 96-3195, 32nd AIAA/ASME/SAE/ASEE Joint Propulsion Conference, Lake Buena Vista, FL.
- JANES, G. & LOWDER, R. 1966 Anomalous Electron Diffusion and Ion Acceleration in a Low-Density Plasma. *Phys. Fluids* **9**, 1115-1123.
- LENTZ, C. A. 1990 Transient One Dimensional Numerical Simulation of Hall thrusters. S.M. thesis, MIT.
- MEEZAN, N., HARGUS, W. & CAPPELLI, M. 2001 The anomalous electron mobility in a coaxial Hall discharge plasma. *Phys. Review E*. **63**, 26410-26416.
- MOROZOV, A., ESINCHUK, Y., TILININ, G., TROFIMOV A., SHAROV Y. & SHCHEPKIN G. 1972 Plasma accelerator with closed electron drift and extended acceleration zone. *Sov. Phys. - Tech. Phys.* **17**, 38-45.
- YOSHIKAWA, S. & ROSE, D. 1962 Anomalous diffusion of a plasma across a magnetic field. *Phys. Fluids*. **3**, 334-340.

Page intentionally left blank

Hartmann effect on MHD turbulence in the limit $Rm \ll 1$

By B. Knaepen[†], Y. Dubief AND R. Moreau[‡]

This work is an attempt to model the actual MHD flows at the laboratory scale ($Rm \ll 1$). It essentially focuses on how to take into account the influence of the Hartmann layers on the turbulence present in the core flow, namely when the applied magnetic field is large enough to impose a quasi-2D regime. The model studied is obtained from the classical theory of Hartmann layers and consists in extra damping terms in the evolution equation of the fluid. Numerical results show that the model predicts the expected behavior of the core flow between Hartmann layers. A striking property is however that the component of the velocity field parallel to the magnetic field does not evolve to an anisotropic state as observed for the perpendicular components. This behavior is supported by an analytical analysis.

1. Introduction

Most of the experiments on MHD achievable at the laboratory scale concern fluids, such as liquid metals, whose magnetic diffusivity $\eta = 1/(\mu\sigma)$ (μ stands for their magnetic permeability and σ for their electrical conductivity) is extremely large in comparison with their kinematic viscosity ν . This implies that the magnetic Reynolds number $R_m = UL/\eta$ (U is a typical velocity scale, L a typical length scale) is often much smaller than unity (typically in the range 10^{-4} - 10^{-2}), whereas the ordinary Reynolds number $Re = UL/\nu$ is much larger than unity (typically in the range 10^3 - 10^5). As a consequence, the distribution of the magnetic field is controlled by diffusion, what means that the actual field is negligibly disturbed by the fluid flow. Then, the magnetic field may be considered as given, and in the following it is supposed uniform and denoted \mathbf{B} .

Many experiments have been performed in such conditions, first in Riga and in Purdue (see Lielausis 1975; Tsinober 1990) then in Beer-Sheva (Branover 1978) and in Grenoble (A. Alemany & Frisch 1979; Sommeria 1986; Messadek & Moreau 2002), which have provided a fairly good knowledge of the specific properties of this kind of MHD turbulence. The understanding of the mechanisms by which the magnetic field is influencing this turbulence has also received significant attention (A. Alemany & Frisch 1979; Sommeria & Moreau 1982; Davidson 1995, 1997). The numerical modeling of this kind of MHD turbulence has also started (Zikanov & Thess 1998; Lee & Choi 2001; Knaepen & Moin 2004) but the tools to compute such flows are still far from being capable to include all the majors effects of the magnetic field. It will be seen, later on, that one of the major properties of this MHD turbulence is to become quasi-two-dimensional (Q2D). Then, an inverse cascade of energy is substituted to the familiar direct cascade in ordinary turbulence. As a consequence, the relevant length scales are larger than in ordinary turbulence and the computation domain must also be larger, as well as the computation time. One

[†] Université Libre de Bruxelles, Brussels, Belgium

[‡] Laboratoire EPM, ENSHMG, Grenoble, France

may also notice that the small scales become less relevant and expect that this kind of turbulence be particularly well adapted to large eddy simulations (LES).

This report is organized as follows. In section 2, the classical theory of Hartmann layers and their influence on the core flow are outlined. The main section of our report follows in section 3. The model describing the influence of the Hartmann layers on the core flow is formulated and numerical results testing its predictions are presented. The emphasis is put on the evolution of the kinetic energy of the flow and on the anisotropy that develops in the flow. We conclude this report in section 4 and highlight indicate lines of future research.

2. Basic ideas on the Hartmann damping

Among the effects of the magnetic field on the turbulence, the first one is the development of an anisotropy, which becomes quite pronounced when the magnetic field is very large. In the case of homogeneous turbulence, this anisotropy is particularly clear in the Fourier space, since the Fourier transform of the Lorentz force is depending on the direction of the wave vector, but independent of its magnitude (A. Alemany & Frisch 1979). Indeed, the energy carried by wave vectors parallel to \mathbf{B} is rapidly damped out, in a time scale of the order of $\tau_J = \rho/(\sigma B^2)$ (ρ is density, τ_J is usually named the Joule time scale and B is the norm of \mathbf{B}), whereas the energy carried by wave vectors perpendicular to \mathbf{B} is not directly damped by the Lorentz force. However, inertia is capable to withdraw some energy from these wave vectors perpendicular to \mathbf{B} and to transfer it to wave vectors more rapidly damped. Such inertial transfer mechanisms, between wave vectors of similar magnitudes but different directions, are far from being well understood as they have not been the subject of as many investigations as the usual energy transfers between different wave numbers. What is generally accepted is that their time scale is still the eddy turnover time $\tau_{tu} = l/u$ (here l and u are length and velocity scales of turbulent eddies). And the net result of the competition between the Joule damping and inertia still leads to a time decay following a power law of the form t^{-n} with $n \approx 1.7$ instead of 1.1 or 1.2 in ordinary isotropic turbulence (A. Alemany & Frisch 1979).

There is another way to understand the development of this anisotropy, without using Fourier transforms and wave vectors, which has the advantage to be valid in non-homogeneous turbulence. It is based on the fact that, when $Rm \ll 1$, the well known Alfvén waves degenerate into a diffusion along the magnetic field lines (Sommeria & Moreau 1982). Due to this mechanism, any initial eddy elongates in the direction parallel to \mathbf{B} according to a law

$$\frac{l_{\parallel}}{l_{\perp}} \sim \left(\frac{\sigma B^2 t}{\rho} \right)^{\frac{1}{2}}. \quad (2.1)$$

So, substituting τ_{tu} instead of t , one may easily guess what the anisotropy of any given eddy may be during its life time. One should notice that eddies with significantly large l_{\perp} may get a length scale l_{\parallel} of the same order as or larger than the width of the whole domain h . Then, such eddies are column-like and one may say that this turbulence becomes Q2D, after a duration of the order of

$$\tau_{2D} = \tau_J \left(\frac{h}{l_{\perp}} \right)^2. \quad (2.2)$$

Other very important effects come from the influence of the Hartmann walls on the

turbulence. This influence is at least twofold. First, the presence of the walls just forces the velocity component perpendicular to them to be zero, because it cannot vary significantly through the thin Hartmann boundary layer. Then, within the Q2D columns, the velocity vectors tend to remain within planes perpendicular to the magnetic field. The second influence of the Hartmann walls has its origin in one of the striking properties of the Hartmann boundary layer, which is not a passive layer like the Blasius layer, but which is a primary layer, capable to react on the core flow. This property is the fact that a significant Joule damping remains present within the layer where the velocity cancels whereas the electric field \mathbf{E} does not. As a consequence, the balance between \mathbf{E} and $\mathbf{u} \times \mathbf{B}$, which is present in the core and minimizes the current density, is destroyed and the current density is locally very important (of the order of $\sigma B u$, whereas it is Ha less within the core, $Ha = \sqrt{\sigma/(\rho\nu)} B h$ being the Hartmann number built with the width between the Hartmann walls h). On this basis, Sommeria & Moreau (1982) have shown that the effective Joule damping time, which is then named the Hartmann time, is $\tau_H = Ha\tau_J = h/B\sqrt{\rho/(\sigma\nu)}$. It may be much larger than τ_J , since it varies as B^{-1} (not B^{-2} as τ_J).

3. Damping of the homogeneous core flow in a Hartmann channel

3.1. Formulation

Since the Hartmann layers are very thin (their thickness $\delta = B^{-1}\sqrt{\rho\nu/\sigma}$ may be around $30 \mu\text{m}$ in mercury with a magnetic field of 1 Tesla), the fluid velocity is uniform in the main part of the channel. Then, except in those layers where the shear is localized, the turbulence may be homogeneous. According to what was described in the former section, it is also Q2D as soon as τ_{2D} is significantly shorter than the eddy turn over time $\tau_{tu} = l_{\perp}/u_{\perp}$. Then the velocity component parallel to the magnetic field, which may be non-zero in the initial state, is submitted to a linear damping in a time scale of the order of τ_{2D} . This may be easily modeled with the addition of the term $-u_{\parallel}/\tau_{2D}$ in the right hand side of the equation for u_{\parallel} . The velocity components in the plane perpendicular to \mathbf{B} are also affected by some damping, but much less rapidly, as explained in section 2. Indeed, they are only submitted to the Hartmann damping, which may be expressed by the addition of the term $-u_{\perp}/\tau_H$ in the right hand side of the equation for u_{\perp} . The damping force F_i associated with the Hartmann layers is therefore tentatively modeled by

$$F_x = -u_x/\tau_H, \quad F_y = -u_y/\tau_H, \quad F_z = -u_z/\tau_{2D}, \quad (3.1)$$

where the z -direction has been chosen as the wall-normal direction. The form 3.1 cannot be used as such since it would not respect the incompressibility of the flow. However it can easily be projected on its solenoidal part F_i^S . Using the Fourier representation, F_i^S can be written as

$$F_i^S = (\delta_{ij} - \frac{k_i k_j}{k^2}) F_j. \quad (3.2)$$

Again in Fourier representation, the actual components of F_i^S are then,

$$F_x^S = -u_x/\tau_H + (1/\tau_{2D} - 1/\tau_H) \frac{k_x k_z}{k^2} u_z \quad (3.3)$$

$$F_y^S = -u_y/\tau_H + (1/\tau_{2D} - 1/\tau_H) \frac{k_y k_z}{k^2} u_z \quad (3.4)$$

Resolution	256 ³
Box size ($l_x \times l_y \times l_z$)	$2\pi \times 2\pi \times 2\pi$
Rms velocity	2.35
Viscosity	0.006
Integral length-scale ($L = 3\pi/4 \times (\int \kappa^{-1} E(\kappa) d\kappa / \int E(\kappa) d\kappa)$)	0.944
$Re = uL/\nu$	370
Dissipation (ϵ)	14.56
Dissipation scale ($\gamma = (\nu^3/\epsilon)^{1/4}$)	0.0110
$k_{max}\gamma$	1.41
Microscale Reynolds number ($R_\lambda = \sqrt{15/(\nu\epsilon)}u^2$)	72.36
Eddy turnover time ($\tau = L/u$)	0.402

TABLE 1. Turbulence characteristics of the initial velocity field. All quantities are in MKS units.

$$F_z^S = -u_z/\tau_{2D} + (1/\tau_{2D} - 1/\tau_H) \frac{k_z k_z}{k^2} u_z \quad (3.5)$$

Aside from a simple linear damping, incompressibility thus requires also a wavevector dependent contribution in order to take into account the effect of Hartmann layers. In 3.5, we see that this k -dependent contribution has exactly the same functional form as the traditional Joule damping term. It comes however with the opposite sign. When τ_{2D} and τ_J are of the same order, the traditional Joule damping can therefore be compensated by this extra term (since in general $\tau_H \gg \tau_J$) and it is thus expected that anisotropy in the parallel component will remain weak in that case. Its decay will be dominated by the simple damping term $-u_z/\tau_{2D}$ at all times.

For the perpendicular components, two phases of decay have to be distinguished. In the first one, $0 < t < \tau_{2D}$, the k -dependent terms will exert their effects. In the second one, $\tau_{2D} < t$, their influence will become negligible as u_z is damped very rapidly. In this second phase, the decay will proceed as a simple damping with characteristic time τ_H .

3.2. Numerical results

The set of equations we are solving are:

$$\partial_t u_i = -\partial_i(p/\rho) - u_j \partial_j u_i - \frac{A^2}{\eta} \Delta^{-1} \partial_z \partial_z u_i + F_i^S + \nu \Delta u_i, \quad (3.6)$$

where F_i^S is given by 3.3-3.5 (here $A = B/\sqrt{\mu\rho}$ denotes the Alfven velocity). These equations are solved using a pseudo-spectral code in a cubic geometry. The resolutions of our run is 256³ Fourier modes. The initial condition for the velocity consists of a developed turbulence field that is adequately resolved in the computational domain adopted (it is obtained from a purely hydrodynamic case). Some of its characteristics are listed in table 1. In order to induce a sufficient amount of anisotropy in the flow, we have chosen a moderate value of the interaction number: $N = \tau_{tu}/\tau_J = 10$. Given the values of u and L (see Table 1), this implies that the Joule time is equal to $\tau_J = L/(uN) = 0.0402$. In this run we also assume that $\tau_{2D} = 0.0402 = \tau_J$ (looking at 2.2 this corresponds to a case where the channel width is equal to the initial l_\perp). From these values, one also easily computes that $Ha = 60.8$ and $\tau_H = 2.45$.

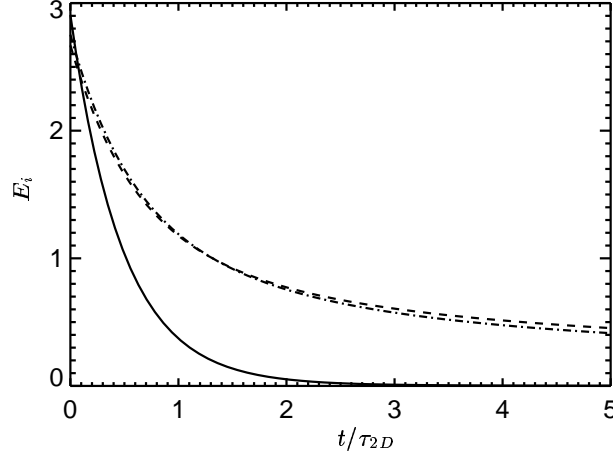


FIGURE 1. Evolution with time of the kinetic energy. Solid line: $\langle \|\frac{1}{2}u_z\|^2 \rangle$; dashed line: $\langle \|\frac{1}{2}u_x\|^2 \rangle$; dashed-dot line: $\langle \|\frac{1}{2}u_y\|^2 \rangle$.

3.2.1. Decay of kinetic energy

At the beginning of the simulation all three components of the velocity field have approximately equal energy (the initial flow is isotropic). As displayed in Fig. 1, the energy of the parallel component is dissipated much faster than the one of the perpendicular components (since $\tau_{2D} \ll \tau_H$). After a time $t = 2\tau_{2D}$, the parallel component has been virtually completely dissipated.

3.2.2. Spectra of kinetic energy

The kinetic spectra presented in figure 2 indicate that the flow is well resolved in the simulation. A close examination shows that the slopes of the spectra for the perpendicular components tend to become steeper as time evolves, though this effect is small. The slope for the parallel direction exhibits the opposite trend and this is very marked in the different plots.

3.2.3. Anisotropy

To measure anisotropy we use the following diagnostics:

$$G_{ij,kl} = \frac{\langle (\partial_i u_j)^2 \rangle}{\langle (\partial_k u_l)^2 \rangle}. \quad (3.7)$$

They measure the relative strength of velocity gradients in different directions and for different components of the velocity field. For instance, it is easy to show that in isotropic turbulence one should have (Pope 2000):

$$G_{11,21} = G_{11,31} = 0.5, \quad G_{12,22} = G_{13,33} = 2, \quad G_{12,32} = G_{13,23} = 1. \quad (3.8)$$

In our simulations, the mean magnetic field is directed along the z direction (parallel direction). If the flow becomes 2D perpendicular to this direction, then one must have:

$$G_{3j,\alpha l} \rightarrow 0, \quad \text{for } (j,l) \in (1,2,3) \quad \text{and} \quad \alpha \in (1,2). \quad (3.9)$$

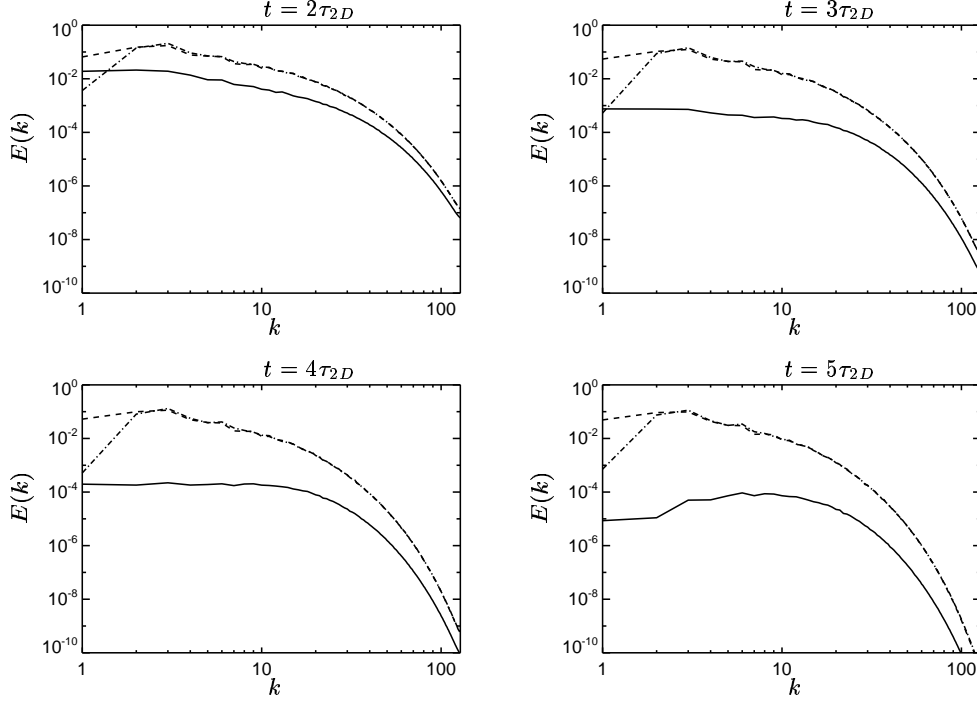


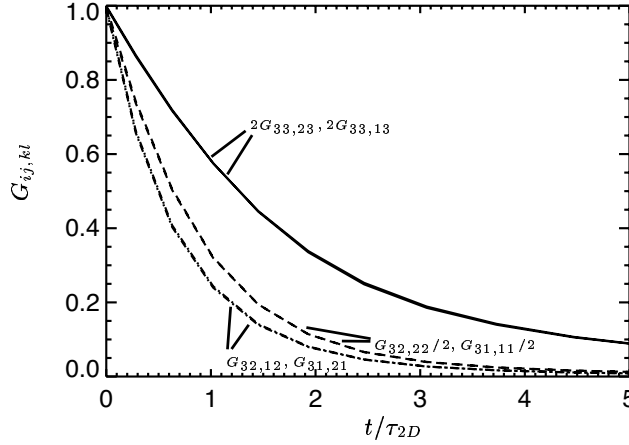
FIGURE 2. Kinetic spectra of the three velocity components at several times during the flow decay. Dashed line: u_x ; dash-dot line: u_y ; solid line: u_z .

In figure 3 several of the $G_{ij,kl}$ are plotted. From the figure it is clear that the symmetry $x \leftrightarrow y$ is well respected. Also, the component u_z remains significantly more isotropic than the perpendicular components with respect to this diagnostics, although with time it also evolves to a state with weaker variations along the parallel direction compared to the perpendicular directions. This behavior is well in line with the discussion contained in section 3.1.

On dimensional grounds, all the $G_{ij,kl}$ displayed in Fig. 3 should be of the order l_\perp^2/l_\parallel^2 . Here we see that this ratio depends on the component of the velocity field considered. The ratio is larger for the parallel component than for the perpendicular components. As a consequence we see that eq. 2.1 becomes component dependent in the presence of the Hartmann damping modeling 3.3-3.5.

3.2.4. 3D visualizations of the flow

The diagnostics presented in Fig. 3 provide a quantitative measure of the anisotropy of the flow. It is also worth to examine more qualitatively how the flow structures evolve with time. This is shown in Figs 4–6 where the energy density of the three velocity components are plotted. These plots confirm the information provided in Fig. 3: the parallel component of the velocity field remains more isotropic than the perpendicular components which become noticeably elongated in the direction of the magnetic field.

FIGURE 3. Anisotropy coefficients $G_{ij,kl}$. See figure for legend.

4. Conclusions

The idea of a pre-existing isotropic turbulence suddenly submitted to a uniform magnetic field, initially introduced by Moffatt (1967), is a purely idealized concept, since, in any experiment, during the growth of the magnetic field, eddy currents and the associated Lorentz forces are generated, which are completely neglected in section 3. In spite of this assumption, which would deserve quite a complex analysis and may be not justified at all in many experimental situations, following Moffatt and others, we focus on the mechanisms by which the homogeneous turbulence tends to become 2D and decays. Contrary to previous numerical studies on 3D homogeneous turbulence subject to a constant mean magnetic field, we try to incorporate the influence of distant Hartmann layers on the flow. The spirit behind the model introduced in section 3 is to reproduce the damping generated by the Hartmann layers through damping terms of appropriate damping times. However, to respect the incompressibility condition, wavevector dependent contribution to the model have to be considered. The effect of the model is therefore twofold. First, the velocity component parallel to the magnetic field undergoes a much more rapid damping than the perpendicular components. Less obviously, this parallel component remains largely isotropic throughout the decay due to the wavevector dependent contribution in the model.

Because of time constraints, our numerical simulations have been limited to times $0 \leq t \leq 5\tau_{2D} \ll \tau_H$. It has thus been only possible to observe the early transition from 3D to 2D turbulence. In future work, simulation runs with $t \sim \tau_H$ will be performed. These will make possible the study of typical 2D turbulence features like inverse energy cascade and its influence on the slope of the kinetic energy spectra.

In addition to the problem described in section 3, during the summer program, another study was started aiming at the simulation of the MATUR experiment (Messadek & Moreau 2002). This experiment, immersed in a mean applied magnetic field, uses a difference of electric potential to force a radial flow between two discs. In this system, anodes are located on one of the discs and the side wall closing the apparatus is the cathode. The MHD equations were implemented in a second-order staggered finite difference code in cylindrical coordinates. Several numerical difficulties were encountered due to the extreme thinness of the Hartmann layers which must be modeled very accurately since the whole electric current passing in the turbulent core must be close via those layers,

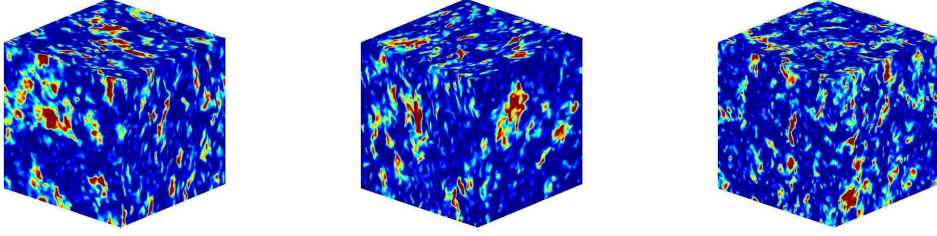


FIGURE 4. 3D visualizations of the energy density of the components of the velocity field at $t = 2\tau_J$; u_x (left), u_y (center), u_z (right). Note that the colormap of the plot corresponding to u_z is not equal to the colormap in the other two plots since the level of energy in u_z is much lower. The colormaps are not provided since the figures are meant to highlight the qualitative shapes of the turbulent structures.

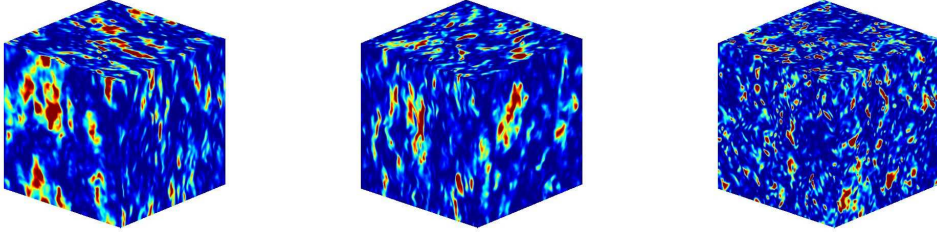


FIGURE 5. See caption of figure 4. Here $t = 3\tau_{2D}$.

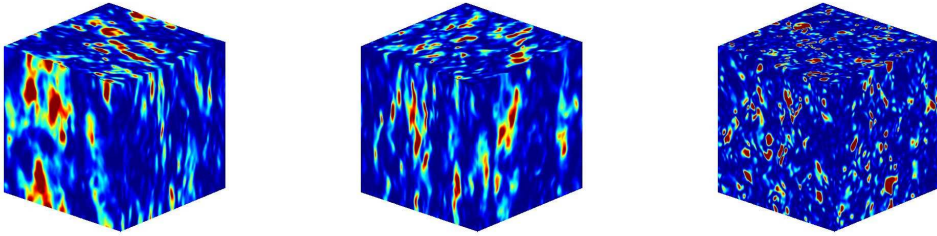


FIGURE 6. See caption of figure 4. Here $t = 5\tau_{2D}$.

which react on the core flow proportionally to the Hartmann current. As a consequence, the grid must be significantly refined in the Hartmann layers yielding very small time steps. Another important issue is the accurate representation of a series of point-like electrodes distributed on a circle at mid way between the center of the apparatus and the side wall (cathode). The difficulty here is caused by the singularities present in the experiment between the insulating parts of the Hartmann wall and the electrically conducting parts. The appropriate way to solve those difficulties without introducing any significant artifact has itself been the subject of detailed investigations. The refinement required by this set-up is very detrimental to the time step in cylindrical coordinates due

to the small radial grid-spacing at the center. To relax such a constraint and study the possibility of local refinement for both the electrodes and the Hartmann layers, current investigations have shifted to the unstructured code CDP- α developed by the ASCI program at Stanford. It is our purpose to complete this work soon and to publish the results of this benchmark in an other paper.

5. Acknowledgements

The authors are grateful to CTR for supporting this research project during the Summer Program 2004. Fruitful discussions with the other participants of the MHD session concerning this work are gratefully acknowledged.

REFERENCES

- A. ALEMANY, R. MOREAU, P. L. S. & FRISCH, U. 1979 Influence of an external magnetic field on homogeneous turbulence. *J. de Mécanique* **18** (2), 275.
- BRANOVER, H. 1978 *Magnetohydrodynamic flow in ducts*. Halsted.
- DAVIDSON, P. A. 1995 Magnetic damping of jets and vortices. *J. Fluid Mech.* **299**, 153.
- DAVIDSON, P. A. 1997 The role of angular momentum in the magnetic damping of turbulence. *J. Fluid Mech.* **336**, 123.
- KNAEPEN, B. & MOIN, P. 2004 Large-eddy simulation of conductive flows at low magnetic Reynolds number. *Phys. Fluids* **16** (5), 1255.
- LEE, D. & CHOI, H. 2001 Magnetohydrodynamic turbulent flow in a channel at low magnetic Reynolds number. *J. Fluid Mech.* **439**, 367.
- LIELAUSIS, O. 1975 Liquid metal magnetohydrodynamics. *Atomic Energy Review* **13**, 527.
- MESSADEK, K. & MOREAU, R. 2002 An experimental investigation of mhd quasi-two-dimensional turbulent shear flows. *J. Fluid Mech.* **456**, 137.
- MOFFATT, H. K. 1967 On the suppression of turbulence by a uniform magnetic field. *J. Fluid Mech.* **28**, 571.
- POPE, S. B. 2000 *Turbulent flows*. Cambridge University Press.
- SOMMERIA, J. 1986 Experimental study of two-dimensional inverse energy cascade in a square box. *J. Fluid Mech.* **170**, 139.
- SOMMERIA, J. & MOREAU, R. 1982 Why, how, and when, MHD turbulence becomes two-dimensional. *J. Fluid Mech.* **118**, 507.
- TSINOBER, A. 1990 MHD flow drag reduction. In *Viscous drag reduction in boundary layers* (ed. D. M. Bushnell & J. N. Hefner), p. 327. AIAA Prog. Astron. Aeron. Series.
- ZIKANOV, O. & TRESS, A. 1998 Direct numerical simulation of forced mhd turbulence at low magnetic Reynolds number. *J. Fluid Mech.* **358**, 299.

LES and numerical simulations

The development and the test of new concepts in large-eddy simulation (LES) traditionally plays a central role in the CTR summer program. This year is no exception with not less than 10 participants, 4 hosts and 5 research projects in the LES group. It might appear surprising to keep such an important “fundamentals” activity while LES are applied more and more routinely in industrial applications and in many fields of physics and engineering as confirmed by its intensive use in other groups of this summer program. There is however still room for improvements in the LES techniques. As a sign of this search for a better LES formalism, participants from several groups – magnetohydrodynamics, solar turbulence and combustion – have chosen to be directly involved in research projects on LES fundamentals. The most striking property of the projects presented hereafter is the integrated approach adopted. The LES problem is treated globally, including the definition of the resolved field, the numerical method and the modelling strategy. The possible interconnections between these different aspects of LES are fully recognized and exploited in the development of the projects.

The first project is a perfect example of this integrated approach. Goldstein, Vasilyev & Kevlahan use the wavelet representation of the velocity field to propose a new LES formalism. Wavelet filters are able to capture energetic structures by simultaneously resolving them in physical and wave number space. A specific numerical scheme is proposed, the dynamically adaptive wavelet collocation (DAWC) method. It is able to track energetic structures without ad-hoc assumptions for the grid adaptation. Also, an eddy-viscosity model based on a dynamic procedure redefined in terms of two wavelet threshold filters is implemented and a fully adaptive LES simulation is achieved. This approach, named stochastic coherent adaptive large eddy simulation (SCALES), implies a direct coupling of the grid evolution to both the flow and the subgrid-scale model. Results in isotropic decaying turbulence show that this approach competes with traditional LES. Providing a local version of the dynamic procedure exploiting the intrinsically local character of the numerical method is the next challenge for the SCALES approach.

The idea that the definition of the resolved field, the numerical method and the modelling strategy have to be considered as a global issue in LES is also omnipresent in the second project by Oberai, Gravemeier & Burton. Ideal LES solutions are introduced to refer to the fields obtained by truncating direct numerical simulation (DNS) solutions. The Smagorinsky model performances are evaluated in an *a-priori* study of the transfer of energy from the resolved scales, split into coarse and fine resolved scales, to the subgrid scales. When the ideal solution is defined as a truncated Fourier representation of the DNS solution, the energy transfer from the fine resolved scales is the dominant contribution and the Smagorinsky model is overly dissipative in the coarse resolved scales. When the ideal LES solution is identified as the nodal interpolant on a coarse finite element mesh, contributions from both the coarse and the fine resolved scales are important and the model is found to perform reasonably well in both coarse and fine resolved scales. The variational multiscale formulation of LES in which different models are used for the fine and the coarse resolved scales could thus be justified in spectral codes but not necessarily in finite element cases.

In the third project, Debliquy, Knaepen, Carati & Wray propose a LES formalism based on sampling operators. Samplings have several attracting properties in LES. They

directly transform continuous signal into discrete data and always commute with products. However, samplings never commute with spatial derivatives. A model is needed for this commutation error, which is the discretization error associated to the numerical scheme. Hence, here again, an integrated approach is proposed in which the definition of the resolved field, the numerical scheme and the model are treated simultaneously. A dynamic procedure, based on samplings on embedded grids, is proposed and tested in isotropic decaying turbulence. The Smagorinsky model is chosen and, despite its ability to represent discretization errors is questionable, reasonable results are obtained. As a by-product of this formalism, interpolation functions compatible with finite difference schemes have been proposed. These functions play the same role as the plane waves in the Fourier analysis.

In the fourth project, Nakayama, Hori & Street have focused their research on the definition of the LES velocity field close to a rough solid boundary. An explicit filtering is used to treat in a unified formalism all the effects due to the lack of resolution, both in the core flow and in the wall region. In addition to the traditional subgrid scale stress, the resulting LES equations contain extra stress-like terms that can be identified as subgrid-scale roughness contributions and that need to be modeled. Here again, the coupling between the definition of the resolved field, the resolved domain and modelling is thus fully acknowledged. Preliminary LES calculations have been conducted for turbulent channel flows over flat and wavy rough surfaces. It is suggested that the rough boundary effects may be modeled by boundary resistance and slip velocity effects. The results are obtained with pre-assigned values of the model constants. However, the formalism is compatible with a dynamic procedure which is presented in the report.

In the last project, Moureau, Vasilyev, Angelberger & Poinso have investigated the importance of the temporal commutation errors (TCE) in LES. The coupling between the definition of the resolved field and the modelling is again the primary motivation of this work. When the filter is a function of time, the LES equations contain an unknown term due to the non commutation of the filter operator and the partial time derivative. A general form of TCE has been derived and the error magnitude has been estimated in a numerical square-piston experiment. In particular, the influence of the crank speed and the compression ratio have been studied. It has been shown that the magnitude of TCE remains small even for large values of these parameters. It is thus tempting to conclude that TCE can be neglected. It should be underlined however that in piston-engines the flow and the mesh deformation are generated by the same phenomenon: the piston motion. In some other cases with automatic local mesh refinement, TCE may be less correlated to the flow and may not remain negligible.

Daniele Carati

Adaptive LES of 3D decaying isotropic turbulence

By D. E. Goldstein[†], O. V. Vasilyev[†] AND N. K.-R. Kevlahan[‡]

In this work SCALES simulations of decaying incompressible isotropic turbulence are compared to DNS and LES results. Current Large Eddy Simulation (LES) relies on, at best, a zonally adapted filter width to reduce the computational cost of simulating complex turbulent flows. While an improvement over a uniform filter width, this approach has two limitations. First, it does not capture the high wave number components of the coherent vortices that make up the organized part of turbulent flows, thus losing essential physical information. Secondly, the flow is over-resolved in the regions between the coherent vortices, thus wasting computational resources. The Stochastic Coherent Adaptive Large Eddy Simulation (SCALES) approach addresses these shortcomings of LES by using a dynamic grid adaptation strategy that is able to resolve and “track” the most energetic coherent structures in a turbulent flow field. This corresponds to a dynamically adaptive local filter width. Unlike Coherent Vortex Simulation (CVS), which is able to recover low order statistics with no subgrid scale stress model, the higher compression used in SCALES necessitates that the effect of the unresolved subgrid scale (SGS) stresses must be modeled. These SGS stresses are approximated using a new dynamic eddy viscosity model based on Germano’s classical dynamic procedure redefined in terms of two wavelet thresholding filters.

1. Introduction

Turbulence is characterized by energetic eddies that are localized in space and scale, yet most numerical methods for turbulent flow simulations do not take advantage of this localization. In this work we explore the possibility of making use of this localization by “compressing” the turbulence problem such that a simulation with a subset of the total modes captures the dynamics of the most energetic eddies in the flow. A recent method for simulating turbulence called Coherent Vortex Simulation (CVS), introduced by Farge *et al.* (1999), uses a wavelet filter to dynamically resolve and “track” the energetic coherent eddies or vortices in a turbulent flow. It has been shown that the resulting subgrid scale (SGS) field with CVS is near Gaussian white noise (Goldstein & Vasilyev 2004; Farge *et al.* 2001), which results in practically no SGS dissipation. Therefore, a CVS simulation can be run with no SGS model if only low order statistics are required. It is important to note that there is still significant energy transfer between the resolved and SGS modes and visa-versa, but the statistical average or net energy transfer is zero. If higher order statistics are required, then a purely stochastic subgrid scale stress model can be used to reproduce the effect of the subgrid scales. One of the challenges with the CVS method is how to determine on the fly during an actual simulation the “ideal” wavelet compression, which results in a purely incoherent subgrid scale field. Even if it can be found in a cost effective manner it is still likely that the associated adaptive grid will be too fine to be

[†] University of Colorado at Boulder, CO

[‡] McMaster University at Hamilton, ON, Canada

cost effective for simulating high Re number flows, since the computational cost of CVS falls between DNS and LES.

Recently a new methodology called Stochastic Coherent Adaptive Large Eddy Simulation (SCALES) (Goldstein & Vasilyev 2004) has been introduced that shares with CVS the ability to dynamically resolve and “track” the most energetic part of the coherent eddies in a turbulent flow field, but with the higher computational efficiency associated with LES. With SCALES the maximum number of modes in the simulation are resolved, given the balance between computing resources and user defined acceptable simulation error. With a field compression in the range of that used with typical LES applications the SGS modes are no longer near Gaussian white noise, as with CVS, so a SGS model is required. Yet at the same field compression as LES, using a spectral cutoff filter, the wavelet filter used with SCALES results in a significantly reduced level of total SGS dissipation that will have to be modeled (Goldstein & Vasilyev 2004). In this work we apply the Stochastic Coherent Adaptive Large Eddy Simulation (SCALES) method to the problem of three-dimensional decaying isotropic turbulence.

An eddy viscosity type SGS model for SCALES is also investigated in this work. Since the wavelet threshold filter lacks a clearly defined global filter width, an alternative model scaling based on the wavelet threshold parameter (ϵ) is proposed. Results using a modified Smagorinsky (Smagorinsky 1963) eddy viscosity SGS stress model using both a constant model coefficient and a dynamic coefficient determined by a new dynamic procedure are shown.

In this research the SCALES method has been implemented using a Dynamically Adaptive Wavelet Collocation (DAWC) method (Vasilyev & Bowman 2000; Vasilyev 2003). The DAWC method is ideal for implementing the SCALES methodology as it combines the resolution of the energetic coherent modes in a turbulent flow with the simulation of their temporal evolution (Vasilyev & Kevlahan 2002; Kevlahan *et al.* 2003). The wavelet collocation method employs wavelet compression as an integral part of the solution such that the solution is obtained with the minimum number of grid points for a given accuracy.

The rest of this paper is organized as follows. In section 2 background theory and results relevant to this work are presented. In Section 3 a Dynamically Adaptive Wavelet Collocation Solver is introduced that has been used to implement the SCALES method. In Section 4 the implementation of SCALES along with the introduction of a new dynamic SGS model is presented. Then in Section 5 fully adaptive SCALES simulations of three-dimensional decaying incompressible isotropic turbulence based on the DAWC method are presented. In the final section conclusions and discussion of future work are provided.

2. Background

2.1. General Properties of Wavelets

Wavelets are basis functions, which are localized in both physical space (due to their finite support) and wavenumber space. A field $u(\mathbf{x})$ can be represented in terms of wavelet basis functions as

$$u(\mathbf{x}) = \sum_{\mathbf{l} \in \mathcal{L}^0} c_{\mathbf{l}}^0 \phi_{\mathbf{l}}^0(\mathbf{x}) + \sum_{j=0}^{+\infty} \sum_{\mu=1}^{2^n-1} \sum_{\mathbf{k} \in \mathcal{K}^{\mu,j}} d_{\mathbf{k}}^{\mu,j} \psi_{\mathbf{k}}^{\mu,j}(\mathbf{x}), \quad (2.1)$$

where $\phi_{\mathbf{k}}^0(\mathbf{x})$ and $\psi_{\mathbf{k}}^{\mu,j}$ are respectively n -dimensional scaling functions and wavelets of different families (μ) and levels of resolution (j). One may think of a wavelet decomposition as a multilevel or multiresolution representation of a function, where each level of

resolution j (except the coarsest one) consists of wavelets ψ_1^j or family of wavelets $\psi_1^{\mu,j}$ having the same scale but located at different positions. Scaling function coefficients represent the averaged values of the field, while the wavelet coefficients represent the details of the field at different scales. The wavelet functions have a zero mean, while the scaling functions do not. Note that in n -dimensions there are $2^n - 1$ distinctive n -dimensional wavelets (Daubechies 1992). Also note that due to the local support of both scaling functions and wavelets, there is a one-to-one correspondence between the location of each scaling function or wavelet with a grid point. As a result each scaling function coefficient c_1^0 and each wavelet coefficient $d_{\mathbf{k}}^{\mu,j}$ is uniquely associated with a single grid point with the indices \mathbf{l} and \mathbf{k} respectively.

For this study we use a set of second generation wavelets known in the literature as lifted interpolating wavelets (Vasilyev & Bowman 2000; Sweldens 1998). In particular, simulations with the Dynamically Adaptive Wavelet Collocation (DAWC) solver are run using a lifted interpolating wavelet of order 6. For a more in-depth discussion on the construction of these wavelets the reader is referred to the papers by Sweldens (1998) and Vasilyev and Bowman (2000). For a more general discussion on wavelets we refer to the books of Daubechies (1992) and Mallat (1999).

2.2. Wavelet Filters

Wavelet filtering is performed in wavelet space using wavelet coefficient thresholding, which can be considered as a non-linear filter that depends on each flow realization. The wavelet thresholding filter is defined by,

$$u_{\geq}(\mathbf{x}) = \sum_{\mathbf{l} \in \mathcal{L}^0} c_1^0 \phi_1^0(\mathbf{x}) + \sum_{j=0}^{+\infty} \sum_{\mu=1}^{2^n-1} \sum_{\substack{\mathbf{k} \in \mathcal{K}^{\mu,j} \\ |d_{\mathbf{k}}^{\mu,j}| \geq \epsilon}} d_{\mathbf{k}}^{\mu,j} \psi_{\mathbf{k}}^{\mu,j}(\mathbf{x}). \quad (2.2)$$

The reconstruction error due to wavelet filtering with threshold ϵ can be shown to be (Donoho 1992; Vasilyev 2003):

$$||u(\mathbf{x}) - u_{\geq}(\mathbf{x})|| \leq C\epsilon, \quad (2.3)$$

for a sufficiently smooth function $u(\mathbf{x})$, where C is of order unity.

An important property of the wavelet thresholding filter is that in a dynamic simulation the grid required to support the wavelet filtered field will be changing in time and it will be collocated with the resolved wavelet coefficients. Thus, the grid defined by the wavelet collocation points will track the areas of locally significant energy in physical space.

2.3. Wavelet Compression and Wavelet De-noising

The major strength of wavelet filtering decomposition (Eq. 2.2), is the ability to compress signals. For functions that contain isolated small scales on a large-scale background, most wavelet coefficients are small, thus, we can retain good approximation even after discarding a large number of wavelets with small coefficients. Intuitively, the coefficient $d_1^{\mu,j}$ will be small unless $u(\mathbf{x})$ has variation on the scale of j in the immediate vicinity of wavelet $\psi_1^{\mu,j}(\mathbf{x})$.

Another important property of wavelet analysis used in this work is the ability of wavelets to de-noise signals. The wavelet de-noising procedure, also called wavelet-shrinkage, originally introduced by Donoho (1993), can be briefly described as following: given a function that consists of a smooth function with superimposed noise, one performs a

forward wavelet transform and sets to zero “noisy” wavelet coefficients, if the square of the wavelet coefficient is less than the noise variance σ^2 , otherwise the wavelet coefficient is kept. This procedure is known as hard or linear thresholding. Donoho (1993) demonstrated that hard thresholding is optimal for de-noising signals in the presence of Gaussian white noise, because wavelet-based estimators minimize the maximal L^2 -error for functions with inhomogeneous regularity. In the CVS method discussed in this work the “noise” is actually the SGS modes.

3. Dynamically Adaptive Wavelet Collocation Method

A key component in the implementation of the SCALES method has been a Dynamically Adaptive Wavelet Collocation (DAWC) (Vasilyev 2003; Vasilyev & Bowman 2000) solver that is ideally suited to the simulation of turbulence since wavelets adapt the numerical resolution naturally to the localized turbulent structures that exist at all wave numbers in fully developed turbulence. The wavelet collocation method takes advantage of the fact that wavelets are localized in both space and scale, and as a result, functions with localized regions of sharp transition are well compressed using wavelet decomposition. The adaptation is achieved by retaining only those wavelets, whose coefficients are greater than an *a priori* given threshold (ϵ). Thus, high resolution computations are carried out only in those regions, where sharp transitions occur. With this adaptation strategy, a solution is obtained on a near optimal grid that “tracks” the coherent vortices in the field, *i.e.* far fewer grid points are needed for wavelets than for conventional finite-difference, finite-element, or spectral methods. By varying the threshold parameter ϵ this method can be used to implement any of the wavelet based methods discussed above, namely CVS or SCALES.

Let us briefly outline the main features of the numerical method. Details can be found in (Vasilyev & Bowman 2000; Vasilyev 2003). In the wavelet collocation method there is a one-to-one correspondence between grid points and wavelets, which makes calculation of nonlinear terms simple and allows the grid to adapt automatically and dynamically to the solution by adding or removing wavelets. Very briefly, at each time step we take the wavelet transform of the solution, remove all wavelets with coefficient magnitude less than a threshold ϵ , and then reconstruct the solution. It can be shown that the L_∞ error of this approximation is $O(\epsilon)$. To account for the evolution of the solution over one time step the computational grid needs to be extended to include grid points associated with wavelets whose coefficients are or can possibly become significant during the time integration step (Vasilyev 2003). To do this we add grid points that are adjacent in both position and scale to each significant wavelet coefficient. While the cost of this added adjacent zone is significant at low compression ratios it becomes much less so at higher compression ratios. This diminishing cost of the adjacent zone with increased compression will be the case for any numerical problem that has inherent local structures that dominate the field being simulated. Figure 1 shows the compression ratio vs. the wavelet filter threshold ϵ for a wavelet collocation grid adapted to a DNS field of isotropic turbulence ($Re_\lambda = 168$) with and without an adjacent zone. We can see clearly that the added overhead of the adjacent zone becomes insignificant for compression ratios over 98%. This is the case because in turbulent flows, like the one considered, the flow is dominated by localized energetic coherent vortices. Since each wavelet corresponds to a single grid point this procedure allows the grid to automatically follow the evolution of the solution in position and scale. We use second generation wavelets (Sweldens 1998), which allow the order of the wavelet (and hence of the numerical method) to be easily

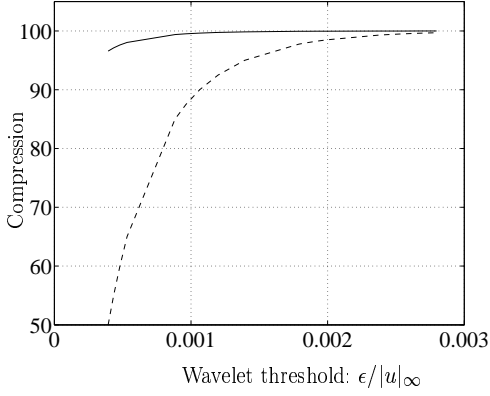


FIGURE 1. Field compression vs. normalized wavelet threshold $\epsilon/||u||_\infty$ using velocity wavelet filtering without adjacent zone (—) and with adjacent zone (----) for field F_{256} . It can be seen that as ϵ increases the loss in compression due to the adjacent zone becomes less significant.

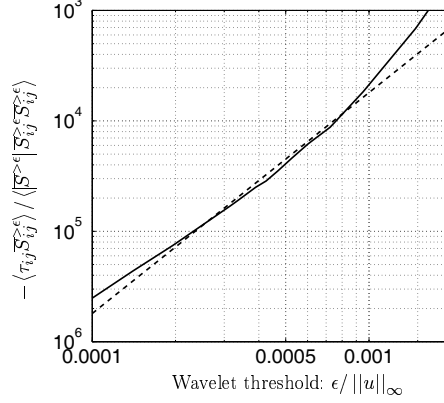


FIGURE 2. $\langle \tau_{ij} \bar{S}_{ij}^{\epsilon} \rangle / \langle |\bar{S}^{\epsilon}| \bar{S}_{ij}^{\epsilon} \bar{S}_{ij}^{\epsilon} \rangle$ vs. normalized wavelet threshold $\epsilon/||u||_\infty$ using velocity wavelet filtering without adjacent zone (—) for field F_{256} . The dashed line is $(\epsilon/||u||_\infty)^2$. This range of $\epsilon/||u||_\infty$ corresponds to a field compression over the range of 78.5% to 99.95%. It can be seen that $\langle \tau_{ij} \bar{S}_{ij}^{\epsilon} \rangle / \langle |\bar{S}^{\epsilon}| \bar{S}_{ij}^{\epsilon} \bar{S}_{ij}^{\epsilon} \rangle$ scales roughly as ϵ^2 . The scaling begins to deviate at $\epsilon/||u||_\infty = 0.001$, which corresponds to 99.4% compression.

varied. The method has a computational complexity $O(N)$, where N is the number of wavelets retained in the calculation (*i.e.* those wavelets with coefficients greater than ϵ plus nearest neighbors).

In summary, the dynamically adaptive wavelet collocation method is an adaptive, variable order method for solving partial differential equations with localized structures that change their location and scale in space and time. Because the computational grid automatically adapts to the solution (in position and scale), we do not have to know *a priori* where the regions of high gradients or structures exist. In related work the dynamically adaptive wavelet collocation method has been combined with the Brinkman penalization method (Vasilyev & Kevlahan 2002) to define solid structures in the domain for the simulation of complex geometry flows.

4. SCALES Implementation

The SCALES method is based on the premise that the most energetic coherent vortices (or structures) of a turbulent flow dominate mixing, heat transfer and other quantities of engineering interest, while the smaller incoherent background is only of interest because of how they effect the energetic coherent vortices (Goldstein & Vasilyev 2004). The SCALES equations for incompressible flow, that describe the evolution of the most energetic coherent vortices in the flow field, can be written as:

$$\frac{\partial \bar{u}_i^{\epsilon}}{\partial x_i} = 0, \quad (4.1)$$

$$\frac{\partial \bar{u}_i^{\epsilon}}{\partial t} + \frac{\partial (\bar{u}_i^{\epsilon} \bar{u}_j^{\epsilon})}{\partial x_j} = -\frac{1}{\rho} \frac{\partial \bar{p}^{\epsilon}}{\partial x_i} + \nu \frac{\partial^2 \bar{u}_i^{\epsilon}}{\partial x_j \partial x_j} - \frac{\partial \bar{\tau}_{ij}^{\epsilon}}{\partial x_j}, \quad (4.2)$$

where

$$\overline{\tau_{ij}}^{>\epsilon} = \overline{u_i u_j}^{>\epsilon} - \overline{u_i}^{>\epsilon} \overline{u_j}^{>\epsilon} \quad (4.3)$$

and u_i is the velocity field, ρ is density, ν is kinematic viscosity, p is pressure and $\overline{(\cdot)}^{>\epsilon}$ represents spatial filtering with a wavelet thresholding filter. As a result of the filtering process the unresolved quantity $\overline{\tau_{ij}}^{>\epsilon}$, commonly referred to as the Subgrid Scale (SGS) stress, is introduced. Note that $\overline{\tau_{ij}}^{>\epsilon}$ is a function of the unfiltered velocity field u_i . However in order to close Eqs. 4.1-4.2 and realize the benefits of SCALES, a low order model for the SGS stress, which is based on the resolved quantities, is needed.

4.1. SCALES SGS Modeling

The standard Smagorinsky (Smagorinsky 1963) eddy viscosity SGS stress model defines an eddy viscosity that is proportional to the filter width and the characteristic filtered rate of strain. In the case of the non-linear wavelet thresholding filter used in SCALES there is no clearly defined filter width, so instead the wavelet threshold (ϵ) is used to properly scale the eddy viscosity:

$$\nu_T = C_s \epsilon^\alpha \left| \overline{S}^{>\epsilon} \right|, \quad (4.4)$$

where

$$\overline{S_{ij}}^{>\epsilon} = \frac{1}{2} \left(\frac{\partial \overline{u_i}^{>\epsilon}}{\partial x_j} + \frac{\partial \overline{u_j}^{>\epsilon}}{\partial x_i} \right), \quad (4.5)$$

is the strain rate of the resolved scales. We will show in Section 4.2 that appropriate scaling is obtained with $\alpha = 2$. The new linear eddy viscosity model is then used to define a model for the subgrid scale stress (Eq. 4.3),

$$\overline{\tau_{ij}^M}^{>\epsilon} \equiv -2\nu_T \overline{S_{ij}}^{>\epsilon}, \quad (4.6)$$

where ν_T is the turbulent eddy viscosity.

The new Germano dynamic formulation for the model coefficient C_s is based on the wavelet filter threshold parameter (ϵ). For the dynamic procedure the grid filter is defined as $\overline{(\cdot)}^{>\epsilon}$ and the “test” filter is defined as $\overline{(\cdot)}^{>2\epsilon}$. The adjacent zone is excluded in both cases to obtain the proper model scaling. The dynamic procedure is then based on the original SGS stress, Eq. 4.3, and an alternative subgrid scale stress,

$$\overline{T_{ij}}^{>2\epsilon} = \overline{\overline{u_i u_j}^{>\epsilon}}^{>2\epsilon} - \overline{\overline{u_i}^{>\epsilon} \overline{u_j}^{>\epsilon}}^{>2\epsilon}, \quad (4.7)$$

which would result from applying the wavelet thresholding “test” filter ($\overline{(\cdot)}^{>2\epsilon}$) to Eqs. 4.1-4.3. Note that the wavelet filter is a projection operator so by definition:

$$\overline{(\cdot)}^{>\epsilon_C} \equiv \overline{\overline{(\cdot)}^{>\epsilon_A} \overline{(\cdot)}^{>\epsilon_B}}, \quad (4.8)$$

where $\epsilon_C = \max(\epsilon_A, \epsilon_B)$. Filtering Eq.4.3 at the “test” filter level and subtracting it from Eq.4.7 results in the modified Germano’s identity (Germano *et al.* 1991)

$$\overline{T_{ij}}^{>2\epsilon} - \overline{\overline{\tau_{ij}}^{>\epsilon}}^{>2\epsilon} = \overline{\overline{u_i}^{>\epsilon} \overline{u_j}^{>\epsilon}}^{>2\epsilon} - \overline{\overline{u_i}^{>\epsilon} \overline{u_j}^{>\epsilon}}^{>2\epsilon}. \quad (4.9)$$

Then substituting modeled SGS stresses at the two filter levels to Eq. 4.9 gives:

$$\begin{aligned} \overline{T_{ij}}^{>2\epsilon} - \overline{\overline{\tau_{ij}}^{>\epsilon}}^{>2\epsilon} &\approx \overline{T_{ij}^M}^{>2\epsilon} - \overline{\tau_{ij}^M}^{>\epsilon} \\ &= 2C_s(2\epsilon)^2 \left| \overline{S}^{>2\epsilon} \right| \overline{S_{ij}}^{>2\epsilon} - 2C_s \epsilon^2 \left| \overline{S}^{>\epsilon} \right| \overline{S_{ij}}^{>\epsilon} \end{aligned} \quad (4.10)$$

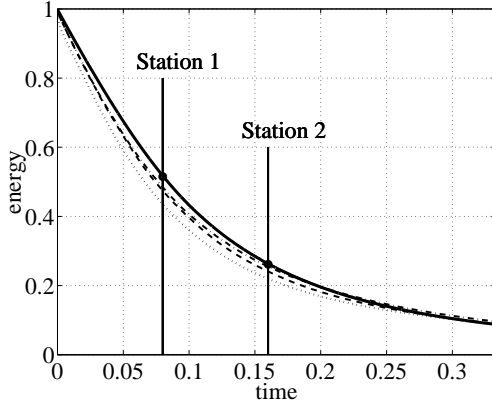


FIGURE 3. Energy decay for SCALES with dynamic SGS model (---), SCALES with SGS model coefficient $C_s \epsilon^2 = 0.0001$ (-.-.-), LES with dynamic SGS model (.....) and for comparison DNS (—). Two stations are shown at which energy spectra will be presented.

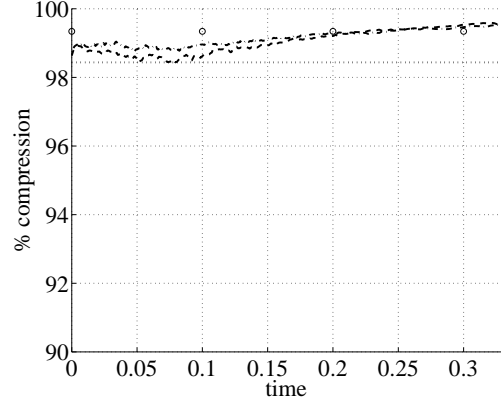


FIGURE 4. Field compression for SCALES with dynamic SGS model (---), SCALES with SGS model coefficient $C_s \epsilon^2 = 0.0001$ (-.-.-) and LES with dynamic SGS model (.....). The more conservative interpretation of the LES compression based on the 3/2 rule is shown as small circles.

Following Lilly's (1992) notation we define L_{ij} and M_{ij} as follows:

$$L_{ij} = \overline{\overline{u_i}^{>\epsilon} \overline{u_j}^{>\epsilon}}^{>2\epsilon} - \overline{\overline{u_i}^{>\epsilon}}^{>2\epsilon} \overline{\overline{u_j}^{>\epsilon}}^{>2\epsilon}, \quad (4.11)$$

$$M_{ij} = 2\epsilon^2 \overline{\overline{S}^{>\epsilon} \overline{S_{ij}}^{>\epsilon}}^{>2\epsilon} - 2(2\epsilon)^2 \overline{\overline{S}^{>2\epsilon}} \overline{\overline{S_{ij}}^{>2\epsilon}}, \quad (4.12)$$

where L_{ij} is a wavelet filtered analog to the Leonard stress. This results in an overdetermined system of equations that can be used to determine C_s

$$C_s M_{ij} = L_{ij}. \quad (4.13)$$

Following Lilly's (1992) least square solution to this system, we obtain the following expression for the local Smagorinsky model coefficient:

$$C_s = \frac{L_{ij} M_{ij}}{M_{ij} M_{ij}}. \quad (4.14)$$

With this model formulation C_s can be locally positive or negative allowing for local backscatter. In practice it has been found that locally negative values of C_s cause numerical instabilities in SCALES, as in LES, so we average over the domain:

$$C_s = \frac{\langle L_{ij} M_{ij} \rangle}{\langle M_{ij} M_{ij} \rangle}, \quad (4.15)$$

where $\langle \cdot \rangle$ denotes volume averaging.

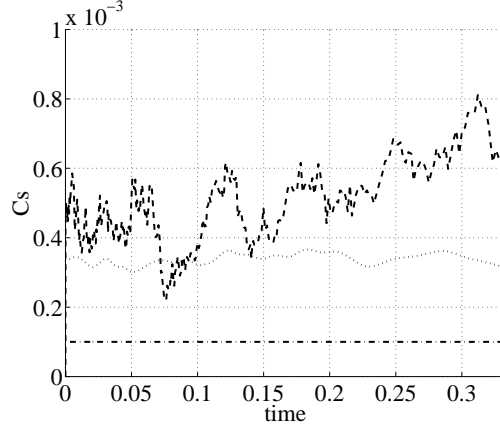


FIGURE 5. Dynamic SGS model coefficient for SCALES with dynamic SGS model (---), SCALES with SGS model coefficient $C_s \epsilon^2 = 0.0001$ (—) and LES with dynamic SGS model (.....).

4.2. Model Scaling

If we make the assumption that, with an appropriate value for α , the eddy viscosity model (Eq.4.4-4.6) provides the right dissipation it is easy to show,

$$2C_s \epsilon^\alpha = - \frac{\langle \tau_{ij} \bar{S}_{ij}^{\epsilon} \rangle}{\langle |\bar{S}^{\epsilon}| \bar{S}_{ij}^{\epsilon} \bar{S}_{ij}^{\epsilon} \rangle}, \quad (4.16)$$

where α is the scaling law. The correct scaling is determined from *a priori* testing of a turbulent field obtained from a 256^3 DNS simulation of forced isotropic turbulence (Jimenez *et al.* 1993) with $Re_\lambda = 168$. Note that this turbulent field will hereafter be referred to as F_{256} . In Figure 2 the scaling of $-\langle \tau_{ij} \bar{S}_{ij}^{\epsilon} \rangle / \langle |\bar{S}^{\epsilon}| \bar{S}_{ij}^{\epsilon} \bar{S}_{ij}^{\epsilon} \rangle$ is shown over a range of $\epsilon / \|u\|_\infty$ that corresponds to a field compression over the range of 78.5% to 99.95%. The slope of the curve in log-log axis determines the appropriate ϵ scaling. As can be seen, the quantity $\langle \tau_{ij} \bar{S}_{ij}^{\epsilon} \rangle / \langle |\bar{S}^{\epsilon}| \bar{S}_{ij}^{\epsilon} \bar{S}_{ij}^{\epsilon} \rangle$ scales roughly as ϵ^2 for a wide range of compressions. However some deviation from this scaling is observed above 99.4% compression. Based on this *a priori* test of scaling, the new dynamic Smagorinsky-type eddy viscosity model (Eq. 4.4) has been implemented. The results of simulations with this new SGS model are shown in Section 5.

5. Results

To validate the SCALES method, numerical simulations of decaying incompressible isotropic turbulence are considered. For this work the incompressible Navier Stokes equations (Eqs. 4.1-4.3) are solved with the DAWC solver. Continuity (Eq. 4.3) is enforced using a multi-step pressure correction time integration method (Guermond & Shen 2003). An adaptive wavelet collocation multilevel elliptic solver is used in solving the Poisson equation for pressure at each time step.

Results of decaying incompressible isotropic turbulence with initial $Re_\lambda = 72$ are presented. The simulations were initialized with a 128^3 forced isotropic turbulence DNS field from a de-aliased pseudo-spectral code. The spectral content of the initial DNS field is fully resolved by doubling the non-adaptive field resolution to 256^3 in the simulations.

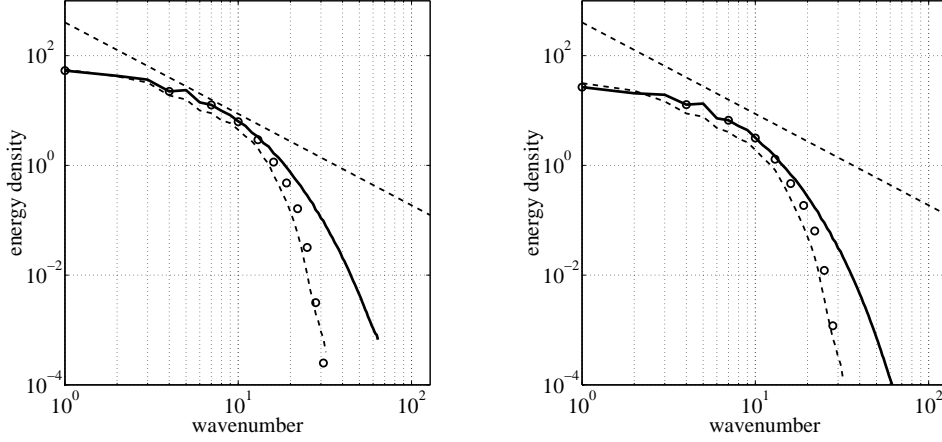


FIGURE 6. Energy spectra for LES with dynamic SGS model (----) at time $t = 0.08$ (left), and $t = 0.16$ (right). For comparison the DNS (—) and filtered DNS (\circ) are shown. A $k^{-5/3}$ straight dashed black line is shown to indicate the inertial range.

This is required because the DAWC solver uses finite differencing, which is not adequate for resolving the full spectral content of the spectral DNS field at the original resolution. The results are compared to DNS of decaying isotropic turbulence performed with the same de-aliased pseudo-spectral code used to generate the initial DNS field.

In these simulations a normalized wavelet threshold is specified. The wavelet threshold is specified as relative to the L_2 norm of the velocity field. During the simulation the relative wavelet threshold ϵ_2 is specified for the whole simulation and the actual absolute wavelet threshold used at each time step is $\epsilon = \epsilon_2 \|u\|_2$.

5.1. SCALES Constant Coefficient and Dynamic SGS Stress Model

SCALES simulations have been performed with the constant coefficient Smagorinsky eddy viscosity model (Eq. 4.4) and the new dynamic Smagorinsky eddy viscosity SGS stress model described in Section 4.1. The model coefficient ($C_s \epsilon^2 = 0.0001$) for the SCALES_{Cs} case was chosen to best match the DNS results. For the SCALES_{dyn} case the volume averaged version of the dynamic model coefficient is used (Eq. 4.15). These SCALES simulations, hereafter for brevity called SCALES_{Cs} and SCALES_{dyn} respectively, are compared to DNS and LES simulations. For both SCALES_{Cs} and SCALES_{dyn} cases ϵ_2 is set to 0.5. The LES simulation is performed in the DAWC solver with a regular 64^3 grid. The simulation is de-aliased by performing a wavelet transform on the velocity field and zeroing the highest level wavelet coefficients, thus resulting in a 32^3 solution at the end of the time step. This is more expensive than would be required in a spectral code using the 3/2 rule. In Figure 3 it can be seen that the resolved kinetic energy decay for the SCALES_{dyn} and SCALES_{Cs} cases closely matches that of the DNS. The LES deviates a small amount more from the DNS. In Figure 4 the compression for the SCALES_{dyn}, SCALES_{Cs} and LES cases are shown. If we consider the overhead of the modes used for de-aliasing, the LES could be considered to have a compression of 98.44%. The modes used for de-aliasing in LES can be considered as analogous to the adjacent zone in SCALES so for a realistic comparison we can consider that if the LES was performed in a spectral code, using the 3/2 rule for de-aliasing, the effective compression would be 99.34% (shown in Fig. 4 as small circles). This is close to the initial

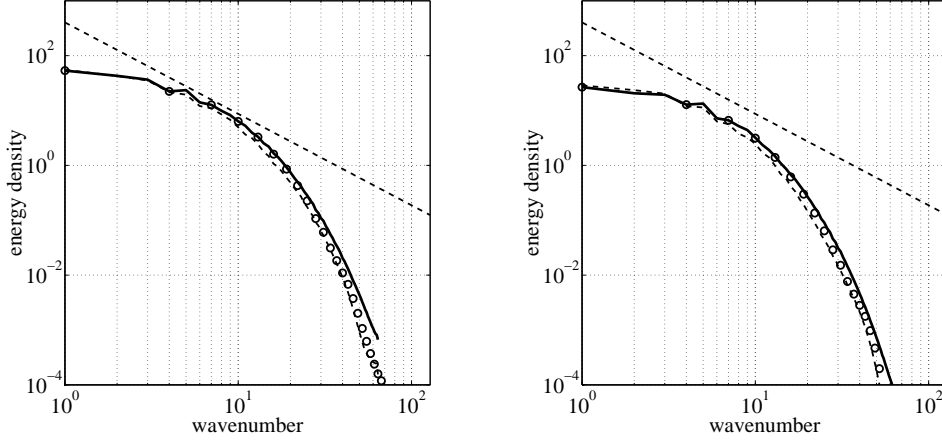


FIGURE 7. Energy spectra for SCALES with SGS model coefficient $C_s \epsilon^2 = 0.0001$ (----) at time $t = 0.08$ (left), and $t = 0.16$ (right). For comparison the DNS (—) and filtered DNS (\circ) are shown. A $k^{-5/3}$ straight dashed black line is shown to indicate the inertial range.

compression of the SCALES_{dyn} simulation, but as the SCALES simulations progress the compression increases. Therefore, it can be said that the SCALES_{dyn} and SCALES_{Cs} simulations were able to capture the energy decay with a compression similar to a de-aliased LES simulation. In Figure 5 we see that the dynamic model coefficient for SCALES_{dyn} is more variable in comparison to the LES case. It is hypothesized that this variability could be reflective of the sensitivity of the SCALES_{dyn} model to actual localized events such as energetic coherent vortex interactions that cause local high resolved stresses that are reflective of the proper instantaneous SGS dissipation. Further research is needed to understand this phenomenon. In Figures 6-8 the energy spectra for the two stations shown in Figure 3 are compared to the appropriately filtered DNS for the SCALES_{dyn}, SCALES_{Cs} and LES cases. It can be seen that, while there is reasonable agreement for the LES case (Fig. 6), the agreement with the filtered DNS is significantly improved for the SCALES_{Cs} (Fig. 7) and SCALES_{dyn} cases (Fig. 8). At both stations, in the dissipative range, the SCALES_{Cs} and SCALES_{dyn} simulations reproduce more of the high wave number energy. At the second station it can be seen in the inertial range that the LES has dissipated slightly more than the SCALES_{Cs} and SCALES_{dyn} cases. It is of particular interest to note that the wavelet filtered DNS in Figures 7 and 8 are closer to the full DNS spectra over the full spectral range. Thus, the ability of SCALES to closely recover the filtered DNS, results in a solution that has a spectral content close to the original unfiltered DNS solution, over the whole DNS spectral range.

6. Conclusions

In this work dynamic simulation results of decaying incompressible isotropic turbulence using a new methodology for simulating turbulent flows called Stochastic Coherent Adaptive Large Eddy Simulation (SCALES) (Goldstein & Vasilyev 2004) are presented. The SCALES method has been implemented using a Dynamically Adaptive Wavelet Collocation (DAWC) method that is ideal for CVS, and SCALES as it combines the resolution of the energetic coherent modes in a turbulent flow with the simulation of their temporal evolution (Vasilyev & Bowman 2000; Vasilyev 2003; Kevlahan *et al.* 2003).

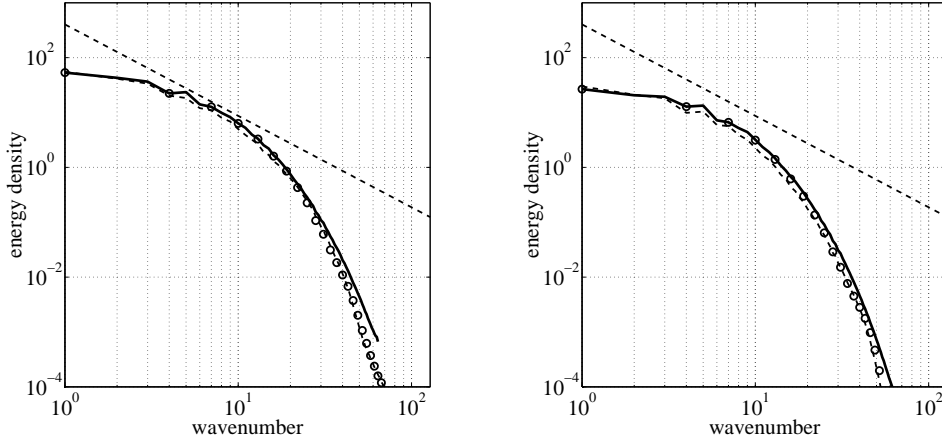


FIGURE 8. Energy spectra for SCALES with dynamic SGS model (---) at time $t = 0.08$ (left), and $t = 0.16$ (right). For comparison the DNS (—) and filtered DNS (\circ) are shown. A $k^{-5/3}$ straight dashed black line is shown to indicate the inertial range.

In this work a new dynamic SGS stress modeling procedure has been introduced based on a variation of the classical Smagorinsky (Smagorinsky 1963) model formulation. In this model the scaling of the eddy viscosity is based on ϵ^2 , instead of the standard scaling, $\overline{\Delta}^2$. *A priori* results using forced incompressible isotropic turbulence have been presented that show this scaling holds, for a wide range of compression. The new dynamic procedure is similar in spirit to the classical dynamic procedure of Germano's (Germano *et al.* 1991), except that the new scaling law, based on ϵ^2 , is used.

Dynamic simulations of SCALES and LES of decaying isotropic turbulence with a Taylor Reynolds number of $Re_\lambda = 72$ have been compared to DNS results to validate the SCALES method with the DAWC solver. The SCALES results with the dynamic model are shown to reproduce the DNS energy decay with only 1 % of the modes being initially resolved. These SCALES results are also compared to fully de-aliased LES calculations. The SCALES results moderately outperformed those of the LES at a similar field compression.

While it is expected that for Reynolds numbers higher than the ones considered in this study the reduced SGS dissipation and increased incoherency of the SCALES SGS stress will provide a tangible improvement in SGS model accuracy, this is not in and of itself the greatest potential benefit of the SCALES method. Real world flows of engineering and scientific interest occur in complex domains with great temporal and spatial variation in turbulence intensity. Therefore, an efficient simulation method must be capable of dynamically, often with limited *a priori* knowledge, adapting to the local resolution over a wide range of Reynolds numbers often including large regions of laminar flow. A good example of this is flow over a modern aircraft that spans the gamut of flows from a nearly laminar far field to areas of intense turbulence in the control surfaces regions. Another area of great potential benefit is in the simulation of fluid structure interaction, where, often no detailed *a priori* information to build cost effective computational grids is available. Therefore, the trade off between costly grid refinement over regions of potentially high turbulence intensity versus the loss of simulation accuracy must be weighed. With the SCALES methodology the collocation grid automatically adapts to the local flow in order to maintain an *a priori* described accuracy threshold, which is the *a priori*

determined wavelet filter threshold (ϵ). For these reasons even if the SCALES methodology can do no better than match the cost of classical LES methods in unit test problems, like the ones conducted in this work, there is strong evidence to believe that SCALES will be able to outperform classical LES in many complex real world flows. To realize the benefits of SCALES in such highly non-homogenous flows in complex geometries a local SGS model will be required. Work on such a model is currently underway.

REFERENCES

- DAUBECHIES, I. 1992 *Ten Lectures on Wavelets*. CBMS-NSF Series in Applied Mathematics 61. Philadelphia: SIAM.
- DONOHO, D. 1993 Unconditional bases are optimal bases for data compression and for statistical estimation. *Appl. Comput. Harmon. Anal.* **1**, 100–115.
- DONOHO, D. L. 1992 Interpolating wavelet transforms. *Tech. Rep.* 408. Department of Statistics, Stanford University.
- FARGE, M., PELLEGRINO, G. & SCHNEIDER, K. 2001 Coherent vortex extraction in 3d turbulent flows using orthogonal wavelets. *Physical Review Letters* **87** (5).
- FARGE, M., SCHNEIDER, K. & KEVLAHAN, N. 1999 Non-Gaussianity and coherent vortex simulation for two-dimensional turbulence using an adaptive orthogonal wavelet basis. *Phys. Fluids*. **11** (8), 2187–2201.
- GERMANO, M., PIOMELLI, U., MOIN, P. & CABOT, W. 1991 A dynamic subgrid-scale eddy viscosity model. *Phys. Fluids A* **3** (7), 1760–1765.
- GOLDSTEIN, D. A. & VASILYEV, O. V. 2004 Stochastic coherent adaptive large eddy simulation method. *Phys. Fluids* **16** (7), 2497–2513.
- GUERMOND, J.-L. & SHEN, J. 2003 Velocity-correction projection methods for incompressible flows. *To appear in SIAM J. Num. Anal.* **41** (1), 112–134.
- JIMENEZ, J., WRAY, A., SAFFMAN, P. & ROGALLO, R. 1993 The structure of intense vorticity in isotropic turbulence. *J. Fluid Mech.* **225**, 65–90.
- KEVLAHAN, N. K.-R., VASILYEV, O. V. & GOLDSTEIN, D. E. 2003 A three-dimensional adaptive wavelet method for fluid-structure interaction. In *Proceedings of Direct and Large-Eddy Simulation Workshop 5*. Technical University of Munich, Germany.
- LILLY, D. K. 1992 A proposed modification to the Germano subgrid-scale closure model. *Phys. Fluid* **3**, 633–635.
- MALLAT, S. G. 1999 *A Wavelet Tour of Signal Processing*. Paris: Academic Press.
- SMAGORINSKY, J. S. 1963 General circulation experiments with the primitive equations. *Mon. Weather Rev.* **91**, 99–164.
- SWELDENS, W. 1998 The lifting scheme: A construction of second generation wavelets. *SIAM J. Math. Anal.* **29** (2), 511–546.
- VASILYEV, O. V. 2003 Solving multi-dimensional evolution problems with localized structures using second generation wavelets. *Int. J. Comp. Fluid Dyn.*, Special issue on High-resolution methods in Computational Fluid Dynamics **17** (2), 151–168.
- VASILYEV, O. V. & BOWMAN, C. 2000 Second generation wavelet collocation method for the solution of partial differential equations. *J. Comp. Phys.* **165**, 660–693.
- VASILYEV, O. V. & KEVLAHAN, N. K.-R. 2002 Hybrid wavelet collocation - Brinkman penalization method for complex geometry flows. *Int. J. Numerical Methods in Fluids* **40**, 531–538.

Transfer of energy in the variational multiscale formulation of LES

By A. A. Oberai [†], V. Gravemeier AND G. C. Burton

The transfer of energy from the resolved scales to the subgrid scales in homogeneous isotropic turbulence is studied, within the context of the variational formulation of large eddy simulation. In particular, the relative contributions to this transfer from the coarse and the fine resolved scales are evaluated and their dependence on the choice of an ideal LES solution is examined. It is found that when the L_2 projection of the DNS solution onto a truncated Fourier space is selected as the ideal LES solution, the energy transfer from the fine resolved scales is the dominant contribution. On the other hand, when the ideal LES solution is defined to be the nodal interpolant of the DNS solution on a coarse finite element mesh, contributions from both the coarse and the fine resolved scales are important. These observations are made by performing *a-priori* analysis using a DNS database and are also explained using an analytical theory of turbulence closure. These results indicate that within the variational formulation of LES, the definition of a “good model” is closely tied to the choice of the ideal LES solution, which in turn is dependent on the function spaces utilized in solving the problem.

1. Introduction

The variational multiscale (VMS) formulation for large eddy simulation (LES) of turbulent flows (Hughes, Mazzei & Jansen 2000; Collis 2001) differs from the filtered formulation in that models are introduced in the weak form of the Navier Stokes equations and are used to account for the approximation of infinite-dimensional function spaces by their finite-dimensional counterparts. Another feature of the VMS formulation is that different models are introduced in the equations for the coarse and the fine resolved scales. In most applications to date, no model has been used in the coarse scale equations and the Smagorinsky model has been used in the fine scale equations (see for example Hughes, Oberai & Mazzei 2001). In a spectral discretization, this choice is easily motivated by the characteristics of the spectral eddy viscosity, which is small for low wavenumbers and large for wavenumbers close to the cutoff.

A closer look at the VMS formulation reveals that the choice of an ideal model is closely linked to the choice of what constitutes an ideal LES solution, which in turn depends on the basis used to solve the problem. Hence what might be a good model when using a spectral basis (say Fourier modes) may not be a good model for a typical finite element basis. This observation has an analog in the filtered LES formulation, where ideal models (in terms of predicting the right energy transfer) for a sharp cutoff filter and a Gaussian filter are very different (see for example Leslie & Quarini 1979; Cerutti, Meneveau, & Knio 2000). With this in mind we explore in this manuscript what constitutes an ideal model (in terms of multiscale transfer of energy) for the VMS formulation, for different definitions of ideal LES solutions. We use DNS data to perform our analysis and thereafter

[†] Department of Aerospace and Mechanical Engineering, Boston University.

explain our results using analytical theories of turbulence. We consider two different ideal LES solutions. The first corresponds to the Fourier truncation of the DNS solution onto a smaller space. The second corresponds to the nodal interpolant of the DNS solution on a coarse grid constructed using typical finite element basis. Through our investigations we conclude that the scale dependence of the transfer of energy to the subgrid scales for these two ideal LES solutions is significantly different.

2. Variational Model and an Ideal LES Model

2.1. Strong and Weak Forms

We consider the motion of an incompressible fluid in $Q = \Omega \times]T_1, T_2[$, where $\Omega = [0, 2\pi]^3$ is the spatial domain and $]T_1, T_2[$ is the time period of interest. The strong form of the problem is given by

$$\mathbf{u}_{,t} + \nabla \cdot (\mathbf{u} \otimes \mathbf{u}) + \nabla p - \nu \nabla^2 \mathbf{u} = \mathbf{f}, \text{ in } Q \quad (2.1)$$

$$\nabla \cdot \mathbf{u} = 0, \text{ in } Q. \quad (2.2)$$

In the above equations \mathbf{u} is the fluid velocity field and p is the pressure, ν is the kinematic viscosity and the symbol \otimes denotes the outer product of two vectors. In addition, since we are restricting our analysis to homogeneous isotropic turbulence, we assume that the solution satisfies periodic boundary conditions.

We consider a weak or a variational formulation of the Navier Stokes equations (see for example Foias, Manley, Rosa & Temam 2001) given by: Find $\mathbf{U}(\cdot, t) = [\mathbf{u}(\cdot, t), p(\cdot, t)]^T \in \mathcal{V}$, such that

$$B(\mathbf{W}, \mathbf{U}) = (\mathbf{W}, \mathbf{F}), \quad \forall \mathbf{W} = [\mathbf{w}, q]^T \in \mathcal{V}, \forall t \in]T_1, T_2[, \quad (2.3)$$

where the semi-linear form $B(\cdot, \cdot)$ is defined as

$$B(\mathbf{W}, \mathbf{U}) = (\mathbf{w}, \mathbf{u}_{,t}) - (\nabla \mathbf{w}, \mathbf{u} \otimes \mathbf{u}) + (\mathbf{w}, \nabla p) + 2\nu(\nabla^S \mathbf{w}, \nabla^S \mathbf{u}) - (\nabla q, \mathbf{u}), \quad (2.4)$$

and where

$$(\mathbf{W}, \mathbf{F}) = (\mathbf{w}, \mathbf{f}). \quad (2.5)$$

Throughout this text (\cdot, \cdot) is used to denote the L_2 inner product.

The infinite dimensional function space \mathcal{V} is defined as

$$\mathcal{V} = \left\{ \mathbf{V} = [\mathbf{v}, r]^T \mid \mathbf{v} \in H^1(\Omega); r \in L_2(\Omega) \right\}. \quad (2.6)$$

In the equation above $H^1(\Omega)$ denotes the Sobolev space of vector-valued functions that are square-integrable and whose derivatives are also square-integrable. This implies that the energy and the enstrophy of the weak solutions remain finite. $L_2(\Omega)$ denotes the space of scalar functions that are square integrable. In addition, we assume that the periodic boundary conditions (though not explicitly stated) are built into the definition of \mathcal{V} .

Let $\mathcal{V}^h \subset \mathcal{V}$ be a finite dimensional subspace. Note that since \mathcal{V}^h is a subspace of \mathcal{V} , (2.3) implies that the exact solution \mathbf{U} satisfies

$$B(\mathbf{W}^h, \mathbf{U}) = (\mathbf{W}^h, \mathbf{F}), \quad \forall \mathbf{W}^h \in \mathcal{V}^h, \forall t \in]T_1, T_2[. \quad (2.7)$$

The Galerkin method when applied to (2.3) yields the following equation for the approximate solution \mathbf{U}^h . Find $\mathbf{U}^h(\cdot, t) \in \mathcal{V}^h$, such that

$$B(\mathbf{W}^h, \mathbf{U}^h) = (\mathbf{W}^h, \mathbf{F}), \quad \forall \mathbf{W}^h \in \mathcal{V}^h, \forall t \in]T_1, T_2[. \quad (2.8)$$

2.2. Ideal LES Model

The Galerkin solution essentially corresponds to a Direct Numerical Simulation (DNS) of the original problem. It is well known that if the space \mathcal{V}^h is unable to represent the large inertial scales of motion as well as the fine dissipative scales, the Galerkin solution will be inaccurate. In particular, it will be corrupted by an unphysical pile up of energy at the finest resolved scales. This solution may be improved upon by adding a model term to the Galerkin approximation. This leads to the following variational equation, which we shall refer to as the modeled equation: Find $\mathbf{U}^h(\cdot, t) \in \mathcal{V}^h$, such that

$$B(\mathbf{W}^h, \mathbf{U}^h) + M(\mathbf{W}^h, \mathbf{U}^h; h, \mathbf{c}) = (\mathbf{W}^h, \mathbf{F}), \quad \forall \mathbf{W}^h \in \mathcal{V}^h, \forall t \in]T_1, T_2[. \quad (2.9)$$

In (2.9), $M(\mathbf{W}^h, \mathbf{U}^h; h, \mathbf{c})$ is the model term that is linear in \mathbf{W}^h and non-linear in \mathbf{U}^h . It also depends on the mesh size h and a vector of parameters \mathbf{c} . Note that due to the presence of the model, the solution of (2.9) and the Galerkin solution are distinct, even though they are represented by the same \mathbf{U}^h in our development.

We now introduce the concept of an optimal solution in the space \mathcal{V}^h . For this we define a *restriction operator* $\mathcal{P}^h : \mathcal{V} \rightarrow \mathcal{V}^h$, such that $\mathcal{P}^h \mathbf{U} \in \mathcal{V}^h$ is the optimal representation of \mathbf{U} in \mathcal{V}^h . For example, $\mathcal{P}^h \mathbf{U}$ may be the nodal interpolant or a suitable projection (L_2 or H^1 in our case) of \mathbf{U} in \mathcal{V}^h , in which case \mathcal{P}^h will be the interpolation or the projection operator, respectively. We would like to select our model term in (2.9) such that the solution \mathbf{U}^h is optimal. Thus requiring $\mathbf{U}^h = \mathcal{P}^h \mathbf{U}$ in (2.9) we have

$$M(\mathbf{W}^h, \mathcal{P}^h \mathbf{U}; h, \mathbf{c}) = (\mathbf{W}^h, \mathbf{F}) - B(\mathbf{W}^h, \mathcal{P}^h \mathbf{U}), \quad \forall \mathbf{W}^h \in \mathcal{V}^h, \forall t \in]T_1, T_2[. \quad (2.10)$$

Using (2.7) in (2.10) we arrive at

$$M(\mathbf{W}^h, \mathcal{P}^h \mathbf{U}; h, \mathbf{c}) = B(\mathbf{W}^h, \mathbf{U}) - B(\mathbf{W}^h, \mathcal{P}^h \mathbf{U}), \quad \forall \mathbf{W}^h \in \mathcal{V}^h, \forall t \in]T_1, T_2[. \quad (2.11)$$

This equation defines the model required to generate the optimal solution. The net energy transferred by the ideal model to the subgrid scales is obtained by setting $\mathbf{W}^h = \mathbf{V}^h \equiv \mathcal{P}^h[\mathbf{u}, 0]^T$ in the above equation and is given by

$$T^h \equiv M(\mathbf{V}^h, \mathcal{P}^h \mathbf{U}; h, \mathbf{c}) = B(\mathbf{V}^h, \mathbf{U}) - B(\mathbf{V}^h, \mathcal{P}^h \mathbf{U}). \quad (2.12)$$

In this study we wish to estimate the scale dependence of this energy transfer. In other words we wish to quantify the proportion of the total transfer from the coarse and the fine resolved scales in \mathcal{V}^h . For this purpose we split \mathcal{V}^h as follows

$$\mathcal{V}^h = \bar{\mathcal{V}}^h \oplus \acute{\mathcal{V}}^h, \quad (2.13)$$

and likewise split \mathbf{V}^h as

$$\mathbf{V}^h = \bar{\mathbf{V}}^h + \acute{\mathbf{V}}^h, \quad (2.14)$$

where $\bar{\mathbf{V}}^h \in \bar{\mathcal{V}}^h$ represents the coarse resolved scales and $\acute{\mathbf{V}}^h \in \acute{\mathcal{V}}^h$ represents the fine resolved scales. Now the net transfer of energy due to the model can be split into a coarse and a fine scale part such that

$$T^h = \bar{T}^h + \acute{T}^h, \quad (2.15)$$

where

$$\bar{T}^h \equiv M(\bar{\mathbf{V}}^h, \mathcal{P}^h \mathbf{U}; h, \mathbf{c}) = B(\bar{\mathbf{V}}^h, \mathbf{U}) - B(\bar{\mathbf{V}}^h, \mathcal{P}^h \mathbf{U}), \quad (2.16)$$

$$\acute{T}^h \equiv M(\acute{\mathbf{V}}^h, \mathcal{P}^h \mathbf{U}; h, \mathbf{c}) = B(\acute{\mathbf{V}}^h, \mathbf{U}) - B(\acute{\mathbf{V}}^h, \mathcal{P}^h \mathbf{U}). \quad (2.17)$$

In the following section, using the DNS data, we will compute the ratios \bar{T}^h/T^h and \dot{T}^h/T^h when the function space \mathcal{V}^h is constructed from Fourier modes and typical finite element shape functions.

The above equations represent the “ideal” transfer of energy. We will also compare this transfer to the transfer predicted by the Smagorinsky model (Smagorinsky 1963). The Smagorinsky transfer is given by is given by

$$\bar{T}_{\text{smag}}^h \equiv M_{\text{smag}}(\bar{\mathbf{V}}^h, \mathcal{P}^h \mathbf{U}; h, \mathbf{c}) \quad (2.18)$$

$$\dot{T}_{\text{smag}}^h \equiv M_{\text{smag}}(\dot{\mathbf{V}}^h, \mathcal{P}^h \mathbf{U}; h, \mathbf{c}), \quad (2.19)$$

where the Smagorinsky term is defined as

$$M_{\text{smag}}(\mathbf{W}, \mathbf{U}; h, \mathbf{c}) = 2(ch)^2 (\nabla^S \mathbf{w}, |\nabla^S \mathbf{u}| \nabla^S \mathbf{u}). \quad (2.20)$$

3. Numerical Results

In this section we present the numerical results of our *a-priori* analysis. The DNS solution used in our analysis is the solution to a forced, homogeneous, isotropic problem with $Re_\lambda = 168$ (see Jimenez, Wray, Saffman & Rogallo 1993 for details).

3.1. Spectral Basis

We expand the DNS solution and its restrictions to the finite dimensional spaces using Fourier modes. We approximate \mathcal{V} with the space spanned by Fourier modes with wavenumber less than k_c . Note that $k_c > k_d$, the dissipation wavenumber, so that \mathcal{V} which is infinite dimensional may be accurately represented by this finite dimensional space. The space \mathcal{V}^h is also spanned by Fourier modes, but with wavenumbers less than k_c^h where $k_c^h \ll k_d$. The restriction operator \mathcal{P}^h is the L_2 projection of \mathcal{V} onto \mathcal{V}^h . As a result

$$\mathbf{U}(\mathbf{x}) = \sum_{\mathbf{k} \leq k_c} \hat{\mathbf{U}}(\mathbf{k}) e^{i\mathbf{k} \cdot \mathbf{x}} = \sum_{\mathbf{k} \leq k_c} [\hat{\mathbf{u}}(\mathbf{k}), \hat{p}(\mathbf{k})]^T e^{i\mathbf{k} \cdot \mathbf{x}} \quad (3.1)$$

$$\mathcal{P}^h \mathbf{U}(\mathbf{x}) = \sum_{\mathbf{k} \leq k_c^h} \hat{\mathbf{U}}(\mathbf{k}) e^{i\mathbf{k} \cdot \mathbf{x}} = \sum_{\mathbf{k} \leq k_c^h} [\hat{\mathbf{u}}(\mathbf{k}), \hat{p}(\mathbf{k})]^T e^{i\mathbf{k} \cdot \mathbf{x}} \quad (3.2)$$

$$\mathbf{V}^h(\mathbf{x}) = \sum_{\mathbf{k} \leq k_c^h} \hat{\mathbf{V}}(\mathbf{k}) e^{i\mathbf{k} \cdot \mathbf{x}} = \sum_{\mathbf{k} \leq k_c^h} [\hat{\mathbf{u}}(\mathbf{k}), 0]^T e^{i\mathbf{k} \cdot \mathbf{x}}, \quad (3.3)$$

where $\mathbf{k} = |\mathbf{k}|$. For this study we choose $k_c = 256$ and $k_c^h = 32$.

In order to compute the multiscale transfer of energy we define $\bar{\mathcal{V}}^h$ to be the space spanned by Fourier modes with wavenumbers less than $k_c^h/2 = 16$. Thus

$$\bar{\mathbf{V}}^h(\mathbf{x}) = \sum_{\mathbf{k} \leq k_c^h/2} \hat{\mathbf{V}}(\mathbf{k}) e^{i\mathbf{k} \cdot \mathbf{x}} = \sum_{\mathbf{k} \leq k_c^h/2} [\hat{\mathbf{u}}(\mathbf{k}), 0]^T e^{i\mathbf{k} \cdot \mathbf{x}} \quad (3.4)$$

$$\dot{\mathbf{V}}^h(\mathbf{x}) = \mathbf{V}^h(\mathbf{x}) - \bar{\mathbf{V}}^h(\mathbf{x}). \quad (3.5)$$

Using (3.1), (3.2), (3.4) and (3.5) in (2.16) and (2.17) we compute the energy transfer from the coarse and fine resolved scales. We note that due to the properties of the restriction operator and the Fourier modes, there is no contribution to the energy transfer from the linear terms. The values of the multiscale transfers are reported in the first column of Table 1. We observe that the energy transfer to the subgrid scales exclusively from the

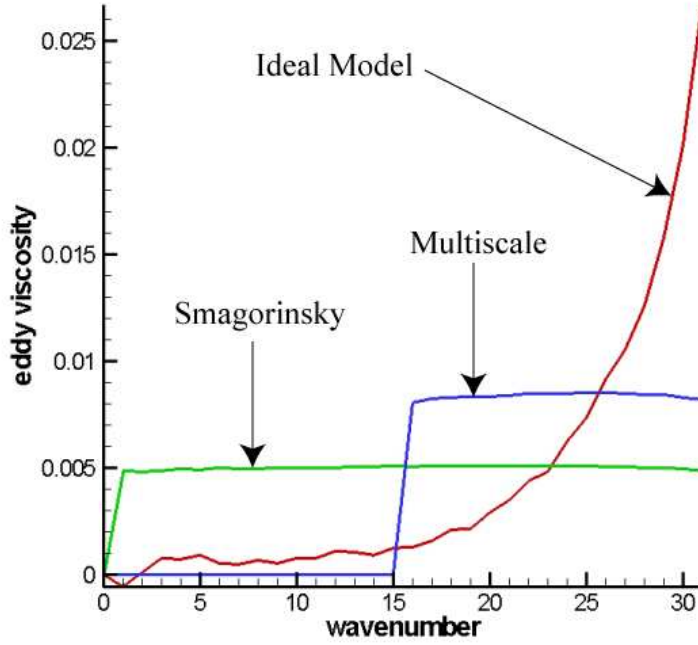


FIGURE 1. Spectral eddy viscosity as a function of wavenumber (results obtained using DNS database). Results for the Ideal model, the Smagorinsky model and the variational multiscale approach are shown. Viscosities are scaled such that the total energy transfer for every model is the same.

coarse resolved scales (modes with wavenumber less than $k_c^h/2$) is a very small fraction of the total energy transfer. Most of the energy transfer to the subgrid scales is from modes with wavenumbers close to the cut-off k_c^h . This observation is consistent with the picture of local energy transfer in wavenumber space reported by several researchers (see also Figure 1).

In the third column of Table 1, we have reported the ratios of energy transfer implied by the Smagorinsky model. These values have been obtained by using (3.2), (3.4) and (3.5) in (2.18) and (2.19). We observe that this model predicts a more equal transfer from the coarse and the fine scales, which is in conflict with true transfer. This observation may be interpreted as a motivation for the variational multiscale approach (Hughes, Mazzei & Jansen 2000; Hughes, Mazzei, Oberai & Wray 2001), which involves applying the Smagorinsky model to the fine scales and applying no model to the coarse scales (see Figure 1).

3.2. Finite Element Basis

We expand the DNS solution and its restrictions to finite dimensional spaces using typical finite element basis functions. In particular, we use shape functions with trilinear interpolation. We utilize an equal number of grid points in each direction. The space \mathcal{V} is spanned by N^3 such functions. Likewise \mathcal{V}^h is spanned by $(N^h)^3$ functions, with

$N^h \ll N$. The restriction operator \mathcal{P}^h is the nodal interpolant of \mathcal{V} onto \mathcal{V}^h . As a result

$$\mathbf{U}(\mathbf{x}) = \sum_{a,b,c=1,2,\dots}^N \mathbf{U}(x_a, y_b, z_c) \phi_a^\delta(x) \phi_b^\delta(y) \phi_c^\delta(z) \quad (3.6)$$

$$\mathcal{P}^h \mathbf{U}(\mathbf{x}) = \sum_{a,b,c=\alpha,2\alpha,\dots}^N \mathbf{U}(x_a, y_b, z_c) \phi_a^h(x) \phi_b^h(y) \phi_c^h(z) \quad (3.7)$$

$$\mathbf{V}^h(\mathbf{x}) = \sum_{a,b,c=\alpha,2\alpha,\dots}^N [\mathbf{u}, 0]^T(x_a, y_b, z_c) \phi_a^h(x) \phi_b^h(y) \phi_c^h(z), \quad (3.8)$$

where δ is the mesh size associated with the DNS solution and h is the mesh size associated with the ideal LES solution. The ratio $\alpha = N/N^h$ and

$$\phi_a^h(\xi) = \begin{cases} (x - x_a + h)/h, & x \in (x_a - h, x_a) \\ (x_a + h - x)/h, & x \in (x_a, x_a + h) \\ 0, & \text{otherwise.} \end{cases} \quad (3.9)$$

To be consistent with the spectral case we select $N = 512$ and $N^h = 64$, which implies $\alpha = 8$.

Using (3.6), (3.7) and (3.8) in (2.12) we compute the net energy transferred to the subgrid scales. In this case, in contrast to the spectral case, the contribution from the linear terms in the Navier-Stokes equations is not zero. However we have verified that it accounts for only about 10% of the total transfer. Hence, most of the subgrid transfer is due to the nonlinear term in the Navier Stokes equation. Based on this observation we now compute the proportion of this transfer from the coarse and fine resolved scales.

In order to compute the multiscale transfer of energy we define $\bar{\mathcal{V}}^h$ to be the space spanned by shape function of mesh size $2h$. The dimension of this space is $(N^h/2)^3$ and

$$\bar{\mathbf{V}}^h(\mathbf{x}) = \sum_{a,b,c=2\alpha,4\alpha,\dots}^N [\mathbf{u}, 0]^T(x_a, y_b, z_c) \phi_a^{2h}(x) \phi_b^{2h}(y) \phi_c^{2h}(z) \quad (3.10)$$

$$\dot{\mathbf{V}}^h(\mathbf{x}) = \mathbf{V}^h(\mathbf{x}) - \bar{\mathbf{V}}^h(\mathbf{x}). \quad (3.11)$$

Using (3.6), (3.7), (3.10) and (3.11) in (2.16) and (2.17) we compute the energy transfer from the coarse and fine resolved scales. The values of the multiscale transfers are reported in the second column of Table 1. We observe that the energy transferred to the subgrid scales exclusively from the coarse resolved scales is a now a significant proportion of the total energy transfer. It is in fact greater than the energy transfer to the subgrid scales from the fine resolved scales. This picture is very different from the Fourier case, where the transfer from the fine resolved scale is seen to dominate.

In the fourth column of Table 1, we have also reported the transfer predicted by the Smagorinsky model, obtained by using (3.7), (3.10) and (3.11) in (2.18) and (2.19). We observe that in this case the ratios of transfer predicted by the Smagorinsky model are closer to the ideal values. Furthermore the multiscale approach of removing the Smagorinsky model from the coarse scales does not appear to be warranted.

	Numerical Estimate for Ideal Model		Numerical Estimate for Smagorinsky		Analytical Estimate for Ideal Model	
	Fourier	FEM	Fourier	FEM	Fourier	FEM
$ \bar{T}^h/T^h $	0.04	0.65	0.30	0.42	0.25	0.49
$ \dot{T}^h/T^h $	0.96	0.35	0.70	0.58	0.75	0.51

TABLE 1. Estimates of the ratios of multiscale transfer of energy due to the subgrid term.

4. Explanation of the Transfer

We now explain the numerical results of the previous section. Our analysis is based on the EDQNM analysis (see Kraichnan 1976; Leslie & Quarini 1979). We first consider the spectral case and then the finite element case.

4.1. Spectral Basis

In Leslie & Quarini 1979 the authors have reported the subgrid spectral viscosity $\nu_n(k)$ corresponding to the sharp cut-off filter. Their results appear in Figure 2 of Leslie & Quarini 1979. Once this viscosity is known, the transfer between any two wavenumbers k_1 and k_2 is estimated by evaluating $T(k_1, k_2) = 2 \int_{k_1}^{k_2} \nu(k) k^2 E(k) dk$, where $E(k) = K_o \epsilon^{2/3} k^{-5/3}$. It may be easily verified that in the spectral case, the coarse and the fine scale energy transfers we wish to compute are given by $\bar{T}^h = T(0, k_c^h/2)$ and $\dot{T}^h = T(k_c^h/2, k_c^h)$. Using these expressions, and reading off the value of the spectral eddy viscosity from the figure, we numerically compute $\bar{T}^h/T^h = 0.25$ and $\dot{T}^h/T^h = 0.75$. These results once again indicate that the transfer is dominated by interactions that are local in the wavenumber space. Note that this estimate is obtained for a spectrum with an infinite inertial range. When the spectrum is flatter than $k^{-5/3}$ in the low wavenumbers and steeper than $k^{-5/3}$ in the high wavenumbers, as it must be for any realistic problem, the plateau in the eddy viscosity is lowered. The net result then is that the transfer from the coarse modes is further reduced.

4.2. Finite Element Basis

To understand the energy transfer within the finite element basis using a similar approach, we take the Fourier transform of (3.7). This yields

$$\widehat{\mathcal{P}^h \mathbf{U}}(\mathbf{k}) = \sum_{a,b,c=\alpha, 2\alpha, \dots}^N \mathbf{U}(x_a, y_b, z_c) \widehat{\phi}_a^h(k_x) \widehat{\phi}_b^h(k_y) \widehat{\phi}_c^h(k_z), \quad (4.1)$$

where $\widehat{\phi}_a^h$, which denotes the Fourier transform of ϕ_a^h , is obtained from (3.9) and is given by

$$\widehat{\phi}_a^h(k_x h) = \frac{2\pi}{N^h} e^{ik_x x_a} b(k_x h), \quad (4.2)$$

where

$$b(\eta) = \frac{2(1 - \cos \eta)}{\eta^2}. \quad (4.3)$$

Utilizing (4.2) in (4.1) we arrive at

$$\widehat{\mathcal{P}^h \mathbf{U}}(\mathbf{k}) = \left[\left(\frac{2\pi}{Nh} \right)^3 \sum_{a,b,c=\alpha,2\alpha,\dots}^N \mathbf{U}(x_a, y_b, z_c) e^{i(k_x x_a + k_y y_b + k_z z_c)} \right] b(k_x h) b(k_y h) b(k_z h) \quad (4.4)$$

In the equation above, the term within the square brackets represents the Fourier coefficients of \mathbf{U} , evaluated using a finite, uniform quadrature rule. Replacing these approximate Fourier coefficients with their exact values, we arrive at

$$\widehat{\mathcal{P}^h \mathbf{U}}(\mathbf{k}) = \hat{\mathbf{U}}(\mathbf{k}) b(k_x h) b(k_y h) b(k_z h). \quad (4.5)$$

From the equation above we conclude that $\mathcal{P}^h \mathbf{U}$ may be approximated by a filtered version of \mathbf{U} where the filter, represented by the tensor product involving b is anisotropic. However since we are dealing with isotropic turbulence, following Leslie & Quarini 1979, we may replace this filter (by inducing a small error) with its isotropic component. Thus we have,

$$\widehat{\mathcal{P}^h \mathbf{U}}(\mathbf{k}) = \hat{\mathbf{U}}(\mathbf{k}) G(kh), \quad (4.6)$$

where

$$G(kh) = (4\pi)^{-1} \int_{\Gamma} b(k_x h) b(k_y h) b(k_z h) d\Gamma. \quad (4.7)$$

In the equation above the integral is taken over all angular directions for a fixed k . Thus comparing (4.6) with (3.2) we conclude that the Fourier transforms of both the spectral and the finite element forms of $\mathcal{P}^h \mathbf{U}$ may be written in the general form given by (4.6) with different interpretations of the filter G . For the finite element case the filter is given by (4.7) and for the spectral case the filter is a sharp cutoff filter with a cutoff at $k = k_c^h$. Both these filters are plotted in Figure 2. In addition, in this figure we have also plotted the Gaussian filter and isotropic component of the top-hat filter described in Leslie & Quarini 1979.

In Figure 2, we observe that the filter implied by the finite element basis is a graded filter, much like the Gaussian and the top-hat filters. Thus based on the analysis presented in Leslie & Quarini 1979, for the finite element basis we expect an eddy viscosity that is similar to that for the Gaussian or the top-hat filters. This viscosity, which is plotted in Figure 3 in Leslie & Quarini 1979 is constant for $kh \in (0, 1)$ and thereafter reduces smoothly to zero. Beyond $kh > 2\pi$, it is almost zero. Assuming for now that the viscosity for the filter induced by the finite element shape functions is the same, we calculate the expected values of transfers T^h and \bar{T}^h . Recognizing that

$$\widehat{\mathcal{P}^h \mathbf{V}}(\mathbf{k}) = \hat{\mathbf{V}}(\mathbf{k}) G(2kh), \quad (4.8)$$

it may be verified that these transfers are given by

$$T^h = 2 \int_0^\infty \nu(k) k^2 E(k) G^2(kh) dk \quad (4.9)$$

$$\bar{T}^h = 2 \int_0^\infty \nu(k) k^2 E(k) G^2(2kh) dk \quad (4.10)$$

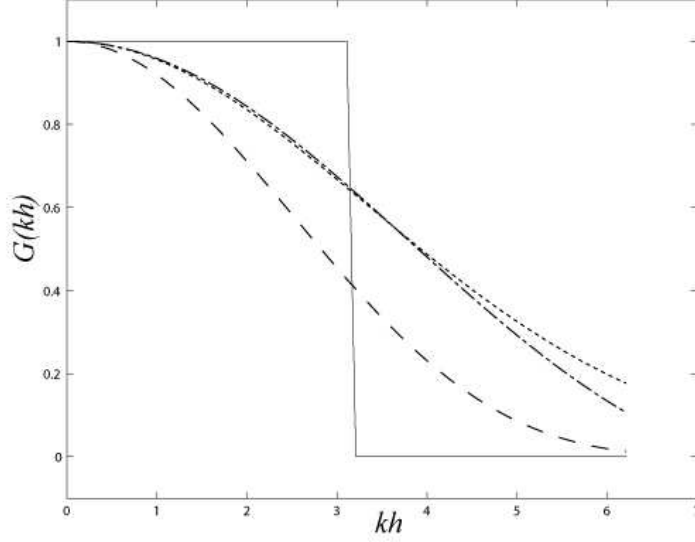


FIGURE 2. Plot of various Filters. Solid line: sharp cutoff filter; Dashed: Filter induced by the FEM basis; Dash-dot: Top-hat filter; Dotted line: Gaussian filter

$$\dot{T}^h = T^h - \bar{T}^h. \quad (4.11)$$

Once again assuming an infinite inertial range, we can explicitly calculate the ratios $\bar{T}^h/T^h = 0.49$ and $\dot{T}^h/T^h = 0.51$. Thus in this case we conclude that the transfer of energy from the coarse and the fine resolved scales is about the same. When compared with the spectral case, this increase in the contribution from the coarse scales for the finite element case, is consistent with the numerical results reported in Table 1.

5. Conclusions

In this manuscript we have performed an *a-priori* study of the transfer of energy from the resolved scales to the subgrid scales in the large eddy simulation of homogeneous isotropic turbulence. Our goal was to uncover the scale dependence of this transfer and the effect of the choice of an ideal resolved scale (LES) solution. In this regard, we found

(a) When the ideal LES solution is defined to have the same Fourier coefficients as the exact solution up to the cut-off wavenumber, then the energy transfer is predominantly from the fine resolved scales represented by modes that are close to the cutoff wavenumber.

(b) When the ideal LES solution is defined as the nodal interpolant of the exact solution on a typical finite element basis then the transfer from both the coarse and the fine resolved scales is significant.

We also analyzed the ability of the Smagorinsky model to replicate the transfer described above. We found that in spectral case the model is overly dissipative in the coarse scales, hence justifying the variational multiscale approach of Hughes, Mazzei, Oberai & Wray 2001. However, in the finite element case we found that the model performs reasonably well in imposing the right proportion of dissipation from the coarse and the fine

resolved scales. Thus indicating that in this case the multiscale modification does not appear to be warranted.

Finally, we provided a theoretical justification of our numerical observations based on the EDQNM closure. Using the results of Leslie & Quarini 1979, we demonstrated the dominance of the energy transfer from the fine resolved sales in the spectral case. In addition, we established that the ideal finite element solution could be obtained applying a graded filter to the exact solution. Thereafter, by assuming that the effective subgrid viscosity for this filter is the same as that of a Gaussian filter, we demonstrated that the energy transfer from the coarse resolved scales is significant.

REFERENCES

- CERUTTI, C., MENEVEAU, C. & KNIO, O.M. 2000 Spectral and Hyper Eddy Viscosity in High-Reynolds-Number Turbulence. *Journal of Fluid Mechanics*, **421**:307–338.
- COLLIS, S.S. 2001 Monitoring unresolved scales in multiscale turbulence modeling. *Physics of Fluids*, **13**(6):1800–1806.
- FOAIS, C., MANLEY, O., ROSA, R. & TEMAM, R. 2001 *Navier-Stokes Equations and Turbulence*. Cambridge University Press, Cambridge.
- HUGHES, T.J.R., MAZZEI, L. & JANSEN, K. E. 2000 Large Eddy Simulation and the Variational Multiscale Method. *Computing and Visualization in Science*, **3**:47–59.
- HUGHES, T. J. R., MAZZEI, L., OBERAI, A. A., & WRAY, A. A. 2001 The Multiscale Formulation of Large Eddy Simulation: Decay of Homogeneous Isotropic Turbulence. *Physics of Fluids*, **13**(2):505–512.
- HUGHES, T. J. R., OBERAI, A. A. & MAZZEI, L. 2001 Large Eddy Simulation of Turbulent Channel Flows by the Variational Multiscale Method. *Physics of Fluids*, **13**(6):1784–1799.
- JIMENEZ, J., WRAY, A. A., SAFFMAN, P. G. & ROGALLO, R. S. 1993 The Structure of Intense Vorticity in Isotropic Turbulence. *Journal of Fluid Mechanics*, **225**:65–90.
- KRAICHNAN, R.H. 1976 Eddy Viscosity in Two and Three Dimensions. *Journal of the Atmospheric Sciences*, **33**:1521–1536.
- LESLIE, D. & QUARINI, G. 1979 The Application of Turbulence Theory to the Formulation of Subgrid Modelling Procedures. *Journal of Fluid Mechanics*, **91**:65–91.
- SMAGORINSKY, J. 1963 General Circulation Experiments with the Primitive Equations. I. The Basic Experiment. *Monthly Weather Review*, **91**:99–164.

Sampling versus filtering in Large-Eddy simulations

By O. Debliquy, B. Knaepen & D. Carati [†] AND A. A. Wray[‡]

A LES formalism in which the filter operator is replaced by a sampling operator is proposed. The unknown quantities that appear in the LES equations originate only from inadequate resolution (discretization errors). The resulting viewpoint seems to make a link between finite difference approaches and finite element methods. Sampling operators are shown to commute with nonlinearities and to be purely projective. Moreover, their use allows an unambiguous definition of the LES numerical grid. The price to pay is that sampling never commutes with spatial derivatives and the commutation errors must be modelled. It is shown that models for the discretization errors may be treated using the dynamic procedure. Preliminary results, using the Smagorinsky model, are very encouraging.

1. Introduction

The analysis presented here owes its origin to the unique practical motivation for Large-Eddy Simulations (LES's), i.e. the lack of adequate computational power. Indeed, LES is a discretization of the Navier-Stokes equations on a grid which is too coarse. Traditionally, the LES equations are presented as a smoothed version of the Navier-Stokes equations. The smoothing operation generates an unknown term that must be modelled. The solution of the LES equations also requires numerical schemes with, unavoidably, discretization errors. Since resolution is always the driving constraint in LES, the discretization errors are expected to play a significative role (Ghosal 1996; Kravchenko & Moin 1997; Chow & Moin 2003). However, several attempts have been proposed in order to minimize their effect on the large scale dynamics (Vasilyev *et al.* 1998; Marsden *et al.* 2002).

The viewpoint adopted in the approach developed here is very different, to such an extent that it might be viewed as provocative. This is however not the objective. The strategy that has been investigated is to abandon the idea of using smoothing filters. In that case, the discretization errors become the only term that requires a modelling effort. This viewpoint should not be confused with the MILES (Monotone Integrated Large Eddy Simulation) approach (Park *et al.* 2004) in which the numerical errors are expected to dissipate the correct amount of energy and to stabilize the under-resolved simulation. On the contrary, in the following, a real modelling effort is developed in order to account for the discretization errors. In particular, using the successful dynamic procedure, two embedded grids are used to optimize the model for the discretization errors.

[†] Université Libre de Bruxelles, Brussels, Belgium

[‡] NASA Ames Research Center, Moffett Field, USA

In spectral codes, filtering or reducing the resolution are two indistinguishable operations. In that sense, for these codes, the discretization errors and the modelling errors are identical and the methodology developed in this report would reduce to a simple re-interpretation of the LES equations without any practical consequence. For finite difference codes the situation is different. The filter width Δ_f and the grid spacing Δ_g may be considered as two independent parameters. In the limit $\Delta_g/\Delta_f \rightarrow 0$, the discretization errors are supposed to be negligible with respect to the “sub-filter” term. Due to finite computational resources, such a limit is however never used in practice. A reasonable compromise is to consider that $\Delta_g/\Delta_f \lesssim 1$. In the following, the opposite limit ($\Delta_g/\Delta_f \rightarrow \infty$), obtained when no smoothing filter is used, is investigated for finite difference schemes. A bridge between this approach and the traditional viewpoint is also proposed. The discretization scheme is considered to result from a sampling operation that shares some properties with filters.

2. Definitions

The purpose of this section is to introduce the sampling operators and to make the link between two apparently incompatible viewpoints on LES. The first one is the traditional filtering approach in which the Navier-Stokes velocity field u_i is transformed into a continuous filtered velocity \tilde{u}_i . The second viewpoint is the discrete representation \bar{u}_i of the velocity field on a numerical grid in the actual LES simulation. In the filtering approach, the LES velocity \tilde{u}_i is given by the following expression

$$\tilde{u}_i(\vec{x}) = \int G(\vec{x}, \vec{y}) u_i(\vec{y}) d^3y, \quad (2.1)$$

in which, $G(\vec{x}, \vec{y})$ is the filter kernel. In general, the filtered field depends on values of the original velocity field from the entire integration domain $\Omega \subset \mathbb{R}^3$. Very few constraints are imposed on the filter kernel $G(\vec{x}, \vec{y})$ except that $G(\vec{x}, \vec{y}) = 0$ for $\vec{y} \notin \Omega$ and the normalization condition:

$$\int G(\vec{x}, \vec{y}) d^3y = 1. \quad (2.2)$$

When considering the discrete representation of the signal u_i on the LES grid, the sampled signal is not a function from Ω into \mathbb{R} anymore, but a mapping from the set of grid points $\{\vec{x}^\ell\}$ into \mathbb{R} . It is however possible to keep the same type of expression,

$$\bar{u}_i(\vec{x}) = \int H(\vec{x}, \vec{y}) u_i(\vec{y}) d^3y. \quad (2.3)$$

In order to make the link with sampling and finite difference schemes, the discrete-filtered function $\bar{u}_i(\vec{x})$ should depend only on the grid values of $u_i(\vec{y})$, so that the general form of the kernel H has to be:

$$H(\vec{x}, \vec{y}) = \sum_{\ell} h^\ell(\vec{x}) \delta(\vec{y} - \vec{x}^\ell), \quad (2.4)$$

and the discrete-filtered signal is given by:

$$\bar{u}_i(\vec{x}) = \sum_{\ell} h^\ell(\vec{x}) u_i(\vec{x}^\ell). \quad (2.5)$$

Such an expression amounts to assuming an interpolation of the signal between the grid points. However, only the values of the Navier-Stokes velocity on the grid are required

to construct \bar{u}_i . Imposing a normalization condition on the discrete-filtering operator is also desirable. Since only the grid point values of \bar{u}_i matter, it is sufficient to impose the normalization condition on the grid:

$$\int H(\vec{x}^{\ell_1}, \vec{y}) d^3y = \sum_{\ell_2} H^{\ell_1 \ell_2} = 1, \quad (2.6)$$

where the square matrix $H^{\ell_1 \ell_2} = h^{\ell_2}(\vec{x}^{\ell_1})$ has the dimensions $N \times N$ where N is the number of grid points. However, in general, the interpolation of a constant signal on a grid should also be a constant signal between the grid points and it is very natural to impose the normalization condition between the grid points as well:

$$\int H(\vec{x}, \vec{y}) d^3y = \sum_{\ell} h^{\ell}(\vec{x}) = 1. \quad (2.7)$$

The process of sampling a signal is very similar to a projection. However, the transformation (2.5) does not necessarily correspond to the application of a projective operator to $u_i(x)$. Indeed, if the signal is discrete-filtered again, the result is given by

$$\bar{\bar{u}}_i(\vec{x}) = \sum_{\ell_1} h^{\ell_1}(\vec{x}) \sum_{\ell_2} h^{\ell_2}(\vec{x}^{\ell_1}) u_i(\vec{x}^{\ell_2}), \quad (2.8)$$

and, introducing the N -dimensional vectors $u_i^{\ell_1} = u_i(x^{\ell_1})$, the discrete-filtering operator must satisfy the following constraint

$$\sum_{\ell_2} H^{\ell_1 \ell_2} u_i^{\ell_2} = u_i^{\ell_1}, \quad (2.9)$$

in order to be considered as a projector. Remarkably enough, the same condition ensures that the discrete-filtered signal takes the same value as the Navier-Stokes signal on the grid points since the right-hand-side of relation (2.9) is simply $\bar{u}_i(\vec{x}^{\ell_2})$. The three vectors $u_i^{\ell_2}$ ($i = 1, 2, 3$) are thus eigenvectors of the square matrix $H^{\ell_1 \ell_2}$ with the eigenvalue $\lambda = 1$. These constraints, for three independent signals u_1 , u_2 and u_3 , are difficult to satisfy and, although no attempt will be done to prove it, the only solution seems to be:

$$H^{\ell_1 \ell_2} = \delta^{\ell_1 \ell_2}. \quad (2.10)$$

This choice automatically satisfies the normalization constraint as well.

It is also interesting that, imposing the projector constraint, the derivatives of these functions at the grid points entirely define the numerical scheme that has to be used when solving the discrete-filtered Navier-Stokes equations. Indeed, the derivatives of \bar{u}_i on the grid are given by

$$\partial_m \bar{u}_i(\vec{x}^{\ell_1}) = \sum_{\ell_2} D_m^{\ell_1 \ell_2} u_i(\vec{x}^{\ell_2}) = \sum_{\ell_2} D_m^{\ell_1 \ell_2} \bar{u}_i(\vec{x}^{\ell_2}), \quad (2.11)$$

$$\partial_{mn}^2 \bar{u}_i(\vec{x}^{\ell_1}) = \sum_{\ell_2} D_{mn}^{\ell_1 \ell_2} u_i(\vec{x}^{\ell_2}) = \sum_{\ell_2} D_{mn}^{\ell_1 \ell_2} \bar{u}_i(\vec{x}^{\ell_2}), \quad (2.12)$$

where the differentiation matrices are given by

$$D_m^{\ell_1 \ell_2} = \frac{\partial h^{\ell_2}}{\partial x_m}(\vec{x}^{\ell_1}), \quad (2.13)$$

$$D_{mn}^{\ell_1 \ell_2} = \frac{\partial^2 h^{\ell_2}}{\partial x_m \partial x_n}(\vec{x}^{\ell_1}). \quad (2.14)$$

The normalization constraint imposes:

$$\sum_{\ell_2} D_m^{\ell_1 \ell_2} = 0, \quad (2.15)$$

$$\sum_{\ell_2} D_{mn}^{\ell_1 \ell_2} = 0. \quad (2.16)$$

These constraints are fairly easy to satisfy.

3. Example

The simplest example of a finite difference scheme is probably the second order centered difference scheme on a regular one dimensional grid. In that case, the grid points are given by $x^\ell = L \ell / N$ where $\ell = 1 \cdots N$. The signals will be assumed to be periodic and two grid points are added to the grid: $x^0 \equiv x^N$ and $x^{N+1} \equiv x^1$. The first and second derivatives of the discrete signal are given by:

$$\frac{\partial \bar{u}(x^\ell)}{\partial x} = \frac{\bar{u}(x^{\ell+1}) - \bar{u}(x^{\ell-1})}{2\Delta} \equiv \partial_x^\Delta \bar{u}, \quad (3.1)$$

$$\frac{\partial^2 \bar{u}(x^\ell)}{\partial x^2} = \frac{\bar{u}(x^{\ell+1}) - 2\bar{u}(x^\ell) + \bar{u}(x^{\ell-1}))}{\Delta^2} \equiv (\partial_x^\Delta)^2 \bar{u}, \quad (3.2)$$

where $\Delta = L/N$ is the grid spacing. The choice of function $h^\ell(x)$ is not unique, even when imposing (3.1) and (3.2). In order to simplify the structure of the function $h^\ell(x)$, only compact support functions will be considered. Moreover, since a homogeneous grid is assumed, it is reasonable to assume that the functions h^ℓ have all the same shape and are characterized by a single function:

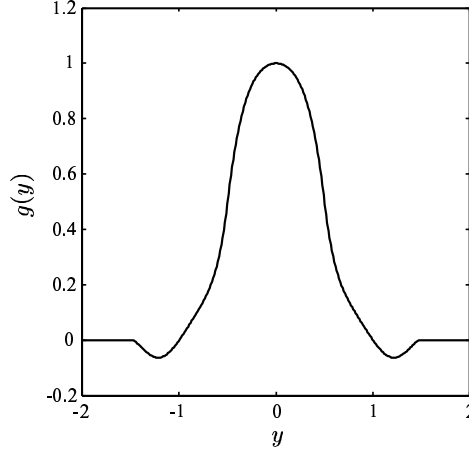
$$h^\ell(x) = g\left(\frac{x - x^\ell}{\Delta}\right) \quad (3.3)$$

Since the constraints (3.1) and (3.2) only concern the first two neighbor points, the support will be assumed to be $[-3/2, 3/2]$ so that only three points are included in it. The connection points at $y = \pm 3/2$ might lead to discontinuities. However, as an additional constraint, the function g is assumed to be C^1 . The second derivative is thus allowed to be discontinuous, but only between grid points. In that case, it is actually much easier to define $g(y)$ separately for three intervals as follows:

$$\begin{aligned} g(y) = & p_a(y) \Theta\left(\frac{1}{2} + y\right) \Theta\left(\frac{1}{2} - y\right) \\ & + p_b(-y) \Theta\left(\frac{3}{2} + y\right) \Theta\left(-\frac{1}{2} - y\right) + p_b(y) \Theta\left(\frac{3}{2} - y\right) \Theta\left(-\frac{1}{2} + y\right), \end{aligned} \quad (3.4)$$

where $\Theta(y)$ is the Heaviside function. This choice implies that $g(y) = g(-y)$, which is reasonable for a centered difference scheme. The constraint (2.10) imposes that $p_a(0) = 1$ and $p_b(1) = 0$. Taking into account (1) the fact that the functions h^ℓ are assumed to be all the same (3.3) and (2) the compact support of g , the normalization constraint reduces to $g(y) + g(y+1) + g(y-1) = 1$. Considering the structure (3.4), this imposes:

$$p_a(y) + p_b(y+1) + p_b(-y+1) = 1 \quad (3.5)$$

FIGURE 1. The function $g(y)$ defined by the expressions (3.4,3.6-3.7).

The lowest order polynomials that can be found to satisfy these constraints as well as the continuity of g and of its derivative at $y = \pm 3/2$ and $y = \pm 1/2$ are given by:

$$p_a(y) = 1 - y^2 - 4 y^4, \quad (3.6)$$

$$p_b(y) = 2 (1 + y) \left(\frac{3}{2} + y \right)^2 (2 + 5 y + 4 y^2). \quad (3.7)$$

The resulting function g is shown in the Figure 1. For summarizing the properties of the discrete-filtering operator, the above choice for the function g ensures that (on the grid):

$$\begin{aligned} \bar{u} &= u \\ \overline{u^2} &= \bar{u}^2, \\ \frac{\partial \bar{u}(x^\ell)}{\partial x} &= \frac{\bar{u}(x^{\ell+1}) - \bar{u}(x^{\ell-1})}{2\Delta} = \partial_x^\Delta \bar{u}(x^\ell), \\ \frac{\partial^2 \bar{u}(x^\ell)}{\partial x^2} &= \frac{\bar{u}(x^{\ell+1}) - 2\bar{u}(x^\ell) + \bar{u}(x^{\ell-1}))}{\Delta^2} = (\partial_x^\Delta)^2 \bar{u}(x^\ell), \end{aligned}$$

and that (everywhere):

$$\bar{\bar{u}}(x) = \bar{u}(x). \quad (3.8)$$

For three-dimensional systems, the function $h^\ell(\vec{x})$ is simply a product of one-dimensional functions g and the grid point coordinate x^ℓ can be characterized by a vector of indices (l_x, l_y, l_z) :

$$h^{\{l_x, l_y, l_z\}}(\vec{x}) = g\left(\frac{x - x^{\ell_x}}{\Delta_x}\right) g\left(\frac{y - y^{\ell_y}}{\Delta_y}\right) g\left(\frac{z - z^{\ell_z}}{\Delta_z}\right), \quad (3.9)$$

and $\vec{x}^\ell = (x^{\ell_x}, y^{\ell_y}, z^{\ell_z})$.

4. Interpolation and diagnostics

In the preceding sections, interpolation functions compatible with a given finite difference scheme have been introduced. They correspond to functions for which the derivatives on the grid are evaluated exactly by the spatial discretization scheme. The functions $h^{\ell_1}(\vec{x})$ thus play the same role for finite difference schemes as the plane waves $e^{i\vec{k} \cdot \vec{x}}$ for

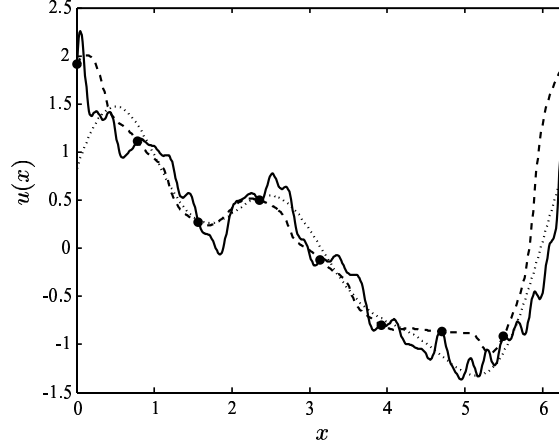


FIGURE 2. The comparison between the sampling operator and a sharp Fourier cutoff is shown for a one dimensional signal. The solid line corresponds to the original periodic signal on the interval $[0, 2\pi]$ built using 32 modes with random amplitudes. The dashed curve corresponds to the sampled signal on a 8 point grid reconstructed using the interpolation functions $h^\ell(x)$. The dotted line is obtained by applying a Fourier cutoff keeping 8 modes.

spectral methods. In that sense, their introduction improves the mathematical grounding of finite differences, though they do not modify the practical implementation of these numerical methods. The approach developed here could then be considered at first sight as an interesting mathematical framework for finite difference schemes but without practical implications. There are however practical implications. The first one is in the post-processing of results obtained using a finite difference scheme. Many quantities are routinely computed in a numerical simulation. It is not the purpose of this work to derive the influence of the interpolation function on the exhaustive list of possible diagnostics. Only two important quantities, the energy and the dissipation will be considered. Moreover, in order to simplify the discussion, the following developments are restricted to one-dimensional systems.

By definition, the one-dimensional kinetic energy is given by

$$E = \frac{1}{2} \int dx \, \bar{u}(x) \, \bar{u}(x), \quad (4.1)$$

$$= \frac{1}{2} \sum_{\ell_1 \ell_2} \bar{u}(x^{\ell_1}) \, Q^{\ell_1 \ell_2} \, \bar{u}(x^{\ell_2}), \quad (4.2)$$

where

$$Q^{\ell_1, \ell_2} = \int dx \, h^{\ell_1}(x) \, h^{\ell_2}(x). \quad (4.3)$$

In spectral methods, thanks to the Parseval theorem, the matrix $Q^{\ell_1 \ell_2}$ reduces to δ^{ℓ_1, ℓ_2} . It is possible to impose this constraint for finite difference schemes at the expense of an increase in the degree of the polynomials used in the definition of the functions $h^{\ell_1}(\vec{x})$. However, the choice for the set of most relevant diagnostics is problem dependent. Any attempt to simplify their expression would thus make the definition of the function $h^\ell(\vec{x})$ problem dependent as well. To avoid this undesirable feature, the “simplest” functions $h^{\ell_1}(\vec{x})$ derived in the previous section and compatible with the continuity and normalization constraints as well as with the numerical scheme will be kept. Consequently, for

the one dimensional second order centered finite difference scheme, the matrix $Q^{\ell_1 \ell_2}$ is not diagonal but can be evaluated explicitly:

$$Q^{\ell_1, \ell_2} = q_1 \delta^{\ell_1, \ell_2} + q_2 (\delta^{\ell_1, \ell_2+1} + \delta^{\ell_1, \ell_2-1}) + q_3 (\delta^{\ell_1, \ell_2+2} + \delta^{\ell_1, \ell_2-2}), \quad (4.4)$$

where $q_1 = 11339/13860$, $q_2 = 121/1260$ and $q_3 = -47/9240$. The property $q_1 + 2q_2 + 2q_3 = 1$ can be derived from the normalization properties of the functions $h^\ell(\vec{x})$.

Similarly, the one dimensional dissipation is defined by:

$$\mathcal{E} = 2\nu \int dx (\partial_x \bar{u}(x)) (\partial_x \bar{u}(x)), \quad (4.5)$$

$$= 2 \frac{\nu}{\Delta^2} \sum_{\ell_1 \ell_2} \bar{u}(x^{\ell_1}) W^{\ell_1 \ell_2} \bar{u}(x^{\ell_2}), \quad (4.6)$$

where

$$W^{\ell_1, \ell_2} = \int d\vec{x} (\partial_x h^{\ell_1}(\vec{x})) (\partial_x h^{\ell_2}(\vec{x})). \quad (4.7)$$

The matrix $W^{\ell_1 \ell_2}$ can also be evaluated and is given by:

$$W^{\ell_1, \ell_2} = w_1 \delta^{\ell_1, \ell_2} + w_2 (\delta^{\ell_1, \ell_2+1} + \delta^{\ell_1, \ell_2-1}) + w_3 (\delta^{\ell_1, \ell_2+2} + \delta^{\ell_1, \ell_2-2}), \quad (4.8)$$

where $w_1 = 1009/315$, $w_2 = -179/105$ and $w_3 = 13/126$. The property $w_1 + 2w_2 + 2w_3 = 0$ can also be derived from the normalization properties of the functions $h^\ell(\vec{x})$.

5. Dynamic Procedure

Another place where the sampling viewpoint has a direct influence is in the implementation of the dynamic procedure. Indeed, the definition of the velocity on the test-level grid requires the explicit definition of the coarsening operator.

There is no reason to expect the dynamic Smagorinsky model to be a good candidate for representing the effect of the commutation error between the discrete-filtering operator and the spatial derivative. However, since this model has been thoroughly benchmarked and, at the very least, has the property to be dissipative so that it should stabilize the simulation, there is some rationale to evaluate and test the dynamic procedure for this model as a first step.

Numerical simulations, both DNS and LES, can be seen as the time advancement of a discrete-filtered velocity. We will consider three grids: The DNS grid \mathcal{G}^{Δ_0} , the LES grid \mathcal{G}^{Δ_1} and a test grid \mathcal{G}^{Δ_2} that is used only in the implementation of the dynamic procedure. In order to stress that the discrete-filtering operator is really based on the sampling concept, its application to the incompressible Navier-Stokes velocity is denoted by:

$$u_i^{\Delta_0} = \mathcal{S}^{\Delta_0} \circ u_i, \quad (5.1)$$

where $u_i^{\Delta_0}$ is the DNS field and the LES and test fields will be noted respectively $u_i^{\Delta_1}$ and $u_i^{\Delta_2}$. The three grids are assumed to be successively embedded $\mathcal{G}^{\Delta_2} \subset \mathcal{G}^{\Delta_1} \subset \mathcal{G}^{\Delta_0}$. This is enough to guarantee that

$$\mathcal{S}^{\Delta_2} = \mathcal{S}^{\Delta_2} \circ \mathcal{S}^{\Delta_1} = \mathcal{S}^{\Delta_2} \circ \mathcal{S}^{\Delta_1} \circ \mathcal{S}^{\Delta_0}, \quad (5.2)$$

$$\mathcal{S}^{\Delta_1} = \mathcal{S}^{\Delta_1} \circ \mathcal{S}^{\Delta_0}, \quad (5.3)$$

since only the grid point values of the velocity are used to construct the $u_i^{\Delta_0}$, $u_i^{\Delta_1}$ and

$u_i^{\Delta_2}$ velocities. The DNS equation can be written as:

$$\partial_t u_i^{\Delta_0} = \underbrace{-\partial_j^{\Delta_0} u_i^{\Delta_0} u_j^{\Delta_0} - \partial_i^{\Delta_0} p^{\Delta_0} + \nu \Delta^{\Delta_0} u_i^{\Delta_0}}_{N_i^{\Delta_0}(u^{\Delta_0})}, \quad (5.4)$$

where the differentiation operators $\partial_i^{\Delta_0}$ and Δ^{Δ_0} define the numerical scheme used in the DNS. By definition, the discretization error and, in particular, the difference between the discrete-filtered value of the velocity derivative $(\partial_j u_i)^{\Delta_0}$ and its evaluation on the grid $\partial_j^{\Delta_0} u_i^{\Delta_0}$ is supposed to be small enough so that it need not be modelled. This is obviously not the case in the LES equation:

$$\partial_t u_i^{\Delta_1} = \underbrace{-\partial_j^{\Delta_1} u_i^{\Delta_1} u_j^{\Delta_1} - \partial_i^{\Delta_1} p^{\Delta_1} + \nu \Delta^{\Delta_1} u_i^{\Delta_1}}_{N_i^{\Delta_1}(u^{\Delta_1})} + \mathcal{E}_i^{\Delta_1, \Delta_0}, \quad (5.5)$$

and the additional term

$$\mathcal{E}_i^{\Delta_1, \Delta_0} = \mathcal{S}^{\Delta_1} \circ N_i^{\Delta_0}(u^{\Delta_0}) - N_i^{\Delta_1}(u^{\Delta_1}), \quad (5.6)$$

has to be modelled. It contains three contributions from the pressure, the convective and the viscous terms. Actually, these terms should be constructed using the Navier-Stokes equations instead of the DNS equations. However, since it is assumed that the DNS velocity is a fair representation of the actual velocity, the expression (5.6) is acceptable and allows a more homogeneous presentation. Using the same notations, the test-level equations can be written as

$$\partial_t u_i^{\Delta_2} = \underbrace{-\partial_j^{\Delta_2} u_i^{\Delta_2} u_j^{\Delta_2} - \partial_i^{\Delta_2} p^{\Delta_2} + \nu \Delta^{\Delta_2} u_i^{\Delta_2}}_{N_i^{\Delta_2}(u^{\Delta_2})} + \mathcal{E}_i^{\Delta_2, \Delta_0}, \quad (5.7)$$

and the additional term that has to be modelled at the test-level reads:

$$\mathcal{E}_i^{\Delta_2, \Delta_0} = \mathcal{S}^{\Delta_2} \circ N_i^{\Delta_0}(u^{\Delta_0}) - N_i^{\Delta_2}(u^{\Delta_2}). \quad (5.8)$$

Equivalently, the equations for $u_i^{\Delta_2}$ can be obtained by applying \mathcal{S}^{Δ_2} on the LES equations:

$$\partial_t u_i^{\Delta_2} = \mathcal{S}^{\Delta_2} \circ N_i^{\Delta_1}(u^{\Delta_1}) + \mathcal{S}^{\Delta_2} \circ \mathcal{E}_i^{\Delta_1, \Delta_0}, \quad (5.9)$$

Consistency between these two formulations imposes the following identity:

$$\mathcal{E}_i^{\Delta_2, \Delta_1} = \mathcal{E}_i^{\Delta_2, \Delta_0} - \mathcal{S}^{\Delta_2} \circ \mathcal{E}_i^{\Delta_1, \Delta_0}, \quad (5.10)$$

where

$$\mathcal{E}_i^{\Delta_2, \Delta_1} = \mathcal{S}^{\Delta_2} \circ N_i^{\Delta_1}(u^{\Delta_1}) - N_i^{\Delta_2}(u^{\Delta_2}). \quad (5.11)$$

Equation (5.10) is nothing else the equivalent of the Germano identity for discrete-filtering operators, written at the vector level instead of the tensor level. The term (5.11) is known in terms of the LES velocity only (since $u_i^{\Delta_2} = \mathcal{S}^{\Delta_2} \circ u_i^{\Delta_1}$) and plays the role of the Leonard tensor in the Germano identity. The right-hand-side depends on the terms that have to be modelled at both LES and test levels.

If the Smagorinsky model is used at both LES and test levels, the identity is only an approximation that reads:

$$\mathcal{E}_i^{\Delta_2, \Delta_1} \approx 2 C M_i^{\Delta_2} \quad (5.12)$$

where

$$M_i^{\Delta_2} = \Delta_2^2 \partial_j^{\Delta_2} |S^{\Delta_2}| S_{ij}^{\Delta_2} - \mathcal{S}^{\Delta_2} \circ \Delta_1^2 \partial_j^{\Delta_1} |S^{\Delta_1}| S_{ij}^{\Delta_1}. \quad (5.13)$$

The tensor $S_{ij}^{\Delta_1}$ and $S_{ij}^{\Delta_2}$ represents the strain tensors evaluated on the LES and test grids respectively. The LES and test grid spacings are, respectively, Δ_1 and Δ_2 . In this formulation, it is assumed that the Smagorinsky parameter C is constant in the entire volume and is the same at both LES and test levels. Its optimal value is given by:

$$C \approx \frac{1}{2} \frac{\langle \mathcal{E}_i^{\Delta_2, \Delta_1} M_i^{\Delta_2} \rangle}{\langle M_i^{\Delta_2} M_i^{\Delta_2} \rangle}. \quad (5.14)$$

Assuming that $\alpha = \Delta_2/\Delta_1$ is a constant, the dynamic procedure can be used to compute directly the constant $c = C\Delta_1^2$:

$$c \approx \frac{1}{2} \frac{\langle \mathcal{E}_i^{\Delta_2, \Delta_1} m_i^{\Delta_2} \rangle}{\langle m_i^{\Delta_2} m_i^{\Delta_2} \rangle}, \quad (5.15)$$

where

$$m_i^{\Delta_2} = \alpha^2 \partial_j^{\Delta_2} |S^{\Delta_2}| S_{ij}^{\Delta_2} - S^{\Delta_2} \circ \partial_j^{\Delta_1} |S^{\Delta_1}| S_{ij}^{\Delta_1}, \quad (5.16)$$

and the model that has to be implemented in the code reads:

$$\mathcal{E}_i^{\Delta_1, \Delta_0} \approx 2 c \partial_j^{\Delta_1} (|S^{\Delta_1}| S_{ij}^{\Delta_1}). \quad (5.17)$$

6. Numerical results

This model has been implemented in a pseudo-spectral code with modified wave vectors in order to mimic the behavior of a second-order centered finite difference scheme. Although this method is not computationally optimal, it has the advantage to be very easy to implement both for the DNS and for the LES. The computational domain is a cubic $2\pi \times 2\pi \times 2\pi$ box. The DNS grid, \mathcal{G}^{Δ_0} , corresponds to a 256^3 resolution and the modified wave vectors for the finite difference scheme $\vec{\mathbf{k}}^{\text{FD}}$ are defined by:

$$\vec{\mathbf{k}}^{\text{FD}} = (k_x^{\text{FD}}, k_y^{\text{FD}}, k_z^{\text{FD}}) = \frac{1}{\Delta_0} (\sin(k_x^{\text{S}} \Delta_0), \sin(k_y^{\text{S}} \Delta_0), \sin(k_z^{\text{S}} \Delta_0)), \quad (6.1)$$

$$(k^2)^{\text{FD}} = \frac{4}{\Delta_0^2} \left(\sin^2 \left(\frac{k_x^{\text{S}} \Delta_0}{2} \right) + \sin^2 \left(\frac{k_y^{\text{S}} \Delta_0}{2} \right) + \sin^2 \left(\frac{k_z^{\text{S}} \Delta_0}{2} \right) \right), \quad (6.2)$$

where $\vec{\mathbf{k}}^{\text{S}}$ is the usual wave vector in the pseudo-spectral code. Note that, in the finite difference scheme, the discretization of the second order derivative is not obtained as the “square” of the first order derivative and consequently different definitions are used for the modified wave vectors entering the first and the second order derivatives. The quantity $(k^2)^{\text{FD}}$ is only used in the viscous term. The incompressibility condition is enforced by projecting the velocity $\vec{u}(\vec{\mathbf{k}}^{\text{FD}})$ on the plane perpendicular to $\vec{\mathbf{k}}^{\text{FD}}$.

The sampling operators \mathcal{S}^{Δ_1} and \mathcal{S}^{Δ_2} are implemented straightforwardly in real space. It should be acknowledged however that enforcing incompressibility is an operation that now depends on the resolution. Consequently, it slightly modifies the properties of the sampling operators, and the velocity values on the grids \mathcal{G}^{Δ_0} , \mathcal{G}^{Δ_1} and \mathcal{G}^{Δ_2} do not coincide exactly. The combination of the sampling and the incompressibility projections remains nevertheless a projective operator.

The LES field is thus obtained by sampling using \mathcal{S}^{Δ_1} on a 32^3 grid. The computations in the implementation of the dynamic procedure that corresponds to the grids \mathcal{G}^{Δ_1} and \mathcal{G}^{Δ_2} are then performed by a simple re-definition of the modified wave vectors.

The preliminary tests, though made with a modified spectral code and a limited resolution, are quite illuminating. First, it shows clearly that a model is required for the

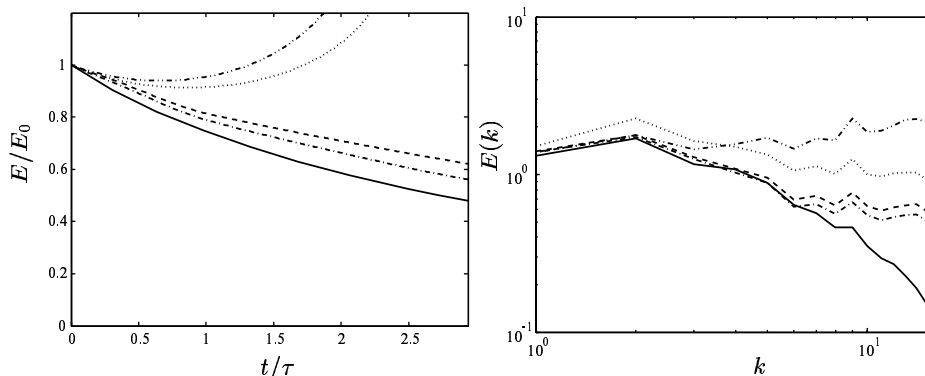


FIGURE 3. Left : Energy decay. Comparison between the sampled DNS (—), the LES curves without model (·····) and with the dynamic Smagorinsky model with the parameter C computed using both convective and viscous contributions (----), the convective contribution only (-·-·-) and the viscous contribution only (---). Right : Energy spectrum at the end of the computation, same symbols. τ is the large-eddy turnover time.

decaying turbulence case. The under-resolved DNS (LES without model) exhibits an increase of the energy after a short decaying period. The dynamic Smagorinsky model has been implemented in three versions. Indeed, the “Leonard” vector $\mathcal{E}_i^{\Delta_2, \Delta_1}$ (5.11) contains two contributions originating respectively from the convective+pressure terms and from the viscous term. In the computation of the dynamic Smagorinsky constant C , the purely convective, the purely viscous, and the full Leonard vectors have been implemented. Not surprisingly, the purely viscous version does not perform satisfactorily. It is actually even worse than the no-model case. Also, the purely convective version produces the best agreement with the sampled DNS. The final spectra are also presented. They all exhibit a piling-up of the energy in the high wave-number range. However, the no-model and the purely viscous dynamic model both overpredict the low wave-number energy range, while the dynamic models that account for the convective discretization errors both correctly predict the low k spectrum.

Although it would be quite hazardous to make definitive and strong statements on the basis of these preliminary numerical results, they indicate that (1) the implementation of a dynamic procedure with sampling operators yields reasonable predictions in the homogeneous decaying turbulence test case and (2) the Smagorinsky model is acceptable for modelling the numerical discretization errors on the convective term but not for the viscous term.

7. Discussion

The methodology presented here is unusual in the sense that no filter is used to define the LES fields. The unknown quantities that appear in the LES equations thus originate only from the lack of resolution (discretization errors) and filters are replaced by sampling operators. The resulting viewpoint seems to make the link between finite difference approaches and finite element methods. The sampling operators have some very pleasant properties. They commute with nonlinearities, they are projections and they explicitly define the numerical grid. The obvious drawback is that they do not commute with spatial derivatives and the commutation errors must be modelled. It has been shown that models for the discretization errors may be treated using the dynamic procedure. Prelim-

inary results, using the Smagorinsky model, are very encouraging, though the modelling of discretization errors by an eddy viscosity term may be debatable.

Considering the encouraging numerical results obtained in the very simple tests presented in section VI, it can be concluded that the methodology in which a LES is defined by sampling operators deserves, at the very least, further investigations. It is however not the purpose of this last section to oversell the sampling-based LES approach. We have thus chosen to close this discussion by pointing out two difficulties that have been raised in the course of the Summer Program and that definitively deserve some attention.

First, as mentioned before, the sampling operators do not preserve the incompressibility of the flow. This difficulty has to be expected since the incompressibility condition involves spatial derivatives:

$$\partial_i u_i = 0. \quad (7.1)$$

The non-commutation of the sampling operator and the spatial derivative thus generates an unknown term in the sampled version of Eq. (7.1). This unknown term has been neglected in the preliminary tests presented here. The modelling of such a term would probably be fairly difficult and might change the nature of the numerical scheme itself since the incompressibility condition is a very strong constraint in most numerical methods. To the best of our knowledge, the commutation error in the incompressibility condition has never been taken into account in more traditional LES in which non-commutative filters are also used. It might turn out that the only practical strategy is to ignore this effect, but numerical and theoretical investigations of the commutation error in the incompressibility condition would be welcome.

The second difficulty has been pointed out by O. Vasilyev: the sampling operators do not conserve the mean of the original signal. This can easily be seen if a sine wave with zero mean is sampled systematically at the minima, the resulting sampled signal would be constant and negative. This is a special case of aliasing due to too coarse sampling. Whether this is an important issue or not is not yet clear. Obviously, it has no damaging consequences in the isotropic turbulence tests. However, the consequences in complex geometries with mean flows remain to be explored.

REFERENCES

- GHOSAL, S. 1996, An analysis of numerical errors in large-eddy simulations of turbulence. *J. Comp. Phys.* **125**, 187-206.
- KRAVCHENKO, A.G. & MOIN, P. 1997 On the effect of numerical errors in large eddy simulations of turbulent flows. *J. Comp. Phys.* **131**, 310-322.
- CHOW, F.K. & MOIN, P. 2003 A further study of numerical errors in large-eddy simulations. *J. Comp. Phys.* **184**, 366-380.
- VASILYEV, O.V., LUND, T.S. & MOIN, P. 1998 A general class of commutative filters for LES in complex geometries. *J. Comp. Phys.* **146**, 105-123.
- MARSDEN, A.L., VASILYEV, O.V. & MOIN, P. 2002 Construction of Commutative Filters for LES on Unstructured Meshes. *J. Comp. Phys.* **175**, 584-603.
- PARK, N., YOO, J.Y. & CHOI, H. 2004 Discretization errors in large eddy simulation: on the suitability of centered and upwind-biased compact difference schemes. *J. Comp. Phys.* **198**, 580-616.
- MORINISHI, Y. & VASILYEV, O.V. 1998 Subgrid scale modeling taking the numerical

error into consideration. *Annual Research Briefs*, Center for Turbulence Research, NASA Ames-Stanford University.

IVAN FEDIOUN, I., LARDJANE, N. & GÖKALP, I. 2001 Revisiting numerical errors in direct and large eddy simulations of turbulence: physical and spectral spaces analysis. *J. Comp. Phys.* **174**, 816-851.

Filtering and LES of flow over irregular rough boundary

By A. Nakayama [†], K. Hori [†] AND R. L. Street

Formal explicit filtering defined by the convolution integral over a flow region has been applied to derive fundamental equations of Large Eddy Simulation (LES) for turbulent flows over complex boundaries with small-scale roughness which is not resolved in full. It allows smoothing of the boundary at the same level of filtering as for the flow. It indicates that extra stress-like terms appear in the equations due to the smoothing. DNS data for a flow over a doubly wavy boundary are analyzed to examine the distributions of these terms and other quantities that need modeling. It is found that these stress terms are due to the pressure drag acting on smoothed-out roughness. Preliminary LES calculations have also been made to examine a model for these terms. It is suggested that the modeling of the boundary resistance terms must be done with appropriate modeling of the boundary conditions. A dynamic procedure to determine model constants is proposed.

1. Introduction

Numerical calculation of large scale flows appearing in natural environments almost always involves simplification of the boundary geometry. It is not only impossible but also meaningless to represent all the details of the terrain with trees and vegetation, not to mention smaller objects, in simulating an atmospheric wind field. Flows in rivers and oceans have an additional complex boundary on the free surface. The overall effects of small and random irregularities may be accounted for as roughness but larger undulations would have to be considered a part of the boundary shape. In fact the roughness and the boundary shape cannot be discriminated so easily. The numerical resolution of the flow field determines what should be considered roughness and what should be considered the boundary shape. If the small scale irregularities are smoothed out or ignored, the motion associated with the details is lost. In the context of large eddy simulation (LES), this will give rise to additional subgrid-scale stresses. It was suggested that small details of irregularities of bed materials like stones of various sizes and shapes in natural rivers are better treated by spatial averaging (Nikora *et al.* 2001), which also leads to an additional stress referred to as dispersion effects. In simulation of atmospheric boundary layers, the extra resistance due to the canopy is added in the flow (e.g. Brown *et al.* 2001; Chow & Street 2002).

In the previous report, we have conducted a Direct Numerical Simulation of a model flow over a doubly wavy surface. The small-scale waviness was intended to simulate roughness and the large-scale waviness the boundary shape. Here we consider modeling of such a flow over a complex boundary with superimposed roughness. First we derive the basic LES equations that result from filtering the instantaneous Navier-Stokes equations over the finite and irregular flow domain. Filtering in a finite domain introduces extra terms or commutation error terms. Modeling of the resulting equations is attempted

[†] Kobe University

making use of the DNS results. The flow field considered in the present work is assumed to be simply connected so that there are no pores or isolated objects in flow.

2. Filtering in complex finite flow domain

In order to explicitly filter the flow over finite boundary, we use the filtering operation defined by

$$\overline{f(\mathbf{x})} = \iiint_D G(\mathbf{x}, \boldsymbol{\xi}) f(\boldsymbol{\xi}) d\boldsymbol{\xi}, \quad (2.1)$$

where D is the actual flow domain and the filter function $G(\mathbf{x}, \boldsymbol{\xi})$ is related to a symmetric weight function $w(\mathbf{x} - \boldsymbol{\xi})$ by the normalization relation

$$G(\mathbf{x}, \boldsymbol{\xi}) = \frac{w((\mathbf{x} - \boldsymbol{\xi})/\Delta)}{W(\mathbf{x})}, \quad (2.2)$$

where Δ is the filter size and $W(\mathbf{x})$ is the total weight of w in the flow region,

$$W(\mathbf{x}) = \iiint_D w\left(\frac{\mathbf{x} - \boldsymbol{\xi}}{\Delta}\right) d\boldsymbol{\xi}. \quad (2.3)$$

The filter width Δ may be taken to depend on position, but here we consider the case when it is constant. If this filtering is applied to the divergence of a vector $\mathbf{F}(\mathbf{x})$, and the volume integral is evaluated by the divergence theorem, we have

$$\begin{aligned} \overline{\nabla \cdot \mathbf{F}(\mathbf{x})} &= \iiint_D G(\mathbf{x}, \boldsymbol{\xi}) \nabla_{\boldsymbol{\xi}} \cdot \mathbf{F}(\boldsymbol{\xi}) d\boldsymbol{\xi} \\ &= \iint_S G(\mathbf{x}, \boldsymbol{\xi}) \mathbf{F}(\boldsymbol{\xi}) \cdot \mathbf{n} dS_{\boldsymbol{\xi}} - \iiint_D \nabla_{\boldsymbol{\xi}} G(\mathbf{x}, \boldsymbol{\xi}) \cdot \mathbf{F}(\boldsymbol{\xi}) dV_{\boldsymbol{\xi}} \\ &= \iint_S G(\mathbf{x}, \boldsymbol{\xi}) F_n(\boldsymbol{\xi}) dS_{\boldsymbol{\xi}} - \iiint_D \frac{-\nabla_{\mathbf{x}}(w(\mathbf{x} - \boldsymbol{\xi})/\Delta)}{W(\mathbf{x})} \cdot \mathbf{F}(\boldsymbol{\xi}) dV_{\boldsymbol{\xi}} \\ &= \iint_S G(\mathbf{x}, \boldsymbol{\xi}) F_n(\boldsymbol{\xi}) dS_{\boldsymbol{\xi}} - \iiint_D \left[-\nabla_{\mathbf{x}} G(\mathbf{x}, \boldsymbol{\xi}) - G(\mathbf{x}, \boldsymbol{\xi}) \frac{\nabla_{\mathbf{x}} W(\mathbf{x})}{W(\mathbf{x})} \right] \cdot \mathbf{F}(\boldsymbol{\xi}) dV_{\boldsymbol{\xi}} \\ &= \overline{F_n}^S(\mathbf{x}) + \nabla \cdot \overline{\mathbf{F}(\mathbf{x})} + \frac{\nabla W}{W} \cdot \overline{\mathbf{F}(\mathbf{x})} \end{aligned} \quad (2.4)$$

where \mathbf{n} is the unit vector outward normal to the boundary S of flow domain D and subscript n is used to indicate the component of a vector in the direction of \mathbf{n} . The first term in the last line of this equation is the flux through the boundary filtered over the boundary, the second term is the divergence of the filtered \mathbf{F} and the last term is a quantity arising from the spatial variation of the total weight $W(\mathbf{x})$. An additional term would appear if Δ was a function of \mathbf{x} , corresponding to the commutation error due to varying filter size. If we take the filtered or "smoothed" boundary to be the surface given by $W(\mathbf{x}) = W_0 = \text{Const.}$ (Figure 1), the last term in Eq.(2.4) can be rewritten as follows

$$\frac{\nabla W}{W} \cdot \overline{\mathbf{F}} = \frac{\nabla W}{|\nabla W|} \frac{|\nabla W|}{W} \cdot \overline{\mathbf{F}} = -\chi \overline{\mathbf{n}} \cdot \overline{\mathbf{F}} = -\chi \overline{F_{\overline{\mathbf{n}}}} \quad (2.5)$$

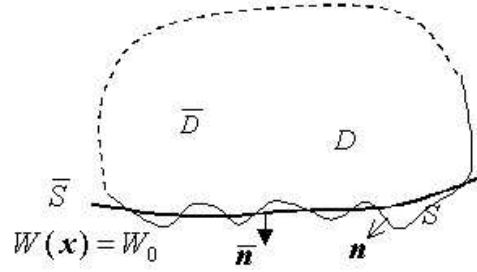


FIGURE 1. Filtering in complex flow domain.

where $\bar{\mathbf{n}} = -\nabla W/|\nabla W|$ is the outward unit normal vector on the smoothed boundary, $\chi = |\nabla W|/W$ is the relative change of the total weight and subscript \bar{n} indicates the component of a vector in the direction of $\bar{\mathbf{n}}$. χ is nonzero only in the layer next to the boundary with thickness roughly equal to the sum of the height of the smoothed boundary and the filter size. The last expression means that it is proportional to the filtered flux through the smoothed boundary.

Using this, Eq.(2.4) can be written as

$$\overline{\nabla \cdot \mathbf{F}(\mathbf{x})} = \nabla \cdot \overline{\mathbf{F}(\mathbf{x})} + \overline{F_n^S}(\mathbf{x}) - \chi \overline{F_{\bar{n}}}. \quad (2.6)$$

This means that the filter of a divergence is the divergence of the filter plus the difference between the flux through the original boundary and the filtered flux through the smoothed boundary. The corresponding formula for the gradient of a scalar function f can be obtained by noting that $\nabla f = \nabla \cdot (f\mathbf{I})$, where \mathbf{I} is the second-order identity tensor

$$\overline{\nabla f(\mathbf{x})} = \nabla \overline{f(\mathbf{x})} + \overline{f\mathbf{n}^S} - \chi \overline{f\bar{\mathbf{n}}}. \quad (2.7)$$

3. Filtered equations of motion

Now the basic LES equations are derived using the above relations. The filtered continuity equation can be obtained by setting $\mathbf{F} = \mathbf{u}$ in Eq.(2.6) and using the continuity equation for the unfiltered velocity. It is

$$\nabla \cdot \bar{\mathbf{u}} = \chi \bar{u}_{\bar{n}}, \quad (3.1)$$

if the velocity on the original boundary is zero.

Using Eqs.(2.6) and (2.7), the momentum equations may be filtered as

$$\begin{aligned} \frac{\partial \bar{\mathbf{u}}}{\partial t} + \nabla \cdot (\bar{\mathbf{u}} \bar{\mathbf{u}}) &= -\frac{1}{\rho} \overline{\nabla p} + \nu \overline{\nabla \cdot \nabla \mathbf{u}}, \\ \frac{\partial \bar{\mathbf{u}}}{\partial t} + \nabla \cdot (\bar{\mathbf{u}} \bar{\mathbf{u}}) - \chi \overline{\mathbf{u} \bar{u}_{\bar{n}}} &= -\frac{1}{\rho} (\nabla \bar{p} + \bar{p} \bar{\mathbf{n}}^S - \chi \bar{p} \bar{\mathbf{n}}) + \nu \left(\nabla \cdot \bar{\nabla} \bar{\mathbf{u}} + \frac{\partial \bar{\mathbf{u}}^S}{\partial \bar{n}} - \chi \frac{\partial \bar{\mathbf{u}}}{\partial \bar{n}} \right) \end{aligned} \quad (3.2)$$

Noting that $\bar{\nabla} \bar{\mathbf{u}} = \nabla \bar{\mathbf{u}} - \chi \bar{\mathbf{u}} \bar{\mathbf{n}}$ and $\nabla \cdot \bar{\nabla} \bar{\mathbf{u}} = \nabla^2 \bar{\mathbf{u}} - \nabla \cdot (\chi \bar{\mathbf{u}} \bar{\mathbf{n}})$, the above equation can be written as

$$\begin{aligned} \frac{\partial \bar{\mathbf{u}}}{\partial t} + \nabla \cdot (\bar{\mathbf{u}} \bar{\mathbf{u}}) &= -\frac{1}{\rho} \nabla \bar{p} + \nabla \cdot (\nu \nabla \bar{\mathbf{u}} - \nu \chi \bar{\mathbf{u}} \bar{\mathbf{n}} - \boldsymbol{\tau}) \\ &+ \mathbf{P} + \mathbf{T} + \chi \left(\overline{\mathbf{u} \bar{u}_{\bar{n}}} - \nu \frac{\partial \bar{\mathbf{u}}}{\partial \bar{n}} \right), \end{aligned} \quad (3.3)$$

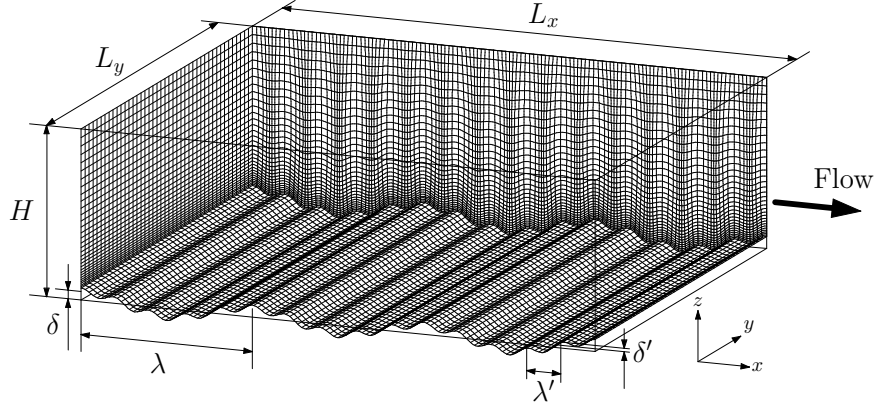


FIGURE 2. DNS of flow over doubly wavy surface.

where

$$\mathbf{P} = \frac{1}{\rho} \overline{p\mathbf{n}}^S = \frac{1}{\rho} \iint_S G(\mathbf{x}, \boldsymbol{\xi}) p(\boldsymbol{\xi}) \mathbf{n} dS_{\boldsymbol{\xi}}, \quad (3.4)$$

$$\mathbf{T} = \nu \overline{\frac{\partial \mathbf{u}}{\partial n}}^S = \nu \iint_S G(\mathbf{x}, \boldsymbol{\xi}) \frac{\partial \mathbf{u}}{\partial n}(\boldsymbol{\xi}) dS_{\boldsymbol{\xi}} \quad (3.5)$$

and $\boldsymbol{\tau}$ is the usual subgrid-scale stress

$$\boldsymbol{\tau} = \rho(\overline{\mathbf{u}\mathbf{u}} - \overline{\mathbf{u}}\overline{\mathbf{u}}). \quad (3.6)$$

We see that in the filtered equations of motion a number of terms appear in addition to the usual subgrid stress. \mathbf{P} and \mathbf{T} are the surface integrals of the pressure and the skin friction over the original surface. Terms associated with χ are quantities that will be important in the near boundary region where χ is nonzero. It should be noted that χ is known once the exact form of the weight function is chosen and the characteristics of the original boundary are given. The terms that need modeling are the surface-average terms \mathbf{P} and \mathbf{T} . These are extra resistances due to the pressure variation and the friction on the smoothed shape of the boundary. Therefore, the direct effects of smoothing the boundary are to introduce extra forces in the momentum equations. The boundary condition of the filtered velocity on the filtered boundary is

$$\overline{\mathbf{u}}(\mathbf{x}_{\overline{S}}) = \iiint_D G(\mathbf{x}_{\overline{S}}, \boldsymbol{\xi}) \mathbf{u}(\boldsymbol{\xi}) d\boldsymbol{\xi}, \quad (3.7)$$

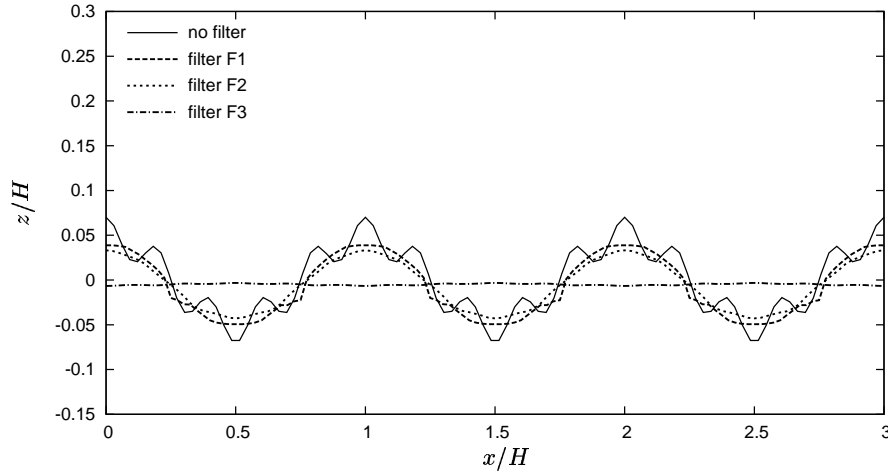
where $\mathbf{x}_{\overline{S}}$ is a point on \overline{S} . We will examine these terms and explore how they may be modeled in the next sections.

4. DNS data of flow over doubly wavy boundary

In order to obtain ideas about how to model the equations derived in the previous section, we have conducted a DNS simulation of a flow over doubly wavy surface, in which the small waviness was intended to simulate roughness and the large waviness the boundary shape (Nakayama & Sakio 2002). Figure. 2 shows the flow field and the

TABLE 1. Size of filters.

Filter	$\Delta_x \times \Delta_y \times \Delta_z$
Filter F1	$\lambda' \times \delta' \times \delta'$
Filter F2	$2\lambda' \times 2\delta' \times 2\delta'$
Filter F3	$2\lambda \times 2\delta \times 2\delta$

FIGURE 3. Smoothed boundary defined by $W_0 = 0.5$.

numerical grid used in this DNS study together with the definition of notation. The details of this simulation are given in Nakayama & Sakio 2002. We explicitly filter the results of this simulation using Eq.(2.1) with different filters. Table 1 shows the sizes of three filters used. They are all top-hat functions for w with Δ_x, Δ_y and Δ_z as the filter width Δ in the x, y , and z directions, respectively. Filter F1 has the same size as the small waviness, F2 is twice as large while F3 is twice as large as the large waviness.

Figure 3 shows the shapes of the smoothed boundary defined by $W_0 = 0.5$. As expected, the shape obtained by filtering with filter F1 removes most of the small waviness, that obtained by filtering with F2 removes the small waviness completely but leaves the large waviness. It is seen that the boundary obtained by filtering with F1 shows a slightly angular shape due to the rectangular top-hat filter used. Filter F3 is large enough to remove all undulations, resulting in an almost flat boundary.

Figure 4 shows the instantaneous flow fields of the DNS results depicted by the surface of constant values of the second invariant of the velocity-gradient tensor. Figure 4(a) is the original unfiltered DNS result while Figure 4(b) is the flow filtered with filter F2. Along with the flow, the boundary is seen to be smoothed and the small structures in the original simulation results are removed. However streaky vortex structures with scales larger than the filter size are still seen. These are what must be reproduced by appropriate LES simulation that does not resolve scales smaller than the filter size.

The components of \mathbf{P} and \mathbf{T} , tangent to the smoothed boundary, P_s and T_s have been

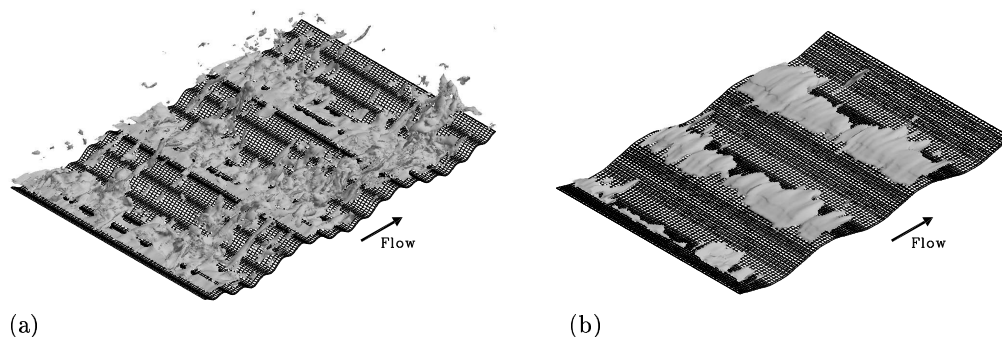


FIGURE 4. Iso-surface of second invariant of velocity gradient tensor in instantaneous DNS results and its filtered flow. (a) unfiltered DNS, (b) filtered DNS.

evaluated using the DNS data and Eqs.(3.4) and (3.5) in order to obtain an idea about these quantities.

Figure 5 shows instantaneous distributions of these terms when filtered with the three filters. It is seen that these terms have significant values in the region near the smoothed boundary. Both terms tend to have positive values where the flow is locally accelerated by the roughness that is smoothed. The pressure integral term P_s tends to have broader distribution and retain large values than the friction integral term as the filter size is increased. The distributions of Figures 5(c) and (f), corresponding to the largest filter size, correspond roughly to the friction and the pressure resistances of the entire waviness.

In addition to the flow over the doubly wavy surface, the flow over a flat surface with small waves has been simulated in order to validate the flow of simpler case of flat rough wall. The small waviness is exactly the same as the small waves of the doubly wavy surface case.

5. Modeling LES equations for rough boundary

Here we consider a method of modeling the LES equations obtained in the previous section. From the analysis it has been seen that it is not just the additive terms in the equations of motion that need modeling but the boundary conditions, and even the position of the boundary, must be modeled. First, as to the position of the boundary, we have already indicated the position where W_0 takes the value $1/2$ for the test flow for which DNS was conducted. The position of the boundary of the computational region and the boundary conditions in LES are related and there may be other choices. We choose the position $W_0 = 0.5$ which corresponds to the real boundary for smooth surface. At this position, however, the filtered velocity is not quite zero and the gradient of W is large but χ is of moderate value. It is not easy to allow leakage through the boundary and nonzero divergence while not violating overall continuity. Here we choose to set the divergence to be zero throughout the analysis region and to require the velocity component normal to the smoothed boundary to vanish. The filtered tangential velocity at the smoothed boundary is roughly the mean velocity in the boundary region. It is closely related to

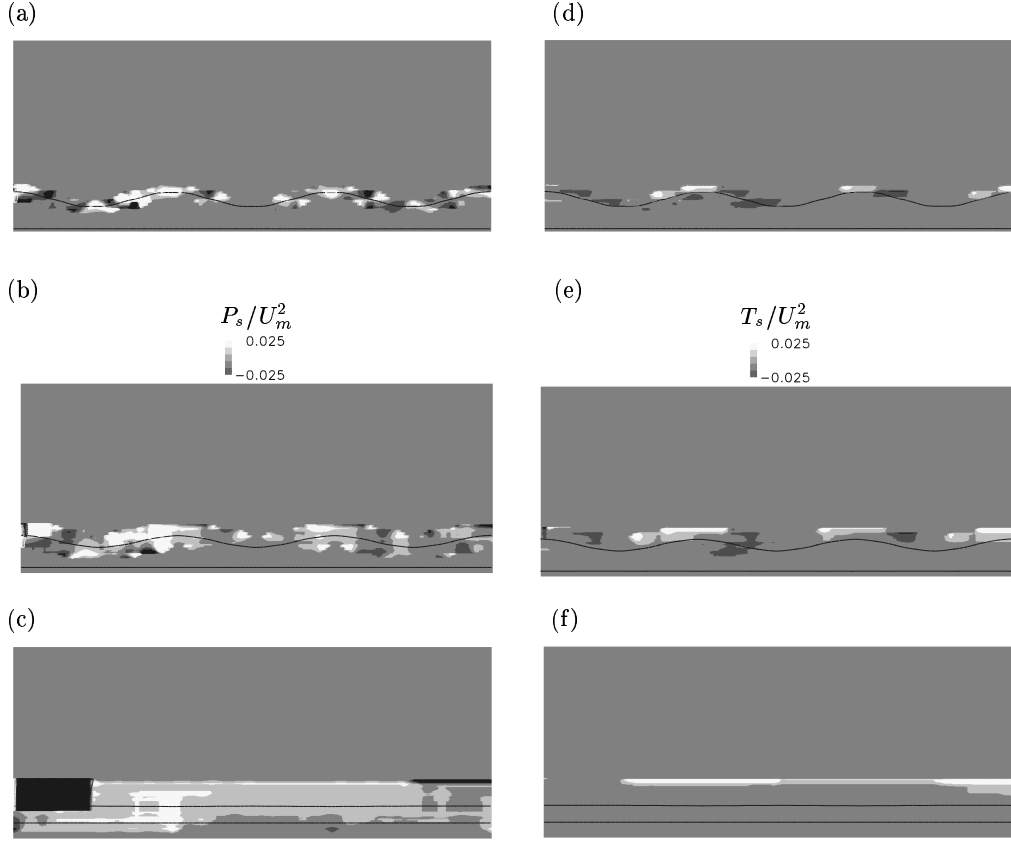


FIGURE 5. Instantaneous distribution of the boundary integral terms P_s/U_m^2 and T_s/U_m^2 .
(a)(d) Filter F1, (b)(e) Filter F2, (c)(f) Filter F3.

the resistance in the same direction. There are a number of resistance formula in various situations including channel flows and even porous flow fields. Generally for flows with high roughness Reynolds numbers, the resistance is proportional to the square of the mean velocity and it is natural to assume a relation like

$$\overline{u_s} = -C_{sl} \text{sign}(R_s) |R_s|^{1/2} \quad (5.1)$$

where R_s is the total resistance $P_s + T_s + \tau_s + \mu \frac{\partial \overline{u_s}}{\partial n}$ at the smoothed boundary, and C_{sl} is a constant. For lower Reynolds numbers, C_{sl} will have to be made a function of the Reynolds number based on the smoothed roughness. Determination of C_{sl} is a critical part of the procedure and it may better be determined dynamically as discussed later.

At this stage it is useful to know what kind of values and distributions that are taken by the quantity χ . They have been calculated for the doubly wavy boundary for the three filters. They are shown in Figure 6. The widths of the distribution are roughly proportional and the magnitudes are inversely proportional to the filter size. The distributions are seen to be more or less linear and this fact may be used in modeling of a rough surface with a given roughness height and filter size.

As to the additional terms in the equations of motion, we propose the following model

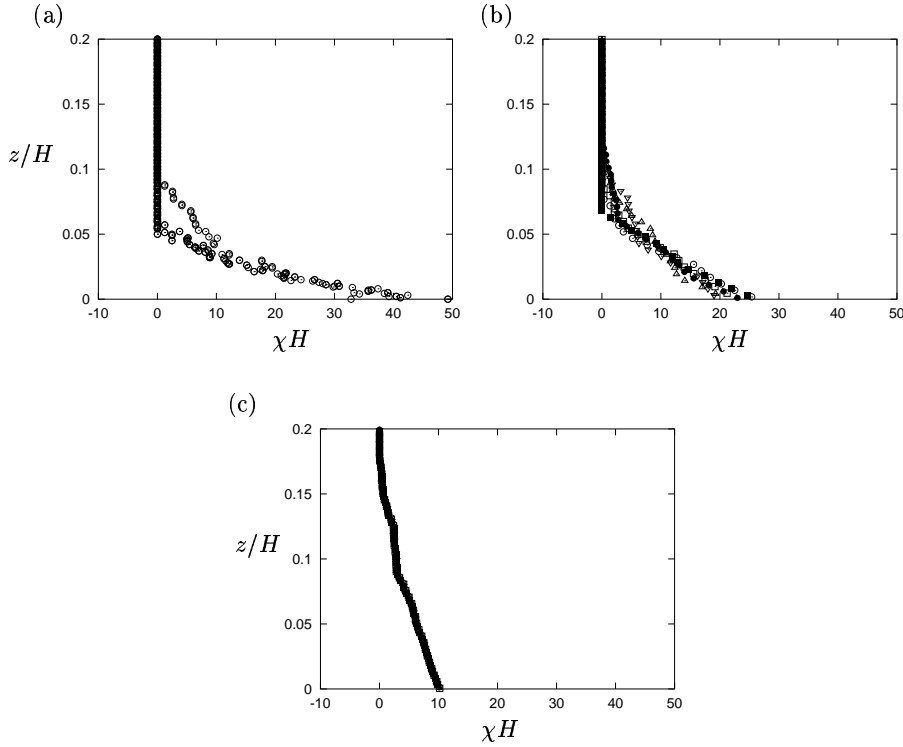


FIGURE 6. Boundary roughness parameter χ . (a) Filter F1, (b) Filter F2, (c) Filter F3, different symbols mean different x locations

for \mathbf{P} and \mathbf{T} .

$$\mathbf{P} = C_d \chi_\Delta \frac{A_\Delta}{\Delta^2} \|\mathbf{u}\|, \quad (5.2)$$

$$\mathbf{T} = C_f \chi_\Delta \frac{\Sigma_\Delta}{\Delta^2} \|\mathbf{u}\|, \quad (5.3)$$

where A_Δ and Σ_Δ are the area projected in the direction tangent to the smoothed boundary and the surface area contained in the region proportional to the filter width Δ and C_d and C_f are drag and friction coefficients. We use subscript Δ for χ , A and Σ emphasizing that these depend on the filter size. It should also be noted that the term \mathbf{T} appears even in the case of smooth surface, while \mathbf{P} appears only for rough surfaces. Modeling of \mathbf{T} may then be tested first for simpler smooth surface flow.

6. Test Calculations

Before testing with rough-surface flows, it is useful to see if smooth-surface flow is simulated correctly. The term \mathbf{T} and the boundary conditions are needed for smooth-surface flows and should work as a wall model. It is known that if the laminar sublayer is resolved to a good degree, LES with a Smagorinsky model, either dynamic or standard with appropriate near-wall damping simulates the smooth-wall channel flow. Here a preliminary test calculation has been conducted using two grids with non-slip and slip boundary conditions. The flow is a channel flow with the bulk Reynolds number of 6760.

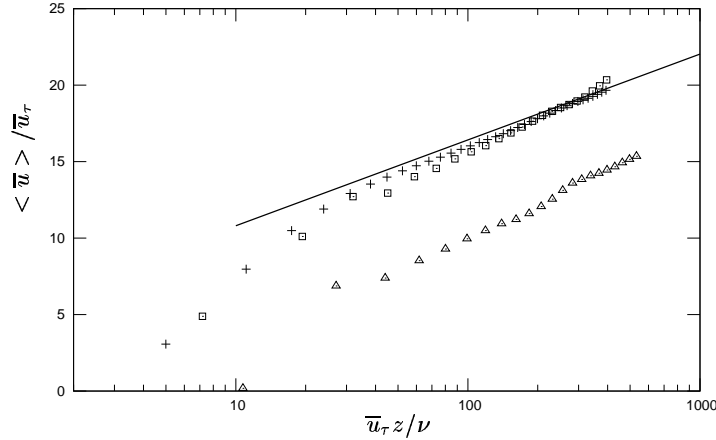


FIGURE 7. The mean velocity profile in smooth-wall channel flow. $-$: standard log-law, $+$: fine grid LES resolving viscous sublayer, \square : coarse grid LES with $C_{sl} = 6$, \triangle : coarse grid LES with $C_{sl} = 0$.

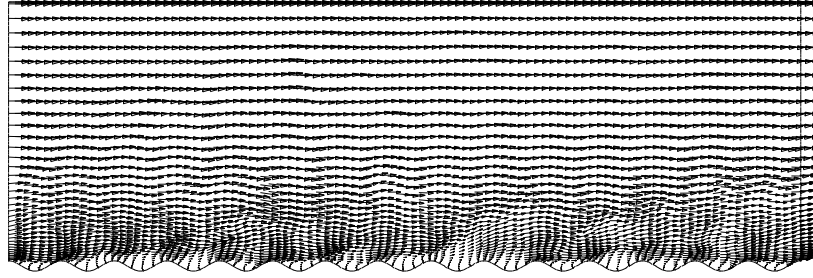
The fine grid has 36 points in the wall-normal direction and the first point near the bottom is about 1.0 viscous length from the wall. The coarse grid has 22 points and the first point is about 10 viscous units away from the boundary. They assume $C_f = 0.002$ and linear distribution for χ with zero filter width.

Figure 7 shows that a LES with fine grid with $C_{sl} = 0$ does reproduce the standard log-law profile. In this smooth-surface case, Σ_Δ / Δ^2 in \mathbf{T} is constant. A coarse-grid LES, however, predicts a mean velocity distribution that is too low. This cannot be improved by adjusting the resistance term \mathbf{T} . The results with $C_{ls} = 6$ is also shown in this figure which indicates the appropriate slip velocity for this Reynolds number. This corresponds to finding the correct off-wall boundary condition and should depend on the Reynolds number and the local flow conditions. Again a dynamic procedure of determining C_{sl} will be more generally applicable.

Next, the flow over flat surface with wavy roughness has been computed. Figure 8(a) shows a snapshot of the velocity field obtained by DNS for this flow. The bulk Reynolds number is again 6760 and the waviness is the same as that of Figure 2. The grid used in LES is $75 \times 36 \times 40$. Figure 8(b) shows the distribution of the time-averaged streamwise velocity component $\langle \bar{u} \rangle$ obtained by LES compared with the DNS results. \bar{u}_τ is the friction velocity defined from the streamwise pressure gradient. The standard smooth-wall log-law is also shown for reference. The boundary drag term now becomes important. In this calculation it is assumed that $C_d = 0.006$ is assumed. It is seen that there is a slight difference in the slope of the logarithmic profile, they agree fairly well, particularly the amount of shift from the smooth line.

Figure 9 now shows the results of the LES calculation of the flow over wavy surface with roughness for which the DNS results have been presented in section 3. The LES grid resolution is such that the small roughness is not resolved but the large waviness is well defined. Figure 9(a) compares the profiles $\langle \bar{u} \rangle$ of the LES with DNS at four locations, at the peak of the waviness, half way to the trough, at the trough and half way to the next peak. Note that the boundary shape used in this calculation is sinusoidal

(a)



(b)

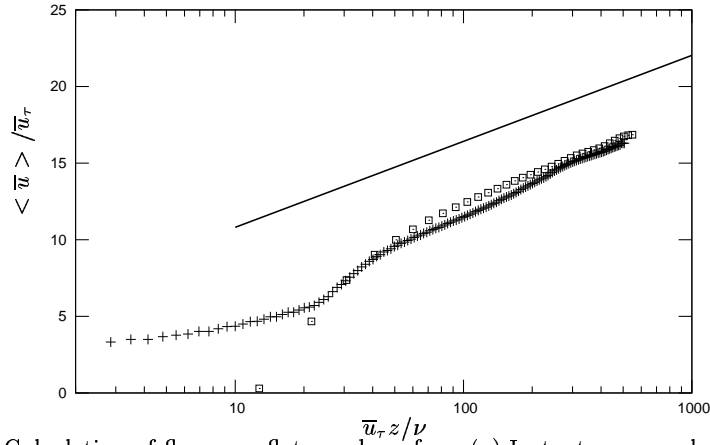


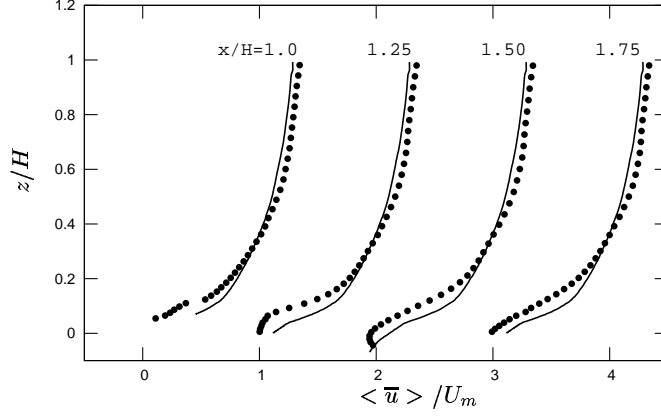
FIGURE 8. Calculation of flow over flat rough surface. (a) Instantaneous velocity distribution from DNS, (b) Mean velocity profile, \square : LES, $+$: DNS, $-$: standard smooth log-law.

and z is the distance from the mean boundary position. The values of the constants C_f , C_d and C_{sl} are same as those used for smooth and flat rough surface flows. The profile at the peak is not quite as full as the DNS results and the recirculation region is larger. It implies that the slip velocity is not large enough. The qualitative feature of vortex structure shown in Figure 9(b) seems similar to the filtered DNS flow field shown in Figure 4(b).

7. Dynamic procedure for determining model constants

The test calculations described in the previous section used somewhat ad-hoc values for the model constants. The choice of the values of these constants influences the results very much and they depend on the local and temporal flow conditions. A dynamic method of determining these constants is preferred. Although no detailed calculations are carried out in the present work, a procedure of dynamically determining the model constants has been formulated. The dynamic determination assumes that the same model relation is valid for the filter size implied in the LES calculation and test filtering of larger size. We consider a test filter of size $\tilde{\Delta}$ which is larger than the grid filter size Δ . First it is

(a)



(b)

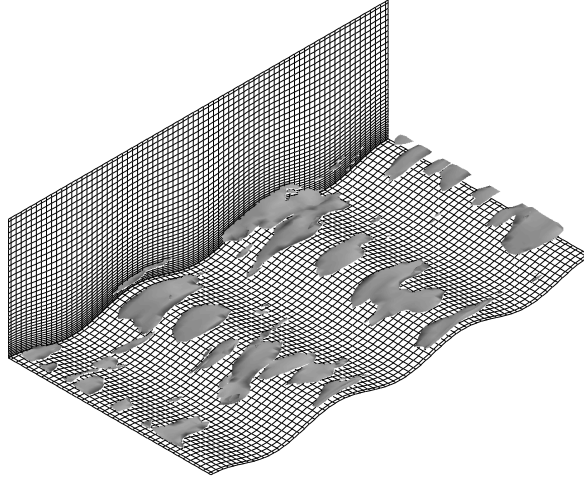


FIGURE 9. Calculation of flow over wavy boundary with roughness. (a) Mean velocity profiles compared with DNS, $-$: DNS, \bullet : LES, profiles for $x/H > 1.0$ shifted horizontally, (b) iso-vorticity surface of LES instantaneous flow results.

noted that test filtering of grid-filtered quantity in finite domain is equal to the single filtering with filter function,

$$G_{\tilde{\tilde{\Delta}}}(x, \xi) = \iiint_D G_{\tilde{\Delta}}(x, \xi') G_{\tilde{\Delta}}(\xi', \xi) d\xi', \quad (7.1)$$

where $\tilde{\tilde{\Delta}}$ is the effective filter width of the double filtering. Then we can follow the procedure of Germano *et al.* (1991) and Lilly (1992). The equation for determining constant C_d is as follows.

$$C_d = \frac{\mathbf{R}_p \cdot \mathbf{U}_p}{\mathbf{U}_p \cdot \mathbf{U}_p}, \quad (7.2)$$

where

$$\mathbf{R}_p = \frac{1}{\rho} \bar{p} \bar{\mathbf{n}}^S, \quad (7.3)$$

is the resistance term resulting from test filtering of size $\bar{\Delta}$ and

$$\mathbf{U}_p = \frac{A_{\bar{\Delta}}}{\bar{\Delta}^2} \chi_{\bar{\Delta}} \left| \tilde{\mathbf{u}} \right| \tilde{\mathbf{u}} - \frac{A_{\bar{\Delta}}}{\bar{\Delta}^2} \chi_{\bar{\Delta}} \left| \tilde{u} \right| \tilde{u}, \quad (7.4)$$

Similar equations can be written for constants C_f . Formulation for C_{sl} is a bit different but a similar derivation is possible.

8. Conclusions

Formal explicit filtering defined by the convolution integral over a flow region has been applied to derive fundamental equations of Large Eddy Simulation (LES) for turbulent flows over complex boundaries with small-scale roughness that cannot be resolved. Formal filtering in finite and complex domain allows filtering of the flow and boundary at the same time and indicates that extra stress-like terms appear in the equations. In addition, the boundary condition is no longer nonslip and the boundary velocity must also be modeled. DNS data obtained in a flow over doubly wavy boundary are analyzed to examine the distributions of these terms and to help model these terms. Preliminary LES calculations have been conducted for flow over flat rough surface and the flow over wavy rough surface. It is suggested that the rough boundary effects may be modeled rationally by combination of the boundary resistance and the slip velocity. Although the presently obtained results are with pre-assigned values of the model constants, dynamic procedure to determine model constants has been formulated and its implementation is hoped to make model more general.

REFERENCES

- BROWN, A.R., HOBSON, J.M. & WOOD, N. 2001 Large-eddy simulation of neutral turbulent flow over rough sinusoidal ridges. *Boundary-Layer Meteorology* **98**, 411-441.
- CHOW, F.K. & STREET, R.L. 2002 Modeling unresolved motions in LES of field-scale flows *15th symp. on Boundary Layers and Turbulence*, American Meteorological Society, 432-435, Wageningen, The Netherlands.
- GERMANO, M., PIOMMELLI, U., MOIN, P. & CABOT, W. 1991 A dynamic subgrid-scale eddy viscosity model. *Phys. Fluids* **A3**, 1760-1765.
- LILLY, D.K. 1992 A proposed modification of the Germano subgrid-scale closure method. *Phys. Fluids* **A4**, 633-635.
- NAKAYAMA, A. & SAKIO, K. 2002 Simulation of Flows Over Wavy Rough Boundaries *Center for Turbulence Research, Annual Research Briefs 2002, Stanford University/NASA Ames Research Center*, pp.313-324
- NIKORA, V., GORING, D., MCEWAN, I. & GRIFFITHS, G. 2001 Spatially averaged open-channel flow over rough bed. *J. Hydr. Engrg, ASCE* **127**, 123-133.

Commutation errors in Large Eddy Simulation on moving grids : Application to piston engine flows

By V. R. Moureau †, O. V. Vasilyev ‡ C. Angelberger ¶ AND T. J. Poinso ||

A theoretical framework is developed to evaluate the Temporal Commutation Errors (TCE) in piston-engine flows. These errors occur when the Large-Eddy Simulation (LES) filter is a function of time, implying for the temporal partial derivative not to commute with filtering. TCE are derived for structured and unstructured grids, highlighting the contributions of width and shape variations. Finally they are evaluated on LES simulations of a square-piston experiment and the influence of the crank speed and the compression ratio are studied. It is found that the TCE may be neglected to first order if the flow field and mesh deformation are generated by the same boundary movement.

1. Introduction

The design of modern combustion devices with the aim to reduce fuel consumption and pollutant emissions is often complicated by combustion instabilities and more generally by the intrinsic unsteadiness. This is the case of industrial or aeronautic gas turbines, rocket engines and piston engines. Large-Eddy Simulation (LES) may become a key tool that could give engineers the means to better predict operation ranges and specifications. Recent improvements of LES codes have shown encouraging simulations of gas turbines (Kaufmann *et al.* 2002; Selle *et al.* 2004; Prière *et al.* 2004) but in spite of these first successes further developments are needed before obtaining satisfactory results, *e.g.* on realistic piston-engine geometries (Celik *et al.* 2001). This gap can be explained by the fact that piston-engine flows are very confined and walls play therefore a major role. Moreover piston-engine combustion chambers are strongly deformed while operating and that induces big pressure variations and meshing problems.

The LES principle is to reduce the simulation time compared to Direct Numerical Simulations (DNS) by filtering the governing equations, resulting in a reduction of the spectral content of the flow. Then the difficulty is to model the effects of the removed small scales on the resolved large eddies. Supposing that the filtering operator commutes with partial derivatives, the filtered equations are similar to unfiltered ones with unclosed extra terms. The Smagorinsky model (Smagorinsky 1963) is commonly used for turbulent unclosed terms in the momentum equation. The assumption that filtering commutes with partial derivatives is generally considered valid on fixed grids with uniform cell width. On deforming unstructured grids this is not the case anymore and commutation errors may have to be considered. In the past spatial commutation errors (SCE) have extensively been studied with the aim to apply LES to complex geometries. The first theoretical analysis is due to Ghosal (Ghosal & Moin 1995; Ghosal 1999) who has given the order of convergence of SCE on structured grids. Some numerical estimations of SCE can also

† IFP and CERFACS, 42 av. G. Coriolis, 31057 Toulouse CEDEX

‡ University of Colorado at Boulder, UCB 427, Boulder, CO 80309

¶ IFP, 1 et 4 av. Bois Preau, 92500 Reuil Malmaison

|| IMF Toulouse, INP de Toulouse and CNRS, 31400 Toulouse CEDEX, France

be found for turbulent channel flows (Fureby & Tabor 1997). Then the SCE derivation formalism has been improved to deal with boundaries, and commuting filters have been defined for structured grids (Vasilyev *et al.* 1998) and unstructured grids (Marsden *et al.* 2002; Haselbacher & Vasilyev 2003). The most recent developments have been focused on the local spectrum of SCE (Vasilyev & Goldstein 2004) and the influence of filter shape or width variations on spectral content has been highlighted.

Because most LES computations have been performed on fixed meshes, very few studies on temporal commutation errors (TCE) are available. Their possible importance in piston-engine simulations has been stressed by Franke (Franke & Frank 2001) but no evaluation on realistic geometry has been carried out. TCE are *a priori* increasing with the instantaneous deformation rate of the mesh as SCE are increasing with filter-width spatial stretching. This deformation rate is itself a function of crank speed and compression ratio.

This study aims at quantifying TCE in a piston-engine like geometry. First TCE are derived for different grid types ordered by increasing connectivity complexity : one dimensional grids (Section 2), three-dimensional structured grids (Section 3) and three-dimensional unstructured grids (Section 4). Then TCE for the momentum equation are evaluated on a piston-engine like configuration (Section 5), consisting of a square-piston engine for which experimental data are available. Since the DNS of this type of experiment is not feasible, the exact derivation of TCE could not be computed directly. Instead an *a priori* model for TCE is proposed and evaluated in LES simulations of the square-piston experiment for different crank speeds and compression ratios.

2. One dimensional derivation

As a first step TCE are studied for one dimensional grids. Given a function ϕ of space and time the filtered function $\bar{\phi}$ is defined by the following convolution product :

$$\bar{\phi}(x, t) = \frac{1}{\Delta(x, t)} \int_{a(t)}^{b(t)} G\left(\frac{x-y}{\Delta(x, t)}, x, t\right) \phi(y, t) dy \quad (2.1)$$

The filter G is assumed to have the most general form, *i.e.* non-uniform filter width and shape. In Eq. (2.1) the variable filter width Δ has been taken out of the filter, which thus only contains information about its shape. This is justified by the fact that width and shape variations do not have the same influence on the local spectrum (Vasilyev & Goldstein 2004) and that the shape is often supposed constant during simulations. Then TCE are defined by :

$$\text{TCE}[\phi] = \frac{\partial \bar{\phi}}{\partial t} - \frac{\partial \phi}{\partial t} \quad (2.2)$$

To obtain an expression for TCE it is necessary to change the non-uniform space $[a(t), b(t)]$ into a uniform mapping space $[A(x, t), B(x, t)]$ with the change of variables :

$$\xi = \frac{x-y}{\Delta(x, t)}, \quad A(x, t) = \frac{x-a(t)}{\Delta(x, t)}, \quad B(x, t) = \frac{x-b(t)}{\Delta(x, t)} \quad (2.3)$$

Then the filtering process can be rewritten :

$$\bar{\phi}(x, t) = \int_{A(x, t)}^{B(x, t)} G(\xi, x, t) \phi(x - \Delta(x, t)\xi, t) d\xi \quad (2.4)$$

And if $\phi(x - \Delta(x, t)\xi, t)$ can be expanded in Taylor series :

$$\phi(x - \Delta(x, t)\xi, t) = \sum_{k=0}^{\infty} \frac{(-1)^k \Delta^k(x, t) \xi^k}{k!} \frac{\partial^k \phi}{\partial x^k}(x, t) \quad (2.5)$$

Introducing the filter moments $\mathcal{M}^{(k)}$:

$$\mathcal{M}^{(k)}(x, t) = - \int_{A(x, t)}^{B(x, t)} G(\xi, x, t) \xi^k d\xi \quad (2.6)$$

$\bar{\phi}$ can be expressed as a series expansion of spatial partial derivatives of ϕ :

$$\bar{\phi}(x, t) = - \sum_{k=0}^{\infty} \frac{(-1)^k \Delta^k(x, t)}{k!} \mathcal{M}^{(k)}(x, t) \frac{\partial^k \phi}{\partial x^k}(x, t) \quad (2.7)$$

The series' convergence in Eq. (2.5) and Eq. (2.7) has been discussed by Vasilyev (Vasilyev *et al.* 1998). Using the fact that turbulent flows have a bounded spectrum, the authors have demonstrated that the convergence of Eq. (2.5) is absolute and thus uniform even if Δ is spatially varying. They have also proven that Eq. (2.7) converges for arbitrary Δ if the filter has a finite support. If the filter has an infinite support but the filter moments do not grow faster than factorial (*e.g.* the Gaussian filter) then the series converges provided that Δ is less than a number of Kolmogorov scales. Finally if ϕ is spectrally bounded then $\partial\phi/\partial t$ is also spectrally bounded and Eq. (2.7) can therefore be used to reformulate TCE :

$$\text{TCE}[\phi] = - \sum_{k=0}^{\infty} \frac{(-1)^k}{k!} \left[\Delta^k(x, t) \mathcal{M}^{(k)}(x, t) \frac{\partial^k}{\partial x^k} \frac{\partial \phi}{\partial t} - \frac{\partial}{\partial t} \left(\Delta^k(x, t) \mathcal{M}^{(k)}(x, t) \frac{\partial^k \phi}{\partial x^k} \right) \right] \quad (2.8)$$

$$\text{TCE}[\phi] = \sum_{k=1}^{\infty} \frac{(-1)^k}{k!} \frac{\partial}{\partial t} \left(\Delta^k(x, t) \mathcal{M}^{(k)}(x, t) \right) \frac{\partial^k \phi}{\partial x^k} \quad (2.9)$$

In Eq. (2.9) the filter width $\Delta(x, t)$ is a function of time and of the Eulerian abscissa x . But $\Delta(x, t)$ is generally a function of the local cell volume and on deforming grids the cells are moving and stretching. It is therefore more convenient to introduce the Arbitrary Lagrangian-Eulerian (ALE) coordinate $X(x, t)$ to express the filter width $\Delta(x, t) = \delta(X, t)$. If $\delta(X, t)$ is equal to the cell volume $V_{\omega}(X, t)$ multiplied by a constant factor then $\delta(X, t)$ can be written as a function of cell-volume spatial variations and of the mean deformation rate $\overline{\nabla \cdot \dot{X}}$:

$$\frac{\partial \Delta}{\partial t}(x, t) = \frac{\partial \delta(X(x, t), t)}{\partial t} = \dot{X} \frac{\partial \delta}{\partial X} + \delta(X, t) \overline{\nabla \cdot \dot{X}} \quad (2.10)$$

where the mean deformation rate is defined by :

$$\overline{\nabla \cdot \dot{X}} = \frac{1}{\delta(X, t)} \frac{\partial \delta}{\partial t}(X, t) = \frac{1}{\omega(X, t)} \int_{\omega(X, t)} \frac{\partial \dot{X}}{\partial x} dx \quad (2.11)$$

In Eq. (2.10) the first right-hand term is due to the cell translation and the spatial stretching and the second is due to the cell contraction or dilatation. Then TCE can be

decomposed into three different contributions :

$$\begin{aligned} \text{TCE}[\phi] = & \overline{(\nabla \cdot \dot{X})} \sum_{k=1}^{\infty} \frac{(-1)^k \delta^k}{(k-1)!} \mathcal{M}^{(k)}(x, t) \frac{\partial^k \phi}{\partial x^k} \\ & + \dot{X} \sum_{k=1}^{\infty} \frac{(-1)^k \delta^{(k-1)}}{(k-1)!} \frac{\partial \delta}{\partial X} \mathcal{M}^{(k)}(x, t) \frac{\partial^k \phi}{\partial x^k} \\ & + \sum_{k=1}^{\infty} \frac{(-1)^k \delta^k}{k!} \frac{\partial \mathcal{M}^{(k)}}{\partial t}(x, t) \frac{\partial^k \phi}{\partial x^k} \end{aligned} \quad (2.12)$$

The first right-hand term arises from the cell temporal stretching. Its sign depends on the deformation type : contraction or dilatation. The second term is a spatial commutation error multiplied by the translation speed of the cell. This term is zero on uniform grids and when the mesh is not uniform it can be treated using a spatially commutative filter (Vasilyev *et al.* 1998; Marsden *et al.* 2002; Haselbacher & Vasilyev 2003). Finally the third term is due to shape variations. For example if during a simulation the filter shape changes from top-hat to Gaussian it will produce TCE through this third term. For simplicity the filter shape is assumed constant throughout the computations. The term of interest is therefore the first one which directly depends on the deformation rate of the combustion chamber.

3. Three dimensional derivation for structured grids

The TCE analysis of Section 2 can be performed in a very similar manner for multi dimensional structured grids because a filter width in each main direction can be easily defined. Then the differences come from the Taylor series expansion or from the filtering definition that becomes :

$$\bar{\phi}(\mathbf{x}, t) = \frac{1}{\Delta_1(\mathbf{x}, t) \Delta_2(\mathbf{x}, t) \Delta_3(\mathbf{x}, t)} \iiint_{\Omega_{\mathbf{x}}(t)} G\left(\frac{x_i - y_i}{\Delta_i(\mathbf{x}, t)}, \mathbf{x}, t\right) \phi(\mathbf{y}, t) d^3 \mathbf{y} \quad (3.1)$$

where $\mathbf{x} = (x_1, x_2, x_3)^T$. Then the same change of variable $\Delta \boldsymbol{\xi} = (\Delta_i \xi_i)^T = (x_i - y_i)^T$ as for the one dimensional derivation can be carried out :

$$\bar{\phi}(\mathbf{x}, t) = - \iiint_{\Omega_{\boldsymbol{\xi}}(\mathbf{x}, t)} G(\boldsymbol{\xi}, \mathbf{x}, t) \phi(\mathbf{x} - \Delta \boldsymbol{\xi}, t) d^3 \boldsymbol{\xi} \quad (3.2)$$

Using the gradient operator ∇ , the Taylor expansion of $\phi(\mathbf{x} - \Delta \boldsymbol{\xi}, t)$ reads :

$$\begin{aligned} \phi(\mathbf{x} - \Delta \boldsymbol{\xi}, t) &= \sum_{l=0}^{\infty} \frac{(-1)^l}{l!} (\Delta \boldsymbol{\xi} \cdot \nabla)^l \phi(\mathbf{x}, t) \\ &= \sum_{i=0}^{\infty} \sum_{j=0}^{\infty} \sum_{k=0}^{\infty} \frac{(-1)^{i+j+k}}{i! j! k!} (\Delta_1 \xi_1)^i (\Delta_2 \xi_2)^j (\Delta_3 \xi_3)^k \nabla_1^i \nabla_2^j \nabla_3^k \phi(\mathbf{x}, t) \end{aligned} \quad (3.3)$$

The 3D filter moments are defined as follows :

$$\mathcal{M}^{(ijk)}(\mathbf{x}, t) = \iiint_{\Omega_{\boldsymbol{\xi}}(\mathbf{x}, t)} G(\boldsymbol{\xi}, \mathbf{x}, t) \xi_1^i \xi_2^j \xi_3^k d^3 \boldsymbol{\xi} \quad (3.4)$$

Finally the 3D equivalent of Eq. (2.9) which gives the Taylor expansion of TCE is

written :

$$\text{TCE}[\phi] = \sum_{i=0}^{\infty} \sum_{j=0}^{\infty} \sum_{k=0}^{\infty} \frac{(-1)^{i+j+k}}{i! j! k!} \frac{\partial}{\partial t} \left[\Delta_1^i \Delta_2^j \Delta_3^k \mathcal{M}^{(ijk)} \right] \nabla_1^i \nabla_2^j \nabla_3^k \phi(\mathbf{x}, t) \quad (3.5)$$

If the commutation errors that come from grid non-uniformity and filter shape variations are neglected then TCE can be reformulated as follows to have the mean deformation rate in each direction appear :

$$\begin{aligned} \text{TCE}[\phi] = \sum_{i=0}^{\infty} \sum_{j=0}^{\infty} \sum_{k=0}^{\infty} \frac{(-1)^{i+j+k}}{i! j! k!} \left(i(\overline{\nabla \cdot \dot{X}})_1 + j(\overline{\nabla \cdot \dot{X}})_2 + k(\overline{\nabla \cdot \dot{X}})_3 \right) \\ \delta_1^i \delta_2^j \delta_3^k \mathcal{M}^{(ijk)} \nabla_1^i \nabla_2^j \nabla_3^k \phi(\mathbf{x}, t) \end{aligned} \quad (3.6)$$

and the mean deformation rate of the cell ω in the direction i is :

$$(\overline{\nabla \cdot \dot{X}})_i = \frac{1}{\omega_i(\mathbf{X}, t)} \int_{\omega_i(\mathbf{X}, t)} \frac{\partial \dot{X}_i}{\partial x_i} dx_i \quad (3.7)$$

For symmetric filters ($\mathcal{M}^{(ijk)} = 0$ if i, j or k is odd) the TCE leading terms \mathcal{L} of Eq. (3.6) are diffusive or anti-diffusive depending on the cell deformation :

$$\begin{aligned} \mathcal{L} = & (\overline{\nabla \cdot \dot{X}})_1 \delta_1^2 \mathcal{M}^{(2,0,0)} \nabla_1^2 \phi(\mathbf{x}, t) \\ & + (\overline{\nabla \cdot \dot{X}})_2 \delta_2^2 \mathcal{M}^{(0,2,0)} \nabla_2^2 \phi(\mathbf{x}, t) \\ & + (\overline{\nabla \cdot \dot{X}})_3 \delta_3^2 \mathcal{M}^{(0,0,2)} \nabla_3^2 \phi(\mathbf{x}, t) \end{aligned} \quad (3.8)$$

4. Three dimensional derivation for unstructured grids

The derivation of TCE for unstructured grids is different compared to structured grids because generally no main direction exists anymore. Only a unique filter width can be defined and it becomes useless to take this width out of the filter definition G . The filter width is therefore defined implicitly and the filtering convolution reads :

$$\bar{\phi}(\mathbf{x}, t) = \iiint_{\Omega_{\mathbf{x}}(t)} G(\mathbf{x} - \mathbf{y}, \mathbf{x}, t) \phi(\mathbf{y}, t) d^3 \mathbf{y} \quad (4.1)$$

Then the filter width does not appear anymore in the variable change $\boldsymbol{\xi} = \mathbf{x} - \mathbf{y}$ to switch to the mapping space :

$$\bar{\phi}(\mathbf{x}, t) = \iiint_{\Omega_{\boldsymbol{\xi}}(\mathbf{x}, t)} G(\boldsymbol{\xi}, \mathbf{x}, t) \phi(\mathbf{x} - \boldsymbol{\xi}, t) d^3 \boldsymbol{\xi} \quad (4.2)$$

This is also the case in the Taylor expansion of $\phi(\mathbf{x} - \boldsymbol{\xi}, t)$ that reads :

$$\phi(\mathbf{x} - \boldsymbol{\xi}, t) = \sum_{i=0}^{\infty} \sum_{j=0}^{\infty} \sum_{k=0}^{\infty} \frac{(-1)^{i+j+k}}{i! j! k!} \xi_1^i \xi_2^j \xi_3^k \nabla_1^i \nabla_2^j \nabla_3^k \phi(\mathbf{x}, t) \quad (4.3)$$

Considering the same filter moment definition as Eq. (3.4) TCE for unstructured grids are finally equal to:

$$\text{TCE}[\phi] = \sum_{i=0}^{\infty} \sum_{j=0}^{\infty} \sum_{k=0}^{\infty} \frac{(-1)^{i+j+k}}{i! j! k!} \frac{\partial}{\partial t} \left[\mathcal{M}^{(ijk)} \right] \nabla_1^i \nabla_2^j \nabla_3^k \phi(\mathbf{x}, t) \quad (4.4)$$

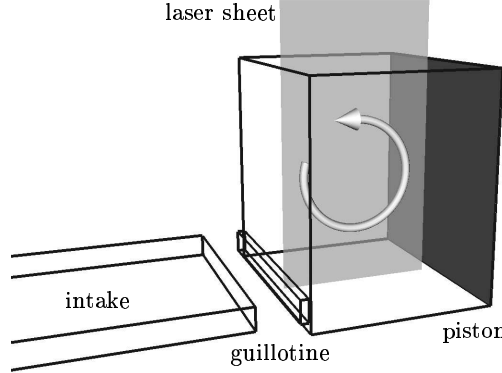


FIGURE 1. Square-piston experiment sketch.

It is important to note that in Eq. (4.4) the different TCE contributions from the cell deformation or from the filter shape variations can not be analysed separately like in the structured case. They are all included in the filter moment derivative $\partial \mathcal{M}^{(ijk)} / \partial t$.

5. Evaluation of TCE on a piston-engine like configuration

The choice of a piston-engine like configuration to evaluate the TCE magnitude has been guided by the following considerations :

- geometrical simplicity to avoid meshing issues,
- four-stroke operating mode to have a piston-engine like behaviour in terms of pressure and density variations,
- availability of experimental measurements to validate numerical simulations.

5.1. Description of the square-piston experiment

The square-piston experiment has been designed and operated at Institut de Mécanique des Fluides de Toulouse (IMFT) to study the compression and the disruption of tumble vortices that occur in Spark-Ignition (SI) engines (Marc *et al.* 1997; Boree *et al.* 2002). This device has been specifically designed to validate LES computations, offering many Particle Image Velocimetry (PIV) measurements for different piston positions. This experiment consists of :

- a square piston that has a sinusoidal motion,
- a rectangular intake channel that is also used as exhaust channel,
- a guillotine that closes the intake channel during compression and expansion strokes,
- a plenum at constant pressure connected to the intake channel.

A sketch of this experiment is given on Fig. (1). The position of the intake channel on the chamber head ensures the generation of a strong tumble motion that is then compressed when the guillotine is closed. Because of synchronisation issues between the PIV device and the piston position, the crank speed is very moderate at 206 rotations per minute (*rpm*). The compression ratio t_c is equal to 4 and the stroke is 75 mm long. The dimensions of the piston are $100 \times 100 \text{ mm}^2$ and those of the channel are $300 \times 96 \times 10 \text{ mm}^3$. PIV measurements are done in the symmetry plane of the configuration, where two velocity components are available. For each chosen piston position more than one hundred instantaneous PIV shots are available. Mean and fluctuating fields computed from these are also available.

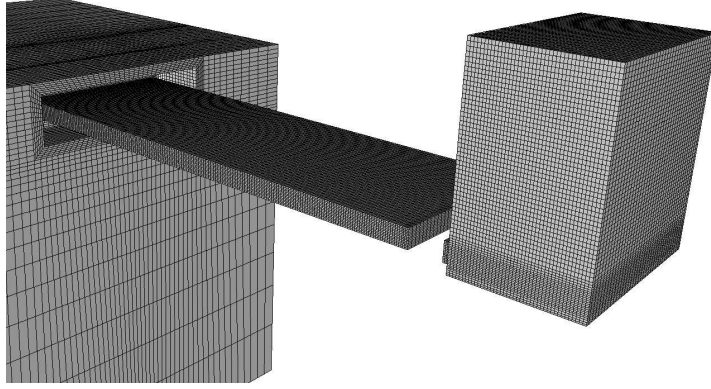


FIGURE 2. Square-piston experiment mesh comprising combustion chamber, intake channel and plenum.

5.2. Large-Eddy Simulation computations

5.2.1. Code description

The AVBP code (<http://www.cerfacs.fr/cfd/software.php>) is used for the following LES computations. This tool is co-developed by CERFACS and IFP and target applications are gas turbines, rocket propellers and piston engines. AVBP solves explicitly the full compressible Navier-Stokes equations on unstructured hybrid 2D and 3D meshes. To better predict the combustion process in industrial applications the heat capacities of the flow can vary in function of temperature and composition. Sensible energy and enthalpy of each species are therefore tabulated for a wide temperature range and mean quantities (molecular weight, mean heat capacities, mean heat capacity ratio) are calculated according to the species mixing. Both second-order and third-order convective schemes (Colin & Rudgyard 2000) are available. These schemes and the NSCBC-based boundary conditions (Poinsot & Lele 1992) have been improved (Moureau *et al.* 2004) to deal with variable heat capacities.

AVBP offers different turbulent models such as the Smagorinsky model (Smagorinsky 1963) or the WALE model (Nicoud & Ducros 1999). Flame/turbulence interactions are taken into account by the thickened flame model (Angelberger *et al.* 2000; Colin *et al.* 2000; Légier *et al.* 2000).

5.2.2. Numerical set-up

3D simulations have been carried out on relatively coarse grids, *i.e.* between 250000 and 300000 cells for the whole device (see Fig. (2)). Because of the combustion chamber compression the grid connectivity has to be modified during the computations to keep a reasonable mesh quality. At several times during the simulations cells are removed or added, the mesh is remapped and the flow is interpolated from the old to the new mesh. The number of connectivity changes is conditioned by the compression ratio as shown on Fig. (3). It represents a mean cell width $\delta = V_\omega^{1/3}$ as a function of the crank angle before top-dead center (BTDC) during the compression stroke. The discontinuities on both curves correspond to connectivity changes, which occur more often for $t_c = 10$.

5.2.3. Validation of LES simulations

LES simulations are validated performing the comparison with PIV data of the square-piston experiment. LES computations have been carried out with the Lax-Wendroff con-

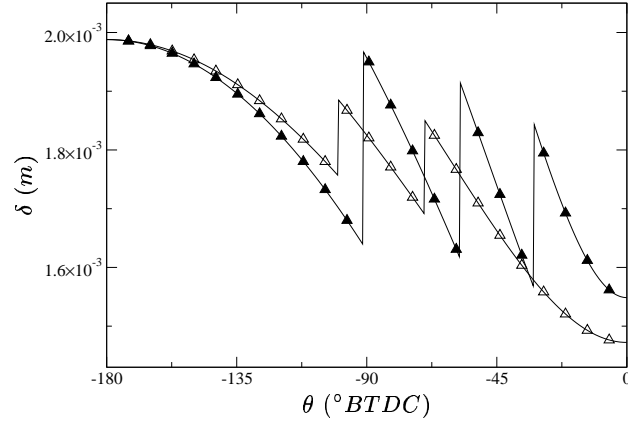


FIGURE 3. Evolution of the mean cell width δ during the compression stroke. \triangle : $t_c = 4$; \blacktriangle : $t_c = 10$.

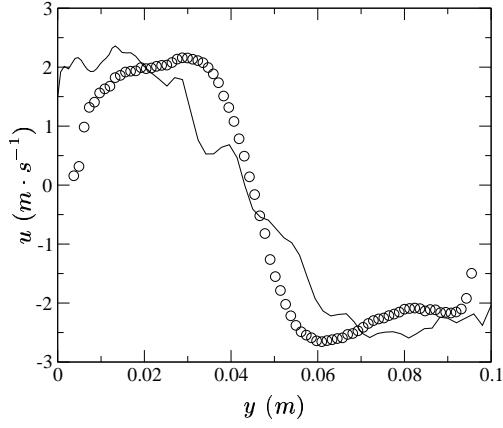


FIGURE 4. Middle x-plane mean profile. \circ : experiments ; — : LES.

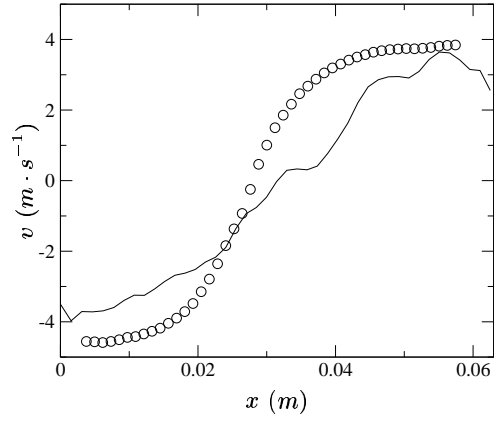


FIGURE 5. Middle y-plane mean profile. \circ : experiments ; — : LES.

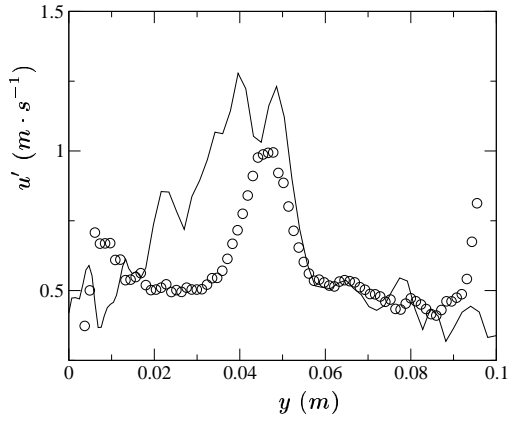


FIGURE 6. Middle x-plane fluctuation profile. \circ : experiments ; — : LES.

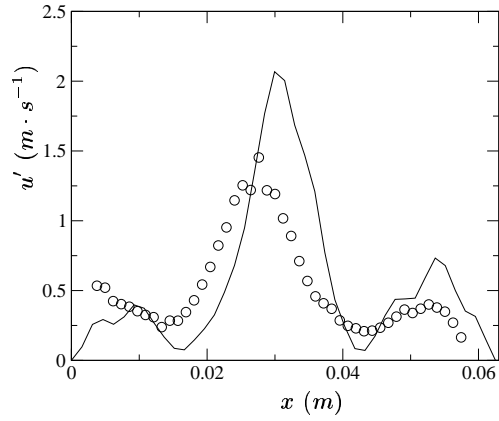


FIGURE 7. Middle y-plane fluctuation profile. \circ : experiments ; — : LES.

vective scheme, the Smagorinsky model and a simple logarithmic wall-law model. Six consecutive LES cycles are averaged to obtain mean and fluctuation profiles. Results at the half of the compression stroke ($-90^\circ BTDC$) are presented on Fig. (4) to Fig. (7). Fig. (4) and Fig. (5) show the mean velocity profiles in the middle of the symmetry plane whereas Fig. (6) and Fig. (7) represent resolved velocity fluctuations u' in the same location. Mean profiles are in good agreement with experimental data indicating that the tumble intensity is well predicted. The fact that the maxima of fluctuations occur at the center of the rotating tumble indicates that they are mainly due to the precession motion of the tumble. This is reproduced by the LES findings.

5.3. Estimation of TCE

5.3.1. Filter choice for the TCE evaluation

As stated in Section 4 mesh cells do not have orthogonal main directions on unstructured grids and the filter can not be written as the combination of three filters in each main direction. Different filters for unstructured grids are found in the litterature. For instance filters that commute with spatial partial derivatives are based on weighting functions of surrounding nodes (Vasilyev *et al.* 1998; Vasilyev & Goldstein 2004). Filters have to satisfy several properties to be usable for LES :

- integral over the domain must be unity,
- filter shape has to be well defined and not to vary too much in space
- filter support has to be as compact as possible for practical calculation issues

The simplest filter for LES computations on unstructured grids is the Gaussian filter. This filter needs a characteristic length that can be expressed as a function of the cell volume $\Delta(\mathbf{x}, t) = \delta(\mathbf{X}, t) = V^{\frac{1}{3}}(\mathbf{X}, t)$:

$$G(\boldsymbol{\xi}, \mathbf{x}, t) = \left(\frac{6}{\pi}\right)^{\frac{3}{2}} \frac{1}{\Delta^3(\mathbf{x}, t)} \exp\left(-6 \frac{\xi_1^2 + \xi_2^2 + \xi_3^2}{\Delta^2(\mathbf{x}, t)}\right) \quad (5.1)$$

This filter satisfies $\mathcal{M}^{(0,0,0)} = 1$ and since this filter is symmetric the first non-zero moments are $\mathcal{M}^{(2,0,0)} = \mathcal{M}^{(0,2,0)} = \mathcal{M}^{(0,0,2)} = \Delta^2/12$.

5.3.2. TCE modeling

The only mean to evaluate exactly the TCE magnitude would be to perform a DNS of the square-piston engine experiment. Since this is not feasible a TCE model for the momentum equation is proposed and evaluated on LES simulations. TCE are indeed appearing on the whole Navier-Stokes equations but without combustion, spatial variations of density ρ and total energy ρE are small compared to momentum $\rho \mathbf{u}$ variations.

The simplest TCE modeling is to keep only the leading terms of Eq. (4.4). This is reasonable since the main LES hypothesis requires that the filter width should be noticeably smaller than the integral length scale. In this case the higher-order terms in Eq. (4.4) are negligible compared to the leading terms. For the Gaussian filter defined on Eq. (5.1) the proposed model is thus :

$$\text{TCE}[\phi] = \frac{1}{12} \Delta \frac{\partial \Delta}{\partial t} \nabla \cdot (\nabla \phi(\mathbf{x}, t)) \quad (5.2)$$

Then if the filter width is a function of the local cell width it is more convenient to do the same decomposition as Eq. (2.10) :

$$\text{TCE}[\phi] = \frac{\delta}{12} (\dot{\mathbf{X}} \cdot \nabla \delta) \nabla \cdot (\nabla \phi(\mathbf{x}, t)) + \frac{\delta^2}{12} \left(\frac{1}{3} \overline{\nabla \cdot \dot{\mathbf{X}}}\right) \nabla \cdot (\nabla \phi(\mathbf{x}, t)) \quad (5.3)$$

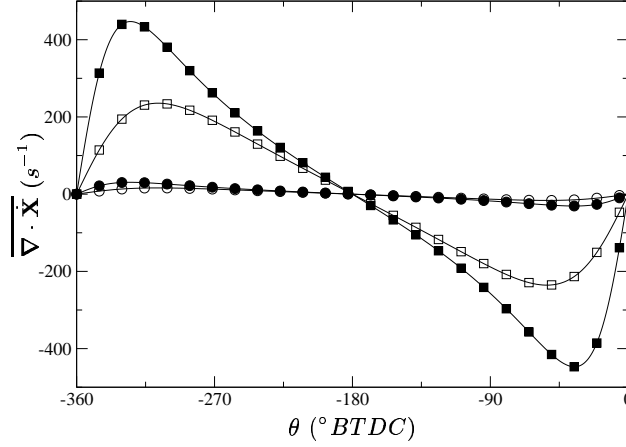


FIGURE 8. $\overline{\nabla \cdot \dot{\mathbf{X}}}$ as a function of crank angle. —○— : 206 rpm , $t_c = 4$; —●— : 206 rpm , $t_c = 10$; —□— : 3000 rpm , $t_c = 4$; —■— : 3000 rpm , $t_c = 10$.

The first term of Eq. (5.3) is a spatial commutation error that vanishes when the cell width δ is uniform. Only the second right-hand term is of interest in this study. This term is a diffusion or anti-diffusion term depending on the sign of the factor $\delta^2(\nabla \cdot \dot{\mathbf{X}})/36$ that has the dimension of a viscosity. In this factor δ^2 is almost constant during the simulation thanks to connectivity changes as shown on Fig. (3). The mean deformation rate $\overline{\nabla \cdot \dot{\mathbf{X}}}$ depends only on engine parameters such as crank speed and compression ratio t_c . This dependence is illustrated on Fig. (8) for a simple sinusoidal law during intake ($\theta \in [-360^\circ, -180^\circ]$) and compression ($\theta \in [-180^\circ, 0^\circ]$) strokes. This rate expressed as a function of the crank angle scales linearly with crank speed and non-linearly with compression ratio.

5.3.3. Evaluation in the code

TCE are evaluated in the LES code only for the momentum equation. As seen in Section 5.3.2 TCE on unstructured grids with a Gaussian filter are diffusive or anti-diffusive. It means that the effective momentum diffusion in a LES simulation will be the sum of the molecular, turbulent and TCE diffusion. Since momentum diffusion corresponds to kinetic energy dissipation a good mean to compare the turbulent diffusion to the TCE diffusion is to study the ratio \mathcal{R} between the resolved kinetic energy dissipated by TCE and by molecular plus turbulent diffusion :

$$\mathcal{R} = \frac{\langle \bar{u}_i \frac{\delta^2}{12} \left(\frac{1}{3} \overline{\nabla \cdot \dot{\mathbf{X}}} \right) \nabla \cdot (\nabla \bar{\rho} \bar{u}_i) \rangle}{\langle \bar{u}_i \frac{\partial \bar{\tau}_{ij}}{\partial x_j} + \bar{u}_i \frac{\partial \bar{t}_{ij}}{\partial x_j} \rangle} \quad (5.4)$$

where the brackets $\langle \rangle$ correspond to the spatial averaging operator. In Eq. (5.4) the different terms are not proper dissipation rates but the sum of kinetic energy dissipation rates plus kinetic energy transport by momentum diffusion :

$$\langle \bar{u}_i \frac{\partial \bar{\tau}_{ij}}{\partial x_j} \rangle = \langle -\frac{\partial \bar{u}_i}{\partial x_j} \bar{\tau}_{ij} \rangle + \langle \frac{\partial \bar{u}_i}{\partial x_j} \bar{\tau}_{ij} \rangle \quad (5.5)$$

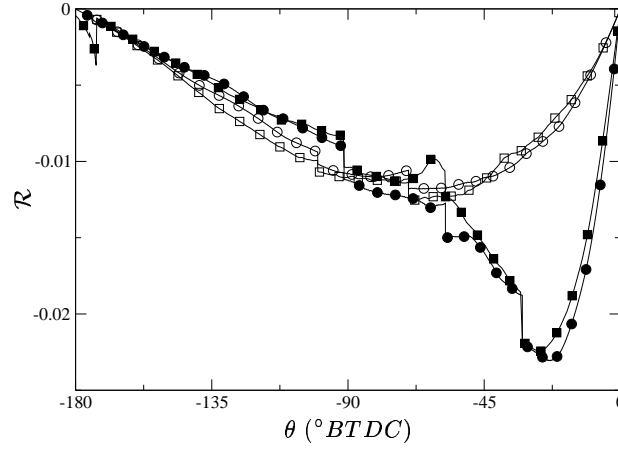


FIGURE 9. Ratio \mathcal{R} of TCE and molecular plus turbulent dissipation as a function of crank angle. —○—: 206 rpm, $t_c = 4$; —●—: 206 rpm, $t_c = 10$; —□—: 3000 rpm, $t_c = 4$; —■—: 3000 rpm, $t_c = 10$.

The second right-hand term of Eq. (5.5) is a boundary term that is nearly zero and \mathcal{R} is therefore a dissipation ratio.

Four single-cycle simulations have been performed to evaluate TCE and the effect of the crank speed and of the compression ratio. Results are presented on Fig. (9). The first remark is that the TCE levels are small compared to molecular plus turbulent dissipation. A maximum of about 1.2% for $t_c = 4$ and 2.5% for $t_c = 10$ is found at the end of the compression stroke. The second remark is that the evaluated ratio \mathcal{R} does only marginally depend on crank speed. It means that TCE and physical dissipation scale in the same manner relatively to crank speed. This is not the case for the compression ratio, leading to some differences at the end of the compression stroke when almost all resolved eddies have been dissipated. Compared to the numerical dissipation of numerical schemes and other uncertainties, TCE can therefore be neglected for applications that operate in about the same range of parameters.

6. Conclusions

TCE have been derived for structured and unstructured grids and models have been proposed. These models have been evaluated on a square-piston experiment and it was shown that kinetic energy dissipation due to TCE can be neglected compared to the turbulent dissipation in piston-engine like applications. It should be underlined that in piston-engines the flow and the mesh deformation are generated by the same phenomenon that is the piston motion. But in some other cases as flame computations with automatic local mesh refinement, TCE are not correlated anymore to local turbulence and they may not remain negligible.

REFERENCES

- ANGELBERGER, C., VEYNANTE, D. & EGOLFOPOULOS, F. 2000 LES of chemical and acoustic forcing of a premixed dump combustor. *Flow Turb. Comb.* **65** (2), 205–222.
- BOREE, J., MAUREL, S. & BAZILE, R. 2002 Disruption of a compressed vortex. *Phys. Fluids* **14** (7), 2543–2556.

- CELIK, I., YAVUZ, I. & SMIRNOV, A. 2001 Large Eddy Simulations of In-Cylinder turbulence for IC engines: A review. *Int. J. of Engine Research* **2** (2).
- COLIN, O., DUCROS, F., VEYNANTE, D. & POINSOT, T. 2000 A thickened flame model for LES of turbulent premixed combustion. *Phys. Fluids* **12** (7), 1843–1863.
- COLIN, O. & RUDGYARD, M. 2000 Development of high-order Taylor-Galerkin schemes for LES. *J. Comp. Phys.* **162** (2), 338–371.
- FRANKE, J. & FRANK, W. 2001 Temporal commutation errors in Large-Eddy Simulation. *Zeitschrift Fur Angewandte Mathematik Und Mechanik* **81** (S3), S467–S468.
- FUREBY, C. & TABOR, D. 1997 Mathematical and physical constraints on Large-Eddy Simulations. *Theor. Comp. Fluid Dyn.* **9** (2), 85–102.
- GHOSAL, S. 1999 Mathematical and physical constraints on Large-Eddy Simulation of turbulence. *AIAA J.* **37** (4), 425–433.
- GHOSAL, S. & MOIN, P. 1995 The basic equations for the Large-Eddy Simulation of turbulent flows in complex-geometry. *J. Comp. Phys.* **118** (1), 24–37.
- HASELBACHER, A. & VASILYEV, O. 2003 Commutative discrete filtering on unstructured grids based on least-squares techniques. *J. Comp. Phys.* **187** (1), 197–211.
- KAUFMANN, A., NICOD, F. & POINSOT, T. 2002 Flow forcing techniques for numerical simulation of combustion instabilities. *Comb. Flame* **131**, 371–385.
- LÉGIER, J.-P., POINSOT, T. & VEYNANTE, D. 2000 Dynamically thickened flame LES model for premixed and non-premixed turbulent combustion. In *Proc. 2000 Summer Program*, pp. 157–168. Center for Turbulence Research, Stanford, USA.
- MARC, D., BOREE, J., BAZILE, R. & CHARNAY, G. 1997 PIV and LDV measurements of tumbling vortex flow in a model square section motored engine. *Soc. Auto. Eng. Paper* (972834).
- MARSDEN, A., VASILYEV, O. & MOIN, P. 2002 Construction of commutative filters for LES on unstructured meshes. *J. Comp. Phys.* **175** (2), 584–603.
- MOUREAU, V., LARTIGUE, G., SOMMERER, Y., ANGELBERGER, C., COLIN, O. & POINSOT, T. 2004 Numerical methods for unsteady compressible multi-component reacting flows on fixed and moving grids. *accepted for publication in J. Comp. Phys.*
- NICOD, F. & DUCROS, F. 1999 Subgrid-scale stress modelling based on the square of the velocity gradient tensor. *Flow Turb. Comb.* **62** (3), 183–200.
- POINSOT, T. & LELE, S. 1992 Boundary conditions for direct simulations of compressible viscous flows. *J. Comp. Phys.* **101** (1), 104–129.
- PRIÈRE, C., GICQUEL, L. Y. M., KAUFMANN, A., KREBS, W. & POINSOT, T. 2004 LES of mixing enhancement : LES predictions of mixing enhancement for jets in cross-flows. *J. Turb.* **5**, 1–30.
- SELLE, L., LARTIGUE, G., POINSOT, T., KOCH, R., SCHILDMACHER, K.-U., KREBS, W., PRADÉ, B., KAUFMANN, P. & VEYNANTE, D. 2004 Compressible Large-Eddy Simulation of turbulent combustion in complex geometry on unstructured meshes. *Comb. Flame* **137** (4), 489–505.
- SMAGORINSKY, J. 1963 General circulation experiments with the primitive equations: 1. the basic experiment. *Mon. Weath. Rev.* **91**, 99–164.
- VASILYEV, O. & GOLDSTEIN, D. 2004 Local spectrum of commutation error in Large Eddy Simulations. *Phys. Fluids* **16** (2), 470–473.
- VASILYEV, O., LUND, T. & MOIN, P. 1998 A general class of commutative filters for LES in complex geometries. *J. Comp. Phys.* **146** (1), 82–104.

RANS modeling and applications

Reynolds-Averaged Navier-Stokes (RANS) techniques are the method of choice for flow predictions in industry in spite of well-known limitations of conventional turbulence closures. Traditionally, RANS efforts during the summer program have focused on the introduction or the evaluation of novel modeling approaches to tackle such limitations. This year, the project led by Stavros Kassinos represents one of such attempts. On the other hand, the other two efforts included in this group explore critical aspects of the application of RANS techniques. Francesco Capizzano's research work aimed at establishing the accuracy in predicting flows with control devices, whereas, Stephane Moreau's group compared RANS techniques to other approaches to compute noise sources in the flow around an airfoil.

Kassinos *et al.* explore the limitations of linear eddy viscosity models in predicting flows in rotating devices. The approach they followed is based on the use of structure-based modeling to construct an algebraic representation of the Reynolds-stress such that the turbulence anisotropy and its response to frame rotation is represented. In this approach the eddy viscosity model is *only* used to build a representative turbulence time scale. The results are extremely encouraging and indicate that over a range of Reynolds and Rossby numbers this approach correctly predicts the effect of rotation on the mean flow and the corresponding turbulent stresses.

Capizzano investigates the predictive capabilities of various RANS closures in computing boundary layer flows with active flow-separation control devices. In particular, the interest is mainly aimed at the simulation of flows with synthetic jets (oscillatory blowing/suction devices). In addition, preliminary work on the development of a lumped model to capture the unsteadiness introduced by synthetic jets was carried out. In this approach the steady-state flow equations are considered and *suitable* body-forces (corresponding to the injection of momentum related to the action of the oscillating jet) are introduced. Initial results are promising.

Moreau *et al.* report on a comparison between various numerical approaches to compute the flow around an airfoil. The main interest is in predicting the pressure fluctuations at the airfoil trailing edge as it has direct implications on the self-generated noise. Conventional RANS techniques, detached eddy simulations and the Lattice Boltzmann method are compared to experimental data. In addition, two Large Eddy Simulations (using a body-fitted mesh and a Cartesian-grid immersed boundary approach) are performed and compared to the other predictions. The results in terms on mean flow characteristics, average wall pressure and velocity profiles in the wake, do not show substantial differences. On the other hand, the analysis of pressure fluctuations spectrum clearly reveals the inadequacy of all but LES techniques to predict the experimental data especially in the high frequency range.

Gianluca Iaccarino

Page intentionally left blank

Combining eddy-viscosity models and the algebraic structure-based Reynolds stress closure

By G. Kalitzin, G. Iaccarino AND C. A. Langer, S. C. Kassinos†

Two linear eddy-viscosity models, the v^2 - f and k - ω models, have been combined with an algebraic structure-based algorithm for the evaluation of the Reynolds stresses. This closure was originally designed as an integral part of the algebraic structure-based model (ASBM) to capture the turbulent anisotropy occurring in rotating wall bounded flows. It is shown that the algebraic structure-based evaluation of the Reynolds stresses can be used directly with *conventional* turbulence models sensitizing them to rotation. Significant improvement in the prediction of anisotropic turbulent flow can be achieved without an additional tuning of the closure coefficients.

The models are evaluated for spanwise rotating channel flow. The sensitivity to the Reynolds and Rossby numbers is investigated. The results are compared with DNS data.

1. Motivation and objectives

Linear eddy-viscosity models are known to be inaccurate in predicting the effect of strong streamline curvature and frame rotation. There is no shortage of modifications and adjustments proposed in the literature to correct their behavior. For example in the work by Shih *et al.* (1995) the k - ϵ model is modified by introducing a coefficients in the ϵ -equations that depend on the shear rate and frame rotation. A more consistent redesigning of the ϵ equation for flows with rotational effects has been proposed by Haire & Reynolds (2003). Another recent attempt by Durbin & Pettersson Reif (2001) consists in the modification of the eddy-viscosity coefficient (again by introducing dependency on the shear rate and frame rotation). In the latter case the justification for the choice of the selected functional dependency comes from the study of close form solutions of second-moment models in the case of homogeneous rotating shear. Although these modifications are shown to provide encouraging predictions for simple flows with rotation (namely channel flows), their accuracy for more complex situations remains unclear. Differential Reynolds stress models, on the other hand, possess the obvious advantage that the turbulence production terms and the stress anisotropy are automatically accounted for. Unfortunately, the difficulties in modeling the stress redistribution terms and their inherent numerical stiffness make them not amenable to mainstream use in engineering calculations.

Algebraic Reynolds stress models have received a substantial amount of attention given the potential benefit of introducing stress anisotropy in the *controlled* environment of an eddy-viscosity closure. Several models have been devised with various degree of success (Gatski & Speziale 1993; Wallin & Johansson 2002). The basic idea behind these models is to express the Reynolds stress tensor as a function of one or more (up to ten) different tensors. This is not different from what is used to derived the so-called non-linear

† Mechanical and Manufacturing Engineering, University of Cyprus and CTR

eddy-viscosity models where additional (high-order) terms are added to the Boussinesq relationship between mean strain and Reynolds stresses. Reynolds and coworkers (e.g. Reynolds 1994, Kassinos & Reynolds 1994, Kassinos *et al.* 1993) have repeatedly argued that for adequate modeling and description of rotating turbulence, information about the turbulence structure is crucial. The Reynolds stresses only characterize the componentality of turbulence, *i.e.*, which velocity components are more energetic. The turbulent field has much more information than that contained in the Reynolds stresses, which is important in presence of rotation, and which is described by the turbulence structure. For instance, the dimensionality of the flow is important. This carries information about which directions are favored by the more energetic turbulent eddies: if the turbulent eddies are preferentially aligned with a given direction, then the dimensionality is smaller along that direction. Here hypothetical turbulent eddies are used to bring awareness of turbulence structure into the turbulence model. Averaging over an ensemble of eddies produces a set of one-point statistics, representative of the eddy field, and a set of equations of state relating the Reynolds stresses to these statistics.

The structure-based approach to build the Reynolds stress closure has lead in Langer & Reynolds (2003) to the development of the Algebraic Structure-Based Model (ASBM) in conjunction with a *novel* two-equation model based on the transport equation for turbulent kinetic energy, k , and large scale vorticity ω^2 . The model has been calibrated for channel flow simulations and the results have shown excellent agreement with available DNS data.

The primary objective of this research project was to implement ASBM in a three-dimensional Reynolds-Averaged Navier-Stokes (RANS) solver to perform simulations of complex flows. In this report, we describe the combination of the ASBM Reynolds stress evaluation with conventional turbulence model, namely the k - ω and v^2 - f models. Results are presented for channel flow with and without spanwise rotation. For the primary objective some modifications to the original ASBM formulations have been developed to ease its numerical implementation. In particular, a scalar diffusivity has been introduced to the transport equations of the turbulent scalars and a new definition of the length scale that identifies the near-wall viscous dominated region has been introduced.

2. The structure-based algebraic stress model

The eddy-axis concept Kassinos & Reynolds (1994) is used to relate the Reynolds stress and the structure tensors to parameters of a hypothetical turbulent eddy field. Each eddy represents a two-dimensional turbulence field, and is characterized by an eddy-axis vector, a_i . The turbulent motion associated with this eddy is decomposed in a component along the eddy axis, the jetal component, and a component perpendicular to the eddy axis, the vortical component. This motion can be further allowed to be flattened in a direction normal to the eddy axis (a round eddy being characterized by a random distribution of kinetic energy around its axis). Averaging over an ensemble of turbulent eddies gives statistical quantities representative of the eddy field, along with constitutive equations relating the normalized Reynolds stresses and turbulence structure to the statistics of

the eddy ensemble.

$$r_{ij} = \frac{\overline{u'_i u'_j}}{2k} = (1 - \phi)\frac{1}{2}(\delta_{ij} - a_{ij}) + \phi a_{ij} \quad (2.1)$$

$$+ (1 - \phi)\chi[\frac{1}{2}(1 - a_{nm}b_{mn})\delta_{ij} - \frac{1}{2}(1 + a_{nm}b_{mn})a_{ij} - b_{ij} + a_{in}b_{nj} + a_{jn}b_{ni}]$$

$$+ (-\gamma\Omega_k^T/\Omega^T)(\epsilon_{ipr}a_{pj} + \epsilon_{jpr}a_{pi})\{\frac{1}{2}[1 - \chi(1 - a_{nm}b_{mn})]\delta_{kr} + \chi b_{kr} - \chi a_{kn}b_{nr}\}$$

The eddy-axis tensor, $a_{ij} = \langle V^2 a_i a_j \rangle$, is the energy-weighted average direction cosine tensor of the eddy axes. The eddy-axis tensor is determined by the kinematics of the mean deformation. Eddies tend to become aligned with the direction of positive strain rate, and they are rotated kinematically by mean or frame rotation.

Motion around the eddy is called vortical, and motion along the axis is called jetal. The eddy jetting parameter ϕ is the fraction of the eddy energy in the jetal mode, and $(1 - \phi)$ is the fraction in the vortical mode. Under irrotational mean deformation, eddies remain purely vortical ($\phi = 0$). Shear produces jetal eddies, and in the limit of infinite rapid distortion $\phi \rightarrow 1$ for shear in a non-rotating frame. For shear in a rotating frame, ϕ ranges from 1 for zero frame rotation to 0 for frame rotation that exactly cancels the mean rotation in the frame, for which the mean deformation in an inertial frame is irrotational.

The eddy helix vector γ_k arises from the correlation between the vortical and jetal components. Hence $\gamma_k = 0$ for purely vortical turbulence ($\phi = 0$) or for purely jetal turbulence ($\phi = 1$). Typically γ_k is aligned with the total rotation vector Ω_k . The eddy-helix vector is the key factor in setting the shear stress in turbulent fields.

Flattening is used to describe the degree of asymmetry in the turbulent kinetic energy distribution around an eddy. A round eddy has no preferential distribution. If the motion is not axisymmetric around the eddy axis, the eddy is called flattened. The eddy-flattening tensor, b_{ij} , is the energy-weighted average direction cosine tensor of the flattening vector. The intensity of the flattening is given by the flattening parameter, χ . Under rapid irrotational deformation in a fixed frame eddies remain axisymmetric. Rotation tends to flatten the eddies in planes perpendicular to the rotation direction.

Following Reynolds *et al.* (2000), the eddy-axis tensor, a_{ij} , is computed on the analysis frame, where the turbulence might be at equilibrium or very close to it. The eddy-axis tensor is computed with no reference to the frame rotation, as it is only kinematically rotated by it (Kassinos & Reynolds 1994, Haire & Reynolds 2003). The evaluation is divided in two parts. Initially a strained eddy-axis tensor, a_{ij}^s , is evaluated based on the irrotational part of the mean deformation. Next a rotation operation is applied, sensitizing the eddy-axis tensor to mean rotation. This procedure produces eddy-axis tensor states that mimic the limiting states produced under RDT for different combinations of mean strain with on-plane mean rotation, while guaranteeing realizability of the eddy-axis tensor.

The strained a_{ij}^s is given by

$$a_{ij}^s = \frac{1}{3}\delta_{ij} + \frac{(S_{ik}^* a_{kj}^s + S_{jk}^* a_{ki}^s - \frac{2}{3}S_{mn}^* a_{nm}^s \delta_{ij})\tau}{a_0 + 2\sqrt{\tau^2 S_{kp}^* S_{kp}^* a_{pq}^s}}, \quad (2.2)$$

where $S_{ij}^* = S_{ij} - S_{kk}\delta_{ij}/3$ is the traceless strain-rate tensor with $S_{ij} = (\partial u_i/\partial x_j + \partial u_j/\partial x_i)/2$, τ is a time scale (Eq. 3.4), and $a_0 = 1.6$ is a “slow” constant. This gives realizable states for the eddy-axis tensor under irrotational deformations.

The final expression for the homogeneous eddy-axis tensor, a_{ij} (for near-wall regions

see Equation 2.13), is obtained by applying a rotation transformation to the strained eddy-axis tensor, a_{ij}^s ,

$$a_{ij} = H_{ik} H_{jl} a_{kl}^s, \quad H_{ij} = \delta_{ij} + h_1 \frac{\Omega_{ij}}{\sqrt{\Omega_{pp}^2}} + h_2 \frac{\Omega_{ik} \Omega_{kj}}{\Omega_{pp}^2}, \quad (2.3)$$

where $\Omega_{pp}^2 = \Omega_{pq} \Omega_{pq}$. The orthonormality conditions $H_{ik} H_{jk} = \delta_{ij}$ and $H_{ki} H_{kj} = \delta_{ij}$ require

$$h_1 = \sqrt{2h_2 - h_2^2/2}. \quad (2.4)$$

h_2 is determined with reference to RDT for combined homogeneous plane strain and rotation (see Reynolds *et al.* 2000, Haire & Reynolds 2003),

$$h_2 = \begin{cases} 2 - 2\sqrt{\frac{1}{2}(1 + \sqrt{1-r})} & \text{if } r \leq 1 \\ 2 - 2\sqrt{\frac{1}{2}(1 - \sqrt{1-1/r})} & \text{if } r \geq 1 \end{cases}, \quad r = \frac{a_{pq} \Omega_{qr} S_{rp}^*}{S_{kn}^* S_{nm}^* a_{mk}}. \quad (2.5)$$

The flattening tensor b_{ij} is modeled in terms of the mean rotation rate vector, Ω_i , and the frame rotation rate vector, Ω_i^f ,

$$b_{ij} = \frac{(\Omega_i + C_b \Omega_i^f)(\Omega_j + C_b \Omega_j^f)}{(\Omega_k + C_b \Omega_k^f)(\Omega_k + C_b \Omega_k^f)}, \quad C_b = -1.0. \quad (2.6)$$

The helix vector γ_k is taken as aligned with the total rotation vector,

$$\gamma_k = \gamma \frac{\Omega_k^T}{\sqrt{\Omega_k^T \Omega_k^T}}, \quad \gamma = \beta \sqrt{\frac{2\phi(1-\phi)}{1+\chi}}. \quad (2.7)$$

Modeling ϕ , β (see Eq. 2.7), and χ is a crucial part in the construction of the model. The equations for these scalars are found by analyzing target turbulent states corresponding to a mean deformation. Throughout the model development there is a strong effort to make it consistent with RDT solutions, aiming to improve model dependability and realizability for a wide range of mean deformations, as well as to obtain guidance in the functional shape chosen for the structure parameters. Tentative functional forms for the structure parameters are thus chosen with reference to RDT. A set of parameter values is chosen to mimic the isotropic turbulent state (the eddy structure is expected to consist of axisymmetric ($\chi = 0$), vortical ($\phi = 0$) eddies). Finally interpolation functions (along with model constants) are chosen to bridge these limiting states (isotropy and RDT). They are selected specially to match a canonical state of sheared turbulence, observed in the log region of a boundary layer.

The structure scalars are parameterized in terms of η_m , η_f , and a^2 , representatives of the ratio of mean rotation to mean strain, frame rotation to mean strain, and a measure of anisotropy respectively. These in turn are defined in terms of $\hat{\Omega}_m^2 \tau^2$, $\hat{\Omega}_T^2 \tau^2$, and $\hat{S}^2 \tau^2$; measures of the strength of the mean rotation, total rotation, and mean strain respectively. τ represents a time scale of the turbulence (Eq. 3.4).

$$\eta_m \equiv \sqrt{\frac{\hat{\Omega}_m^2}{\hat{S}^2}}, \quad \eta_f \equiv \eta_m - \text{sign}(X) \sqrt{\frac{\hat{\Omega}_T^2}{\hat{S}^2}}, \quad a^2 \equiv a_{pq} a_{pq}, \quad (2.8)$$

$$\hat{\Omega}_m^2 \equiv -a_{ij}\Omega_{ik}\Omega_{kj}, \quad \hat{\Omega}_T^2 \equiv -a_{ij}\Omega_{ik}^T\Omega_{kj}^T, \quad \hat{S}^2 \equiv a_{ij}S_{ik}S_{kj}, \quad X \equiv a_{ij}\Omega_{ik}^TS_{kj}. \quad (2.9)$$

In order to evaluate the structure parameters, they are first defined in a generic a^2 plane, along the mean-shear line, $\eta_m = 1$, and along the plane-strain line, $\eta_m = 0$. They are then interpolated or extrapolated in the same a^2 plane, depending on the flow location in this a^2 plane, specified in terms of η_f and η_m . The structure parameters are then sensitized to the degree of anisotropy of the turbulence, measured along the a^2 direction.

In the following, the subscripts “0” and “1” applied to ϕ , β , and χ , refer to values along the lines $\eta_m = 0$ and $\eta_m = 1$, respectively. The superscript “*” is used to denote values on the a^2 plane where $\eta_m = 0$ and $\eta_m = 1$ were evaluated.

The structure parameters are then defined with help from the auxiliary functions given by Tables 1–3.

$$\phi = \phi^* \left(\frac{(\eta_m - \eta_f)^2}{(\eta_m - \eta_f)^2 + (1 - a^2)^2} \right) \left(\frac{|\eta_m - \eta_f| \sqrt{\frac{3}{2}(a^2 - \frac{1}{3})}}{|\eta_m - \eta_f| \sqrt{\frac{3}{2}(a^2 - \frac{1}{3})} + p_0(1 - a^2)} \right), \quad (2.10)$$

$$\beta = \beta^*, \quad (2.11)$$

$$\chi = \chi^* \left[\frac{3}{2} \left(a^2 - \frac{1}{3} \right) \right]^{p_1}. \quad (2.12)$$

As a no-slip wall is approached, the velocity is driven to zero through the action of viscous forces. Furthermore, the velocity vector is reoriented into planes parallel to the wall through an inviscid mechanism (wall blocking) which acts over distances far larger than the viscous length scale. Thus the velocity component normal to the wall is driven to zero faster than the tangential components. In the structure-based model it is postulated that the eddy orientation shall also be parallel to the wall. A wall-blocking procedure is then introduced to reorient the eddies into planes parallel to the wall. The structure parameters are also sensitized to wall blocking, such that the modeled Reynolds stresses are consistent with the expected near wall asymptotic behavior.

Following Reynolds *et al.* (2000), the homogeneous eddy-axis tensor, a_{ij}^h , is computed based on the homogeneous algebraic procedure, Equations 2.2 and 2.3 (note that the superscript “h” has been added in the current section). It is then partially projected onto planes parallel to the wall,

$$a_{ij} = H_{ik}H_{jl}a_{kl}^h, \quad H_{ik} = \frac{1}{D_a}(\delta_{ik} - B_{ik}), \quad D_a^2 = 1 - (2 - B_{kk})a_{mn}^h B_{nm}, \quad (2.13)$$

where H_{ik} is the partial-projection operator, and D_a^2 is such that the trace of a_{ij} remains unity. The blockage tensor B_{ij} gives the strength and the direction of the projection. If the wall-normal direction is x_2 , then B_{22} is the sole non-zero component, and varies between 0 (no blocking) far enough from the wall, to 1 (full blocking) at the wall. B_{ij} is computed by

$$B_{ij} = \frac{\Phi_{,i}\Phi_{,j}}{\Phi_{,k}\Phi_{,k}} \Phi \quad \text{if} \quad \Phi_{,k}\Phi_{,k} > 0. \quad (2.14)$$

If all gradients of Φ vanish, the denominator in (2.14) has been clipped setting effectively B_{ij} to zero.

The blocking parameter, Φ , is computed by an elliptic relaxation equation

$$L^2 \frac{\partial^2 \Phi}{\partial x_k \partial x_k} = \Phi, \quad L \frac{u_\tau}{\nu} = 23, \quad (2.15)$$

	ϕ_1	β_1	χ_1
$\eta_f < 0$	$\frac{\eta_f - 1}{3\eta_f - 1}$	$\left[1 - b_0 \frac{\eta_f}{(1 - a^2)} \left(1 + \sqrt{(a^2 - 1/3)}\right)\right]^{-1}$	$\frac{1}{2}\beta_1$
$0 < \eta_f < 1$	$(1 - \eta_f)$	1	$\frac{1}{2} + \frac{1}{2} \left[1 - \frac{(1 - \eta_f)^2}{1 + b_1 \eta_f / (1 - a^2)}\right]$
$\eta_f > 1$	$\frac{\eta_f - 1}{3\eta_f - 1}$	$\left[1 + b_2 \frac{(\eta_f - 1)}{(1 - a^2)} \eta_f \sqrt{(a^2 - 1/3)}\right]^{-1}$	$1 - \frac{(1 - \beta_1)(\eta_f - 1)}{(1 - a^2) + (\eta_f - 1)}$

TABLE 1. Turbulence structure scalars: a^2 plane, $\eta_m = 1$ line

	ϕ_0	β_0	χ_0
$\eta_f \leq \sqrt{3}/4$	$0.145 \left[\frac{(2\eta_f)^2}{3/4} - \left(\frac{(2\eta_f)^2}{3/4} \right)^9 \right]$	1	$-\left[0.342 \frac{(2\eta_f)^2}{3/4} + (1 - 0.342) \left(\frac{(2\eta_f)^2}{3/4} \right)^6 \right]$
$\eta_f > \sqrt{3}/4$	$(1 + \chi_0)/3$	$-\chi_0$	$-\left[1 + b_3 \frac{(\eta_f - \sqrt{3}/4)}{(1 - a^2)} \eta_f \sqrt{(a^2 - 1/3)} \right]^{-1}$

TABLE 2. Turbulence structure scalars: a^2 plane, $\eta_m = 0$ line

η_m	ϕ^*	β^*	χ^*
< 1	$\phi_0(\eta_*) + [\phi_1(\eta_*) - \phi_0(\eta_*)]\eta_m^2$	$\beta_0(\eta_*) + [\beta_1(\eta_*) - \beta_0(\eta_*)]\eta_m^2$	$\chi_0(\eta_*) + [\chi_1(\eta_*) - \chi_0(\eta_*)]\eta_m^4$
> 1	$\frac{1/3 + \frac{(\phi_1(\eta_f) - 1/3)}{1 + (\eta_m - 1)/(1 - a^2)}}{1 + (\eta_m - 1)/(1 - a^2)}$	$\frac{\beta_1(\eta_f)}{1 + (\eta_m - 1)/(1 - a^2)}$	$\frac{\chi_1(\eta_f)}{1 + (\eta_m - 1)/(1 - a^2)}$

TABLE 3. Turbulence structure scalars: a^2 plane, interpolation along the (η_m, η_f) directions.
 $\eta_* \equiv -\eta_m + [4/\sqrt{3} + (2 - 4/\sqrt{3})\eta_m]\eta_f$.

with $\Phi = 1$ at solid boundaries, and $\Phi_{,n} \equiv \partial\Phi/\partial x_n = 0$ at open boundaries, where x_n is the direction normal to the boundary.

To recover proper asymptotic behavior of the Reynolds stresses, $r_{12} \propto O(x_2)$ and $r_{22} \propto O(x_2^2)$, as the wall at $x_2 = 0$ is approached, the homogeneous jetal, ϕ^h , and helix, γ^h , parameters are modified using

$$\phi = 1 + (\phi^h - 1)(1 - B_{kk})^2, \quad (2.16)$$

$$\gamma = \gamma^h(1 - B_{kk}). \quad (2.17)$$

A consequence of this approach is that realizability is automatically satisfied for r_{ij} .

3. Rotating channel flow computed with conventional turbulence models combined with ASBM

The steady RANS equations governing the motion of an incompressible viscous fluid in a Cartesian rotating frame of reference are given by conservation of mass and momentum as Greenspan (1968):

$$\frac{\partial u_i}{\partial x_i} = 0, \quad (3.1)$$

$$u_j \frac{\partial u_i}{\partial x_j} + 2\epsilon_{ijk}\Omega_j^f u_k = -\frac{\partial P}{\partial x_i} + \nu \frac{\partial^2 u_i}{\partial x_k \partial x_k} + \frac{\partial}{\partial x_j} \left(-\overline{u'_i u'_j} \right). \quad (3.2)$$

where u_i is the mean velocity measured in the coordinate system rotating with constant angular velocity Ω_j^f , and x_j , P , ρ , and ν represent respectively the position vector, reduced pressure, density and kinematic viscosity. The reduced pressure is given by

$$P = \frac{p}{\rho} + \mathcal{U} - \frac{1}{2}(\epsilon_{ijk}\Omega_j^f x_k)(\epsilon_{lpq}\Omega_p^f x_q), \quad (3.3)$$

where p is the thermodynamic pressure, \mathcal{U} is such that a conservative body force per unit mass (*e.g.* gravity) is given by $\partial\mathcal{U}/\partial x_i$, and the last term represents the centripetal acceleration.

For fully-developed channel flow in a spanwise rotating frame the mean velocity is given by $u_j = u(y)$ where y is the wall normal direction. The frame rotation rate vector is given by $\Omega_j^f = \Omega_z^f$ with z being the spanwise direction. The wall-normal mean velocity component vanishes by continuity for a fully developed channel flow with zero velocity at the walls. This simplifies the momentum equation; only the momentum equation in streamwise direction x needs to be solved and the term containing the angular velocity Ω^f is zero.

The Reynolds stress in equation (3.2) is obtained with the algebraic structure-based procedure described in Section 2. The complete ASBM model, described in Langer & Reynolds (2003), includes two scalar transport equations for the turbulent kinetic energy k and the large-scale turbulent enstrophy ω^2 . The purpose of these two quantities is to provide the field distribution of k and of the turbulence time scale τ . The latter has the following relation to k and ϵ :

$$\tau^2 = \left(\frac{k}{\epsilon} \right)^2 + \left(2.0 \sqrt{\frac{\nu}{\epsilon}} \right)^2. \quad (3.4)$$

In this work, field distributions of k and τ have been obtained from the k - ω model by Wilcox (1993) and v^2 - f model by Lien & Durbin (1996). In addition, low-Re modifications given in Wilcox (1993) for the k - ω model have been considered. For the k - ω model, the time scale is computed as $\tau^2 = 1/(\beta^*\omega)^2 + 4.0\nu/(k\omega\beta^*)$ while equation (3.4) is used directly for v^2 - f which includes transport equations for k and ϵ .

The time scale is used to scale the vorticity Ω_{ij} and strain S_{ij} tensors that are obtained from the mean flow velocity distribution. The blockage tensor B_{ij} is obtained as described above from an elliptic equation. The tensors τS_{ij} , $\tau \Omega_{ij}$ and B_{ij} as well as k and τ and the frame rotation vector $\tau \Omega_j^f$ provide the necessary information for the ASBM Reynolds stresses $\tau_{ij} = -\overline{u'_i u'_j}$.

Following equation (3.2), the Reynolds stress enters only the diffusion term in the momentum equation. In an incompressible RANS flow solver based on a standard SIMPLE

algorithm the diffusion term is usually treated implicitly for stability. This is straightforward when the Reynolds stress is computed over the Boussinesq approximation and an eddy-viscosity is used. With the ASBM procedure the Reynolds stress is computed explicitly and an explicit correction to the momentum equation is used. For the implementation of the ASBM procedure in the IBRANS code by Kalitzin & Iaccarino (2003) the last two terms in equation (3.2) have been re-written as:

$$\frac{\partial}{\partial x_j}[(\nu + \nu_t^n) \frac{\partial u_i^{n+1}}{\partial x_j}] - \frac{\partial}{\partial x_j}[\nu_t^n \frac{\partial u_i^n}{\partial x_j} - \frac{\tau_{ij}^n}{\rho}] \quad (3.5)$$

where n is the current iteration. The terms with the eddy-viscosity are equal to each other when the solution is converged. The eddy-viscosity used is as defined by the k - ω or v^2 - f model.

The Reynolds stress enters only the production term $P_k = \tau_{ij} \partial u_i / \partial x_j$ in the transport equations of the turbulence models. The eddy-viscosity is retained in the diffusion terms and no additional modifications of the turbulence equations have been performed in respect to the frame rotation.

Haire & Reynolds (2003) also looked at using alternative scale equations along with an earlier version of the ASBM, for free shear flows. A few distinctions are present in the current investigation. Briefly, (i) the turbulent transport term in the scale equations has a tensorial form in Haire & Reynolds (2003), whilst here a scalar diffusion model is investigated, for its simplicity makes it possible to use the ASBM in available CFD packages. (ii) Haire and Reynolds concentrated on free shear flows. The analysis here regards wall-bounded flows, and (iii) the algebraic equations that constitute the current ASBM formulation are different from the earlier version explored by them.

The channel flow computations have been performed as streamwise periodic flow with one cell in flow direction. The pressure and velocity components at the outflow have been copied to the inflow and a source term has been added to the momentum equation to account for the pressure loss.

4. Numerical results

Channel flow simulations in orthogonal mode rotation have been performed for a variety of Reynolds and Rossby numbers. The first objective of these simulations is to identify the steps necessary to combine the ASB Reynolds stress evaluation and a *conventional* eddy-viscosity model. As shown earlier the RANS equations are *closed* when the eddy-viscosity is introduced; therefore, the first, preliminary, step is to use the ASB procedure as a post-processing tool to evaluate the Reynolds stresses. Successive steps consist of introducing different levels of coupling between ASB and the overall solution procedure; first, only the mean equations are modified by discarding the eddy-viscosity and evaluating the divergence of the Reynolds stresses directly. Finally, a fully coupled solution is obtained when the Reynolds stresses are also used to close terms in the equations for turbulent quantities. The results obtained are summarized in Fig. 1 for the k - ω and the v^2 - f models in a channel flow without rotation. Not surprisingly, the best match with the experiments is obtained when the full coupling is employed; it is also very interesting to note that the use of ASB as a post-processing is already sufficient to obtain the correct level of anisotropy as opposed to the standard application of the eddy-viscosity models. This situation is clearly a peculiarity of this specific test case because the stress anisotropy does not affect the mean flow transport. Another important observation is

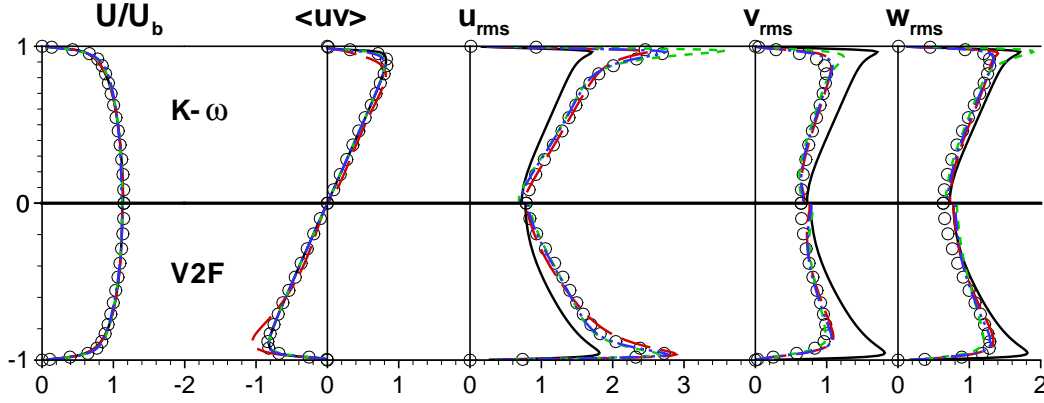


FIGURE 1. Channel flow at $Re = 395$ computed with low- Re $k-\omega$ (upper half) and v^2-f (lower half) models as: — : Reynolds stress computed from Boussinesq approximation for linear model, — : ASB Reynolds stress from linear model, --- : ASB Reynolds stress used only in the mean flow, -.- : ASB Reynolds stress used in the mean flow and in the production term of models, o : DNS by Moser *et al.* (1999).

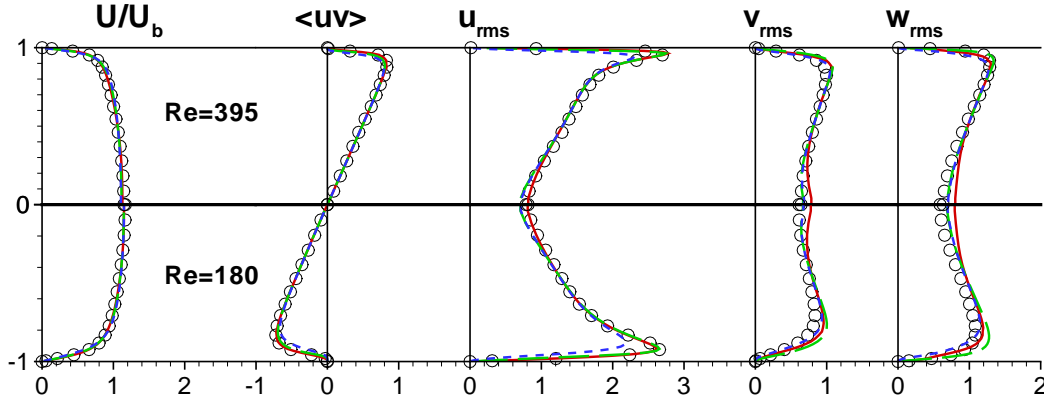


FIGURE 2. Channel flow at $Re = 395$ (upper half) and $Re = 180$ (lower half). — : ASB v^2-f , — : ASB low- Re $k-\omega$, --- : ASB high- Re $k-\omega$, o : DNS by Moser *et al.* (1999).

that the inclusion of the ASB stress evaluation in the turbulent kinetic energy production is necessary to obtain accurate results. It must be noted that in the original ASBM approach by Langer & Reynolds (2003), a tensorial turbulent diffusivity is also included whereas in the present implementation a scalar coefficient is used.

Fig. 2 shows the effect of the Reynolds number for flow without rotation. In this case the high- and low- Re ASB $k-\omega$ as well as the ASB v^2-f models are reported. Here we added the ASB prefix to the models to indicate that the Reynolds stresses are evaluated with the ASB procedure. The latter two produce results that are satisfactory for both Reynolds numbers whereas the high- Re ASB $k-\omega$ under-predicts the peak of the u_{rms} in particular for $Re = 180$.

The application of the fully-coupled approach for the flow in a channel with rotation is reported in Fig. 3 and Fig. 4 for a channel flow at two different Rossby numbers. The Rossby number is defined here as $Ro = \frac{\Omega^f 2h}{u_b}$ where Ω^f is the magnitude of the frame rotation rate, h is the half-height of the channel and u_b is the bulk velocity in the channel.

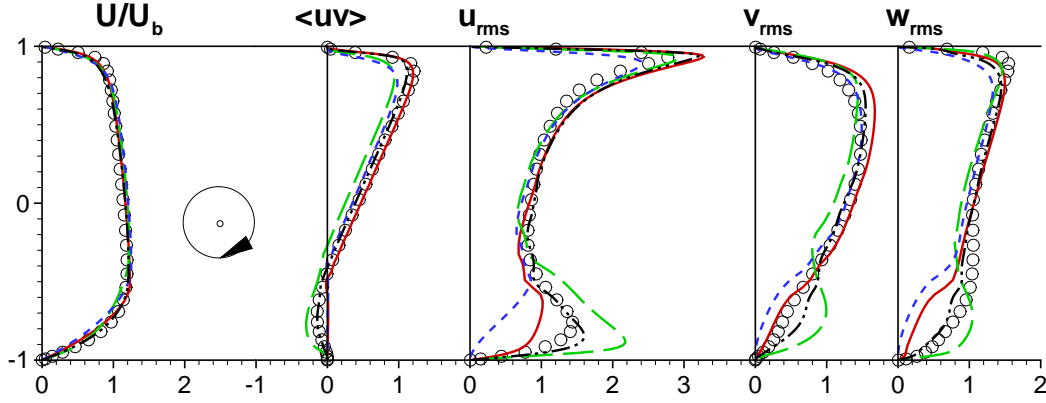


FIGURE 3. Rotating channel flow at $Re = 180$ and $Ro = 0.22$. — : ASB v^2-f , — : ASB low-Re $k-\omega$, --- : ASB high-Re $k-\omega$, - · - : ASBM, o: DNS by Alvelius (1999).

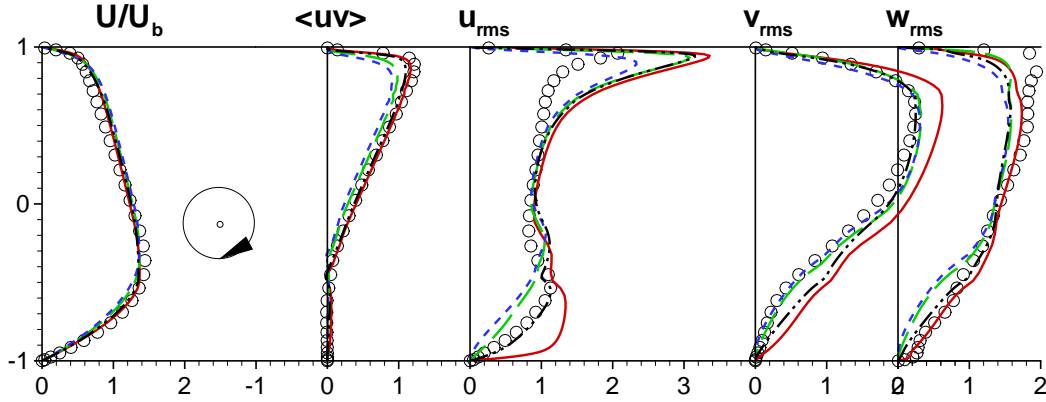


FIGURE 4. Rotating channel flow at $Re = 180$ and $Ro = 0.77$. — : ASB v^2-f , — : ASB low-Re $k-\omega$, --- : ASB high-Re $k-\omega$, - · - : ASBM, o: DNS by Alvelius (1999).

In these plots DNS data and the original ASBM are compared to ASB $k-\omega$ and ASB v^2-f predictions. The asymmetry in the mean velocity profile is properly captured even for the high Rossby case. In addition, the Reynolds stress anisotropy is remarkably close to the DNS results at the turbulence-enhanced side of the channel. Notice that at the pressure-side of the channel (lower side in the Fig. 3 and Fig. 4) turbulence intensity is reduced and, eventually, the turbulent stresses are negligible with respect to the viscous stresses. The correspondence between mean flow predictions and correct level of anisotropy is very encouraging. The difference between the full ASBM approach and the current combined approach is also very small especially when v^2-f is used.

Further simulations have been performed at a variety of Rossby numbers in the $[0 - 0.77]$ interval. The results obtained using the v^2-f and the ASB v^2-f are presented. The mean velocity profile and the turbulent kinetic energy are reported in Fig. 5 and Fig. 6, respectively. As expected from the results previously shown, the current model and the DNS agree remarkably well.

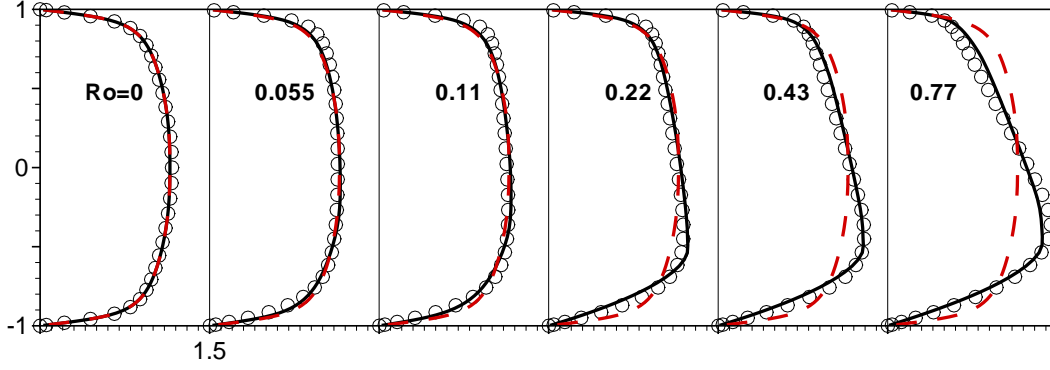


FIGURE 5. Velocity profiles for channel flow at $Re = 180$ and $Ro = 0, 0.055, 0.11, 0.22, 0.43$ and 0.77 ; --- : v^2-f , — : ASB v^2-f , o: DNS by Alvelius (1999)

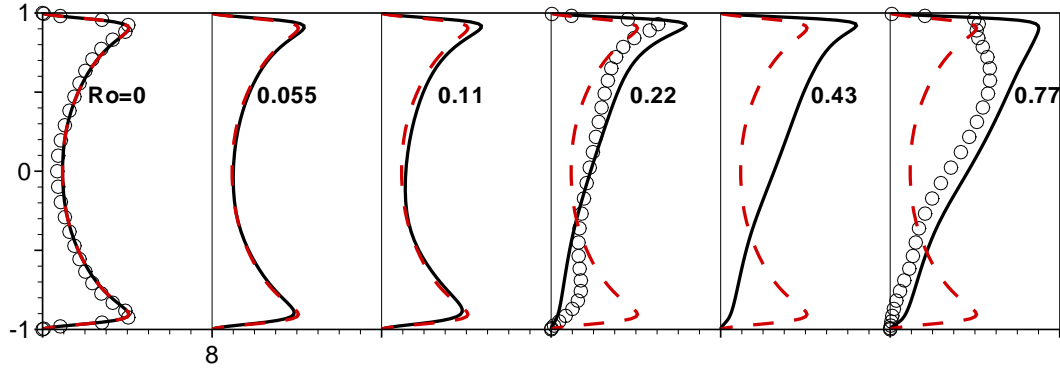


FIGURE 6. Turbulent kinetic energy for channel flow at $Re = 180$ and $Ro = 0, 0.055, 0.11, 0.22, 0.43$ and 0.77 ; --- : v^2-f , — : ASB v^2-f , o: DNS by Alvelius (1999)

5. Conclusions and future plans

The algebraic structure-based model has been used in this work in combination with conventional linear eddy-viscosity models to evaluate the Reynolds stress in the RANS equations. This approach has proven to be very accurate in predicting the mean flow and the stress anisotropy in rotating channel flow as opposed to the baseline eddy-viscosity predictions that are typically insensitive to frame rotation. Several modifications, that have not been reported in this paper, have been introduced to the ASBM model in order to facilitate its application to more general flow problems. In particular, a scalar turbulent diffusion coefficient is introduced in lieu of the original tensorial diffusivity and a modified formulation for the blockage effect that includes a new definition of the relevant length scale has been derived.

The current combination of the ASB Reynolds stress evaluation with the v^2-f and $k-\omega$ models is carried out in a full three-dimensional flow solver. However, only channel flow simulations were performed. Preliminary computations of flows in square-ducts appeared encouraging. Convergence for this flow was poor indicating that further work on

the numerical scheme and the ASB algorithm is needed. Current work focuses on the clarification of this issue.

REFERENCES

- ALVELIUS K. 1999 Studies of Turbulence and its Modeling through Large Eddy- and Direct Numerical Simulation. *Ph.D. thesis*, Dept. Mech. Eng., KTH, Stockholm, Sweden.
- DURBIN, P. A. & PETTERSSON REIF B. A. 2001 *Statistical Theory and Modeling for Turbulent Flows*. John Wiley & Sons.
- GATSKI, T.B. & SPEZIALE, C.G. 1993 On explicit algebraic stress models for complex turbulent flows. *J. Fluid Mech.*, **254**, 59-78.
- GREENSPAN, H.P. 1968 *The Theory of Rotating Fluids*. Cambridge University Press.
- HAIRE, S., L. & REYNOLDS, W. C. 2003 Toward an Affordable Two-Equation Structure-Based Turbulence Model. *Technical Report No. TF-84*, Mech. Eng. Dept., Stanford Univ.
- KALITZIN, G. & IACCARINO G. 2003 Toward Immersed Boundary Simulation of High Reynolds Number Flows. *CTR Annual Research Briefs*, 369-378.
- KASSINOS, S.C. & REYNOLDS, W.C. 1994 A Structure-Based Model for the Rapid Distortion of Homogeneous Turbulence. *Technical Report TF-61*. Mech. Eng. Dept., Stanford Univ.
- KASSINOS, S.C., REYNOLDS, W.C., & ROGERS, M.M. 1993 One-Point Turbulence Structure Tensors. *J. Fluid Mech.*, **249**, 337-71.
- KASSINOS S.C., LANGER C.A., HAIRE S.L. & REYNOLDS W.C. 2000 Structure-Based Turbulence Modeling for Wall-Bounded Flows. *Int. J. Heat Fluid Flow*, **21**, 599-605.
- LANGER, C. A. & REYNOLDS, W. C. 2003 A New Algebraic Structure-Based Turbulence Model for Rotating Wall-Bounded Flows. *Technical Report No. TF-85*, Mech. Eng. Dept., Stanford Univ.
- LIEN, F. S. & DURBIN, P. A. 1996 Non-linear $k-\epsilon-v^2$ modeling with application to high-lift. *CTR summer proceedings*.
- MOSER R., KIM J. & MANSOUR N. 1999 Direct Numerical simulation of turbulent channel flow up to $Re_\tau = 590$ *Phys. Fluids*, **11**, 943-945.
- REYNOLDS W.C. 1994 Towards a Structure-Based Turbulence Model. In T. B. Gatski, S. Sarkar, and C. G. Speziale (Eds.), *Studies in Turbulence*. Lumley 60th birthday Symposium, 76-80, Springer-Verlag, New York.
- REYNOLDS W.C., KASSINOS S.C., LANGER C.A. & HAIRE S.L. 2000 New Directions in Turbulence Modeling. Presented at the *Third International Symposium on Turbulence, Heat, and Mass Transfer*. Nagoya, Japan April 3-6. Available at url:<http://asbm.stanford.edu/asbm.ps>.
- SHIH, T. H., LIOU, W. W., SHABBAR, A. & ZHU J 1995 A new $k-\epsilon$ eddy-viscosity model for high Reynolds number turbulent flows. *Comp. Fluids* **24** 227-238.
- WALLIN S. & JOHNASSEN A. V. 2002 Modelling streamline curvature effects in explicit algebraic Reynolds stress turbulence models. *Int. J. Heat and Fluid Flow*, **23** (5), 721-730.
- WILCOX D. C. 1993 Turbulence Modeling for CFD. *DCW Industries Inc.*, La Canada, California.

Synthetic jet modeling for U-RANS

By F. Capizzano[†] AND G. Iaccarino

This work focuses on different approaches for the numerical simulation of a Synthetic Jet device via RANS codes. The objective is to explore possible RANS techniques to utilize in a more general design loop with flow control purposes. A turbulent flow over a hump model with a contoured slot in three different working conditions (no-flow control, steady suction and oscillatory control) is considered for our validation tests. The device itself is not simulated but its effects are modeled using specially designed boundary conditions (BC). Comparisons of numerical results obtained with various BC formulations and experimental data are carried out.

In the second part of the paper a preliminary study of a lumped model in which the time averaged flow field is resolved using a steady state approach is presented. A source term is added in the momentum equation to account for the unsteadiness generated by the pulsating jet. The source term is related to a scalar quantity whose field is governed by a classical convection-diffusion type transport equation.

1. Introduction

The study of devices for controlling the boundary layer characteristics is receiving renewed interest due to the introduction of a new family of piezoelectric actuators named Synthetic Jets (SJ). They consist of a deforming membrane oscillating into a close cavity. A periodic suction/blowing flow is established at its small exit orifice. SJs add momentum into the external boundary layer like classical continuous jets but have the advantages of requiring low electrical power supply and no piping. A good review of SJ applications along with unresolved questions has been given by Kral *et al.* (1997).

Computational fluid dynamics is currently heavily used to investigate both the basic operating principles of SJs; in the near future fast, reliable prediction tools based on CFD will be required to design control systems based on these devices. Direct numerical simulations and large eddy simulations have been performed with good results (Catalano *et al.* 2002; Conrad *et al.* 2002; Rumsey *et al.* 2004). These simulations, though of key interest for the understanding of complicated interactions between an external cross flow and a single SJ, require massive resources and are too time consuming when used to answer to practical aerodynamic design questions (such as the number and positions of the actuators over a wing). On the contrary Reynolds-Averaged Navier-Stokes (RANS) simulations offer sufficient predicting performances with relative low computational costs. In this paper, we are interested in evaluating the feasibility and the accuracy of RANS modeling for the simulation of turbulent flows controlled by synthetic jets. Recently a workshop (CFDVAL2004) on numerical simulation of synthetic jets and turbulent separation control was held under joint sponsorship by NASA and ERCOFTAC. Results collected in Rumsey *et al.* (2004) illustrate the substantial equivalence between BC models and direct simulation of the cavity (plenum) flow. This was partly due to the inherent difficult characterization of the membrane motion that introduces uncertainties. Another

[†] CIRA Italian Aerospace Research Center, Via Maiorise 81043 Capua (CE), Italy

interesting question raised at the workshop was: is it possible to capture the unsteady effects of a SJ in an external boundary layer as a steady problem?

In previous works such as Kral *et al.* (1997) and Iaccarino *et al.* (2003), RANS modeling coupled with specific boundary conditions is preferred to an explicit simulation of the jet cavity. Several contributors in the CFDVAL2004 workshop used BC models especially for the hump model case (separation control). This case has been studied experimentally in the NASA Langley Transonic Cryogenic Tunnel with CFD validation in mind. A low mach number 2D flow ($Mach = 0.1$) passes over a hump wall; in the recovery region a slot exit is applied to control the natural separation bubble. The first part of the paper deals with steady/unsteady simulations in which an appropriate boundary condition model is applied at the slot exit.

The objective of the second part of our research project was to investigate the feasibility of a lumped model to approximate synthetic jets in the context of steady-state RANS simulations. The rationale is that synthetic jets inject momentum in the external flow but do not add mass (as opposed to conventional active control devices based on blowing). This implies that, if we solve the steady-state governing equations with suitable forcing terms in the momentum equations, we will be able to duplicate the time-average effect of an oscillating jet. The idea of unsteady phenomena modeled as a body force goes back to Lighthill acoustic streaming theory. Recently Riley (2001) developed a theory for an oscillatory nonconservative body force in homogeneous fluids. Pes *et al.* (2002) add, in the momentum equation, a source term containing information about unsteady characteristics of the SJ/crossflow interactions. They evaluate the source term using a deterministic neural-network based code. The real difficulty is related to the evaluation of the source term. The method proposed here links the source term to a scalar field containing information about SJ characteristic parameters identified by experimentalists, Glezer & Amitay (2002), Smith *et al.* (2003) (e.g. the stroke length L_0 and the impulse associated with the discharge phase I_0). An expression for the source term is proposed along with the scalar field transport equation and the relative boundary condition.

2. Numerical method

The numerical analysis presented here has been carried out using the CIRA U-ZEN multi-zone flow solver (Catalano *et al.* 2003). It is a multiblock structured grid code able to solve steady and unsteady compressible Reynolds-Averaged Navier-Stokes equations around complex 3D geometries. A cell-centered finite volume approach with Jameson-type artificial dissipation is used as a discretization technique for the equations in conservation form. A steady state solution is obtained using an iterative multistage Runge-Kutta scheme which is accelerated using a local time stepping process and an implicit residual averaging. Geometric multigrid based on the the RK scheme is used to accelerate the convergence to steady state. Time-accurate solutions are obtained using a dual time stepping method. Several eddy viscosity turbulence models are available in U-ZEN including non linear models. All the numerical tests have been performed assuming a fully turbulent 2D incompressible flow ($Mach = 0.1$) using Myong & Kasagi (1990) $\kappa - \epsilon$ and the Menter (1994) SST $\kappa - \omega$ as closure models. Some modifications have been introduced in the original version of U-ZEN for a correct integration of SJ boundary condition models.

3. Boundary condition model

In this section the boundary condition models adopted for the steady and unsteady simulations are discussed. Hereafter a non-dimensional formulation is considered based on the free-stream flow quantities and the hump chord, c . As outlined above, the SJ effect on the external boundary layer is modeled by a space and time dependent jet-velocity distribution

$$\mathbf{u} = \mathbf{U}_J(\xi, \eta, t) \quad (3.1)$$

where (ξ, η) is a curvilinear reference system along an imaginary line leveled with the hump surface and $\mathbf{U}_J = U_{Jn}\hat{\eta} + U_{Jt}\hat{\xi}$.

3.1. Steady model

For a steady blowing/suction control analysis, the coefficients of mass and momentum at the slot exit are considered

$$C_{\dot{m}} = \rho_J U_{Jn} h \quad (3.2)$$

$$C_{\mu} = 2\rho_J U_J^2 h \quad (3.3)$$

respectively, where $\rho_J = \rho_J^*/\rho_{\infty} = 1$, $U_J = U_J^*/U_{\infty}$ and $h = h^*/c$ are the non-dimensional jet density, velocity and slot width. The first option to model $\mathbf{U}_J(\xi, \eta, t)$ is a top-hat velocity distribution based on the integral information $C_{\dot{m}}$

$$\text{1st model} \quad \begin{cases} U_{Jn} = C_{\dot{m}}/\rho_j/h \\ \mathbf{u}(\xi) = U_{Jn}\hat{\eta} \end{cases} \quad (3.4)$$

In this case C_{μ} is not directly used but rather verified *a posteriori*. A similar BC was chosen by Viken *et al.* (2003) for their numerical tests. Their results show discrepancies in the pressure recovery region between numerical and experimental data as for suction and blowing. As pointed out by the authors many factors, such as the BC model deficiencies, turbulence model and 3D effects during experiments, play a role. Analogous discrepancies were found by Iaccarino *et al.* (2003) who also compared numerical solutions with and without cavity flow. A second option, as described by Marongiu *et al.* (2004), is to take advantage of both integral information $C_{\dot{m}}$ and C_{μ} to introduce a tangential component U_{Jt} at the slot exit

$$\text{2nd model} \quad \begin{cases} U_{Jn} = C_{\dot{m}}/\rho_j/h \\ U_{Jt} = U_{Jn} \tan(\theta) \\ \tan(\theta) = \sqrt{C_{\mu}/(2U_{Jn}^2 h)} \\ \mathbf{u}(\xi) = U_{Jn}\hat{\eta} + U_{Jt}\hat{\xi} \end{cases} \quad (3.5)$$

Top-hat velocity distributions used in the above two models are poor approximations of the complex flow near the orifice. A further BC model uses a spatially varying velocity distribution at the SJ cavity, using zero gradient extrapolation from the domain interior. During the iterative process, to ensure the correct integral mass flow rate, the following

procedure is used

$$\text{3rd model} \quad \left\{ \begin{array}{l} U_{Jn} = C_{\dot{m}}/h \\ \frac{\partial}{\partial \eta} \mathbf{u}(\xi) = 0 \implies \mathbf{u}(\xi)|_{extrapol.} \\ \Delta \mathbf{u}(\xi) = U_{Jn} \hat{\xi} - \mathbf{u}(\xi)|_{extrapol.} \\ \mathbf{u}(\xi) = \mathbf{u}(\xi)|_{extrapol.} + \Delta \mathbf{u}(\xi) \end{array} \right. \quad (3.6)$$

The procedure based on (3.6) is physically correct in the case of suction but it does not satisfy the characteristics of blowing because no information, except for the pressure field, can be extrapolated from inside the domain. A revised procedure (3.6) for blowing starts from the following extrapolation:

$$\frac{\partial}{\partial \eta} p(\xi) = 0 \implies p(\xi)|_{extrapol.} \quad (3.7)$$

A fully developed incompressible laminar flow coming from the slot duct can be assumed and a pressure-corrected velocity distribution, on center line, is derived as

$$\text{blow correction} \quad \left\{ \begin{array}{l} U_{Jn} = \sqrt{(2/3C_{\dot{m}}/h)^2 + 2(1 - p(\xi)|_{extrapol.})} \\ \mathbf{u}(\xi) = U_{Jn} \hat{\eta} \end{array} \right. \quad (3.8)$$

This correction takes the place of $\frac{\partial}{\partial \eta} \mathbf{u}(\xi) = 0$ in the procedure (3.6).

An additional modification can be included to account for the exact geometrical shapes in proximity of the slot exit

A Neumann boundary condition on the orifice exit for the turbulent variables is enforced for each of the three models.

3.2. Unsteady model

During oscillatory suction/blowing, a zero net mass flux through the orifice is established:

$$\frac{1}{T} \int_0^T \mathbf{u}(\xi, t) dt = 0 \quad (3.9)$$

where $T = 1/f$ is the device forcing period.

Although there is no guarantee that this integral condition is satisfied locally each point on the orifice and given the limited experimental information for the spatial and temporal variations, we simply use the membrane forcing as the one-mode frequency:

$$C_{\dot{m}}(t) = \rho_j h U_J^{max} \sin(2\pi f t) \quad (3.10)$$

where f is the suction/blowing frequency and U_J^{max} is the peak velocity out of slot during blowing part of the cycle. The application of the three spatial model (3.4), (3.5) and (3.6), requires the instantaneous mass flux condition

$$\frac{1}{h} \int_0^\xi \mathbf{u}(\xi, t) d\xi = C_{\dot{m}}(t) / \rho_j / h \quad (3.11)$$

Compared to the first and second models, this means a constant velocity distribution which remains self-similar when modulated by a certain time frequency. Otherwise when

the third model is applied, the resulting $\mathbf{u}(\xi)$ can change its spatial form during the temporal process, thus obtaining a new way of characterizing the expression (3.1).

As for steady simulations, a Neumann condition is assumed for the turbulent variables.

4. The hump model case

The configuration selected for the present study is a $2D$ channel flow with a bottom wall mounted Glauert-Goldschmied half-airfoil (Figs. 1 and 2). The non-dimensional domain based on the hump chord length ($c = 0.42m$) extends approximately $2c$ and $4c$ upstream and downstream of the hump respectively and $0.9c$ in the normal direction. A collection of experimental data are available for the steady cases (base-flow and steady suction) at a Reynolds and Mach number of $Re = 9.36 \times 10^5$ and $M_\infty = 0.1$ based on a free-stream velocity $U_\infty = 34.6m/s$. Two end-plates in the span-wise direction are used in the experiment to guarantee a nominal $2D$ flow in the center plane; they introduce a considerable blockage effect and, therefore, in the simulations a contoured shape of the top wall is introduced to mimic the acceleration introduced by the plates. In the no-flow control case a natural separation occurs near 65% of the chord followed by a reattachment near the $x/c = 1.11$ location. The resulting separation bubble extends $\Delta/c = 0.435$ approximately. A slot is introduced near 65% chord to control flow separation. Two computational single-block grids are built both counting 728×198 cells at the finest of three grid levels, having a first cell height $\Delta y/c$ of $1 \cdot 10^{-5}$; this leads to an acceptable resolution of the viscous sublayer ($y^+ \leq 0.5$). The two grids differ in the contouring of the upper wall shape. The cavity region is not meshed and the slot exit is discretized using 64 grid cells in the stream-wise direction with clustering near the corners. In Table 1 are summarized the boundary conditions adopted for the no flow-control case simulations. Experimental velocity u profile is prescribed at the inflow along with a turbulent kinetic energy (k) distribution derived by the available experimental turbulent stresses u'^2 using an empirical correlation to link the root-mean-squared turbulent velocities u' , v' and w' (fully-developed turbulent boundary layer on a flat plate)

$$k = \frac{1}{2}(u'^2 + v'^2 + w'^2) \approx \frac{1}{2}[u'^2 + (\frac{1}{2}u')^2 + (\frac{3}{4}u')^2] = .90625 \cdot (u')^2 \quad (4.1)$$

In Figs. 3 and 4, C_P and C_f distributions are compared using the two grids described above. The corrected top wall grid matches more closely the expansion peak and therefore the pressure plateau into the bubble. Hereafter we present only results obtained on the profiled upper wall grid. The C_P and C_f distributions, obtained with SST $\kappa-\omega$ and $\kappa-\epsilon$ closure models, are compared in Figs. 5 and 6. Both models produce acceptable expansion peak (at the beginning of the recovery region) and pressure level inside the bubble. On the contrary they over-predict the recirculation zone extension delaying the experimental reattachment point from $x/c \approx 1.11$ to $x/c = 1.62$, using $\kappa-\epsilon$, and $x/c = 1.27$ using $\kappa-\omega$. Comparisons of stream-wise velocity (Figs.7 and 8) and turbulent kinetic energy (Figs.9 and 10) in two stations fore (65% chord) and aft (80% chord) the slot exit suggest a low level of turbulent shear stress. It is evident inside the bubble (Fig. 10) an under-prediction of the turbulent kinetic energy respect to the experimental data.

5. Separation control: results and discussions

Steady and unsteady separation control are analyzed in this section. A detailed experimental database is available for steady suction (CFDVAL2004) allowing a sufficient

TABLE 1. No-flow control case: boundary conditions

	u	v	p	κ
<i>Inflow</i>	experim.	0	experim.	experim.
<i>Outflow</i>	extrapol.	extrapol.	$p/p_\infty = 0.99944$	extrapol.
<i>Upper – wall</i>	slip	slip	extrapol.	κ_∞
<i>Bottom – wall</i>	no-slip	no-slip	extrapol.	0

calibration of the numerical boundary conditions. The experimental steady suction mass flow rate is $C_{\dot{m}} = 1.509 \cdot 10^{-3}$ reported to the slot exit width $h/c = 4.5 \times 10^{-3}$ at level with the hump surface. Three kinds of steady boundary condition are explored. Numerical tests, not reported here, show little difference between these three BC models in terms of C_p and C_f distributions. For brevity only the results obtained with the 3rd model are reported. Steady suction pressure coefficient (Fig. 11) shows an acceptable pressure level in the separation bubble but its extension is over-predicted compared to the experimental data. Skin friction comparison (Fig. 12) confirms this deficiency even if the bubble extension reduction ($\approx 25\%$) is of the same order of experimental one. Comparisons of stream-wise velocity and turbulent kinetic energy at two stations upstream (65% chord) and downstream (80% chord) the slot exit are shown in Figs. 13–16. As expected, the main reason for the over-predicted bubble extension is due to low mixing in the separated region (Fig. 16).

Unsteady computations are carried out applying the third BC model with the blow-phase correction (3.8). This one is less stiff in respect to top-hat BC models which impose singularities at the slot exit corners. Turbulence closure is obtained by Myong & Kasagi $\kappa - \varepsilon$ model. An experimental zero-net-mass-flux oscillatory suction/blowing frequency of $f = 138.5Hz$ is imposed. Peak velocity out of slot during blowing part of cycle is $U_j^{max} = 26.6m/s$. Its position is unknown. The non-dimensional forcing period is $T = U_j^{max} / (fc) = 1/St = 0.5948$ (where St is the Strohal number) is divided into 720 time steps. To ensure periodicity, a number of 20 synthetic jet characteristic cycles are carried out. When periodicity is achieved a further cycle is run to average the flow field. A comparison between numerical and experimental mean C_p distribution, Fig. 17, shows a qualitative feasibility of the BC model in place of a complete SJ device simulation. The quality of the prediction (cfr. Figs. 18 and 19) can be improved using a different turbulence model, e.g. $SST\kappa - \omega$ model, as verified in the steady cases. In the Fig. 20, u and v velocity power spectra in two zones of the controlled boundary layer are reported: $x/c = 0.86$ (steady bubble zone), $x/c = 2.0$ (downstream reattachment point). The forcing frequency and its harmonics are clearly represented within the flow.

6. A preliminary study of a body force approach for a time averaged steady state simulation: a simple laminar case

Steady state approach to periodic unsteady phenomena has been formalized in the *steady streaming* theory for homogeneous fluids (Riley 2001). When an oscillating non-conservative forcing (of the form $\sin(\omega t)$) is present in an incompressible flow field, fluctuating vorticity is generated inside the fluid. At leading order, the above vorticity field has non-zero time-average value. This concept is utilized by Pes *et al.* (2002) to approach

the problem of a synthetic jet from a steady point of view. They model synthetic jet unsteadiness using a neural network-based deterministic source term which is added to the right hand side of the momentum equations. However repeated unsteady computations are necessary to train the neural network based algorithm with different combination of the input parameters. Here an alternative way of obtaining the source term is illustrated. The basic idea is to use a scalar to describe the momentum transfer from the synthetic jet to the external flow. Experimental studies of Glezer & Amitay (2002) and Smith *et al.* (2003) of synthetic jet fluid mechanics in cross flow, identify characteristic length and velocity scales

$$L_0 = \int_0^{T/2} u_0(t) dt \quad (6.1)$$

$$U_0 = L_0 f = f \int_0^{T/2} u_0(t) dt \quad (6.2)$$

where $u_0(t)$ is the center line velocity averaged over the area of the orifice and $T = 1/f$ is the oscillation period. It is natural to relate the transported scalar to these quantities. One choice is the product of the oscillating frequency and the velocity scale U_0 (this quantity has the dimension of an acceleration, i.e. is appropriate as a momentum body force)

$$\phi = fU_0. \quad (6.3)$$

The value of this scalar quantity is known at the jet orifice and it is there prescribed as a boundary condition (note that the orifice is a no-slip boundary for the steady-state mean flow). The evolution of the scalar is governed by a convection/diffusion equation. The momentum transfer is described via a body force \mathbf{F} on the basis of the scalar value and eventually its gradient

$$\mathbf{F} = L_0 \nabla \phi \quad (6.4)$$

In order to design the corresponding forcing terms, we performed few simulations of a synthetic jets in a time-accurate mode and then extracted, for each case, the "exact" forcing terms that would reproduce the time-averaged flow field. These forcing terms have been derived in terms of the most important design parameters for synthetic jets: frequency, maximum blowing velocity, cross-flow velocity and Reynolds number, etc. The configuration selected is a simple two-dimensional jet in a flat plate boundary layer. Initial work during the summer has focused on the construction of this database of time-accurate solutions. Preliminary results are very encouraging.

7. Future works

Unsteady RANS simulations have been carried out for flows with active flow control devices. The present results demonstrate a qualitative capability of modeling synthetic jets using simple boundary conditions. The details of the velocity distributions at the orifice exit do not seem to have a strong influence on the results. Turbulent variables of closure models are treated, at orifice, with a zero gradient conditions: more sophisticated conditions will be explored in the future.

A preliminary work has been carried out to develop a scalar transport equation for the modeling synthetic jets in a steady-state fashion. The major advantage of this approach is that once the tuning is completed, the present procedure can be implemented in a close-form within any CFD code. If it is successful, the proposed model would be substantially

faster than conventional time-dependent methods to study these control devices, and would make design and optimization of active flow control systems affordable.

8. Acknowledgments

The authors wish to thank Dr. N. Mansour at NASA Ames, and Prof. Paul Durbin at Stanford University, for the helpful discussions during the summer program and Dr. D. You for reviewing the manuscript.

REFERENCES

- CATALANO, P., WANG, M., IACCARINO, G., SBALZARINI, L. & KOUMOUTSAHOS, P. 2002 Optimization of cylinder flow control via actuators with zero-mass flux. *Proc. of 2002 Summer Program*, Center for Turbulent Research, 297–304.
- CATALANO, P., AMATO, M. 2003 An evaluation of RANS turbulence modeling for aerodynamic applications. *Aerospace science and Technology*, **7-7**, 493–590.
- CONRAD, Y. L. & GOLDSTEIN, D.B. 2002 Two-dimensional synthetic jet simulation. *AIAA J.* **40**, 510–516.
- GLEZER, A. & AMITAY, M. 2002 Synthetic jets. *Annu. Rev. Fluid Mech.* **34**, 503–529.
- IACCARINO, G., MARONGIU, C., CATALANO, P., AMATO, M. 2003 RANS simulation of the separated flow over a bump with active control. *Annual Research Briefs*, Center for Turbulence Research, NASA Ames/Stanford University.
- KRAL, L. D., DONOVAN, J. F., ALAN, B. C. & CARY, A. W. 1997 Numerical simulation of synthetic jet actuators. *AIAA Paper* 1997-1824.
- MARONGIU, C., IACCARINO, G., CATALANO, P., AMATO, M. 2004 CASE 3: Investigation of a boundary condition model for the simulation of controlled flows. *CFD Validation Workshop on Synthetic Jets and Turbulent Separation Control*. **1**, March 29-31 Williamsburg, Virginia.
- MENTER, F. R. 1994 Two equation eddy viscosity turbulence models for engineering applications. *AIAA J.* **32**, 1598–1605.
- MYONG, H., KASAGI, N. 1990 A new approach to the improvement of the $\kappa - \varepsilon$ turbulence model for wall bounded shear flows. *JSME Intern. J.* **33-1**, 63–72.
- PES, M., LUKOVIC, B., ORKWIS, P. & TURNER, M. 2002 Modeling of two dimensional synthetic jet unsteadiness using neural network-based deterministic source terms. *AIAA Paper*. 2002-2860.
- RILEY, N. 2001 Steady streaming. *Annu. Rev. Fluid Mech.* **33**, 43–65.
- RUMSEY, C.L., GATSKI, T.B., SELLERS, W.L., VATSA, S.A., VIKEN, S.A. 2004 Summary of the 2004 CFD validation workshop on synthetic jets and turbulent separation control. *AIAA Paper*. 2004-2217.
- SMITH, B.L., SWIFT, G.W. 2003 A comparison between synthetic jets and continuous jets. *Experiments in fluids*. **34**, 467–472.
- VIKEN, S. A., VATSA, V. N., RUMSEY, C. L., CARPENTER, M. H. 2003 Flow control analysis of the hump model with RANS tools. *AIAA Paper* 2003-0218.
- RUMSEY, C.L., GATSKI, T.B., 2004 CFD validation of synthetic jets and turbulent separation control. *Contributed Papers*. vol. 1-3. <http://cfdval2004.larc.nasa.gov/>.

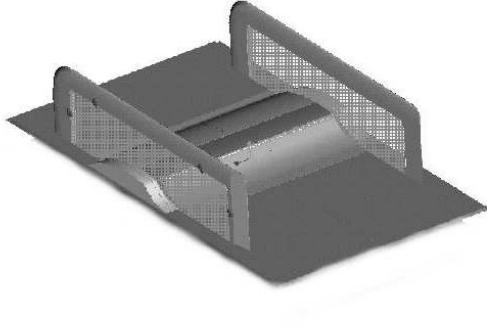


FIGURE 1. Hump model experimental set-up.

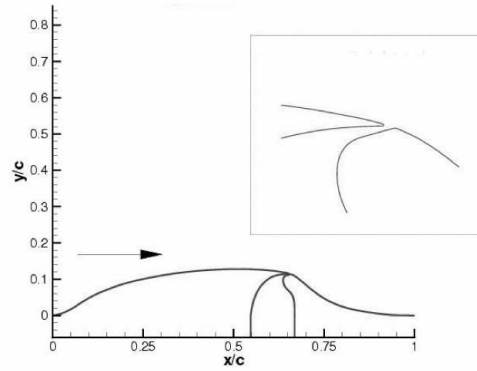
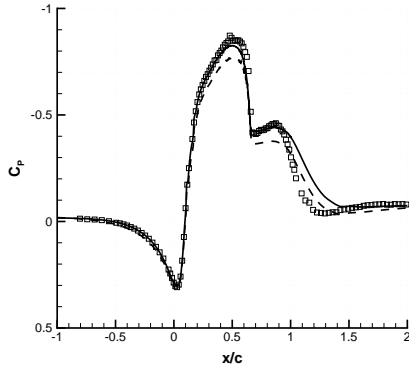
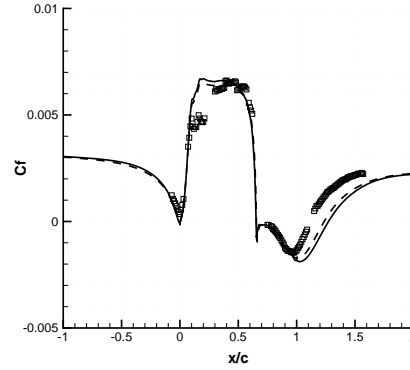
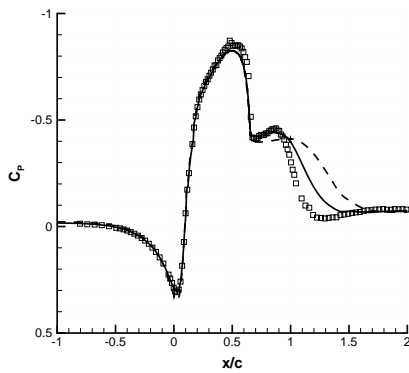
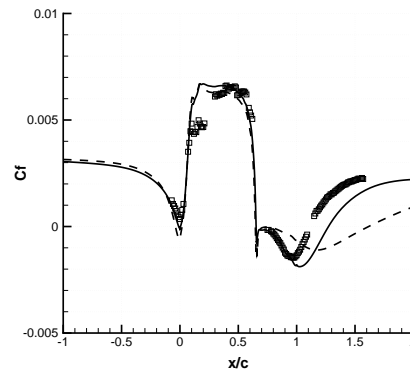


FIGURE 2. Hump model: 2D sketch.

FIGURE 3. No control c_p : Exp. (symbol), contoured top wall grid (solid), flat top wall grid (dashed).FIGURE 4. No control c_f : Exp. (symbol), contoured top wall grid (solid), flat top wall grid (dashed).FIGURE 5. No control case c_p : Exp. (symbol), SST $\kappa-\omega$ (solid), $\kappa-\epsilon$ Myong & Kasagi (dashed).FIGURE 6. No control case c_f : Exp. (symbol), SST $\kappa-\omega$ (solid), $\kappa-\epsilon$ Myong & Kasagi (dashed).

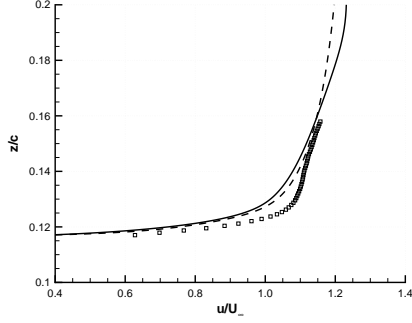


FIGURE 7. No control case: stream-wise velocity at $x/c = 0.65$. Exp. (symbol), SST $\kappa-\omega$ (solid), $\kappa-\varepsilon$ Myong & Kasagi (dashed).

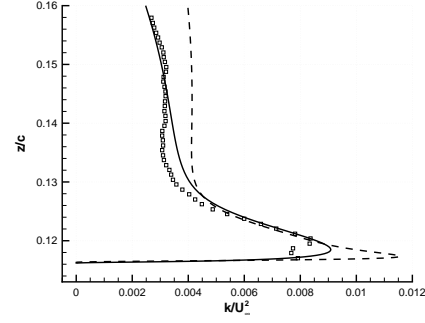


FIGURE 8. No control case: turbulent kinetic energy at $x/c = 0.65$. Exp. (symbol), SST $\kappa-\omega$ (solid), $\kappa-\varepsilon$ Myong & Kasagi (dashed).

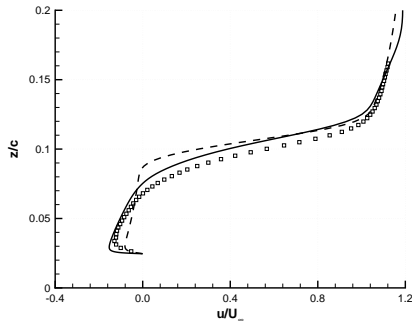


FIGURE 9. No control case: stream-wise velocity at $x/c = 0.80$. Exp. (symbol), SST $\kappa-\omega$ (solid), $\kappa-\varepsilon$ Myong & Kasagi (dashed).

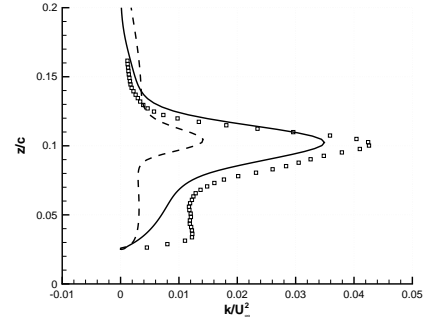


FIGURE 10. No control case: turbulent kinetic energy at $x/c = 0.80$. Exp. (symbol), SST $\kappa-\omega$ (solid), $\kappa-\varepsilon$ Myong & Kasagi (dashed).

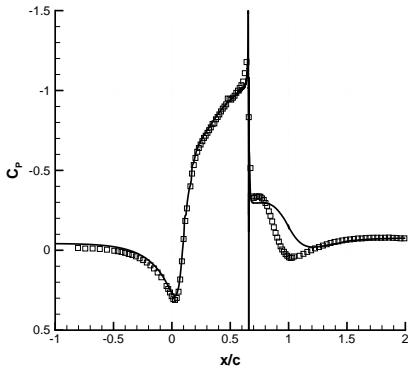


FIGURE 11. Steady suction c_p : Exp. (symbol), SST $\kappa-\omega$ (solid).

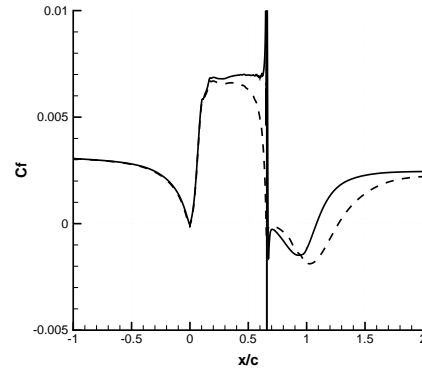


FIGURE 12. c_f distribution with SST $\kappa-\omega$: steady suction (solid), baseflow (dashed).

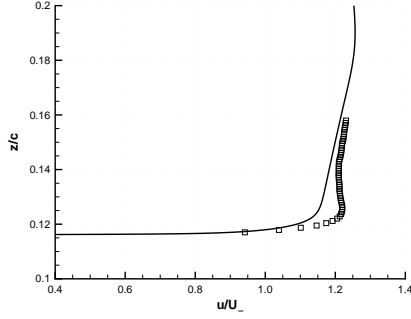


FIGURE 13. Steady suction: stream-wise velocity at $x/c = 0.65$. Exp. (symbol), SST $\kappa - \omega$ (solid), $\kappa - \varepsilon$ Myong & Kasagi (dashed).

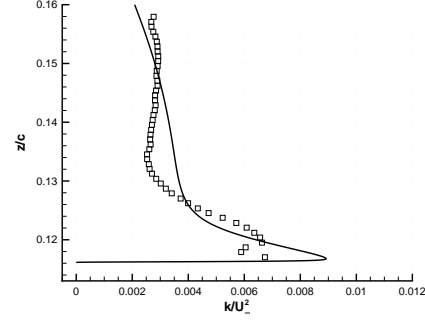


FIGURE 14. Steady suction: turbulent kinetic energy at $x/c = 0.65$. Exp. (symbol), SST $\kappa - \omega$ (solid), $\kappa - \varepsilon$ Myong & Kasagi (dashed).

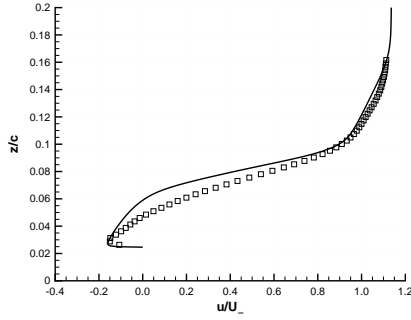


FIGURE 15. Steady suction: stream-wise velocity at $x/c = 0.80$. Exp. (symbol), SST $\kappa - \omega$ (solid), $\kappa - \varepsilon$ Myong & Kasagi (dashed).

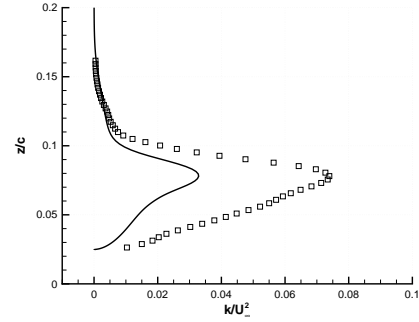


FIGURE 16. Steady suction: turbulent kinetic energy at $x/c = 0.80$. Exp. (symbol), SST $\kappa - \omega$ (solid), $\kappa - \varepsilon$ Myong & Kasagi (dashed).

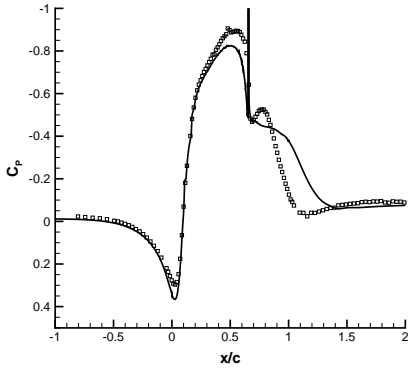


FIGURE 17. Unsteady case; mean c_p : Exp. (symbol), $\kappa - \varepsilon$ Myong & Kasagi (solid).

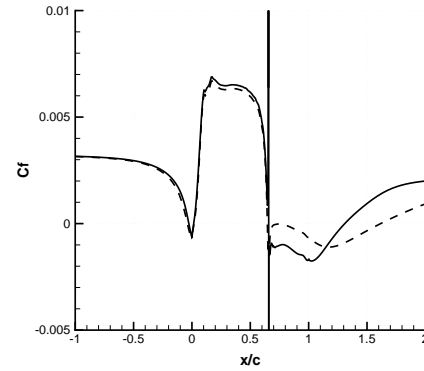


FIGURE 18. Unsteady case; mean c_f : base-flow (dashed), oscillatory control (solid) . $\kappa - \varepsilon$ Myong & Kasagi model.

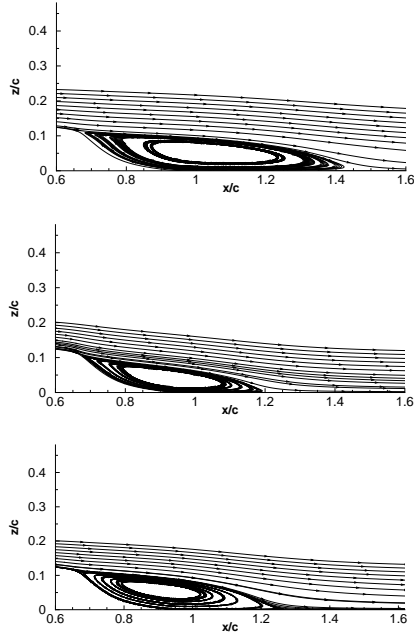


FIGURE 19. Separation bubble: no control (top), steady suction (middle), synthetic jet (bottom). $\kappa - \varepsilon$ Myong & Kasagi.

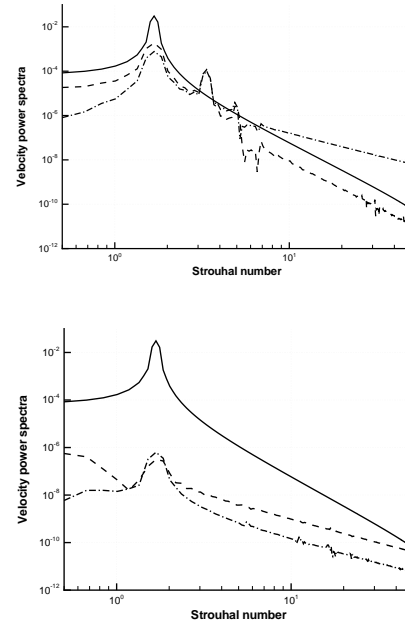


FIGURE 20. Velocity component power spectra in the boundary layer: $x/c = 0.86$ steady bubble zone (top), $x/c = 2.0$ downstream reattachment point (bottom). velocity magnitude (solid), u component (dashed), v component (dash-dot).

Numerical simulation of a low speed fan blade

By Stéphane Moreau [†]
G. Iaccarino, S. Kang, Y. Khalighi AND M. Wang

The feasibility of using various unsteady turbulence models for the prediction of the wall pressure fluctuations or self-noise sources on a Controlled Diffusion airfoil is evaluated. The aim is to find a possible alternative to a classical body-fitted Large Eddy Simulation for a complex automotive engine cooling fan blade. These unsteady simulations have been compared to wall pressure and wake velocity profiles measured in the large anechoic chamber of Ecole Centrale de Lyon, and to a reference body-fitted Large Eddy Simulation using the dynamic subgrid scale model previously achieved at CTR.

1. Introduction

Broadband self noise or trailing edge noise is due to the scattering of boundary layer vortical disturbances into acoustic waves at the trailing edge of a fan blade. As the only noise contribution in a homogeneous stationary flow, it is a matter of primary interest when addressing the problem of the noise generated by fans (Sharland 1964; Wright 1976; Fukano, Kodama & Senoo 1977; Caro & Moreau 2000), wind turbines (Glegg, Baxter & Glendinning 1987; Hubbard & Shepherd 1991; Parchen *et al.* 1999) and high-lift devices (Pérennès & Roger 1998; Singer, Lockard & Brentner 2000). Self-noise can be reduced if its origin and leading parameters are clearly identified, in terms of flow variables that can be modified through a proper blade design. The prediction of the corresponding broadband noise sources is therefore the prime goal of this study. A first step towards this goal is to study the noise sources of a Controlled-Diffusion (CD) airfoil specifically developed for low Reynolds number automotive engine cooling applications by Valeo. The corresponding set of experiments run in the anechoic wind tunnels of Ecole Centrale Lyon provide the reference aeroacoustic experimental database (Moreau *et al.* 2003; Roger & Moreau 2004).

A first large-eddy simulation (LES) of the flow over the Valeo CD profile (Wang *et al.* 2004) showed that a high quality and fine grid was necessary to achieve numerical stability and yield comparable wall pressure statistics to those obtained experimentally. The sensitivity of the body-fitted single block structured mesh approach to the grid quality and the large computational cost of this airfoil simulation preclude its extension to a realistic automotive engine cooling fan. The latter involves a complex blade geometry with a large variation of blade twist (stagger angle) and rapidly varying blade sweep and rake (highly bowed blades), which makes it hard to reach a high quality single block structured grid over the entire blade span. Moreover the tip clearance involves a much more complex labyrinth than the one considered by You *et al.* (2004), making a local structured body-fitted grid hard to design. Therefore to reach the goal of accurate predictions of wall pressure fluctuations for low speed fan blades, alternative methods need to be explored. The present study will test several numerical approaches as potential

[†] Valeo Motors and Actuators, France

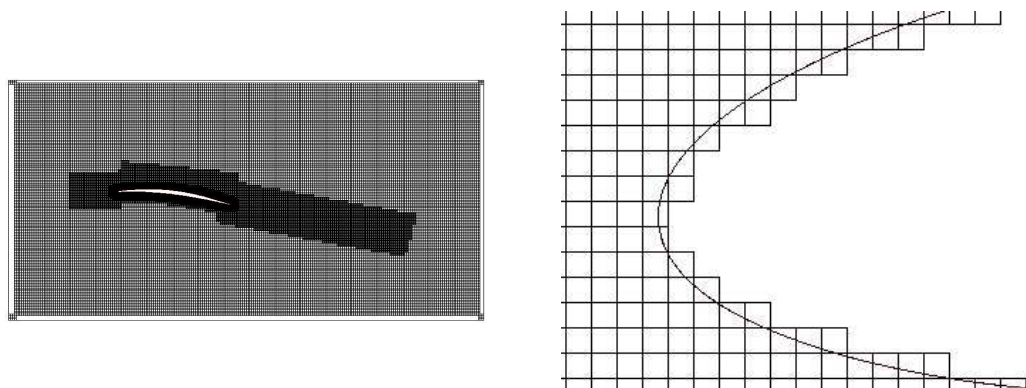


FIGURE 1. Left: Full grid around the CD airfoil used for the Lattice Boltzmann method. Right: Close-up at the leading edge.

alternatives. The Valeo CD airfoil is again considered and the body-fitted LES results serve as reference numerical data.

One way to circumvent the inherent topological difficulties associated with a body-fitted grid for a complex fan blade is to resort to non-boundary conforming methods. Two such promising methods have emerged recently for aerodynamic predictions. The Lattice Boltzmann method (LBM) relies on a pseudo-particle approach and is based on microscopic models and mesoscopic kinetic equations that describe the interaction between the pseudo-particles (Chen & Doolen 1998). The incompressible Navier-Stokes equations are recovered by taking a multi-scale expansion (Chapman-Enskog) of the velocity moments of the particle distribution functions, in the limit of small Knudsen and Mach numbers. On the other hand, the Immersed Boundary method still relies on the direct discretization of the Navier Stokes equations but imposes the boundary conditions indirectly through an additional source term or forcing function added to the flow equations (Mittal & Iaccarino 2005). Both methods employ an “easy-to-generate” non-body conforming Cartesian grid and have a low per-grid-point operation count and massively parallelized algorithms that should lead to fast turn-around simulations. Finally, assuming that the low frequency part of the spectrum is due to the largest vortical structures mainly found in the outer zone of the boundary layer, a Detached Eddy Simulation on a body-fitted grid might also provide an interesting alternative to the more computationally intensive Large Eddy Simulation. This will be the third method tested here. These three methods are first outlined in the next section, with some details on the associated grid and simulation parameters for the CD airfoil. The results are then presented for a Reynolds number based on the chord length of 1.5×10^5 corresponding to the ECL experimental data and the associated reference LES. This transitional Reynolds number represents a real challenge for both Cartesian methods.

2. Numerical approaches

2.1. Lattice Boltzmann method

The LBM originates from lattice gas (LG) automata, e.g. a simplified, fictitious and discrete particle kinetics on a discrete lattice with a discrete time. Whereas LG method describes the evolution of a set of Boolean variables, e.g. integers, that represent the particle occupation at the lattice nodes, the LBM method solves for the particle distribution

functions f_i at the lattice nodes i . These real functions are the solutions of the following discrete kinetic equations:

$$f_i(\mathbf{x} + \mathbf{e}_i \Delta t, t + \Delta t) = f_i(\mathbf{x}, t) + \Omega_i(f(\mathbf{x}, t)) \quad (2.1)$$

where \mathbf{e}_i are the local particle velocities and $\Omega_i(f(\mathbf{x}, t))$ is the collision operator which represents the rate of change of f_i resulting from collisions. The macroscopic properties of the fluid are moments of the distribution functions f_i :

$$\rho = \sum_i f_i \quad \rho \mathbf{u} = \sum_i f_i \mathbf{e}_i \quad (2.2)$$

If the local particle distribution is further assumed to relax to an equilibrium state at a single rate τ , the collision operator in equation (2.1) reduces to the lattice Bhatnagar-Gross-Krook (BGK) collision term:

$$\Omega_i(f(\mathbf{x}, t)) = -\frac{f_i - f_i^{eq}}{\tau} \quad (2.3)$$

In the low Knudsen limit, the rate τ is much smaller than the shortest hydrodynamic time scale and the LBM reproduces the direct simulation of the Navier-Stokes equations (LB-DNS mode). For high Reynolds number, the shortest hydrodynamic time scale or Kolmogorov scale becomes prohibitively small and the rate τ can be replaced by an effective turbulent relaxation time $\tau_{turb} = \tau_0 + C_\mu \frac{k^2}{\epsilon T \sqrt{(1+\eta^2)}}$, where τ_0 is the bare molecular relaxation time, T the absolute temperature, $\eta = \frac{Sk}{\epsilon}$, k the specific turbulent kinetic energy, ϵ the specific dissipation rate, C_μ and S model constants. It can then be shown that the resulting model is similar to a k - ϵ RNG model (LB-RANS model, see Chen *et al.* 2003). All present simulations have been obtained with the commercial code Powerflow from EXA Corporation; the method used (namely Digital Physics) is an extension of the above LBM (Chen, Teixeira & Molvig 1997).

The grid topology around the CD profile, shown in Figure 2 (left), is a rectangular box of similar size as the reference LES grid. The boundary conditions on the box, as in the LES simulation, involve the velocity components on three sides extracted from the RANS simulation of the full ECL test rig and a constant pressure at the outlet. The resulting cartesian grid has 73551 voxels and 1491 surfels in a two-dimensional slice. It involves five levels of consecutive grid refinements. The smallest cell at the leading edge, shown in Figure 2 (right), is five times larger than that in the body-fitted LES grid. The corresponding three-dimensional grid has 3.64 millions voxels and 1.12 million surfels. To improve the resolution at the leading and trailing edges, it includes eight levels of grid refinements (Figure 5c). The highest resolution achieved has 5120 grid points along the chord length. Yet the grid spanwise extension has been limited to 5% of the chord length because of the restriction of the current LBM to cubic voxels.

2.2. LES with immersed boundary method

Mittal & Iaccarino (2005) classified several implementations of the immersed boundary method. The present approach belongs to the discrete forcing approach with direct boundary condition imposition. The interpolation scheme is an extension of the interpolation scheme of Fadlun *et al.* (2000). The velocity components at the first grid point off the immersed boundary (IB) are obtained either by using the discretized Navier-Stokes equation or by linear interpolation as in Fadlun *et al.* (2000). A modified version of the latter is used here.

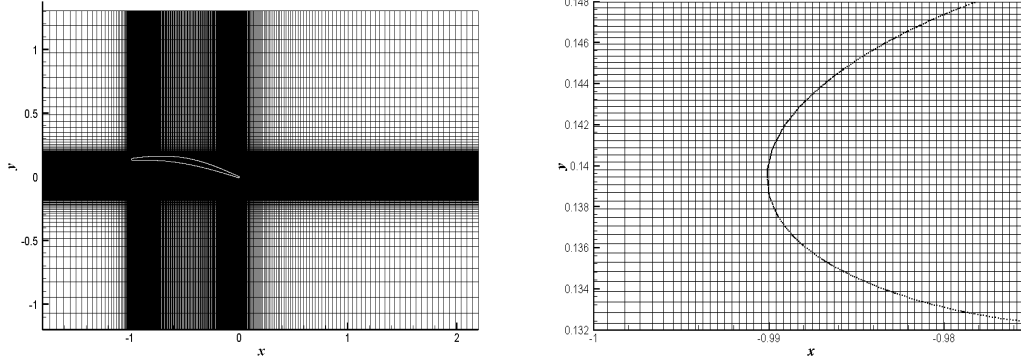


FIGURE 2. Left: Full grid around the CD airfoil used for the immersed boundary method.
Right: Close-up at the leading edge.

The interpolation scheme can be written as:

$$\begin{aligned} \hat{u}_{i,c}^k &= w_{i,1} \hat{u}_{i,1}^k + w_{i,2} \hat{u}_{i,2}^k + w_{i,IB} \hat{u}_{i,IB}^k \\ &+ \psi \left(u_i^{k-1} - w_{i,1} u_{i,1}^{k-1} - w_{i,2} u_{i,2}^{k-1} - w_{i,IB} u_{i,IB}^{k-1} \right) \\ &- (\gamma_k + \rho_k) \Delta t \left(\frac{\partial p^{k-1}}{\partial x_i} \Big|_c - w_{i,1} \frac{\partial p^{k-1}}{\partial x_i} \Big|_1 - w_{i,2} \frac{\partial p^{k-1}}{\partial x_i} \Big|_2 - w_{i,IB} \frac{\partial p^{k-1}}{\partial x_i} \Big|_{IB} \right), \end{aligned} \quad (2.4)$$

where the subscripts 1 and 2 denote adjacent velocity nodes in the x_1 and x_2 directions, and subscript IB denotes the point on the IB which is the boundary-normal projection of the velocity node c , and w_i is an interpolation coefficient determined by the geometric configuration. Δt is the time step, k is the sub-step index, γ_k and ρ_k are coefficients used in the third order Runge-Kutta scheme, and $\psi = \sqrt{(w_{i,1} + w_{i,2})/w_{i,IB}}$ ($\psi \leq 1$). Note that if the last two terms in equation (2.4) are omitted the standard linear interpolation formula is recovered. The present approach is based on the fractional step method (Kim & Moin 1985) with Crank-Nicolson scheme for the diffusion terms and the third-order Runge-Kutta scheme for the convective terms. The second-order central difference is used for all the terms in a staggered grid system. The dynamic subgrid scale model (Lilly 1992) is used for LES.

To find an intermediate velocity field $\hat{u}_{i,H}^k$ which provides reduced error in the pressure field, the following correction to \hat{u}_i^k is considered:

$$\hat{u}_{i,H}^k = \hat{u}_i^k - (\gamma_k + \rho_k) \Delta t \left(\frac{\partial}{\partial x_i} \right)_H f,$$

where f is a potential field determining the amount of correction and the subscript H denotes a formal finite volume discrete operator. The expression for f is given as:

$$\begin{aligned} \left(\frac{\partial^2}{\partial x_j \partial x_j} \right)_H f &= \left(\frac{\partial^2}{\partial x_j \partial x_j} \right)_H p^{k-1} + \frac{1}{(\gamma_k + \rho_k)} \left[\gamma_k \left(\frac{\partial}{\partial x_i} \frac{\partial}{\partial x_j} \right)_H (u_i u_j)^{k-1} \right. \\ &\quad \left. + \rho_k \left(\frac{\partial}{\partial x_i} \frac{\partial}{\partial x_j} \right)_H (u_i u_j)^{k-2} \right] + \frac{1}{(\gamma_k + \rho_k) \Delta t} \left(\frac{\partial}{\partial x_i} \right)_H \hat{u}_i^k. \end{aligned}$$

The grid topology around the CD profile is similar to the LB grid and the same boundary conditions are imposed. A first cartesian grid, termed *Grid1* and shown in

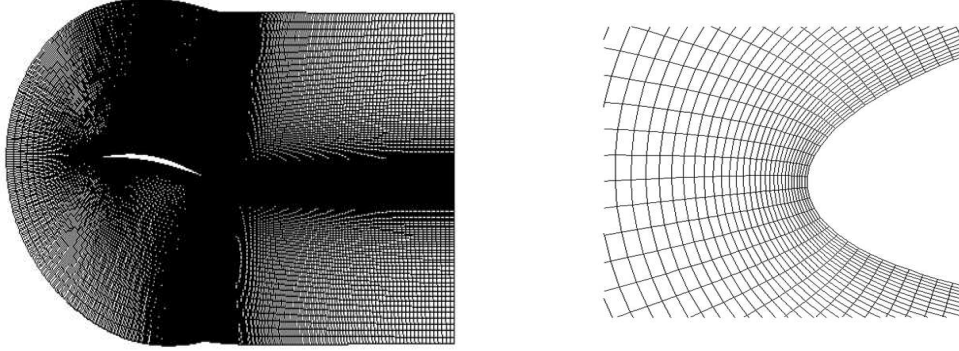


FIGURE 3. Left: Full grid around the CD airfoil used for the DES method. Right: Close-up at the leading edge.

Figure 2 (left), had some local grid stretching which limits the number of points in a two-dimensional slice to 150,000 nodes shown in Figure 2 (left). To avoid numerical problems at the leading edge, the grid spacing is locally uniform as shown in Figure 2 (right). The smallest grid cell at the leading edge is still 2.5 times larger than the one on the body-fitted LES grid. Adding 32 nodes in the spanwise direction, extending over 5% of the chord length, led to a 4.8 millions grid in 3D.

3. Detached-eddy simulation

Spalart *et al.* (1997) proposed a hybrid technique known as detached eddy simulations (DES), which combines URANS and LES models by non-zonal blending. Near the wall a standard RANS model is used and in the outer region of the boundary layer where large detached turbulent structures occur, the URANS equations are modified such that they take a LES-like form. The switching is achieved by modifying the length scale l_{turb} of the turbulence model according to the local grid dimension $\Delta = \max(\Delta_x, \Delta_y, \Delta_z)$: $\tilde{l} = \min(l_{turb}, C_{DES} \Delta)$. The present simulations obtained with Fluent 6.1.22 are based on the modification of the Spalart-Allmaras transport equation for the modified turbulent kinetic viscosity $\tilde{\nu}$:

$$\frac{\partial \tilde{\nu}}{\partial t} + u_i \frac{\partial \tilde{\nu}}{\partial x_i} = c_{b1} \tilde{S} \tilde{\nu} - c_{w1} f_w \left[\frac{\tilde{\nu}}{\tilde{l}} \right]^2 + \frac{1}{\sigma} \frac{\partial}{\partial x_j} \left[(\nu + \tilde{\nu}) \frac{\partial \tilde{\nu}}{\partial x_j} \right] + \frac{c_{b2}}{\sigma} \left(\frac{\partial \tilde{\nu}}{\partial x_j} \right)^2 \quad (3.1)$$

The value for C_{DES} of 0.65 is based on the validation of the model for decaying isotropic turbulence. This scheme is far less expensive than LES but is supposed to capture the large scale motions in regions with significant eddy content. Recent applications of the DES to aeroacoustic experiments have yielded promising results: Mendonça, Allen & de Charentenay (2003) have investigated the acoustics of several cavities with the DES method; Greschner *et al.* (2004) have applied the DES method to the complex flow past a rod-airfoil configuration. In the latter, a good agreement was found with the experimental velocity spectra up to 2000 Hz, which corresponds to the frequency range over which significant sound is generated.

Two three-dimensional grids have been built from the original LES grids to yield reduced models that could be run on single-processor 32-bits PC workstations. The first one, termed *DES-Grid1*, stems from the LES grid in a two-dimensional slice but has a

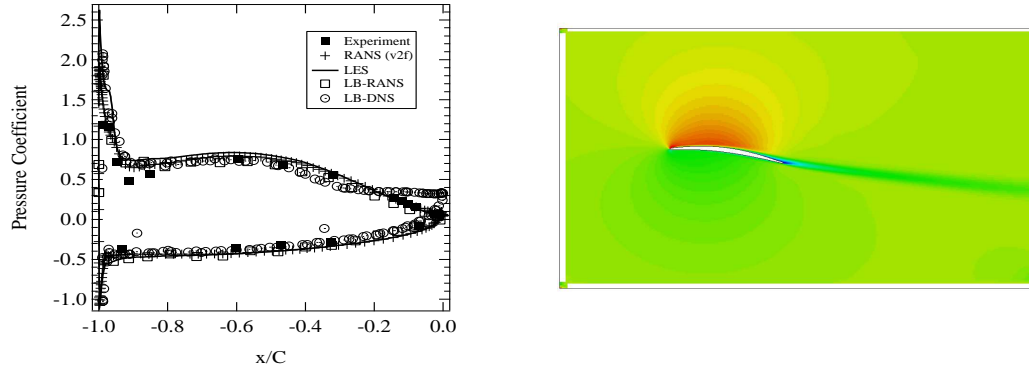


FIGURE 4. Left: Pressure coefficient $-C_p$. Right: LB-RANS velocity contours.

reduced spanwise extent of 5% of the chord length with 16 equidistant points (Figure 3). The total size of the grid is then $(960 \times 84 \times 16)$ and has therefore 1.3 million nodes. A second grid, termed *DES-Grid2*, keeps the original span 10% of the chord length of the reference LES. Yet to limit the overall grid size, two levels of coarsening are applied away from the profile (Figure 5b).

4. Simulation results

The LB method was first run in a URANS mode with a time step of 2.4×10^{-7} s. The DNS mode was later switched on with a time step of 1.9×10^{-7} s. To speed up the computation, the Mach number has been increased from 0.04 to 0.2. Figure 4 (left) shows a comparison of the pressure coefficient of these LB simulations with the corresponding ones from the body fitted RANS performed with Fluent by Moreau *et al.* (2003) and the reference LES simulation by Wang *et al.* (2004). The agreement of the LB-RANS simulation with the other methods is very good even though some oscillations are present, which are even more pronounced in the friction coefficient. Figure 4 (right) is the corresponding flow field, which again matches closely the previous RANS simulation. No unsteadiness is found as in the body fitted RANS results: neither pressure fluctuations along the blade, nor vortical structures in the wake. Results have been gathered for 11 non-dimensional flow-through times based on the chord and free-stream velocity. Switching off the turbulence model and refining the grid produces the so-called LB-DNS results. The refined grid is shown in Figure 5c. The DNS simulation has been run for 6.7 flow-through times. Pressure fluctuations are now produced. Yet, more oscillations on the mean pressure coefficient than in the RANS mode are also obtained. These larger wiggles are apparently generated by the stairstep-like boundary representation and, possibly, the grid refinement. These have been filtered out in Figure 4. The leading edge region is similar. Yet at the trailing edge, the larger adverse pressure gradient triggers a turbulent flow separation not evidenced in the experiment. This is also clearly shown by the darker zones in the streamwise velocity contours (Figures 6c and 7c). The boundary layer is consequently thicker at the trailing edge. This flow separation may have been triggered by a too rapid grid refinement in the aft region of the profile, in the streamwise direction. Finally, the wake exhibits a clear vortex shedding not seen in the reference LES. This is most likely caused by the limited spanwise extent of the grid: achieving the proper

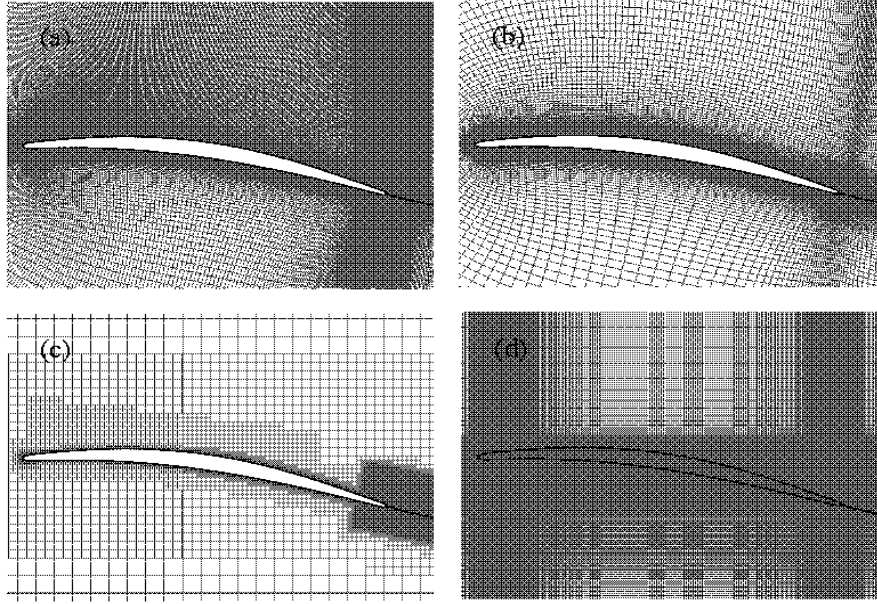


FIGURE 5. Final grids: a) LES, b) DES, c) LB, d) LES-IB.

grid resolution in this direction would require prohibitively expensive three-dimensional simulations.

With the LES-IB method, a first simulation was run at a Reynolds number of 1.5×10^4 on the grid *IB-Grid1*. The Immersed Boundary method yielded a complex three-dimensional laminar wake behind the airfoil. Primary roll-up vortices and secondary rib vortices are found, which are typical structures of three-dimensional vortex shedding. When switching to the actual Reynolds number of 1.5×10^5 , numerical instabilities occurred close to the trailing edge and in the wake where the grid stretching is the largest. This motivated switching to the more uniform and finer grid termed *IB-Grid2*. This final grid is shown in Figure 5d. The time step is 1.5×10^{-5} s. The simulation has been run for 5 non-dimensional time after the transient period. At the leading edge, Figure 9 (left) shows a similar pressure plateau as in the reference LES, evidence of a small laminar flow separation. The agreement with experiment is also excellent on both suction and pressure sides. This small recirculation bubble oscillates and triggers small vortices that are then convected along the profile. At the trailing edge, the large vortex shedding shown at the lower Reynolds Number of 1.5×10^4 is no longer observed. Smaller turbulent structures are convected in the wake as shown in the close-up view of both streamwise and spanwise velocity contours at the trailing edge (Figures 7d and 8d). At the trailing edge, the structures are now different from the reference body-fitted simulation. Figure 6 also suggests that the boundary layer is locally thicker. In the aft portion of the profile, the grid spacing is most likely still too large (two to three times larger in the streamwise direction and ten times larger in the wall-normal direction than in the reference body-fitted LES).

The DES simulations have first been run on the shorter grid *DES-Grid1*. The reduced time step selected is 0.025 or a physical time step of about 2×10^{-4} s. This is about one order of magnitude larger than that for the LES simulations. The total simulation

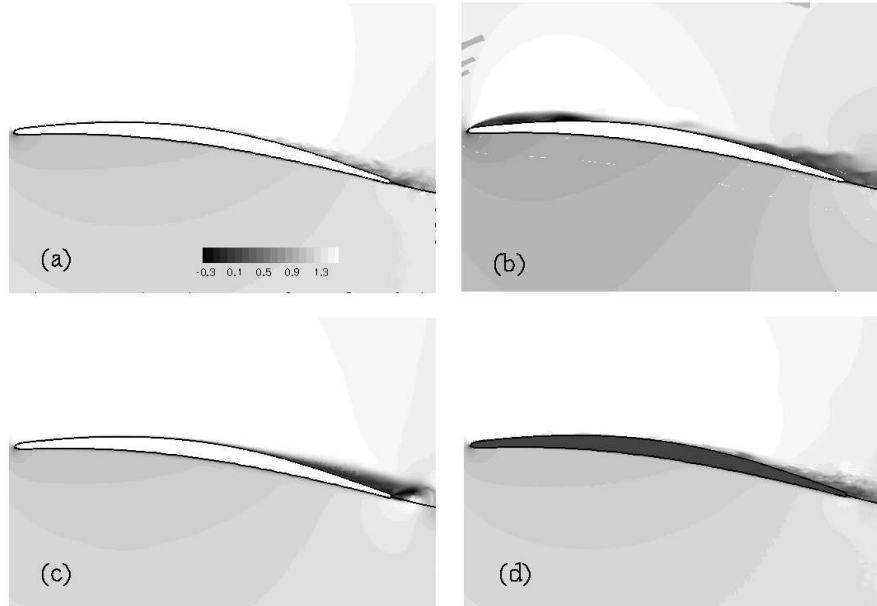


FIGURE 6. Streamwise velocity: a) LES, b) DES, c) LB, d) LES-IB.

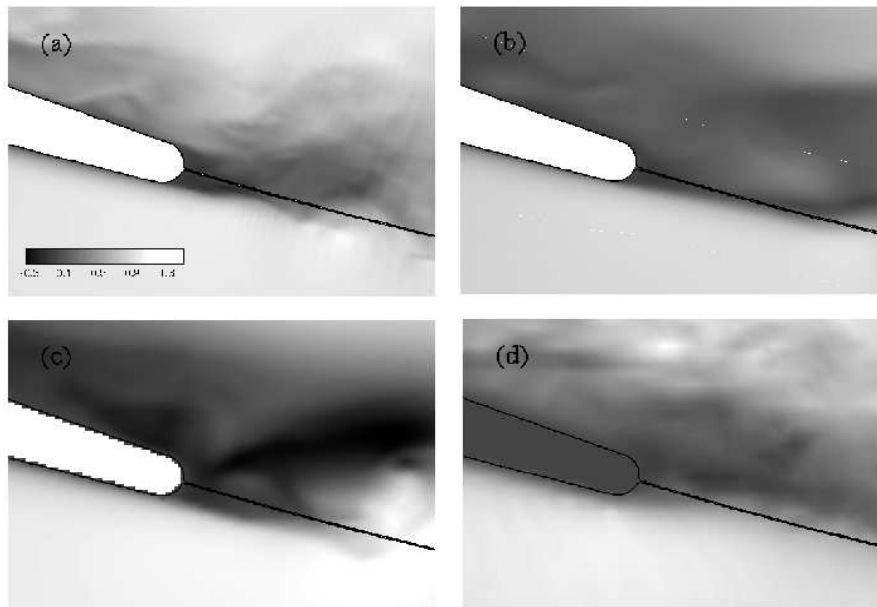


FIGURE 7. Close-up view of streamwise velocity: a) LES, b) DES, c) LB, d) LES-IB.

involved about 800 time steps in 24 hours or 20 flow-through times. Figure 9 (left) shows the corresponding wall pressure distribution. A too-large flow separation at the leading edge is generated yielding the large pressure plateau. The pressure recovery at the trailing edge is however in good agreement with experiment and the other LES simulations. Figure 9 (right), representing an iso-surface of vorticity, clearly shows some

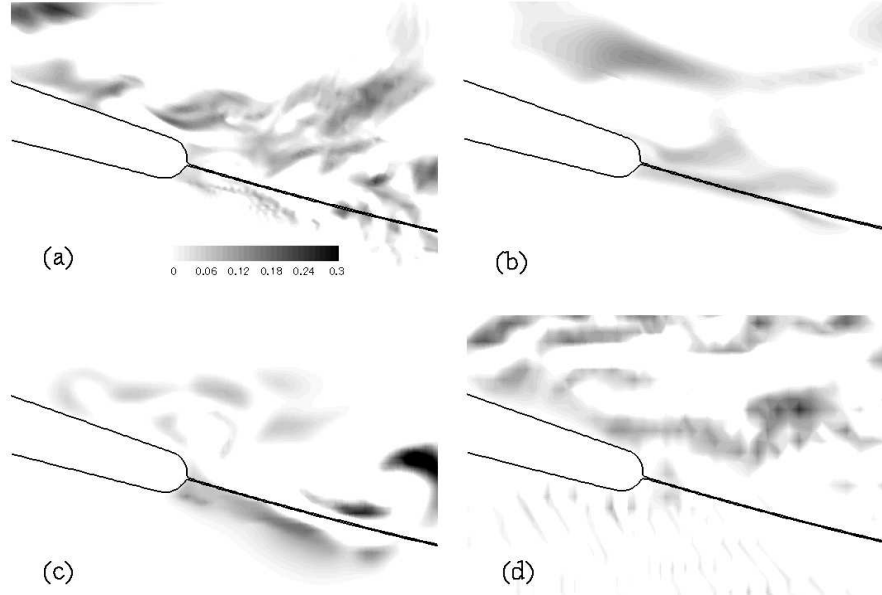


FIGURE 8. Close-up view of spanwise velocity: a) LES, b) DES, c) LB, d) LES-IB.

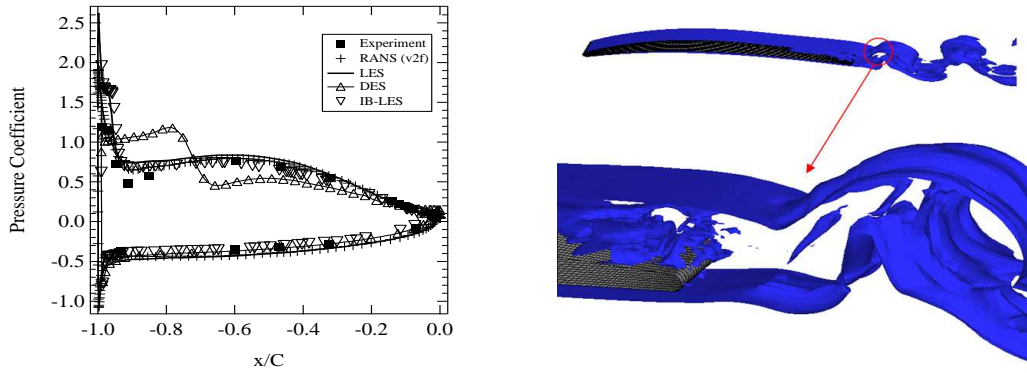


FIGURE 9. Left: Pressure coefficient $-C_p$. Right: DES iso-surface of vorticity magnitude.

three-dimensional unsteadiness produced close to the trailing edge. Smaller scales are created besides large scale vortex shedding and pressure fluctuations are produced close to the trailing edge. The main structures are much larger than in the LES and exhibit a definite large scale vortex shedding as in the LBM case. This has motivated an extension of the spanwise domain size to yield the grid *DES-Grid2* shown in Figure 5b. Figure 6b represents the streamwise velocity which still exhibits the vortex shedding pattern, but the domain extension has clearly reduced it. The boundary layer thickness is still the largest, which then leads to the widest wake shown in Figure 10.

In this plot, all simulations exhibit a larger wake thickness and a larger velocity deficit both at $x/C = 0.1$ and $x/C = 0.2$ (the trailing edge is located at $x/C = 0$), which suggests a thinner suction side boundary layer at the trailing edge in the experiment. The velocity profile of the reference LES is the closest to the experimental one. The

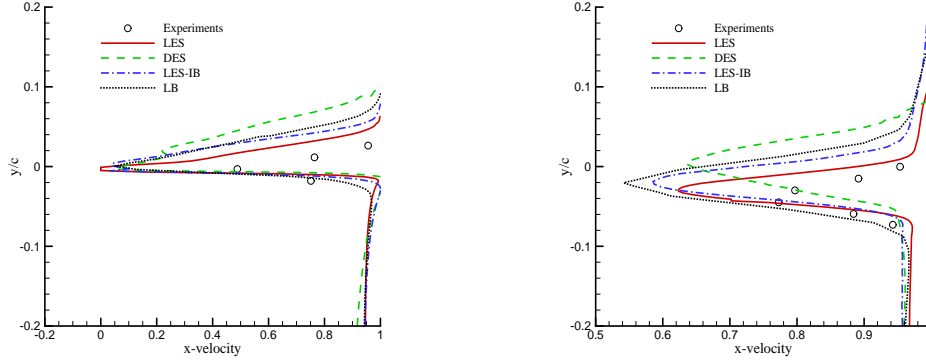


FIGURE 10. Wake Velocity Profiles. Left: $x/C = 0.1$. Right: $x/C = 0.2$.

LES-IB profile is thicker but its spreading is the same. This can again be attributed to the lower grid resolution compared to the reference LES. The LB-DNS profile is only slightly thicker at the first station but it spreads faster and the wake thickness is now wider on both suction and pressure sides. This might be due to a local grid discontinuity. The DES profile at the first station has the same thickness on the pressure side as the experiment and the other methods. On the suction side, however, it first follows the two LES profiles and then becomes suddenly larger, because of the observed larger structures. The switch in the model might be the cause of this sudden jump in the velocity profile. Downstream, at the second station, the wake thickness is similar to the LB-DNS one and the wake spreading is similar to the experiment. Yet the profile is shifted, suggesting a wake that is almost straight, which should not be the case due to the lift of the cambered CD airfoil. Finally, it should be stressed that the experimental grid for the X-wire probe is probably not fine enough to capture the minimum velocity and that the measurement at this location also carries the largest measurement uncertainty in this region.

To compare the pressure fluctuations obtained by all methods, the wall pressure power spectral density (PSD) has been computed at the sensor closest to the trailing edge, located at $x/C = -0.02$ on the suction side. These PSDs are compared in Figure 11. The reference LES provides a very good agreement with the fluctuations measured by the remote microphone probe. All other simulations yield much higher spectral levels at low frequencies. These overpredictions of lower frequency fluctuations and faster decay at higher frequencies may be partly attributable to the lower grid resolution in the trailing edge region for the LB-DNS and LES-IB methods. Other issues, such as the boundary treatment in LES-IB and the lack of a SGS model in LB-DNS also need to be examined. In the DES, the same grid is used in the inner region as in the reference LES, which might explain the good agreement at high frequencies. Yet the large unphysical flow structures cause an overprediction in the low and intermediate frequency range of the spectrum. The LB-DNS exhibits a broad peak around 350 Hz which can be attributed to the wake vortex shedding seen in the simulation. The lack of small structures in this simulation causes the faster decay of LB-DNS spectrum at high frequencies. By examining the pressure traces, some transients are found to be still present in the DES and LB simulations, which suggests that the solutions have not fully settled down to a statistically steady state, or that some pressure reflections (numerical noise) might be present at the boundaries.

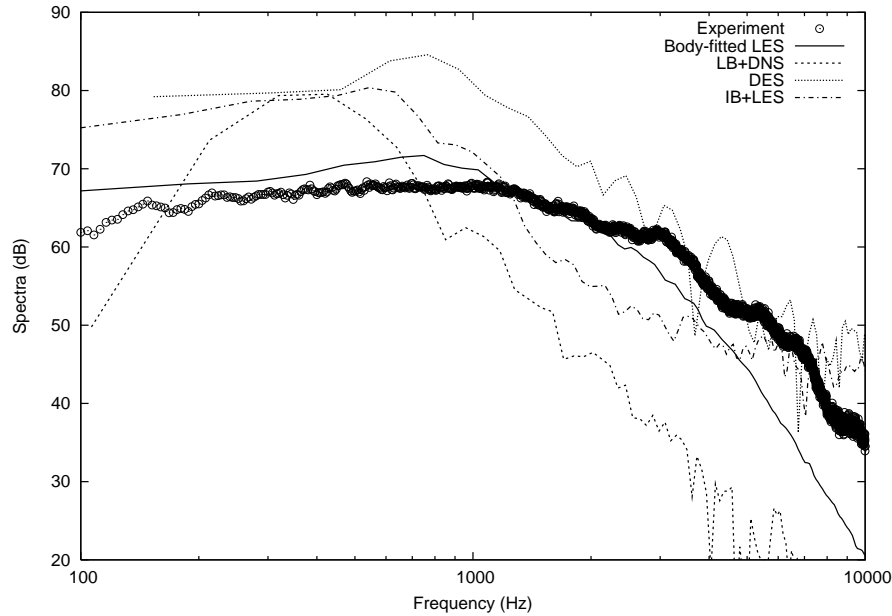


FIGURE 11. Power spectral density of wall pressure near the trailing edge ($x/C = -0.02$ on suction side): a) LES, b) DES, c) LB, d) LES-IB.

5. Conclusions

The ability to perform LES with an immersed boundary method at high Reynolds number has been demonstrated. The current simulation has provided good resolution of the small structures developing along the airfoil and a proper mean wall pressure distribution. The grid resolution is still too coarse in the trailing edge area, which may have caused the less favorable wall pressure spectra and wider velocity profile in the wake. Moreover, the grid requirements of a single block structured cartesian grid are as restrictive as the body-fitted approach. A lot of grid nodes have to be clustered in the airfoil region and a very regular, quasi-uniform grid distribution has to be used to prevent numerical instability or numerical wiggles in the solution. A possible solution is to use local grid refinement as shown by Mittal & Iaccarino (2005). The effect of the immersed boundary treatment on the wall pressure spectra also needs to be investigated.

The LBM is clearly not suited for this type of simulation yet. The grid requirements are similar to those of the IB method in the streamwise and wall-normal directions. The local grid refinement capability clearly helps reduce the number of surfels in the profile plane. However too rapid grid refinements in the trailing edge region produce a flow separation not seen experimentally. Moreover, the restriction to cubic voxels does not allow a sufficient extension of the three-dimensional grid in the spanwise direction, which prevents the proper stretching of the vortical structures in the wake. In fact, all simulations on grids that have a limited spanwise extent have triggered unphysical two-dimensional vortex shedding. At least a spanwise extension of 10% of the chord length is required. The current grid topology of Powerflow is the main limitation of this LBM implementation. It should also be remembered that the LB simulation is an under-resolved DNS, making it difficult to compare the results with other LES solutions.

The DES does not provide a physical flow topology even on the fine reference LES

grid, with too large a flow separation at the leading edge and too large flow structures and too thick a boundary layer at the trailing edge. The numerical treatment of the inlet boundary condition in Fluent 6.1.22 may not be sufficient to prevent some wave reflection and random noise generation that consequently modify the wall pressure fluctuations.

In summary, none of the methods tested here can yet provide a satisfactory alternative to the body-fitted LES to tackle the larger and more complex three-dimensional flow over a fan blade with its complex tip clearance labyrinth.

REFERENCES

- CARO, S. & MOREAU, S. 2000 Aeroacoustic modeling of low pressure axial flow fans. *AIAA Paper 2000-2094*, 6th AIAA/CEAS Aeroacoustics Conference, Lahaina, Hawaii.
- CHEN, S., TEIXEIRA, C. & MOLVIG, K. 1997 Digital physics approach to computational fluid dynamics: some basic theoretical features. *Int. J. Modern Phys. C* **8**, 675-684.
- CHEN, S. & DOOLEN, D. 1998 Lattice Boltzmann method for fluid flows. *Annu. Rev. Fluid Mech.* **30**, 329-364.
- CHEN, S., KANDASAMY, S., ORSZAG, S., SHOCK, R., SUCCI, S. & YAKHOT, V. 2003 Extended Boltzmann kinetic equation for turbulent flows. *Science* **301**, 633-636.
- FADLUN, E. A., VERZICCO, R., ORLANDI, P. & MOHD-YUSOF, J. 2000 Combined immersed-boundary/finite-difference methods for three-dimensional complex flow simulations. *J. Comput. Phys.* **161**, 35-59.
- FUKANO, T., KODAMA, Y. & SENOO, Y. 1977 Noise generated by low pressure axial flow fans. 1 - Modelling of the turbulent noise. *J. Sound Vib.* **50**, 63-74.
- GLEGG, S. A. L., BAXTER, S. M. & GLENDINNING, A. G. 1987 The prediction of broadband noise from wind turbines. *J. Sound Vib.* **118**, 217-239.
- GRESCHNER, B., THIELE, F., CASALINO, D. & JACOB, M. C. 2004 Influence of turbulence modeling on the broadband noise simulation of complex flows. *AIAA Paper 2004-2926*, 10th AIAA/CEAS Aeroacoustics Conference, Manchester, United Kingdom.
- HUBBARD, H. H. & SHEPHERD, K. P. 1991 Aeroacoustics of large wind turbines. *J. Acoust. Soc. Am.* **89**, 2495-2507.
- KIM, J. & MOIN, P. 1985 Application of a fractional-step method to incompressible Navier-Stokes equations. *J. Comput. Phys.* **59**, 308-323.
- LILLY, D. K. 1992 A proposed modification of the Germano subgrid-scale closure method. *Phys. Fluids A* **4**, 633-635.
- MENDONÇA, F., ALLEN, R. & DE CHARENTENAY, J. 2003 CFD prediction of narrow-band and broadband cavity acoustics at $M = 0.85$. *AIAA Paper 2003-3303*, 9th AIAA/CEAS Aeroacoustics Conference, Hilton Head, South Carolina.
- MITTAL, M. & IACCARINO, G. 2005 Immersed boundary methods. To be published in *Annu. Rev. Fluid Mech.*
- MOREAU, S., HENNER, M., IACCARINO, G., WANG, M. & ROGER, M. 2003 Analysis of flow conditions in free-jet experiments for studying airfoil self-noise. *AIAA J.* **41**, 1895-1905.
- PARCHEN, R., HOFFMANS, R., GORDNER, A., BRAUN, K. A., VAN DER BORG, N. J. C. & DASSEN, M. AND A.G.M. 1999 Reduction of airfoil self-noise at low Mach

- number with a serrated trailing edge. 6th International Congress on Sound and Vibration, Copenhagen, Denmark, pp. 3433-3440.
- PÉRENNÈS, S. & ROGER, M. 1998 Aerodynamic noise of a two-dimensional wing with high-lift devices. *AIAA Paper 98-2338*, 4th AIAA/CEAS Aeroacoustics Conference, Toulouse, France.
- ROGER, M. & MOREAU, S. 2004 Trailing edge noise measurements and prediction for a subsonic loaded fan blade. *AIAA J.* **42**, 536-544.
- SHARLAND, I. J. 1964 Sources of noise in axial flow fans. *J. Sound Vib.* **1**, 302-322.
- SINGER, B. A., LOCKARD, D. P. & BRENTNER, K. S. 2000 Computational aeroacoustic analysis of slat trailing-edge flow. *AIAA J.* **38**, 1558-1564.
- SPALART, P. R., JOU, W. H., STRELETS, M. & ALLMARAS, S. R. 1997 Comments on the feasibility of LES for wings and a hybrid RANS/LES approach. 1st AFSOR International Conference on DNS/LES, Aug. 4-8; see also: *Advances in DNS/LES*. C. Liu and Z. Liu Eds, Greyden Press, Columbus, OH.
- WANG, M., MOREAU, S., IACCARINO, G. & ROGER, M. 2004 LES prediction of wall pressure spectra on a low speed airfoil. *Annual Research Briefs-2004*, Center for Turbulence Research, Stanford Univ./NASA Ames.
- WRIGHT, S.E. 1976 The acoustic spectrum of axial flow machines. *J. Sound Vib.* **45**, 165-223.
- YOU, D., MITTAL, M., WANG, M. & MOIN, P. 2004 Computational methodology for large-eddy simulation of tip-clearance flows. *AIAA J.* **42**, 271-279.

Page intentionally left blank

Stability and acoustics

There were three projects in this group, all of which investigated the utility of analytical tools in conjunction with advanced flow simulations. The first investigated by-pass transition mechanisms in boundary layers, which are important in numerous aerodynamics applications. It is well known that boundary layers rarely transition to turbulence via a saturation of their most unstable linear modes (Tollmien-Schlichting waves); by-pass transition refers to any other mechanism leading to nonlinear saturation and turbulence. Visitor P. Ricco and hosts P. Durbin and T. Zaki worked to evaluate and extend the Boundary Region Theory of Lieb, Wundrow & Goldstein to describe a nonlinear by-pass transition mechanism involving receptivity to a free-stream mode. They found that the linear Boundary Region Theory concurs with Orr-Sommerfeld theory concerning which modes can efficiently penetrate the boundary layer, suggesting that inclusion of non-parallel flow effects is not crucial in models. They have also developed a nonlinear formulation of this theory to study two-mode interactions, which Durbin & Zaki have suggested to be important in by-pass transition.

The second project was an application of a new general flow-field decomposition—the multiscale window transform—which has certain attractive properties. It employs special basis functions that allow the energy in user selected nominal scales of an inhomogeneous flow to be unambiguously defined. This property then allows one to define the transfer of energy between these scales, the control of which is often the target of flow control applications. For drag control, for example, extraction of energy from the mean by large-scale turbulence should be suppressed. In this project, visitor X. S. Liang, who developed the multiscale window transform, worked with host M. Wang to make a precise designation of this inter-scale transfer in the wake of a circular cylinder. They defined scales corresponding to the mean flow and largest turbulence structures and identified locations of high energy transfer between these scales. These are thought to correspond to the most effective points at which to apply control in order to disrupt this transfer.

The final project was motivated by the prediction of jet noise, which is an important problem facing aircraft and engine makers. To do this, one typically defines a noise source, which is modeled using turbulence theory, and a wave propagation operator, which is inverted to compute the radiated noise. Unfortunately, since sound perturbations cannot be decoupled from other fluctuations in a compressible turbulent flow, there is no unique decomposition of the flow into a noise source and inhomogeneous wave equation. Many such formulations have been proposed over the last fifty years, but since all are exact consequences of the flow equations, it is hard to demonstrate clearly why one might be better than another. J. B. Freund and S. K. Lele addressed this issue in a new way using DNS data by evaluating the robustness of different formulations to errors intentionally introduced into the noise sources. They found a clear differences in the performance for different formulations.

Jon Freund

Page intentionally left blank

A study of turbulent wake dynamics using a novel localized stability analysis

By X. S. Liang [†] AND M. Wang

This paper briefly presents a unified, localized treatment of hydrodynamic stability relating the stability theory to experimental and numerical results, which are in general highly nonlinear, intermittent, and involve multiple scales in space and time. The localization in time is achieved with the multiscale window transform, a mathematical machinery developed by Liang & Anderson (2004); while the spatial dimension is localized through “transfer-transport separation”, which is made precise with the introduction of the concept *perfect transfer*. The theory is applied to investigate the dynamics of cylinder wakes. A remarkable observation is that *rapid amplification in perturbation energy does not necessarily correspond to instability*. In a saturated laminar wake, an absolute instability is identified with two local transfer lobes attached to the cylinder surface. In the turbulent case, the instability is located far away downstream and has distinct patterns. The dynamics is structured on three scale windows, among which the meso-scale window hosts a regularly growing mode. This mode is maintained through a primary instability. Although its energy can be ultimately traced to the base flow, the turbulent or sub-mesoscale motion is sustained through two different mechanisms: The first is directly from the background, and is distributed rather symmetrically as two side lobes along the wake boundary; the second comes from a secondary instability of the regular meso-scale process, appearing mainly as a form of monopole in the center. On all the instability maps, there exist sporadic inverse transfer spots. This inverse transfer or self-laminarization has profound implications for vortex suppression, allowing us to propose a generic strategy to get turbulence under efficient control.

1. Introduction

We introduce a novel localized hydrodynamic stability analysis and show how it can be utilized for turbulence research, particularly, for wake dynamics research. Like any infinite dimensional dynamical process, hydrodynamic instabilities are generally localized in space and time. This is especially apparent in the turbulence context, where processes are usually highly nonlinear and tend to occur intermittently over limited domains with irregularity and mobility. A hydrodynamic stability analysis thus should be able to unravel dynamics on a local basis in order to allow for a faithful representation of nature. The challenge is, however, that the conventional concept of stability is a notion over a system (e.g., Lin 1966; Drazin & Reid 1982), to which every location belongs, and hence it is difficult to localize a dynamically isolated hotspot for such an analysis to be performed. This problem is not new. Specific approximate approaches have been sought in tackling certain problems. An example is the parcel stability analysis, which has been applied to the symmetric instability study (see Holton 1992). Other approaches include those used in the study of absolutely and convectively unstable flows (e.g., Pierrehumbert & Swanson 1995; Huerre & Monkewitz 1990), in the treatment of localized standing

[†] Address: Harvard University DEAS, Pierce Hall, 29 Oxford St, Cambridge, MA 02138

Rankine-Hugoniot shocks (Chakrabarti 1989), and in the investigation of plasma instability (e.g., Chu *et al.* 1996). These analyses are either linear (e.g., WKB method) or formulated in the Lagrangian sense, and as a result their utility is limited.

Liang *et al.* (2004) developed a novel approach to give this old problem a unified solution. Their generalized hydrodynamic stability analysis is localized, nonlinear, and hence applicable to fluid flows on a generic basis. In the following section, we give a brief introduction to the theory. In particular, we show how the interaction between background and perturbation structures can be computed as a field-like (Eulerian) variable in a real time mode. The theory is then applied to study the wake dynamics involving vortex shedding behind a circular cylinder. We first examine a laminar wake (Sec. 3), investigating how it is evolved and sustained. This is followed by an analysis of a turbulent wake (Sec. 4) to study its distinct physics and draw contrast to the laminar case. In Sec. 5, conclusions are drawn and a strategy for optimal turbulence control is proposed.

2. Multiscale window transform and localized stability analysis

Hydrodynamic stability in the classical Lyapunov formalism is essentially an energetic analysis. That is to say, a system is unstable provided that disturbances grow. Here disturbances are measured by a norm, or energy, over the whole domain under concern. The novelty of our new stability analysis approach is to localize the Lyapunov norm to make it a field-like variable. We need to consider the localization both in time and in space.

2.1. Time localization - Multiscale window transform

At the heart of the localized stability analysis is how processes in the context of a function space are organized into some subspaces or scale windows with distinct ranges of time scales, as well as time instants. In a classical framework, multiscale decomposition is at odds with energy localization. In Liang *et al.* (2004), this difficulty is overcome through the development of a machinery, multiscale window transform (MWT), which we briefly introduce hereafter. For details, see Liang & Anderson (2004).

MWT tailored specifically to stability analysis can be introduced with the aid of a highly localized scaling basis[†] $\phi(t)$ (Fig. 1a). The basis is obtained through orthonormalization of the cubic spline. Fig. 1b shows its periodized counterpart $\phi_n^j(t)$. Given a field $p = p(t)$, $t \in [0, 1]$ a scaling reconstruction (e.g., Strang & Nguyen 1997) can be utilized to fulfill an orthogonal (in $L_2[0, 1]$) decomposition to obtain a large scale part $p^{\sim 0}$, and an eddy part $p^{\sim 1}$ or more. These parts are further transformed on a space spanned by $\{\phi_n^{j_1}\}_n$, $n = 0, 1, \dots, 2^{j_1} - 1$, with 2^{-j_1} the smallest scale that the given dataset resolves. This transform, which involves scale ranges or windows, rather than individual scales as in traditional transforms, is termed “multiscale window transform”. Specifically, we have a large-scale window transform and an eddy window transform in a two-window decomposition.

MWT has a property called “marginalization” which allows one to express the energy for a scale window simply as the square of the transform coefficient for that window. Given a time series $p(t)$, we denote the MWT as $\hat{p}_n^{\sim \varpi}$, where $\varpi = 0, 1, \dots$ signify large-scale window, eddy-scale window, and so forth. The marginalization, which we will henceforth write as \mathcal{M}_n , is a special operator of summation over time steps n .

[†] This is a special case. An MWT in a generic sense does not rely on the choice of basis. This is one aspect where MWT differs from other localized analysis such as wavelet transform.

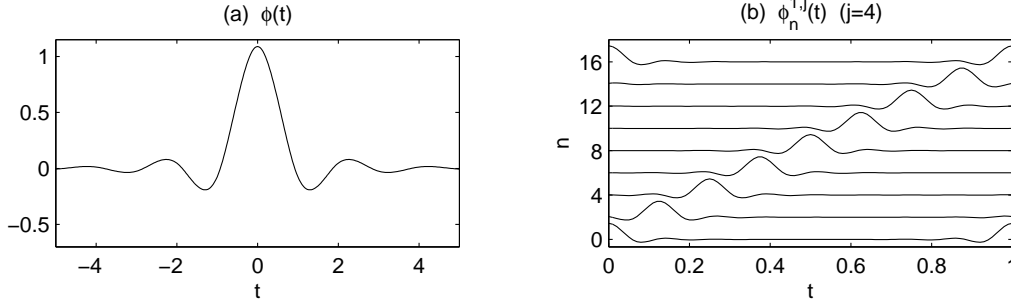


FIGURE 1. (a) Scaling function ϕ constructed via orthonormalization from cubic splines (see Strang & Nguyen 1997). (b) The periodized basis $\phi_n^j(t) = \sum_{\ell=-\infty}^{+\infty} \phi(2^j(t + \ell) - n)$.

2.2. Space localization - Transfer-transport separation

The spatial dimension localization is another crucial issue. In a local sense, perturbation amplification does not necessarily correspond to instability, as energy needed to fuel the growth could be transported from other places into the domain. Liang *et al.* (2004) termed this issue as “transfer-transport separation”. In the following, we briefly present their approach to this problem.

Consider an ideal and incompressible fluid flow. The governing equation is

$$\frac{\partial \mathbf{v}}{\partial t} = -\nabla \cdot (\mathbf{v}\mathbf{v}) - \frac{1}{\rho} \nabla P. \quad (2.1)$$

Take an MWT for time step n and window ϖ on both sides and dot with $\hat{\mathbf{v}}_n^{\sim \varpi}$. It gives

$$\dot{K}_n^{\varpi} = NL_n^{\varpi} + Q_{P,n}^{\varpi}, \quad (2.2)$$

where $\dot{K}_n^{\varpi} \approx \frac{1}{2} \hat{\mathbf{v}}_n^{\sim \varpi} \cdot \hat{\mathbf{v}}_n^{\sim \varpi}$, $Q_{P,n}^{\varpi} = -\frac{1}{\rho} \nabla \cdot (\hat{\mathbf{v}}_n^{\sim \varpi} \hat{P}_n^{\sim \varpi})$, and the nonlinear term $NL_n^{\varpi} = -\left[\nabla \cdot (\mathbf{v}\mathbf{v})_n^{\sim \varpi} \right] \cdot \hat{\mathbf{v}}_n^{\sim \varpi}$ is a representation of processes intertwined with transport $Q_{K,n}^{\varpi}$ and transfer T_n^{ϖ} . The major issue of spatial localization is how to have these processes precisely separated. This is achieved with the introduction of a concept *perfect transfer*. By definition a perfect transfer T_n^{ϖ} is a process which mediates among scale windows such that $\mathcal{M}_n \sum_{\varpi} T_n^{\varpi} = 0$, i.e., a redistribution of energy among scale windows which does not generate nor destroy energy as a whole. Liang *et al.* (2004) established that NL_n^{ϖ} can be precisely decomposed into a transport and a perfect transfer, and the decomposition is unique. In the incompressible 2-D flow case,

$$T_n^{\varpi} = -\frac{1}{2} \left\{ (\hat{u}_n^{\sim \varpi})^2 \nabla \cdot \mathbf{v}_u + (\hat{v}_n^{\sim \varpi})^2 \nabla \cdot \mathbf{v}_v \right\}, \quad (2.3)$$

where $\mathbf{v}_S = \frac{(\mathbf{v}S)_n^{\sim \varpi}}{S_n^{\sim \varpi}}$, for $S = u$, and v . For 3-D flow, the third dimension can be added likewise.

Liang *et al.* (2004) showed that, with the aid of T_n^{ϖ} , it is possible to introduce a metric to measure the localized stability. Specifically, they showed that, except for an opposite sign, $CR = (T_n^{\varpi})^{(\varpi+1) \rightarrow \varpi}$ followed by a horizontal filtering is in compliance with Lyapunov's norm for a system losing stability from window ϖ to window $\varpi + 1$. Here the superscript $(\varpi + 1) \rightarrow \varpi$ means an interaction analysis that selects out the transfer from window $\varpi + 1$ to window ϖ from the nonlinearly intertwined processes. When $CR < 0$,

the flow system is locally unstable, and vice versa. Note CR is a field-like variable, and is hence capable of handling any highly localized analysis. For more realistic flows, CR may be modified accordingly to ensure consistency with Lyapunov's formalism. But as this nonlinear transfer has essentially captured the dynamics, we might just define it this way.

Note hydrodynamic stability may be understood with $(T_n^{\varpi+1})^{\varpi \rightarrow (\varpi+1)}$, as well as from $(T_n^{\varpi})^{(\varpi+1) \rightarrow \varpi}$, depending on what a time scale one chooses to observe the problem. They are identical when marginalized, except for the opposite sign. In this case, a system is unstable if $CR > 0$ and vice versa.

Also worthwhile to note is the concept of Reynolds stress.[†] Conventionally Reynolds stress has been understood as the transfer mechanism between scale windows. Liang *et al.* (2004) established that it does not conserve energy, and as a result, it is problematic in representing transfer processes.

We close this section by remarking that many problems in fluid dynamics are made easy in our framework. In $CR = (T_n^{\varpi})^{(\varpi+1) \rightarrow \varpi}$, by switching ϖ from 0 to 1 one may accordingly introduce the concepts of primary instability and secondary instability. Another good example is about convective and absolute instabilities (e.g., Pierrehumbert & Swanson 1995; Huerre & Monkewitz 1990; Oertel 1990 and references therein): A moving negative CR means convective instability, while a persisting negative CR center implies absolute instability. Likewise, local/global instability can also be studied simply by examining the variation of the influential range of CR .

3. Wakes behind a circular cylinder: The laminar case

In this section, we investigate a laminar wake behind a circular cylinder. We particularly want to explore the aspect of the dynamics that sustains the Karman vortex street, through the convenience of the “stability structure” brought forth by our analysis.

3.1. Model description

We utilize a numerical model to generate the necessary dataset. The model solves the incompressible Navier-Stokes equations on a C -type mesh using an energy-conserving, hybrid finite-difference/spectral code described in Mittal and Moin (1997). The numerical scheme employs second-order central differences in the streamwise and cross-stream directions, and Fourier collocation in the spanwise direction. The time advancement is of the fractional step type in combination with the Crank-Nicholson method for viscous terms and third order Runge-Kutta scheme for the convective terms. The Poisson equation for pressure is solved using a multigrid iterative procedure at each Runge-Kutta substep.

Dimensionless variables are used in the following analysis, with the cylinder diameter d as the length scale, free-stream velocity U_∞ as the velocity scale, and d/U_∞ as the time scale. We use x , y , and z to denote the streamwise, cross-stream, and spanwise coordinates, respectively, with x and y origins located at the cylinder center.

The laminar flow simulation (2-D) is performed at $Re = 200$ on a 513×129 mesh, covering a computation domain $-40 \leq x \leq 25$; $-50 \leq y \leq 50$. The simulation is initiated with an “impulsive start”, and is run until a quasi-steady state is achieved. The results

[†] Our formalism is equivalent to the classical Reynolds formalism when $j_0 = 0$ and a periodical extension is adopted (see Liang *et al.* 2004).

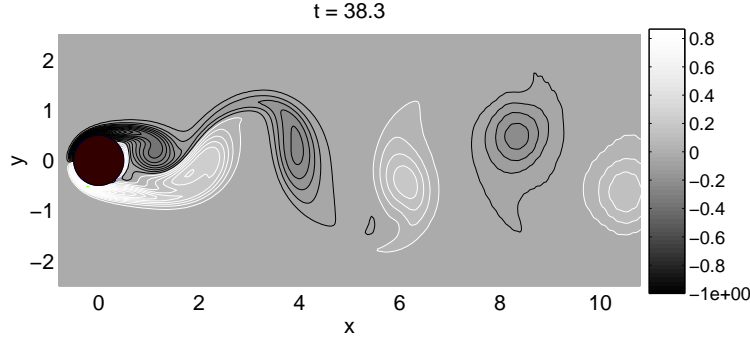


FIGURE 2. A snapshot of the simulated vorticity in a cylinder wake ($Re = 200$).

are then uniformly mapped onto a cartesian coordinate with $\Delta x = \Delta y = 0.04$, and time stepsize $\Delta t = 0.152$. Shown in Fig. 2 is a snapshot of the simulated vorticity field.

3.2. Stability structure

We now investigate the localized stability. It is analyzed from the standing point of energy loss to eddy structures from the large-scale window (that is to say, we analyze it on window 0). This helps us to grasp the stability from a longer time span, without paying too much attention to short scale details. We present only the results after the system reaches an equilibrium, since the transient period is artificial and highly dependent on initial conditions. In this case, a consistent choice of large-scale window bound is $j_0 = 0$. (We have proved in Liang *et al.* (2004) that when $j_0 = 0$ the large-scale window reconstruction is equivalent to the duration average.)

The stability metric in terms of energy loss from the base flow to the eddy window is thereby computed. The result is nearly invariant to time for all the time steps considered because the wake flow is quasi-steady. As shown in Fig. 3 for $t = 38.3$, two negative centers sit symmetrically about the axis $y = 0$. These centers, which embrace the near wake and characterize the energy transfers from the basic flow toward the eddy window, show clearly that the system is absolutely unstable, and the instability is mainly limited within the two negative lobes attached to the cylinder. An analysis using the initial evolution data (not shown here) exhibits how this absolute instability is invoked.

Also shown in Fig. 3a is that CR is non-positive everywhere throughout the domain. That is to say, a global instability has been excited. In contrast to the classical notion, the global instability does not just mean a uniform energy transfer everywhere. Rather, it has a spatial structure.

It is conventional to read instability by examining perturbation growth from simulations. Here we also plot the perturbation/eddy energy growth \dot{K}^{eddy} . Shown in Fig. 3b is the \dot{K}^{eddy} for the same time instant as in Fig. 3a. Apparently, the distributions in these two maps are different. Eddy energy grows very fast along $y = 0$ in the near wake, while in the same region the transfer is virtually zero. It can be misleading to assess the stability of a flow system by visual inspection of the simulated fields.

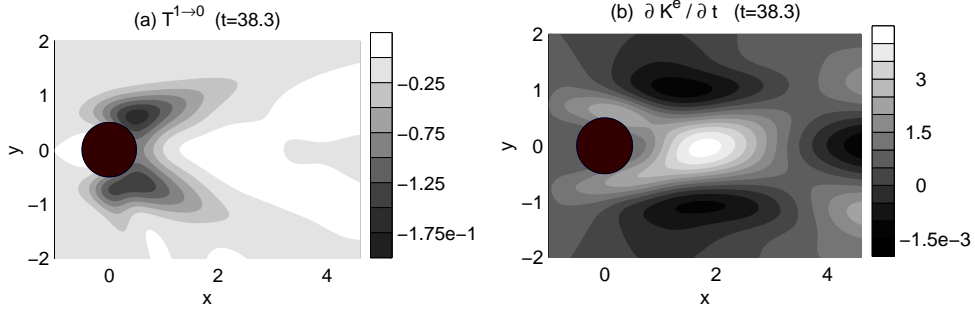


FIGURE 3. (a) Instability metric for $t = 38.3$ in terms of energy loss from the large-scale window to the eddy window. Negative transfer indicates instability. (b) Time rate of change of eddy energy \dot{K}^{eddy} for $t = 38.3$. Positive \dot{K}^{eddy} means gain in eddy energy.

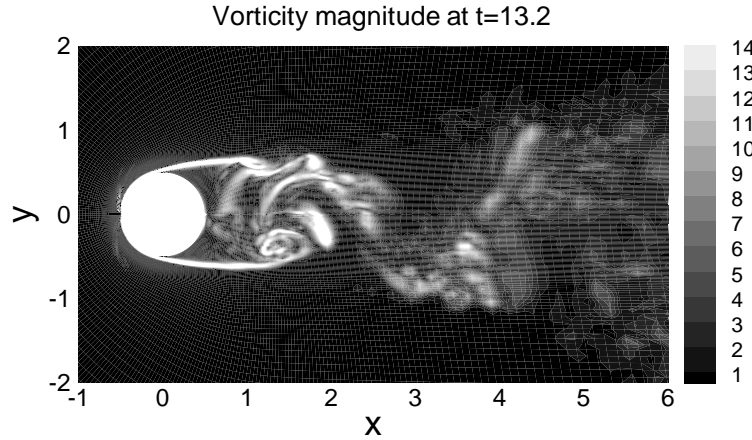


FIGURE 4. A snapshot of the instantaneous vorticity magnitude for the turbulent wake. The Reynolds number is 3900.

4. Wakes behind a circular cylinder: The turbulent case

4.1. Model description

To generate a turbulent dataset at $Re=3900$, we adopt the same numerical model as in the preceding section except that the Navier-Stokes equations are solved in conjunction with the dynamic subgrid scale model (Germano *et al.* 1991; Lilly 1992). In the simulation, $401 \times 120 \times 48$ grid points are used, and the domain size is given by $-22 \leq x \leq 17$, $-24 \leq y \leq 24$, and $-\pi/2 \leq z \leq \pi/2$. The computational solutions have been validated against previous results in terms of key parameters such as the drag coefficient and vortex-shedding frequency (Strouhal number). After the computation reaches a statistical equilibrium, we interpolate the results onto a uniform cartesian mesh ($\Delta x = 0.04$, $\Delta y = 0.02$, $\Delta z = \pi/48$) and $2^8 = 256$ equal time steps with $\Delta t = 0.0387$. Fig. 4 shows the instantaneous vorticity magnitude in a spanwise section at $t = 13.2$ (arbitrary starting time).

4.2. Window bound determination

Turbulence problems involve more complicated scale window structures. Before moving on to stability analysis, we need to determine the respective scale window bounds. We

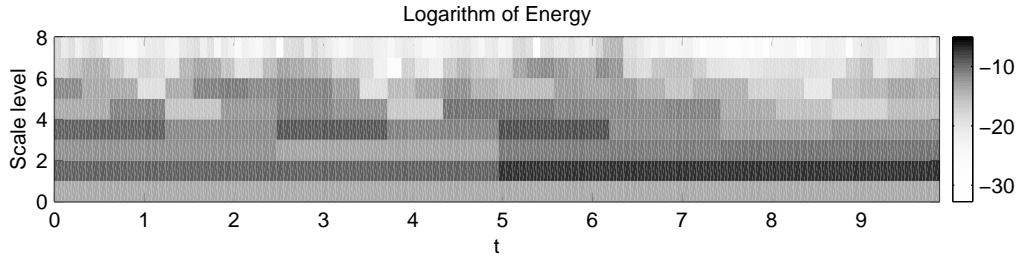


FIGURE 5. Time wavelet spectrum analysis for u at point $(2, -0.5, 0)$. Unfolded on the map is the logarithm of the square of wavelet transform coefficients. The abscissa is time, and the ordinate scale level j , which is defined such that $2^{-j}T$ (T = time duration) is the time scale.

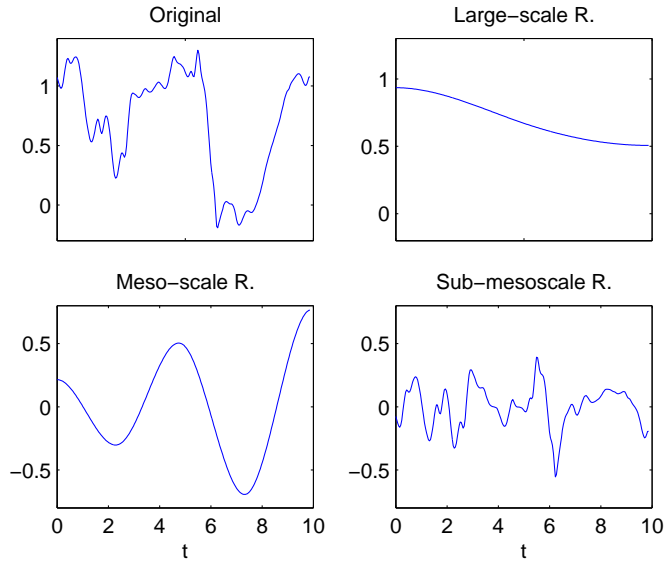


FIGURE 6. Reconstructions of the time series of u in Fig. 5. Parameters used are $j_0 = 1$, and $j_1 = 2$.

use a wavelet time spectrum analysis for this purpose. The time series are chosen from the velocity components at several typical points within the wake.

We only present the analysis of one time series. Fig. 5 displays the spectrum for u at point $(2, -0.5, 0)$. For clarity, the time average has been removed from the signal. We see from the figure that there is a clear peak at scale level $j = 1$, and another one between $j = 3$ and 4. This implies that the choice $j_0 = 0$ and $j_1 = 2$ allows for a demarcation of the function space into a well-defined large-scale window, a meso-scale window, and a sub-mesoscale window. The reconstructions with these parameters (Fig. 6) present from another point of view this partition. The growing oscillating meso-scale reconstruction hosts the time scale of vortex shedding, which is modulated by the slower varying large-scale reconstruction. The sub-mesoscale window represents the rapidly varying small scale turbulence. We are to investigate how the meso-scale window arises, and where the turbulent sub-mesoscale structure derives its energy.

4.3. Turbulence structure analysis

As in the laminar case, we continue to analyze the hydrodynamic stability from a longer-time span point of view. That is to say, we use energy loss from one window to another, rather than energy gain within a window, as the criterion. The results are presented in a spanwise plane, although the analysis is fully three-dimensional. The turbulent flow field is statistically equivalent in all the spanwise planes, but over the time period considered, the stability metric is not invariant to the spanwise location.

Figure 7 shows how energy is transferred from the background to the meso-scale structure. Here negative value indicates instability. There are two centers of instability for all the time steps shown. From the sequence, two evolutionary patterns are evident. The first is the orientation evolution: In the beginning the two centers are aligned in a northwest-southeast pattern; their relative location varies gradually into a juxtaposition symmetric around $y = 0$, and finally they evolve into a southwest-northeast orientation. The second is the relative transfer strength between these two centers. Originally, the southern center is much weaker than the northern one, but beginning at $t = 4.1$, they switch status, and by $t = 8.8$, a pattern opposite to the original appears.

In comparison to Fig. 7, the energy lost from the background to the turbulent structures are fairly symmetric about the x -axis (see Fig. 8). This is to some degree similar to the laminar case, although the transfer strength oscillates, and the hotspots are detached from the cylinder.

The above computations are based on the large-scale window. Interactions between the meso-scale and sub-mesoscale processes also require analysis for the meso-scale window. Shown in Fig. 9 is the energy loss from the meso-scale process to the turbulent processes. In contrast to the dipole structure in Figs. 7 and 8, here the transfer is mainly within a monopole except in the beginning. And, moreover, the monopole lies near the x -axis. The energy gained by the meso-scale process from the basic flow then cannot be used directly to fuel the turbulence. It must be first transported from the two lobes to the center before the transfer occurs.

The above observations suggest that there is clearly a primary instability, followed by a secondary instability, in the turbulent wake. The primary instability is composed of two parts: one accounts for the meso-scale growing mode; another for the turbulence along the wake boundary. The meso-scale dynamics is regular, as is shown in Fig. 6. The wake becomes asymmetric about the x -axis because this process is excited in an asymmetric way. The secondary instability occurs mainly in the middle near the x -axis. It funnels energy to sustain the turbulence there. Both the turbulent motions along the wake boundary and in the middle acquire energy in a fairly symmetric way, indicating that the system is in a statistical equilibrium.

A remarkable feature in the transfer maps in Figs. 7, 8 and 9 is the positive spots/centers sandwiched in the instability structures. These inverse transfers indicate that, even though the flow is turbulent, there exist processes which introduce orders rather than chaos to the system. We will see later in the discussion that these inverse transfers may have profound implications for turbulence control.

5. Discussion and conclusions

We have briefly introduced a localized hydrodynamic stability analysis to relate stability theory to experimental and numerical data, which are in general highly nonlinear

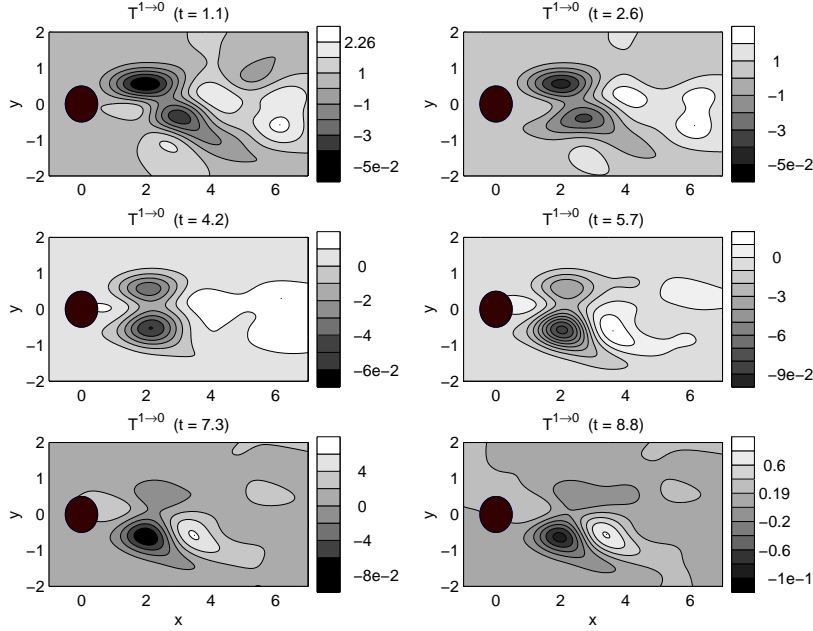


FIGURE 7. Stability metric CR in terms of energy transfer from the large-scale window to the meso-scale window for the turbulent wake. Negative values indicate instability.

and intermittent in space and time. We have utilized the theory to investigate the wake behind a cylinder, both in a laminar flow and in a turbulent flow.

The localized stability analysis is developed on a subspace decomposition-based and localized mathematical machinery, multi-scale window transform. In this analysis, a flow system is organized into some appropriately defined time scale windows. The classical formalism in the sense of Lyapunov is then localized in time to obtain a metric to measure the hydrodynamic instability. The key to spatial localization is the transfer-transport separation, which is made possible through introducing the concept of *perfect transfer*. For a fluid flow, the resulting criterion of instability bears a spatio-temporal structure, which is conceptually different from the classical formalism where stability is a notion over the whole system. This allows for much more flexibility in investigating flows with regions of interest that are difficult to demarcate. It is particularly useful for open flows, and flows with dynamics mobile in nature, such as those involving convective instability and absolute instability.

The theory has been applied to investigate the wake dynamics behind a circular cylinder. We have examined two different cases: a laminar wake ($Re=200$), and a turbulent wake ($Re=3900$). In the laminar case, the metric shows a symmetric transfer pattern, with two lobes of local absolute instability attached to the cylinder surface. A global instability mode is also seen at the stage. In contrast to the classical formalism, the eddy energy growth pattern does not necessarily imply instability.

The turbulent wake case shows a more complicated and interesting instability structure. Processes involved are structured on three distinct scale windows, among which the meso-scale flow sees a clear regularly growing mode for the time period analyzed. A primary instability is identified, with transfer centers appearing in pair along the wake boundary. It provides energy both for the meso-scale window and for the sub-mesoscale

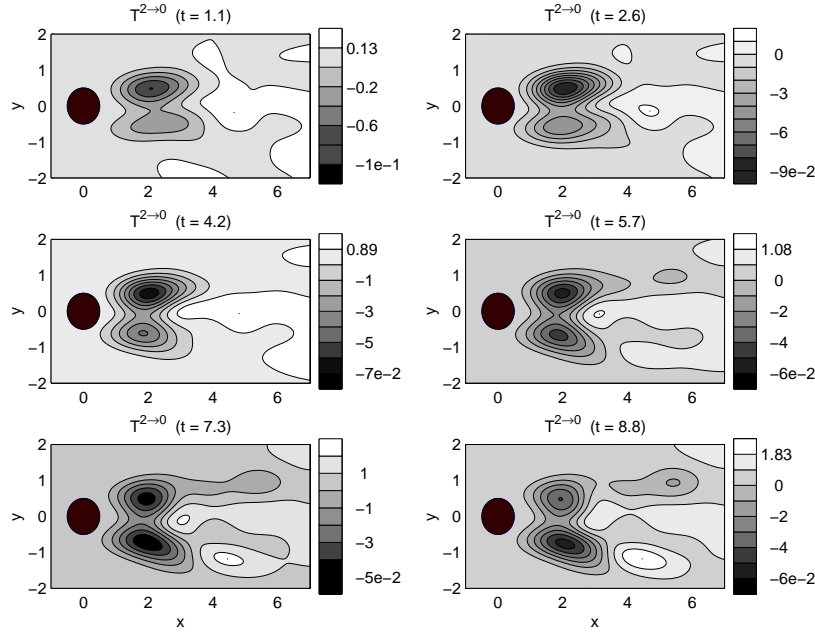


FIGURE 8. Stability metric CR in terms of energy transfer from the large-scale window to the sub-mesoscale window for the turbulent wake. Negative values indicate instability.

turbulence window. The transfer-center pair for the meso-scale window oscillates in orientation as well as strength, accounting mostly for the asymmetry of the wake vortex shedding, while that for the sub-mesoscale window adopts a pattern fairly symmetric in location around the x -axis. The turbulence also derives its energy from the meso-scale window. This secondary instability is in a monopole form and appears mainly in the center around the x -axis. Both the primary instability and the secondary instability are absolute in character.

A potential application of the above research is flow control. Based on previous studies (e.g., Huerre & Monkewitz 1990), absolute instability plays a pivotal role in vortex shedding, and as a result, a crucial step in suppressing the formation of the Karman vortex street is to identify the absolute instability regions. Our methodology provides a natural and easy way to achieve this. Although there is still some distance to go before a mature scheme of vortex suppression is formulated, it seems reasonable to suggest that control should be best applied at the maximum energy transfer centers or at locations directly upstream of these centers. In the laminar case the instability lobes are attached to the cylinder surface and their centers are downstream of the top and bottom of the cylinder, suggesting that applying control near these locations may be effective. Indeed, our simple numerical experiments using surface suction show that the areas between 70 to 90 degrees and between -70 to -90 degrees from the x -axis are the most effective suction locations for suppressing vortex shedding and reducing drag on the cylinder. Controls in areas below 50 degrees and above -50 degrees are counterproductive. We will explore this in a more systematic fashion in the future.

We have seen that on all the instability patterns there are sandwiched stable centers. These stable structures indicate that, although the flow is turbulent, processes of inverse transfer or self-laminarization may exist. This phenomenon has profound implications.

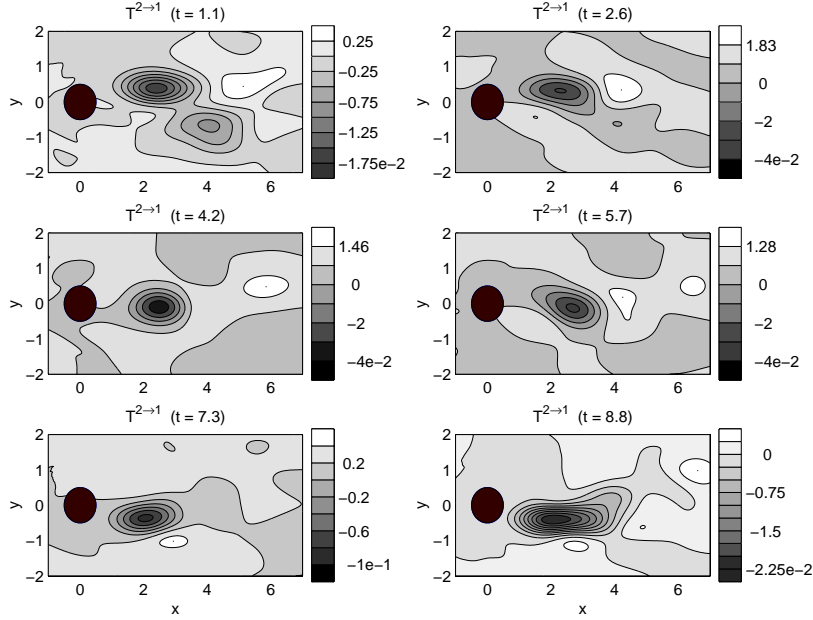


FIGURE 9. Stability metric \mathcal{CR} in terms of energy transfer from the meso-scale window to the sub-mesoscale window for the turbulent wake. Negative values indicate instability.

As is well known, the objective of turbulence control is to inhibit eddy energy from being generated, and accordingly, the traditional control strategy is based on suppression of turbulence growth. The problem is, *looking solely at the turbulence growth could be misleading, as energy increase does not necessarily occur in accordance with transfer* (cf. Fig. 3). In a region with eddy energy growing the transfer could be toward the large-scale flow. This is best illustrated in the two-point system in Fig. 10, where eddy energy (K_1^{eddy} and K_2^{eddy}) grows at both locations 1 and 2, while the transfer at location 2 is toward the large-scale window. Control of the perturbation energy growth at both points 1 and 2 indeed helps to suppress the onset of turbulence, but it is not optimal in terms of energy savings. At point 2, there is an intrinsic trend of laminarization. Suppression of K_2^{eddy} defeats this trend as well, and therefore reduces the control performance. To take advantage of this laminarization, the control should be applied at point 1 only, and the optimal objective functional should be chosen to be T_1 , rather than $K_1^{eddy} + K_2^{eddy}$.

REFERENCES

- CHAKRABARTI, S. K. 1989 Standing Rankine-Hugoniot shocks in the hybrid model flows of the black hole accretion and winds. *Astrophys. J.* **347** (1), 365-372.
- CHU, M. S., GREENE, J. M., LAO, L. L., MILLER, R. L., BONDESON, A., SAUTER, O., RICE, B. W., STRAIT, E. J., TAYLOR, T. S., & TURNBULL, A. D. 1996 Resistive interchange modes in negative central shear tokamaks with peaked pressure profiles. *Phys. Rev. Lett.* **77**(13), 2710-13.
- DRAZIN, P. G., & REID, W. H. 1982: *Hydrodynamic Stability*. Cambridge University Press. Cambridge, UK.

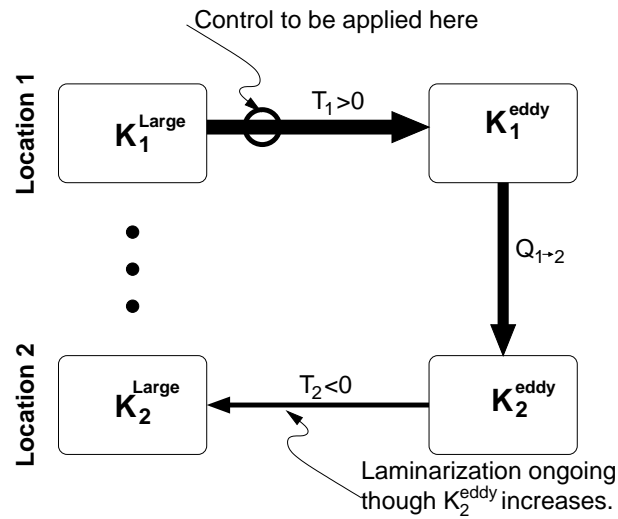


FIGURE 10. Schematic of the eddy energy transport and transfer for a two-point turbulent system. T and Q signify transfer and transport, respectively. An arrow indicates the direction of an energy flow, with its thickness standing for strength. In this case, transfer is toward the large scale at point 2, but K_2^{eddy} still grows because of the transport (advection) of K_1^{eddy} from point 1. For optimal results, control should be placed at location 1 only.

- GERMANO, M., PIOMELLI, U., MOIN, P., & CABOT, W. H. 1991 A dynamic subgrid-scale eddy viscosity model. *Phys. Fluids A* **3**, 1760–1765.
- HOLTON, J. R. 1992 *An Introduction to Dynamic Meteorology*. Academic Press. San Diego, California.
- HUERRE, P. & MONKEWITZ, P. 1990 Local and global instabilities in spatially developing flows. *Annu. Rev. Fluid Mech.* **22**, 473–537.
- LIN, C. C. 1966 *The Theory of Hydrodynamic Stability*. Cambridge U Press. Cambridge, UK.
- LIANG, X. S. & ANDERSON D. G. M 2004 Multiscale window transform. (in preparation).
- LIANG, X. S., STONE, H. A., ANDERSON, D. G. M., & WANG, M. 2004 A unified localized hydrodynamic instability analysis for incompressible fluid flows. (in preparation).
- LILLY, D. K. 1992 A proposed modification of the Germano subgrid scale closure method. *Phys. Fluids A* **4**, 633–635.
- MITTAL, R. & MOIN, P. 1997 Suitability of upwind-biased finite difference schemes for large-eddy simulation of turbulence flows. *AIAA J.* **35**, 1415–1417.
- OERTEL, H., JR. 1990 Wakes behind blunt bodies. *Annu. Rev. Fluid Mech.* **22**, 539–559.
- PIERREHUMBERT, R. T., & SWANSON, K. L. 1995 Baroclinic Instability. *Ann. Rev. Fluid Mech.* **27**, 419–467.
- STRANG, G. & NGUYEN, T. 1997 *Wavelets and Filter Banks*. Wellesley-Cambridge Press. Wellesley, MA.

Nonlinear evolution of velocity fluctuations in a laminar boundary layer excited by free-stream vortical disturbances

By P. Ricco [†], P. A. Durbin, T. Zaki AND X. Wu [†]

The response of an incompressible laminar boundary layer to vortical disturbances in the free-stream is investigated. For sufficiently long-wavelength components, the unsteady boundary-region equations are employed at a streamwise location where the boundary-layer thickness becomes of the order of the inverse of the transverse fundamental wavenumber. The equations account for the transverse ellipticity and the pressure gradient induced by the displacement effect produced by the developing boundary layer. The free-stream turbulence is modeled by one vortical mode and the nonlinear generation of modes of higher frequency within the boundary layer is considered. This study confirms that low-frequency disturbances penetrate into the viscous region and induce laminar streamwise-elongated streaks, whereas high-frequency disturbances are confined in the outer edge layer. Results show that the streamwise and vertical wavenumbers have opposite effects on the penetration of modes into the boundary layer and that there is consistency between the linear boundary-region solution and the continuous spectrum of the Orr-Sommerfeld equation. Nonlinear effects are more intense for lower values of streamwise wavenumber for a fixed level of turbulence intensity.

1. Introduction

1.1. Background

The instability of laminar flows and transition to turbulence have interested researchers for over a century. Both the complexity of the physical mechanisms and the large range of applications have been the main factors for such research efforts. Since flows in engineering systems primarily exist in fully turbulent states, it is important to attain a sound understanding of the processes by which a laminar flow evolves to a turbulent regime. The ultimate engineering purpose is to design techniques for controlling these phenomena in order to reduce wall friction drag and noise, or to enhance heat transfer and mixing in combustion.

The first successful attempts to solve the problem of laminar instability in boundary layers date back to Tollmien (1929) and Schlichting (1933). For the first time, the neutral curve of instability for the Blasius boundary layer was calculated and the unstable waves were thus named Tollmien-Schlichting (TS) waves, which were later first observed experimentally by Schubauer & Skramstad (1947). They successfully reduced the free-stream turbulence to a very low level ($Tu = 0.01 - 0.03\%$) to suppress the undesired perturbations and detected the generation and evolution of TS waves excited by a vibrating ribbon. The TS waves were thus recognized as the key feature in laminar-turbulent flow transition. Laboratory observations by Dryden (1936) and Taylor (1939) had however

[†] Department of Mathematics, Imperial College, London, United Kingdom.

showed that, when a laminar boundary layer was subjected to a high level of free-stream turbulence, low-frequency disturbances within the viscous region significantly amplified and distorted the flow. In this case the classical TS mechanism did not seem to play a significant role. This second type of disturbances found renewed interest with the investigations by Klebanoff (1971) and Arnal & Juillen (1978). They confirmed the findings by Dryden (1936) and Taylor (1939) and observed the existence of streak-like structures elongated in the streamwise direction. The transition process was not initiated by modal growth mechanisms, that is the TS viscous instability was *bypassed*. It thus appears that in the search for a sound understanding of instability and transition in wall-bounded flows it is necessary to determine when and how the TS process is excited as predicted by stability theory, and when the external level of perturbations is significant such that the growth of disturbances inside the viscous layer is not of the TS type. The problem is not trivial because it must additionally account for the different types of external disturbances which may excite the system.

It is known that the so-called *receptivity* process provides a mechanism capable of converting the wavelengths of the external disturbances into the wavelength proper of a TS wave. This may for example occur in the case of low-intensity free-stream turbulence ($Tu \sim 1\%$ or lower) interacting with wall-roughness and/or with other heterogeneities such as rapid changes in wall curvature and acoustic disturbances (Goldstein 1984; Goldstein 1985; Ruban 1985; Goldstein & Hultgren 1989; Wu 2001). On the contrary, in the cases of distortion of the free-stream flow and of higher free-stream turbulence levels, the route to wall-bounded turbulence does not follow the classical TS wave mechanism. Wu & Choudhari (2003) showed that moderate free-stream turbulence may induce substantially excessive growth rates so that the modified amplification of TS waves is higher than in the case of the undisturbed Blasius boundary layer. They also argued that, when the distortion exceeds a certain threshold, the mean profile shows a near-wall inflection point which drives the system to inviscid instability. For even higher free-stream turbulence levels ($Tu > 2 - 3\%$), bypass transition appears to take effect, which still remains mysterious. The boundary layer acts like a filter, allowing low-frequency perturbations to penetrate into the boundary layer, convect downstream and intensify (Reshotko 1976; Morkovin 1984; Suder *et al.* 1988; Goldstein *et al.* 1992; Goldstein & Leib 1993; Goldstein & Wundrow 1998; Andersson *et al.* 2001). As outlined by Jacobs & Durbin (2001), the laminar boundary layer initially undergoes a phase during which the skin-friction is only slightly higher than in the purely laminar regime. Laminar streamwise-elongated streaks, known as breathing modes or “Klebanoff modes” (Kendall 1991; Westin *et al.* 1994) dominate the core of the viscous region in this first stage of external excitation. Although these structures are called “modes”, they are not modes in the strict mathematical sense, namely they are not solutions to an eigenvalue problem. The next stage of transition is the generation of small scales of motion which eventually lead to the formation of turbulent spots. The turbulent boundary layer is then formed by the merging of the spots. Figure 1 shows a top view of the downstream evolution of streamwise velocity fluctuations inside the boundary layer when excited by free-stream turbulence. The formation of the laminar streaks (left), their instability and breakdown to turbulent spots and the merging to fully-developed turbulence (right) are clearly pictured.

Recent effort has been directed to providing a mathematical description of the linear growth of the laminar streaks. It has been found that in a laminar wall-bounded flow, three-dimensional disturbances with very long or infinite streamwise wavelength may undergo transient temporal algebraic growth to form streaks (Ellingsen & Palm



FIGURE 1. Contour plot of streamwise velocity fluctuations in a plane parallel to the wall in the core of the boundary layer during bypass transition induced by free-stream turbulence. The flow is from left to right. DNS simulation by Zaki & Durbin (2004).

1975; Landhal 1980; Hultgren & Gustaffson 1981; Gustavsson 1991; Butler & Farrell 1992; Trefethen *et al.* 1993; Reddy & Henningson 1993). More recently, it was shown that three-dimensional disturbances of similar form may exhibit substantial spatially-transient downstream growth in a flat-plate boundary layer (Luchini 1996; Luchini 2000; Cathalifaud & Luchini 2000; Tumin 2001; Zuccher *et al.* 2004). All these works revealed an important characteristic concerning the development of streamwise vortices which are already present within the boundary layer. Even the predicted profiles of the perturbation agree fairly well with experimental measurements. However, these works did not explain the key process of how these perturbations are generated by free-stream disturbances, and so these theories do not fully describe the bypass transition induced by external turbulence.

We argue that any research attempt aimed at understanding bypass transition must explicitly account for the forcing of external disturbances, which appear to be the predominant cause for this unique phenomenon. The model must thus be an inhomogeneous problem with non-zero boundary conditions at the edge of the boundary layer in order to synthesize the effects of the interaction of the viscous layer with external perturbations such as free-stream turbulence.

Steps in this direction have been taken by Leib *et al.* (1999) (denoted as LWG), and by the DNS study by Jacobs & Durbin (2001) and Zaki & Durbin (2004). In these last two works, the free-stream turbulence is expanded in continuous spectrum modes. The penetration depth of these modes provides a characterization of the ability of the external disturbance to generate amplifying disturbances inside the boundary layer. In contrast to the studies of algebraic growth, where the boundary-layer excitation is modeled as a homogeneous problem, they investigated the entrainment of free-stream velocity disturbances into a flat-plate boundary layer.

1.2. Organization of the paper

Nonlinear unsteady boundary-region solution

The mathematical formulation first hinges on the boundary-layer equations which provide a valid description of the response relatively close to the leading edge. The elliptic boundary-region equations, however, must be invoked farther downstream where the boundary-layer thickness grows to a size comparable with a length scale representative of the transverse vortical motion. The linear variant of these equations (LUBR) was solved by LWG. The nonlinear extension is not trivial, and represents the major challenge of the present analysis. The equations of continuity, x -, y - and z -momentum for the disturbances are solved by employing a second-order backward finite-difference scheme. The solution of this system requires an initial field, as well as upstream and free-stream boundary conditions.

Mean laminar steady flow

The boundary-layer equations for the mean laminar flow are first solved to obtain

the background flow on which the perturbations evolve. The equations are cast into the usual nondimensional form which employs the similarity variable η and gives the well-known Blasius solution (Schlichting & Gersten 2000). The system is solved through a second-order finite-difference scheme which employs Newton's method (Cebeci 2002).

Inviscid free-stream flow and outer boundary conditions

The mean inviscid flow is affected at leading order by the displacement effect induced by the viscous region. The free-stream solution is matched with the solution of the large- η form of the equations to find the $\eta \rightarrow \infty$ boundary conditions.

Initial condition

These profiles are needed in order to initiate the boundary-region calculation. They are obtained by means of a composite solution, constructed from the large- η solution and a power series valid for $\eta = \mathcal{O}(1)$, and by using the additive rule.

1.3. Objective

The objective of the present analysis is twofold. Our main focus is to extend the calculations of LWG, restricted to the linear evolution of very small perturbations, to the nonlinear interaction of fluctuations within the boundary layer forced by one free-stream mode.

Although LWG showed that the linear unsteady boundary-region equations describe well the behavior of low-amplitude fluctuations relatively close to the leading edge, nonlinearity must be necessarily accounted for as the magnitude of disturbances grows downstream. As LWG and Wundrow & Goldstein (2001) point out, its effects are likely to be the enhancement of transverse-length-scale components and the generation of high-frequency disturbances. In another paper of theirs, Leib *et al.* (1999b) report preliminary results for the nonlinear evolution of the peak level of the transverse-averaged r.m.s. component of the streamwise velocity as a function of the boundary-layer thickness. The solution was obtained by solving the *steady* boundary-region equations with one free-stream mode. The nonlinear solution agrees well with the linear one for short streamwise distances, while the nonlinear trend is lower than the linear one farther downstream.

The second objective is to study the effect of the parameters of the free-stream modes on the penetration of disturbances into the boundary layer. The frequencies of the modes in the streamwise and wall-normal directions are varied independently and the linear boundary-region equations are solved. The results are compared with the penetration of the modes given by the Orr-Sommerfeld equations. The comparison of the two different approaches is motivated by the work of Jacobs & Durbin (2001), where the continuous spectrum of the OS modes is used to synthesize the inflow condition for a DNS of bypass transition.

2. Problem formulation: scaling and equations of motion

The two-dimensional flow of uniform velocity U_∞ past an infinitely-thin flat plate on which homogeneous three-dimensional, statistically-stationary turbulent velocity fluctuations are superposed is considered. These perturbations are of the convected "gust" type, i.e. they passively convect with the mean flow. The mean velocity of the oncoming flow is significantly smaller than the speed of sound so that the flow can be considered incompressible. The * symbol indicates dimensional quantities. The Cartesian coordinate system is represented by the vector $\mathbf{x} = x\hat{\mathbf{i}} + y\hat{\mathbf{j}} + z\hat{\mathbf{k}} = x_1\hat{\mathbf{i}} + x_2\hat{\mathbf{j}} + x_3\hat{\mathbf{k}}$, which defines the streamwise, wall-normal and transverse directions, respectively. In LWG, these coordinates and all the other lengths are nondimensionalized by the transverse integral scale

of turbulence Λ , which is defined as follows:

$$\Lambda = \Lambda(x^*, y^*) = \int_0^\infty R_{ww}(x^*, y^*, \tau) d\tau,$$

where the correlation of the transverse velocity component is

$$R_{ww}(x^*, y^*, \tau) = \frac{\overline{w_\infty(x^*, y^*, z^* + \tau, t^*) w_\infty(x^*, y^*, z^*, t^*)}}{(\overline{w_\infty(x^*, y^*, z^*, t^*)})^2}.$$

The overbar indicates time-averaged quantities and it is considered that $x^* \rightarrow -\infty$ and $y^* \rightarrow \infty$ so that Λ is constant. For our case of one mode in the free-stream, it occurs that:

$$R_{ww} = \cos(k_3^* \tau),$$

so that Λ is not defined. We thus choose to scale all the lengths by the inverse of the transverse fundamental wavenumber k_3^* . For clarity, we still call this reference length $\Lambda = 1/k_3^*$, hence $k_3 = 1.0$. The velocity quantities are made dimensionless by U_∞ . The pressure p^* is normalized by ρU_∞^2 and the time t^* by Λ/U_∞ .

Due to the hypothesis of homogeneity and stationarity of the statistical quantities, such fluctuations are mathematically represented as a superposition of sinusoidal disturbances:

$$\mathbf{u} - \hat{\mathbf{i}} = \epsilon \mathbf{u}_\infty(x - t, y, z) = \epsilon \hat{\mathbf{u}}^\infty e^{i(\mathbf{k} \cdot \mathbf{x} - k_1 t)} + c.c., \quad (2.1)$$

where $\hat{\mathbf{u}}^\infty = \{\hat{u}_1^\infty, \hat{u}_2^\infty, \hat{u}_3^\infty\}$ and $\mathbf{k} = \{k_1, k_2, k_3\}$ are real vectors and $\hat{u}_{1,2,3}^\infty = \mathcal{O}(1)$. From the incompressibility condition, it follows that:

$$\nabla \cdot \mathbf{u}_\infty = 0, \text{ namely } \hat{\mathbf{u}}^\infty \cdot \mathbf{k} = 0. \quad (2.2)$$

Differently from the linear analysis by LWG where the turbulent Reynolds number

$$r_t = \epsilon R_\Lambda \ll 1,$$

we have $r_t = \mathcal{O}(1)$, where

$$R_\Lambda = \frac{U_\infty \Lambda}{\nu}$$

is the Reynolds number based on Λ and on the kinematic viscosity of the fluid ν . We also assume to work in the high-Reynolds-number regime, i.e. $R_\Lambda \gg 1$. It has been shown by Goldstein (1997) that, as $\epsilon \rightarrow 0$ while r_t is kept at $\mathcal{O}(1)$, the flow domain can be divided into four distinct asymptotic regions, shown in figure 2. Here is a brief description of the regions:

Region I: This region of dimensions $\mathcal{O}(\Lambda)$ in the vertical and streamwise directions includes the inviscid linear flow approaching the leading edge of the plate. In this region, the disturbances are treated as small perturbations of the oncoming uniform flow. The behavior of the solution in the very proximity of the leading edge is not considered. Instead, the analysis concentrates on the downstream asymptotic evolution of the disturbances at a large distance from the edge, allowing the derivatives with respect to the streamwise direction to be neglected.

Region II: This region is located under Region I and it comprises the viscous flow as it develops from the leading edge of the plate. The disturbances are governed by the linearized unsteady boundary-layer equations (LUBL) (Goldstein 1983; LWG). The solution eventually becomes invalid when the boundary-layer thickness δ^* becomes of the

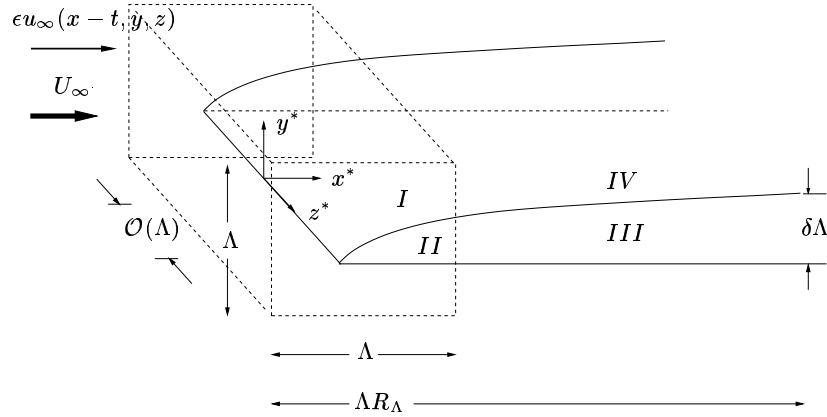


FIGURE 2. Flow field domain representation.

order of Λ . Since δ^* evolves as:

$$\delta^* = \Lambda \delta = \mathcal{O}(x^* R^{-1/2}),$$

where $R = x^* U_\infty / \nu$, setting $\delta^* = \mathcal{O}(\Lambda)$ implies that the boundary-layer approximation becomes invalid at a downstream location where $x^* = \mathcal{O}(\Lambda R_\Lambda)$, namely where

$$x/R_\Lambda = \mathcal{O}(1).$$

The flow then becomes fully three-dimensional and the ellipticity in the transverse direction must be considered. The initial condition for LUBL is used to construct the initial condition for the flow in Region III.

Region III: The flow in this region is mathematically described by the unsteady boundary-region equations (Kemp 1951), which are a simplified version of the full Navier–Stokes equations, obtained by discarding the streamwise derivatives in the viscous and pressure-gradient terms. These equations are different from the ones of LWG because the nonlinear terms are not neglected any longer.

Region IV: This region describes the outer inviscid flow above Region III and the solution is influenced at leading order by the displacement effect due to the increased thickness of the viscous layer. The flow should generally be considered nonlinear since turbulence experiences equilibrium decay in this region. However, as argued by LWG, the flow can be regarded as linear over a range of streamwise distances if the turbulent Reynolds number $r_t \ll 1$ and the flow behaves locally as a convected perturbation gust of the type of Region I. This happens when the distance $x_L \ll 1/\epsilon = R_\Lambda/r_t$. Following the study by LWG, the stationary and homogeneous turbulence $\epsilon \mathbf{u}_\infty$ is specified at a distance $-x_L^\dagger$ upstream of the leading edge where:

$$1 \ll -x_L^\dagger \ll R_\Lambda. \quad (2.3)$$

The boundary condition (2.1) can thus be applied independently of the mean flow. Despite the fact that the linear flow in the free-stream suitably provides the outer boundary conditions for the nonlinear boundary-region equations, the effects of nonlinearity in the free-stream deserve further analysis. Additional comments on this issue can be found in section 2.2.

The flow in Region I is inviscid and treated as a flow of uniform velocity to which gust-like velocity perturbations are superposed. The inviscid perturbations can be determined

by rapid distortion theory (Hunt 1973; Goldstein 1978), which describes the interaction of a gust-like disturbance with a body of arbitrary shape, in our case an infinitely-thin flat plate. The inviscid perturbation $\{u_{1,w}, u_{2,w}, u_{3,w}\}$ at the surface of the plate gives the outer boundary conditions for the viscous flow in Region II:

$$u_{1,w} = \hat{u}_1^\infty + \frac{ik_1}{\gamma} \hat{u}_2^\infty, \quad (2.4)$$

$$u_{3,w} = \hat{u}_3^\infty + \frac{ik_3}{\gamma} \hat{u}_2^\infty, \quad \gamma = \sqrt{k_1^2 + k_3^2}, \quad (2.5)$$

where the first terms on the right-hand side are the components of the unperturbed gust disturbance. The second terms represent the influence of the underlying flat surface and are related to the potential flow induced by the gust interacting with the plate. These large- η conditions are employed to obtain the initial profiles for the flow in Region II, which, in turn, are used to determine the boundary conditions for Region III. The complete analysis can be found in LWG.

2.1. The unsteady nonlinear boundary-region equations

For a single Fourier component of the disturbance, the physical solution in the viscous region can be expressed as:

$$\begin{aligned} \{u, v, w, p\} = & \{F', \left(\frac{1}{2\bar{x}R_\Lambda}\right)^{1/2} (\eta F' - F), 0, -\frac{1}{2}\} + \\ & + \epsilon \{\bar{u}_0(\bar{x}, \eta, z, t), \left(\frac{2\bar{x}k_1}{R_\Lambda}\right)^{1/2} \bar{v}_0(\bar{x}, \eta, z, t), \bar{w}_0(\bar{x}, \eta, z, t), \bar{p}_0(\bar{x}, \eta, z, t)\}, \end{aligned} \quad (2.6)$$

where:

$$\eta = y \left(\frac{R_\Lambda}{2x}\right)^{1/2},$$

and $\bar{x} = k_1 x$. $F = F(\eta)$ is the Blasius function, solution of:

$$F''' + FF'' = 0,$$

with $F(0) = 0$, $F'(0) = 0$ and $F \rightarrow \bar{\eta} = \eta - \beta$ ($\beta = 1.2168$) as $\eta \rightarrow \infty$. As in LWG and Gulyaev *et al.* (1989), the perturbation solution is expressed as the sum of a two-dimensional part $\{\bar{u}^{(0)}, \bar{v}^{(0)}, 0, \bar{p}^{(0)}\}$ and a three-dimensional part, as follows:

$$\bar{u}_0 = \bar{u}^{(0)} + \sum_{m,n=-\infty}^{+\infty} \hat{u}_{m,n} e^{ink_3 z - imk_1 t}, \quad (2.7)$$

$$\bar{v}_0 = \bar{v}^{(0)} + \sum_{m,n=-\infty}^{+\infty} \hat{v}_{m,n} e^{ink_3 z - imk_1 t}, \quad (2.8)$$

$$\bar{w}_0 = \sum_{m,n=-\infty}^{+\infty} \hat{w}_{m,n} e^{ink_3 z - imk_1 t}, \quad (2.9)$$

$$\bar{p}_0 = \bar{p}^{(0)} + \sum_{m,n=-\infty}^{+\infty} \hat{p}_{m,n} e^{ink_3 z - imk_1 t}. \quad (2.10)$$

The equations of motion are then obtained by inserting expressions (2.7)-(2.10) into the nonlinear boundary-region equations and by retaining the three-dimensional components only:

Continuity equation

$$\frac{\partial \hat{u}_{m,n}}{\partial \bar{x}} - \frac{\eta}{2\bar{x}} \frac{\partial \hat{u}_{m,n}}{\partial \eta} + \frac{\partial \hat{v}_{m,n}}{\partial \eta} + n\Omega \hat{w}_{m,n} = 0; \quad (2.11)$$

x-Momentum equation

$$\begin{aligned} & \left(-im - \frac{\eta F''}{2\bar{x}} + n^2 \kappa^2 \right) \hat{u}_{m,n} + F' \frac{\partial \hat{u}_{m,n}}{\partial \bar{x}} - \frac{F}{2\bar{x}} \frac{\partial \hat{u}_{m,n}}{\partial \eta} - \frac{1}{2\bar{x}} \frac{\partial^2 \hat{u}_{m,n}}{\partial \eta^2} + \\ & + F' \hat{v}_{m,n} = -\epsilon \frac{\partial(\widehat{u_R u_R})}{\partial \bar{x}}|_{m,n} + \frac{\epsilon \eta}{2\bar{x}} \frac{\partial(\widehat{u_R u_R})}{\partial \eta}|_{m,n} + \\ & -\epsilon \frac{\partial(\widehat{u_R v_R})}{\partial \eta}|_{m,n} - \epsilon n \Omega \widehat{u_R w_R}|_{m,n}; \end{aligned} \quad (2.12)$$

y-Momentum equation

$$\begin{aligned} & \frac{1}{4\bar{x}^2} (F - \eta F' - \eta^2 F'') \hat{u}_{m,n} + \left(-im + \frac{F'}{2\bar{x}} + \frac{\eta F''}{2\bar{x}} + n^2 \kappa^2 \right) \hat{v}_{m,n} + \\ & + F' \frac{\partial \hat{v}_{m,n}}{\partial \bar{x}} - \frac{F}{2\bar{x}} \frac{\partial \hat{v}_{m,n}}{\partial \eta} - \frac{1}{2\bar{x}} \frac{\partial^2 \hat{v}_{m,n}}{\partial \eta^2} + \frac{R_\Lambda}{2\bar{x} k_1} \frac{\partial \hat{p}_{m,n}}{\partial \eta} \\ & = -\frac{\epsilon}{2\bar{x}} \widehat{u_R v_R}|_{m,n} - \epsilon \frac{\partial(\widehat{u_R v_R})}{\partial \bar{x}}|_{m,n} + \\ & + \frac{\epsilon \eta}{2\bar{x}} \frac{\partial(\widehat{u_R v_R})}{\partial \eta}|_{m,n} - \epsilon \frac{\partial(\widehat{v_R v_R})}{\partial \eta}|_{m,n} - \epsilon n \Omega \widehat{v_R w_R}|_{m,n}; \end{aligned} \quad (2.13)$$

z-Momentum equation

$$\begin{aligned} & (-im + n^2 \kappa^2) \hat{w}_{m,n} + F' \frac{\partial \hat{w}_{m,n}}{\partial \bar{x}} - \frac{F}{2\bar{x}} \frac{\partial \hat{w}_{m,n}}{\partial \eta} - \frac{1}{2\bar{x}} \frac{\partial^2 \hat{w}_{m,n}}{\partial \eta^2} \\ & + n\Omega \hat{p}_{m,n} = -\epsilon \frac{\partial(\widehat{u_R w_R})}{\partial \bar{x}}|_{m,n} + \frac{\epsilon \eta}{2\bar{x}} \frac{\partial(\widehat{u_R w_R})}{\partial \eta}|_{m,n} \\ & -\epsilon \frac{\partial(\widehat{v_R w_R})}{\partial \eta}|_{m,n} - \epsilon n \Omega \widehat{w_R w_R}|_{m,n}, \end{aligned} \quad (2.14)$$

where

$$\kappa \equiv \frac{k_3}{(k_1 R_\Lambda)^{1/2}} = \mathcal{O}(1), \quad (2.15)$$

and $\Omega = ik_3/k_1$. The $\widehat{}$ symbol on the nonlinear terms indicates the Fourier transform operation and the subscript R denotes the three-dimensional component of velocity in equations (2.7)-(2.10). The equations are parabolic in the \bar{x} direction and elliptic in the z direction. A second-order backward finite-difference scheme is employed to march in \bar{x} and the block tri-diagonal system is solved with a standard block-elimination algorithm. The pressure component is computed on a grid staggered in the η direction with respect to the grid of the velocity components. The nonlinear terms are evaluated explicitly using

the pseudospectral method, namely the velocity quantities at the previous \bar{x} location are transformed back to the physical space to perform the product operations and are subsequently Fourier transformed again to the spectral space. This is a standard procedure for similar flow simulations in order to avoid the computationally expensive convolution operations (Kim *et al.* 1987). Dealiasing is performed by expanding the number of collocation points by a factor of (at least) 3/2 before going from the spectral to the physical space (Canuto *et al.* 1988; Moin & Mahesh 1998; Pope 2000). This operation avoids the spurious energy cascade from the unresolved high-frequency modes into the resolved low-frequency ones and it is found to be essential for the stability of the numerical results when the effect of nonlinearity is significant. An odd number of modes $N_t = N_z = 9$ is employed and is sufficient for capturing the nonlinear effects. The domain extends to $\eta = 20$ and 500 grid points are used in this direction. The typical step size in the marching direction is $\Delta\bar{x} = 0.005$.

2.2. Initial and boundary conditions

The initial condition is the same as in LWG and corresponds to the mode $(m, n) = (1, 1)$. Null initial velocity and pressure profiles are specified for all the other modes. The initial conditions are then:

$$\hat{u}_{1,1} \rightarrow \Omega u_{3,w} \left(2\bar{x}U_0 + (2\bar{x})^{3/2}U_1 \right), \quad (2.16)$$

$$\begin{aligned} \hat{v}_{1,1} \rightarrow \Omega u_{3,w} \left((V_0 + (2\bar{x})^{1/2}V_1 + \frac{i}{(\kappa_2 - i|\kappa|)(2\bar{x})^{1/2}} (e^{i\kappa_2(2\bar{x})^{1/2}\bar{\eta} - (\kappa^2 + \kappa_2^2)\bar{x}} - \right. \\ \left. + e^{-|\kappa|(2\bar{x})^{1/2}\bar{\eta}}) - \left(\frac{3}{4}\beta - \frac{1}{2}g_1|\kappa|(2\bar{x})^{1/2} \right) e^{-|\kappa|(2\bar{x})^{1/2}\bar{\eta}} + \right. \\ \left. + \bar{\eta} + \frac{3}{4}\beta - (2\bar{x})^{1/2} \left(-\frac{i}{2}(\kappa_2 + i|\kappa|)(\bar{\eta}^2 + 1) + \frac{3}{4}\beta|\kappa|\bar{\eta} + \frac{1}{2}|\kappa|g_1 \right) \right), \end{aligned} \quad (2.17)$$

$$\begin{aligned} \hat{w}_{1,1} \rightarrow u_{3,w} \left(W_0 + (2\bar{x})^{1/2}W_1 + \frac{1}{(\kappa_2 - i|\kappa|)} \left(\kappa_2 e^{i\kappa_2(2\bar{x})^{1/2}\bar{\eta} - (\kappa^2 + \kappa_2^2)\bar{x}} + \right. \right. \\ \left. \left. - i|\kappa| e^{-|\kappa|(2\bar{x})^{1/2}\bar{\eta}} \right) - \frac{3}{4}\beta|\kappa|(2\bar{x})^{1/2} e^{-|\kappa|(2\bar{x})^{1/2}\bar{\eta}} - 1 + \right. \\ \left. - (2\bar{x})^{1/2} \left(i(\kappa_2 + i|\kappa|)\bar{\eta} - \frac{3}{4}\beta|\kappa| \right) \right), \end{aligned} \quad (2.18)$$

$$\hat{p}_{1,1} \rightarrow \frac{ik_3}{R_\Lambda} u_{3,w} \left(P_1 + \left(g_1 - \frac{3}{4} \frac{\beta}{|\kappa|(2\bar{x})^{1/2}} \right) e^{-|\kappa|(2\bar{x})^{1/2}\bar{\eta}} - g_1 - \frac{3}{4}\beta\bar{\eta} \right), \quad (2.19)$$

where the functions U_0, V_0, W_0 and U_1, V_1, W_1, P_1 are solutions to two linear systems given in Appendix B, pag. 199 of LWG. It is also given that

$$\kappa_2 \equiv \frac{k_2}{(k_1 R_\Lambda)^{1/2}}, \quad (2.20)$$

and the condition $k_1 \ll k_2, k_3$ applies. The complex constant g_1 is also given in Appendix B, pag. 200 of LWG and is obtained by matching the large- η solution of the linear boundary-region equations with the initial condition for the linear boundary-layer equations. The no-slip boundary condition is applied at the wall for the velocity components

Case	k_1	k_2	k_3	\bar{x}
1	0.00053	-0.667	1.0	0.1
2	0.0011	-0.667	1.0	0.2
3	0.011	-0.667	1.0	2.0
4	0.063	-0.667	1.0	12.0
5	0.212	-0.667	1.0	40.0

TABLE 1. Parameters for the mode comparison at $R_\Lambda = 212$ depicted in figures 3 and 5 for the LUBR and the OS solutions, respectively.

of all the modes. Thanks to the staggered grid, no boundary condition for the pressure fluctuation is required at the wall. The boundary conditions as $\eta \rightarrow \infty$ for the forcing mode $(m, n) = (1, 1)$ capture the turbulent viscous decay in the free-stream and are of the mixed type:

$$\hat{u}_{1,1} \rightarrow 0, \quad (2.21)$$

$$\frac{\partial \hat{v}_{1,1}}{\partial \eta} + |\kappa|(2\bar{x})^{1/2} \hat{v}_{1,1} \rightarrow -\Omega u_{3,w} e^{i(\bar{x} + \kappa_2(2\bar{x})^{1/2}\bar{\eta})} e^{-(\kappa^2 + \kappa_2^2)\bar{x}}, \quad (2.22)$$

$$\frac{\partial \hat{w}_{1,1}}{\partial \eta} + |\kappa|(2\bar{x})^{1/2} \hat{w}_{1,1} \rightarrow i u_{3,w} \kappa_2 (2\bar{x})^{1/2} e^{i(\bar{x} + \kappa_2(2\bar{x})^{1/2}\bar{\eta})} e^{-(\kappa^2 + \kappa_2^2)\bar{x}}, \quad (2.23)$$

$$\frac{\partial \hat{p}_{1,1}}{\partial \eta} + |\kappa|(2\bar{x})^{1/2} \hat{p}_{1,1} \rightarrow 0. \quad (2.24)$$

For the other modes generated by nonlinearity within the viscous region, the boundary conditions as $\eta \rightarrow \infty$ are:

$$\hat{u}_{m,n} = \hat{v}_{m,n} = \hat{w}_{m,n} = \hat{p}_{m,n} = 0, \text{ for } (m, n) \neq (1, 1). \quad (2.25)$$

Small and bounded oscillations appear in the profiles of these velocity components at short downstream distances and eventually die away as \bar{x} increases. These oscillations are probably due to the null initial profiles and to the fact that these large- η boundary conditions indeed only represent the asymptotic behavior as $\bar{x} \rightarrow \infty$. It must be also remarked that nonlinear effects might be present in the free-stream. This issue was already pointed out by LWG. Nonlinear terms should then be retained in the free-stream equations and in the large- η boundary-region equations, which are both employed to find the outer boundary conditions. We observe that, albeit generated within the boundary layer, the v , w and p component of the nonlinearly-excited modes with $(m, n) > (1, 1)$ extend well beyond the limit of the boundary layer at $\eta \approx 3.5$. For the present status of the analysis we have tried to overcome this problem by employing a very large domain extending to $\eta = 20$.

Case	k_1	k_2	k_3	\bar{x}
a	0.1333	-1.0	1.0	32.0
b	0.1333	-1.167	1.0	32.0
c	0.1333	-1.333	1.0	32.0
d	0.1333	-1.5	1.0	32.0

TABLE 2. Parameters for the mode comparison at $R_\Lambda = 167$ depicted in figures 4 and 6 for the LUBR and the OS solutions, respectively.

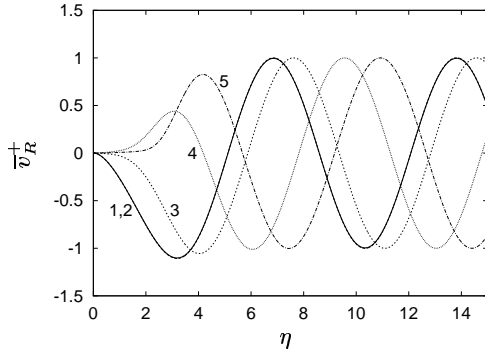


FIGURE 3. Instantaneous profiles of vertical velocity component for different values of k_1 - OS solution - $R_\Lambda = 212$.

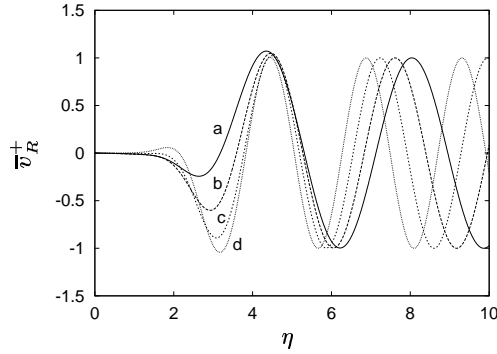


FIGURE 4. Instantaneous profiles of vertical velocity component for different values of k_2 - OS solution - $R_\Lambda = 167$.

3. Results

3.1. Penetration of modes into the boundary layer

The values of the wavenumbers k_1 and k_2 are independently varied to study the penetration of the free-stream modes into the boundary layer and are given in tables 1 and 2. We analyze the shape of the real component of the three-dimensional linear boundary-layer solution $\{\bar{u}_R^+, \bar{v}_R^+, \bar{w}_R^+\}$ for $t = 0$ and $z = 0$ at fixed downstream location x . The superscript $+$ indicates quantities scaled by the maximum free-stream value. The OS and LUBR equations are employed for comparison. Lower values of k_1 generate a more penetrating \bar{v}_R^+ (figures 3 and 5) and \bar{u}_R^+ components (not shown). The same effect is detected on the transverse component of velocity, but it is less intense than on the other components. The present results underline the importance of k_1 on the penetration of the modes into the viscous region. Similarly to what Jacobs & Durbin (2001) and LWG observed, the boundary layer acts as a low-pass filter, so that high-frequency fluctuations are sheltered and do not diffuse toward the wall. Figures 4 and 6 show that k_2 has the opposite effect of k_1 : lower values of k_2 give less penetration of the modes into the boundary layer. The OS equations give qualitatively similar results to the LUBR equations, thus indicating that the non-parallel effects do not play a major role in the penetration of modes into the boundary layer. The non-parallel effects may however become significant during the downstream evolution for the *lift-up* phenomenon detected in the DNS simulations by Jacobs & Durbin (2001), although nonlinearity probably plays a more critical role.

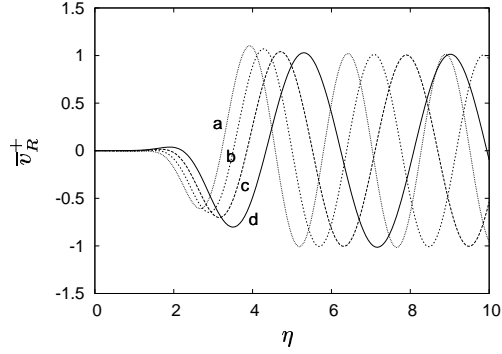
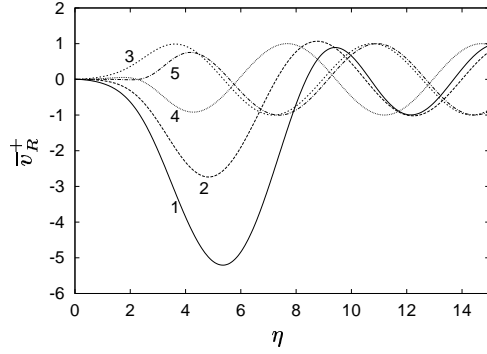


FIGURE 5. Instantaneous profiles of vertical velocity component for different values of k_1 - LUBR solution - $R_\Lambda = 212$. FIGURE 6. Instantaneous profiles of vertical velocity component for different values of k_2 - LUBR solution - $R_\Lambda = 167$.

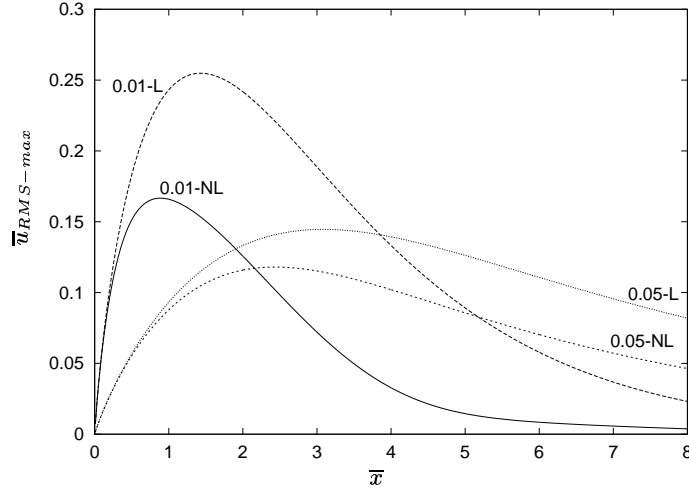


FIGURE 7. Effect of variation of streamwise wavenumber k_1 on the maximum r.m.s. of the streamwise velocity for $\epsilon \hat{u}_{1,2,3}^\infty = 0.015$, $k_2 = -k_3 = -1.0$ and $R_\Lambda = 400$. The numbers in the graph indicate the values of k_1 and NL and L indicate the nonlinear and the linear case, respectively.

3.2. Nonlinear evolution of disturbances in the boundary layer

In order to quantify the effect of the external forcing within the boundary layer, we study the \bar{x} evolution of the maximum value along η of the r.m.s of the fluctuating streamwise velocity component. The r.m.s. is defined as:

$$\bar{u}_{RMS} = \epsilon \left(\sum_{m=-(N_t-1)/2}^{(N_t-1)/2} \sum_{n=-(N_z-1)/2}^{(N_z-1)/2} |\hat{u}_{m,n}|^2 \right)^{1/2}, \quad (m, n) \neq (0, 0).$$

The peak of this quantity is then compared with the peak of the r.m.s. of the linear solution, namely:

$$\bar{u}_{RMS} = \epsilon \sqrt{2} |\Omega u_{3,w} \bar{u}|,$$

where \bar{u} is the same as in LWG.

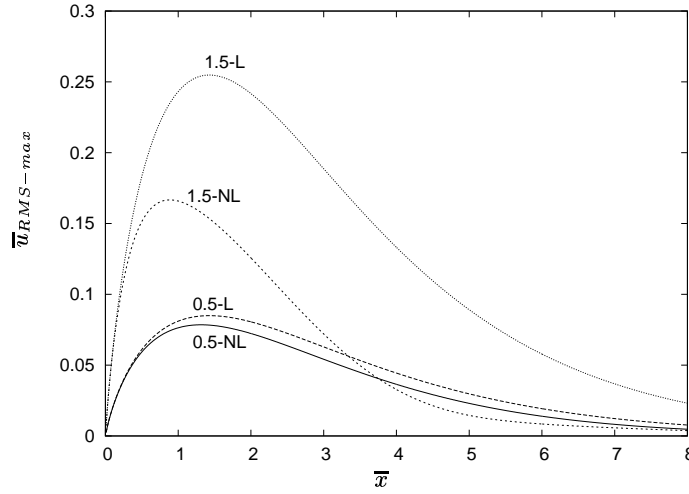


FIGURE 8. Effect of variation of turbulence intensity on the maximum r.m.s. of the three-dimensional streamwise velocity for $\epsilon = 0.01$, $k_1 = 0.01$, $k_2 = -k_3 = -1.0$ and $R_\Lambda = 400$. The numbers in the graph indicate the values of $\hat{u}_{1,2,3}^\infty$.

Nonlinearity has a stabilizing influence on the evolution of the r.m.s signal. The linear trend coincides with the nonlinear one at short downstream distances, and the effect becomes gradually more important as the flow develops downstream until it saturates. As shown in figures 7 and 8, lower values of streamwise frequencies k_1 and higher values of free-stream Tu amplify this effect, with a more marked influence of the latter. This is in agreement with the observation that low frequency modes are the most penetrating ones.

LWG partly attributed the discrepancy between their high-frequency linear results (LWG Figure 10 - page 192) and the experimental data by Kendall (unpublished) to nonlinear effects. In our study, these effects are captured, but do not explain the divergence in LWG's results at high frequency because the low-frequency fluctuations are the ones which are most influenced by nonlinearity. It should be noted, however, that high-frequency disturbances are the ones most likely to be affected by streamwise ellipticity effects, neglected both in LWG's work and in ours. Also, LWG's solution is the continuous spectrum given by rapid distortion theory, whereas our result is obtained by forcing the boundary layer with one free-stream mode only.

The fact that LWG found good agreement between their low-frequency-band results and the experimental data by Kendall in the same frequency range (Figure 10 - page 192) could be due to the mild effect of nonlinearity at the downstream locations of comparison and to the low value of free-stream turbulence intensity. Our result is in qualitative agreement with the one presented by Leib *et al.* (1999b), who solved the *steady* nonlinear boundary-region equations forced by one free-stream mode. They found that nonlinearity is not influential at short downstream distances, but progressively brings about less intense fluctuations with respect to the linear case. This qualitative accordance seems to further indicate that the low-frequency streamwise disturbances behave in a quasi-steady manner during the early stage of the downstream evolution. Wu & Choudhari (2003) however remarked that unsteadiness is likely to play a critical role in the near-wall torsion of the Blasius profile, thereby enhancing the TS-breakdown mechanism.

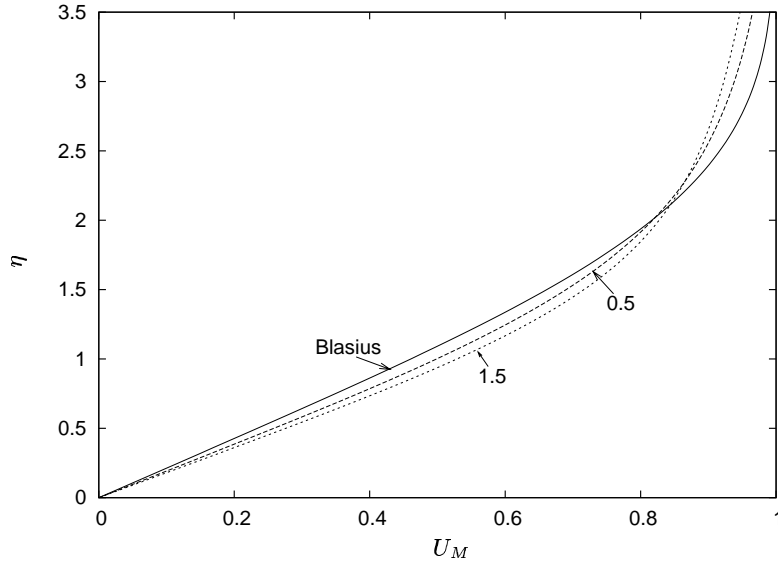


FIGURE 9. Evolution of mean streamwise velocity profile at different downstream locations for $\epsilon \hat{u}_{1,2,3} = 0.015$, $k_1 = 0.01$, $k_2 = -k_3 = -1.0$, and $R_\Lambda = 400$. Numbers in the graph denote the downstream location \bar{x} .

The new mean flow U_M is as follow:

$$U_M = U_M(\bar{x}, \eta) = F'(\eta) + \hat{u}_{0,0}(\bar{x}, \eta).$$

We observe that the canonical Blasius profile is modified by the nonlinear interactions in that higher values of streamwise velocity are detected near the wall (increased wall-shear stress), whereas the opposite phenomenon occurs in the proximity of the free-stream (figure 9). This finding accords with the DNS calculations of Jacobs & Durbin (2001) and Zaki & Durbin (2004), who reported the existence of forward jets in the proximity of the wall and backward jets in the outer edge layer.

LWG also point out that the two-dimensional components, which are asymptotically smaller for isotropic free-stream turbulence in the linear case, might become important in the nonlinear case and interact with the three-dimensional ones.

4. Future work

Future studies with multi-mode forcing in the free-stream are of interest, in particular the nonlinear interaction of two modes, one with low and the other one with high frequency. Recent results by Zaki & Durbin (2004) show that transition can occur with two modes of this kind. This finding is encouraging for our further research on bypass transition, since, as also envisioned by LWG, the nonlinear simulation with the continuous free-stream spectrum appears too computationally expensive at the present time. However, since the boundary-region formulation is accurate only for low values of k_1 , it might not be possible to investigate the case with the high-frequency free-stream forcing.

It is also important to analyze the secondary instability of the new flow generated by the nonlinear interaction of the modes within the viscous region. This stability analysis has also been suggested by LWG. The purpose is to set a theoretical basis on the most prominent transition mechanism observed in the DNS simulations by Jacobs &

Durbin (2001), namely the Kelvin-Helmholtz type of instability of the lifted backward perturbation jets. This intriguing mechanism has been first recognized as relevant by Wu *et al.* (1999) in their extensive work on bypass transition due to periodically passing wakes. These unstable phenomena eventually lead to the formation of “top-down” turbulent spots, so called since they are originated by a high-level of free-stream turbulence located *on top* of them. The merging of the spots then completes the transition to fully-developed turbulence.

It is also undoubtedly of interest to look for analogies with the recent results by Wu & Choudhari (2003) of a Blasius boundary layer perturbed by Klebanoff modes. They found that such free-stream perturbations can significantly distort the base mean flow to produce the inviscid growth of modified TS waves, which can be much higher than in the case of the unmodified Blasius flow. Furthermore, the analysis by Cossu & Brandt (2002) and the experiments by Boiko *et al.* (1994) indicate that moderate free-stream turbulence intensities are capable of generating a spatial amplification rate of disturbances which is lower than in the canonical case. However, they also observed that inflectional instability occurs for higher values of turbulence intensity, thereby enhancing the transition process. These peculiar behaviors deserve further investigation, which might lead us to a better understanding of the relation between the TS-wave breakdown and the lift-up mechanism of the laminar streaks. We however note that the new base flow for the secondary instability analysis should include the contribution of the streak modulation at fixed time. It should be possible to parametrize the effect of time on the streamwise velocity profile inasmuch as the laminar streaks evolve on a much longer time scale.

Acknowledgements

Pierre Ricco would like to acknowledge the hospitality and financial support of the Center for Turbulence Research at Stanford and to thank Professor S. Lele, Z. Xiong, Y. Liu for the useful and illuminating discussions. Part of PR's expenses during the Summer Research Program was covered by EPSRC grant GR/S59635/01.

REFERENCES

- ANDERSSON, P., BRANDT, L., BOTTARO, A. & HENNINGSON, D.S. 2001 On the breakdown of boundary layer streaks. *Journal of Fluid Mechanics*, **428**, 29–60.
- ARNAL, D. & JUILLEN, J.C. 1978 Contribution expérimental à l'étude de la receptivité d'une couche limite laminaire, à la turbulence de l'écoulement général. *CERT RT 1/5018 AYD - ONERA*.
- BOIKO, A.V., WESTIN, K.J.A., KLINGMANN, K.G.B., KOZLOV, V.V. & ALFREDSSON, P.H. 1994 Experiments in a boundary layer subjected to free stream turbulence. Part 2 the role of TS-waves in the transition process. *Journal of Fluid Mechanics*, **281**, 219–245.
- BUTLER, K.M. & FARRELL, B.F. 1992 Three-dimensional optimal perturbations in viscous shear flow. *Physics of Fluids*, **4**, 8, 1637–1650.
- CANUTO, C., HUSSAINI, M.Y., QUARTERONI, A. & ZANG, T.A. 1988 *Spectral Methods in Fluid Dynamics*. Springer-Verlag, New York.
- CATHALIFAUD, P. & LUCHINI, P. 2000 Algebraic growth in boundary layers: optimal control by blowing and suction at the wall. *Eur. J. Mech. B - Fluids*, **19**, 469–490.
- CEBECI, T. 2002 *Convective Heat Transfer*. Springer-Verlag.

- COSSU, C. & BRANDT, L. 2002 Stabilization of Tollmien-Schlichting waves by finite amplitude optimal streaks in the Blasius boundary layer. *Physics of Fluids*, **14**, 8, L57–L60.
- DRYDEN, H. L. 1936 Air flow in the boundary layer near a plate. *NACA Rep.* 562.
- ELLINGSEN, T. & PALM, E. 1975 Stability of linear flow. *Physics of Fluids*, **18**, 4, 487–488.
- GOLDSTEIN, M.E. 1978 Unsteady vortical and entropic distortions of potential flows round arbitrary obstacles. *Journal of Fluid Mechanics*, **89**, 433–468.
- GOLDSTEIN, M.E. 1983 The evolution of Tollmien-Schlichting waves near a leading edge. *Journal of Fluid Mechanics*, **127**, 59–81.
- GOLDSTEIN, M.E. 1984 Generation of instability waves in flows separating from smooth surfaces. *Journal of Fluid Mechanics*, **145**, 71–94.
- GOLDSTEIN, M.E. 1985 Scattering of acoustic waves into Tollmien-Schlichting waves by small streamwise variations in surface geometry. *Journal of Fluid Mechanics*, **154**, 509–529.
- GOLDSTEIN, M.E. 1997 Response of the pre-transitional laminar boundary layer to free-stream turbulence - Otto Laporte Lecture. *Bull. Am. Phys. Soc.*, **42**, 2150.
- GOLDSTEIN, M.E. & HULTGREN, L.S. 1989 Boundary layer receptivity to long-wave free-stream disturbances. *Ann. Rev. Fluid Mechanics*, **21**, 137–166.
- GOLDSTEIN, M.E., LEIB, S.J. & COWLEY, S.J. 1992 Distortion of a flat plate boundary layer by free stream vorticity normal to the plate. *Journal of Fluid Mechanics*, **237**, 231–260.
- GOLDSTEIN, M.E. & LEIB, S.J. 1993 Three-dimensional boundary layer instability and separation induced by small-amplitude streamwise vorticity in the upstream flow. *Journal of Fluid Mechanics*, **246**, 21–41.
- GOLDSTEIN, M.E. & WUNDROW, D.W. 1998 On the environmental realizability of algebraically growing disturbances and their relation to Klebanoff modes. *Theor. Comput. Fluid Dyn.*, **10**, 171–186.
- GULYAEV, A.N., KOZLOV, V.E., KUZNETSOV, V.R., MINEEV, B.I. & SEKUNDOV, A.N. 1989 Interaction of a laminar boundary layer with external turbulence. *Izv. Akad. Nauk. SSSR Mekh. Zhid. Gaza*, **6**, 700–710.
- GUSTAVSSON, L.H. 1991 Energy growth of three-dimensional disturbances in plane Poiseuille flow. *Journal of Fluid Mechanics*, **224**, 241.
- HULTGREN, L.S. & GUSTAFSSON, L.H. 1981 Algebraic growth of disturbances in a laminar boundary layer. *Physics of Fluids*, **24**, 6, 1000–1004.
- HUNT, J.C.R. 1973 A theory of turbulent flow round two-dimensional bluff bodies. *Journal of Fluid Mechanics*, **61**, 625–706.
- JACOBS, R.G. & DURBIN, P.A. 2001 Simulation of bypass transition. *Journal of Fluid Mechanics*, **428**, 185–212.
- KEMP, N. 1951 The laminar three-dimensional boundary layer and a study of the flow past a side edge. *M.Ac.S. Thesis, Cornell University*.
- KENDALL, J.M. 1985 Experimental study of disturbances produced in a pre-transitional boundary layer. *AIAA Paper 85-1695*.
- KENDALL, J.M. 1991 Studies on laminar boundary layer receptivity to free-stream turbulence near a leading edge. In *Boundary Layer Stability and Transition to Turbulence* (ed. D.C. Reda, H.L. Reed & Kobayashi). ASME FED, vol. 114, 23–30.

- KIM, J., MOIN, P. & MOSER, R. 1987 Turbulence statistics in fully developed channel flow at low Reynolds number. *Journal of Fluid Mechanics*, **177**, 133–166.
- KLEBANOFF, P.S. 1971 Effect of free-stream turbulence on a laminar boundary layer. *Bull. Am. Phys. Soc.*, **16**.
- LANDHAL, M.T. 1980 A note on an algebraic instability of inviscid parallel shear flows. *Journal of Fluid Mechanics*, **98**, 243–251.
- LEIB, S.J., WUNDROW, D.W. & GOLDSTEIN, M.E. 1999 Effect of free-stream turbulence and other vortical disturbances on a laminar boundary layer. *Journal of Fluid Mechanics*, **380**, 169–203.
- LEIB, S.J., WUNDROW, D.W. & GOLDSTEIN, M.E. 1999b Generation and growth of boundary-layer disturbances due to free-stream turbulence. *AIAA Paper 99-0498*.
- LUCHINI, P. 1996 Reynolds-number-independent instability of the boundary layer over a flat surface. *Journal of Fluid Mechanics*, **327**, 101–115.
- LUCHINI, P. 2000 Reynolds-number-independent instability of the boundary layer over a flat surface: optimal perturbations. *Journal of Fluid Mechanics*, **404**, 289–309.
- MOIN, P. & MAHESH, K. 1998 Direct numerical simulation: a tool in turbulence research. *Annu. Rev. Fluid Mech.*, **30**, 539–578.
- MORKOVIN, M.V. 1984 Bypass transition to turbulence and research desiderata. *NASA CP-2386 Transition in Turbines*, 161–204.
- POPE, S. B. 2000 *Turbulent Flows*. Cambridge University Press.
- REDDY, S.C. & HENNINGSON, D.S. 1993 Energy growth in viscous channel flows. *Journal of Fluid Mechanics*, **252**, 209–238.
- RESHOTKO, E. 1976 Boundary layer stability and transition. *Ann. Rev. Fluid Mech.*, **8**, 311–349.
- RUBAN, A.I. 1985 On the generation of Tollmien-Schlichting waves by sound. *Fluid Dynamics*, **25**,(2), 213–221.
- SCHLICHTING, H. 1933 Zur Entstehung der Turbulenz bei der Plattenströmung., *In Math. Phys. Klasse (181–208). Nach. Ges. Wiss. Göttingen*.
- SCHLICHTING, H. & GERSTEN, K. 2000 *Boundary-Layer Theory*. Springer.
- SCHUBAUER, G.B. & SKRAMSTAD, H.K. 1947 Laminar boundary-layer oscillations and transition on a flat plate. *NACA TN 909*.
- SUDER, K.L., O'BRIEN, J.E. & RESHTKO, E. 1988 Experimental study of bypass transition in a boundary layer. *NASA TM 100913*.
- TAYLOR, G.I. 1939 Some recent developments in the study of turbulence. *In proc. Fifth Intl Congr. for Applied Mechanics (ed. J.P. Den Hartog & Peters)*, 294–310.
- TOLLMIE, W. 1929 Über die Entstehung der Turbulenz 1. Mitteilung., *In Math. Phys. Klasse (21–44). Nach. Ges. Wiss. Göttingen (Translated into English as NACA TM 609 (1931))*.
- TREFETHEN, L.N., TRAFETHEN, A.E., REDDY, S.C. & DRISCOLL, T.A. 1993 Hydrodynamic stability without eigenvalues. *Science*, **261**, 578–584.
- TUMIN, A. 2001 A model of spatial algebraic growth in a boundary layer subjected to a streamwise pressure gradient. *Physics of Fluids*, **13**, 5, 1521–1523.
- WESTIN, K.J.A., BOIKO, A.V., KLINGMANN, B.G.B., KOZLOV, V.V. & ALFREDSSON, P.H. 1994 Experiments in a boundary layer subjected to free stream turbulence. Part I. Boundary layer structure and receptivity. *Journal of Fluid Mechanics*, **281**, 193–218.

- WU, X. 2001 Receptivity of boundary layers with distributed roughness to vortical and acoustic disturbances: A second-order asymptotic theory and comparison with experiments. *Journal of Fluid Mechanics*, **431**, 91–133.
- WU, X. & CHOUDHARI, M. 2003 Linear and non-linear instabilities of a Blasius boundary layer perturbed by streamwise vortices. Part II. Intermittent instability induced by long-wavelength Klebanoff modes. *Journal of Fluid Mechanics*, **483**, 249–286.
- WU, X., JACOBS, R.G., HUNT, J.C.R. & DURBIN, P.A. 1999 Simulation of boundary layer transition induced by periodically passing wakes. *Journal of Fluid Mechanics*, **398**, 109–153.
- WUNDROW, D.W. & GOLDSTEIN, M.E. 2001 Effect on a laminar boundary layer of small-amplitude streamwise vorticity in the upstream flow. *Journal of Fluid Mechanics*, **426**, 229–262.
- ZAKI, T. & DURBIN, P.A. 2004 Mode interaction and the bypass route to transition. *Journal of Fluid Mechanics*, submitted.
- ZUCCHER, S., LUCHINI, P. & BOTTARO, A. 2004 Algebraic growth in a Blasius boundary layer: optimal and robust control by mean suction in the nonlinear regime. *Journal of Fluid Mechanics*, **513**, 135–160.

The robustness of acoustic analogies

By J. B. Freund[†], S. K. Lele AND M. Wei [†]

Acoustic analogies for the prediction of flow noise are exact rearrangements of the flow equations $\mathcal{N}(\vec{q}) = 0$ into a nominal sound source $\mathcal{S}(\vec{q})$ and sound propagation operator \mathcal{L} such that $\mathcal{L}\vec{q} = \mathcal{S}(\vec{q})$. In practice, the sound source is typically modeled and the propagation operator inverted to make predictions. Since the rearrangement is exact, any sufficiently accurate model of the source will yield the correct sound, so other factors must determine the merits of any particular formulation. Using data from a two-dimensional mixing layer direct numerical simulation (DNS), we evaluate the robustness of two analogy formulations to different errors intentionally introduced into the source. The motivation is that since \mathcal{S} can not be perfectly modeled, analogies that are less sensitive to errors in \mathcal{S} are preferable. Our assessment is made within the framework of Goldstein's generalized acoustic analogy, in which different choices of a base flow used in constructing \mathcal{L} give different sources \mathcal{S} and thus different analogies. A uniform base flow yields a Lighthill-like analogy, which we evaluate against a formulation in which the base flow is the actual mean flow of the DNS. The more complex mean flow formulation is found to be significantly more robust to errors in the energetic turbulent fluctuations, but its advantage is less pronounced when errors are made in the smaller scales.

1. Introduction

Jet noise remains a major contributing component of aircraft noise, especially at take-off, and is especially challenging to reduce without decreasing jet exit velocities. Design tools with sufficient reliability to explore configurations (*e.g.* nozzle geometries) significantly different from those against which modeling parameters were tuned are lacking. Thus, the industry currently relies in part on an expensive Edisonian trial-and-error approach for seeking improvements. The principal difficulty is that the noise radiated by a jet depends in a complex way upon the details of the *unsteady* flow turbulence, which makes it harder to predict than the simpler mean statistics typically targeted by turbulence models.

Most approaches to predicting jet noise have three elements: designation of a noise source and propagation operator, modeling of the source, and solution of the radiated sound. Just as there is no clear separation of sound from the rest of the flow in nonlinear compressible turbulence, there is also no unique designation of a noise source in such a flow. Near flow Mach number M of unity, which is where jets on civilian aircraft typically operate, many of the length and time scale separations common in acoustic analysis are unavailable to assist this designation. As a result, there are numerous possible choices for decomposing the flow equations, written compactly here for flow field \vec{q} as $\mathcal{N}(\vec{q}) = 0$, into a nominal noise source \mathcal{S} and propagation \mathcal{L} operator: $\mathcal{L}\vec{q} = \mathcal{S}(\vec{q})$. This procedure is known as acoustic analogy; the rearrangement is exact, but $\mathcal{S}(\vec{q})$ is treated analogously to an externally applied noise source. The (usually linear) wave operator \mathcal{L} provides the means to compute \vec{q} in the far field which is the radiated noise.

[†] Theoretical and Applied Mechanics, University of Illinois at Urbana-Champaign

Lighthill (1952) introduced the acoustic analogy framework, selecting \mathcal{L} to be a homogeneous-medium scalar wave operator acting on the density perturbation ρ' ,

$$\mathcal{L}\vec{q} = \frac{\partial^2 \rho'}{\partial t^2} - a_\infty^2 \nabla^2 \rho' = \mathcal{S}(\vec{q}), \quad (1.1)$$

with the source

$$\mathcal{S}(\vec{q}) = \frac{\partial^2}{\partial x_i \partial x_j} \left(\rho v_i v_j + (p' - a_\infty^2 \rho') \delta_{ij} - \tau_{ij} \right), \quad (1.2)$$

where a_∞ is the constant ambient speed of sound, $\rho' = \rho - \rho_\infty$ is density perturbation, $p' = p - p_\infty$ is pressure perturbation, and v_i are velocity components.[†] Inversion of the wave operator is trivial in this case, but modeling the source in absence of precise space-time near-field information is not.

Lighthill recognized from the beginning (Lighthill 1952) that his decomposition was in a sense artificial. Since the propagation operator \mathcal{L} in (1.1) does not redirect sound, refraction is effectively lumped into \mathcal{S} in (1.2) and is thus indistinguishable from a true noise source. The separation of propagation and generation has troubled the aeroacoustic community ever since. It can be argued that \mathcal{L} and \mathcal{S} that better separate true sources from propagation provide a firmer platform upon which to begin modeling the sources. The linearized Lilley equation (Lilley 1974; Goldstein 1976) is a common choice for this. In this formulation, a parallel base flow and any refraction it causes is explicit in \mathcal{L} . However, it does not provide any obvious simplification of the source \mathcal{S} , still leaving complex combinations of terms (*e.g.* Colonius *et al.* 1997) which must be modeled in making predictions. Since there is no clear simplification that comes about by including more propagation physics into \mathcal{L} , it can therefore also be argued that the Lighthill approach is no worse off than such a more sophisticated approach. Since acoustic analogies are exact, an accurate representation of the source in the simpler Lighthill analogy provides the correct sound despite the multiple physical effects grouped into it. Which approach is best can be argued back and fourth, but since different acoustic analogies require different source models, it is difficult to make clear head-to-head comparisons between them and thus difficult to judge if one is preferable to others. Also, since the source is complex, there are typically sufficient free parameters to make it match data for any particular jet.

In this paper, we take a new approach and empirically assess the *robustness* of different acoustic analogies to modeling errors in their respective \mathcal{S} 's. Since \mathcal{S} will never be modeled exactly in practice, we explore whether some $\mathcal{L}\vec{q} = \mathcal{S}(\vec{q})$ decompositions are more robust to errors than others. It is known, for example, that small errors in the source for the Lilley equation can lead to large (order of magnitude) errors in the noise predicted (Colonius *et al.* 1997). To make our assessment, we employ Goldstein's recently developed generalized acoustic analogy, which provides a single clear framework for a family of consistent \mathcal{L} 's and \mathcal{S} 's. The formulation is described in section 2.1. The noise source data are taken from a direct numerical simulation (DNS) described in section 2.2, with errors of types purposely introduced as described in section 2.3. Specifically, we consider Lighthill's homogeneous-medium wave equation approach and a formulation in which \mathcal{L} includes the exact mean flow taken from the DNS.

[†] This form of Lighthill's equation is equivalent to his formulation and more convenient.

2. Preliminaries

2.1. Formulation

The propagation operator in Goldstein's (2003) generalized acoustic analogy is similar to linearized Euler equations:

$$\bar{\rho} \frac{\bar{D}}{Dt} \frac{\rho'}{\bar{\rho}} + \frac{\partial}{\partial x_j} \bar{\rho} u'_j = 0 \quad (2.1a)$$

$$\bar{\rho} \left(\frac{\bar{D}}{Dt} u'_i + u'_j \frac{\partial \tilde{v}_i}{\partial x_j} \right) + \frac{\partial p'_e}{\partial x_i} - \rho' / \bar{\rho} \frac{\partial \tilde{\tau}_{ij}}{\partial x_j} = \frac{\partial}{\partial x_j} (e'_{ij} - \tilde{e}_{ij}) \quad (2.1b)$$

$$\frac{1}{\gamma - 1} \left(\frac{\bar{D} p'_e}{Dt} + \gamma p'_e \frac{\partial \tilde{v}_j}{\partial x_j} + \gamma \frac{\partial}{\partial x_j} \bar{\rho} u'_j \right) - u'_i \frac{\partial \tilde{\tau}_{ij}}{\partial x_j} = \frac{\partial}{\partial x_j} (\eta'_j - \tilde{\eta}_j) + (e'_{ij} - \tilde{e}_{ij}) \frac{\partial \tilde{v}_i}{\partial x_j}, \quad (2.1c)$$

where

$$\frac{\bar{D}}{Dt} \equiv \frac{\partial}{\partial t} + \tilde{v}_j \frac{\partial}{\partial x_j} \quad (2.2)$$

and

$$\tilde{\tau}_{ij} \equiv \delta_{ij} \bar{p} - \tilde{T}_{ij} - \tilde{\sigma}_{ij}. \quad (2.3)$$

The base flow which defines the specific analogy has density $\bar{\rho}$, pressure \bar{p} , and velocity \tilde{v}_i and satisfies exact equations with sources \tilde{T}_{ij} , \tilde{H}_{ij} and \tilde{H}_0 (Goldstein 2003). For example, the governing equations for a time-averaged base flow has Reynolds stresses as sources. Perturbations from this base flow are ρ' , p' , and v'_i . To put (2.1) into its relatively clean form, new dependent variables were constructed from nonlinear combinations of the primitive variables as

$$p'_e \equiv p' + \frac{\gamma - 1}{2} \rho v_i v_i + (\gamma - 1) \tilde{H}_0 \quad \text{and} \quad u'_i \equiv \rho \frac{v'_i}{\bar{\rho}}, \quad (2.4)$$

which become $p'_e = p'$ and $u_i = v_i$ in the linear acoustic limit.

The source terms on the right-hand side of (2.1b) and (2.1c) are the \mathcal{S} discussed in section 1. They are

$$e'_{ij} \equiv -\rho v'_i v'_j + \frac{\gamma - 1}{2} \delta_{ij} \rho v'_k v'_k + \sigma'_{ij} \quad (2.5a)$$

$$\tilde{e}_{ij} \equiv \tilde{T}_{ij} - \delta_{ij} (\gamma - 1) \tilde{H}_0 \quad (2.5b)$$

$$\eta'_i \equiv -\rho v'_i h'_0 - q'_i + \sigma_{ij} v'_j \quad (2.5c)$$

$$\tilde{\eta}_i \equiv \tilde{H}_i - \tilde{T}_{ij} \tilde{v}_j, \quad (2.5d)$$

where σ is a viscous stress tensor and q is a diffusive heat flux. The enthalpy h'_0 is $h'_0 \equiv h' + v'_i v'_i / 2$, where h' is a perturbation to the base flow thermodynamic enthalpy.

We consider two base flow choices in this paper. The first is a uniform flow,

$$\bar{\rho} = \rho_\infty \quad \bar{p} = p_\infty \quad \tilde{v}_1 = V_1 \quad \text{and} \quad \tilde{v}_2 = \tilde{v}_3 = 0, \quad (2.6)$$

which gives a Lighthill-like formulation for a uniform velocity homogeneous medium. V_1 is the velocity of the slow speed side of the mixing layer. In this case, \tilde{T}_{ij} , \tilde{H}_{ij} and \tilde{H}_0

are all zero, so the sources are

$$e'_{ij} - \bar{e}_{ij} = -\rho v'_i v'_j + \frac{\gamma - 1}{2} \delta_{ij} \rho v'_k v'_k \quad (2.7)$$

and

$$\eta'_i - \bar{\eta}_i = -\rho v'_i h'_0, \quad (2.8)$$

where we have omitted molecular diffusion terms as we do throughout in the discussion and in the numerical calculations. In this case, perturbations are from the uniform flow (2.6), not the mean flow.

In the second case, we use the time averaged DNS flow to be the base flow. An overbar ($\bar{\cdot}$) indicates a time average with corresponding Favre average ($\overline{\cdot}$). Thus we have noise sources

$$e'_{ij} - \bar{e}_{ij} = -\rho v'_i v'_j + \overline{\rho v'_i v'_j} + \frac{\gamma - 1}{2} \delta_{ij} (\rho v'_k v'_k - \overline{\rho v'_k v'_k}) \quad (2.9)$$

and

$$\eta'_i - \bar{\eta}_i = -\rho v'_i h'_0 + \overline{\rho v'_i h'_0}, \quad (2.10)$$

which have zero mean.

2.2. DNS Data and Acoustic Analogy Solution

We will study the robustness of these two acoustic analogies for a two-dimensional mixing layer flow between Mach 0.9 and Mach 0.2 free streams of the same temperature. The instantaneous vorticity is visualized in figure 1, which also shows that the physical domain of the simulation extends from $x = 0$ to 200δ downstream and from $y = -80\delta$ to 80δ in the transverse direction, where δ is the vorticity thickness at the inflow boundary. The Reynolds number based on the velocity difference and δ is 500. The physical domain was surrounded by a boundary zone on all sides to absorb outgoing disturbance. The flow was excited by low amplitude random forcing applied in the inflow boundary zone at 8 frequencies randomly distributed between zero and twice the most unstable frequency predicted by linear stability analysis. To simulate the flow, the compressible flow equations were solved using high-order finite differences and fourth-order Runge-Kutta time advancement and without modeling approximations. Full details of the numerical method and simulation procedure, including the specifics of the inflow excitation, are provided elsewhere (Wei & Freund 2004). The only difference here is that the present x domain is twice as long as that considered in those mixing layer control studies and the simulation time is doubled.

Flow fields were saved every four numerical time steps during simulation. All necessary averages, correlations, and source terms needed for the acoustic analogies were computed directly from this stored DNS data. The left-hand sides of (2.1) were solved directly on the same mesh as the direct numerical simulation using a similar algorithm with the same numerical time step as the DNS. The source was interpolated in time as necessary using a cubic spline with 16 knots. For both the DNS data and the analogy solutions, the sound was extrapolated into the far-field by a semi-analytic solution of the wave equation in the same manner as by Freund (2001). The full details of this procedure are also documented elsewhere (Wei & Freund 2004).

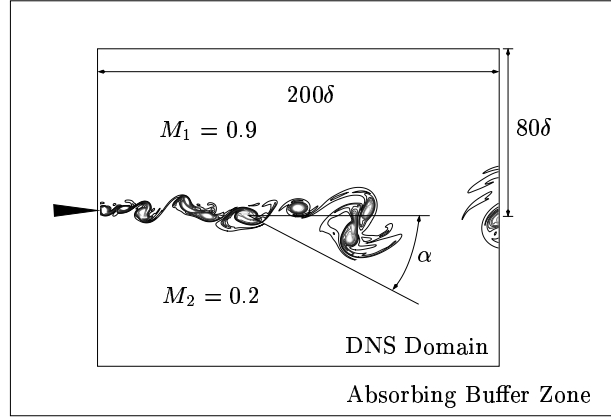


FIGURE 1. Schematic of the computational domain with vorticity magnitude showing the mixing layer.

2.3. Source Errors

As discussed in section 1, the primary objective of this work is to assess the robustness of the noise predictions to errors in the nominal noise source, so we must somehow specify these errors. For now, we only consider errors that arise from omitting part of the flow solution from the source computation. In practice, this error might be the missing small-scale turbulence in a large-eddy simulation or due to imperfect modeling of the larger turbulent scale in, say, a parabolized Navier-Stokes model of a mixing layer or jet (Bertolotti & Colonius 2003; Chueng & Lele 2004), but we make no attempt to rigorously represent to any particular source of error. Instead, the flow was simply decomposed into empirical Karhunen-Loeve (KL) eigenfunctions $\vec{\psi}_i(\mathbf{x})$ (Holmes, Lumley & Berkooz, 1996), also commonly called Proper Orthogonal Decomposition or POD modes, with time coefficients $a_i(t)$ such that the flow \vec{q} is reconstructed as

$$\vec{q}(\mathbf{x}, t) = \sum_{i=1}^N a_i(t) \vec{\psi}_i(\mathbf{x}). \quad (2.11)$$

In this study, the kinetic energy norm

$$E = \int_{\mathcal{V}} \rho u_i u_i d\mathcal{V} \quad (2.12)$$

defines the eigenfunctions in the usual way. Subsets of these modes were used to reconstruct flow and calculate approximations to e_{ij} and η_i defined in (2.5). To compute $\vec{\psi}_i$, we used the method of snapshots (Sirovich, 1987) with 558 data fields sampled at regular intervals from the 3907 available fields stored from the simulation. The resulting KL modes are used only to define a spectral decomposition of the flow which has attractive properties for our purposes, so special significance is given to any particular modes. An alternative approach to introducing error would be to specify length and time scales at which to filter the data. While that approach might better connect the present errors to the class of errors expected in a large-eddy simulation, it requires that several filtering parameters be specified and would not provide a single framework for all the types of error we wish to introduce. The empirical eigenfunctions on the other hand follow directly from the definition of the energy norm (2.12). The modes in approximately homogeneous

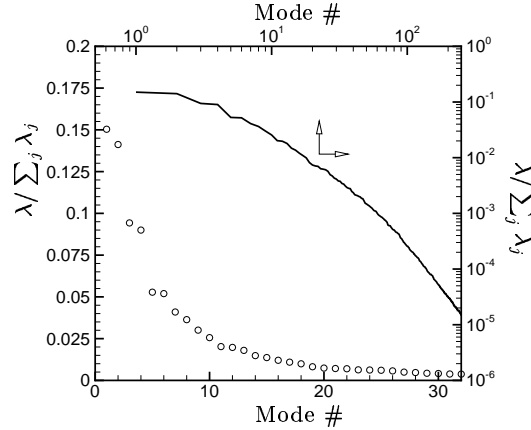


FIGURE 2. Fraction of kinetic energy defined by (2.12) of each mode. The — line corresponds to the top and right logarithmic axes.

flows, such as the streamwise coordinate direction in the present case, can be related to Fourier like modes via WKB analysis (Moser 1994).

The fraction of the total energy contained by each KL modes is shown in figure 2. The lowest-order modes contain most of this energy and seem to come in pairs. Similar pairing has been observed even in turbulent jets (Freund & Colonius 2002) and is necessitated by the advection of slowly evolving structures downstream. The pairs appear as $\pi/2$ phase shifted WKB-like wave packets in x which fit together like sine's and cosine's. The higher-order modes have the exponential energy decay expected for any such spectral representation of a low-Reynolds-number flow. Figure 3 shows the spatial form of the y -velocity component of selected modes and their corresponding time coefficients $a_i(t)$. Clearly, the lower-order modes are larger scale and lower frequency.

We consider two types of erroneous reconstruction for our robustness assessment. The first is simple truncation of the reconstruction series in (2.11) as

$$\vec{q}(\mathbf{x}, t) = \sum_{i=1}^{N_t} a_i(t) \vec{\psi}_i(\mathbf{x}), \quad (2.13)$$

where N_t is less than the total number of 558 modes available. Specifically, we consider cases with $N_t = 16, 32$, and 128 , which represent 81.2, 91.3, and 99.3 percent of the energy, respectively. The other error we introduce is a reduction in the coefficient of a low-order mode. The flow field in this case is reconstructed by (2.13) with $N_t = 128$, but with a_i reduced for selected small i . In particular, we take $a_1 = 0.5a_1$ and $a_3 = 0.5a_3$.

3. Results

Table 1 describes the six cases for which we present results. Sound spectra for all these cases are presented in figures 4 to 6 at directivity angles $\alpha = 40^\circ, 90^\circ$, and 140° , where α is measured from the downstream x axis toward the slow speed stream (see figure 1). At all angles the full source case (a) produces nearly a perfect match with the DNS directivity, as it should if implemented correctly. The small differences are believed to be due to boundary conditions and other numerical errors and are much smaller than the disagreement we will see in the other cases.

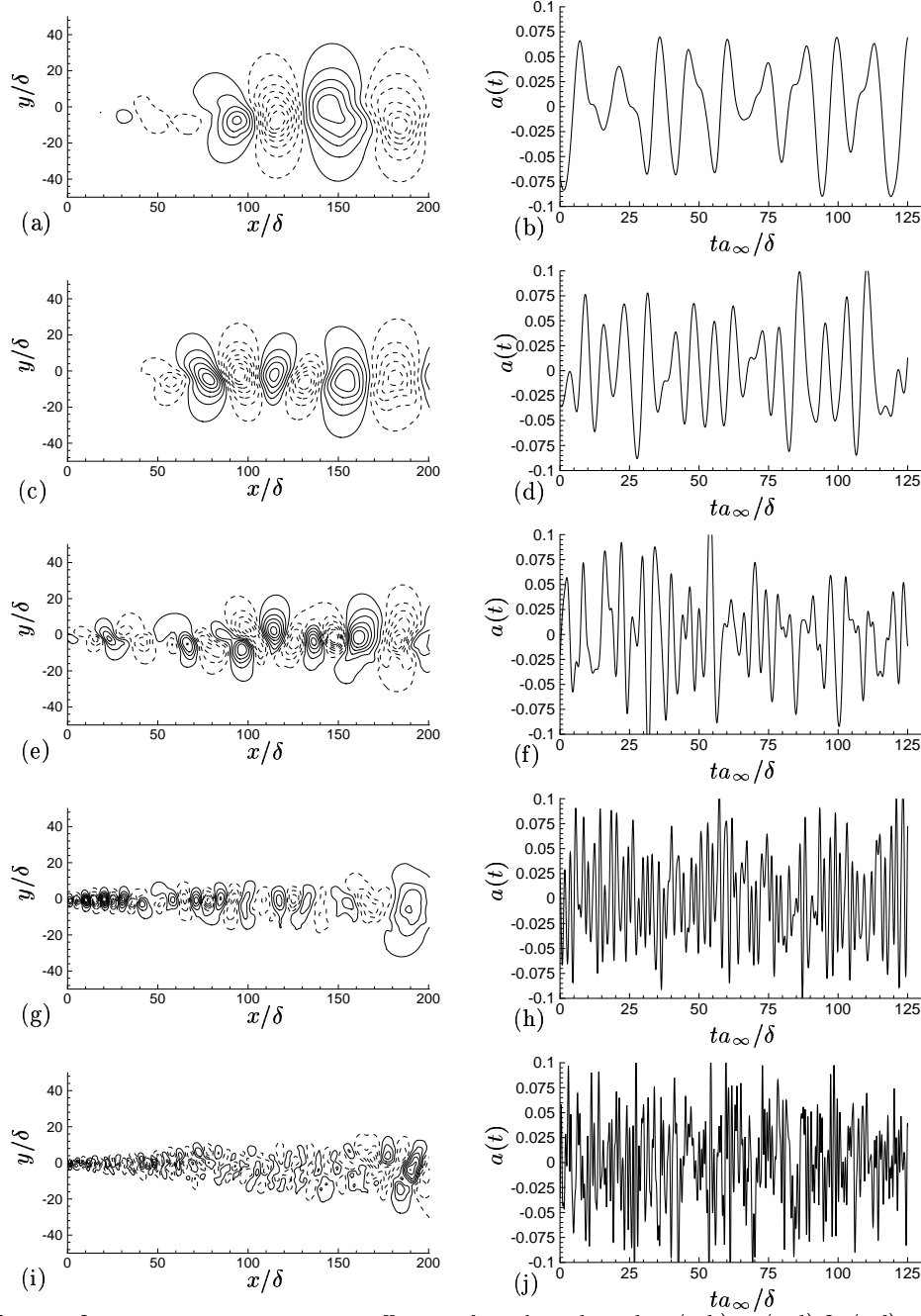


FIGURE 3. Mode shape and time coefficients for selected modes: (a-b) 1, (c-d) 3, (e-f) 16, (g-h) 32, and (i-j) 128.

Despite representing nearly all the kinetic energy of the mixing layer, retaining 128 KL modes (case b) for both cases produce significant errors in the higher frequencies, especially at $\alpha = 90^\circ$. The mean-flow analogy is slightly closer to the DNS at $\alpha = 40^\circ$, but

Case	Energy Retained	Description
a	100.0%	Full source information
b	99.3%	128 modes
c	91.3%	32 modes
d	81.2%	16 modes
e	92.5%	Modes with $a_1 = a_1/2$
f	95.3%	Modes with $a_3 = a_3/2$

TABLE 1. Cases presented.

otherwise the errors are effectively the same, giving neither formulation a clear advantage. Both make the noise too intense at these high frequencies indicating that the error is due to a disruption of cancellations that occur with the full source. Retaining fewer modes as in cases (c) and (d) leads to similar errors, but at lower and lower frequencies, which is in accord with our observation that the lower order modes have relatively lower frequencies. For the 16-mode case (d), the high frequencies are also under predicted, apparently because they are completely missing from the source in this case. The mean-flow analogy performs slightly better, but does not show a strong advantage.

A much more significant difference is observed when we disrupt the lower frequency, larger-scale structures by altering the lowest-order KL modes. The (e) and (f) frames of figures 4 to 6 show these cases. Since modes only up through 128 were retained, we expect the same errors as in case (b) at high frequencies, but at $\alpha = 40^\circ$ and 140° we also now see large over prediction errors in the low frequencies for the uniform-flow (Lighthill) analogy. The mean-flow analogy case behaves significantly better. Clearly, the complexity introduced by better distinguishing propagation from true acoustic sources is worthwhile in this case.

4. Discussion

There are two ways that we can anticipate acoustic analogies being used in a time dependent formulation of the type tested here. The first would be in conjunction with a large-eddy simulation or similar accelerated solution of the flow equations which represents only the larger, more energetic scales of the flow. The analogy in this case might be used in conjunction with a sub-grid-scale source model to predict the noise from the missing scales (*e.g.* Bodony & Lele 2003). The quantitative details of our assessment are not to be heavily relied upon in this case since the flow we have studied is two dimensional, though the mean flow itself is similar to that of a turbulent mixing layer so we do not anticipate any fundamental difference with that case. This application best corresponds to error models in which we truncated (2.11) sum at finite N_t , omitting for the most part smaller scale unsteadiness from the computation.

The second type of time dependent acoustic analogy application we envision would be in conjunction with a model for the largest scales of a turbulent flow, such as a solution of the parabolized Navier-Stokes equation (Bertolotti & Colonius 2003; Chueng & Lele 2004) or a dynamic model constructed by projecting KL modes onto the governing equations. Such a representation would, of course, contain some errors, which we modeled by altering the time coefficient of the lowest-order modes.

The results above suggest that neither formulation has a clear advantage for modeling the contribution of the missing small scales to the higher frequencies in the noise

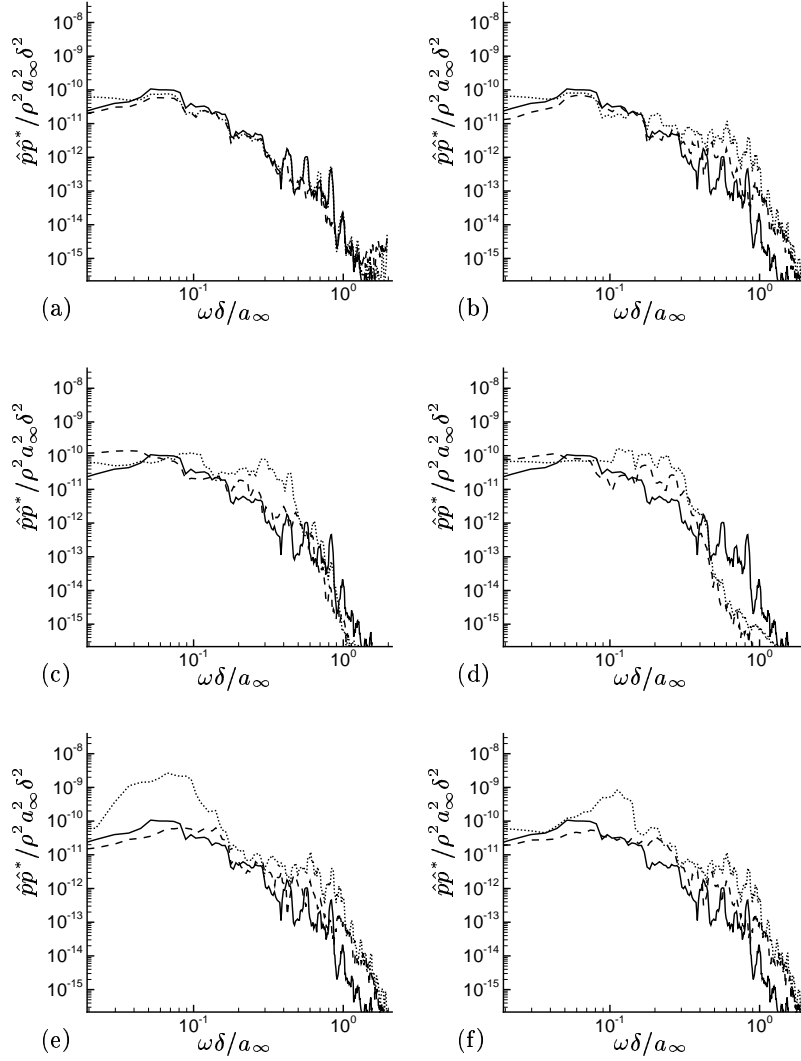
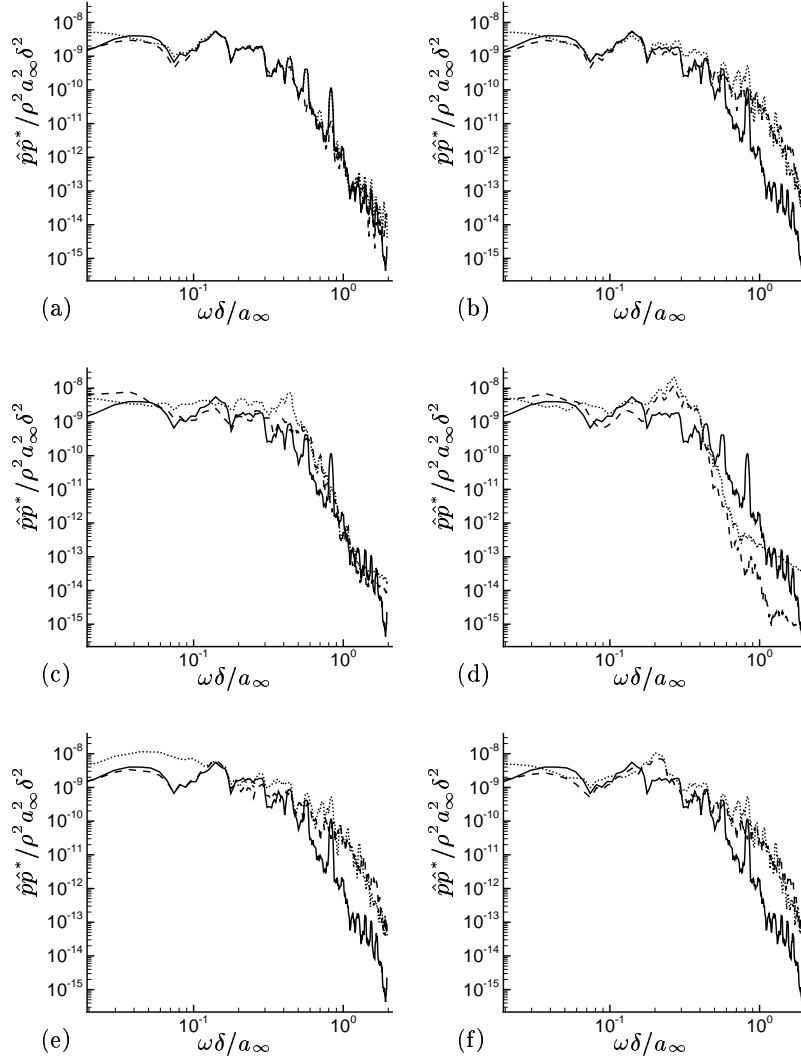


FIGURE 4. Sound pressure spectra at $\alpha = 40^\circ$: — DNS; ---- DNS-mean base flow analogy; uniform base flow (Lighthill) analogy. Frames (a) through (f) show cases a through f as defined in table 1.

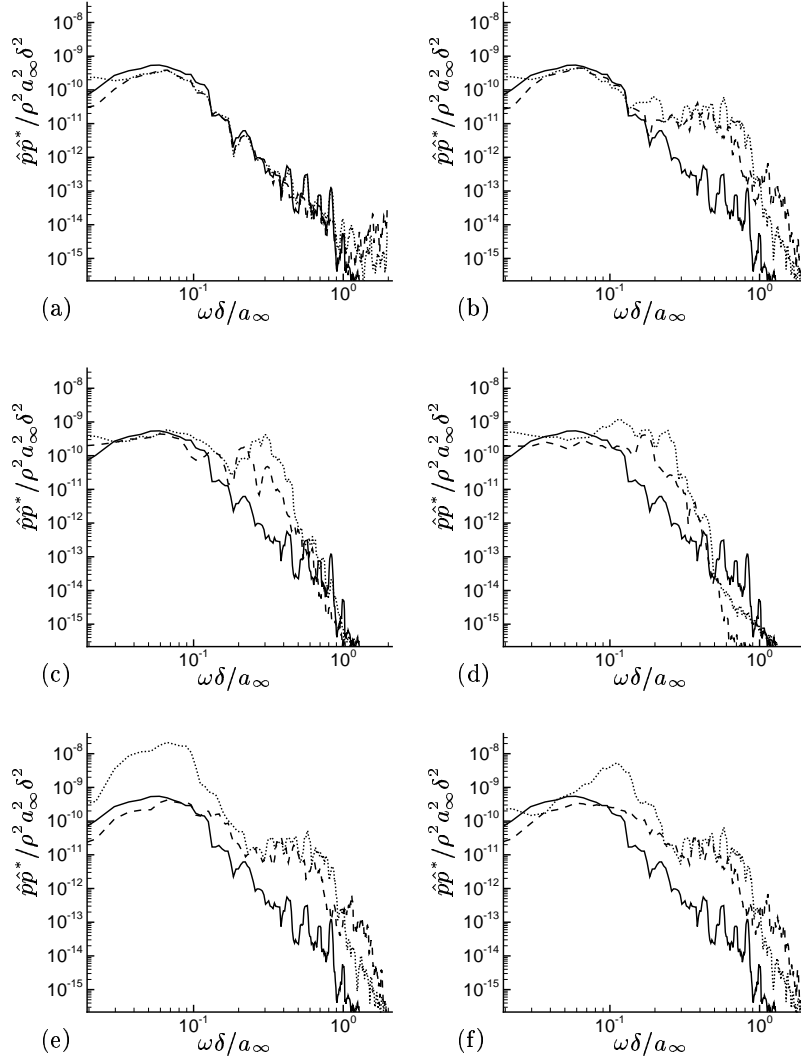
spectrum, though this might, of course, depend upon the specifics of the particular formulation used. However, the mean-flow analogy formulation does seem to be preferable in the second case, where the Lighthill-like formulation shows significant errors.

A purported disadvantage of the mean-flow analogy is that the resulting linearized Euler equations support instability wave homogeneous solutions, which have the potential to overwhelm the solution. Methods have been proposed for removing or reducing these (*e.g.* Bogey, Bailly & Juvé 2002) but, as anticipated by Goldstein (2003), no special treatment was required in the present case. The homogeneous solution is excited, but does not degrade the acoustic predictions.

FIGURE 5. Same as figure 4 at $\alpha = 90^\circ$.

5. Conclusions

The key conclusion is that formulating the acoustic analogy with the mean flow appearing in the propagation operator within Goldstein's (2003) formulation leads to a significantly more robust formula for the far-field sound. The errors we introduced into the low frequency, larger-scales do not in this case disproportionately affect the sound field. The same errors introduced into the source when the base flow is uniform, which corresponds to the Lighthill analogy, cause order-of-magnitude errors in the noise spectrum radiated to both upstream and downstream angles. The mean flow analogy is therefore more attractive by this measure for predicting noise when an imprecise dynamic model is used for the large-scale structures. However, both formulations show similar robustness when errors are introduced into the small-scale higher-frequency components of the

FIGURE 6. Same as figure 4 at $\alpha = 140^\circ$.

source by our method, which by our measure indicates that neither has a clear advantage. Further testing with a turbulent flow is warranted.

JBF gratefully acknowledges support from NASA. The mixing layer DNS simulation were supported by AFOSR.

REFERENCES

- BERTOLOTTI, F. & COLONIUS, T. 2003 On the noise generated by shear-layer instabilities in turbulent jets. AIAA Paper 2003-1062.

- BODONY, D. J. & LELE, S. K. 2003 A statistical subgrid scale noise model: formulation. AIAA Paper 2003-3252.
- BOGEY, C., BAILLY, C. & JUVÉ, D. 2002 Computation of flow noise using source terms in linearized Euler's equations. *AIAA J.* **40** (2), 235.
- CHEUNG, L. & LELE, S. 2004 Acoustic radiation from subsonic and supersonic mixing layers with nonlinear PSE. AIAA Paper 2004-0363.
- COLONIUS, T., LELE, S. K. & MOIN, P. 1997 Sound generation in a mixing layer. *J. Fluid Mech.* **330**, 375–409.
- FREUND, J. B. 2001 Noise sources in a low-Reynolds-number turbulent jet at Mach 0.9. *J. Fluid Mech.* **438**, 277–305.
- FREUND, J. B. & COLONIUS, T. 2002 POD analysis of sound generation by a turbulent jet. AIAA Paper 2002-0072.
- GOLDSTEIN, M. E. 1976 *Aeroacoustics*. McGraw-Hill Book Co.
- GOLDSTEIN, M. E. 2003 A generalized acoustic analogy. *J. Fluid Mech.* **488**, 315–333.
- HOLMES, P., LUMLEY, J. L. & BERKOOZ, G. 1996 *Turbulence, Coherent Structures, Dynamical Systems and Symmetry*. Cambridge: Cambridge University Press.
- LIGHTHILL, M. J. 1952 On sound generated aerodynamically: I. General theory. *Proc. Royal Soc. Lond. A* **211**, 564–587.
- LILLEY, G. M. 1974 On the noise from jets. *Tech. Rep.* CP-131. AGARD.
- MOSER, R. D. 1994 Kolmogorov inertial range spectra for inhomogeneous turbulence. *Phys. Fluids* **6** (2), 794–801.
- SIROVICH, L. 1987 Chaotic dynamics of coherent structures. Parts I–III. *Quarterly of Applied Math.* **XLV** (3), 561–582.
- WEI, M. & FREUND, J. B. 2004 A quiet free shear flow. submitted *J. Fluid Mech.*

The combustion and multiphase group

Over recent years, much progress has been made in the development of combustion models for numerical simulations of engineering systems. Although much of the theory is still unclear, the application of these models to real systems seems to be in reach. It is hence not surprising that industrial and commercial interests were well represented in the combustion and multiphase group. However, the main emphasis of most of the projects was in fundamental theory and modeling. The combustion and multiphase group was the largest group of this years' summer program. It had contributions in the general areas of multiphase and combustion science and modeling, but also in fires and radiation, and combustion instabilities and control. This section includes reports on twelve projects: Two related to multiphase flows, five in the area of combustion science and modeling, two related to fires and radiation, and three on combustion instabilities and control.

The projects in multiphase flows are related to liquid gas interfaces and Lagrangian spray models. It is well known that the level set approach to simulate two-phase flows does not guarantee mass conservation of the individual phases. To insure mass conservation, the level set scalar has to be appropriately corrected, for example by a volume of fluid method. The project of Boersma *et al.* explores the effect of such a level set correction method on the higher order interface properties, for instance the curvature. It is found that local correction methods introduce significant errors in the interface curvature. A correction extension method is then proposed addressing this problem and leading to a significant reduction of curvature errors. LES/Lagrangian spray modeling of multiphase flows is critical in simulating practical combustion devices. In a different project, Pozorski *et al.* studied the impact of sub-grid turbulence on particle motion. It was shown from DNS data that filtering affects preferential concentration. A stochastic model was proposed for reconstructing the residual velocity field.

Recent breakthroughs in premixed combustion modeling has increased the computational accessibility of such systems. Bilger recently proposed a new marker field method to track combustion in low Damköhler number premixed configurations. Using a fictional scalar field, the project of Bilger *et al.* analyzed a direct mapping between this field and the reaction progress-variable. DNS of low-Damköhler number premixed combustion is used for an *a priori* testing of the model. A second project related to premixed combustion is that of Huh *et al.*, who recently proposed a premixed turbulent combustion model based on zone-conditional averages. In contrast to Bilger's model, this model has been formulated for the high Damköhler number case. The aim of the present project was to test closure assumptions for the turbulent burning velocity using DNS data. An entirely different approach to combustion modeling in LES is the filtered-density function approach. In such LES-FDF methods, the integration of the chemical source term is computationally expensive. Pope *et al.* studied the use of ISAT to accelerate this computation for LES-FDF. Using several parallel computation paradigms, they identified potential bottlenecks in using ISAT algorithms and demonstrated substantial speed-up compared with the direct integration.

From an industrial perspective, combustion models must be computationally inexpensive. With this constraint in mind, Goldin *et al.* proposed the constructed-PDF model as a possible extension of conventional laminar-flamelet models. By using detailed chemistry and the Linear-Eddy Model to model a simplified flow configuration, a look-up

table is created. Using this lookup table, simulations have been performed for a series of turbulent diffusion flame, showing good agreement with experimental data. A real-world application of combustion modeling was the objective of the project of Kim *et al.*. A simulation of a Pratt & Whitney aircraft engine combustor was initiated. One of the obstacles encountered was the modeling of the injection process, which involves a liquid jet impingement on a wall and the formation and development of a liquid wall film. As a result of the project, different film models have been developed and simulations for the combustor have been initiated.

Another highly complex problem of practical interest is the simulation of accidental fires. Tieszen *et al.* studied mixing in such flows by performing LES for a buoyant helium plume. It was found that conventional sub-filter modeling was insufficient and could not reproduce the Rayleigh-Taylor instabilities at the base of the plume. Different models have been proposed and applied in simulations with varying filter width. Also related to accidental fires was the project by Jensen *et al.*. A comparative study of different solution methods of the radiative transfer equation was performed using the temperature fields from simulations of a 2 m pool fire. The applied models include discrete transfer method, different discrete ordinate techniques, and a moment method using the so called M_1 closure.

Another group investigated specific issues related to the design and optimization of combustion devices. In such systems, a major issue is to develop fast optimization processes to be able to adjust, for example, the positions and flow rate distribution of dilution jets in a gas turbine burner in order to reach a predefined outlet temperature profile. This issue was the focus of the work of Debiante *et al.* who applied modern optimization methods to a model flame and showed the potential of their approach to control the flame length, temperature and NO_x emission. Recent experimental experience shows that optimization procedures can also be dangerous: optimizing performances and pollution often leads to instabilities. The development of LPP devices (Lean Premixed Prevaporize) for gas turbines is a good example of experimental design optimization which meets most performance and pollution objectives, but in many cases, leads to high and unacceptable instability levels. Studying and predicting such instabilities using numerical tools was the topic of the other projects. The computation of acoustic resonators (such as combustion chambers) is indeed still a challenge because of the lack of an appropriate formulation of boundary conditions. Prosser and Schlüter proposed and studied a new original boundary condition formulation based on a low-Mach number approximation to improve existing characteristic methods for compressible codes. The objective of the project of Martin *et al.* was to revisit the Rayleigh criterion which is the most commonly used tool to describe instabilities: the recent development of compressible LES for combustion allows now to replace this criterion by a detailed analysis of the budget of acoustic energy. Such a budget was studied in the case of a staged turbulent combustor in which the level of oscillation was controlled by the outlet boundary condition. Finally, as LES will still remain very expensive for a long time, additional tools are needed for design and optimization of thermoacoustic oscillations in industry: the last project (Benoit *et al.*) shows how acoustic analysis can be coupled to LES to predict the growth rates of all acoustic modes in a reacting configuration. Here the objective was to show that LES information can be injected into a Helmholtz acoustic solver to retrieve the unstable modes and eventually control them through different outlet conditions.

Direct numerical simulation of turbulent premixed flames with a marker field and application to RANS and LES

By R. W. Bilger †, S. H. Kim AND S.M. Martin

Direct numerical simulations of turbulent premixed combustion in isotropic homogeneous turbulence have been carried out. The simulations incorporate solutions for the marker field produced for a scalar having a simple source term proportional to the mean density. The mapping of the reaction progress field from this marker field is investigated at low to moderate Damkohler number and the results suggest that this could be a feasible way for closing the progress variable field in RANS and LES. Preliminary results for RANS calculations for a combustor with a backward-facing step are presented.

1. Introduction

Recently, methods of generating a simple marker field in turbulent premixed combustion have been proposed by Bilger (2004). In turbulent nonpremixed combustion, the mixture fraction has been a very powerful concept - its conservation equation is readily modeled and solved to give fields for its mean and variance in approaches involving Reynolds Averaged Navier Stokes (RANS) equations, see Bilger (1980) and Peters (2000). These fields provide a marker for the mixing, with reaction occurring near the instantaneous surfaces having the stoichiometric value of the mixture fraction. The progress variable, C , has been widely used in studies of turbulent premixed combustion (Peters 2000). While conceptually an ideal marker in turbulent premixed combustion, equations for its mean and variance have proved difficult to model satisfactorily in RANS and in Large Eddy Simulation (LES); it has the difficulty that its filtered values tend to be zero or unity everywhere in the flow except for a single surface of grid cells.

The new marker field, S , obeys the simple conservation equation Bilger (2004)

$$\rho \frac{\partial S}{\partial t} + \rho \mathbf{U} \cdot \nabla S - \nabla \cdot (\rho D \nabla S) = \rho / \tau_S \quad (1.1)$$

where the constant time scale, τ_S , may be arbitrarily chosen - it merely sets the scaling for S . Equations for the mean and variance of S are obtained for stationary flow as

$$\bar{\rho} \tilde{\mathbf{U}} \cdot \nabla \tilde{S} + \nabla \cdot \overline{\rho \mathbf{u} s} = \bar{\rho} / \tau_S \quad (1.2)$$

$$\bar{\rho} \tilde{\mathbf{U}} \cdot \nabla (\overline{s'^2}) + \nabla \cdot \overline{\rho \mathbf{u} s^2} + 2 \overline{\rho \mathbf{u} s} \cdot \nabla \tilde{S} = -2 \bar{\rho} \tilde{N}_s \quad (1.3)$$

where

$$\tilde{S} \equiv \overline{S} / \bar{\rho}; S = \tilde{S} + s \quad (1.4)$$

† The University of Sydney

$$\tilde{s}' \equiv \left(\frac{\overline{\rho s^2}}{\bar{\rho}} \right)^{1/2} \quad (1.5)$$

$$N_s \equiv D \nabla S \cdot \nabla S; \tilde{N}_s \equiv \overline{\rho N_s} / \bar{\rho} \quad (1.6)$$

It may be noticed that there are no unclosed chemical source terms in Eqs. 1.2 and 1.3. It is expected that standard RANS closures for the turbulent fluxes and for the scalar dissipation will be satisfactory, but this needs to be investigated.

It is conjectured in Bilger (2004) that for a statistically stationary one-dimensional turbulent premixed flame in homogeneous isotropic turbulence that the C field will be able to be mapped non-linearly from the S field at low to moderate Damhohler Numbers (Da). This is investigated here using 3D Direct Numerical Simulations (DNS). The DNS is described in the next section. The mapping of the C and S fields is investigated in Section 3, including conditional moment closure for obtaining C statistics from the S statistics. Application of the approach to a premixed combustor with a backward facing step is described in Section 4.

2. Direct numerical simulations

Direct numerical simulations of one dimensional premixed flames are carried out. The fully compressible Navier-Stokes equations with single step chemistry are solved:

$$\frac{\partial \rho}{\partial t} + \frac{\partial \rho u_i}{\partial x_i} = 0 \quad (2.1)$$

$$\frac{\partial \rho u_i}{\partial t} + \frac{\partial}{\partial x_j} (\rho u_i u_j) = - \frac{\partial p}{\partial x_i} + \frac{\partial \tau_{ij}}{\partial x_j} \quad (2.2)$$

$$\frac{\partial \rho e}{\partial t} + \frac{\partial}{\partial x_j} [(\rho e + p) u_j] = \frac{\partial u_j \tau_{ij}}{\partial x_i} + \frac{\partial}{\partial x_i} \left(\lambda \frac{\partial T}{\partial x_i} \right) + Q \omega \quad (2.3)$$

$$\frac{\partial \rho Y_R}{\partial t} + \frac{\partial}{\partial x_j} (\rho u_j Y_R) = \frac{\partial}{\partial x_i} \left(\rho D \frac{\partial Y_R}{\partial x_i} \right) - \omega \quad (2.4)$$

where

$$\rho e = \frac{1}{2} \rho u_i u_i + \frac{p}{\gamma - 1} \quad (2.5)$$

$$\tau_{ij} = \mu \left(\frac{\partial u_i}{\partial x_j} + \frac{\partial u_j}{\partial x_i} - \frac{2}{3} \delta_{ij} \frac{\partial u_k}{\partial x_k} \right) \quad (2.6)$$

$$\omega = A \rho Y_R \exp\left(-\frac{T_a}{T}\right) \quad (2.7)$$

p is pressure, e is the internal energy and Q is the heat of reaction per unit mass of fresh mixture. A is the pre-exponential factor. T_a is the activation temperature. The gas mixture is assumed to be a perfect gas with a specific heat ratio of $\gamma=1.4$. Y_R is the normalized mass fraction of the deficient reactant. The reaction progress variable is defined here as $C \equiv 1 - Y_R$. The thermal conductivity, λ , and the diffusion coefficient,

Case	u'/s_L	l_t/l_F	ρ_u/ρ_b	T_a/T_b	Da	Re_λ
I	16.7	0.87	4	4	0.05	47
II	12.9	1.23	4	4	0.1	47
III	6.8	2.29	4	4	0.34	47

TABLE 1. Characteristics of the premixed flames

D , are given as

$$\lambda = \mu c_p / Pr \text{ and } D = \mu / (\rho Sc) \quad (2.8)$$

The viscosity, μ , is given as

$$\mu = \mu_u (T/T_u)^{0.76} \quad (2.9)$$

The Prandtl number, Pr , and the Schmidt number, Sc , are set to be 0.7. This formulation corresponds to a very lean fuel-air mixture (Trouve & Poinot 1994).

The computation domain is a cube with inflow and outflow in the x_1 direction and periodic in the x_2 and x_3 directions. The equations are integrated using a low storage fourth order Runge Kutta method with a sixth order compact finite difference scheme for spatial discretization (Kennedy *et al.* 2000; Lele 1992). A nonreflecting boundary condition is used for the outflow boundary (Poinot & Lele 1992). The equations are solved on a $178 \times 128 \times 128$ grid. Initial and inflow turbulence is homogeneous and isotropic. The characteristics of the premixed flames are shown in Table 1. The laminar flame thickness, l_F , is based on the maximum gradient of the progress variable. The results in Figs. 1-5 are those at $\tau \approx 1.5$, where the nondimensional time, τ , is normalized by the initial eddy turn over time of the fresh mixture.

3. Mapping of the C and S fields

The conditional average of the reaction progress variable can be defined as

$$Q(\mathbf{x}, t, \varphi) \equiv \langle C(\mathbf{x}, t) | S(\mathbf{x}, t) = \varphi \rangle \quad (3.1)$$

where φ is the sample space variable of the marker, S . When the C and S fields are well correlated, the conditional fluctuations, $c \equiv C - Q$, will be small enough for the conditional moment closure (CMC) model to be applied for the closure of the nonlinear chemical reaction rate. Once the solution for Q is obtained, the statistics of C can be deduced from those of S , e.g.,

$$\tilde{C} = \int \tilde{P}(\varphi) \langle C | \varphi \rangle d\varphi \quad (3.2)$$

where $\tilde{P}(\varphi)$ is the Favre probability density function (PDF) of S . In this section the mapping of the C and S fields will be investigated using the 3D DNS data. Figure 1 shows the conditional average, Q , and r.m.s. fluctuations, $\langle c^2 | \varphi \rangle^{1/2}$, for Case I. The maximum $\langle c^2 | \varphi \rangle^{1/2}$ is about 0.08, which occurs at $\varphi \approx 1.6$. Figure 2 shows spatial distributions of C and S for Case I. The contour steps in S are uniform, while those in C are taken from the corresponding conditional average, Q , in Fig. 1. Note the strong similarity between the C and S fields mapped in this way.

The Q equation (derived below) involves the conditionally averaged reaction rate of

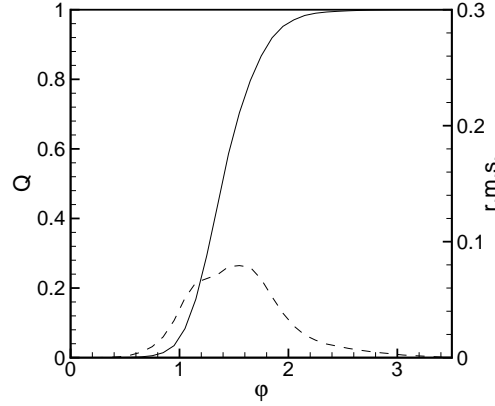


FIGURE 1. Conditional average and r.m.s. fluctuations of the reaction progress variable for Case I.

the progress variable, C . Conditional averaging suppresses fluctuations of reactive scalars when a proper conditioning variable is chosen. In the CMC model the nonlinear chemical reaction rates are closed using the conditional moments. First-order closure estimates of the conditional mean reaction rate in the conditionally averaged equation for the reaction progress variable using the conditional averages of reactive scalars:

$$\langle \omega(\rho, Y_R, T) | \varphi \rangle = \omega(\rho_\varphi, \langle Y_R | \varphi \rangle, \langle T | \varphi \rangle) = \omega(Q) \quad (3.3)$$

This closure is limited to 1-step chemistry. The closure model of Eq. (3.3) is tested in Fig. 3 giving excellent results for low Da .

Figure 4 shows the conditional average, Q , and r.m.s. fluctuations, $\langle c^2 | \varphi \rangle^{1/2}$, for higher Da cases, Cases II and III. As Da increases the slope of Q with respect to S increases so that the flame is in a narrower region of φ space. Also, the r.m.s., $\langle c^2 | \varphi \rangle^{1/2}$, increases with Da so that the mapping between the C and S fields is not as good. This can also be seen from the contour plots in Fig. 5. The structures of the C and S fields are still similar for Case II. For Case III, however, the similarity between the S and C fields is not as good as in the lower Da cases, while the S and C fields are likely to have similar large scale wrinkling.

Figure 6 shows the conditional mean reaction rates for Cases II and III. The CMC closure for the reaction rate remains quite good, while the correlation between the C and S fields is not as good. It is not as good as at lower Da , but may still be sufficiently good for modelling purposes.

Next the Q equation is derived following Bilger (2004). Using the decomposition method described in Klimenko & Bilger (1999) the progress variable is split into a conditioned average and fluctuating component.

$$C(x, t) = Q(S(x, t), x, t) + c(x, t) \quad (3.4)$$

Derivatives are taken of this equation with respect to time and space and substituted into the conservation equation for the progress variable (given below), which after rearranging

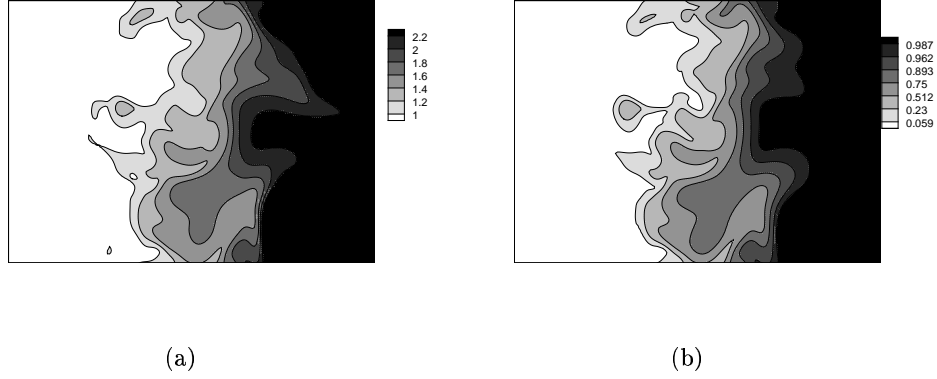
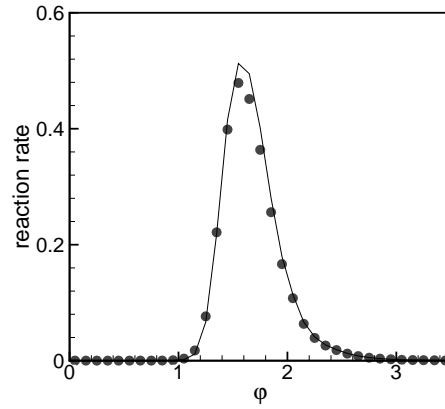
FIGURE 2. Distributions of C and S in a x_1 - x_3 plane for Case I (a) S (b) C 

FIGURE 3. Conditional mean reaction rates for Case I(symbol: DNS, line: CMC).

gives

$$\begin{aligned} \rho \dot{Q} + \rho \mathbf{U} \cdot \nabla Q - \rho N_s Q'' + \left[\rho \frac{\partial S}{\partial t} + \rho \mathbf{U} \cdot \nabla S - \nabla \cdot (\rho D \nabla S) \right] Q' = \\ \rho W_c / \tau_c - \rho \frac{\partial c}{\partial t} - \rho \mathbf{U} \cdot \nabla c + \nabla \cdot (\rho D \nabla c) \end{aligned} \quad (3.5)$$

$N_s = D \nabla S \cdot \nabla S$ is the scalar dissipation rate of S . Here the Q' signifies a derivative with respect to S . The fourth term on the LHS of Eq. 3.5 is simplified using Eq. 1.1 and the entire equation is divided by the density to give

$$\dot{Q} + \mathbf{U} \cdot \nabla Q - N_s Q'' + [1/\tau_s] Q' = W_c / \tau_c - \frac{\partial c}{\partial t} - \mathbf{U} \cdot \nabla c + \nabla \cdot (\rho D \nabla c) / \rho \quad (3.6)$$

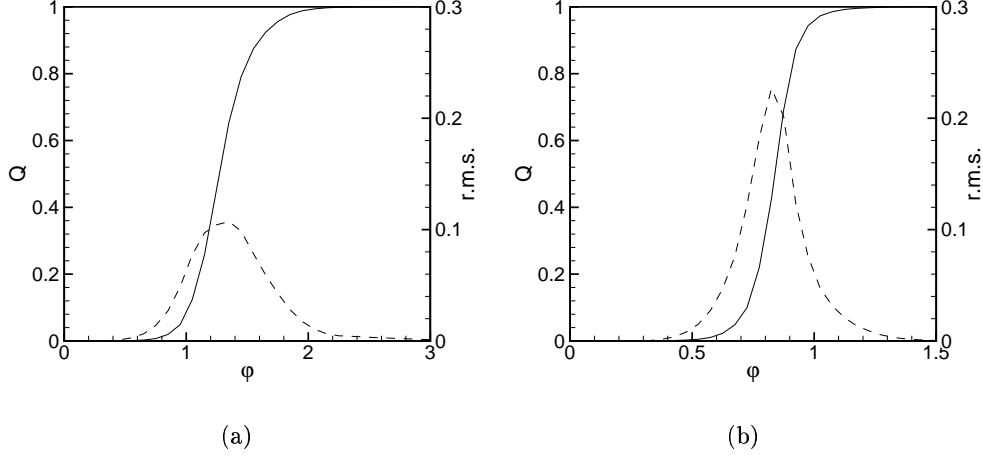


FIGURE 4. Conditional average and r.m.s. fluctuations of the reaction progress variable (a) Case II (b) Case III.

The equation is conditionally averaged following Bilger (2004) to give

$$\dot{Q} + \langle \mathbf{U} | \varphi \rangle \cdot \nabla Q - \langle N_s | \varphi \rangle Q'' + Q' / \tau_s = \langle W_c | \varphi \rangle / \tau_c + e_c \quad (3.7)$$

$$e_c = \left\langle -\frac{\partial c}{\partial t} - \mathbf{U} \cdot \nabla c + \nabla \cdot (\rho D \nabla c) / \rho | \varphi \right\rangle \quad (3.8)$$

The boundary conditions are $Q = 0$ at $S = -\infty$ and $Q = 1$ at $S = \infty$. To make the solution more tractable several simplifying assumptions are made. First only steady state problems are addressed, so the time derivatives drop out. Based on a first order closure it is assumed that the first and third e_c terms are negligible. The reaction rate term is closed using Eq. 3.3. The S time scale is closed by $\tau_s = L/U_u$, where L and U_u are the inlet characteristic length and velocity, respectively. For 2D flow Eqs. 3.7 and 3.8 become

$$\langle u | \varphi \rangle \cdot \frac{\partial Q}{\partial x} + \langle v | \varphi \rangle \cdot \frac{\partial Q}{\partial y} - \langle N_s | \varphi \rangle Q'' + U_u / L Q' = W_c(Q) / \tau_c - \frac{\nabla [P(\varphi) \langle u c | \varphi \rangle]}{P(\varphi)} \quad (3.9)$$

A model is required to close the conditional velocity terms. Next the premixed CMC is derived and solved with Eq. 1.2 and 1.3 in a RANS model to show how C and S are related when Reynolds averaged. Solving Eq. 3.9 is left to future work.

4. RANS application to a combustor

The premixed CMC method was originally proposed by Bilger (1993) and Smith (1994) and first implemented by Martin *et al.* (2003) and Martin (2003). The premise of the theory is that most of the fluctuations of the reactive scalars are correlated with a progress variable. The conservation equations for the species and energy are derived conditioned on the progress variable. This increases the dimensionality of the problem by one, while providing an improved closure for the reaction rates over other methods.

Next an outline of the derivation and the closure assumptions are given, followed by

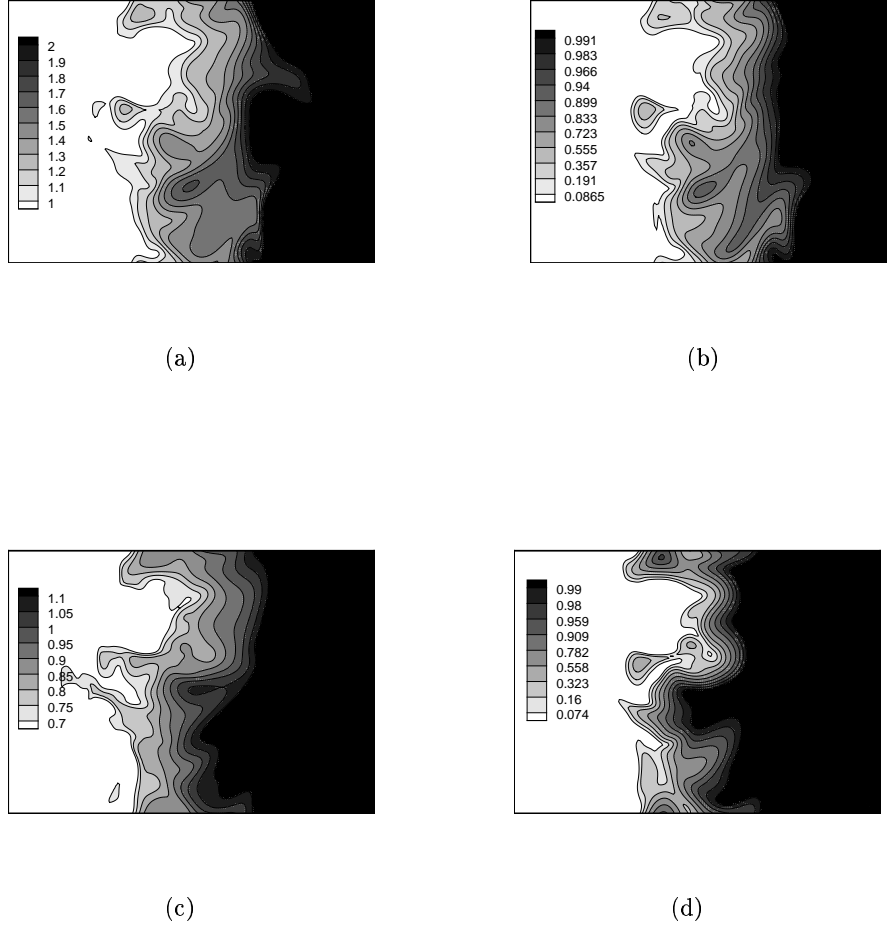


FIGURE 5. Distributions of C and S in a x_1 - x_3 plane (a) S for Case II (b) C for Case II (c) S for Case III (d) C for Case III

the marker field implementation for RANS. Results are presented and future work is discussed.

4.1. Derivation of the Premixed CMC Method

The premixed CMC method can be derived by two methods, following the non-premixed CMC. The first is the joint PDF method of Klimenko and the second is the decomposition method of Bilger, see Klimenko & Bilger (1999) for the details of the non-premixed derivations. Here the decomposition method is used. See Martin (2003) for a detailed derivation of both methods.

The derivation starts with the Favre averaged conditional expectation of the reactive

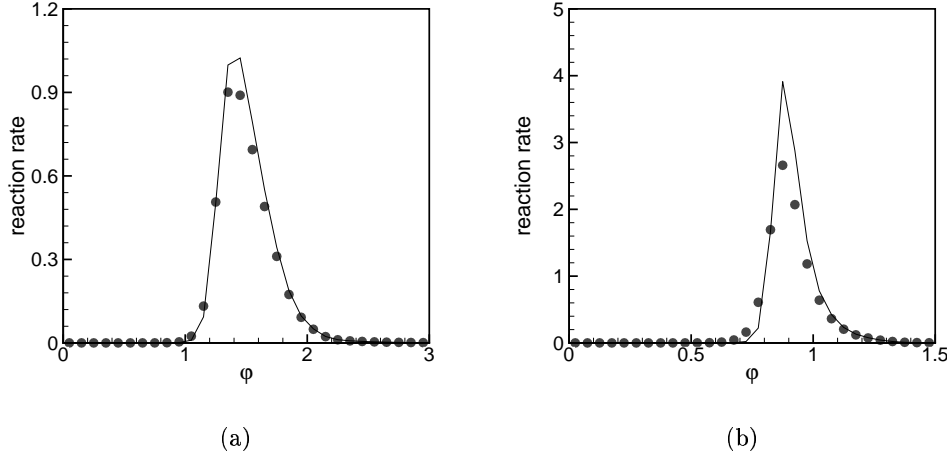


FIGURE 6. Conditional mean reaction rates (a) Case II (b) Case III(symbol: DNS, line: CMC).

scalar defined as

$$Q_i(\zeta, x, t) \equiv \frac{\langle \rho(x, t) Y_i(x, t) | C(x, t) = \zeta \rangle}{\langle \rho(x, t) | C(x, t) = \zeta \rangle} \quad (4.1)$$

Here Y is the species mass fraction and ζ is the sample space variable corresponding to the progress variable C . The mass fractions are made up of the conditional averaged component and the fluctuation about this averaged value, shown below.

$$Y_i(x, t) = Q_i(C(x, t), x, t) + y_i(x, t) \quad (4.2)$$

This equation is substituted into the conservation equation for the species mass fractions shown below.

$$\rho \frac{\partial Y_i}{\partial t} + \rho \mathbf{U} \cdot \nabla Y_i - \nabla \cdot (\rho D \nabla Y_i) = \rho \omega_i \quad (4.3)$$

After simplification and employing the conservation equation for the progress variable the premixed CMC equation is obtained, shown below.

$$\langle \rho | \zeta \rangle \dot{Q}_i + \langle \rho u | \zeta \rangle \cdot \nabla Q_i = \langle \rho \omega_i | \zeta \rangle + \langle \rho D_i \nabla C \cdot \nabla C | \zeta \rangle Q_i'' - \langle \rho S_c | \zeta \rangle Q_i' + e_Q + e_y \quad (4.4)$$

$$e_Q = \langle [\nabla \cdot (\rho D_i \nabla Q_i) + \rho D_i \nabla C \cdot \nabla Q_i' + Q_i' \nabla \cdot (\rho (D_i - D_h) \nabla C)] | \zeta \rangle \quad (4.5)$$

$$e_y = -\langle [\rho \frac{\partial y_i}{\partial t} + \rho u \cdot \nabla y_i - \nabla \cdot (\rho D_i \nabla y_i)] | \zeta \rangle \quad (4.6)$$

$$\rho S_c = \frac{-\rho \sum \omega_i h_{f,i}}{h_{ad}^s - h_u^s} \quad (4.7)$$

Here the gradient operator signifies derivatives in real space, the primes indicate derivatives in C space and the dot indicates a time derivative. Note that S_c used here is the source term for the equation and is not the S from the marker field used above. Equation 4.4 is similar in form to the non-premixed CMC equation, with the third term on the

RHS of the equation the main difference. This term comes from C being a non-conserved scalar and can be thought of as a convective velocity in C space. This term makes the premixed equations stiffer than their non-premixed counterparts. In Eq. 4.7 $h_{f,i}$ is the heat of formation for the i th species and h^s is the sensible enthalpy. The ad subscript signifies adiabatic equilibrium conditions and the u indicates unburned conditions. Eq. 4.4 is in non-conserved form, the conserved form is obtained from the joint PDF derivation. The transport equation for the PDF of C can be used to convert between the two formulations.

To make the above equations more tractable several simplifying assumptions are made. The first is to assume steady state, so the time derivative terms drop out. The next assumption is that the conditioned mass fractions are constant in physical space, this eliminates the second term on the RHS of Eq. 4.4. This avoids the need for a closure model for the conditioned velocity. It is assumed that all diffusivities are constant and equal. The remaining terms in Eqs. 4.5 and 4.6 are assumed to be negligible for high Re flows. Klimenko & Bilger (1999) and Martin (2003) give a more detailed discussion on the magnitude of these terms. This gives the simplified premixed CMC equation as

$$\langle \rho D \nabla C \cdot \nabla C | \zeta \rangle Q_i'' - \langle \rho S_c | \zeta \rangle Q_i' + \langle \rho \omega_i | \zeta \rangle = 0 \quad (4.8)$$

This equation is decoupled from the flow field equations, with the conditioned scalar dissipation rate, $\rho N_c = \langle \rho D \nabla C \cdot \nabla C | \zeta \rangle$, the only value needed from the flow field (the dimensionality of the equations are reduced). This allows the simplified premixed CMC equations to be solved offline and saved in tabular format, greatly reducing the computation time. This is a system of $ns+1$ equations, where ns is the number of species in the system, the extra equation is for the enthalpy. The equations reduce to a set of second order ODE's of the boundary value type, with the values at $C = 0$ set to the unburned values and at $C = 1$ set to the adiabatic equilibrium values. For adiabatic problems the enthalpy equation is not required.

4.2. Closure Assumptions for RANS

The progress variable, C , is defined as the non-dimensional sensible enthalpy.

$$C \equiv \frac{h^s - h_u^s}{h_{ad}^s - h_u^s} \quad (4.9)$$

Using the sensible enthalpy instead of the temperature accounts for non-constant specific heats. The conservation equation for the Favre averaged C comes from the energy equation and the above definition.

$$\frac{\partial \bar{\rho} \tilde{C}}{\partial t} + \nabla \cdot (\bar{\rho} \tilde{\mathbf{U}} \tilde{C}) - \nabla \cdot (\mu_t / \sigma_c \nabla \tilde{C}) = \bar{\rho} \tilde{S}_c \quad (4.10)$$

$\sigma_c = 0.7$, is the turbulent Schmidt number. S_c is the conditioned source term as defined in Eq. 4.7. Similarly the conservation equation for the variance of the progress variable is derived.

$$\frac{\partial \bar{\rho} \tilde{c}^2}{\partial t} + \nabla \cdot (\bar{\rho} \tilde{\mathbf{U}} \tilde{c}^2) - \nabla \cdot (\mu_t / \sigma_c \nabla \tilde{c}^2) = C_{c1} \mu_t (\nabla \tilde{C})^2 - C_{c2} \bar{\rho} \frac{\tilde{\epsilon}}{\bar{k}} \tilde{c}^2 - 2 \bar{\rho} \tilde{S}_c'' \quad (4.11)$$

A closure for the fluctuation of the source term, the last term on the RHS of Eq. 4.11 is obtained by doing a Taylor series expansion, see Martin (2003) for the details. $C_3 = 100$,

other values were tried with little affect on the solution.

$$\widetilde{S}_c' = C_3 \frac{\widetilde{c}^2}{\widetilde{T}(\widetilde{C} + \frac{\widetilde{T}_u}{T_{ad} - \widetilde{T}_u})} \widetilde{S}_c \quad (4.12)$$

The conditioned scalar dissipation is approximated by the unconditioned value as.

$$\langle \widetilde{N} | \zeta \rangle \simeq \widetilde{N} = 2 \frac{\widetilde{\epsilon}}{\widetilde{k}} \widetilde{c}^2 \quad (4.13)$$

The solution procedure is to solve the simplified premixed CMC equations for a range of scalar dissipation values and store the density, source term and species mass fractions in a table. Fluent ver. 6.1.22 (Fluent 2004) is used to solve the fluid equations along with the RNG turbulence model for the 2-dimensional backward facing step of El Bahawy *et al.* (1983). Premixed methane and air are flowed over the step and the flame is stabilized in the recirculation zone. The equivalence ratio is 0.9 and the full GRI2.11 mechanism is used (Bowman *et al.* 1998). An initial mesh of 300 x 80 cells is used with grid adaption in the flame zone and along the wall to meet the log-wall criteria for the wall boundary conditions. Equations for the progress variable and its variance are added as scalar equations to (Fluent 2004) using its user defined function (UDF) capabilities. The inlet values are zero and the outlet and walls are set to zero gradient for the scalars.

At each computational cell, the mean progress variable and scalar dissipation is used to retrieve the conditioned density, reaction rate source term and mass fractions from the table. The progress variable and its variance are used with an assumed shape beta-function PDF to obtain the non-conditioned values, which are used in the next iteration of the CFD code. This process is continued until steady state is reached.

4.3. Marker Field Implimentation

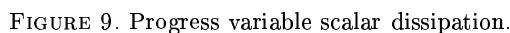
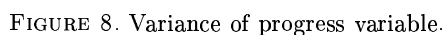
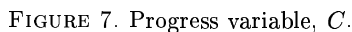
Here a comparison is made between the C field using Eq. 4.8 and the S field, without using Eq. 3.9. Future work will calculate the C field using Eq. 3.9.

Equations 1.2 and 1.3 are also added to (Fluent 2004) as additional UDF's. The inlet values for S are $-20(1 - y/h)$, where y is the vertical coordinate of the step and h is the step height. Standard RANS closure is used for the turbulent fluxes. There is no feed back from the marker field equations to the other equations. The scalar dissipation of S is calculated as follows.

$$\langle \widetilde{N} | \zeta \rangle \simeq \widetilde{N} = 2 \frac{\widetilde{\epsilon}}{\widetilde{k}} \widetilde{s}^2 \quad (4.14)$$

4.4. RANS Results

Figures 7 and 8 show the progress variable and its variance, showing the location of the flame front. Figure 9 shows the scalar dissipation of the progress variable. The large values in these figures at the tip of the step are due to limitations in the turbulence model and are not physical. Figure 10 shows the marker field. The contours in the flame zone are nearly parallel with the progress variable contours, indicating a potential mapping between the progress variable and the marker field. Figure 11 shows the variance of the marker field, which is very different then the variance of the progress variable. The variance of the marker variable was nearly zero until reaching its peak at the flame zone, then slowly tapering off. The variance of the marker field is largest prior to the flame and tappers off as the flame zone is approached. Figure 12 shows the scalar dissipation of the marker field. The peak values are in the flame zone, as was the case with the progress variable, but it also has large values prior to the flame zone.



Here 3D DNS using 1-step chemistry was used to show the mapping between the progress variable and the marker field for a 1D flame. At low Damkohler number the marker field equation provided a good closure for the conditioned reaction rate term. At higher Damkohler numbers the closure was not as good, but may still be good enough for RANS and LES modeling. The premixed CMC method was incorporated into a RANS model along with the mean and variance of the marker field. This showed that the progress variable and marker field look similar in RANS providing further evidence that the marker field may provide a viable closure. Next steps include generating a 3D DNS database with more realistic chemistry and incorporating the conditioned marker field into RANS and LES.

BILGER, R. W. 2004 Marker fields for turbulent premixed combustion. *Combust. Flame* **138**, 188-194.

BILGER, R. W. 1993 Conditional Moment Closure Modelling and Advanced Laser Measurements in *Turbulence and Molecular Processes in Combustion*, T. Takeno, Ed. **138**, 188-194.

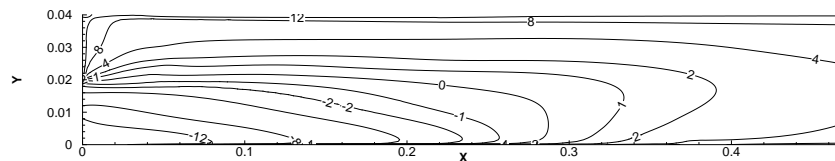
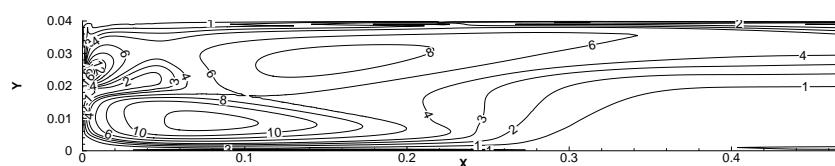
FIGURE 10. Marker variable, S .

FIGURE 11. Variance of marker variable.

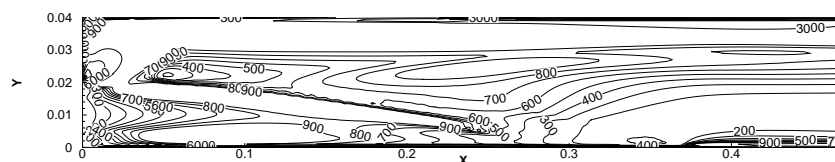


FIGURE 12. Marker variable scalar dissipation.

- BILGER, R. W. 1980 in *Turbulent Reacting Flows*, P.A. Libby and F.A. Williams, Eds., pp267-285 Elsevier Science Publishers.
- BOWMAN, C.T., HANSON, R.K., DAVIDSON, D.F., GARINER JR., W.C., LISSANSKI, V., SMITH, G.P., GOLDEN, D.M., FRENKLACH, M. & GOLDENBERG, M. 1998 www.me.berkeley.edu/gri-mech/GRI2.11.
- EL BANHAWY, Y., SIVASEGARAM, S. & WHITELAW, L.H. 1983 Premixed, Turbulent Combustion of a Sudden-Expansion Flow. *Combust. Flame* **50**, 153-165.
- FLUENT CFD CODE, 2004 www.fluent.com.
- KENNEDY, C. A., CARPENTER, M. H. & LEWIS, R. M. 2000 Low-storage, explicit Runge-Kutta schemes for the compressible Navier-Stokes equations. *Appl. Num. Math.* **35**, 177.
- KLIMENKO, A.Y. & BILGER, R. W. 1999 Conditional Moment Closure for Turbulent Combustion. *Prog. Eng. Comb. Sci.* **25**, 595-697.
- LELE, S. K. 1992 Compact finite difference schemes with spectral-like resolution. *J. Comp. Phys.* **103**, 16.
- MARTIN, S.M., KRAMLICH, J.C., KOSALY, G. & RILEY, J.J. 2003 The Premixed Conditional Moment Closure Method Applied to Idealized Lean Premixed Gas Turbine Combustors. *Journal of Engineering for Gas Turbines and Power, Transactions of the ASME* **125**, 895-900.

- MARTIN, S.M. 2003 *Ph.D Thesis, The Conditional Moment Closure Method for Modeling Lean Premixed Turbulent Combustion*. The University of Washington.
- PETERS, N. 2000 *Turbulent Combustion*. Cambridge University Press.
- POINSOT, T. J. & LELE, S. K. 1992 Boundary conditions for direct numerical simulations of compressible viscous flows. *J. Comp. Phys.* **101** 104.
- SMITH, N.S.A. 1994 *Ph.D Thesis, Development of the Conditional Moment Closure Method for Modelling Turbulent Combustion*. The University of Sydney.
- TROUVE, A. & POINSOT, T. 1994 The Evolution Equation for the Flame Surface Density in Turbulent Premixed Combustion. *J. Fluid Mech.* **278**, 1-31.

Page intentionally left blank

Validation of an asymptotic zone conditional expression for turbulent burning velocity against DNS database

By K. Y. Huh[†], S. H. Kim and S. Kim[†]

Zone conditional formulations for the Reynolds averaged reaction progress variable are used to derive an asymptotic expression for turbulent burning velocity. New DNS runs are performed for validation in a statistically one dimensional steady state configuration. A parametric study is performed with respect to turbulent intensity, integral length scale, density ratio and laminar flame speed. Results show good agreement between DNS results and the asymptotic expression in terms of measured maximum flame surface density and estimated turbulent diffusivity in unburned gas.

1. Motivation and objectives

There has been controversy about the definition of turbulent burning velocity, which is the mean propagation speed of a flame brush in turbulent premixed combustion. Although it is a quantity of engineering significance in many combustion devices, experimental correlations have shown much scatter in different flame configurations and test conditions. There are some theoretical or analytical expressions with arbitrary tuning constants (Peters 1999), which have similar functional forms with experimental correlations (Abdel-Gayed *et al.* 1987). The current consensus is that there is yet no predictive formula reliable in a wide range of combustion situations. A pessimistic view is that there may be no unique measurable quantity to be defined as the turbulent burning velocity in any given experimental condition (Driscoll 2003). However confusion may come from the fact that we have not considered a complete list of relevant parameters or physical phenomena to characterize a turbulent premixed flame, e. g., external pressure gradient imposed in stagnating (Liu & Lenze 1988) or buoyant flow (Khokhlov *et al.* 1996) or flame instability to increase flame surface density at a higher ambient pressure (Kobayashi *et al.* 1996).

Some form of averaging is essential to handle randomly fluctuating scalars and reaction rates in turbulent combustion. Conditional averaging has proved useful to reduce such fluctuation, while unconditional Favre averaging does not allow a logical approach for closure of the nonlinear mean reaction rate. The conditional moment closure model (Klimenko & Bilger 1999) which involves conditional averaging with respect to mixture fraction has been successful in turbulent nonpremixed combustion problems (Kim & Huh 2004). Choice of the conditioning variable may be arbitrary as long as it contributes to significant reduction of fluctuation from any conditional mean value. Zone conditional averaging is a reasonable choice for turbulent premixed combustion at a high Damkohler number. It is because much of the fluctuation originates from transition between burned and unburned regions in addition to generic turbulent fluctuation in each region. In

[†] Mechanical Eng. Dept. Pohang University of Science and Technology, Korea

previous work the zone conditionally averaged mass and momentum equations were derived with the closure assumptions for unknown surface average quantities (Lee & Huh 2004; Lee *et al.* 2004). Validation was performed against the DNS database of a steady flame brush (Nishiki *et al.* 2002), although at relatively low turbulence Reynolds and Damkohler numbers. In this study new DNS runs are made to validate the predictive formula for turbulent burning velocity with parametric study to evaluate independently the effects of turbulent intensity, integral length scale, density ratio and laminar flame speed.

2. Mathematical Formulation

2.1. Definition of zone conditional averaging

We introduce the Heaviside function defined as

$$H_{c^*}(\mathbf{x}, t, c) = H(c - c^*) = \begin{cases} 1 & \text{if } c(\mathbf{x}, t) \geq c^* \\ 0 & \text{otherwise} \end{cases} \quad (2.1)$$

where c^* is set equal to 0.5. The idea is to separate the instantaneous reaction field into three distinct zones; unburned ($\rho = \rho_u$), burned ($\rho = \rho_b$) and thin reaction zone ($\rho_b < \rho < \rho_u$). The iso- c surface defines the flame surface which separates the zone of $c(\mathbf{x}, t) \geq c^*$ from the zone of $c(\mathbf{x}, t) \leq c^*$. In the limit of a high Damkohler number the reaction zone thickness is less than any turbulence length scale and the probability of $0 < c < 1$ becomes negligibly small. Then the expectation of H_{c^*} is equal to Reynolds averaged reaction progress variable as

$$\langle H_{c^*} \rangle = \bar{c}. \quad (2.2)$$

The overbar and $\langle \cdot \rangle$ notation with no subscript represent an unconditional ensemble average and may be used interchangeably. For any quantity, Φ , it holds that

$$\langle H_{c^*} \Phi \rangle = \bar{c} \langle \Phi \rangle_b \quad (2.3)$$

$$\langle (1 - H_{c^*}) \Phi \rangle = (1 - \bar{c}) \langle \Phi \rangle_u \quad (2.4)$$

where $\langle \Phi \rangle_b$ and $\langle \Phi \rangle_u$ are the conditional averages in burned and unburned region respectively. Define that

$$\Phi_i = \langle \Phi \rangle_i + \Phi'_i \quad (2.5)$$

where the subscript i can be any of u , b , su or sb . The notations, sb and su , represent the conditional quantities in burned and unburned gas adjacent to the thin reaction zone as shown in Fig. 1. The prime notation may represent an unconditional or a conditional fluctuation according to the definition of the average. The two averages, $\langle \Phi \rangle_u$ and $\langle \Phi \rangle_{su}$ (or $\langle \Phi \rangle_b$ and $\langle \Phi \rangle_{sb}$), are not in general equal to each other. When integrated over volume, the former represents a volumetric average in unburned (or burned) gas while the latter represents a surface average on the unburned (or burned) side of a flame surface. Conditional density fluctuation is ignored as negligible with constant ρ_b and ρ_u . Since variable density and chemical reaction are confined to the thin reaction zone, all reaction terms can be represented as simple interfacial transfer in terms of the surface average quantities, su or sb , on either side of a flame surface.

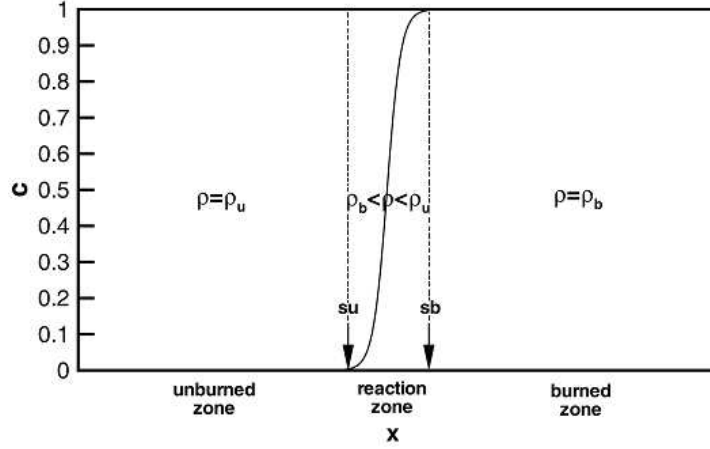


FIGURE 1. Illustration of instantaneous reaction field around a flamelet surface.

2.2. Derivation of \bar{c} transport equation

The instantaneous local balance equation for reaction progress variable is written as,

$$\frac{\partial c}{\partial t} + \mathbf{v} \cdot \nabla c = S_d |\nabla c| \quad (2.6)$$

where the reaction progress variable, c , is defined as,

$$c = \frac{T - T_u}{T_b - T_u} \quad \text{or} \quad c = \frac{Y_F - Y_F^u}{Y_F^b - Y_F^u}. \quad (2.7)$$

T , T_u and T_b are respectively local, unburned and burned gas temperatures. Y_F , Y_F^u and Y_F^b are the fuel mass fractions of local, unburned and burned gas. The two definitions in Eq. (2.7) are equivalent for a unity Lewis number with no heat loss and compressibility effects. Temporal and spatial derivatives of the Heaviside function are given as,

$$\frac{\partial H(c - c^*)}{\partial t} = \delta(c - c^*) \frac{\partial c}{\partial t} \quad (2.8)$$

$$\nabla H(c - c^*) = \delta(c - c^*) \nabla c. \quad (2.9)$$

A balance equation for the Heaviside function, H_{c^*} , can be derived from Eqs. (2.6), (2.8) and (2.9) as,

$$\frac{\partial H_{c^*}}{\partial t} + \mathbf{v} \cdot \nabla H_{c^*} = S_L \Sigma \quad (2.10)$$

where S_d is assumed to be equal to the laminar flame speed S_L . The instantaneous flame surface density Σ is defined as,

$$\Sigma = |\nabla c| \delta(c - c^*) \quad (2.11)$$

Taking an ensemble average of Eq. (2.10) we have a transport equation for the Reynolds averaged reaction progress variable as,

$$\frac{\partial \bar{c}}{\partial t} + \langle \mathbf{v} \rangle_{su} \cdot \nabla \bar{c} = \langle \mathbf{v}'_{su} \cdot \mathbf{n}' \rangle_s \Sigma_f + S_{Lu} \Sigma_f \quad (2.12)$$

where the flame surface density, Σ_f , is an ensemble average of Σ . In Eq. (2.12), the surface average of Φ , $\langle \Phi \rangle_s$, is defined as $\langle \Phi \rangle_s = \langle \Phi \Sigma \rangle / \Sigma_f$, which is different from

the unconditional BML formulation. The surface averages here are taken to be on the unburned side for modelling and interpretation in the following. It is, however, equally valid to write Eq. (2.12) in terms of the surface averages on the burned side for an infinitesimally thin flamelet. \mathbf{n} is a unit normal vector on a flame surface toward the unburned side given as,

$$\mathbf{n}(\mathbf{x}, t) = -(\nabla c / |\nabla c|)_{c=c^*}. \quad (2.13)$$

Note that $\nabla H_{c^*} = -\mathbf{n}\Sigma$. The laminar flame speed, S_{Lu} , is the displacement speed relative to adjacent unburned gas, i.e. $\mathbf{v}_s = \mathbf{v}_{su} + \mathbf{n}S_{Lu}$, where \mathbf{v}_s is the velocity of the iso- c flame surface. In case counter-gradient diffusion is dominant over gradient transport with a large heat release parameter and weak turbulence, the flame surface density, Σ_f , may be modelled simply as,

$$\Sigma_f = 4\Sigma_{max}\bar{c}(1 - \bar{c}) \quad (2.14)$$

where Σ_{max} is the maximum at $\bar{c} = 0.5$. This parabolic profile is shown to be accurate in many experiments (Deschamps *et al.* 1992), while the peak \bar{c} tends to increase with increasing gradient diffusion (Lee *et al.* 2000).

2.3. Asymptotic expression for turbulent burning velocity

The transport equation, Eq. (2.12), for the Reynolds averaged reaction progress variable can be rewritten as,

$$\frac{\partial \bar{c}}{\partial t} + \langle \mathbf{v} \rangle_u \cdot \nabla \bar{c} = (\langle \mathbf{v} \rangle_u - \langle \mathbf{v} \rangle_{su}) \cdot \nabla \bar{c} + \langle \mathbf{v}'_{su} \cdot \mathbf{n}' \rangle_s \Sigma_f + S_{Lu} \Sigma_f. \quad (2.15)$$

The first term on the RHS of Eq. (2.15) is modelled as,

$$(\langle \mathbf{v} \rangle_u - \langle \mathbf{v} \rangle_{su}) \cdot \nabla \bar{c} = f(u' / S_{Lu}^0, Ka) D_{tu} \nabla^2 \bar{c} \quad (2.16)$$

where D_{tu} is turbulent diffusivity in unburned gas and the function, f , represents the effect of nonpassive nature of a flame surface in terms of the ratio, u' / S_{Lu}^0 , and the Karlovitz number. The difference between the surface and volume average velocities comes from diffusive turbulent eddy motions in unburned gas without any externally imposed pressure gradient. The second term on the RHS of Eq. (2.15) is modelled as (Lee & Huh 2004),

$$\langle \mathbf{v}'_{su} \cdot \mathbf{n}' \rangle_s \Sigma_f = K \langle k \rangle_u^{0.5} \langle \mathbf{n}' \cdot \mathbf{n}' \rangle^{0.5} \Sigma_f = K \langle k \rangle_u^{0.5} (1 - \langle \mathbf{n} \rangle_s \cdot \langle \mathbf{n} \rangle_s)^{0.5} \Sigma_f \quad (2.17)$$

where I_0 is the mean stretch factor for laminar flame speed. K is a dimensionless constant of order unity. The quantity, $\langle \mathbf{v}'_{su} \cdot \mathbf{n}' \rangle_s$, is shown to be positive and approximately constant through a flame brush in the DNS database (Nishiki *et al.* 2002). The transport equation for the Reynolds averaged reaction progress variable can now be written for a one-dimensional steady propagating flame as,

$$U_T \frac{d\bar{c}}{dx} = f(u' / S_{Lu}^0, Ka) D_{tu} \frac{d^2 \bar{c}}{dx^2} + K \langle k \rangle_u^{0.5} (1 - \langle \mathbf{n} \rangle_s \cdot \langle \mathbf{n} \rangle_s)^{0.5} \Sigma_f + I_0 S_{Lu}^0 \Sigma_f \quad (2.18)$$

where the turbulent flame speed, U_T , may be obtained asymptotically by assuming exponential decay of \bar{c} as \bar{c} approaches zero.

$$\frac{d\bar{c}}{dx} = a_1 \bar{c} \quad \text{as } \bar{c} \rightarrow 0 \quad (2.19)$$

The following relationships should hold asymptotically at the leading edge.

$$\frac{d^2\bar{c}}{dx^2} = a_1^2\bar{c}, \quad \langle n_x \rangle_s = 1, \quad \Sigma_f = \frac{d\bar{c}}{dx} = a_1\bar{c} \quad \text{as } \bar{c} \rightarrow 0 \quad (2.20)$$

The magnitude of the mean unit normal vector, $\langle n_x \rangle_s$, should approach unity as $\bar{c} \rightarrow 0$ or $\bar{c} \rightarrow 1$, as burned or unburned gas may exist only on one side of a plane normal to the propagation direction. The constant a_1 is determined as $4\Sigma_{max}$ according to Eqs. (2.14) and (2.20). Then, an asymptotic formula for U_T is given from Eq. (2.18) as,

$$U_T = 4f(u'/S_{Lu}^0, Ka)\Sigma_{max}D_{tu} + I_0S_{Lu}^0. \quad (2.21)$$

Note that the modeled term in Eq. (2.17) does not affect the asymptotic expression for turbulent burning velocity. In the following the function, f , and the mean stretch factor, I_0 , are assumed to be equal to unity for comparison with DNS results. Further investigation is required on these two parameters, while validity of this investigation will not be impaired considering uncertainties in the other estimated quantities, Σ_{max} and D_{tu} .

3. Methodology in DNS

Direct numerical simulation is performed to construct a new database for validation of Eq. (2.21) for turbulent burning velocity. Fully compressible Navier-Stokes equations with single step chemistry are solved:

$$\frac{\partial \rho}{\partial t} + \frac{\partial \rho u_i}{\partial x_i} = 0 \quad (3.1)$$

$$\frac{\partial \rho u_i}{\partial t} + \frac{\partial}{\partial x_j}(\rho u_i u_j) = -\frac{\partial p}{\partial x_i} + \frac{\partial \tau_{ij}}{\partial x_j} \quad (3.2)$$

$$\frac{\partial \rho e}{\partial t} + \frac{\partial}{\partial x_j}[(\rho e + p)u_j] = \frac{\partial u_j \tau_{ij}}{\partial x_i} + \frac{\partial}{\partial x_i}(\lambda \frac{\partial T}{\partial x_i}) + Q\omega \quad (3.3)$$

$$\frac{\partial \rho Y_R}{\partial t} + \frac{\partial}{\partial x_j}(\rho u_j Y_R) = \frac{\partial}{\partial x_i}(\rho D \frac{\partial Y_R}{\partial x_i}) - \omega \quad (3.4)$$

where

$$\rho e = \frac{1}{2}\rho u_i u_i + \frac{p}{\gamma - 1} \quad (3.5)$$

$$\tau_{ij} = \mu \left(\frac{\partial u_i}{\partial x_j} + \frac{\partial u_j}{\partial x_i} - \frac{2}{3}\delta_{ij} \frac{\partial u_k}{\partial x_k} \right) \quad (3.6)$$

$$\omega = A\rho Y_R \exp\left(-\frac{T_a}{T}\right) \quad (3.7)$$

p is the pressure, e is the internal energy and Q is the heat of reaction per unit mass of fresh mixture. A is a pre-exponential factor. T_a is the activation temperature. The gas mixture is assumed to be a perfect gas with a specific heat ratio of $\gamma=1.4$. Y_R is the mass fraction of reactant. The reaction progress variable is defined here as $c \equiv 1 - Y_R$. The thermal conductivity, λ , and the diffusion coefficient, D , are given as

$$\lambda = \mu c_p / Pr \quad \text{and} \quad D = \mu / (\rho Sc). \quad (3.8)$$

The viscosity, μ , is given as

$$\mu = \mu_u (T/T_u)^{0.76}. \quad (3.9)$$

Both the Prandtl number, Pr , and the Schmidt number, Sc , are set to be 0.7. These equations are integrated by a low storage fourth order Runge-Kutta method with a sixth order compact finite difference scheme for spatial discretization. Initial and inflow turbulence are homogeneous and isotropic. The DNS code is based on the finite difference method with inflow and outflow boundary conditions at the inlet and outlet. Periodic boundary conditions are assigned on the sides to represent an infinite planar flame. Nonreflective formulations are employed to avoid a nondissipative transient reflected from inlet or outlet boundary due to an arbitrary guess for the initial state. The number of mesh points is 178x128x128 in the flow direction and the other two normal directions, respectively. It was about the maximum number of mesh points that could be handled by a LINUX PC with 1 Gb RAM.

The simulation is performed from an initial condition for five eddy turnover times to reach a fully developed steady flame. Data are then sampled at a regular interval for a subsequent ten eddy turnover times for averaging and postprocessing. There are 64 sampled data sets during the period of ten eddy turnover times for each case. The inflow boundary condition is adjusted continuously to maintain the steady state and retain the flame brush in the computational domain.

4. Results and Discussion

The simulation conditions for the reference case are summarized in Table 1. The Damkohler number is 7.2, the turbulence Reynolds number is 116.4 and the Karlovitz number is 3.94. These estimations are based on thermal diffusivity, laminar flame speed, turbulent intensity and integral length scale given in the table. The Zeldovich number, Ze , is defined as T_a/T_b , where T_b is burned gas temperature. D_{th} is thermal diffusivity. l_c is chemical length scale given as D_{th}/S_{Lu}^0 , which corresponds to laminar flamelet thickness. Single step chemistry will not be a concern for the zone conditional formulations at a high Da , although the Da here is restricted by computational limitation. Figure 2 shows three dimensional images of a fluctuating flame brush for the reference case. There are about four or five computational cells assigned to resolve the internal structure of a laminar flamelet. The quasi steady flame brush is well confined in the domain throughout the sampling period. Flame surface momentarily forms a long finger protruding into burned gas, which either burns out to disappear or gets detached and convected downstream as an unburned pocket. Although not a serious concern, this may affect conditional statistics as the flame touches the outlet boundary.

Spatial variation of $\bar{\tau}$ and flame surface density in Figs. 3(a) and (b) show significant fluctuation due to stochastic behavior of a limited flame portion in the domain. The relationship between $\bar{\tau}$ and flame surface density is also stochastic to some extent in Fig. 3(c), but falls in the region bounded by a parabolic curve with the peak value of about 1.2. The mean values shown as hollow circles also form an approximate parabolic curve with the peak value of about 0.9 in Fig. 3(c). The instantaneous turbulent burning velocity is set equal to the inflow velocity corrected for minor movement of the flame brush at every time step. The mean turbulent burning velocity is 1.24 in Fig. 3(d) with fluctuation for the same reason as in Fig. 3(a) and (b). Here the turbulent burning velocity is estimated by Σ_{max} on the upper boundary curve, since the asymptotic gradient at the leading edge seems to correlate better with the upper curve than with the average curve

TABLE 1. Reference case

ρ_u/ρ_b	S_{Lu}^0	u'/S_{Lu}^0	u'	l_k	l_c	τ_t	τ_c	ν
4.0	0.314	2.38	0.7471	0.0229	0.0455	1.0424	0.1449	0.005
k	ϵ	ν_t	D_{th}	l_t	Ka	Re_t	Da	Ze
0.8373	0.4539	0.1390	0.0413	0.7788	3.94	116.4	7.2	4.0

in Fig. 3(c). There will be negligible fluctuation with no such ambiguity in experimental measurements or simulations in a much larger domain.

The volume and surface average velocities are shown at different times for the reference case in Fig. 4. Significant fluctuation of the conditional velocities is partly due to an insufficient number of samples for averaging on each cross sectional plane. While $\langle \mathbf{v} \rangle_b$ is greater than $\langle \mathbf{v} \rangle_u$ in most flame regions, crossover between $\langle \mathbf{v} \rangle_b$ and $\langle \mathbf{v} \rangle_u$ should occur near the leading edge for existence of a stabilized flame brush. The surface average velocities are close to the volume average velocities, while deviation occurs near the edges in Fig. 4. Deviation in unburned gas velocities occurs at the leading edge, while deviation in burned gas velocities occurs at the trailing edge. It is clear that the propagation characteristics depends on balance of momentum in the burned and unburned gas as well as transport of scalar quantities in a turbulent premixed flame.

A parametric study is performed for six cases in addition to the reference case with respect to turbulent intensity, integral length scale, density ratio and laminar flame speed as listed in Table 2. Three dimensional flame configurations are compared for all six test cases in Fig. 5. The flame shows more wrinkling with an increased flame surface density for the case D1. A larger density ratio seems to suppress the wrinkling of flame surface to some extent for the reference case. The cases U1 and U2 with lower turbulent intensities show less wrinkling and shorter flame brush thicknesses than the reference case. Although they have the same integral length scale, the characteristic scale of wrinkling shows apparent increase to give a reduced flame surface density at a lower turbulent intensity. Variation with respect to turbulent intensity, however, is not monotonic here, since the case U2 shows a higher peak than the case U1. The case S1 has a thicker laminar flamelet with a lower laminar flame speed than the other cases. The case S1 also has a thicker flame brush and a lower peak flame surface density than the reference case. The cases L1 and L2 have lower integral length scales with the turbulent intensity the same as the reference case. The flame brush thickness tends to decrease with a decreasing integral length scale, while the flame surface density does not show a monotonic behavior.

Flame surface densities for the six parametric cases show a similar trend as for the reference case in Fig. 6. The level of fluctuation varies with the maximum fluctuation for the case D1 and the minimum fluctuation for the case S1. It may be inferred that the fluctuation is partly related with accuracy of the estimation method based on the gradient of instantaneous reaction progress variable in the domain. The case S1 shows less fluctuation since it has a thicker laminar flamelet which allows more accurate estimation of the gradient. As for the reference case the turbulent burning velocity is predicted in

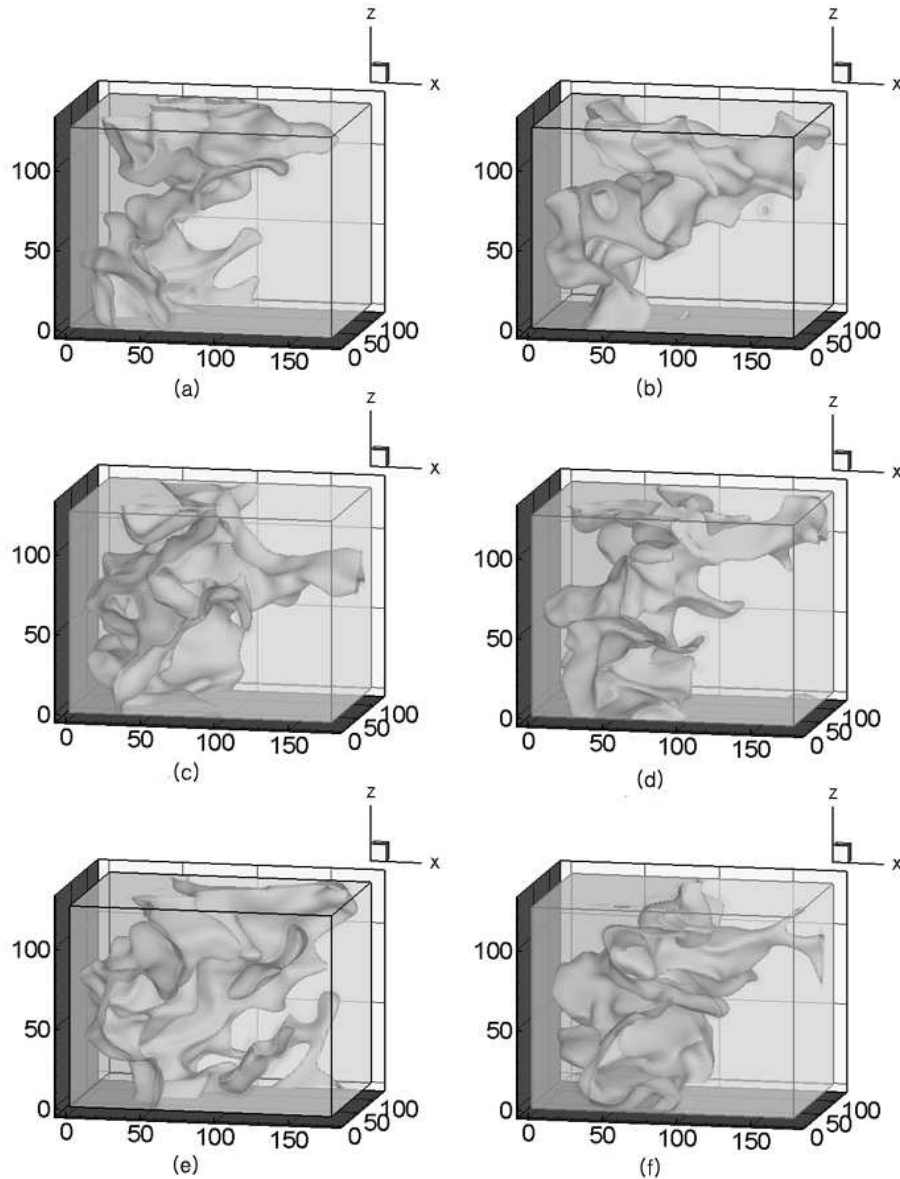


FIGURE 2. Images of a turbulent premixed flame brush at different instants for the reference case. (a) $5.0 \tau_t$, (b) $6.7 \tau_t$, (c) $8.3 \tau_t$, (d) $10.0 \tau_t$, (e) $11.7 \tau_t$ and (f) $13.4 \tau_t$.

terms of the maximum flame surface density on the upper boundary of the scattered points in Fig. 6. Without further study and more test cases in a larger domain it seems difficult to find a consistent trend for the maximum flame surface density and the level of fluctuation in terms of the independent parameters under investigation. Figure 7 shows instantaneous turbulent burning velocities with mean values given as horizontal lines for all cases. There is no obvious correlation between fluctuation in the predicted turbulent burning velocity in Fig. 7 and fluctuation of the flame surface density in Fig. 6.

Comparison is made between the mean turbulent burning velocities from DNS and the

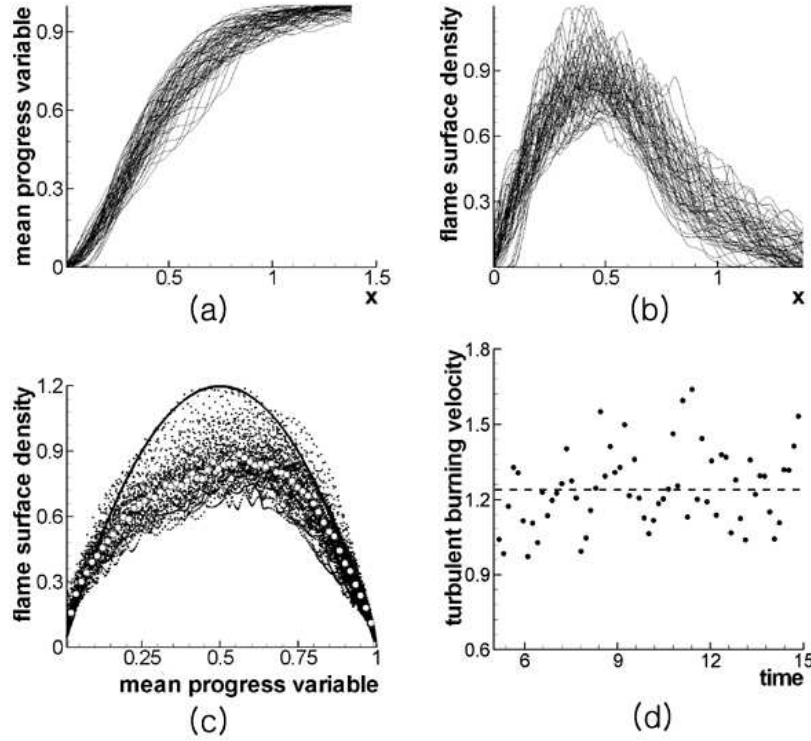


FIGURE 3. DNS results for the reference case.

predictions by Eq. (2.21). The maximum flame surface densities from the upper boundaries of scattered points are listed in Table 3. The function, $f(u'/S_{Lu}^0, Ka)$, and the mean stretch factor, I_0 , are assumed to be equal to unity. Although not a satisfactory practice, this simplifying assumption is not likely to affect overall validity of the comparison in this study. Turbulent diffusivity is estimated from $D_{tu} = u'^2 T_L$ where the Lagrangian integral time scale, T_L , has been estimated or measured in a few previous investigations in the literature. It is given in terms of the constant, C_0 , as $T_L^{-1} = \frac{3}{4} C_0 \frac{\epsilon}{k}$. The constant, C_0 , was estimated to be about 2.1 from thermal wake data, while Pope (1994) reported a value in the range between 4 and 6. By fitting to direct simulation data Sawford (1991) suggested a value of 7, which is employed in the comparison in this report. All the relevant parameters are listed with the measured and estimated turbulent burning velocities in Table 3. There is good agreement between DNS and asymptotic expression in Fig. 8 where the points for all test cases are clustered around the line, $y=x$. The maximum error is about 15%.

5. Conclusions and future work

It is shown that the predictive formula for turbulent burning velocity agrees well with DNS results for a steady turbulent premixed flame in all test cases. There is no external pressure gradient to be taken into account in this one dimensional configuration. A parametric study was performed with respect to turbulent intensity, integral length scale, density ratio and laminar flame speed. Although some uncertainty remains for estimation of stretch factors and turbulent diffusivity, validity of the predictive formula is confirmed

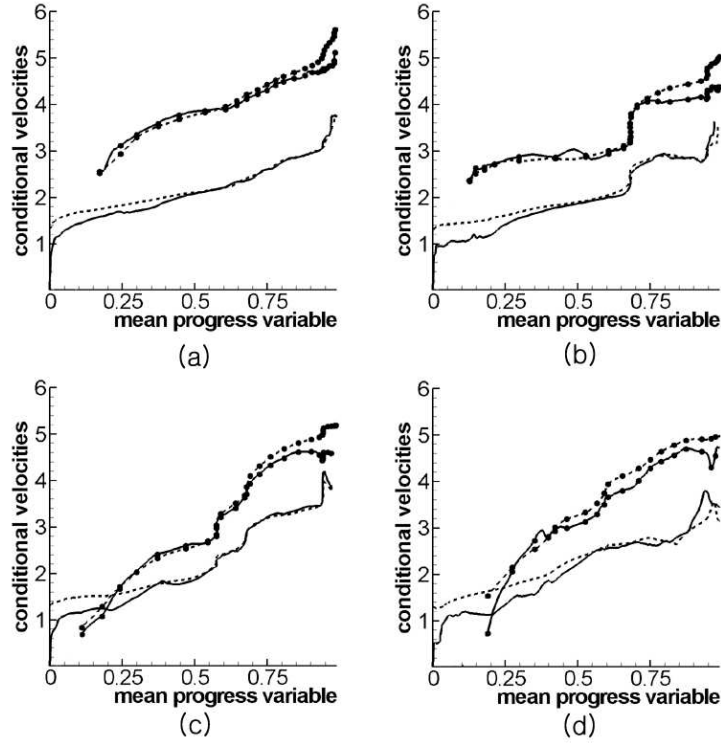


FIGURE 4. Conditional velocities at different instants for the reference case. Solid line for $\langle v \rangle_{su}$, dotted line for $\langle v \rangle_u$, solid line with markers for $\langle v \rangle_{sb}$ and dotted line with markers for $\langle v \rangle_b$.

Case Identification	Parameter Investigated
D1	$\rho_u/\rho_b = 1.0$
U1	$u' = 0.3736$
U2	$u' = 0.1868$
S1	$S_{Lu}^0 = 0.181$
L1	$l_t = 0.5841$
L2	$l_t = 0.3894$

TABLE 2. Six cases for parametric study

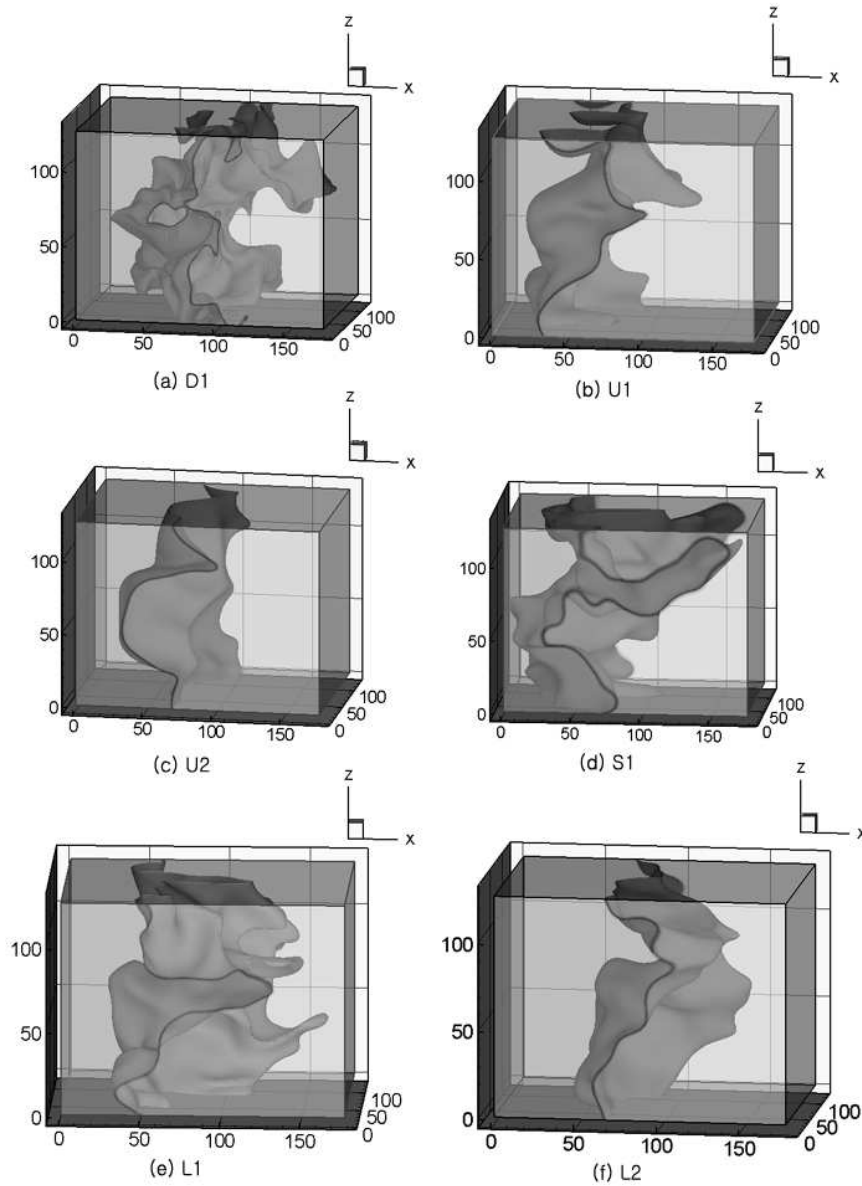


FIGURE 5. Images of turbulent premixed flame brushes for six parametric test cases.

in this investigation. DNS results show significant fluctuation of spatially averaged values on each cross sectional plane due to a limited computational domain and an insufficient number of samples for averaging. Correlation is made in terms of the maximum flame surface density on the upper boundary of scattered data points. Turbulent diffusivity is estimated from the Lagrangian integral time scale with the Kolmogorov constant, C_0 , equal to 7. Further work is needed to reduce fluctuation of statistical averages in a larger computational domain and to perform DNS of a more realistic flame with multistep

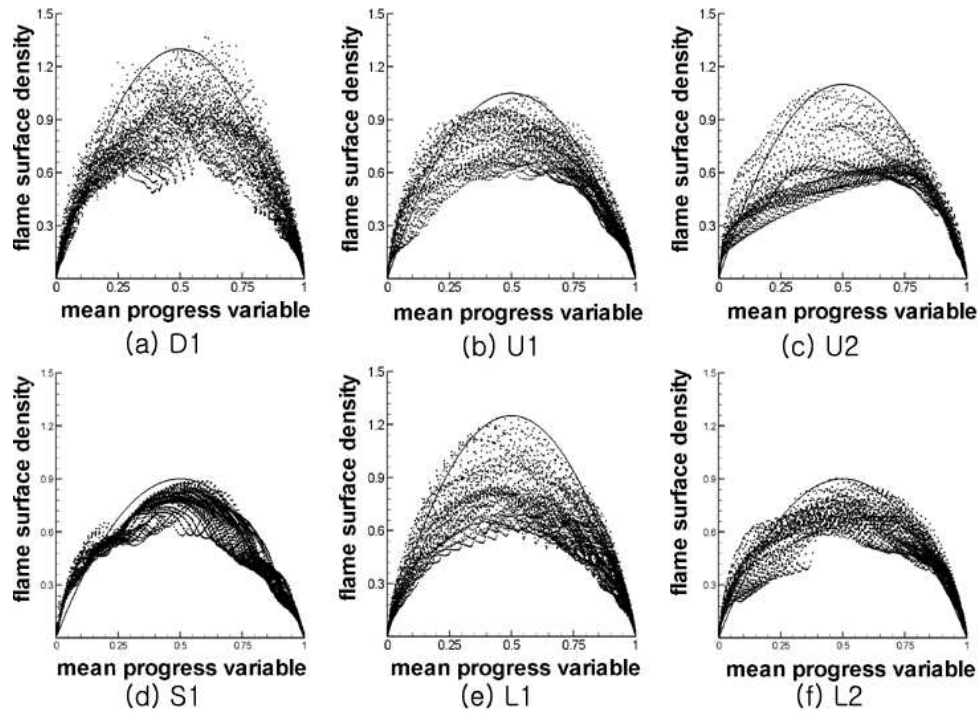
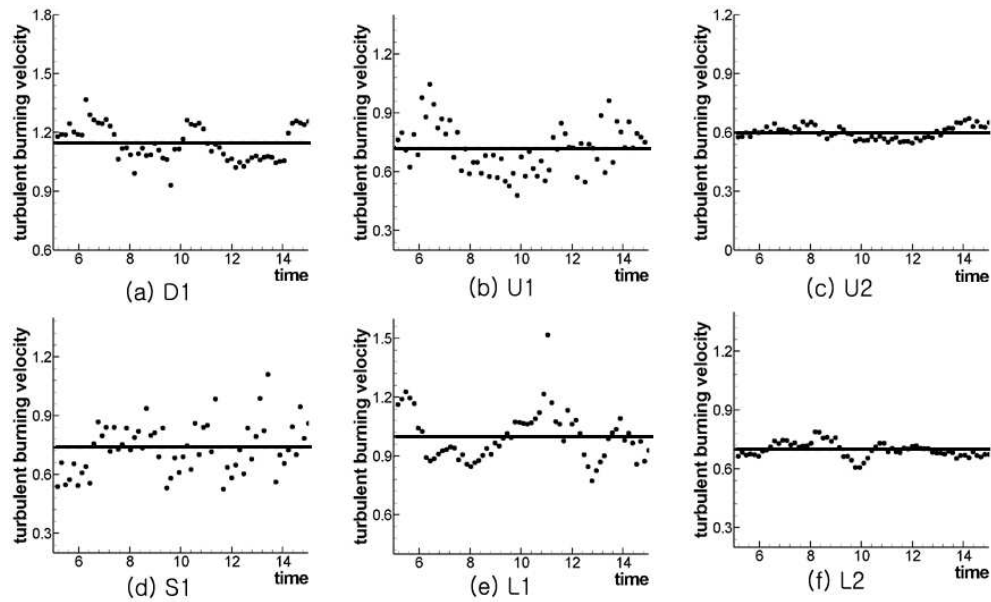
FIGURE 6. Flame surface density vs \bar{c} for six parametric test cases.

FIGURE 7. Turbulent burning velocities for six parametric test cases.

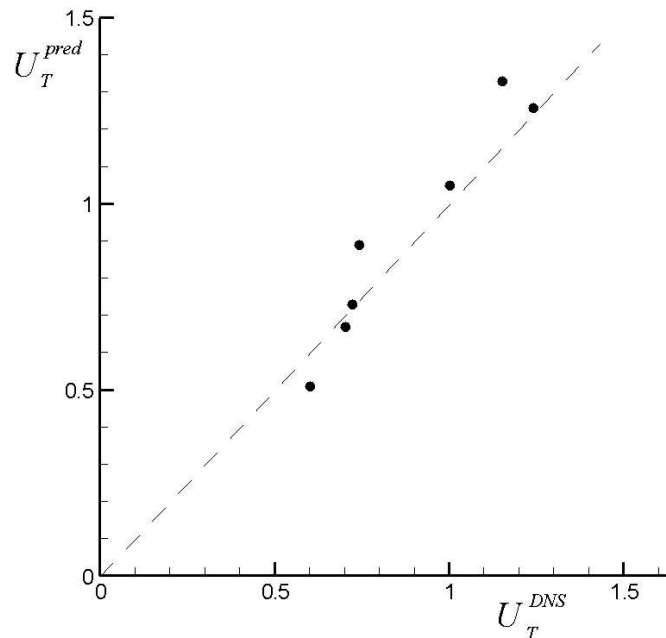
Case	D_{tu}	S_{Lu}^0	Σ_{max}	U_T^{DNS}	U_T^{pred}
ref	0.1961	0.314	1.21	1.24	1.26
D1	0.1916	0.314	1.30	1.15	1.33
U1	0.0981	0.314	1.05	0.72	0.73
U2	0.0438	0.314	1.10	0.6	0.51
S1	0.1961	0.181	0.90	0.74	0.89
L1	0.1471	0.314	1.25	1.00	1.05
L2	0.0981	0.314	0.90	0.70	0.67

TABLE 3. Comparison of turbulent burning velocity from DNS and predictive formula

chemistry and nonunity Lewis numbers. The effect of an external pressure gradient may easily be taken into account in the current steady one dimensional simulation.

REFERENCES

- ABDEL-GAYED, R. G., BRADLEY, D. & D. & LAWES, M. 1987 Turbulent burning velocities: A general correlation in terms of strain rates. *Proc. Roy. Soc. Lond.* **A414**, 389-413.
- DESCHAMPS, B., BOUKHALFA, A., CHAUVEAU, C., GOKALP, L., SHEPHERD, L. G. & CHENG, R. K. *An experimental estimation of flame surface density and mean reaction rate in turbulent premixed flames*. 24th Int. Symp. on Combustion (Combustion Institute), 469-475.
- DRISCOLL, J. F. 2003 *Premixed turbulent combustion - current knowledge and new challenges*. 3rd Joint Meeting of the U.S. Sections of the Combustion Institute, March, Chicago IL.
- IM, Y., HUH, K. Y., NISHIKI, S. & HASEGAWA, T. 2004 *Zone conditional assessment of flame-generated turbulence with DNS database of a turbulent premixed flame*. *Combustion & Flame* **137**, 478-488.
- KHOKHLOV, A. M, ORAN, E. S & WHEELER, J. C. 1996 *Scaling in buoyancy-driven turbulent premixed flames*. *Combustion & Flame* **105**, 28-34.
- KIM, S. H. & HUH, K. Y. 2004 *Second-order conditional moment closure modeling of turbulent piloted Jet diffusion flames*. *Combustion & Flame* in press.
- KLIMENKO, A. Y. & BILGER, R. W. 1999 *Conditional moment closure for turbulent combustion*. *Prog. Energy Combust. Sci.* **25**, 595-687.
- KOBAYASHI, H., TAMURA, T., MARUTA, K., NIIOKA, T. & WILLIAMS, F. A. 1996 *Burning velocity of turbulent premixed flames in a high pressure environment*. 26th Int. Symp. on Combustion (Combustion Institute), 389-396.

FIGURE 8. U_T^{DNS} vs U_T^{pred} .

- LEE, E. & HUH, K. Y. 2004 *Zone conditional modeling of premixed turbulent flames at a high Damkohler number*. Combustion & Flame **138**, 211-224.
- LEE, E., IM, Y. H. & HUH, K. Y. 2004 *Zone conditional analysis of a freely propagating one-dimensional turbulent premixed flame*. 30th Int. Symp. on Combustion (Combustion Institute) in press.
- LEE, G., HUH, K. Y. & KOBAYASHI, H. 2000 *Measurement and analysis of flame surface density for turbulent premixed combustion on a nozzle-type burner*. Combustion & Flame **122**, 43-57.
- LIU, L. & LENZE, B. 1988 *The influence of turbulence on the burning velocity of premixed CH₄-H₂ flames with different laminar burning velocities*. 22nd Int. Symp. on Combustion (Combustion Institute), 747-754.
- NISHIKI, S., HASEGAWA, T., BORGHI, R. & HIMENO, R. 2002 *Modeling of flame generated turbulence based on direct numerical simulation databases*. 29th Int. Symp. on Combustion (Combustion Institute), 2017-2022.
- PETERS, N. 1999 *The turbulent burning velocity for large scale and small scale turbulence*. J. Fluid Mech. **384**, 107-132.
- POPE, S. B. 1994 *Lagrangian PDF methods for turbulent flows*, Annu. Rev. Fluid Mech. **26**, 23-63.
- SAWFORD, B. L. 1991 *Reynolds number effects in Lagrangian stochastic models of turbulent dispersion*, Phys Fluids A **3**(6), 1577-1586.

LES/FDF/ISAT computations of turbulent flames

By L. Lu [†], Z. Ren [†], V. Raman, S. B. Pope [†], AND H. Pitsch

The *in situ* adaptive tabulation (ISAT) algorithm is incorporated in the Stanford structured large eddy simulation (LES) code for the large eddy simulation of turbulent combustion. The subgrid scale (SGS) closure implemented by Raman is based on the scalar filtered mass density function (FDF) methodology. The FDF represents the joint probability density function of the subgrid-scale scalar quantities and is obtained by solution of its modelled transport equation. In this equation, the effect of chemical reactions appears in closed form and the chemistry mechanism is implemented via ISAT; the influences of SGS mixing and convection are modelled. The modelled FDF transport equation is solved by the Lagrangian Monte Carlo scheme which solves the statistically equivalent stochastic differential equations (SDEs). The numerical simulation of a spatially developing mixing layer with a 9-species detailed hydrogen mechanism is performed to examine computational issues arising in the LES/FDF/ISAT methodology. It is shown that the filtered mixture fraction field obtained via the FDF agrees well with that obtained by the ‘conventional’ LES in which the finite difference solution of the transport equation of the filtered mixture fraction is obtained. The performance and load balancing of both the serial and parallel ISAT strategies are investigated. For the simulation in which cheap retrievals are dominant, a speed-up factor of about 300 is obtained for the combustion chemistry compared to using direct integration. And compared to the LES (without FDF), the relative cost of LES/FDF (without reaction) is about 2.8, and the relative cost of LES/FDF/ISAT is about 4.3. For the simulation in which there is a significant fraction of direct integrations, the halving of the time in combustion chemistry is achieved by using the parallel ISAT strategy compared to serial ISAT.

1. Introduction

For the modeling of turbulent combustion, large eddy simulation (LES) has the advantage of accounting for the large scale unsteady motions, which account for the bulk of the spatial transport. Within the past decade, large eddy simulation of turbulent reacting flows has been the subject of widespread investigation. And there are significant recent developments of subgrid scale (SGS) modelling for the large eddy simulation of turbulent reacting flows. One such closure is based on the “filtered density function” (FDF) method, first introduced by Pope (Pope 1990). This method is analogous to the probability density function (PDF) modeling (Pope 1985) which has proved very effective in Reynolds averaged simulations. The composition FDF is considered by many investigators and it provides a complete description of the subfilter-scale compositions fluctuations (Gao & O’Brien 1993; Colucci *et al.* 1998; Jaber *et al.* 1999; Zhou & Pereira 2000; James & Jaber 2000; Cha & Trouillet 2003; Givi 2003; Raman *et al.* 2003a). Due to this property, the effect of chemical reactions appears in closed form and the FDF offers the ability to treat finite-rate chemistry and the turbulence-chemistry interactions. This combined methodology LES/FDF (with very simple chemistry) has been applied to

[†] Cornell University

the Sandia D flame by Sheikhi *et al.* (Sheikhi *et al.* 2004), and to the Sydney bluff-body by Raman *et al.* (Raman *et al.* 2004a; Raman *et al.* 2004b).

While desirable, the computational cost of directly using realistic combustion chemistry in the LES/FDF simulation of turbulent combustion is expensive and usually prohibitive due to strong non-linearities of the reaction source term and the wide range of time scales in the chemical kinetics. The *in situ* adaptive tabulation (ISAT) algorithm (Pope 1997) greatly facilitates the incorporation of realistic combustion chemistry (e.g., of order 10 and 20 species for hydrogen and methane, respectively) and reduces the CPU time dramatically, which makes the LES/FDF simulation of turbulent combustion with realistic chemistry feasible.

In this work, the LES/FDF/ISAT capability for the numerical simulations of turbulent reactive flows with realistic combustion chemistry is developed by incorporating ISAT into the Stanford structured LES code with a Lagrangian Monte Carlo implementation of the composition FDF method. The numerical simulation of a simple spatially developing mixing layer is performed to verify this capability. A detailed hydrogen mechanism, the Li mechanism (Li *et al.* 2003), which has 9 species and 21 reactions, is incorporated via ISAT. In the next sections, the three important ingredients of the LES/FDF/ISAT capability (the LES solver, the FDF formulation and the ISAT algorithm) are briefly reviewed. Then, the results from the mixing layer are discussed, and the ISAT performance and load balancing are investigated.

2. The LES solver

The Stanford parallel structured finite volume code (Pierce 2001; Pierce & Moin 2004), developed specifically for LES of variable density low Mach-number flows, is used in this work. The second order LES scheme uses an energy conserving formulation for the momentum equation. The eddy viscosity and diffusivity are computed using the dynamic Smagorinsky model (Moin *et al.* 1991). The LES scheme also solves the scalar transport equation of filtered mixture fraction $\langle \xi \rangle_L$ using a semi-implicit scheme. The numerical implementation uses an upwind based QUICK scheme that is designed to reduced numerical oscillations but also leads to some amount of numerical dissipation.

3. The filtered density function (FDF) and its Monte Carlo solution

Let ϕ denotes the composition, which consists of species mass fractions and enthalpy in the simulation. The filtered density function (FDF), which describes the sub-filter joint composition density function, is defined as (Pope 1990; Gao & O'Brien 1993)

$$F_L(\psi; \mathbf{x}, t) = \int_{-\infty}^{+\infty} \rho(\mathbf{x}', t) \delta[\psi - \phi(\mathbf{x}', t)] G(\mathbf{x}' - \mathbf{x}) d\mathbf{x}', \quad (3.1)$$

where F_L denotes the filtered mass density function, δ denotes the Dirac delta function, ψ is the sample-space variable corresponding to ϕ and $G(\mathbf{x}' - \mathbf{x})$ is the filter. This definition implies that the FDF is the mass-weighted spatially filtered value of the fine-grained density and the integral properties of the FDF is such that

$$\int_{-\infty}^{+\infty} F_L(\psi; \mathbf{x}, t) d\psi = \int_{-\infty}^{+\infty} \rho(\mathbf{x}', t) G(\mathbf{x}' - \mathbf{x}) d\mathbf{x}' = \bar{\rho}, \quad (3.2)$$

where $\bar{\rho}$ is the filtered density. Using the above definitions, the transport equation for F_L can be derived (Colucci *et al.* 1998; Jaber *et al.* 1999). In the transport equation

for F_L , if the effects of SGS convection are modelled by a gradient diffusion model and and the SGS mixing is closed via the interaction by exchange with the mean (IEM or LMSE) (Villermaux & Devillon 1972; Dopazo & O'Brien 1974) model, the final modelled FDF transport equation is

$$\frac{\partial F_L}{\partial t} + \frac{\partial[\langle u_i \rangle_L F_L]}{\partial x_i} = \frac{\partial}{\partial x_i} \left[(\gamma + \gamma_t) \frac{\partial(F_L/\bar{\rho})}{\partial x_i} \right] + \frac{\partial}{\partial \psi_\alpha} [\Omega_m (\psi_\alpha - \langle \phi_\alpha \rangle_L) F_L] - \frac{\partial[S_\alpha F_L]}{\partial \psi_\alpha}, \quad (3.3)$$

where $\langle u_i \rangle_L$ is the Favre filtered velocity component, $\langle \phi \rangle_L$ is the Favre filtered composition and \mathbf{S} is the rate of change of composition given by the detailed chemical mechanism. The molecular and turbulent diffusivities are denoted by γ and γ_t respectively. The term Ω_m is the SGS mixing frequency (as required in IEM) and is modelled by $\Omega_m = C_\Omega (\gamma + \gamma_t) / (\bar{\rho} \Delta_G^2)$, where C_Ω is a model parameter and Δ_G is the filter width.

The Lagrangian Monte Carlo procedure (Pope 1985) using an ensemble of notional particles is employed for the solution of the high-dimensional equation Eq. 3.3. In this procedure, each of the particles obeys the evolution equations which is obtained from Eq. 3.1 by using techniques similar to the RANS based method. These particles undergo motion in physical space by convection due to the filtered flow velocity and diffusion due to molecular and subgrid diffusivities. The particles move in physical space according to

$$d\mathbf{x}^* = \left(\langle \mathbf{u} \rangle_L + \frac{1}{\bar{\rho}} \nabla(\gamma + \gamma_t) \right) dt + \sqrt{2 \frac{(\gamma + \gamma_t)}{\bar{\rho}}} d\mathbf{W}, \quad (3.4)$$

where \mathbf{x}^* is the instantaneous particle position, $\bar{\rho}$ is the filtered density and \mathbf{W} represents the Wiener process. The particle composition is changed due to mixing and reaction.

$$d\phi^* = [\Omega_m (\langle \phi \rangle_L - \phi^*) + \mathbf{S}(\phi)] dt, \quad (3.5)$$

where ϕ^* is the composition of the particle with the position \mathbf{x}^* . A splitting operation is employed in which the transport in physical and composition space are treated separately (Raman *et al.* 2003b). The transfer of information from the fixed finite difference grid points to the locations of the Monte Carlo particles is conducted via interpolation. Whereas the Favre-filtered statistics such as the filtered species mass fractions on the fixed grid points are obtained via ensemble averaging all the particles in the grid cells.

4. In situ adaptive tabulation (ISAT)

In LES/FDF simulations of turbulent combustion, if a splitting scheme is used to separate the combustion chemistry from other processes such as convective and diffusive species transport as depicted in Fig. 1, the reaction fractional step corresponds to a homogeneous, adiabatic, isobaric system consisting of n_s chemical species. At time t , the full composition is represented by the $n_\phi = n_s + 1$ variables $\phi(t) \equiv \{\phi_1, \phi_2, \dots, \phi_{n_\phi}\}$, which can be taken to be the species mass fractions and enthalpy. Modeling reaction kinetics in this system leads to a set of stiff ordinary differential equations (ODEs)

$$\frac{d\phi(t)}{dt} = \mathbf{S}(\phi(t)), \quad (4.1)$$

where \mathbf{S} is the rate of change of composition given by the detailed chemical mechanism. The task in the reaction fractional step is to determine the solution to Eq. 4.1, the composition $\phi(t + \Delta t)$ after reaction has occurred for the time-step interval Δt starting from the initial composition $\phi(t)$ at time t . Due to strong non-linearities of the reaction

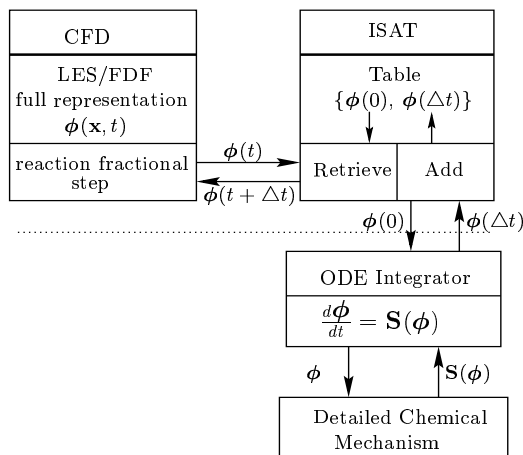


FIGURE 1. Schematic of *in situ* adaptive tabulation used in the reaction fractional step of a CFD computation using LES/FDF approach.

source term and the wide range of time scales in the chemical kinetics, direct integration (DI) of Eq. 4.1 using an ODE integrator is computationally expensive. Further, when the reaction fractional step is performed a huge number of times with many different initial compositions, significant computational resources are required.

An alternative to DI for computing the solution $\phi(t + \Delta t)$ is ISAT, which is a storage-retrieval methodology (with error control) introduced by Pope (1997). As depicted in Fig. 1, an ISAT table stores pairs of values of ϕ before and after reaction $\{\phi(0), \phi(\Delta t)\}$, so that given $\phi(t)$ the corresponding value $\phi(t + \Delta t)$ can be retrieved from the table. (Since the governing ordinary differential equations (ODEs) are autonomous, the value of t is immaterial, and without loss of generality we can set $t = 0$.) As needed, pairs of values $\{\phi(0), \phi(\Delta t)\}$ are added to the table by integrating the governing ODEs with the detailed chemistry. In a large-scale numerical simulation, the reaction fractional step is predominately treated by retrieving from the ISAT table, which is many orders of magnitude less expensive than performing an ODE integration. As a result, ISAT makes the use of realistic combustion chemistry in the LES/FDF simulation of turbulent combustion feasible.

Both the serial and parallel ISAT strategies have been developed. In a parallel LES/FDF simulation of a combustion problem, each processor has its own ISAT table. For the serial ISAT strategy, in the reaction fractional step, particle compositions on one processor are locally processed by using the local ISAT table and there is no message passing. Whereas for the parallel ISAT, the particle composition $\phi(t)$ on one processor may be passed to another processor (using MPI), processed there using the local ISAT table, and then $\phi(t + \Delta t)$ is passed back to the original processor. Two different parallel ISAT strategies are used in this study. One is the uniform random distribution (URAN) method in which all the particle compositions in the simulation are randomly distributed uniformly among the processors to be processed during the reaction fractional step. The other strategy is the local level distribution (LOCLEV) method in which message passing is minimized by passing particle compositions to nearby processors so that all processors have close to the same number of particle compositions to be processed during the reaction fractional step.

5. Flow configuration and numerical specification

The LES/FDF simulation of a two-dimensional, spatially developing, reacting, plane mixing layer is considered. In the simulation, the effect of heat release is neglected and the density is taken to be constant: therefore there is no feedback from the FDF to the LES computation. The primary objective of the simulation is to test the computational performance of the new LES/FDF/ISAT approach and to investigate the ISAT performance for serial and parallel ISAT strategies. No attempt is made to study the numerical accuracy, investigate the effect of models and model parameters, or make comparison with the experimental data.

The flow configuration is set to mimic the Cabra flame which is a turbulent lifted flame of H_2/N_2 issuing into a vitiated co-flow (Cabra *et al.* 2002). In the simulations, a reacting planar mixing layer composed of cold diluted hydrogen in one stream (fuel stream) and hot lean combustion product in the other stream (oxidant stream) is considered. The composition for the fuel stream is taken to be (in volume percentage) N_2 (75%) and H_2 (25%); the temperature is 305K. The composition for the oxidant stream is taken to be (in volume percentage) N_2 (75%), O_2 (15%) and H_2O (10%); the temperature is 1045K.

In the simulation, the flow variables are normalized with respect to selected reference quantities, denoted by the subscript r . The reference velocity U_r is chosen to be the fuel stream velocity 66 m/s, the reference length L_r is taken to be 3.3mm. And the non-dimensional time is given by $t^+ = U_r t / L_r$. The kinematic viscosity ν_r in the simulation is taken to be a constant throughout, which is based on the fuel stream properties. The Reynold number $Re = U_r L_r / \nu_r$ is 15200. The two-dimensional computational domain in non-dimensional units in the simulation is the rectangular region: x^+ from -10 to 50 and y^+ from 0 to 15, where the splitter plate lies in the region: x^+ from -10 to 0 and y^+ from 7.2 to 7.8. The present two-dimensional calculations are performed on a nonuniform mesh with 128 grids nodes in the streamwise direction (x^+) and 64 grid nodes in the tranverse direction (y^+). The mesh in the small region near the splitter plate is refined. The simulation uses parallel computation with 8 processors, and the computational domain is decomposed into 8 blocks in the x^+ direction with each block having the same number of grid cells.

In the simulation, the inlet velocity profiles at $x^+ = -10$ are taken to be laminar plug profiles and turbulence develops in the downstream layer due to the instability of the shear layer. The ratio of oxidant and fuel stream velocities is fixed at 0.4, with the non-dimensional fuel stream velocity being unity, and oxidant stream velocity being 0.4. These values of the free stream velocities are selected so that the flame exists throughout most of the flow, as shown in Fig. 3. The wall boundary conditions at the splitter plate are Neumann conditions for all scalars and pressure, and no-slip Dirichlet conditions for velocity. All the open and outflow boundaries use the convective boundary condition.

In FDF, the Monte Carlo particles are distributed at $t=0$ throughout the calculation domain. The nominal particle number density of 30 particles per cell is use in the simulation. Particle cloning and clustering are utilized to minimize the fluctuation in the number density. New particles are introduced at the inlet at a rate proportional to the local mass flow rate, and the composition of incoming particles is set according to the composition of the fluid at the point of entry. To save computational time, the LES simulation without FDF/ISAT is carried out until the flow field reaches statistical stationarity. Then the LES/FDF simulation without reaction fractional steps is carried out for 1000 time steps. Finally the full LES/FDF/ISAT simulation is performed.

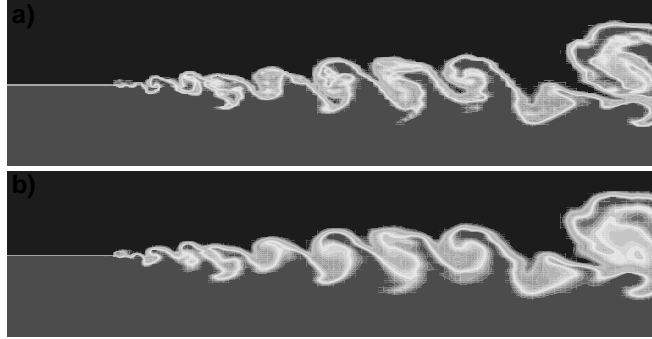


FIGURE 2. Contours of the instantaneous filtered mixture fraction field as predicted by the LES/FDF/ISAT approach via (a) FDF, (b) the LES solver using a standard finite difference scheme.

6. Assessment of the LES/FDF/ISAT approach

To demonstrate the consistency of the FDF formulation, the mixture fraction results obtained via FDF and via the LES solver using the standard finite difference scheme are compared to each other. For the mixing layer studied, any deviations between the results from the FDF and the LES solvers are attributed to the differences in the numerical procedures. Since the accuracy of the finite difference scheme is well established, this comparative analysis provided a means of assessing the performance of the Monte Carlo solution of the FDF. In the FDF for this two-stream problem, the filtered mixture fraction is constructed based on the filtered N_2 mass fraction, $\langle \xi \rangle_L = \frac{\langle Y_{N_2} \rangle_L - Y_{N_2}^o}{Y_{N_2}^f - Y_{N_2}^o}$, where $Y_{N_2}^o$ and $Y_{N_2}^f$ are the N_2 mass fractions of the fuel and oxidant streams respectively. In Fig. 2, the instantaneous contour plots of the mixture fraction are shown as determined by the FDF and LES solvers. This figure provides a simple visual demonstration of consistency of the FDF formulation as the results via the particle method are in agreement with those obtained by the finite difference scheme. In fact, results from the LES solver are somewhat more smeared partially due to the numerical diffusion. Further work should include a quantitative comparison between the filtered mixture fraction fields obtained via FDF and LES as a function of the numerical parameters (e.g., grid size and particle number density).

The LES/FDF/ISAT approach is able to predict the compositional structure of the flame once realistic combustion chemistry is employed. In the simulation, the OH mass fraction, Y_{OH} , is used as a marker of the flame (Cabra *et al.* 2002). Figure 3, which shows one instantaneous filtered OH contour from the particle method, provides a simple visual demonstration of the flame structure. The cold fuel and hot vitiated products mix together with the development of mixing layer and the flame occurs some distance downstream. The reactants must be mixed at the molecular level for reactions to occur. Free-stream fluid that has been entrained into the mixing layer, but remains unmixed, will not undergo reaction as shown in the figure.

7. ISAT performance

One full LES/FDF/ISAT simulation (denoted as CASE1) with constant non-dimensional time step $dt^+ = 0.06$ is performed for 6000 time steps (about two flow-through times). In this simulation, the nominal particle number density of 30 particles per cell is used.

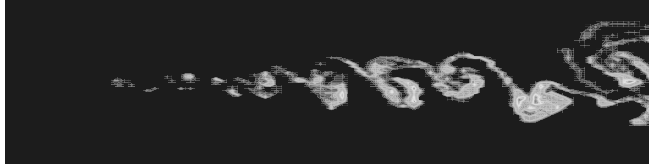


FIGURE 3. The instantaneous filtered OH contour as predicted by the LES/FDF/ISAT approach via FDF.

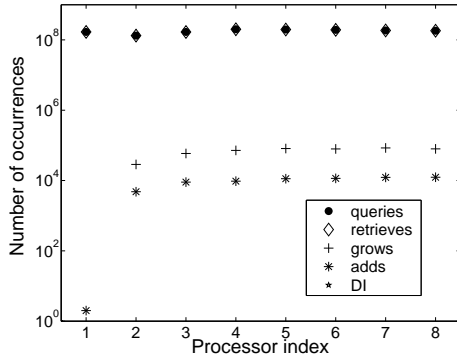


FIGURE 4. Number of occurrences of different events in ISAT (serial) for each processor of CASE1.

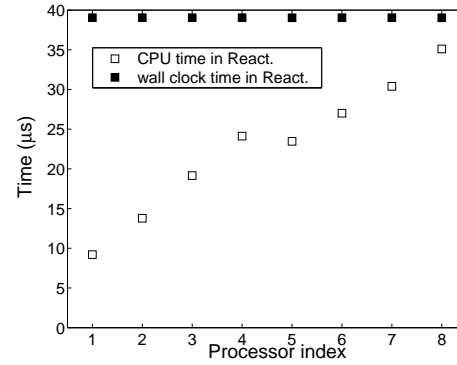


FIGURE 5. The CPU time and wall clock time in reaction fractional step (in microseconds per particle step) for each processor of CASE1.

Each processor has one ISAT table with the maximum assigned storage 300 Mbytes and the ISAT error tolerance used is $\epsilon_{tol} = 1 \times 10^{-5}$.

Figure 4 shows the number of occurrences for different events in ISAT (serial) for each processor. As may be seen from this figure, the number of reaction fractional steps (number of queries) performed is about 2×10^8 for each processor; the cheap retrieves are dominant and there are no direct integrations in the simulation (because the tables are not full).

In the parallel simulations of turbulent combustion, one computational difficulty is how to ensure good load balancing, especially for combustion chemistry. Figure 5 shows the CPU time and wall clock time (per particle step) in the reaction fractional steps for each processor. As may be seen from this figure, even for this simple geometry and chemistry case, the load balancing is not good. The CPU time spent by processor 7 is almost 4 times the CPU time spent by processor 1. And processor 1 has a significant amount of idle time. This is due to the following fact: in the active flame region there are strong chemical reactions and so the reaction fractional step is usually computationally expensive; in the computational domain of processor 1 (adjacent to the inlet), there is no flame at all; whereas for processor 7 (adjacent to the outlet), there is significant flame activity (see Fig. 3).

The load balancing issue for combustion chemistry motivates the development of parallel ISAT strategies. The objective of parallel ISAT strategies is to minimize the wall clock time by trying to achieve good load balancing for the combustion chemistry (i.e., for the reaction fractional step). However, the optimal strategy, which minimizes the wall clock time for the combustion chemistry, may not give the best load balancing. For the two parallel ISAT strategies studied, the uniform random distribution (URAN) method

guarantees good load balancing but requires a large amount of message passing, whereas the local level distribution (LOCLEV) method tries to minimize message passing. A further strategy which can be used in combination with both URAN and LOCLEV is called “Quick Try”. This is done by looping over all the particle compositions on each processor and trying to retrieve by using the local ISAT table before performing the parallel ISAT strategies. Then the parallel ISAT strategies are applied only to those particle compositions whose queries cannot be resolved by retrieves from the local ISAT table. In this study, Quick Try is combined with the parallel ISAT strategies yielding five different modes of ISAT: serial, URAN, URAN-Quick, LOCLEV and LOCLEV-Quick. These parallel strategies are implemented using the *x2f_mpi* software developed by Pope & Lantz (Pope & Lantz 2004).

The success of the parallel ISAT strategies depends on three key time parameters: the average CPU time per retrieve (t_{ret}); the average message passing time per particle composition (t_{MPI}); and the average CPU time per direct integration (t_{DI}). The time t_{ret} increases with n_ϕ^2 ; t_{MPI} increases linearly with n_ϕ ; and t_{DI} increases at least with n_ϕ^3 . Generally, t_{ret} is much smaller than t_{DI} ; and for a combustion process with large n_ϕ , t_{MPI} is smaller than both t_{ret} and t_{DI} . For a particular simulation, if t_{MPI} is greater than both t_{ret} and t_{DI} , then parallel ISAT strategies have no advantages over serial ISAT. (Even though parallel ISAT strategies may achieve better load balancing, the wall clock time for combustion chemistry is larger compared with serial ISAT. As far as wall clock time is concerned, for this case serial ISAT is optimal.) If t_{MPI} is greater than t_{ret} but smaller than t_{DI} , parallel ISAT strategies have no advantages over serial ISAT if the cheap retrieves are dominant and there are no direct integrations in the simulation; however the performance (both for load balancing and wall clock time) of parallel ISAT strategies is better than serial ISAT if there is a significant fraction of direct integrations in the simulation.

For the simulation of the mixing layer with H_2 detailed mechanism, these three key time parameters are listed in the Table 1. As may be seen from the table, the message passing time per particle step is of the same order as the retrieve time (a little more expensive) and both the retrieve time and message passing time are two order of magnitude smaller than the direct integration time. Under these circumstances, for the above simulation (CASE1) where the cheap retrieve is dominant and there are no direct integrations, we observed that serial ISAT is optimal even though the load balancing is not good. For this simulation with simple H_2 chemistry, by using serial ISAT, a speed-up factor of about 300 is obtained for the combustion chemistry compared to using direct integration for the reaction fractional step. The performance of URAN-Quick and LOCLEV-Quick modes is similar to serial ISAT because about 99.5% of particle compositions can be retrieved by Quick Try. Even though the URAN mode achieves the best load balancing, the wall clock time for the combustion chemistry using the URAN mode is about twice the wall clock time using serial ISAT.

In order to study and compare the different ISAT strategies when there is a significant fraction of direct integrations, another simulation (denoted as CASE2) is carried out. In this simulation, all the settings are the same as CASE1 except that the assigned ISAT table storage is 20 Mbytes, the ISAT error tolerance is $\epsilon = 5 \times 10^{-6}$ and the simulation is performed for 4000 time steps. As may be seen from Fig. 6 a, there is a significant number of direct integrations (about 1% for some processors) in the simulation. Figure 6 b-f show the CPU time and wall clock time in combustion chemistry, and the CPU time in Quick Try for each processor for different ISAT strategies. As may be seen from the figure, all

Direct integration (t_{DI}) retrieve (t_{ret}) message passing (t_{MPI})		
$\sim 6000\mu s$	$\sim 15\mu s$	$\sim 20\mu s$

TABLE 1. Time (in microseconds per particle step) for DI, retrieve and message passing.

the parallel ISAT strategies have advantages over serial ISAT both for load balancing and wall clock time. For this particular case, the URAN-Quick is best (in that it gives the smallest wall clock time) whereas URAN gives the best load balancing. For the URAN-Quick and LOCLEV-Quick modes, even though about 98% percents of particle compositions are retrieved using Quick Try, the CPU time of Quick Try accounts for only about 30% of the total CPU time in the reaction fractional step. The effect of quick try depends on the different parallel ISAT strategy. For the case simulated, URAN-Quick gives smaller wall clock time than URAN whereas LOCLEV-Quick gives larger wall clock time than LOCLEV.

8. LES/FDF performance

Besides studying the different ISAT strategies for the combustion chemistry, the computational performance of the LES/FDF methodology in the mixing layer simulation is also analyzed. Figure 7 shows the CPU time and wall clock time in the LES part, in the particle part excluding reaction part and in the reaction fractional part for the simulation CASE1. As may be seen from the figure, the LES solver accounts for less than 25% of the wall clock time, and most time is spent in the particle part. Besides the load balancing issue for the combustion chemistry part, the load balancing of the particle part excluding reaction is also not good, and the first processor takes much more CPU time than other processors. This clearly is a topic for further investigation. Also observe that the LES wall clock time is several times the LES CPU time. The particle wall time excluding the reaction is greater than the wall time in the reaction fractional steps. Compared to the LES (without FDF), the relative cost of LES/FDF (without reaction) is about 2.8, and the relative cost of LES/FDF/ISAT is about 4.3.

9. Conclusion

The LES/FDF/ISAT capability for the numerical simulations of turbulent combustion with realistic chemistry is developed by incorporating ISAT into the Stanford structured LES code with a Lagrangian Monte Carlo implementation of the composition FDF method. The numerical simulation of a two-dimensional spatially-developing mixing layer with a 9-species detailed hydrogen mechanism is performed to examine computational issues arising in the LES/FDF/ISAT methodology. It is shown that there is good consistency between the filtered mixture fractions obtained both from the FDF and LES solvers.

Both the serial ISAT and two different parallel ISAT strategies are studied and compared. For the mixing layer with the simple H_2 chemistry, when the cheap retrieves are dominant and there are no direct integrations in the simulation (such as CASE1), se-

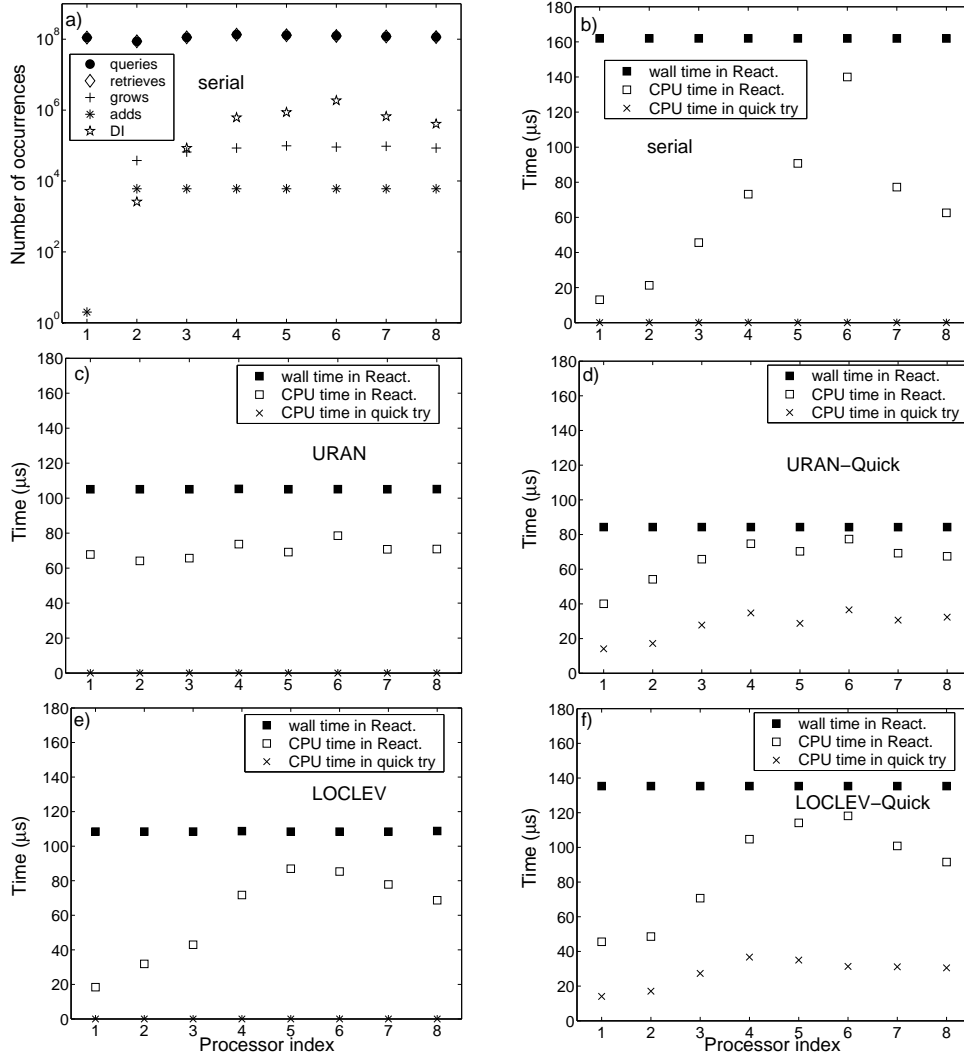


FIGURE 6. (a) Number of occurrences for different events in ISAT (serial) for each processor. (b)-(f) The CPU time and wall clock time in reaction fractional step, and the CPU time in the quick try (in microseconds per particle step) for each processor of CASE2.

rial ISAT gives a smallest wall clock time for the combustion chemistry and therefore is optimal, even though the parallel ISAT strategies may achieve better load balancing. For the simulation CASE1 with serial ISAT, a speed-up factor of about 300 is obtained for the combustion chemistry compared to using direct integration for the reaction fractional step. When there is a significant fraction of direct integrations in the simulation (such as CASE2), all the parallel ISAT strategies have advantages over serial ISAT both for load balancing and in terms of wall clock time. The effect of quick try depends on the different parallel ISAT strategy. For the simulation CASE2, URAN-Quick gives a smaller wall clock time than URAN whereas LOCLEV-Quick gives a larger wall clock time than LOCLEV. For the simulation CASE2, the URAN-Quick is optimal (in that it

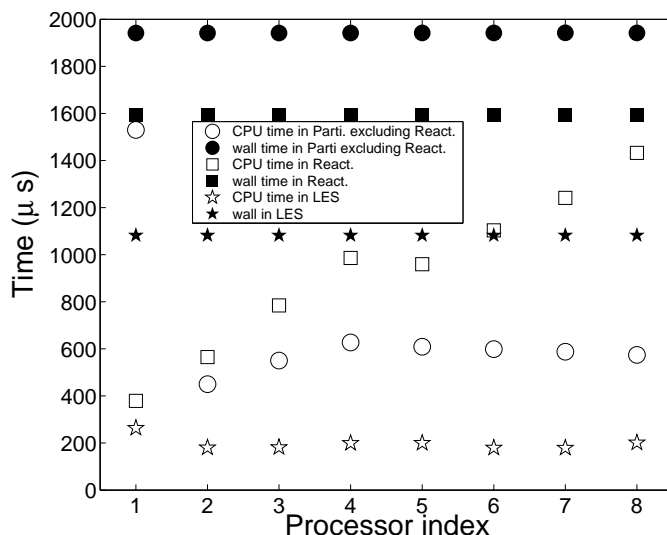


FIGURE 7. The CPU time and wall clock time in the LES solver, in the Monte Carlo particle part (excluding the reaction fractional step) and in the reaction fractional step (in microseconds per cell per time step) of CASE1.

gives the smallest wall clock time) whereas URAN gives the best load balancing. For the simulation CASE1, compared to the LES (without FDF), the relative cost of LES/FDF (without reaction) is about 2.8, and the relative cost of LES/FDF/ISAT is about 4.3.

In the future work, for the LES/FDF, the coupling (such as density) between the LES and FDF should be implemented and more quantitative testing of accuracy and efficiency would be performed. For the ISAT, the quantitative study of the performance of different strategies for different chemical mechanism and in different circumstance would be performed.

Acknowledgements

Part of this research was conducted using the resources of the Cornell Theory Center, which receives funding from Cornell University, New York State, federal agencies, foundations, and corporate partners. This work is supported in part by the Air Force Office of Scientific Research under Grant No. F-49620-00-1-0171.

REFERENCES

- CABRA, R., MYRVOLD, T., CHEN, J. Y., DIBBLE, R. W., KARPETIS, A. N. & BARLOW, R. S. 2002 Simultaneous laser Raman-Rayleigh-Lif measurements and numerical modeling results of a lifted turbulent H-2/N-2 jet flame in a vitiated coflow. *Proc. Combust. Inst.* **29**, 1881-1888
- CHA, C. M. & TROUILLET, P. 2003 A subgrid-scale mixing model for large-eddy simulations of turbulent reacting flows using the filtered density function. *Phys. Fluids* **15**, 1496-1504.
- COLUCCI, P. J., JABERI, F. A., GIVI, P. & POPE, S. B. 1998 Filtered density function for large eddy simulation of turbulent reacting flows. *Phys. Fluids* **10**, 499-515.

- DOPAZO, C. & O'BRIEN, E. E. 1974 Approach to autoignition of a turbulent mixture. *Acta Astronaut.* **1**, 1239-1266.
- GAO, F. & O'BRIEN, E. E. 1993 A large-eddy simulation scheme for turbulent reacting flows. *Phys. Fluids A* **5**, 1282-1284.
- GIVI, P. 2003 Subgrid scale modeling in turbulent combustion: A review. *AIAA Paper*, 2003-5081.
- JABERI, F. A., COLUCCI, P.J., JAMES, S., GIVI, P. & POPE, S. B. 1999 Filtered mass density function for large eddy simulation of turbulent reacting flows. *J. Fluid Mech.* **401**, 85-121.
- JAMES, S. & JABERI, F. A. 2000 Large scale simulations of two-dimensional nonpremixed methane jet flames. *Combust. Flame* **123**, 465-487.
- LI, J., ZHAO, Z., KAZAKOV, A. & DRYER, F. L. 2003 An updated comprehensive kinetic model for H_2 combustion. *Fall Technical Meeting of the Eastern States Section of the Combustion Institute, Penn State University, University Park, PA, October 26-29, 2003*.
- MOIN, P., SQUIRES, K., CABOT, W. & LEE, S. 1991 A dynamic subgrid-scale model for compressible turbulence and scalar transport. *Physics of Fluids A* **3**, 2746-2757.
- PIERCE, C. D. 2001 Progress-variable approach for large-eddy simulation of turbulent combustion. PhD thesis, Stanford University.
- PIERCE, C. D. & MOIN, P. 2004 Progress-variable approach for large-eddy simulation of non-premixed turbulent combustion. *J. Fluid Mech.* **504**, 73-97.
- POPE, S. B. 1985 PDF methods for turbulent reactive flows. *Prog. Energy Combust. Sci.* **11**, 119-192.
- POPE, S. B. 1990 Computations of turbulent combustion: Progress and challenges. *Proc. Combust. Inst.* **23**, 591-612.
- POPE, S. B. 1997 Computationally efficient implementation of combustion chemistry using *in situ* adaptive tabulation. *Combust. Theo. Modelling* **1**, 41-63.
- POPE, S. B. & LANTZ, S. R. 2004 *x2f-mpi* Software for the efficient load distribution of function evaluations in a multi-processor MPI environment. (in preparation)
- RAMAN, V., PITSCH, H. & FOX, R. O. 2003a Quadrature moments method for the simulation of turbulent reactive flows. in: *CTR Annual Research Briefs, Center For Turbulence Research*, 261-275.
- RAMAN, V., FOX, R. O., HARVEY, A. D. & WEST, D. H. 2003b Effect of feed-stream configuration on gas-phase chlorination reactor performance. *Industrial and Engineering Chemistry Research*, **42**, 2544-2557.
- RAMAN, V., PITSCH, H. & FOX, R. O. 2004a LES-transported FDF simulations of a bluff-body stabilized flame. *TNF7 Workshop Proceedings*, 56-57.
- RAMAN, V., PITSCH, H. & FOX, R. O. 2004b Hybrid large-eddy simulation/lagrangian filtered density function approach for simulating turbulent combustion. (submitted)
- SHEIKHI, M. R. H., DROZDA, T. G., GIVI, P., JABERI, F.A. & POPE, S. B. 2004 Large eddy simulation of a turbulent nonpremixed piloted methane jet flame (Sandia flame D). *Proc. Combust. Inst.* **30**, in press.
- VILLERMAUX, J. & DEVILLON, J. C. 1972 in: *Proc. 2nd Int. Symp. on Chemical Reaction Engineering*. Elsevier, New York.
- ZHOU, X. Y. & PEREIRA, J. C. F. 2000 Large eddy simulation (2D) of a reacting plane mixing layer using filtered density function. *Flow, Turbulence and Combustion* **64**, 279-300.

A constructed PDF model for fast CFD with realistic chemistry

By G. M. Goldin [†] AND V. Raman

CFD predictions using a new model to include finite-rate chemistry effects in turbulent flames are presented. The Constructed PDF model assumes that the scalar PDF in a general, complex geometry reacting flow is similar to the scalar PDF in a simple geometry reacting flow. Detailed chemistry simulations are performed in a model of the simple flow over all realizable conditions. The scalar PDF at discrete points in the realizable space is parameterized by a small set of its lower moments, and tabulated. Modeled transport equations for these lower moments are computed in the CFD solver and the PDF table is interpolated for unclosed terms. *A priori* calculation and tabulation of the chemistry and its interaction with the turbulence allow rapid, multi-physics CFD simulations on large meshes. The model is applied to the RANS prediction of turbulent, partially-premixed, piloted jet flames (Sandia flames D and F). Excellent agreement with the experimental data is obtained for temperature, major species and the fast chemistry radical *OH*. Good agreement is obtained for *CO* and the slow chemistry species *NO*.

1. Introduction

Turbulent combustion models that incorporate arbitrary, detailed chemical kinetics in multi-dimensional CFD include the Transported PDF Model (Pope 1985), the Conditional Moment Closure (Klimenko & Bilger 1999) and the Steady and Unsteady Laminar Flamelet Models (Peters 2000). Owing to the tremendous computational cost of solving detailed chemical kinetics in complex three-dimensional geometries, combustion models that tabulate the chemistry and its interaction with the turbulence *a priori* remain prevalent in industry. The most common chemistry tabulation approach is the Steady Laminar Flamelet Model (SLFM) where a stationary flame is computed in a laminar flow configuration and mapped to a reduced variable space, usually mixture fraction and scalar dissipation rate or reaction progress variable. To account for turbulent fluctuations, a shape for the Probability Density Function (PDF) of these reduced variables is assumed, which is invariably a product of Delta functions (specified by first moments), and Beta or Gaussian functions (specified by first and second moments). The flamelet state relationships are convoluted with the assumed PDFs and tabulated as a function of the lower moments. Transport equations for these lower moments are solved in the CFD code, and the table interpolated to retrieve the required thermo-chemistry, such as mean density and mean temperature.

There are two limitations to the SLFM. The first is that the chemistry may be insufficiently represented by the reduced variables. For example, in the case of scalar dissipation rate as a flamelet reduced variable, the chemistry is assumed to respond instantaneously to the strain. This is a poor assumption for slow kinetics such as pollutant formation, which are predicted to be near equilibrium at the combustor outlet where the strain rate

[†] Fluent Inc., Lebanon NH 03766, USA

is small. The second limitation is that it is difficult to prescribe the joint PDF of the reduced variables, especially for those that are not conserved, and statistical independence of variables is invariably assumed.

The objective of this work is to apply the Constructed PDF Model (Goldin & Menon 1997; Goldin & Menon 1998; Goldin 2004) to an *a posteriori* CFD prediction of an experimental flame with comprehensive measurements, and to investigate its accuracy and performance. The Constructed PDF Model assumes that the thermo-chemical PDF in a turbulent reacting flow of arbitrary geometry is similar to the thermo-chemical PDF in a turbulent reacting flow of simple geometry. Reduced models for scalar evolution in simple geometric configurations are available, allowing affordable simulations with detailed chemistry over the entire range of realizable conditions. A suitable set of lower moments are selected to parameterize the PDF, and all required lower moments (such as mean density, mean temperature and if necessary mean reaction rate) are tabulated as a function of these lower moments. As in the SLFM, transport equations for the parameterizing lower moments are solved in the CFD code and all required PDF quantities are interpolated from the table. The Constructed PDF Model is directly comparable with the SLFM because they both pre-compute the turbulence-chemistry interaction and have similar storage and computational costs in the CFD solver. However, the Constructed PDF Model avoids the SLFM assumptions of state relationships and assumed PDF shapes.

2. The Constructed PDF Model

In this work, the joint PDF of species and temperature is constructed from scalar mixing and reaction in the simple geometry of isotropic, homogenous, stationary turbulence. Three dimensional Direct Numerical Simulations (DNS) with full chemistry at high Reynolds numbers is computationally impossible at present, so the Linear Eddy Model (LEM) (Kerstein 1988, Kerstein 1992) is employed to make the computations tractable. The LEM is an excellent approximation of scalar evolution in simple geometries, and accurate statistics of the scalar PDF in homogenous turbulence have been demonstrated (McMurtry *et al.* 1993).

The central assumption of the LEM is that since reaction occurs at the molecular level after species mix, it is critical to resolve the smallest turbulent length scales, which contribute substantially to mixing. Hence, mixing models, such as gradient-diffusion or coalescence-dispersion, are not invoked. To make such DNS affordable, the spatial dimension is reduced from 3D to 1D. Along a 1D line, molecular diffusion and chemical reaction are resolved without approximation, but turbulent convection by 3D eddies must be modeled. This stirring is modeled by random re-arrangements of the scalar elements along the LEM line, where each mapping imitates the effect of a turbulent eddy on the scalar field. The turbulence is hence specified in the LEM by two parameters, namely integral length scale L and Reynolds number Re_t (or equivalently the Kolmogorov length scale $\eta = L/Re_t^{3/4}$). Since the LEM is a Monte-Carlo simulation, statistics must be averaged over a number of realizations.

The LEM scalar field is smoothed by the continuous action of molecular diffusion and sharpened by irregular turbulent stirring events. For large L and small Re_t , the Kolmogorov scale is large and the flame chemistry is near equilibrium[†]. As Re_t increases,

[†] Slowly forming chemical species such as *NO* may be far from chemical equilibrium even at low Re_t .

smaller eddies appear and occur with increased frequency. They cause fine-scale gradients in the scalar field, increasing the rate of molecular diffusion and the degree of chemical non-equilibrium. At moderate Re_t local extinction occurs, and at high Re_t all flame structures in the LEM field blow-out. Although the LEM model has two turbulence inputs (viz. L and Re_t), the scalar PDF is not independent of these two parameters, and similar PDFs are obtained for different L and Re_t combinations (Goldin & Menon 1997). To illustrate this, note that the LEM domain length is equal to L , and the boundary conditions are periodic. Hence, a domain of size $2L$ with a larger Re_t so that both simulations have identical Kolomogorov length scales η will have identical PDFs.

With a specified mechanism and molecular transport properties, the two LEM inputs are the initial scalar field and the LEM turbulence parameters L and Re_t . By varying these two parameters over their realizable ranges, the joint PDF of species and temperature is tabulated as a function of a (small) set of its lower moments.

3. Constructing the PDF Table

The Constructed PDF Model is applied here to non-premixed combustion. Accordingly, the initial scalar field is a slab of fuel adjacent to a slab of oxidizer. A conserved mixture fraction can be defined from the LEM species field, and its Favre mean remains constant during the scalar field development. The mixture fraction variance decays monotonically from a maximum at the start of the simulation, toward zero. In this work, the scalar PDF is parameterized by these first two moments of the mixture fraction. An additional moment is required to parameterize the turbulence: simulations at low turbulence where the chemistry is near equilibrium will take longer to dissipate than high turbulence simulations, but will still pass through the same mixture fraction variance. Here, the mean scalar dissipation rate is used as a third parameter†.

We apply the Constructed PDF Model to CFD predictions of the Sandia piloted jet flames labeled D and F. A well-validated, 19 species chemical mechanism for methane-air combustion is used (Sung *et al.* 2001) which is a CARM reduction from the GRI-Mech 2.11 detailed mechanism. ISAT (Pope 2001) is utilized to accelerate the chemistry calculations and radiative heat loss by an optically thin model is included (Barlow *et al.* 2001). Constant molecular transport properties are assumed, with a Schmidt number of 0.7 and a unity Lewis number. Since the initial condition is cold fuel next to cold oxidizer, ignition is necessary to initiate combustion. Ignition is modeled by equilibrating mixed-but-unburnt elements at early stages in the simulation. Note that the PDF at later times is relatively insensitive to this artifact (Goldin 2004).

The mean mixture fraction uniquely defines the initial scalar field and 16 points are used in mean mixture fraction space. At each mean mixture fraction, we fix L at $0.1m$ and run the LEM at 5 Re_t values of 100, 500, 1000, 1500 and 2000. The mixture fraction variance decays from its maximum to zero in every LEM simulation, and the PDF is tabulated at 24 intermediate variance points. All LEM simulations are ensemble averaged over 100 realizations to remove statistical errors. Approximately 1000 CPU hours are required to build this table.

RANS simulations of flames D and F are performed using this constructed PDF table. For isobaric combustion, the thermo-chemistry couples to the flow through the mean density which is obtained from the table by tri-linear interpolation. The $k-\epsilon$ turbulence

† Mean residence time and mean reaction progress were tested in place of mean scalar dissipation rate and found to be less accurate.

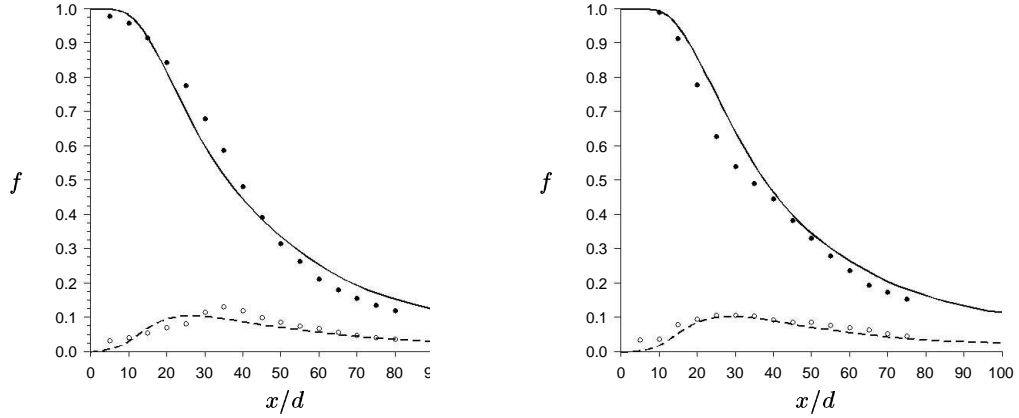


FIGURE 1. Axial plot of mean and RMS mixture fraction (f) for flame D (left) and flame F (right). Solid line is the predicted mean, solid circles are experimental mean, dashed line is the predicted RMS, open circles are experimental RMS

model is used with standard constants except for $c_{\epsilon 1}$, which is increased to 1.56 so that the correct jet spreading is obtained. Standard equations for mean and variance of mixture fraction are solved (Peters 2000), with the turbulent Schmidt number set to 1, and the standard model for the mean scalar dissipation rate is used, with $c_{\phi} = 2$. All RANS simulations are performed on an axi-symmetric mesh and take minutes to converge on a laptop computer.

4. Results

Axial plots of mean and RMS mixture fraction, temperature and OH , CO and NO mass fractions are presented in Figures 1 through 5. Plots on the left correspond to flame D and plots on the right to flame F. The predicted mean and RMS of mixture fraction in Figure 1 show reasonable agreement with the data. Since the mixture fraction is a conserved scalar, this difference is attributed, mostly, to deficiencies in the RANS turbulence model. Mean temperature prediction in Figure 2 show very good agreement for flame D, and moderate agreement for flame F. The Flame F experiment is near global blow-off and exhibits significant local extinction at all measured axial stations, which is difficult to predict. While the LEM is capable of predicting local extinction, parameterizing this by the single variable of mean scalar dissipation rate has limitations. The major species CH_4 , O_2 , CO_2 and H_2O show similar agreement as temperature and are excluded here.

Excellent agreement for mean and variance of OH mass fraction is displayed in Figure 3. In particular, the super-equilibrium increase of OH as the strain is increased from flame D (left) to flame F (right) is captured.

CO mass fraction in Figure 4 is reasonably well computed, but is over-predicted in the rich zones before the flame stoichiometric point at approximately $x/d = 45$. H_2 mass fraction displays similar behaviour as CO , hence plots of H_2 are not included here. In order to better understand the rich-side over-prediction of CO in Figure 4 conditional averages of CO are presented in Figure 5 for axial stations $x/d = 30$ and $x/d = 45$ in flame

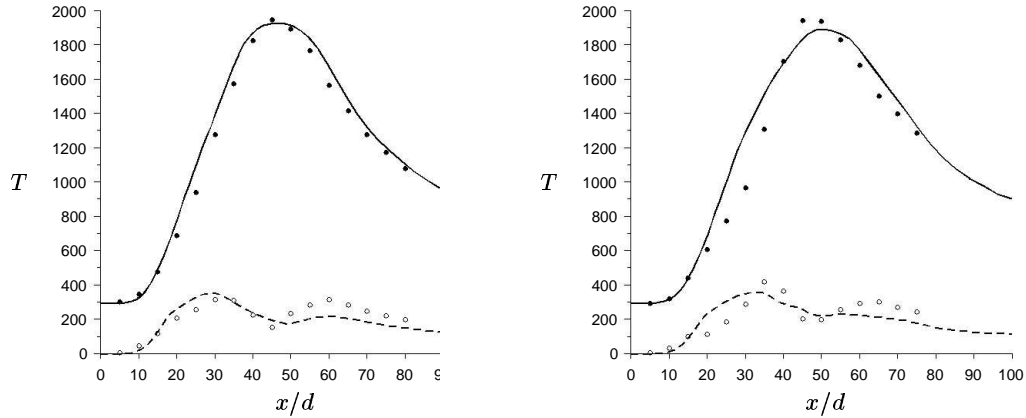


FIGURE 2. Axial plot of mean and RMS temperature (in degrees Kelvin) for flame D (left) and flame F (right). Symbols as in Figure 1.

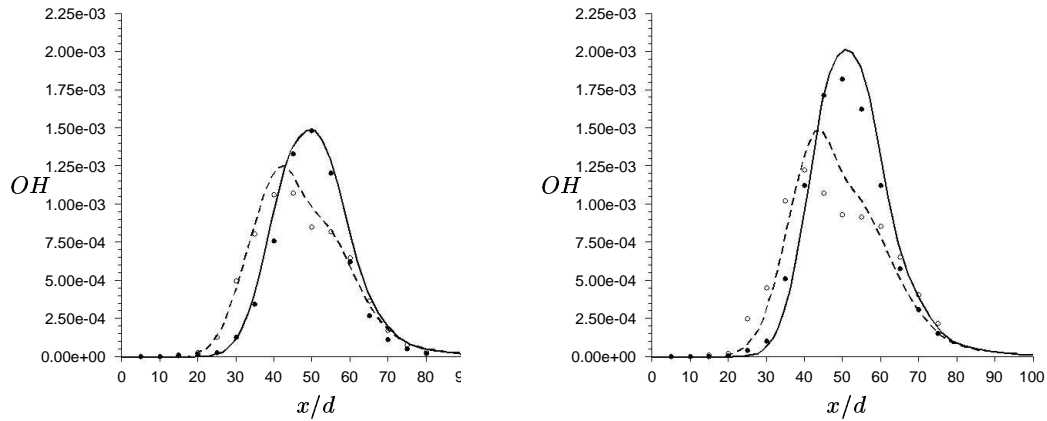


FIGURE 3. Axial plot of mean and RMS OH mass fraction for flame D (left) and flame F (right). Symbols as in Figure 1.

D. Both plots show a slight CO over-prediction in lean mixtures, and substantial CO over-prediction in rich mixtures. The CO over-prediction could be due to contributions from the ignition model, which equilibrates a few points in the LEM field at the start of the simulation, causing initially high CO and H_2 . This artifact is more pronounced at earlier simulation times in the LEM simulation, corresponding to near-nozzle locations in the CFD simulation where the variance is large.

The NO mass fraction in Figure 6 is over-predicted at lean axial down-stream locations. This over-prediction could have contributions from assumptions in the Constructed PDF model, as well as limitations in the original chemical mechanism and its reduction, and limitations in the thin-body radiation model. Figure 7 plots average NO conditional on mixture fraction at axial planes $x/d = 45$ (left) and $x/d = 60$ (right). From the $x/d = 60$ graph it is apparent that the NO over-prediction is confined around the stoichiometric

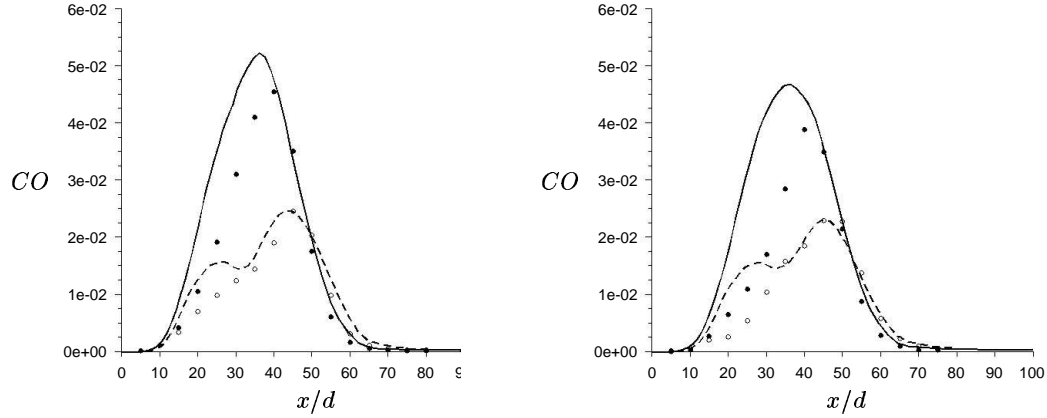


FIGURE 4. Axial plot of mean and RMS CO mass fraction for flame D (left) and flame F (right). Symbols as in Figure 1.

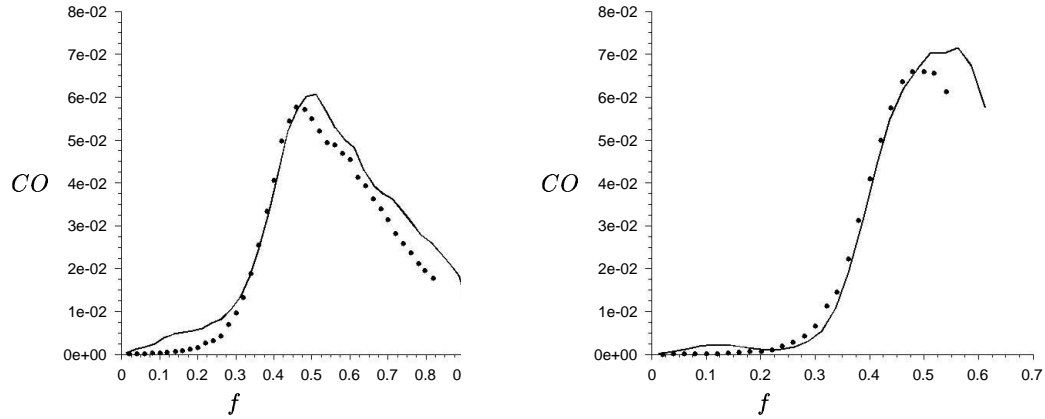


FIGURE 5. Average CO , conditioned on mixture fraction, versus mixture fraction (f) at axial locations $x/d = 30$ (left) and $x/d = 45$ (right), for flame D. Symbols as in Figure 1.

mixture fraction of 0.35. In contrast to the Constructed PDF model, the SLFM predicts NO mass fractions an order of magnitude greater than the measurements, as presented in Figure 8. The error in the SLFM prediction of slow chemical species such as NO is due to disparities in the residence time of the flamelet simulation and the CFD simulation. The flamelet residence time, which is determined by the flamelet strain, will generally not correspond to the residence time in the CFD simulation. In contrast, implicit in the lower moments of the Constructed PDF model (in this case variance of mixture fraction and mean scalar dissipation rate) is a residence time, and a history of entrainment of fuel and oxidizer into reaction zones where NO is accumulated. That is, a given mean mixture fraction, mixture fraction variance and mean scalar dissipation rate correspond to a unique residence time in the non-premixed LEM simulation.

An interesting feature of the Constructed PDF model is the ability to capture local

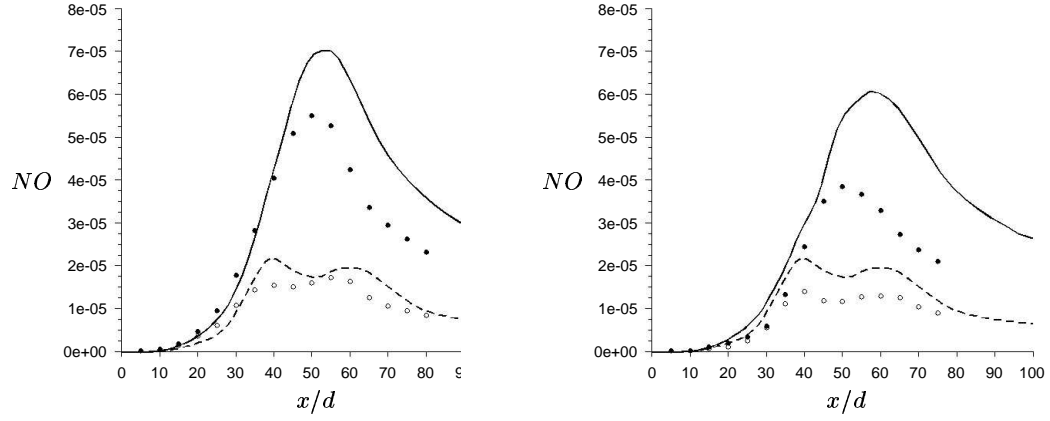


FIGURE 6. Axial plot of mean and RMS NO mass fraction for flame D (left) and flame F (right). Symbols as in Figure 1.

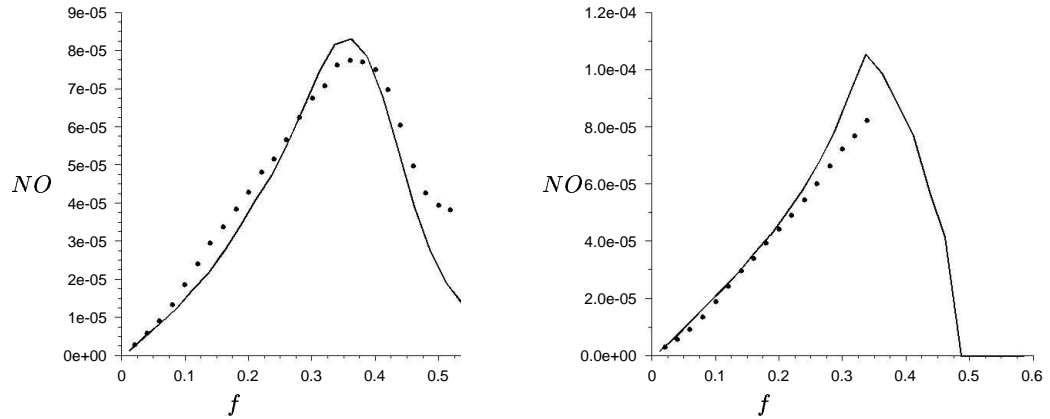


FIGURE 7. Average NO , conditioned on mixture fraction, versus mixture fraction (f) at axial locations $x/d = 45$ (left) and $x/d = 60$ (right), for flame D. Symbols as in Figure 1.

extinction. This is illustrated in Figure 9 which shows scatter plots of temperature in flame F at $x/d = 30$ for the predictions (left) and the experiment (right). The predicted temperatures are obtained from random points in the LEM field, and correspond to the random laser shots of the experiment. Locally extinguished fluid elements are those near the stoichiometric mixture fraction with temperatures well below the equilibrium line. The extent of local extinction is over-predicted in both lean and rich mixtures, which may be due, in part, to the simplified molecular transport assumptions ($Le = 1$). A more accurate modeling of molecular diffusion in the LEM may improve these predictions of local extinction.

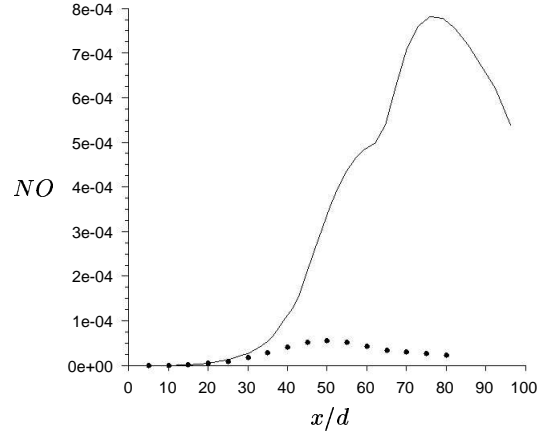


FIGURE 8. Axial plot of mean NO mass fraction for flame D using the Steady Laminar Flamelet Model (SLFM). Symbols as in Figure 1.

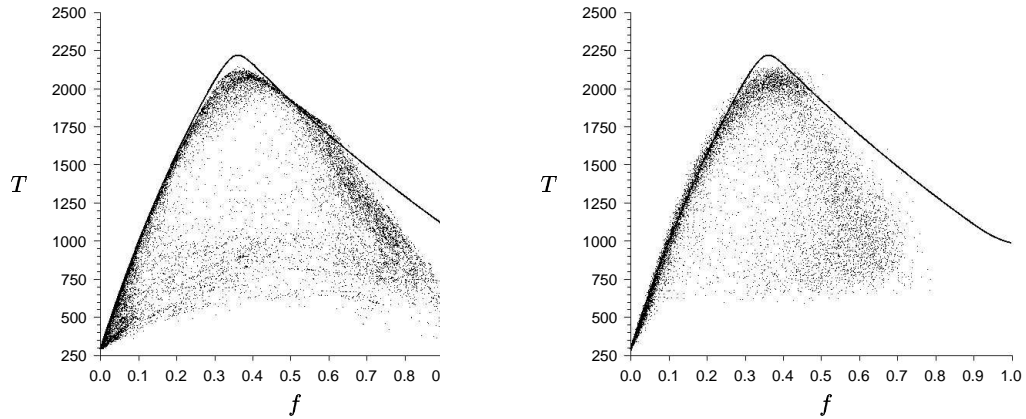


FIGURE 9. Scatter plots of temperature (in degrees Kelvin) versus mixture fraction (f) at $x/d = 30$ for flame F. Predictions (left) and experiment (right) are dots, equilibrium temperature is solid line.

5. Summary and Conclusion

- The Constructed PDF model approximates the joint PDF of species and temperature in an arbitrary geometry reacting flow by the joint PDF of species and temperature calculated in a simple geometry reacting flow.
- Simple geometry simulations are performed over the realizable range of initial conditions, and the thermo-chemical PDF is tabulated as a function of a suitable set of lower moments.
- Once the table is constructed, the PDF is interpolated in a CFD simulation for required lower moments, such as mean and RMS of density, temperature and species mass fractions.

- The Constructed PDF model is similar in this respect to the Steady Laminar Flamelet Model (SLFM) where the turbulence-chemistry interaction is computed *a priori* and tabulated. However, the Constructed PDF model does not assume PDF shapes or chemical state relationships.
- Pre-computing and tabulating the turbulence-chemistry interaction provides very large reductions in the CFD convergence time.
- Scalar decay in homogeneous turbulence is used as the simple geometry, which is modeled with the The Linear Eddy Model (LEM).
- The Constructed PDF model is applied to the prediction of partially-premixed turbulent jet flames, commonly known as Sandia flames D and F.
- A 19 species ARM chemical mechanism (derived from the GRI-Mech 2.11 detailed mechanism) is employed, and ISAT is used to accelerate the chemistry calculations.
- Three lower moments are used to parameterize the PDF, namely mean mixture fraction, mixture fraction variance, and mean scalar dissipation rate.
- Accurate RANS predictions for means and RMS of temperature, major species and *OH* are obtained. *CO* and *NO* predictions agree reasonably well with the measured data, although *CO* is over-predicted in rich regions and *NO* is over-predicted in lean regions.
- Local extinction and re-ignition is captured in the model.

6. Acknowledgements

The first author extends thanks to Dr. Alan Kerstein from Sandia National Labs for several fruitful discussions, and to Drs. Dipankar Choudhury and Nelson Carter from Fluent Inc. for allowing time off to attend the CTR 2004 Summer Program.

REFERENCES

- BARLOW, R. S., KARPETIS, A. N., FRANK, J. H. AND CHEN, J. Y. 2001 Scalar Profiles and NO Formation in Laminar Opposed-Flow Partially Premixed Methane/Air Flames. *Comb. and Flame*, **127**, 2102.
- KERSTEIN, A. R. 1988 Linear Eddy Model of Turbulent Scalar Transport and Mixing. *Comb. Science and Tech*, **60**, 361.
- KERSTEIN, A. R. 1992 Linear Eddy Model of Turbulent Scalar Transport. Part 7. Finite Rate Chemistry and Multi-stream Mixing. *J. Fluid Mech.* **240**, 361.
- KLIMENKO, A. Y. AND BILGER, R. W. 1999 Conditional Moment Closure for Turbulent Combustion. *Prog. Energy Combust. Sci.* **25**, 595.
- PETERS, N. 2000 *Turbulent Combustion*. Cambridge University Press.
- GOLDIN, G. M. AND MENON, S. 1997 A Scalar PDF Combustion Model for Turbulent Non-Premixed Combustion. *Comb. Science and Tech*, **125**, 47.
- GOLDIN, G. M. AND MENON, S. 1998 A Comparison of Scalar PDF Turbulent Combustion Models. *Comb. and Flame*, **113**, 442.
- GOLDIN, G. M. 2004 A priori Investigation of the Constructed PDF Model *Proc. 30th Symp. Comb.*. In Press.
- McMURTRY, P. A., GANSAUGE, T. C., KERSTEIN, A.R. AND KRUEGER, S.K. 1993 Linear Eddy Model Simulations of Mixing in Homogeneous Turbulent Flow. *Physics Fluids A* **5**, 1023.
- PETERS, N. 1984 Laminar Diffusion Flamelet Models in Non Premixed Combustion. *Prog. Energy Combust. Sci.* **110**, 319.

- POPE, S. B. 1985 PDF Methods in Turbulent Reactive Flows. *Prog. Energy Combust. Sci.* **11**, 119.
- POPE, S. B. 2001 Computationally Efficient Implementation of Combustion Chemistry using In Situ Adaptive Tabulation. *Comb. Th. Model.* **1**, 41.
- SUNG, C. J., LAW, C. K. AND CHEN, J. Y. 2001 Augmented Reduced Mechanisms for NO Emission in Methane Oxidation *Comb. and Flame*, **125**, 906.

Liquid film modeling in high shear nozzles

By W.-W. Kim [†], S. Apte, M. Herrmann AND F. Ham

As part of the ongoing development of predictive simulation capabilities for jet engine combustors, two approaches for modeling liquid film formation and evolution in the context of high shear nozzles are investigated. In the first approach, the dense spray region and liquid film formation is modeled by closely packed droplets moving in layers. It is shown that the displacement of gas-phase by droplet finite-size effects can capture the spreading of the liquid film on the injector walls. Collision dominates in the near wall region and is captured using an inter-particle stress model. In the second approach, a transport equation for film-height based on the lubrication theory is solved near the wall. The droplets are represented by the dense spray model until they hit the wall. After impingement, the Lagrangian droplet/parcel is removed and its mass and momentum are transferred to evolve the film-height. We perform a preliminary assessment of these models for two configurations: a liquid jet impinging vertically on a flat plate and a simplified injector consisting of a turbulent channel flow with spray impinging onto one of the channel walls.

1. Introduction

1.1. Problem Description

Modern aero-engine gas turbine combustors employ high shear nozzles to atomize liquid fuel as it enters the combustion chamber. Figure 1 shows a schematic of a high shear nozzle, and illustrates the processes that lead to the final distribution of fuel droplets in the downstream combustion chamber. Fuel is introduced through a small number of radial jets near the center of the nozzle. Instabilities created by the interaction of high shear rates with the liquid column lead to an almost immediate stripping of small droplets from the surface of the jet as it penetrates into the swirling crossflow. The core column remains largely intact, however, and undergoes breakup later at a characteristic length scale L_B (figure 2).

For certain nozzle designs, the breakup length scale L_B can be longer or significantly longer than the nozzle dimensions, and the liquid column impinges on an inner nozzle wall, forming a liquid film. This film interacts with the turbulent boundary layer, eventually leaving the front of the nozzle where it undergoes breakup as it interacts with an additional swirling airflow (figure 3).

1.2. Simulation Challenges

Prediction of droplet size-distributions and size-velocity correlations produced by high shear nozzles plays a crucial role in accurately modeling the dynamics of spray flames, pollutant formation and emissions. While the various physical processes described in the previous subsection are reasonably well understood, the direct numerical simulation of the atomization process remains excessively costly because most of the breakup occurs at

[†] Pratt & Whitney

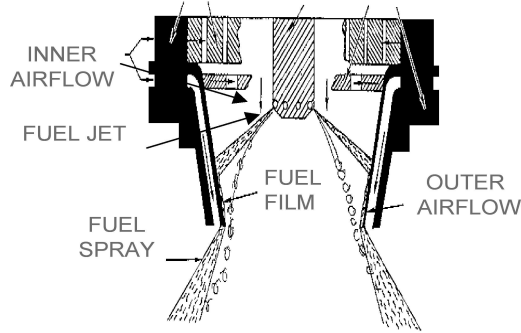


FIGURE 1. Schematic of a high shear nozzle illustrating the liquid fuel breakup and atomization process.

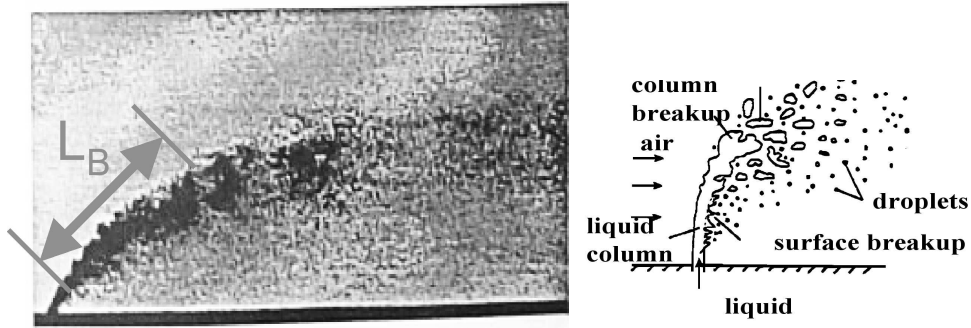


FIGURE 2. Experimental results and schematic illustrating liquid jet breakup process.

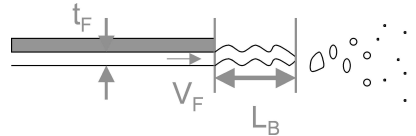


FIGURE 3. Characteristic scales associated with the film breakup process.

length and time scales significantly smaller than those that can be resolved on reasonable computational grids. Consequently subgrid modeling must be used.

In the present investigation, we investigate models for just the liquid film formation and evolution component of the breakup process. While this may seem excessively restrictive, it is expected that a film model can readily be integrated with the existing stochastic breakup models in the LES code CDP (Mahesh *et al.* 2004; CITS report 2004), and used to provide an initial condition (velocity, length scale, and azimuthal distribution) for the Lagrangian point particles/parcels that presently model the disperse liquid phase in the combustion chamber (Apte *et al.* 2003c; Apte *et al.* 2003a).

2. Modeling Approaches and Results

2.1. Approach 1: Dense Spray Model

In this model, the liquid phase is solved in the Lagrangian framework and the carrier or fluid phase in the Eulerian framework. The liquid film is represented by a layer of droplets

flowing together. The important differences between this model and the standard point-particle approach employed for two-phase flows (Apte *et al.* 2003c) are: 1) the inter-particle distances are small and liquid flow is collision dominated, 2) the local liquid-phase volume fraction is large and the standard drag-laws need modification, 3) the carrier fluid is treated as a mixture of liquid and gaseous phases and the continuity and momentum equations as well as properties such as viscosity are modified by the volume fraction. This formulation for dense sprays was first derived by Dukowicz (1980) and also proposed by Joseph & Lundgren (1990) for dense particulate flows. The details of this formulation and its implementation on unstructured grids to simulate dense particulate flows is discussed by Apte *et al.* 2003b. We apply this model to simulate liquid film formation and dense spray regimes in gas-turbine combustors. In addition, this model will be used in the second approach described later to track droplets till they hit a wall and form a liquid film.

In the present work, we focus on the first two parts of the model: viz., inter-droplet collisions and modifications to drag forces experienced by droplets. First we neglect the important effect of fluid displacement due to the presence of droplets, however, prevent overlapping of droplet centroids through the collision model. The effect of dense liquid phase is then indirectly captured through two-way coupling between the two phases. Note that in standard point-particle approach where collisions are neglected, the droplets could overlap and may not be able to sustain a layer of droplets flowing together.

The liquid volume fraction Θ_p is defined as,

$$\Theta_p(\mathbf{x}) = \sum_{k=1}^{N_p} V_k \mathcal{G}_\sigma(\mathbf{x} - \mathbf{x}_{\mathbf{p}_k}) \quad (2.1)$$

where the summation is over all particles N_p . Here $\mathbf{x}_{\mathbf{p}_k}$ is the particle location, \mathbf{x} centroid of a control volume, and V_k the volume of a particle. The function \mathcal{G}_σ is the interpolation operator given as

$$\mathcal{G}_\sigma(\mathbf{x}_p) = \frac{1}{(\sigma\sqrt{2\pi})^3} \exp\left[\frac{-(x-x_p)^2 + (y-y_p)^2 + (z-z_p)^2}{2\sigma^2}\right] \quad (2.2)$$

The resulting Θ_p will be smooth and mass-conserving provided \mathcal{G}_σ is smooth. A Gaussian interpolation function with filter-width (σ) proportional to grid size and satisfying $\int_V \mathcal{G}_\sigma(\mathbf{x} - \mathbf{x}_{\mathbf{p}_k}) dV = 1$ is used.

The liquid phase equations for individual droplets in Lagrangian framework are,

$$\frac{d}{dt}(\mathbf{x}_p) = \mathbf{u}_p \quad (2.3)$$

$$m_p \frac{d}{dt}(\mathbf{u}_p) = F_p = m_p \mathbf{a}_p \quad (2.4)$$

The total force on a particle consists of the standard hydrodynamic drag force, dynamic pressure gradient, gradient of viscous stress in the fluid phase, a generalized buoyancy force, and inter-particle collision. For the present spray application, the density ratio ρ_p/ρ_f is large ($\approx 10^3$), and we neglect the pressure gradient, viscous stress and buoyancy forces, the total acceleration of the particle \mathbf{a}_p is given as

$$\mathbf{a}_p = \frac{(\mathbf{u}_g - \mathbf{u}_p)}{\tau_r} + \mathbf{a}_{coll} + \left(1 - \frac{\rho_f}{\rho_p}\right) \mathbf{g} \quad (2.5)$$

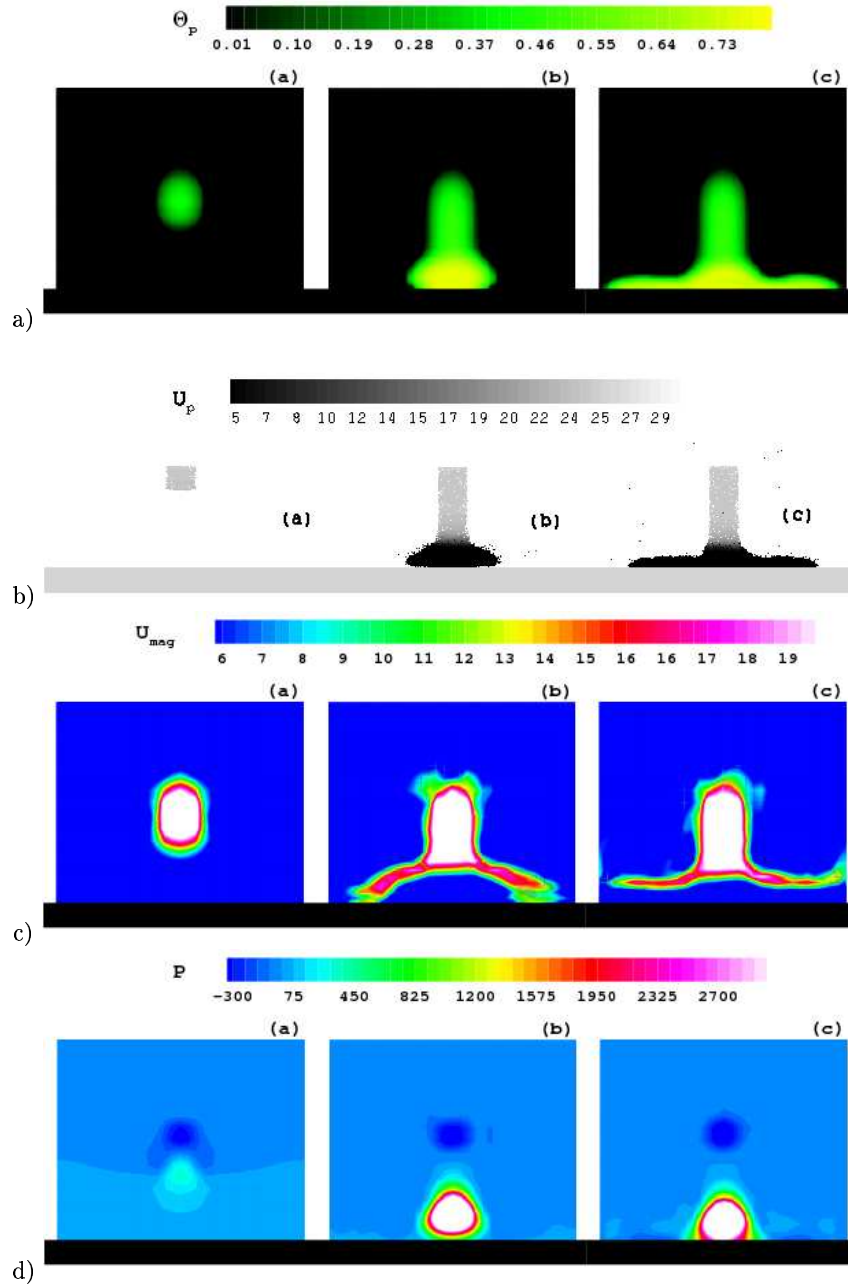


FIGURE 4. Temporal evolution of film formation in direct impact of liquid spray onto a flat plate. Liquid spray is represented by discrete particles of same density. Particles initially clustered at the top move vertically down, impact the flat plate and build up. Particle build up opposes incoming particles, creates a stagnation point, develops a strong gas-phase velocity field through two-way coupling and spreads the film. The present computation includes only the collision model keeping the particle centroids from overlapping each other. (a): Particle volume fraction, (b): particle positions color coded with particle velocity magnitude, (c): gas-phase velocity magnitude, (d): pressure.

The drag force is caused by the motion of a particle through the gas. The standard expression for τ_r , the particle relaxation time is

$$\frac{1}{\tau_r} = \frac{3}{8} C_d \frac{\rho_g}{\rho_p} \frac{|\mathbf{u}_g - \mathbf{u}_p|}{R_p} \quad (2.6)$$

where C_d is the drag coefficient and is dependent on the particle Reynolds number, volume fraction and viscosity given by Andrews & O'Rourke (1996).

$$C_d = \frac{24}{Re} (1 + a Re_p^b) \Theta_g^{-1.8}, \quad \text{for } Re_p < 1000 \quad (2.7)$$

$$= 0.44 \Theta_g^{-1.8}, \quad \text{for } Re_p \geq 1000 \quad (2.8)$$

where C_d is the drag coefficient for spherical particles, $R_p = (3V_p/4\pi)^{1/3}$ is the particle radius. The particle Reynolds number (Re_p) is given as

$$Re_p = \frac{2\rho_g \Theta_g |\mathbf{u}_g - \mathbf{u}_p| R_p}{\mu_g}. \quad (2.9)$$

There is an indirect collective effect in this drag term: when there is a dense collection of particles passing through the fluid interphase momentum exchange term will cause \mathbf{u}_g to approach the particle velocity, \mathbf{u}_p thus decreasing the drag on a particle, a drafting effect. The acceleration of particles due to inter-particle interactions (\mathbf{a}_{coll}) is an important term in dense sprays. A simple model for acceleration of particles due to collision (\mathbf{a}_{coll}) is

$$\mathbf{a}_{coll} = -\frac{1}{\Theta_p \rho_p} \nabla \tau \quad (2.10)$$

where τ is the interparticle stress that provides a pressure type force that prevents packing of particles beyond the close-packing limit. Expression for τ is given as (Harris & Crighton (1994))

$$\tau = \frac{P_s \Theta_p^\beta}{\Theta_{cp} - \Theta_p} \quad (2.11)$$

where P_s has units of pressure, Θ_{cp} is the particle volume fraction at close packing and β is a constant. Here it is assumed that the droplets are rigid spheres and thus there exists a close-packing limit beyond which the droplets would not remain spherical nor rigid. The values for P_s and β are obtained from Andrews & O'Rourke (1996). In this model, the inter-particle acceleration due to particle collision is assumed to be independent of its size and velocity. This model is least expensive in terms of computational cost as particle binary pairs are not formed and the collision force is directly obtained by interpolation from equation (2.10). It should be noted that, this model cannot accurately represent collision between two individual droplets, however, does represent collective behavior of a cluster of droplets and their collisions with others.

Finally, the force on the gas-phase through two-way coupling is given as

$$\mathbf{F}(\mathbf{x}, \mathbf{t}) = -\frac{1}{V} \sum_{\mathbf{x}_p \in V(\mathbf{x})} \mathbf{F}_p \quad (2.12)$$

It should be noted that, in dense spray regime, the liquid mass loading is large and the total force acting on the carrier phase could become large. An explicit treatment of this force gives rise to stability problems in the solution of carrier-phase momentum equations. Owing to this difficulty, in many simulations of practical combustors with dense spray

regimes and liquid atomization, the two-way coupling effects are often neglected. This, however, may give erroneous evolution of the spray near the injector. In order to overcome this difficulty, we implemented an implicit coupling for the drag force.

In brief, the algorithm is as follows: 1) advance the droplet centroids explicitly, 2) compute the volume fraction fields and inter-particle collision forces based on the new droplet locations, 3) represent the carrier-phase velocity interpolated at the particle location in equation 2.6 implicitly and solve the carrier phase equations using a fractional step algorithm on unstructured grids (Mahesh *et al.* 2004), 4) knowing the new velocity field of the carrier phase advance the droplet velocities, 5) recompute the total drag on droplets and correct the carrier-phase velocity fields as a third fractional step using any residual force to discretely conserve momentum transfer between the two phases. In this algorithm, the collision force acting on the droplets is represented explicitly and gives time-step restrictions in advancing the droplet equations. However, the time-steps generally employed in LES do not move the droplets by more than 2-3 times their diameters in one iteration and thus the time-step restriction from the collision model is not severe. The advancement of droplet positions can be made more accurate by sub-dividing the time-step into tiny steps and recomputing the collision force in each sub-step.

Figure 4 shows the results obtained from the dense-spray model for impingement of a liquid jet onto a flat plate. In this model problem, there is no initial gas-phase flow over the flat plate. Liquid jet impinges vertically and spreads to form a film. Here the liquid jet is modeled as a collection of closely packed particles of same density as the liquid. As a first approximation, the particles are assumed as rigid spheres. These particles have an initial velocity of 25 m/s in the vertical direction. They impinge the flat plate and undergo a plastic collision losing all of their normal momentum. A stack of particles builds near the boundary. These stagnant particles oppose the incoming particles through the collision model and spread them in the horizontal plane. The strong momentum coupling between the two-phases creates a velocity field (Fig. 4c) and a pressure field (Fig. 4d). Formation and growth of the liquid film is clearly observed. We plan to perform a detailed validation study of the model and use it for prediction of spray size distributions in a new injector designed by Pratt & Whitney.

Approach 2: Thin Film Model

In this second approach, the liquid film formed by the impact of a fuel spray onto the nozzle walls is treated as a thin film. Introducing the lubrication approximations for thin films into the Navier-Stokes equations, an equation for the evolution of the film height h above a no-slip wall can be derived (Oron *et al.* 1997),

$$\frac{\partial h}{\partial t} + \nabla_1 \cdot \left[\frac{1}{2} h^2 \tau_g + \frac{1}{3} h^3 \nabla_1 \left(N_g - \frac{\text{Re}}{\text{Fr}^2} h + \frac{1}{C} \nabla_1^2 h \right) \right] = 0. \quad (2.13)$$

Here, τ_g and N_g are the tangential respectively normal stresses exerted by the outside gas onto the liquid film surface, cp. Fig. 5, Re and Fr are the Reynolds and Froude number, ∇_1 is the Nabla-operator in the x - y -wall coordinate system, and C is the capillarity number,

$$C = \frac{u_0 \mu_l}{\sigma}, \quad (2.14)$$

with u_0 a reference velocity, μ_l the liquid viscosity, and σ the surface tension coefficient.

To include the effect of the impinging spray, (2.13) has to be extended by appropriate source terms. Assuming, as an initial step, that all drops coming into contact with the

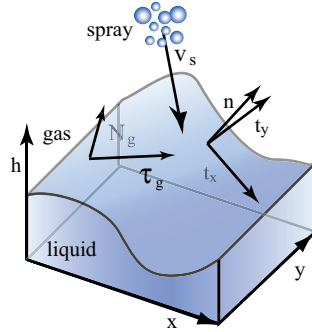


FIGURE 5. Film definition

film surface are fully absorbed into the film such that no splashing occurs, the impinging spray constitutes a mass respectively height source q_s ,

$$q_s = \frac{\dot{m}_s}{\rho_l \Delta A}, \quad (2.15)$$

where \dot{m}_s is the mass flux of the impinging spray, ρ_l is the liquid density, and ΔA is the size of the wall grid cell where impingement occurs. The inclusion of a detailed splashing model is straightforward and will be considered in the future. Besides its mass, each absorbed drop transfers its momentum to the film. Here, we assume that all momentum is transferred to the film within the single grid cell where absorption occurs. This results in additional normal and tangential stresses,

$$N_s = \text{Re} \frac{(m\mathbf{v})_s}{\delta t_I \Delta A} \cdot \mathbf{n} \quad (2.16)$$

$$\boldsymbol{\tau}_s = \text{Re} \frac{(m\mathbf{v})_s}{\delta t_I \Delta A} \cdot \mathbf{t}, \quad (2.17)$$

with $(m\mathbf{v})_s$ the impacting spray momentum, \mathbf{n} and \mathbf{t} the film surface normal and tangential vector, cp. Fig. 5, and δt_I an impact time scale.

Including all spray impingement effects, the evolution equation for the film height then reads

$$\frac{\partial h}{\partial t} + \nabla_1 \cdot \left[\frac{1}{2} h^2 (\boldsymbol{\tau}_g + \boldsymbol{\tau}_s) + \frac{1}{3} h^3 \nabla_1 \left(N_g - \frac{\text{Re}}{\text{Fr}^2} h + N_s + \frac{1}{C} \nabla_1^2 h \right) \right] = q_s. \quad (2.18)$$

Finally, the effect of the liquid film on the outer flow field has to be taken into account by modifying the respective boundary conditions. First, the boundary conditions have to be moved a distance of h away from the wall, and second, the usual no-slip velocities have to be replaced by the film surface velocities,

$$\mathbf{v}^{CDP} = \mathbf{n} \cdot w_h + \mathbf{t} \cdot \mathbf{v}_{t,h}, \quad (2.19)$$

with

$$\mathbf{v}_{t,h} = h \boldsymbol{\tau}_g + \frac{1}{2} \nabla_1 \cdot \left(N_g - \frac{\text{Re}}{\text{Fr}^2} h + N_s + \frac{1}{C} \nabla_1^2 h \right) h^2 \quad (2.20)$$

and

$$w_h = \frac{\partial h}{\partial t} + \mathbf{v}_{t,h} \cdot \nabla_1 h. \quad (2.21)$$

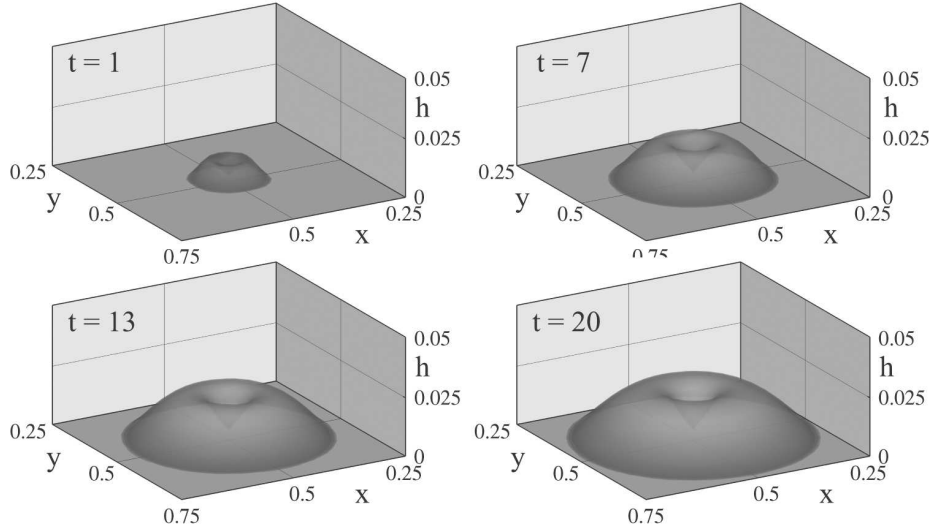


FIGURE 6. Spreading of a film on a flat plate

2.1.1. Numerical method

The film equation, (2.18), constitutes a fourth order PDE with a stable time step restriction of

$$\Delta t_h = \min \left(\alpha_1 \frac{\Delta x_{\min}}{|\tau_g + \tau_s|_{\max} h_{\max}}, \alpha_2 \frac{C \Delta x_{\min}^4}{h_{\max}^3}, \alpha_2 \frac{C \Delta x_{\min}^3}{h_{\max}^2}, \alpha_3 \frac{1}{|q_s|_{\max}}, \alpha_4 \frac{\Delta x_{\min}}{\max(\partial N / \partial x, \partial N / \partial y) h_{\max}^2} \right), \quad (2.22)$$

where α_i are CFL numbers of order 1. Since, in the worst case, $\Delta t_h \sim \Delta x^4$, severe time step restrictions can be imposed on an explicit solver, usually necessitating the use of an implicit solver. However, since (2.18) is incorporated into CDP, the CPU time spent to solve the film equation on a typical CDP grid employing an explicit solver is negligible compared to the CPU time spent in a single CDP time step. This is due to the fact that (2.18) is only two-dimensional.

In practice, (2.18) is solved on a separate, two-dimensional wall grid, using a first order upwind scheme for the advection term involving the tangential stresses and a positivity preserving scheme (Diez & Kondic 2002) employing central differences for all higher order terms. Integration in time is first order. Bilinear interpolation is used to transfer quantities from the wall grid to the CDP grid and vice versa. However, (2.19) has been neglected for now.

To capture the spreading of the film on the underlying wall, a precursor film model is employed (de Gennes 1985; Troian *et al.* 1989). This circumvents the explicit treatment of contact line angles and thereby avoids any contact line singularities.

2.1.2. Thin Film Model Results

The implementation of the film equation has been verified comparing the numerical solutions of traveling surface waves under shear stress to analytical solutions. The obtained results show excellent agreement with the theory.

To demonstrate the performance of the film model in the combustor code CDP, the

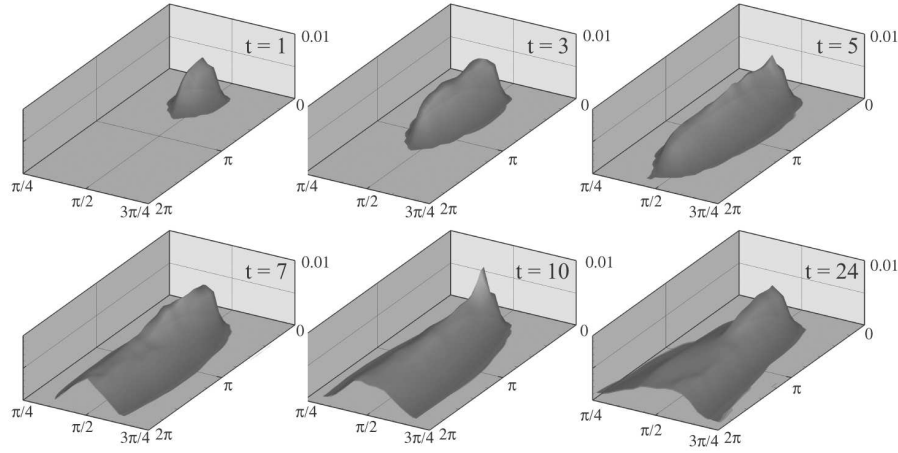


FIGURE 7. Spreading of a film in a turbulent channel

results of two different example cases are presented in the following. In the first case, a spray with density $\rho_l = 850 \text{ kg/m}^3$ and $\dot{m} = 1 \text{ kg/s}$ impacts vertically onto a 1 m^2 square flat plate in a square area of 16 cm^2 located at the center of the plate. The spray is injected just above the film, so that the momentum coupling between the spray and the gas-phase can be neglected. The capillarity number is $C = 0.018$, the Reynolds number $\text{Re}_s = 9700$, and the Froude number $\text{Fr} = 0.023$. Figure 6 shows the spreading of the developing film. The effect of the momentum transfer from the spray to the film is clearly visible in the impact area, where the film is visibly depressed. As time progresses, the film starts to spread and forms a circular wetting area, resulting in a maximum film height of roughly 2 mm .

In the second example, a spray with $\dot{m} = 10.9 \text{ g/s}$ is injected in a 45° angle onto a $2\pi \times \pi$ sized wall of a turbulent channel with Reynolds number $\text{Re} = 395$. The capillarity number is $C = 0.25$, the film Reynolds number $\text{Re} = 1.3 \cdot 10^5$, and the Froude number $\text{Fr} = \infty$. To highlight the effect of the outside flow field on the film evolution, the gas-phase stresses acting on the film surface have been enhanced by a factor of 100. Figure 7 shows the evolution of this film. After the initial impact, the film is quickly pushed along the channel wall by the outside gas-phase flow and starts to spread in the transverse direction. Note that due to the turbulent fluctuations of the gaseous shear stresses, fluctuations in the film height are generated.

3. Conclusions

Two approaches for modeling liquid film formation and evolution in the context of high shear nozzles have been implemented in the unstructured LES code CDP. Both approaches show promise in describing the physics of film formation and evolution, and its impact on the gas phase. As part of an ongoing collaboration with Pratt & Whitney, both models will be validated against cold-flow experimental data in a test rig configuration involving a high shear nozzle. Depending on the results of this validation, one or both approaches will then be used to perform a pre-test prediction of an experimental combustor configuration scheduled for detailed cold and hot flow measurements in early 2005.

REFERENCES

- ANDREWS, M. J., & O'ROURKE, P. 1996 The multiphase particle-in-cell (MP-PIC) method for dense particle flow. *Int. J. Mult. Flow* **22**:379–402.
- APTE, S. V., GOROKHOVSKI, M. & MOIN, P. 2003a LES of atomizing spray with stochastic modeling of secondary breakup. *Int. J. Mult. Flow* **29**:1503–1522.
- APTE, S. V., MAHESH, K., & LUNDGREN, T. 2003b An Eulerian-Lagrangian model to simulate two-phase/particulate flows. *Annual Research Briefs*, Center for Turbulence Research, Stanford University.
- APTE, S. V., MAHESH, K., MOIN, P. & OEFELEIN, J. C. 2003c LES of swirling particle-laden flows in a coaxial-jet combustor. *Int. J. Mult. Flow* **29**:1311–1331.
- CITS Annual technical report 2004. *Center for Integrated Turbulence Simulations, Stanford University*.
- DIEZ, J.A., AND KONDIC, L. 2002 Computing three-dimensional thin film flows including contact lines. *J. Comput. Phys.* **183**:274–306.
- DUKOWICZ, J. K. 1980 A particle-fluid numerical model for liquid sprays. *J. Comput. Phys.* **35**:229–253.
- DE GENNES, P. G. 1985 Wetting: Statistics and dynamics. *Rev. Mod. Phys.* **57**:827–863.
- HARRIS, S.E., & CRIGHTON, D.G. 1994 Solutions, solitary waves and viodage disturbances in gas-fluidized beds. *J. Fluid Mech.* **266**:243–276.
- JOSEPH, D.D., & LUNDGREN, T. 1990 Ensemble averaged and mixture theory equations for incompressible fluid-particle suspensions. *Int. J. Mult. Flow* **16**:35–42.
- MAHESH, K., CONSTANTINESCU, G. & MOIN, P. 2004 A numerical method for large-eddy simulation in complex geometries. *J. Comput. Phys.* **197**:215–240.
- ORON, A., DAVIS, S. H., AND BANKOFF, S. G. 1997 Long-scale evolution of thin liquid films. *Rev. Modern Phys.*, **69**(3):931–980.
- TROIAN, S. M., HERBOLZHEIMER, E., SAFRAN, S. A., AND JOANNY, J. F. 1989 Fingering instabilities of driven spreading films. *Europhys. Lett.* **10**:25–30.

Simulation of dispersed two-phase flow using a coupled Volume-of-Fluid/Level-Set method

By E.R.A. Coyajee[†], M. Herrmann AND B.J. Boersma[†]

In this paper, a coupled Volume-of Fluid/Level-Set interface advection method is considered for the simulation of incompressible two-phase flow. With this method, mass conservation for both phases can be achieved up to specified tolerance in each computational cell. Representation of surface tension forces, however, is found unsatisfactory for the stationary droplet (Laplace) problem, as the procedure to couple the Volume-of-Fluid (VOF) and Level-Set (LS) functions gives rise to increased levels of spurious currents. An attempt to improve the coupling of VOF and LS interface descriptions is reported.

1. Introduction

In many industrial flows, the size distribution of drops in a liquid dispersion is of primary importance to process performance. The size distribution is governed by continuous break-up and coalescence of the dispersed phase. In contrast to break-up, coalescence requires the interaction of multiple droplets. In the past, several studies of droplet interaction have been conducted, e.g. Wang, Zinchenko & Davis (1994) and Loewenberg & Hinch (1997). Most of these studies are performed in the limiting condition of Stokes flow, i.e. occurring in emulsification and polymer blending processes. However, industrial flows are frequently turbulent. In this case, if the droplet Reynolds number is finite, the interaction of droplets and coalescence probability is expected to be influenced by effects of inertia in the flow.

To perform a detailed investigation of the behavior of multiple droplets in an incompressible flow at finite droplet Reynolds number, we aim to apply an appropriate numerical method. In this work, the mass conserving Level-Set (MCLS) method introduced by Van der Pijl, Segal, Vuik & Wesseling (2004) is considered for the simulation of two-phase flows. In the MCLS method, the interface between both fluids is advected by a combined VOF/LS approach, with the purpose of eliminating drawbacks of the individual methods by combining advantages.

1.1. VOF method

In the VOF method the interface is represented implicitly on a fixed grid by a marker function, commonly denoted ψ . Indicating the fractional volume of one of the fluids, the VOF function in a computational cell, Ω , is defined from:

$$\psi = \frac{\int_{\Omega} \chi d\Omega}{\int_{\Omega} d\Omega}, \quad (1.1)$$

where χ is the characteristic function, i.e. $\chi = 1$ in one fluid and $\chi = 0$ in the other fluid. The value of the VOF function is $0 < \psi < 1$ for cells which are cut by the interface and 0 or 1 elsewhere.

[†] J.M. Burgerscenter, Laboratory for Aero and Hydrodynamics, Delft University of Technology, Leeghwaterstraat 21, 2628 CA Delft, The Netherlands.

The main advantage of the VOF method is that interface advection can be performed such that the volume or mass of each phase is conserved. On the other hand, the location of the interface is not explicitly defined by the VOF function. Consequently, geometric reconstruction of the interface (or its normal) has to be performed for advection or the computation of curvature. Over the past years, reconstruction procedures have been advanced from Simple Linear Interface Construction up to Piecewise Linear Interface Construction and even piecewise parabolic approximations in Renardy & Renardy (2002). Therefore, computation of interface normals and curvature have improved considerably. The reconstruction procedures themselves however have become complex and their implementation elaborate.

1.2. *LS method*

An LS approach for simulation of two-phase flow has been introduced by Sussman, Smereka & Osher (1994). In the LS methodology, the interface is represented implicitly on a fixed grid by the zero-level of a marker function, commonly denoted ϕ , i.e. $\phi = 0$ at the interface. Away from the interface, the marker function is required to be a distance function, i.e. $\phi < 0$ in phase '1' and $\phi > 0$ in phase '2'. Using the distance function property, the discontinuous surface tension force and discontinuous phase variables such as viscosity and density are easily regularized and implemented according to the Continuous Surface Force methodology (Brackbill, Kothe & Zemach 1992).

Advection of the interface is performed by advecting the LS function as if it were a material property:

$$\frac{\partial \phi}{\partial t} + \mathbf{u} \cdot \nabla \phi = 0. \quad (1.2)$$

For the numerical solution of equation 1.2, straightforward methods for hyperbolic conservation laws are applied, which are diffusive. The diffusion changes the volume enclosed by $\phi = 0$, causing transport of mass from one phase to another. For the current objective, long-term computation of dispersed flow, mass losses would result in unacceptable changes in the properties of droplets and their behavior.

1.3. *MCLS method*

To overcome the problem of mass diffusion in the LS method, the MCLS method combines both LS and VOF approaches: The LS methodology is used for representation of the interface, while the VOF methodology is used for volume preserving advection of both phases. Such a combined approach requires methods to switch between LS and VOF interface descriptions. The MCLS method uses the following relation introduced in the coupled LS/VOF (CLSVOF) method by Sussman & Puckett (2000):

$$\psi = \frac{\int_{\Omega} H(\phi) d\Omega}{\int_{\Omega} d\Omega}, \quad (1.3)$$

where $H(\phi)$ is the Heaviside function, defined

$$H(\phi) = \begin{cases} 1 & \text{if } \phi > 0 \\ 0 & \text{otherwise.} \end{cases} \quad (1.4)$$

Using equation 1.3 and assuming a piecewise linear interface in each computational cell, Van der Pijl, Segal & Vuik (2004) propose an explicit relation between ψ and ϕ of the form:

$$\psi = f(\phi, \nabla \phi), \quad (1.5)$$

which will be discussed further in section 3.2. In addition to equation 1.5, a coupled VOF/LS method requires a way of computing ϕ from ψ . However, no explicit inverse relation of equation 1.5 seems to be available. Instead, an iterative procedure is performed to correct an approximate solution of the LS function. Unfortunately, our tests indicate that the corrections give rise to enhancement of the so-called spurious currents in the stationary bubble problem. Therefore this work tries to make a contribution to improve the coupling between LS and VOF interface representations.

The organization of this article is as follows. In the next section a set of equations is presented for the description of multiphase flow. Subsequently in section 3, the numerical method of Van der Pijl, Segal & Vuik (2004) is presented, with specific emphasis on the inverse coupling between the LS and VOF function. In section 4, results are presented for the stationary droplet problem. Furthermore, an analysis and proposition for improvement of the VOF/LS coupling in the MCLS method is given, followed by the results of a number of test cases. A discussion concludes the paper.

2. Governing equations

Multiphase flow is described by a set of equations for fluid and interface motion. The motion of the fluids is described by the Navier-Stokes (NS) equations:

$$\rho(\phi) \left(\frac{\partial \mathbf{u}}{\partial t} + \mathbf{u} \cdot \nabla \mathbf{u} \right) = -\nabla p + \nabla \cdot \left(\mu(\phi) \left(\nabla \mathbf{u} + (\nabla \mathbf{u})^T \right) \right) + \mathbf{f} \quad (2.1)$$

and the continuity equation for incompressible flow:

$$\nabla \cdot \mathbf{u} = 0. \quad (2.2)$$

The motion of the interface is described by the following equations for the LS:

$$\frac{\partial \phi}{\partial t} + \mathbf{u} \cdot \nabla \phi = 0 \quad (2.3)$$

and VOF function:

$$\frac{\partial \psi}{\partial t} + \mathbf{u} \cdot \nabla \psi = 0. \quad (2.4)$$

In equation 2.1, ρ , μ , p , $\mathbf{u} = (u, v, w)^T$ and \mathbf{f} respectively represent density, viscosity, pressure, the velocity vector and a volume force. The volume force \mathbf{f} may represent gravity as well as surface tension forces. A continuum description of the discontinuous surface tension force acting at the interface between two fluids:

$$\sigma \kappa(\phi) \nabla H(\phi) \quad (2.5)$$

was introduced by Brackbill, Kothe & Zemach (1992) and cast into LS methodology by Chang, Hou, Merriman & Osher(1996). Here, $\kappa(\phi)$ is the mean curvature, defined from:

$$\kappa(\phi) = \nabla \cdot \frac{\nabla \phi}{|\nabla \phi|}. \quad (2.6)$$

Density $\rho(\phi)$ and viscosity $\mu(\phi)$ are allowed to vary between phase '1' or '2', and are defined:

$$\mu(\phi) = \mu_1 (1 - H(\phi)) + \mu_2 H(\phi), \quad (2.7)$$

$$\rho(\phi) = \rho_1 (1 - H(\phi)) + \rho_2 H(\phi). \quad (2.8)$$

3. Numerical method

In the method of Van der Pijl, Segal & Vuik (2004), the computational domain is a 3D rectangular box. Equations 2.1-2.4 are spatially discretized on a uniform Cartesian mesh. A standard staggered arrangement of variables is used, i.e. velocity components are located on the cell faces, whereas pressure, density, VOF and LS variables are defined at cell centers.

Although the original method allows unequal densities in either phase, in this report only fluids of equal density are considered as our focus is on the effects of the VOF/LS coupling on computation of surface tension. The coupling itself is in no way influenced by the density ratio, and for further details about the implementation of discontinuous density we refer to Van der Pijl, Segal, Vuik & Wesseling (2004).

A single time-step in our code consists of the following sequence. First, for a given interface position (i.e. LS function), the flow field is advanced to obtain the velocity at the new time level. Second, given the velocity, the interface is advected to obtain a new interface position (i.e. LS function).

3.1. Fluid flow

Time integration of equations 2.1 and 2.2 is performed with the second order Adams-Bashforth method in the framework of a pressure correction method. Rewriting equation 2.1 into

$$\frac{\partial \mathbf{u}}{\partial t} = \mathbf{f}(\mathbf{u}, \phi) - \nabla \tilde{p}, \quad (3.1)$$

where $\tilde{p} = p/\rho$ denotes the reduced pressure, the integration scheme is given from:

$$\frac{\mathbf{u}^* - \mathbf{u}^n}{\Delta t} = \frac{3}{2}(\mathbf{f}(\phi^n, \mathbf{u}^n)) - \frac{1}{2}(\mathbf{f}(\phi^{n-1}, \mathbf{u}^{n-1})) + \nabla \tilde{p}^{n-1/2}, \quad (3.2)$$

$$\nabla^2 \tilde{p}^* = \frac{1}{\Delta t} \nabla \cdot \mathbf{u}^*, \quad (3.3)$$

$$\nabla \tilde{p}^{n+1/2} = \nabla \tilde{p}^{n-1/2} + \nabla \tilde{p}^*, \quad (3.4)$$

$$\mathbf{u}^{n+1} = \mathbf{u}^* - \Delta t \nabla \tilde{p}^*. \quad (3.5)$$

Due to the assumption of uniform density, we can use a direct Poisson solver to obtain the pressure from equation 3.3, making the code very efficient. For spatial discretization of equations 2.1 and 2.2, central second order finite differences are used. Finally, the following regularized Heaviside function is used for the computation of the surface tension volume force.:

$$H_\alpha(\phi) = \begin{cases} 0 & \text{if } \phi < -\alpha \\ \frac{1}{2} \left(1 + \frac{\phi}{\alpha} + \frac{1}{\pi} \sin(\pi \phi / \alpha) \right) & \text{if } |\phi| \leq \alpha \\ 1 & \text{if } \phi > \alpha \end{cases}, \quad (3.6)$$

where α is chosen as $\alpha = 3/2$.

3.2. Interface advection

The interface advection procedure in the MCLS method is the following:

1. Given ϕ^n , compute ψ^n ;
2. Advect ψ^n toward ψ^{n+1} ;
3. Advect ϕ^n toward ϕ^* ;

4. Correct ϕ^* to obtain ϕ^{n+1} , such that $|\psi^{n+1} - f(\phi^{n+1}, \nabla \phi^{n+1})| < \epsilon$ in each computational cell.

This procedure will be explained in the following sections.

3.2.1. Computation of VOF from the LS function

As discussed in the introduction, a direct relation is used to compute the VOF from the LS function in 3D:

$$\psi = f(\phi, \nabla \phi). \quad (3.7)$$

In the MCLS method, the interface is assumed to be piecewise linear in each computational cell. As a consequence, the interface is a 2D plane, which can be described by a normal vector and a distance to some position along the normal direction. The normal to the interface is simply described by:

$$\mathbf{n} = \frac{\nabla \phi}{|\nabla \phi|} \approx \nabla \phi \quad (3.8)$$

as the LS function is maintained a distance function in our computations (see section 3.2.3), for which $|\nabla \phi| \equiv 1$. In the actual implementation, $\nabla \phi$ is estimated using central second order finite differences. The description of the interface is completed by the local value of the LS function, describing the distance between the interface and the cell center.

With the assumption of a piecewise linear interface, equation 1.3 is simplified to:

$$\psi = \frac{\int_{\Omega_k} H(\phi_k + \nabla \phi_k \cdot (\mathbf{x} - \mathbf{x}_k)) d\Omega}{\int_{\Omega_k} d\Omega}, \quad (3.9)$$

where ϕ_k and $\nabla \phi_k$ are the discrete values of the LS function and its gradient in a computational cell, Ω_k , and \mathbf{x}_k denotes the position of the cell center. Now, at the piecewise linear interface, described by the local values ϕ_k and $\nabla \phi_k$, the value of the LS function is known: $\phi = 0$. Then, from the location of the planar interface and the local gradient of the LS function, any distance between the interface and the faces of the computational cell can be computed. Therefore, it is possible to determine the VOF value in a computational cell from a geometric computation of the volume for which $H(\phi) = 1$, in accordance with equation 1.3. For the complete mathematical formulation of equation 3.8, we refer to Van der Pijl, Segal & Vuik (2004).

3.2.2. VOF advection

The VOF advection is performed by means of an operator-split method. To this aim, equation 2.4 is rewritten into:

$$\begin{aligned} \frac{\partial \psi}{\partial t} + \frac{\partial(u\psi)}{\partial x} &= \psi \frac{\partial u}{\partial x} \\ \frac{\partial \psi}{\partial t} + \frac{\partial(v\psi)}{\partial y} &= \psi \frac{\partial v}{\partial y} \\ \frac{\partial \psi}{\partial t} + \frac{\partial(w\psi)}{\partial z} &= \psi \frac{\partial w}{\partial z}. \end{aligned} \quad (3.10)$$

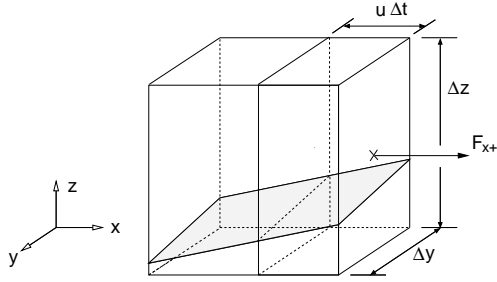


FIGURE 1. Computational cell with flux F_{x+} and its donating region $u\Delta t\Delta y\Delta z$. The interface is indicated by a patterned surface.

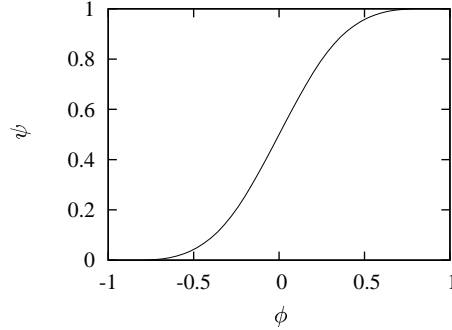


FIGURE 2. Graph of the relation between ϕ and ψ for $\nabla\phi = (\frac{1}{3}\sqrt{3}, \frac{1}{3}\sqrt{3}, \frac{1}{3}\sqrt{3})$.

A conservative numerical approximation of equation 3.10 is obtained by considering fluxes of fluid, denoted F , flowing through the boundary of a cell during time-step Δt :

$$\begin{aligned}
 \frac{\psi^* - \psi^n}{\Delta t} &= -\frac{F_{x+}^n - F_{x-}^n}{\Delta x \Delta y \Delta z \Delta t} + \psi^* \frac{u_+ - u_-}{\Delta x} \\
 \frac{\psi^{**} - \psi^*}{\Delta t} &= -\frac{F_{y+}^* - F_{y-}^*}{\Delta x \Delta y \Delta z \Delta t} + \psi^{**} \frac{v_+ - v_-}{\Delta y} \\
 \frac{\psi^{***} - \psi^{**}}{\Delta t} &= -\frac{F_{z+}^{**} - F_{z-}^{**}}{\Delta x \Delta y \Delta z \Delta t} + \psi^{***} \frac{w_+ - w_-}{\Delta z} \\
 \frac{\psi^{n+1} - \psi^{***}}{\Delta t} &= -\psi^* \frac{u_+ - u_-}{\Delta x} - \psi^{**} \frac{v_+ - v_-}{\Delta y} - \psi^{***} \frac{w_+ - w_-}{\Delta z},
 \end{aligned} \tag{3.11}$$

where subscripts indicate the corresponding face of a cell. The discrete flux is defined:

$$F = \int_{\Omega_D} H(\phi) d\Omega, \tag{3.12}$$

where Ω_D is the donating region, which contains the fluid that will flow through a face during a time-step Δt . An example of a discrete flux, F_{x+} , and its donating region is displayed in figure 1. To compute the magnitude of the particular flux in figure 1, the VOF within the donating region of size: $u\Delta t\Delta y\Delta z$ needs to be considered. To compute the discrete fluxes, equation 3.7 can be used as its formulation enables the computation of a fluid fraction in any rectangular domain.

3.2.3. LS advection

As a final step in the interface advection procedure one would like to obtain ϕ^{n+1} from ψ^{n+1} directly. Unfortunately, no explicit inverse relation of equation 3.7 appears to be available and a different strategy needs to be applied. Although interface advection of the LS function is not preferred as the solutions are not strictly mass conserving, ϕ^n can be advected to obtain an approximate solution of the LS function.

The preliminary update of the LS function, denoted ϕ^* , is obtained by solving equation 2.3. Subsequently, reinitialization is performed to keep the LS function a distance function as in Sussman, Smereka & Osher (1994). First order discretization is used for both advection and reinitialization procedures. Obviously, first order methods suffer from considerable numerical diffusion, resulting in transport of mass from one phase to an-

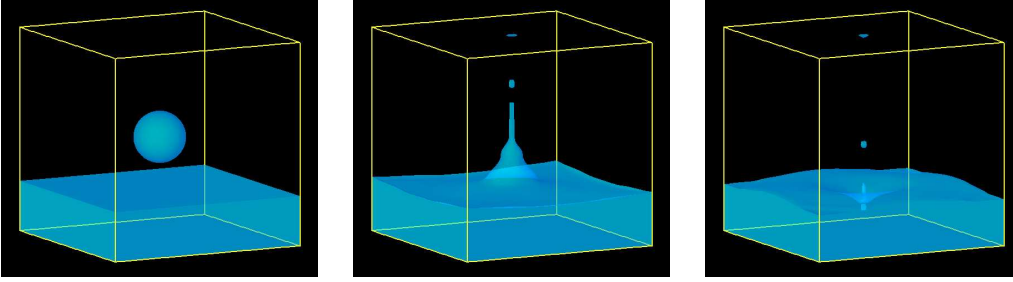


FIGURE 3. Droplet falling into a free surface. Simulation of an air-water flow without surface tension. Courtesy of Sander van der Pijl.

other. However, as mass conservation is ensured by the correction procedure described in the next section, Van der Pijl, Segal, Vuik & Wesseling (2004) argue in favor of a low order method because the diffusion provides a smooth approximate solution for the LS function.

3.2.4. Correction of the LS function

Finally, ϕ^* is corrected, providing a solution ϕ^{n+1} which satisfies:

$$|\psi_k^{n+1} - f(\phi_k^{n+1}, \nabla \phi_k^{n+1})| \leq \epsilon \quad \forall \quad k = 1, 2, \dots, K \quad (3.13)$$

where K is the total number of computational cells and ϵ a tolerance. In this work we use $\epsilon = 1 \cdot 10^{-4}$.

The main idea of the correction procedure is as follows: Keeping $\nabla \phi$ at a constant value, the interface equation 3.7 gives a one-to-one relation between the LS and VOF function:

$$\phi = g(\psi, \nabla \phi). \quad (3.14)$$

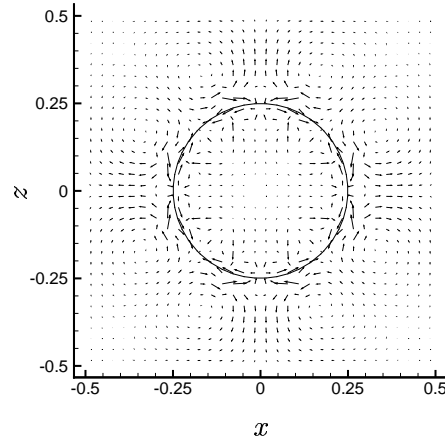
Figure 2 shows an example of the graph of such a relation between the LS and VOF function for $\nabla \phi = (\frac{1}{3}\sqrt{3}, \frac{1}{3}\sqrt{3}, \frac{1}{3}\sqrt{3})$. From figure 2 it will be clear that, while assuming a constant gradient of the LS function, the local value of the LS function in a cell can be adjusted such that the required local value of the VOF function is obtained. We found this procedure similar to the one in Sussman & Puckett (2000), in which a linearly constructed piece of interface is shifted along its normal direction to minimize a mass error. Here, the assumption of a constant gradient is equivalent to solving a linearized problem.

Using equation 3.14, the following iterative procedure is executed to correct the preliminary LS function:

- $\phi^0 = \phi^*$;
- $\delta\psi_k = |\psi_k^{n+1} - f(\phi_k^0, \nabla \phi_k^0)|$;
- Repeat until $\delta\psi_k < \epsilon \quad \forall k$

$$\phi_k^{m+1} = \begin{cases} g(\psi_k^{n+1}, \nabla \phi_k^m) & \text{if } \delta\psi_k > \epsilon \\ \phi_k^m & \text{if } \delta\psi_k < \epsilon; \end{cases}$$
- $\delta\psi_k = |\psi_k^{n+1} - f(\phi_k^{m+1}, \nabla \phi_k^{m+1})|$;
- $\phi^{n+1} = \phi^{m+1}$.

Case	1	2	3	4	5	6	7	8	9	10	11	12
σ	1	0.1	0.01	0.001	1	0.1	0.01	0.001	1	0.1	0.01	0.001
μ	1	1	1	1	0.1	0.1	0.1	0.1	0.01	0.01	0.01	0.01

TABLE 1. Parameter combinations of surface tension σ and viscosity μ for the Laplace problem.FIGURE 4. Laplace problem: Velocity vectors and interface over a cross-section ($y = 0$) of the droplet at time $t = 0.1$. MCLS method used for case 7 with $h = 1/32$.

4. Results

Figure 3 shows three images of a simulation of a droplet falling into a free surface. The maximum relative mass error during this computation is less than $1.6 \cdot 10^{-4}$. Considering the complexity of the interface motion, this result clearly shows the capability of the MCLS method to conserve mass. Nevertheless, the simulation of figure 3 is performed without the surface tension force in equation 2.1. To investigate the surface tension representation in the MCLS method, the Laplace or stationary droplet problem is simulated in this section.

4.1. Laplace problem

The Laplace or stationary bubble/droplet problem is considered an important test case for implementation of surface tension forces (Renardy & Renardy 2002). Here, the Laplace problem is simulated in a computational domain of dimensions $1 \times 1 \times 1$. Boundary conditions are periodic in all directions. Initial conditions are $\mathbf{u} = (0, 0, 0)$ for the fluid velocity and $R_b = 0.25$ for the radius of the droplet. Computations have been performed using $\rho = 1$ and various combinations of σ and μ , listed in table 1. For a grid refinement study, uniform meshes are used with $h = 1/16, 1/32, 1/64, 1/128$. The time-step is $\Delta t = 2 \cdot 10^{-5}$. In the simulations, the magnitude of the parasitic currents is monitored by measuring

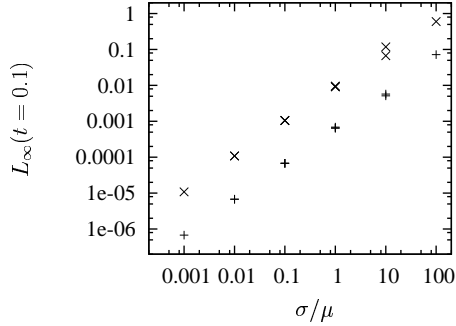


FIGURE 5. Laplace problem: Results of the parameter study for the MCLS method (\times) compared to LS advection ($+$), $h = 1/64$.

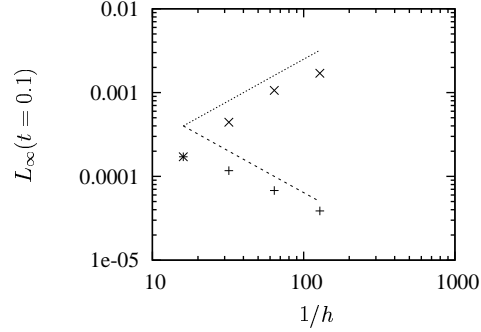


FIGURE 6. Laplace problem: Results of a grid refinement test for the MCLS method (\times) compared to LS advection ($+$), for case 7. (...) Line of slope +1. (---) Line of slope -1.

the maximum norm of the error in velocity, defined from[†]:

$$L_\infty = \max_{1 \leq k \leq K} (|u|_k, |v|_k, |w|_k). \quad (4.1)$$

Simulations have been run for all mesh sizes and combinations of parameters up to $t = 0.1$. At this time, the spurious or parasitic currents (displayed in figure 4) are found to have saturated toward a maximum level. This behavior is similar to the behavior found in Renardy & Renardy (2002). Also in accordance with other authors we find that $L_\infty(t = 0.1)$ increases linearly with the ratio σ/μ (figure 5). Nonetheless, the spurious currents seem rather high. To compare, we have recalculated all cases using only first order LS advection, i.e. disregarding the coupling between the advected VOF and LS functions in the simulation. The results are also given in figure 5 and reveal lower levels of parasitic currents.

From the comparison of results of the LS and MCLS methods, we conjecture the enhancement of spurious currents is caused by the inverse coupling between the LS and VOF functions. In the procedure of section 3.2.4, corrections are only introduced in cells where the local mass error is larger than a certain tolerance. As the corrections are only applied locally, problems may arise in the computation of curvature which involves second order derivatives of the LS function. We have done an analysis of a singular perturbation in ϕ on the curvature, i.e. introducing $\phi = \phi(\mathbf{x}) + \varepsilon$ to the discretized curvature $\kappa(\phi)$. For a singular perturbation $\varepsilon = O(h)$, the resulting error in curvature is found to be $O(1/h)$.

The previous analysis, which suggests that the corrections act as a singular perturbation on the smooth initial LS function, is confirmed by the results of our simulations. Figure 6 shows results of a grid refinement study of the maximum norm for case 7, both for LS advection and the MCLS method. The magnitude of the spurious currents in the MCLS method is found to increase approximately proportional with $1/h$, whereas first order convergence is found for LS advection[‡].

[†] Note that, since the exact solution for the fluid velocity in the Laplace problem is zero velocity everywhere, any velocity measured is equal to an error in the velocity.

[‡] For $h = 1/16$ results are identical for both methods. This is due to the fact that hardly any corrections need to be performed for this mesh, as the displacement of the interface is very small in the relation to the mesh width.

4.2. Regularization of the corrections

The analysis of the previous section indicates that local corrections to the LS function introduce undesirable errors in the curvature. A possible improvement would be to regularize the corrections and retain a smooth spatial representation of the curvature.

In the current method, the surface tension force is treated as a volume force. This requires the curvature to be computed in a small 'band' surrounding the interface. The curvature is defined as the divergence of the normal vector to the interface (equation 2.6). To compute a valid representation of the curvature in a region surrounding the interface, the gradient of the corrected LS function should be constant along the direction normal to the interface. Therefore, the first step in the proposed regularization procedure is to extend the local corrections, defined $\delta\phi = \phi^{n+1} - \phi^*$, along the direction normal to the interface by solving the following equation in pseudo-time τ :

$$\frac{\partial \delta\phi}{\partial \tau} + S(\phi^*) \frac{\nabla \phi^*}{|\nabla \phi^*|} \nabla \delta\phi = 0, \quad (4.2)$$

where $S(\phi^*)$ is the signum function defined:

$$S(\phi^*) = \begin{cases} -1 & \text{if } \phi^* < 0 \\ 0 & \text{if } \phi^* = 0 \\ 1 & \text{if } \phi^* > 0 \end{cases} \quad (4.3)$$

For numerical implementation of equation 4.2, a first order method is used as described in Peng, Merriman, Osher, Zhao & Kang (1999).

In addition to the extension procedure, a filter is applied to smooth the corrections in the direction tangential to the interface. The following interpolation function is applied to the corrections, consecutively in each coordinate direction, to attenuate high-frequency components:

$$\hat{\delta\phi} = \frac{1}{16} (-\delta\phi_{+2} + 4\delta\phi_{+1} + 10\delta\phi + 4\delta\phi_{-1} - \delta\phi_{-2}), \quad (4.4)$$

with $\hat{\delta\phi}$ the filtered corrections.

After treating the initial correction with the additional extension and filtering procedures, modified corrections are obtained and added to the initial approximation of the LS function. Due to the regularization, the effect of the initial correction procedure is altered and equation 3.13 may not necessarily hold. Therefore, the local correction, extension and filtering procedures are repeated iteratively in the following test case.

In our test case, the LS function of a perturbed spherical interface:

$$\phi^* = R(1 - \lambda) - \sqrt{x^2 + y^2 + (z/(1 - \lambda))^2} \quad (4.5)$$

is corrected back to a spherical interface of radius R , whose VOF function is represented by ψ^{n+1} . The perturbation λ is proportional to the mesh width, $\lambda \propto h$, and of such magnitude that the maximum volumetric error in each computational cell k is approximately 10%, i.e. $\max |\psi_k^{n+1} - f(\phi_k^*, \nabla \phi_k^*)| \approx 0.1$. After each iteration cycle of the modified correction procedure, the maximum relative error in curvature:

$$\max_k \left| \frac{\kappa_k^{n+1} - \kappa_k^*}{\kappa_k^{n+1}} \right| \quad (4.6)$$

	Max. relative error κ			Relative mass error		
Mesh width	1/32	1/64	1/128	1/32	1/64	1/128
Local method	$7.87 \cdot 10^{-1}$	1.64	3.60	$4.77 \cdot 10^{-6}$	$2.77 \cdot 10^{-6}$	$1.24 \cdot 10^{-6}$
Regularized method	$2.48 \cdot 10^{-4}$	$3.67 \cdot 10^{-4}$	$7.89 \cdot 10^{-4}$	$6.08 \cdot 10^{-6}$	$1.85 \cdot 10^{-6}$	$9.17 \cdot 10^{-7}$

TABLE 2. Comparison of maximum relative curvature and relative mass errors for the local and regularized correction methods. For the latter, only results after 24 iterations are shown.

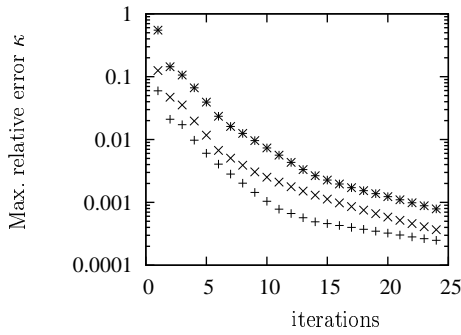


FIGURE 7. Maximum relative error in curvature as a function of iterations. (+) $h = 1/32$, (\times) $h = 1/64$ and (*) $h = 1/128$.

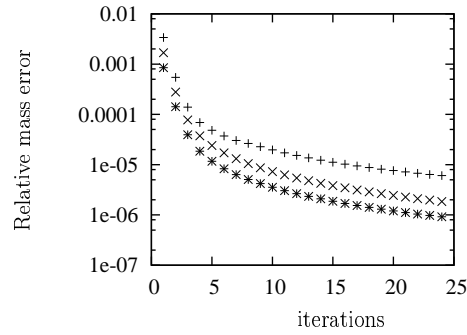


FIGURE 8. Relative mass error as a function of iterations. Symbols as in figure 7.

and the relative mass error

$$\frac{\sum_k \psi_k^{n+1} - f(\phi_k^{n+1}, \nabla \phi_k^{n+1})}{\sum_k \psi_k^{n+1}} \quad (4.7)$$

are computed and stored.

In table 2, results are compared of the local and regularized correction method, showing significant reduction of error in curvature for the new method. Figures 7 and 8 display successful convergence of errors with increasing number of iterations in case of the regularized method for each individual grid size. However, figure 7 also shows that for identical number of iterations, no convergence upon grid refinement is obtained for the maximum relative error in curvature. Furthermore, similar tests for less smoothly perturbed ϕ^* (not shown here) indicate unsatisfactory convergence of the mass error. Therefore actual implementation of the regularized correction procedure is not pursued.

5. Discussion

From the results presented in this work, we conclude that the coupling of LS and VOF interface descriptions by applying local corrections to the LS function should be avoided. The local corrections introduce non-smooth errors in the curvature and therefore surface tension force, because its computation involves second order derivatives of the LS function. As a result of these errors, spurious currents are enhanced, which limits the range of parameters (surface tension coefficient and viscosity) to be used for the

simulation of droplets. Moreover, the errors in surface tension force are shown to grow linearly upon grid refinement, which may affect the convergence and stability of the numerical method in general. Finally, the presented non-localization scheme is insufficient because, although it reduces the magnitude of the error in curvature, still does not guarantee convergence of the error upon grid refinement.

Instead, a global correction procedure could be applied, providing a LS function which is sufficiently smooth. Our proposition is to enforce two conditions on the LS function simultaneously:

$$\psi = f(\phi, \nabla\phi) \quad (5.1)$$

and

$$|\nabla\phi| = 1 \quad (5.2)$$

to obtain a mass conserving distance function to the piecewise linear interface. Currently, a variational LS method is considered, which reinitializes the LS function to accomplish equation 5.2 under the constraint for volume fraction, equation 5.1.

Although a priori estimation is difficult, a variational VOF/LS coupling procedure will be an additional effort in the code. Nonetheless, use of the LS function for the computation of the VOF advection has shown to be highly efficient in the MCLS code. Therefore, we still consider the combined VOF/LS approach an appropriate one to pursue.

Acknowledgments

Sander van der Pijl is greatly acknowledged for developing the MCLS method and providing us access to his code.

REFERENCES

- BRACKBILL, J., KOTHE, D. & ZEMACH, C. 1992 A continuum method for modeling surface tension. *J. Comp. Phys.* **100**, 335-354.
- CHANG, Y., HOU, T., MERRIMAN, B. AND OSHER, S. 1996 A level set formulation of Eulerian interface capturing methods for incompressible fluid flows. *J. Comp. Phys.* **124**, 449-464.
- LOEWENBERG, M. & HINCH, E. J. 1997 Collision of two deformable drops in shear flow. *J. Fluid Mech.* **338** 299-315.
- VAN DER PIJL, S. P., SEGAL, A. & VUIK, C. 2004 *Modeling of three-dimensional bubbly flows with a mass-conserving Level-Set method*. Proceedings European Congress on Computational Methods in Applied Sciences and Engineering, ECCOMAS 2004, Jyväskylä, Finland, July 24-28, 2004.
- VAN DER PIJL, S. P., SEGAL, A., VUIK, C. & WESSELING, P. 2004 A mass-conserving Level-Set method for modeling of multi-phase flows. *To appear in Int. J. Numer. Meth. Fluids*. <http://ta.twi.tudelft.nl>
- PENG, D., MERRIMAN, B., OSHER, S., ZHAO, H. & KANG, M. 1999 A PDE-based fast local Level-Set method. *J. Comp. Phys.* **155**, 410-438.
- RENARDY, Y. & RENARDY, M. 2002 PROST: A parabolic reconstruction of surface tension for the Volume-of-Fluid method. *J. Comp. Phys.* **183**, 400-421.

- SUSSMAN, M., SMERKA, P. & OSHER, S.1994 A Level Set approach for computing solutions to incompressible two-phase flow. *J. Comp. Phys.* **114**, 146-159.
- SUSSMAN, M. & PUCKETT, E. G.2000 A coupled Level Set and Volume-of-Fluid method for computing 3D and axisymmetric incompressible two-phase flows. *J. Comp. Phys.* **162**, 301-337.
- Wang, H., Zinchenko, A. Z. & Davis, R. H.1994 The collision rate of small drops in linear flow fields *J. Fluid Mech.* **265**, 161-188.

Page intentionally left blank

Filtered particle tracking for dispersed two-phase turbulent flows

By J. Pozorski †, S. V. Apte AND V. Raman

Turbulent particulate flows are considered in the Eulerian-Lagrangian approach where the large-eddy simulation of the carrier phase is coupled with the particle tracking. The issue addressed here is the impact of the subgrid scale turbulence on the statistics of particle motion, including preferential concentration. This is accomplished through *a priori* analysis of DNS data in the case of forced isotropic turbulence. A model for filtered particle tracking (FPT) is then proposed. The model aims to reconstruct the residual (subgrid scale) fluid velocity along particle trajectories. The computation results serve to appraise the model through comparisons with available DNS reference data on preferential concentrations for a selection of particle inertia parameters.

1. Introduction

Study of two-phase flows with dispersed droplets or solid particles constitutes an important activity in the realm of turbulence. There are variety of theoretical and modeling issues regarding this class of flows, both in the two-fluid and the trajectory approach (e.g., Simonin 1996; Minier & Peirano 2001). Practical applications involve environmental studies, chemical and process engineering, as well as power engineering, including wet steam flows and combustion of solid or liquid fossil fuels. A relevant industrial example is fuel injection in Diesel engine or a gas turbine combustor where the dispersed phase is present in the form of small droplets (Apte *et al.* 2003). In the paper, the dispersed phase will be assumed dilute; consequently, the one-way momentum coupling is adequate and particle collisions can safely be neglected. Yet, for a sufficiently high load of the dispersed phase, the two-way coupling needs to be accounted for in the momentum and energy equations; moreover, for high particle number densities, the interparticle collisions will affect their dynamics. Additional complexity to the physical picture will be added through the interphase mass and energy transfer in the case of evaporating droplets or volatilizing solid particles. Here, we concentrate on the dynamical aspects only, and precisely on the impact of turbulence on the statistics of the dispersed phase.

The Lagrangian stochastic approach has initially been proposed in its natural context for modeling and prediction of turbulent diffusion and dispersion. In the framework of statistical RANS (Reynolds-averaged Navier-Stokes) description of turbulence, various random walk models for the diffusion of fluid particles and the dispersion of solid particles in two-phase flows have been proposed since then, cf. Stock (1996), Pozorski & Minier (1998), Mashayek & Pandya (2003) and references therein. Following rapid progress in large eddy simulation (LES), the method has also been used with success to compute two-phase dispersed flows. The feasibility of LES to study preferential concentration of particles by turbulence (Wang & Squires 1996) and to compute flows with two-way momentum coupling (Boivin *et al.* 2000) has been reported.

† Institute of Fluid-Flow Machinery, Polish Academy of Sciences, Gdańsk, Poland

Generally speaking, some terms in the filtered LES evolution equations have to be modeled altogether, because relevant physical processes occur at unresolved scales; an example is the source term, due to chemical reactions, in mass and energy balance equations. Some other are partly resolved source terms due to the presence of particles: mass transport (evaporation/condensation), momentum coupling, and energy balance (heating, latent heat of evaporation). The issue of residual (unresolved, subgrid scale) velocity field and its influence on the statistics of particle motion and their preferential concentration has received only limited attention in the literature. It is revisited here with *a priori* tests using filtered DNS velocity fields.

The first aim of the paper is to study the impact of LES filtering on the particulate phase. It will be shown to be non-negligible for a sufficiently coarse LES mesh (judged by a residual kinetic energy content). A quantitative assessment of this effect is accomplished through the statistics of preferential particle concentration: the probability distribution of particle number density and the radial distribution function of the interparticle distance. The second aim of the paper is to develop a filtered particle tracking (FPT) model for the LES of the dispersed phase. The model is meant to reconstruct statistically the residual flow field along particle trajectories. First computation results are reported for the forced isotropic turbulence case.

2. Turbulent dispersion of particles

To determine the evolution of a set of non-interacting solid particles in turbulent flow, particle location \mathbf{x}_p and its velocity \mathbf{U}_p should be known. Another variable of importance for further considerations is the fluid velocity \mathbf{U}^* “seen” or sampled by the particle as it moves across the flow. In terms of the instantaneous Eulerian velocity field $\mathbf{U}(\mathbf{x}, t)$ of the carrier (fluid) phase, we have $\mathbf{U}^* = \mathbf{U}(\mathbf{x}_p, t)$. Respective governing equations for particles are:

$$\frac{d\mathbf{x}_p}{dt} = \mathbf{U}_p, \quad (2.1)$$

$$\frac{d\mathbf{U}_p}{dt} = \frac{\mathbf{U}^* - \mathbf{U}_p}{\tau_p} + \mathbf{g}. \quad (2.2)$$

In general cases (Maxey & Riley 1983), the particle equation of motion (2.2) includes the pressure-gradient, drag, added-mass and Basset forces. Yet, for particles much heavier than the carrier fluid, $\rho_p \gg \rho_f$ (ρ_f and ρ_p stand for fluid and particle densities), an acceptable approximation is to retain only the aerodynamic drag and external force terms \mathbf{g} (if relevant). The drag term is written using the particle relaxation time τ_p .

Obviously, modeling of the fluid velocities sampled by particles is no longer needed when the carrier phase is fully resolved, possibly with source terms that represent the exchange of mass, momentum, and energy between the particles and the flow. This is the DNS with particle tracking where \mathbf{U}^* is simply the instantaneous fluid velocity interpolated at the point-particle location. Since the number of degrees of freedom in turbulent flows scales as $\text{Re}^{9/4}$, this approach is feasible only for simple flow cases at relatively small Re . Nevertheless, the DNS studies are extremely valuable for model testing, as evidenced in the following sections: preferential concentration patterns, first observed in experimental studies, are investigated (Sec. 3.3); the impact of filtering on particle statistics is assessed (Sec. 3.4). For a finite-size particle (comparable to the Kolmogorov scale η or larger), its dynamics, fluctuating lift and drag forces can be computed from “true DNS” studies (Bagchi & Balachandar 2003; Burton & Eaton 2003).

Despite the growing importance of DNS, a reduced (or contracted) description involving far less degrees of freedom is still used for practical, “real-life” flow cases. In particular, RANS remains a standard engineering approach. One of the difficult modeling aspects of turbulent dispersion in RANS is the account of the fluid velocity statistics seen along the solid particle trajectories. They unavoidably differ from the “pure” Lagrangian statistics because of the particle inertia and the external force (such as gravity) effects. Stochastic models based on the Langevin equation have been proposed to account for these effects (Pozorski & Minier 1998; Minier *et al.* 2004). Alternatively, the PDF formalism, initially developed in turbulence modeling (cf. Pope 2000), and particularly useful in turbulent combustion (Fox 2003), has been extended to turbulent dispersion issues, starting with the kinetic equation of Reeks (1992) and further developed by Pozorski & Minier (1999).

In general terms, a physically-sound reconstruction of instantaneous fluid velocity “seen” by the particles \mathbf{U}^* has to be performed out of limited information available (such as the fluid mean velocity $\langle \mathbf{U} \rangle$ or its turbulent kinetic energy). A classical approach goes through the decomposition $\mathbf{U}^* = \langle \mathbf{U} \rangle + \mathbf{u}^*$ with the mean fluid velocity at the particle location, $\langle \mathbf{U} \rangle(\mathbf{x}_p, t)$, determined from the Eulerian RANS solver for the carrier phase. Various stochastic models have been proposed to represent the fluctuating fluid velocity \mathbf{u}^* sampled by particles. They often are extensions of fluid diffusion models, developed in the context of environmental and atmospheric studies, but can suffer from spurious drifts if improperly devised (MacInnes & Bracco 1992). A sound alternative seems to be a stochastic model for \mathbf{U}^* (Pozorski & Minier 1999; Minier *et al.* 2004).

In the context of RANS, there are no instantaneous flow structures resolved; consequently, there is no preferential concentration (which, by definition, denotes correlation of particle locations with certain flow structures). In RANS of non-homogeneous turbulence, spatial gradients of particle number density can develop (even for initially uniform particle distribution) because of the so-called turbophoresis effect. It consists in the net particle displacement in the direction of decreasing turbulence intensity (for $\rho_p > \rho_f$).

In LES, the resolved (large-scale) part of the instantaneous flow field can readily be interpolated to particle locations. The major issue is now to determine whether the remaining (residual or subgrid-scale) part of the flow velocity field can have a noticeable influence on the particulate phase. In most studies reported so far, this influence has been neglected and justified by a low residual energy content. A LES study of particle-laden channel flow was reported by Wang & Squires (1996). Analysis of their data (Fig. 4 there) shows that the ratio of k_{sg} to \bar{u}^2 remains small throughout the viscous sublayer (roughly 10%). Armenio *et al.* (1999) computed channel flow with the one-way momentum coupling. Particles were tracked in a fully-resolved (DNS) velocity field and in filtered fields where up to 20% of the turbulent kinetic energy remained unresolved depending on the filter size; however, there was no filtering in the wall-normal direction. They performed then a corresponding LES with the same filter width. In all cases, the r.m.s. particle dispersion was found to be only slightly affected by the incomplete resolution.

Okong'o & Bellan (2004) performed an *a priori* analysis of a dispersed two-phase flow. They distinguished four possibilities for the reconstruction of SGS fluid velocities “seen”: ideal model (velocity U_i from DNS data), baseline model (velocity \tilde{U}_i from LES), random model (velocity reconstructed as $\tilde{U}_i + \sigma \xi_i$ where ξ_i are Gaussian random numbers) and deterministic model (not explained here). The eddy life-time and interaction-time model known in RANS has been extended to LES by Oefelein (cf. Segura *et al.* 2004) and successfully applied to the channel flow. Also Sankaran & Menon (2002) proposed a simple FPT model, yet its impact on final LES results has not been reported.

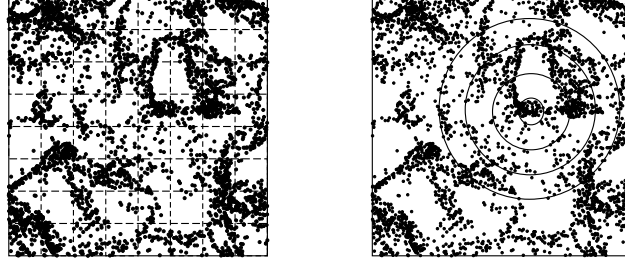


FIGURE 1. Computing the particle number density and the radial distribution function.

3. Preferential concentration of particles in turbulent flows

3.1. Effect of turbulent structures on particles

Instantaneous structures of the turbulent velocity field influence the motion of heavy particles (droplets), depending on their inertia. A convenient definition of the Stokes number goes here through the normalization with the Kolmogorov time scale: $St = \tau_p / \tau_\eta$. Particles of $St = \mathcal{O}(1)$ tend to correlate with certain eddy structures and this leads to the effect of preferential concentration, i.e. accumulation of particles in flow regions of low vorticity and high rate of strain (streams, convergence zones); cf. Eaton & Fessler (1994) for review. Studies reported in the literature include DNS of isotropic turbulence (Squires & Eaton 1991; Wang & Maxey 1993) as well as LES (Wang & Squires 1996).

The preferential concentration changes the physical picture of particulate flows in several ways: it affects the particle deposition on walls (Uijttewaal & Oliemans 1996); it leads to an increase of interparticle collision rates and, possibly, coalescence in a dense two-phase flow regime (Reade & Collins 2000); it influences the particle settling velocity in an external (gravity) field (Wang & Maxey 1993).

3.2. Quantifying preferential concentration

Various measures of preferential concentration have been established in the literature, cf. Hogan & Cuzzi (2001) for a comparative study and sensitivity tests with respect to the Reynolds number and bin size. Preferential concentration can be quantified by the PDF of particle number density based on bin counting, cf. Fig. 1(a). The distribution of particle number $n = N_{PC}$ per bin (or per cell), $f_B(n)$, will depend on St and on the bin size. For a random (uncorrelated) distribution of particles in the domain, the PDF is the discrete Poisson distribution, $f_P(n)$, with the parameter being the mean of the number density (exactly: the average number of particles per cell, $\langle N_{PC} \rangle$)

$$f_P(n) = \frac{e^{-\lambda}}{n!} \lambda^n, \quad \lambda = \langle N_{PC} \rangle. \quad (3.1)$$

A natural measure of the non-uniform particle concentration is the deviation of the actual (measured) number density from the random one (Wang & Maxey 1993):

$$\tilde{D} = \sum_{n=1}^{\infty} [f_B(n) - f_P(n)]^2. \quad (3.2)$$

Another measure of preferential concentration is

$$D = \frac{s - s_P}{\lambda} \quad (3.3)$$

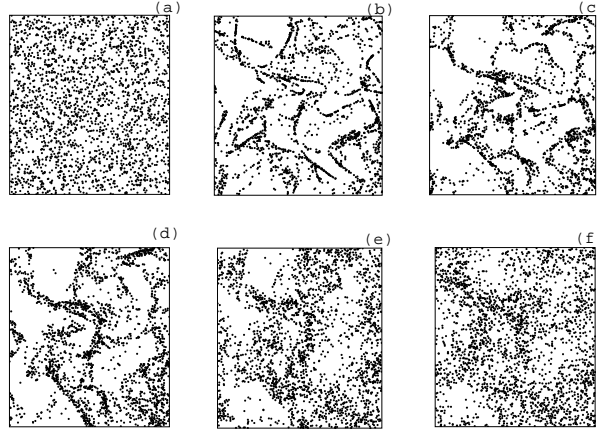


FIGURE 2. Snapshots of particle positions from DNS; runs with various values of the particle inertia parameter: a) $St = 0.01$, b) $St = 0.2$, c) $St = 0.7$, d) $St = 1$, e) $St = 2$, f) $St = 4$.

where s is the standard deviation of the actual number of particles per bin, and $s_P = \lambda^{1/2}$ is the standard deviation of the corresponding Poisson distribution; normally, $D \geq 0$.

Yet another possibility to quantify the non-uniform particle concentration comes from the two-point spatial distribution function. For a statistically isotropic and homogeneous system of particles, Reade & Collins (2000) introduced the radial distribution function (RDF) of particle location, $g(r)$, derived from the two-point RDF $f^{(2)}(r)$ where $r = |\mathbf{x}_2 - \mathbf{x}_1|$ for particles located at points \mathbf{x}_2 and \mathbf{x}_1 , cf. Fig. 1(b). Basically, $g(r)dr$ is the number of particles located in a spherical cell $(r, r+dr)$ around \mathbf{x}_1 , divided by the expected number of particles if their distribution were uniform, and averaged over first-particle locations \mathbf{x}_1 . The RDF is close to unity for a uniformly distributed particle system. Moreover, $g(r)$ can provide a clear estimation of the characteristic length scale of preferential concentration (if any).

3.3. DNS of particle-laden, forced isotropic turbulence

The DNS of forced isotropic turbulence at $Re_\lambda \approx 40$ has been undertaken on a 96^3 grid. The particle tracking has been performed in the DNS velocity field with the assumption of one-way momentum coupling. This has been done for a selection of particle inertia parameters (the Stokes number). The resulting snapshots of particle locations are shown in Fig. 2. As readily noticed, the preferential concentration of particles is most visible for $0.2 < St < 2$, in agreement with earlier observations of Squires & Eaton (1991).

The bin counting has been applied to particle locations in 3D with the bin size varying from the cell size of the DNS ($\Delta_{\text{bin}} = \Delta$) up to 1/6 of the domain size ($\Delta_{\text{bin}} = 32\Delta$). As evidenced by the profiles of f_B in Fig. 3, the random particle pattern (the Poisson distribution) is noticed for the smallest particles tracked ($St=0.01$) for all bin sizes. Also for the largest particles ($St=4$) the pattern is basically random, specially for smaller bin sizes. Intermediate-size particles tend to deviate most from the random distribution. As noticed from Fig. 3(d), the limit behavior for large $\langle N_{PC} \rangle$ (larger bins) is well reproduced, i.e. the Poisson distribution, Eq. (3.1), tends to the Gaussian PDF, $\mathcal{N}(\lambda, \lambda^{1/2})$.

For particles in isotropic turbulence, \tilde{D} computed from Eq. (3.2) is shown in Fig. 4(a); the profile of D , Eq. (3.3), is shown in Fig. 4(b). Both confirm the visual impression from Fig. 2 that the maximum of preferential concentration occurs for particles of $St = \mathcal{O}(1)$.

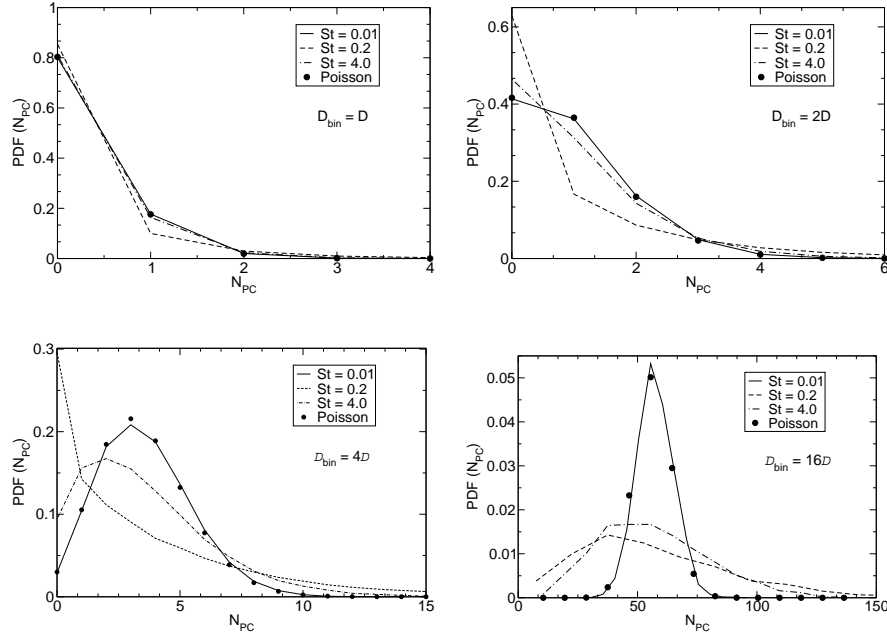
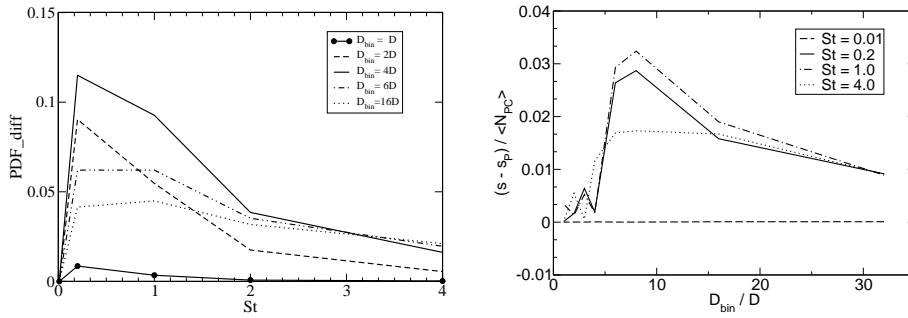
FIGURE 3. PDF of particle number density for different bin sizes: a) Δ , b) 2Δ , c) 4Δ , d) 16Δ .

FIGURE 4. Measures of preferential concentration: a) difference of PDFs of particle number density (actual and Poisson), Eq. (3.2); b) difference of standard deviations, Eq. (3.3).

To illustrate how the RDF $g(r)$ works in practice, we considered three simple, predetermined particle patterns in 3D (Fig. 5): random, ordered with a short length scale l , and ordered at a larger scale L (resulting in a checkered pattern). As quantified by the RDF in Fig. 6(a), neither random nor short-scale ordered pattern ($l < \Delta_{\text{bin}}$) exhibit any preferential concentration. For the checkered pattern ($L > \Delta_{\text{bin}}$), the non-uniformities are reflected in the RDF; moreover, the characteristic scale of the pattern ($\sim L$) is retrieved from the plot. Then, we repeated the procedure for the particles moving in the DNS flow field. The plots in Fig. 6(b) show a departure from the uniform (random) distribution of particle locations in space, most pronounced for $0.2 < St < 2$. The characteristic length scale of the pattern is about 10η .

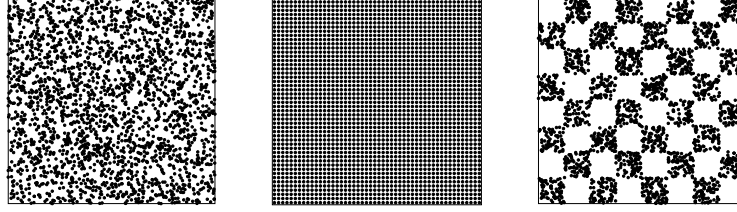
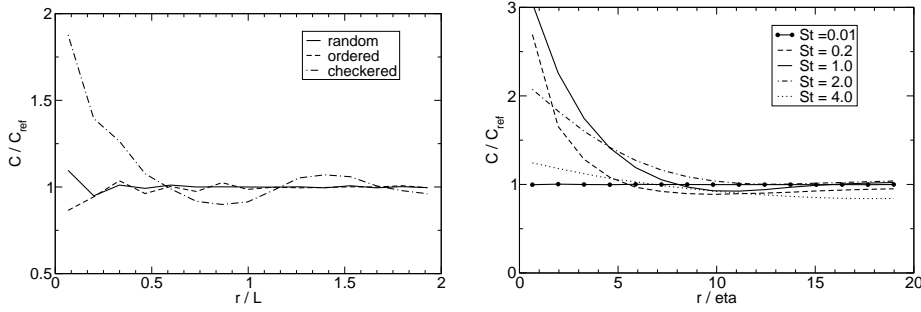
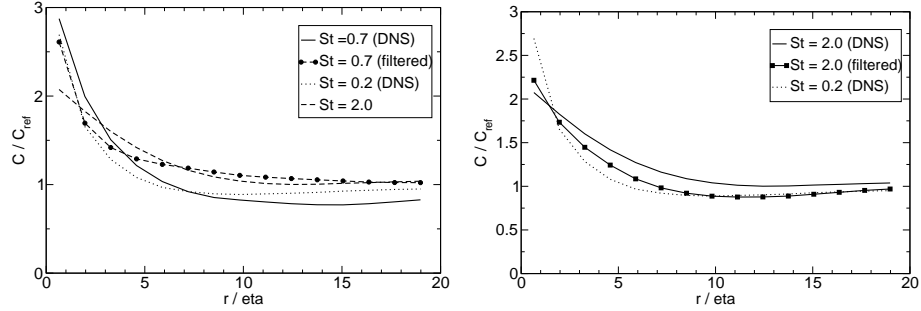


FIGURE 5. Tests for various particle arrangements: a) random, b) ordered, c) checkered.


 FIGURE 6. Particle radial distribution functions: a) pre-arranged pattern, b) DNS at $St = 1$.

 FIGURE 7. RDF of particles tracked in a filtered DNS field. (a) $St = 0.7$; (b) $St = 2.0$.

3.4. A priori tests of preferential concentration: particle tracking in filtered DNS field

To the best of the authors knowledge, the effect of LES filtering on preferential particle concentration has not been studied so far. An interesting finding results from an *a priori* test as follows. The instantaneous DNS velocity field has been filtered so that $k_{\text{filtered}} = 0.65k_{\text{DNS}}$. Then, the particles have been tracked in a smoothed velocity field. To determine the impact of smoothing on preferential concentration, the statistics of the particle number density in the physical space have been gathered. The pattern of preferential concentration is indeed modified by filtering. As noticed from the computed RDF of particle locations (Fig. 7), in filtered velocity field particles behave as though their effective Stokes number were larger; yet, short-scale correlations remain strong. This gives us some hint as to the construction of a FPT model. The snapshots of particle locations moving in the smoothed (LES-like) velocity field are shown in Figs. 8(b) and 9(b).

4. Reconstructing residual fluid velocity field along particle paths

4.1. Reasons behind FPT modeling

In LES, by definition of the method, a major part of the turbulent kinetic energy should be resolved (say, 80%, Pope 2000). Yet, this can be estimated only in simple cases where there is a DNS study at hand. For practically-relevant computations, the resolution often varies in space. The LES is known to face particular difficulties in wall-bounded flows, since the complete near-wall resolution becomes costly as the number of grid nodes scales roughly as $Re^{1.8}$ (cf. Pope 2000) and wall-modeling (or hybrid RANS/LES approach) is preferred. Also in this case, the SGS energy content may be considerable.

Regarding the LES of two-phase dispersed flows, several new issues appear. A concern about LES with the two-way coupling (of mass, momentum, energy) relates to the modeling of carrier phase source terms due to particles. Another concern, of importance here, is the impact of unresolved (subgrid-scale) flow quantities on particles: their dispersion, preferential concentration, deposition on walls. It can vary depending on the particle inertia parameter. In particular, for evaporating spray flow, the droplets unavoidably enter the size range where there is an impact from the flow SGS. In a numerical study of near-wall turbulence, Uijttewaalt & Oliemans (1996) pointed out to the significant deviation of their LES results on particle deposition on the wall with respect to reference data. The LES predicted the particle deposition coefficient to be one order of magnitude smaller than the value found in experiment and DNS. A probable reason was the insufficient resolution of near-wall eddies responsible for deposition of smaller particles, and a need of a model to account for subgrid scale effects on particles was suggested.

4.2. Requirements for a FPT model

To specify criteria of a good SGS dispersion model, let us start from the well-established case of single-phase LES. Arguably, a sound model for the SGS stress should simulate the effects of small eddies without altering the motion at large-eddy scales. For particle-laden turbulent flows, but still with the one-way coupling of mass, momentum, and energy (i.e., no evaporation/condensation, light loading, no heat transfer), a pre-requisite for a good SGS dispersion model, suitable for FPT, is that particle characteristics should remain close to those from a fully-resolved computation. They include the statistics of instantaneous particle locations (preferential concentration, if any), averaged locations (e.g., the r.m.s. particle position in line-source dispersion, the concentration profile in jet or mixing layer), and velocities (turbulent kinetic energy, Lagrangian velocity autocorrelation).

The constraints to be satisfied by a FPT model are: (i) in the limit of fully-resolved computation (LES becomes then DNS, $k_{sg} \rightarrow 0$), the model should have no effect on particle motion; (ii) in the limit of small particles ($\tau_p/\tau_f \rightarrow 0$) the model should boil down to the prediction of fluid diffusion; the velocity filtered density function approach (VFDF) of Gicquel *et al.* (2002) may possibly serve as the limit case to compare with; (iii) in the limit of large particles ($\tau_p/\tau_f \rightarrow \infty$) the model should have no short-time effect on particle motion; (iv) in the presence of external force field (gravity), the model should possibly take it into account; (v) in the limit of under-resolved velocity field (LES becomes then RANS, $k_{sg} \rightarrow k$), the particle turbulent dispersion should be fully modeled; (vi) for pairs of neighboring particles (located within the same cell or closer to each other than $\mathcal{O}(\Delta_f)$), the model should possibly account for relative dispersion effects.

Yet, we perceive the constraints (i)–(iii) as really important for FPT models in the context of LES. The effects of external fields (iv) are, apparently, not well known; the limit of RANS (v) is unlikely to be approached in real-life LES computations. Concerning

the relative dispersion issue (vi), it cannot be accounted for in the one-point approach that is of interest here because of computational efficiency.

An essential ingredient of FPT models is the residual kinetic energy, k_{sg} say. It determines the level of residual velocity fluctuations, also those “seen” by particles. In a particular test case considered here (forced isotropic turbulence), k_{sg} can readily be found from the DNS data (raw and filtered). In general case, the subgrid kinetic energy of the flow can be estimated from its transport equation. Wang & Squires (1996) and Sankaran & Menon (2002) recall the k_{sg} equation based on the Schumann non-equilibrium model.

4.3. Simple FPT model for locally homogeneous and isotropic turbulence

A reasonable assumption about LES is to consider the residual turbulent motion as locally homogeneous and isotropic. Then, the fluid velocity “seen” by particles is computed as $U_i^* = \tilde{U}_i(\mathbf{x}_p, t) + u_i^*$, i.e. the sum of the filtered LES velocity \tilde{U}_i interpolated at the particle location and the residual velocity “seen” by the particle.

Crucial ingredients of an FTP model are the SGS turbulent kinetic energy of the fluid and a SGS time scale. By analogy to modeling turbulent diffusion of fluid elements in the context of statistical (RANS) description (Pozorski & Minier 1999), we assume that \mathbf{u}^* is governed by the Langevin equation

$$du_i^* = -\frac{u_i^*}{\tau_L^*} dt + \sqrt{\frac{2\sigma_{\text{sg}}^2}{\tau_L^*}} dW_i \quad (4.1)$$

where σ_{sg} and τ_L^* stand for the respective velocity and time scales of residual motions “seen” by the particle; moreover, let τ_{sg} denote the time scale of residual motions. They are estimated from

$$\sigma_{\text{sg}} = \sqrt{\frac{2}{3}k_{\text{sg}}}, \quad \tau_L^* = f(\tau_{\text{sg}}, \tau_p, \sigma_{\text{sg}}/g), \quad \tau_{\text{sg}} = C \frac{\Delta_f}{\sqrt{\frac{2}{3}k_{\text{sg}}}}. \quad (4.2)$$

The model constant $C = \mathcal{O}(1)$ accounts for the uncertainty concerning the time scale of the residual velocity autocorrelation. The prediction $\tau_L^* = \tau_{\text{sg}}$ is expected to work well for small St (also in the limit case of fluid diffusion). For larger St, we tentatively propose an extension of the model for RANS particle dispersion (Pozorski & Minier 1999) drawing on the Csanady expressions to account for the crossing-trajectory effect. The time scale will now differ in the directions parallel and perpendicular to the relative velocity $\tilde{\mathbf{U}} - \mathbf{U}_p$

$$\tau_{L,||}^* = \frac{\tau_{\text{sg}}}{\sqrt{1 + \beta^2 \xi^2}}, \quad \tau_{L,\perp}^* = \frac{\tau_{\text{sg}}}{\sqrt{1 + 4\beta^2 \xi^2}} \quad (4.3)$$

where ξ is the normalized drift velocity determined from $\xi = |\tilde{\mathbf{U}} - \mathbf{U}_p|/\sigma_{\text{sg}}$. In the context of RANS, β is the ratio of Lagrangian to Eulerian time scales $\beta = T_L/T_E$; for SGS velocity field we assume $\beta = 1$.

In practical implementation, a discrete version of the model (unconditionally stable, first-order accuracy in time) becomes

$$u_i^{*(n+1)} = au_i^{*(n)} + b\xi_i \quad (4.4)$$

where $\Delta t = t^{(n+1)} - t^{(n)}$ is the time interval and ξ_i are random numbers from the standard Gaussian distribution, $\xi_i \in \mathcal{N}(0, 1)$. The coefficients a and b are given by the explicit solution of the stochastic differential equation (SDE), Eq. (4.1), with frozen coefficients

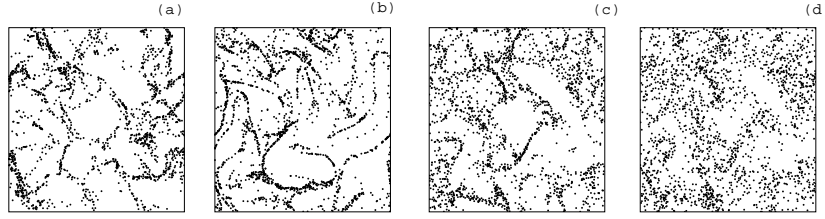


FIGURE 8. Snapshots of particle positions; runs for particles of $St = 0.7$. a) DNS; b) *a priori* LES with no FPT model; c) *a priori* LES with FPT model and $C=0$; d) with $C=0.05$.

over a time step Δt :

$$a = e^{-\Delta t/\tau_L^*}, \quad b = \sigma_{sg} \sqrt{1 - e^{-2\Delta t/\tau_L^*}}. \quad (4.5)$$

In the particular example of Eq. (4.1), which is a SDE with constant coefficients, the solution provided by Eqs. (4.4) and (4.5) is exact. However, the construction of higher-order numerical schemes for general (variable coefficients) SDEs remains an open issue.

Equation (4.4) can be further simplified to the Euler scheme

$$u_i^{*(n+1)} = \left(1 - \frac{\Delta t}{\tau_L^*}\right) u_i^{*(n)} + \sigma_{sg} \sqrt{\frac{2\Delta t}{\tau_L^*}} \xi_i. \quad (4.6)$$

Yet, in contrast to formulation (4.4)–(4.5), discretization (4.6) does impose a time step restriction $\Delta t < \tau_L^*$ because of stability concerns.

It may be interesting to note that in the limit of $\Delta t \gg \tau_L^*$ the scheme (4.4) boils down to generating a series of independent successive velocities \mathbf{u}^* , i.e.

$$\mathbf{u}^{*(n+1)} = \sigma_{sg} \boldsymbol{\xi}. \quad (4.7)$$

However, for a physically-consistent use of Eq. (4.7), it is imperative that the time intervals for generating a series of independent velocity realizations be $2\tau_L^*$ in order to preserve the correlation time scale (cf. Pozorski & Minier 1998).

4.4. First results of the FPT model

We have tested the FPT model (4.1) in *a priori* LES computations of forced isotropic turbulence for the same conditions as those described in Sec. 3.3. The computational results for two values of the Stokes number and some choices of the model constant are shown in Figs. 8 and 9. The impact of the residual velocity field, reconstructed in FPT, is readily noticed. As expected, the one-point stochastic model introduced here has a “randomizing” effect on particle locations. For particle sizes larger than that of maximum preferential concentration effect (roughly $St \approx 1$ in our case) the randomizing effect of small scales is lost (the picture of preferential concentration becomes overly sharp), so the model is meant to restore it, cf. Fig. 9. In the case of smaller particles that are most influenced by smaller eddies and correlated on a shorter length scale, it is shown in Fig. 8 that the filtering does an inverse effect, i.e. it partly kills this short-scale preferential concentration (the picture of preferential concentration becomes somewhat “blurred”), so a potentially successful model for this case should rather be of an “antidiffusive” character (arguably, scale-similarity arguments can be used for its construction).

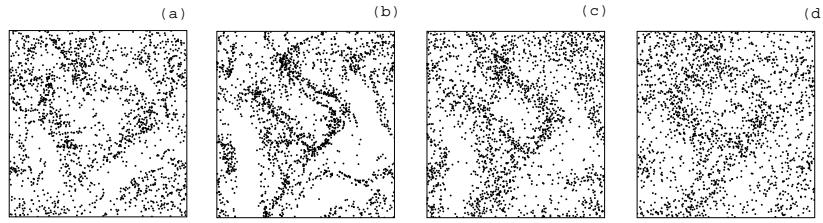


FIGURE 9. Snapshots of particle positions; runs for particles of $St = 2$. a) DNS; b) *a priori* LES with no FPT model; c) *a priori* LES with FPT model and $C=0.05$; d) DNS for $St = 4$.

5. Conclusion and future plans

In the present paper, we have shown the impact of LES filtering on particle motion in turbulent flows. In particular, the particle preferential concentration patterns change. A stochastic model has been proposed to reconstruct the residual velocity field along particle trajectories. First results with the model seem encouraging. A lingering question as to FPT is that it is only a single-realization (one-particle) approach. The statistical interpretation of the model has to be thought over, also in the context of parcels (representing many solid particles). Further developments are warranted for more general flow fields. Arguably, an improved model should consist of a random ingredient (since the details of residual fluid motion are unknown) and possibly also of a deterministic ingredient, dependent on the structure of the resolved field and justified by the hope that the largest unresolved scales are in a sense similar to resolved ones.

A further-term objective is to unify the LES/FPT approach for the dispersed flows, presented above, with the LES/FDF approach for flows with scalars, possibly reactive, developed by Colucci *et al.* (1998). This should ultimately provide a physically-sound, yet efficient, tool for the computation of dispersed turbulent two-phase flows with chemical reactions (spray combustion). In this formulation, the vector of stochastic variables associated with particles will include \mathbf{x}_p , \mathbf{U}_p , \mathbf{U}^* , d_p , T_p , and chemistry-related quantities.

Acknowledgments

We wish to thank Frank Ham and Olivier Desjardins for their assistance. We are grateful to Professor John Eaton for his insightful comments on the manuscript.

REFERENCES

- APTE, S. V., MAHESH, K., MOIN, P. & OEFELEIN, J. C. 2003 LES of swirling particle-laden flows in a coaxial-jet combustor. *Int. J. Multiphase Flow* **29**, 1311–1331.
- ARMENIO, V., PIOMELLI, U. & FIOROTTO, V. 1999 Effect of the subgrid scales on particle motion. *Phys. Fluids* **11**, 3030–3042.
- BAGCHI, P. & BALACHANDAR, S. 2003 Effect of turbulence on the drag and lift of a particle. *Phys. Fluids* **15**, 3496–3513.
- BOIVIN, M., SIMONIN, O. & SQUIRES, K. D. 2000 On the prediction of gas-solid flows with two-way coupling using large eddy simulation. *Phys. Fluids* **12**, 2080–2090.
- BURTON, T. M. & EATON, J. K. 2003 Fully resolved simulations of particle-turbulence interaction. *Rep. No. TSD-151*, Dept. of Mech. Engng., Stanford University.
- COLUCCI, P. J., JABERI, F. A., GIVI, P. & POPE, S. B. 1998 Filtered density function for large eddy simulation of turbulent reacting flows. *Phys. Fluids* **10**, 499–515.

- EATON, J. & FESSLER, J. R. 1994 Preferential concentration of particles by turbulence. *Int. J. Multiphase Flow* **20**, Suppl., 169–209.
- FOX, R. O. 2003 *Computational Models for Turbulent Reacting Flows*. Cambridge University Press.
- GICQUEL, L. Y. M., GIVI, P., JABERI, F. A. & POPE, S. B. 2002 Velocity filtered density function for LES of turbulent flows. *Phys. Fluids* **14**, 1196–1213.
- HOGAN, R. C. & CUZZI, J. N. 2001 Stokes and Reynolds number dependence on preferential particle concentration in simulated 3D turbulence. *Phys. Fluids* **13**, 2938–2945.
- MACINNES, J. M. & BRACCO, F. V. 1992 Stochastic particle dispersion modeling and the tracer-particle limit. *Phys. Fluids A* **4**, 2809–2824.
- MASHAYEK, F. & PANDYA, R. V. R. 2003 Analytical description of two-phase turbulent flows. *Prog. Energy Combust. Sci.* **29**, 329–378.
- MAXEY, M. R. & RILEY, J. J. 1983 Equation of motion for a small rigid sphere in a nonuniform flow. *Phys. Fluids* **26**, 883–889.
- MINIER, J. P. & PEIRANO, E. 2001 The PDF approach to turbulent polydispersed two-phase flows. *Phys. Reports* **352**, 1–214.
- MINIER, J. P., PEIRANO, E. & CHIBBARO, S. 2004 PDF model based on Langevin equation for polydispersed two-phase flows applied to a bluff-body gas-solid flow. *Phys. Fluids* **16**, 2419–2431.
- OKONG'O, N. A. & BELLAN, J. 2004 Consistent large-eddy simulation of a temporal mixing layer laden with evaporating drops. Part 1. Direct numerical simulation, formulation and *a priori* analysis. *J. Fluid Mech.* **499**, 1–47.
- POPE, S. B. 2000 *Turbulent Flows*. Cambridge University Press.
- POZORSKI, J. & MINIER, J. P. 1998 On the Lagrangian turbulent dispersion models based on the Langevin equation. *Int. J. Multiphase Flow* **24**, 913–945.
- POZORSKI, J. & MINIER, J. P. 1999 PDF modeling of dispersed two-phase turbulent flows. *Phys. Rev. E* **59**, 855–863.
- READE, W. C. & COLLINS, L. R. 2000 Effect of preferential concentration on turbulent collision rates. *Phys. Fluids* **12**, 2530–2540.
- REEKS, M. W. 1992 On the continuum equations for dispersed particles in nonuniform flows. *Phys. Fluids A* **4**, 1290–1303.
- SANKARAN, V. & MENON, S. 2002 LES of spray combustion in swirling flows. *J. Turbulence* **3**, art. no. 011.
- SEGURA, J. C., EATON, J. K. & OEFELEIN, J. C. 2004 Predictive capabilities of particle-laden LES. *Rep. No. TSD-156*, Dept. of Mech. Engng., Stanford University.
- SIMONIN, O. 1996 Eulerian numerical approach for prediction of gas-solid turbulent two-phase flows. *Von Karman Institute Lecture Series*, Rhode-St-Genèse, Belgium.
- SQUIRES, K. D. & EATON, J. K. 1991 Preferential concentration of particles by turbulence. *Phys. Fluids A* **3**, 1169–1178.
- STOCK, D. E. 1996 Particle dispersion in flowing gases. *J. Fluids Engng.* **118**, 4–17.
- UIJTTEWAALL, W. S. J. & OLIEMANS, R. V. A. 1996 Particle dispersion and deposition in DNS and LES of vertical pipe flows. *Phys. Fluids* **8**, 2590–2604.
- WANG, L. P. & MAXEY, M. R. 1993 Settling velocity and concentration distribution of heavy particles in homogeneous isotropic turbulence. *J. Fluid Mech.* **256**, 27–68.
- WANG, Q. & SQUIRES, K. D. 1996 Large eddy simulation of particle-laden turbulent channel flow. *Phys. Fluids* **8**, 1207–1223.

Toward the development of a LES-SGS closure model for buoyant plumes

By S. R. Tieszen [†], H. Pitsch, G. Blanquart AND S. Abarzhi

LES simulations of a helium plume based on a dynamic Smagorinski closure model show very strong grid dependency. The authors interpret these results as the inability of diffusive, eddy-viscosity closure models to capture the growth of Rayleigh-Taylor (RT) instabilities, which develop at the plume-air interface, create thin finger-type structures, and lead eventually to strong mixing of air and helium. To capture the RT mixing and to achieve grid independent results, unreasonably high grid densities are required. Our motivation is therefore to develop subgrid models, which could reproduce the robust effect of the RT mixing on the plume dynamics, without having to capture the details of dynamics at small-scales. Preliminary results from a developed model highlight difficulties and suggest directions for future study.

1. Introduction

1.1. Motivation and Objectives

This study is motivated by the need to simulate large, turbulent, reacting plumes, i.e., fires. For fully turbulent fires, the ratio between the height and diameter is on the order of $O(2)$ (Drysdale 1999). Therefore, significant turbulent mixing occurs within the first diameter of a fire. Understanding and predicting this mixing is critical to modeling a fire. Subgrid combustion and soot models are critically dependent on relevant scalar fields and subgrid mixing rate estimates. These models in turn strongly affect the density field and the fields for effective radiative properties. The radiative properties strongly affect heat transfer to fuel sources that sustain the fire. Fundamentally, reactive scalars couple to momentum through three primary pathways, the momentum source term through variable density, advection through dilatation via the continuity condition and the density, and diffusion through changes in viscosity. While all three couplings are present in all reacting flows, fires, as reacting plumes, are very strongly affected by the source term coupling. Due to its importance, it is of interest to study the source term coupling independently from the other couplings. The effects of variable density can be achieved through species alone. In a fire, peak density ratios between reaction zone products and ambient air are of $O(7)$. The density ratio of helium and air is of the same order. For this reason, an iso-thermal helium plume will be used to assess subgrid model requirements to capture the momentum source term coupling for buoyant plumes. The scope of this study is limited to a comparison with experimental data from O'Hern *et al.* (2004) for a 1 meter diameter helium plume.

1.2. Literature Review

Relatively few numerical studies are specifically focused on the near source region of plumes. One reason for this lack of studies is that, until recently, there has been very

[†] Sandia National Laboratory

little plume data available to compare with simulations. Much of the plume literature has focused on the rate at which a plume will become self-similar (elevation/diameter $\gg 2$) and thus is not relevant to the current study. Further, much of the data is derived from buoyant jets that are buoyant in the far field but momentum dominated in the near source region. In addition to the one meter diameter study used here, transient laminar data are available from Cetegen 1997 and data from a moderately turbulent buoyant plume ($Ri = 2.6$, $Re = 291$) are available from Mell 2001.

The most relevant numerical study of the near source region of non-reacting buoyant plumes is the LES study of DesJardin *et al.* 2004. This study demonstrated significant grid dependency of the results with the use of a dynamic Smagorinski model, and concluded that the best results were obtained with the model turned off. The nature of the turbulence was not identified, but it was suggested by the authors that the under-resolution of the sharp density gradients could result in an underprediction of vorticity in the plume. A study by Tieszen *et al.* 2004 using temporally filtered equations with a narrow temporal filter width (relative to the puffing frequency) and a modified $k - \epsilon$ closure model also showed strong grid dependency. The strong grid dependency resulting from these studies clearly indicates that dissipative, eddy viscosity type closures are insufficient descriptions of the turbulent mixing process. LES studies have also been conducted on reacting plumes, i.e., fires, (Xin *et al.* 2002; Mell *et al.* 1996; Tieszen *et al.* 1996). Mell *et al.* 1996 notes that in addition to hydrostatic (gravitational) production of vorticity, hydrodynamic production is also important to capture the puffing behavior. Results from all the above mentioned studies indicate that the puffing frequency is determined by large scale phenomena since it can be captured with relatively coarse gridding. However, simulations by DesJardin *et al.* 2004 and Tieszen *et al.* 2004 of a 1 meter diameter helium plume indicate that relatively small-scale, but essentially non-dissipative, turbulent structures can significantly affect the mean flow field.

The above mentioned studies all use primarily dissipative turbulence closure models. While a number of closure models have been developed in the general LES community that capture more physics than just dissipation, these models primarily capture the off-diagonal stresses at the filter cut-off. To the authors' knowledge, no buoyancy specific non-dissipative models have been developed. The LES community has included buoyant production of turbulence in terms of an enhanced eddy viscosity, see for example Eidson T. M. 1985 and Canuto V. M. 1994. Reynolds averaged closure models that include buoyancy also have included it only as an enhanced eddy viscosity (see for example Nicolette, *et al.* 2004). Clearly there is a need for the development of a buoyant turbulent model that captures key non-dissipative physics.

It is well known that the near source region of plumes and fires are dominated by puffing (Cetegen & Ahmed 1993). The nature of the instability (absolute or convective) that results in puffing is a matter of some discussion (Tieszen 2001). Recent studies strongly argue that, while complicated, the instability is absolute (Soteriou *et al.* 2002). Previous studies on both Rayleigh-Taylor (RT), (Duff *et al.* 1962; Dimonte & Schneider 2000; Debacq *et al.* 2001) and Kelvin-Helmholz (KH) (Wang 1984) instabilities are relevant to the current study. The helium plume entering vertically into air in earth's gravity field can be thought of as a classical RT problem with the complications of finite boundary conditions. The finite boundary conditions give rise to the coherent vertical plume; the large scale dynamics of which are dominated by puffing.

The current study employs a well established LES code to compare with helium plume experimental results. The comparison is described in the next section. The dynamics of

the turbulence are subsequently discussed, from which subgrid modeling approaches and requirements are derived. The relevance of the helium plume to fires is discussed and conclusions are drawn in the final section.

2. Data and LES Comparisons

2.1. Experimental and Numerical Details

The two-dimensional data available from O'Hern *et al.* (2004) consists of Favre-averaged vertical and horizontal velocities, density, and an estimate of the turbulent kinetic energy on a planar surface passing through the centerline of the 1 meter diameter helium plume source. The lower boundary of the data plane is just above the surface of the source and the upper boundary of the plane is about 0.75 meters above the source. The sides of the plane extend just beyond the plume source to capture edge entrainment into the plume. The laser sheet width is 8 mm. The velocity data are acquired through Particle Image Velocimetry (PIV) and the density data through Planar Laser Induced Fluorescence (PLIF). The inlet plume velocity is 0.34 m/s and the molecular weight of the plume is 5.42 g/mol (due to trace gases required for the PLIF). The plume is issued into air. The temperature is 291 K with an ambient pressure of 82 kPa. Details of the experimental geometry can be found in O'Hern *et al.* (2004). Data uncertainties are: for density $\pm 18\%$ of the difference between plume and air density, $\pm 5\%$ of the air density, velocities $\pm 20\%$, and the turbulent kinetic energy $\pm 30\%$.

The current study uses an energy preserving, low mach number LES code (Pierce 2001; Pierce & Moin 2004), unlike the compressible formulation of DesJardin *et al.* 2004 that uses pressure gradient scaling to make the solution affordable, or the non-energy preserving numerics of Tieszen *et al.* 2004. Further, the current study uses a cylindrical formulation of the governing equations on a structured mesh unlike the structured Cartesian solutions of (DesJardin *et al.* 2004) and CVFEM Cartesian solutions of (Tieszen *et al.* 2004). Open boundaries are used except for the floor and inlet. The inlet treatment also differs from the previous studies in that the flow in the diffuser is not specified as a Dirichlet condition, but allowed to develop (ignoring the presence of a honeycomb at the exit).

2.2. Grid Sensitivity Results

For grid sensitivity studies, a dynamic Smagorinsky model was used to close the momentum equations. A mixture fraction equation was solved for the helium mass fraction. Its closure model consists of a gradient-diffusion assumption. Since previous studies showed strong mesh sensitivity, simulations were conducted with three mesh densities. A coarse mesh of nominally 250 K nodes (r, θ, z : $52 \times 64 \times 80$), a medium mesh of nominally 1 M nodes (r, θ, z : $104 \times 64 \times 160$), and fine mesh of nominally 4 M nodes (r, θ, z : $208 \times 64 \times 320$).

Fig. 1 shows contours of plume density at an instant in time. The transient results are time averaged after a quasi-steady puffing mode has been achieved. The time-averaged results are shown in Fig. 2 through 5. Figure 2 shows the time-averaged density contours. As the mesh density is increased from 250 K to 1 M to 4 M, more air is mixed into the plume, increasing the centerline density. Comparing the centerline density between the simulations and the data, a monotonic trend is seen, in which the results of the simulation approach the data as the mesh density is increased.

As seen in Fig. 3, an over-prediction of the centerline vertical velocity occurs for under-resolved meshes. However, as the mesh density is increased the results of the simulation

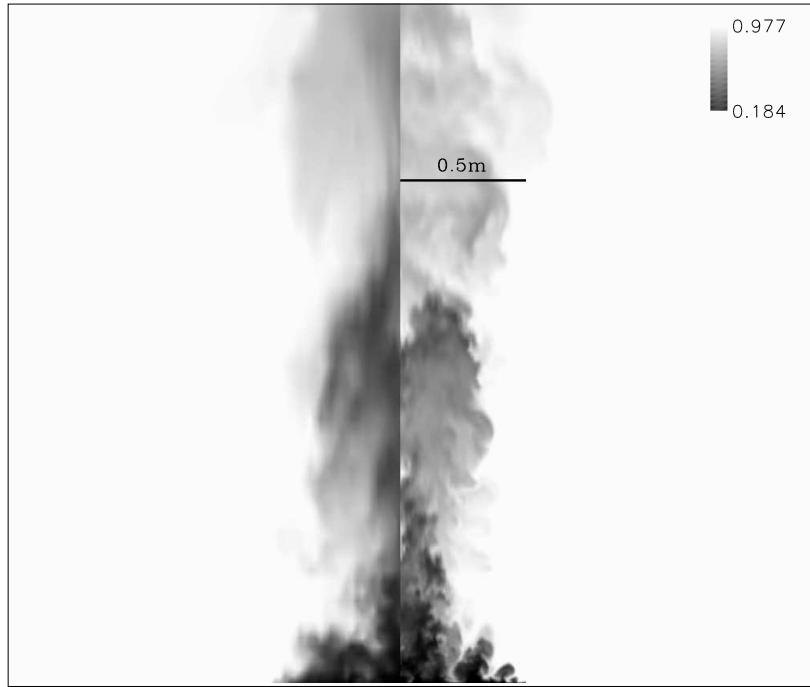


FIGURE 1. Density Contours for a Typical Time Plane. Left Side - 250 K node simulation.
Right Side - 4 M node simulation.

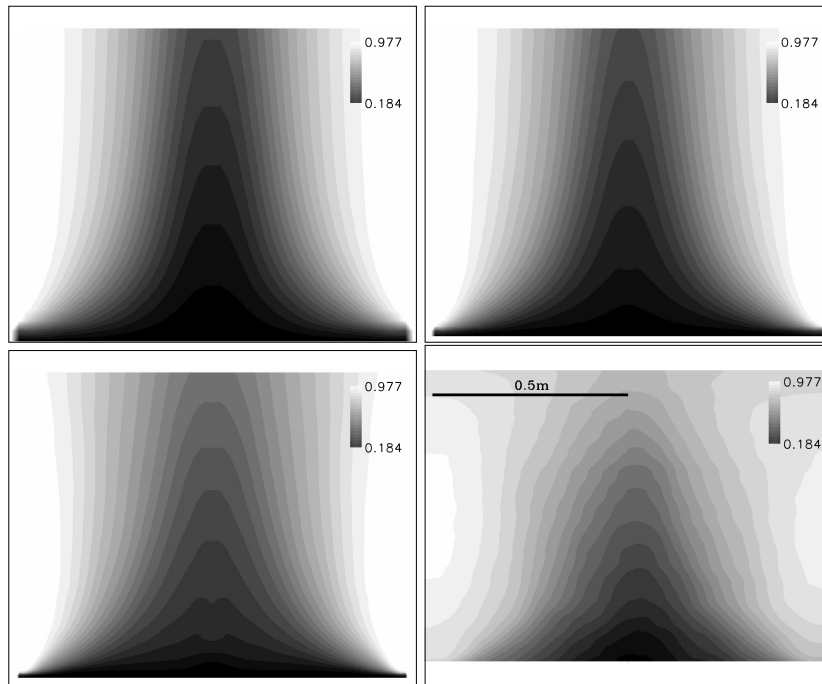


FIGURE 2. Density. Comparison between data (lower right) and simulations with 250 K (upper left), 1 M (upper right) and 4 M nodes (lower left).

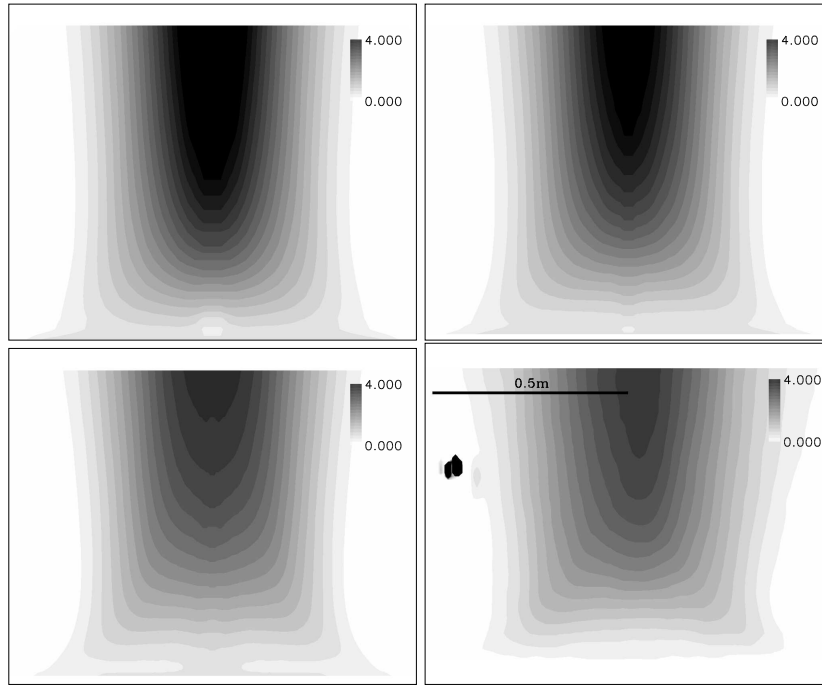


FIGURE 3. Vertical velocity (m/s). Comparison between data (lower right) and simulations with 250 K (upper left), 1 M (upper right) and 4 M nodes (lower left).

approach the data. The centerline velocity overshoot is consistent with the centerline density undershoot at a given mesh density. Both indicate that there is not enough scalar mixing occurring within the plume for the under-resolved simulations. Figure 4 shows the horizontal velocity contours for the simulations and the data. The radial velocity shows relatively little sensitivity to mesh density. This result is somewhat surprising, since continuity must be preserved and there is a relatively large difference in the vertical centerline velocities with mesh density. Comparing Fig. 4 with Fig. 2, it can be seen that the peak velocities occur in a region of high density gradients and the small changes in the locations of the velocity peaks can account for the lack of large changes in the velocity magnitude with grid density. Figure 5 shows the turbulent kinetic energy for the simulations and the data. Since only two-dimensional PIV data was experimentally available, an assumption was made in data processing that the out-of-plane horizontal velocity fluctuations are equal to the inplane horizontal velocity fluctuations. To be consistent, the numerical simulation data is processed in the same fashion. The under-resolved simulations result in too much turbulent kinetic energy along the centerline. Since the turbulent kinetic energy is dominated by the large scale puffing phenomena, this result indicates that the puffs are too strong. A lack of mixing also accounts for this result in that the velocities are too high, and the plume is too coherent. As with the mean statistics, the simulation results approach the data monotonically as the mesh density is increased. The choice of a cylindrical formulation also results in a small artifact along the plume centerline.

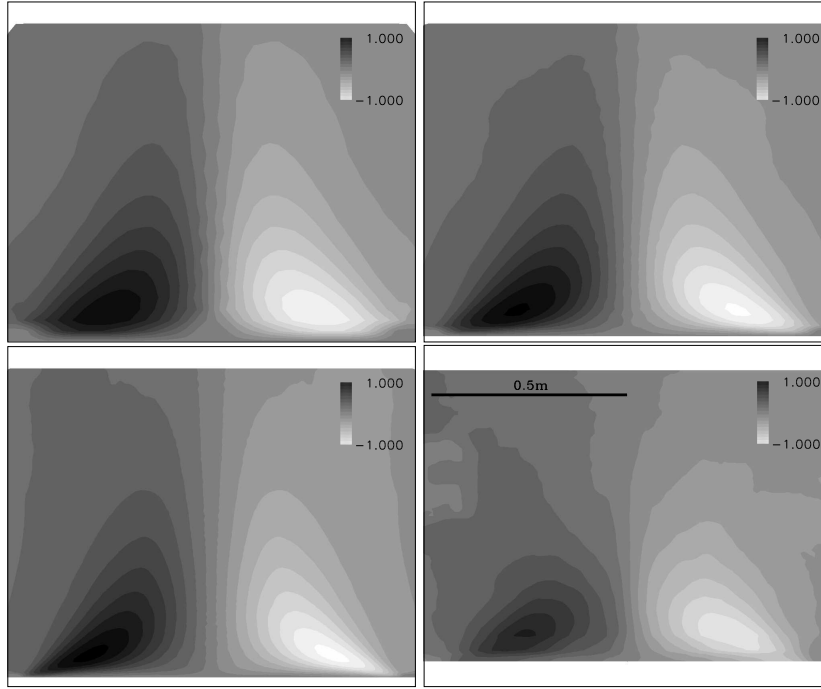


FIGURE 4. Horizontal velocity (m/s). Comparison between data (lower right) and simulations with 250 K (upper left), 1 M (upper right) and 4 M nodes (lower left).

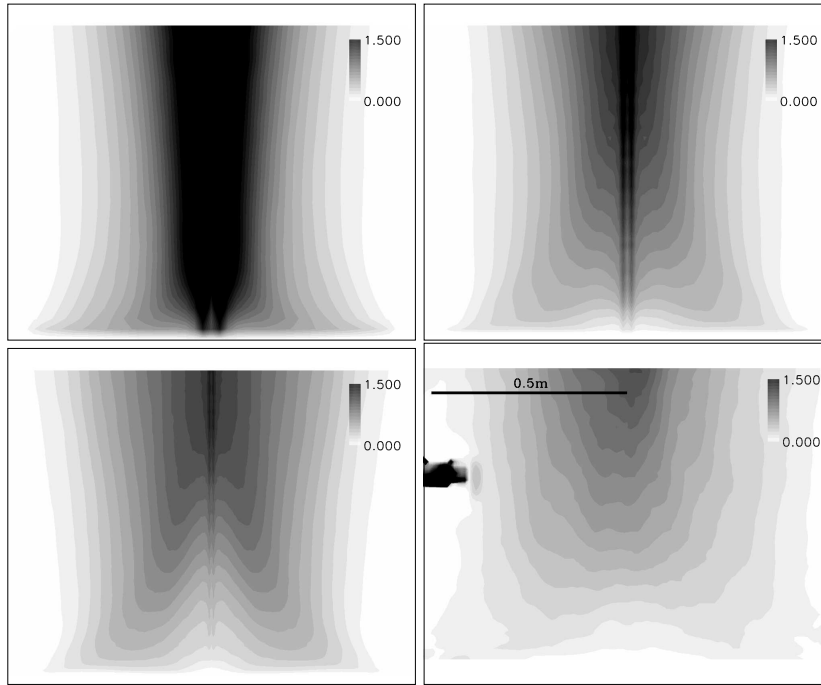


FIGURE 5. Turbulent Kinetic Energy (m^2/s^2). Comparison between data (lower right) and simulations with 250 K (upper left), 1 M (upper right) and 4 M nodes (lower left).

3. Turbulent Dynamics and Subgrid Model Requirements

3.1. Near Plume Source Laminar Instability Dynamics

The grid refinement study compares favorably with the results of DesJardin *et al.* 2004 and Tieszen *et al.* 2004. All studies used different numerics, but all of them use only diffusive, eddy-viscosity type turbulence closure models and all show similar results with strong grid dependencies. The results suggest that the under-resolved turbulent structures are doing more than just dissipating energy. Scalar mixing is clearly being affected in a manner which significantly alters the time-averaged statistics. As the grid is refined, more of the mixing is picked up by the increased grid resolution, resulting in more mixing in the plume. Thus, simple dissipative closures like the dynamic Smagorinski model are not capturing the turbulence mechanisms that result in the mixing for this plume. In order to postulate a model that can capture the mixing physics, it is necessary to understand the mechanisms which govern mixing in the near field of a plume.

Based on the phenomenological arguments, simulations results, and the transient data, an argument can be made that the mixing mechanism that is not being resolved with coarser grids is the growth of Rayleigh-Taylor instabilities. In a buoyancy dominated flow, it is the density difference between the plume and the surroundings that is the driving force for the flow, as can be seen in the time-averaged simulation results. As the simulation results approach the correct density profile with increased grid resolution, all velocity and turbulence statistics approach the data. These results suggest that resolving the circulation evolution is sufficient to resolve the flowfield. A circulation evolution equation, derived from the vorticity transport equation, (Najm *et al.* 1998) is given by

$$\frac{d}{dt}\Gamma = \int_A dA \cdot \left[\frac{1}{\rho} \nabla \rho \times \left(\frac{1}{Fr} g - \frac{D\mathbf{v}}{Dt} \right) + \frac{1}{Re} \frac{\nabla \times \Phi}{\rho} \right]. \quad (3.1)$$

The right hand side of Eq. 3.1 is the motive force for circulation. It implies that it is not necessary to resolve the density gradients to capture the evolution of circulation. It is only necessary to capture density differences normal to the local acceleration field. In other words, for a given discretization, if the cell density is correct for each cell, then the true subgrid density distribution need not be known for circulation to be properly represented. The key is to resolve spatial density fluctuations at the scale they occur. Note that scalar fields are a result of the time history of the flow field, not just the local instantaneous turbulence intensities.

Scalar structures exist across a broad range of scales in a plume. The largest scalar structures are the large toroidal puffs that characterize all plumes, as seen in Figure 1. These large scalar structures are the consequence of the vorticity generated at the edge of the plume and grow from relatively small eddies near the toe of the plume due to the persistency of the density gradient at the plume edge. Figure 6 shows distinct scalar structures that are a result of the mixing caused by the growth of laminar instabilities in the near source region of the flow. The helium bubble and air spike structures will continue to grow until they are rolled up into the large toroidal eddies as part of the puff cycle. A consequence of these dynamics is that air from the RT bubbles and spikes gets swept into the centerline early in the plume development.

The relevant scale of the RT instability can be estimated on the basis of dimensional grounds (Duff *et al.* 1962) which suggests

$$\lambda = \left(\frac{D^2}{Ag} \right)^{\frac{1}{3}} \quad (3.2)$$

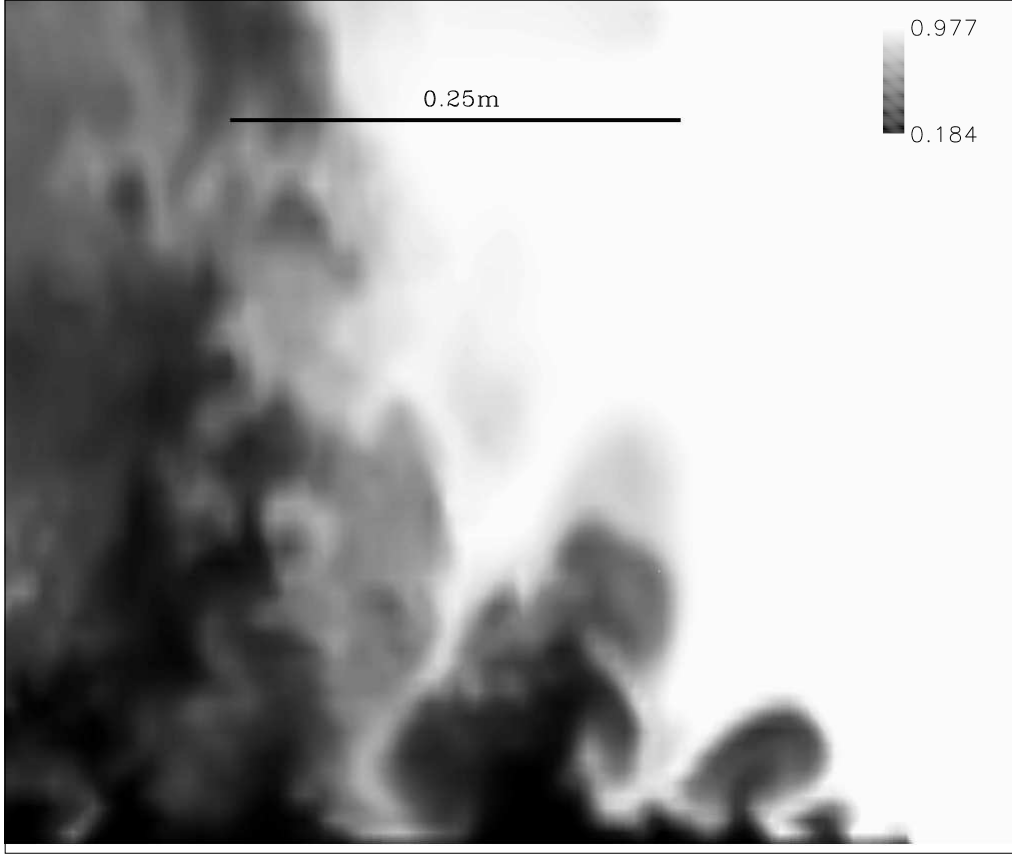


FIGURE 6. Density Contours Near the Plume Source showing Rayleigh-Taylor Bubbles and Spikes. 4 M node simulation results.

where D is the diffusion coefficient between the plume and air, A is the Atwood number (density difference divided by density sum), and g is gravity. For the helium plume (molecular weight = 5.42 g/mol), the Atwood number is 0.685 and D is approximately $7.1 \times 10^{-5} \text{ m}^2/\text{s}$. For these conditions, the fastest growth mode is $O(\text{mm})$. Equation 3.2 is for unforced growth. The scale can be different if the flow is forced, as is possible with all the turbulent instabilities present in the helium plume. The experimental images suggest that the actual air spikes are more like $O(\text{cm})$ wide and somewhat laminar in nature.

RT studies show that in the nonlinear phase of the instability, the amplitude growth is dominated by the characteristic width of the RT structures, i.e. by the horizontal length scale, and it is linear with time (compared to the square of time for turbulent flow dominated by vertical length scales). The amplitude can be approximated by

$$H = \frac{t}{2} \sqrt{gL} \left(\sqrt{\frac{2A}{1+A}} + \sqrt{\frac{2A}{1-A}} \right), \quad (3.3)$$

where t is the growth time and L is the characteristic width of the RT structures, (Di-monte & Schneider 2000).

Dynamically, the RT structures form during the phase of the puff cycle when there is air over the top of the rising helium plume. This phase of the cycle occurs after the large

coherent vortices associated with a puff pull air in over the top of the helium and begin to advect away. As the helium moves into the air, the classical bubble and spike structure begins to form. While the width of the air spikes remains $O(\text{cm})$, the persistence of the density difference between the upward rising bubbles and the downward sinking spikes results in a scalar field in which the scalar structures are much taller than the scale of the laminar instability that creates them. As a first approximation, it can be considered that RT instability persists for about $1/2$ the puff cycle period. The puffing period for this plume is 0.7 seconds based on O'Hern *et al.* (2004), so t can be taken as approximately 0.35 seconds. Using 1 cm as the characteristic width of the RT structure, the height of the structure can reach $O(15 \text{ cm})$ according to Eq. 3.3. This distance is consistent with the structures shown in Fig. 6. The RT growth period ends when vortices formed at the edge of the plume grow strong enough to result in the radial indraw of air. This indraw temporarily cuts off the helium and advects the RT structures up into the core of the plume. The cycle then repeats itself.

The Ph.D. thesis of Wang 1984 is also relevant to the current study. Wang studied curved shear layers with various density ratios. A close comparison of Fig. 2 and 3 shows that there is not a strong velocity difference across the path of strongest density gradient. Hence the Kelvin-Helmholtz instability is not strong for this flow. However, the flow transitions from nearly horizontal to nearly vertical with a mean velocity of $O(2 \text{ m/s})$. Given a radius of curvature of approximately a plume radius, the centripetal acceleration is on the same order as gravity. The heavy fluid, air, is on the inside of the curved interface with the light fluid, helium, on the outside of the curved interface. Wang 1984 shows experimentally under similar conditions that the RT instability dominates the mixing.

3.2. Model Development Paths

From these arguments, it can be concluded that it is necessary to build LES closure models that can capture the effect of mixing by the persistent growth of density gradient driven laminar instabilities. It is likely that grid independent DNS can be achieved for this plume if grid densities of $O(\text{mm})$ can be achieved, i.e., $O(10^9)$ node simulations. As the grid resolution is decreased, more and more of the mixing effects have to be modeled. From the results of the current study, it may be possible to achieve grid independent results if a scalar reconstruction method is used to ensure that the density in the spikes is preserved for meshes > 4 million nodes. If the mesh resolution is to be less than several million nodes, it will be necessary to include the effect of mixing due to the spikes, without actually capturing the spike dynamics. Visualization of the more coarsely refined meshes from this study indicated that the spikes were not present (see Fig. 1). This observation is consistent with the time-averaged plume density being too low along the centerline due to lack of air entrainment.

A model form was selected by dimensional and phenomenological reasoning with the intent of capturing the mixing effects of the bubble and spike structure without resolving the dynamics. It is assumed that the dynamic Smagorinski model is sufficient for capturing the standard turbulent subgrid stresses, but to capture the transient laminar growth of RT instabilities an additional closure model would be required. Seen from a grid resolved level, RT instability induced velocities would appear as spatial fluctuating velocities that are driven by density gradients in a gravitational field. Self-correlation would occur in the direction of the RT spike (vertical in the current study) resulting in a single additional term in the gradient of the Reynold stresses that required closure. Using the vertical density gradient and gravity as a measure of the additional unresolved

vertical stress, results in

$$\text{RT Stress Closure Model} = -\frac{\partial}{\partial x_j} \left(f^2 g_k \frac{\partial \rho}{\partial x_k} e_i e_j \right) \quad \text{where} \quad e_i = \frac{g_i}{|g|} \quad \frac{\partial \rho}{\partial x_k} \geq 0 \quad (3.4)$$

where the directional indices permit only the components aligned with the gravity vector. For positive density gradients, this model results in a spreading force along the helium air interface intending to mimic the growth of the bubble and spike structure. The model has the strongest effect where the density gradients are strongest, scaled by the strength of gravity.

A limited investigation was performed with this model. Unfortunately, with a constant near unity the model effect was not sufficiently strong. Due to time limits other scalings were not tried. Possible improvements could include scaling with the Atwood number in addition to gravity, using horizontal instead of vertical gradients, or to attempt to correct for the fact that on coarse meshes, the density gradient used in the model is under-resolved.

4. Discussion and Conclusions

4.1. Relevance to Fires

The objective of both the experiments and simulations was to evaluate the coupling between the momentum source term and scalar fields in a flow relevant to fires. By studying non-reacting helium, both the scalar and momentum fields can be measured and the complications of combustion, soot formation, and radiation are avoided. As noted in the introduction, there are additional couplings in fires beyond the momentum source term coupling. Also, there are important differences between the helium plume and a reacting fire for the momentum source term. In the plume, the strongest gradients are at the base of the plume, and the mean driving force decreases with elevation as shown in Fig. 2. However, in a fire the gradients are not strongest between fuel and air but hot products and air, and the mean driving force first increases with elevation until the elevation of maximum combustion and then decreases. Most hydrocarbon fuel vapors are actually heavier than air and under these conditions, the fuel vapor is stably stratified. It is the high temperature products that are not stably stratified and will show the development of RT instabilities. Thus, for heavier than air fuels, the fuel core (or vapor dome as it is sometimes referred to) will not necessarily be subject to RT bubbles and spikes like the helium plume.

Equations 3.2 and 3.3 suggest that as the Atwood number gets smaller (i.e., smaller density difference), the wavelength of the instability gets larger, and the growth rate of the bubble and spike structure slows down. Visualization of experiments by Tieszen *et al.* 2004 for methane and hydrogen fires qualitatively show this effect. Even though methane is buoyant relative to air, bubble and spike structure is almost not discernable in the movies. However, in hydrogen, the bubble and spike structure is much stronger than the helium plume, and the puffing is likewise much stronger.

These differences between reacting and non-reacting flows should be kept in mind for scaling studies. For example, for hydrocarbon fires, it may not be necessary to resolve the bubble and spike structure that may occur between the hot products and the air, because to leading order it does not affect the combustion rate of the fuel through enhanced mixing of the fuel vapors and air.

4.2. Conclusions

LES simulations, data for a one meter base diameter helium plume, and theoretical arguments are used to elucidate physics requirements for turbulent LES subgrid closure models for buoyant plumes. Both the data and highly resolved LES simulations show strong Rayleigh-Taylor (RT) instabilities that lead to turbulence and rapid scalar mixing near the base of strongly buoyant plumes. A grid refinement study using a dynamic Smagorinsky model shows strong grid dependency in the mean statistics, with the finest grid (4 million nodes) approaching the data. The authors interpret the temporally resolved results as indicating that the small scale RT structures play a significant role in the mean statistics. The authors argue that these structures must either be resolved or modeled to capture the mean statistics of the plume. In particular, it is noted that RT air spikes with O(mm-cm) widths have the ability to penetrate the plume source in the time-scale of the puffing frequency. The high radial entrainment at the plume base sweeps this air into the centerline of the plume at a very low elevation. The resulting relatively high mean-centerline-density moderates the mean driving force of the plume and results in centerline velocities that are about a factor of two lower than would occur if this mixing mode were not present.

4.3. Acknowledgments

Support for the lead author provided by Sandia, a multiprogram laboratory operated by Sandia Corporation, a Lockheed Martin Company, for the United States Department of Energy under Contract DE-AC04-94AL85000.

REFERENCES

- CANUTO, V. M. 1994 Large Eddy Simulation of Turbulence: A Subgrid Scale Model Including Shear, Vorticity, Rotation, and Buoyancy, *Astrophysical J.* **158**:729-752.
- CETEGEN, B. M. 1997 Measurements of Instantaneous Velocity Field of a Non-Reacting Pulsating Buoyant Plume by Particle Image Velocimetry, *Combust. Sci. and Tech.*, **123**:377-87.
- CETEGEN, B. M. & AHMED T. A. 1993 Experiments on the Periodic Instability of Buoyant Plumes and Pool Fires, *Combustion and Flame*, **93**:157-84.
- DEBACQ, M., FANGUET, V., HULIN, J. P., & SALIN, D. 2001 Self-similar Concentration Profiles in Buoyant Mixing of Miscible Fluids in a Vertical Tube, *Phys. Fluids*, **13**(11):3097-3100.
- DESJARDIN, P. E., O'HERN, T. J., & TIESZEN, S. R. 2004 Large Eddy Simulation and Experimental Measurements of the Near-Field of a Large Turbulent Helium Plume, *Phys. Fluids*, **16**(6):1866-1883.
- DIMONTE, G., & SCHNEIDER, M. 2000 Density Ratio Dependence of Rayleigh -Taylor mixing, *Phys. Fluids*, **12**(2):304-321.
- DRYSDALE, D. 1999 *An Introduction to Fire Dynamics, 2nd Ed.* John Wiley & Sons, NY, NY, p. 161.
- DUFF, R. E., HARLOW, F. H., & HIRT, C. W. 1962 Effects of Diffusion on Interface Instability Between Gases, *Phys. Fluids*, **5**(4):417-425.
- EIDSON, T. M. 1985 Numerical Simulation of the Turbulent Rayleigh-Benard Problem Using Subgrid Modeling. *J. Fluid Mech.*, **158**:245-268.
- O'HERN, T. J., WECKMAN, E. J., GERHART, A. L., TIESZEN, S. R., & SCHEFER, R.

- W. 2004 Experimental Study of a Turbulent Buoyant Helium Plume. *Manuscript in Review*.
- MELL, W. E. 2001 Helium plume data available from author, National Institute of Standards and Technology, Building and Fire Research Laboratory, Gaithersburg, Maryland.
- MELL, W. E., MCGRATTEN, K. B., & BAUM, H. R. 1996 Numerical Simulation of Combustion in Fire Plumes, *26th Symposium (International) on Combustion*. The Combustion Institute, pp. 2715-22.
- NAJM, H. N., SCHEFER, R. B., MILNE, R. B., MUELLER, C. J., DEVINE, K. D., & KEMPKA, S. N. 1998 Numerical and Experimental Investigation of Vortical Flow-Flame Interaction. SAND98-8232 Sandia National Laboratories, Albuquerque, NM.
- NICOLETTE, V. F., TIESZEN, S. R., BLACK, A. R., DOMINO, S. P., & O'HERN, T. J. 2004 A Turbulence Model for Buoyant Flows Based on Vorticity Generation. *Manuscript in Review*.
- PIERCE, C. D. 2001 *Progress-variable Approach for Large Eddy Simulation of Turbulent Combustion*. Ph.D. Thesis, Stanford University.
- PIERCE, C. D. & MOIN, P. 2004 Progress-variable Approach for Large Eddy Simulation of Non-premixed Turbulent Combustion. *J. Fluid Mech.*, **504**:73-97.
- SOTERIOU, M. C., DONG, Y., & CETEGEN, B. M. 2002 Lagrangian Simulation of the Unsteady, Near Field Dynamics of Planar Buoyant Plumes, *Phys. Fluids*, **14**(9):3118-3140.
- TIESZEN, S. R., NICOLETTE, V. F., GRITZO, L. A., HOLEN, J. K., MURRAY, D., & MOYA, J. L. 1996 Vortical Structures in Pool Fires: Observation, Speculation, and Simulation. SAND96-2607 Sandia National Laboratories, Albuquerque, NM.
- TIESZEN, S. R. 2001 On the Fluid Mechanics of Fires, *Annu. Rev. Fluid Mech.*, **33**:67-92.
- TIESZEN, S. R., DOMINO, S. P., & BLACK, A. R. 2004 Validation of a Simple Turbulence Model Suitable for Closure of Temporally-Filtered Navier-Stokes Equations Using a Helium Plume, Sandia National Laboratories, Albuquerque, NM In review.
- TIESZEN, S. R., O'HERN, T. J., WECKMAN, E. J., & SCHEFER, R. W. 2004 Experimental Study of the Effect of Fuel Mass Flux on a One Meter Diameter Methane Fire and Comparison with a Hydrogen Fire, *Combustion and Flame* Accepted for publication.
- WANG, C. 1984 *The Effects of Curvature on Turbulent Mixing Layers*. Ph.D. Thesis, California Institute of Technology.
- XIN, Y., GORE, J., MCGRATTEN, K. B., REHM, R. G., & BAUM, H. R. 2002 Large Eddy Simulation of Pool Fires, *29th Symposium (International) on Combustion*. The Combustion Institute, pp. 259-265.

Radiative transfer modeling of a large pool fire by discrete ordinates, discrete transfer, ray tracing, Monte Carlo, and moment methods

By K. A. Jensen[†], J.-F. Ripoll, A. A. Wray[‡], D. Joseph[¶] AND M. El Hafi[¶]

Five computational methods for solution of the radiative transfer equation in an absorbing-emitting and non-scattering gray medium were compared on a 2 m JP-8 pool fire. The temperature and absorption coefficient fields were taken from a synthetic fire due to the lack of a complete set of experimental data for fires of this size. These quantities were generated by a code that has been shown to agree well with the limited quantity of relevant data in the literature. Reference solutions to the governing equation were determined using the Monte Carlo method and a ray tracing scheme with high angular resolution. Solutions using the discrete transfer method, the discrete ordinate method (DOM) with both S_4 and LC_{11} quadratures, and moment model using the M_1 closure were compared to the reference solutions in both isotropic and anisotropic regions of the computational domain. DOM LC_{11} is shown to be the more accurate than the commonly used S_4 quadrature technique, especially in anisotropic regions of the fire domain. This represents the first study where the M_1 method was applied to a combustion problem occurring in a complex three-dimensional geometry. The M_1 results agree well with other solution techniques, which is encouraging for future applications to similar problems since it is computationally the least expensive solution technique. Moreover, M_1 results are comparable to DOM S_4 .

1. Motivation and objectives

Accurate prediction of the heat flux to an object exposed in a large fire is important for consideration of the thermal hazard to engineered systems, personnel, and facilities. Such fires could potentially occur from a transportation accident. Fires of this scale have relatively low velocities and high temperatures, and therefore the majority of heat transfer to an object is dominated by the radiative emission from high-temperature soot (Gritzo *et al.* 1998). The computational cost for solution of the radiative transfer equation (RTE) is quite high for simulations of fires of this scale. In addition to the common three-dimensional space variables and time, the governing equation also requires integration over all directions of propagation at each point in the domain, adding two angular variables. The challenge, therefore, is to choose a numerical solution method which predicts the radiative flux to objects in fires with sufficient accuracy. Moreover, the radiative source term, which is coupled to the hydrodynamics, must be computed with low cost and sufficient accuracy to ensure a correct prediction of the evolution of the fire.

In this study, five common numerical methods to solve the radiative transfer were

[†] Sandia National Laboratories

[‡] NASA Ames Research Center

[¶] Ecole des Mines d'Albi Carmaux

compared when applied to a realistic, full-field three-dimensional fire data set. The five methods include:

1. Ray tracing: straightforward integration of the integral equation by tracing a specified number of rays originating from each point through the domain. The method is accurate but costly since it normally requires a large number of angles.

2. Discrete transfer method: similar to ray tracing technique, but works in reverse by tracing rays throughout the domain and adding their energy contribution to each cell it passes through.

3. Discrete ordinate method: solution of the transport equation by finite volume methods. The angular integration is performed using selected numerical quadrature schemes. The two quadrature schemes used were S_4 (24 angles) and LC_{11} (96 angles).

4. Moment method with the M_1 closure (Maximum entropy closure): uses moments of the governing equation to convert the angular dependence into a hyperbolic set of four equations for three-dimensional problems. A closure model is required for the radiative pressure term.

5. Monte Carlo, Net Exchange Formulation: statistical Monte Carlo method formulated in terms of net exchange and choosing a form of the probability density function for efficient computations. The cost is normally high due to the number of realizations required for good accuracy.

Of these methods, the M_1 method has theoretically the lowest cost because the angular dependency is handled analytically. However, the accuracy of the M_1 method in complex three-dimensional cases remains unknown. The main questions addressed in this study are: How does each method perform with low angular resolution? How many angles are required for an accurate solution? What is the accuracy of moment methods for fire problems? Which method is most appropriate for a fire?

2. Synthetic fire

The radiative heat transfer in large pool fires is dominated by the thermal emission of high-temperature soot and is gray in nature. Solution of the RTE in the participating medium thus requires knowledge of the gray absorption coefficient and emission temperature throughout the medium. Ideally, a complete, highly-resolved set of experimental measurements would be available for this purpose. However, due to the complex fire dynamics (Tieszen *et al.* 1996), as well as difficulty in instrumenting diagnostics in high temperature, sooting environments, relevant data for large scale fires are not available.

Given the lack of available and relevant data, a synthetic 2-meter JP-8 pool fire was created with the Vulcan fire simulation tool from Sandia National Laboratories. Vulcan, and its predecessor (Holen *et al.* 1990), has been successfully used in recent years for simulating such pool fires which resemble those in the Fire Laboratory for Accreditation of Models and Experiments (FLAME) facility in Albuquerque, New Mexico (Brown & Blanchat 2003). Figure 1 shows, from left to right: the exterior of the FLAME facility, a contour along the centerline plane of the facility showing the fuel pan in the center and the inlet air ring at the bottom of the facility; and the temperature profile of the synthetic fire along the central plane. The facility was discretized with a $92 \times 92 \times 120$ three-dimensional Cartesian grid. The full-field data is axially symmetric with the center defined by the fuel pan. In order to compute the fire, the fluid conservation equations are solved using a Reynolds Averaged Navier Stokes (RANS) approach, with sufficient iterations from ignition to reach a steady-state solution.

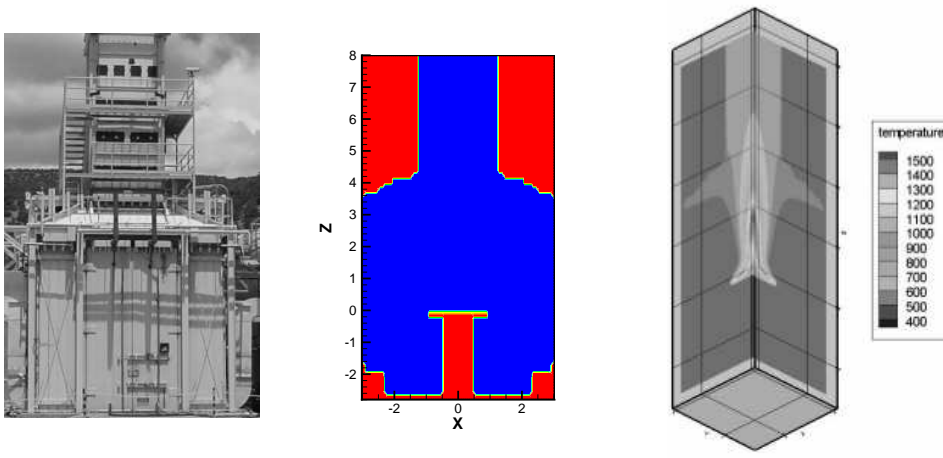


FIGURE 1. The FLAME facility (left), a contour plot of the center plane (center), and the synthetic fire temperature contour (right).

The absorption coefficients calculated by Vulcan depend on contributions from soot as well as from carbon dioxide and water vapor. The model for this coefficient assumes that the medium is gray since soot is the dominant absorbing and emitting species. When the domain of computation is as complex as the FLAME facility (see Fig. 1), prescribing common boundary conditions for five different codes can become problematic. Here, using a ghost cell technique, the walls, the pan, and the fuel source were prescribed a very large constant opacity on the order of $O(10^3)$ and ambient temperature 293 K . At the exhaust opening at the top of the chimney, it is assumed that all energy leaves unimpeded.

3. Solution methods for the radiative transfer equation

3.1. Problem definition

The gray radiative transfer equation (RTE) describes the change in radiation intensity, I , through an absorbing and emitting gray medium along a path of length ds in a solid angle $d\Omega$ (Modest 2003),

$$\frac{dI(\mathbf{s})}{ds} = \kappa I_b - \kappa I(\mathbf{s}) \quad (3.1)$$

where $I_b = \sigma T^4 / \pi$ is the blackbody intensity at temperature T , σ is the Stefan-Boltzman constant, and κ is the absorption coefficient.

For most heat transfer applications, the primary engineering quantities of interest are the net incident radiation G , the radiative heat flux (\mathbf{q}_r) and the divergence of the heat flux ($\nabla \cdot \mathbf{q}_r$), also called radiative source term. These quantities can be derived from the following integrals of the intensity over solid angle

$$G = \int_{4\pi} I(\mathbf{s}) d\Omega, \quad \mathbf{q}_r = \int_{4\pi} I(\Omega) \Omega d\Omega \quad \text{and} \quad \nabla \cdot \mathbf{q}_r = \kappa(4\sigma T^4 - G) \quad (3.2)$$

Solution of the RTE, as well as solutions of Eqs. (3.2), using each solution technique is outlined in the following subsections.

3.2. Discrete transfer method (DTM)

The discrete transfer method (DTM) used in Vulcan is an enhanced version of the original model proposed by Shah (1979). The enhancements were selected to obtain an acceptable compromise between accuracy and calculation speed. This will be tested by comparing the results obtained herein with those obtained from verified and highly accurate Monte Carlo and ray tracing techniques.

Within the computational domain a *radiation box* is defined to speed the calculation by focusing on the region with high thermal emission. This box defines where rays originate in the tracing technique. For this study, the box was defined as the smallest grid-conformal parallelepiped encompassing all control volumes with a temperature greater than 800 K.

For each node on the boundary of the box, a specified number of rays are emitted over a hemisphere and followed to the boundary of the calculation domain; a corresponding ray is followed back from the boundary to the original point. Along these traces, the change of intensity from absorption and emission is calculated over each control volume in the path with proper weighting given to the solid angle and the originating projected area.

The change of intensity for the ray within a control volume is found from a recurrence relation obtained from analytical integration of Eq. (3.1),

$$I_{n+1} = I_n \exp(-\kappa \delta s) + I_b(1 - \exp(-\kappa \delta s)) \quad (3.3)$$

where δs is the distance over which the beam passes through the control volume.

The source term for the energy equation, Eq. (3.2), is found by summing the net gain or loss of radiation energy in each control volume intersected during a ray trace. The contribution to the source term from one beam i passing through a control volume n is given by: $S_{n,i} = (I_{n+1} - I_n)\Omega_i dA d\Omega$, where dA is the area from the element at the ray origin boundary and Ω_i is the solid angle represented by the beam. The total radiant source term for the n th control volume is found by summing over N total beams: $Q_r dV = \sum_{i=1,N} S_{n,i}$

The heat flux to a surface is not calculated throughout the field of Vulcan, but rather at selected surfaces (e.g., cell faces). The hemispherical flux in W/m^2 is derived from this model by integrating all incoming rays on a surface. This integration requires a large number of rays to be traced from each node of the radiation box to be accurate, but from experience it has been found to be quite fast when a limited number of selected surfaces are used. To compare to the other methods, the hemispherical fluxes to the common surface shared by two adjacent cells were summed for the equivalent of a 4π integration.

3.3. Discrete ordinates method (DOM)

The DOM is based on the discretization of the RTE (see Eq. (3.1)) over a chosen number N_{dir} of discrete directions, $\mathbf{s}_i(\mu_i, \eta_i, \xi_i)$, contained in the solid angle 4π and associated with weights w_i . Koch & Becker (2004) compare several types of angular quadratures, two of which are used here: the S_4 (24 directions) for its efficiency and the LC_{11} (96 directions) for its accuracy.

The RTE is solved for every discrete direction \mathbf{s}_i using a finite volume approach. The integration of the RTE over the volume V of an element limited by a surface Σ with outer unit normal \mathbf{n} , and the application of the divergence theorem yield:

$$\int_{\Sigma} I \mathbf{s} \cdot \mathbf{n} d\Sigma = \int_V (\kappa I_b - \kappa I(\mathbf{s})) dV \quad (3.4)$$

The domain is discretized in control volumes (in this study regular hexahedra[†]). Taking I_j to be the average intensity over the j^{th} face, associated with the center of that face, and taking $I_{b,P}$ and I_P to be the average intensities over the volume V , associated with the center of the cell, P , Eq. (3.4) can be discretized as follows:

$$\sum_{j=1}^{N_{face}} I_j(\mathbf{s}_i \cdot \mathbf{n}_j) A_j = \kappa V (I_{b,P} - I_P) \quad (3.5)$$

The scalar product of the i^{th} discrete direction vector with the normal vector of the j^{th} face of the considered cell is defined by $D_{ij} = \mathbf{s}_i \cdot \mathbf{n}_j = \mu_i n_{xj} + \eta_i n_{yj} + \xi_i n_{zj}$.

I_b is assumed to be constant and equal to $I_{b,P}$ over the volume V , and I_j is taken constant over each face. For each cell, the incident radiation G , given in Eq. (3.2) is evaluated at the center by

$$G \simeq \sum_{i=1}^{N_{dir}} w_i I_P(\mathbf{s}_i) \quad (3.6)$$

For a gray medium, one obtains the divergence of the radiative heat flux using Eq. (3.2). To solve Eq. (3.5), a spatial differencing scheme based on the mean flux (DMFS), proposed by Ströhle *et al.* 2001, is used. This scheme uses the following decomposition:

$$I_P = \frac{1}{2} \overline{I_{out}} + \frac{1}{2} \overline{I_{in}} \quad (3.7)$$

where $\overline{I_{in}}$ is the weighted average of the intensities at the entering faces of the cell and $\overline{I_{out}}$ the weighted average of the intensities leaving the cell. Substituting $\overline{I_{out}}$ from Eq. (3.7) into Eq. (3.5) and after some algebra (see Joseph *et al.* 2003 for more details), one obtains:

$$I_P = \left(\frac{1}{2} \kappa V I_b - \sum_{\substack{j \\ D_{ij} < 0}} D_{ij} A_j I_j \right) / \left(\frac{1}{2} \kappa V + \sum_{\substack{j \\ D_{ij} > 0}} D_{ij} A_j \right) \quad (3.8)$$

After the calculation of I_P from Eq. (3.8), the radiation intensities at those cell faces at which $D_{ij} > 0$ are set equal to $\overline{I_{out}}$, obtained from Eq. (3.7).

3.4. Monte Carlo method - net exchange formulation (MCM-NEF)

Monte Carlo Methods (MCM) have been often used to produce highly accurate solutions in the process of validating other numerical methods (Coelho *et al.* 2003; Perez *et al.* 2004). They first appeared in the literature as strict numerical implementations of stochastic photon transport models (Hammersley & Handscomb 1967). The very large number of realizations required to achieve convergence shows the limitations of the classical Monte Carlo algorithms, particularly when optically thick media are encountered (Farmer & Howell 1994). To overcome these difficulties, a mathematical formulation using the Net Exchange Formulation (NEF) (Cherkaoui *et al.* 1996), together with adapted probability density functions, have been proposed to improve the variance reduction procedures (de Lataillade *et al.* 2002). Taking P_i as a point within the volume V_i and P_j within V_j , we denote the position vectors of P_i and P_j as \mathbf{r}_{P_i} and \mathbf{r}_{P_j} . The net radiative exchange between two volumes V_i and V_j , $\varphi_{(V_i, V_j)}$, or a volume V_i and a surface S_j , $\varphi_{(V_i, S_j)}$, or two surfaces S_i and S_j , $\varphi_{(S_i, S_j)}$, is expressed as follows for black walls and

[†] the formulation provided here is also valid for non regular mesh.

non-scattering media

$$\varphi_{(V_i, V_j)} = \int_{V_j} \int_{V_i} \frac{\kappa(\mathbf{r}_{P_i}) \kappa(\mathbf{r}_{P_j}) \tau(s_{ij})}{s_{ij}^2} [I_b(\mathbf{r}_{P_i}) - I_b(\mathbf{r}_{P_j})] dV_i dV_j \quad (3.9)$$

$$\varphi_{(V_i, S_j)} = \int_{S_j} \int_{V_i} \frac{|\mathbf{n}(\mathbf{r}_{P_j}) \cdot \mathbf{s}| \kappa(\mathbf{r}_{P_j}) \tau(s_{ij})}{s_{ij}^2} [I_b(\mathbf{r}_{P_i}) - I_b(\mathbf{r}_{P_j})] dV_i dS_j \quad (3.10)$$

$$\varphi_{(S_i, S_j)} = \int_{S_j} \int_{S_i} \frac{|\mathbf{n}(\mathbf{r}_{P_i}) \cdot \mathbf{s}| |\mathbf{n}(\mathbf{r}_{P_j}) \cdot \mathbf{s}| \tau(s_{ij})}{s_{ij}^2} [I_b(\mathbf{r}_{P_i}) - I_b(\mathbf{r}_{P_j})] dS_i dS_j \quad (3.11)$$

where

$$s_{ij} = s_j - s_i = |\mathbf{r}_{P_j} - \mathbf{r}_{P_i}|, \quad \mathbf{s} = \frac{(\mathbf{r}_{P_j} - \mathbf{r}_{P_i})}{|\mathbf{r}_{P_j} - \mathbf{r}_{P_i}|}, \quad \text{and} \quad \tau(s_{ij}) = \exp\left[-\int_{s_i}^{s_j} \kappa(s) ds\right] \quad (3.12)$$

with \mathbf{n} the normal vector to the surface S , κ the gray absorption coefficient, and $\tau(s_{ij})$ is the spectral transmittance along a straight line between P_i and P_j .

The radiative source term for a volume V_i and the net heat flux at a surface S_i are computed by taking into account their radiative exchanges with all the other volumes and surfaces:

$$S_r(\mathbf{r}_{P_i}) = \int_{V_i} \nabla \cdot \mathbf{q}_r dV_i = \sum_{j=1}^{N_s} \varphi_{(V_i, S_j)} + \sum_{j=1}^{N_v} \varphi_{(V_i, V_j)} \quad (3.13)$$

and

$$q_{w, net, i} = \sum_{j=1}^{N_s} \varphi_{(S_i, S_j)} + \sum_{j=1}^{N_v} \varphi_{(S_i, V_j)} \quad (3.14)$$

where N_s is the number of surfaces and N_v the number of volumes.

One way of evaluating the multiple integrals in the expressions for the net exchange rates, Eqs. (3.9), (3.10), (3.11), is to use a Monte Carlo Method, which is now described.

Considering that each radiative exchange can be represented as an integral \mathcal{I} , of a function f , over a domain D : $\mathcal{I} = \int_D f(x) dx$. An arbitrary probability density function (pdf), p , defined and strictly positive on the integration domain D is introduced. The weight function $W(x) = f(x)/p(x)$ is used to write

$$\mathcal{I} = \int_D \frac{f(x)}{p(x)} p(x) dx = \int_D W(x) p(x) dx$$

Given a random variable X , distributed according to p , and a function of that variable, $g(X)$, we let \mathcal{I} represent the expectation of $g(X)$. Estimating \mathcal{I} with N samples $g(x_i)$, where x_i is the i th realization of the random variable X gives

$$\mathcal{I} = E[g(X)] \approx \frac{1}{N} \sum_{i=1}^N g(x_i) = \langle g(X) \rangle_N, \quad \text{where} \quad \mathcal{I} = \lim_{N \rightarrow \infty} \langle g(X) \rangle_N \quad (3.15)$$

Then the standard deviation of the estimate is calculated as $\sigma(\langle g(X) \rangle_N) = \frac{1}{\sqrt{N}} \sigma(g(X))$, where $\sigma(g(X))$ is the standard deviation of $g(X)$. It will be approximated by

$$\sigma(\langle g(X) \rangle_N) \approx \frac{1}{\sqrt{N}} \sqrt{[\langle g(X)^2 \rangle_N - \langle g(X) \rangle_N^2]} \quad (3.16)$$

In this last expression the variance depends on the function g which itself depends on the

pdf. To perform efficient MC simulations, the choice of the pdf is crucial. More details are described in (de Lataillade *et al.* 2002; Eymet *et al.* 2004). The results presented in this paper have a standard deviation of about 1 percent.

3.5. Ray tracing method

This method treats the RTE as a set of first-order ODEs, with one ODE for each spatial point and directional angle. At each spatial point \mathbf{x} , a set of rays is considered to project inward toward the point, with the set being chosen to sample solid angle space in such a way as to allow accurate integration over that space to compute the net incident radiation and the heat flux. For the fire problem, the rays are followed outward from the chosen point until they intercept a wall or the exit of the chimney. At such a boundary point the initial value of the incoming radiative intensity is set to equilibrium ($I = I_b$). From this initial value, the RTE is integrated forward along the ray to the chosen spatial point, and the value at that point is saved for inclusion in angular integrals involving $I(\mathbf{x}, \Omega)$.

The method of integration along a ray assumes that, within each step of the quadrature, the source I_b and opacity κ are constants equal to their interpolated values at the center of the step. With this assumption, $I(\mathbf{s}, \Omega)$ can be advanced from one end of the step, \mathbf{s}_0 , to the other, \mathbf{s}_1 , according to the following rule

$$I(\mathbf{s}_1, \Omega) = I(\mathbf{s}_0, \Omega) \exp(-\kappa|\mathbf{s}_1 - \mathbf{s}_0|) + I_b(1 - \exp(-\kappa|\mathbf{s}_1 - \mathbf{s}_0|)) \quad (3.17)$$

Once the full set of angular values $I(\mathbf{x}, \Omega)$ is obtained at the point \mathbf{x} , angular integrals, such as those in Eqs. (3.2), are performed to compute quantities of interest.

3.6. Moment methods and the \mathbf{M}_1 closure

A system of equations for two moments, the net incident radiation G and the radiative flux \mathbf{q}_r , can be extracted from the gray RTE, Eq. (3.1), by integrating it over all directions. The system is given by

$$\frac{1}{c} \partial_t G + \nabla \cdot \mathbf{q}_r = \kappa(4\sigma T^4 - G) \quad (3.18)$$

$$\frac{1}{c} \partial_t \mathbf{q}_r + \nabla \cdot (\mathbf{D}_r G) = -\sigma \mathbf{q}_r \quad (3.19)$$

The M_1 closure (Levermore 1984; Fort 1997†) is given by the following Eddington tensor \mathbf{D}_r . It is computed from the Eddington factor χ and the anisotropic factor $\mathbf{f} = \mathbf{q}_r/G$ as follows

$$\mathbf{D}_r = \frac{1-\chi}{2} \mathbf{Id} + \frac{3\chi-1}{2} \frac{\mathbf{f} \otimes \mathbf{f}}{f^2} \quad \text{with} \quad \chi(f) = \frac{3+4f^2}{5+2\sqrt{4-3f^2}} \quad (3.20)$$

where \mathbf{Id} denotes the identity matrix, f the euclidian norm of \mathbf{f} , and \otimes the dyadic product. The Eddington tensor \mathbf{D}_r , which plays the role of a flux limiter, comes from an underlying radiative intensity which is able to describe both a beam (by a Dirac function) as well as isotropic radiation (by a Planck function). Hence, the M_1 model is able to predict radiation in opaque, semi-opaque or transparent media and, as we show below, is particularly suited for the computation of radiation in fires. The numerical scheme used to solve this model is given in Ripoll *et al.* 2002.

† more references concerning this model can be found in Ripoll 2004.

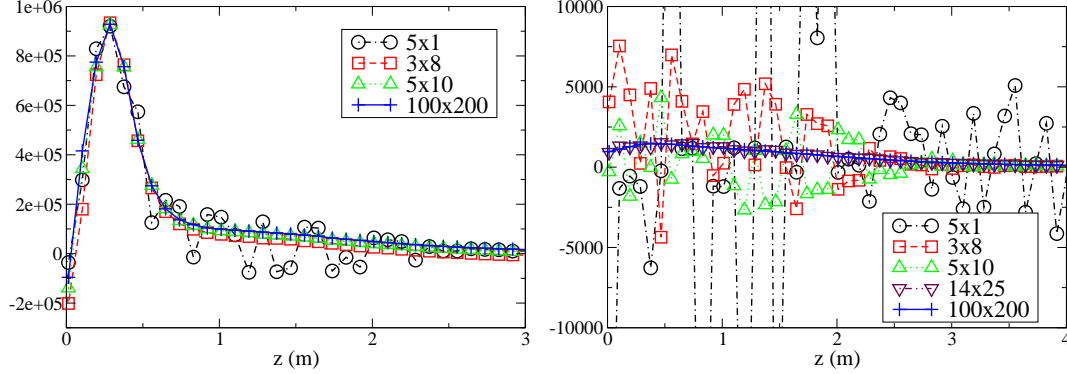


FIGURE 2. Radiative source term (W/m^3) at $r = 0.43 \text{ m}$ (left) and radial heat flux (W/m^2) at $r = 1.03 \text{ m}$ (right) as a function of elevation from the fuel pan computed by ray tracing for several angular resolutions (θ, ϕ).

4. Results and discussion

4.1. Angular resolution and coupling

In this section, the number of angles (or rays) needed for the fire computation is investigated using the ray tracing code, which helped define the required angular resolution and quadrature schemes for comparison of the solution methods. Figures (2) and (3) (left) show the radiative source term and radial heat flux profiles calculated at various angular resolutions. It is found that a low resolution, less than 50 angles, leads to poor results both inside and outside the fire. When only 5 or 10 angles are used, a hot source might be hit or not according to the angles chosen, in other words, ray effects are dominant and the results vary greatly based on this choice.

Inside the fire, it is found that at least 50 rays are needed to get a solution close to the converged one[†] (see Fig. 2). However outside the fire, Fig. 3 (left), it is found that 350 angles are needed to get an acceptable solution and to reduce ray effects. Hence, because such resolutions are needed for accuracy, a high computational cost is expected. Nevertheless, these results must be balanced by the fact that neither special quadratures, nor particular choices of angles have been used herein to try to improve the accuracy of the results for low angular resolution. In the ray tracing solver, angles are uniformly distributed in $\mu = \cos(\theta)$ and ϕ , which is not the optimal choice. Undoubtedly a better choice of angles and/or quadratures would decrease the number of angles needed to get accurate results[‡].

In Fig. 3 (right), it is shown how the angular resolution does affect the time-dependent coupled problem. Here, radiation and hydrodynamics are solved coupled by Vulcan and evolve in time. Radiation is solved by the DTM method. It is found that 24 angles do not lead to an accurate solution and induce strong temporal variation of the radiative flux, which leads to fluctuations in the hydrodynamic quantities. Moreover, since the coupling between radiation and hydrodynamics is very strong in fires, a poor computation of the

[†] Angular convergence was obtained with 20,000 angles (100×200). All results presented with the RTE ray tracing solver in this study were obtained with this resolution.

[‡] The reader might be interested in seeing which angular quadrature is needed for radiation in a solar atmosphere: Stein *et al.* in this volume.

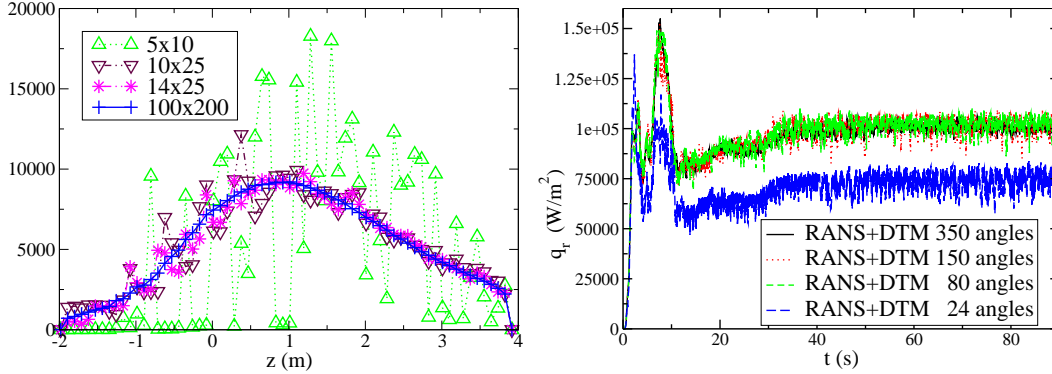


FIGURE 3. Left: Radial component of the radiative flux (W/m^2) as a function of elevation from the fuel pan computed by ray tracing for different resolutions (θ, ϕ) at $r = 2.55$ m from the centerline of the fuel pan. Right: time evolution profiles of the radial component of the radiative flux at $r = 0.5$ and $z = 0.5$ m inside the fire for several angular resolutions using DTM.

radiation can, for instance, lead to extinction or to an over/under-estimation of soot formation.

Starting from 80 angles, which seems to be a good compromise between speed and accuracy, the Vulcan results are close to convergence, but the fluctuations are still significant. Results are considered converged for a resolution of 350 angles. As a result of these observations, the code is usually run with 80 angles to quickly obtain a fully developed fire. The results are converged afterward using 350 angles over a smaller time interval[†].

4.2. Radiative source term

A comparison of the radiative source terms ($div(\mathbf{q}_r)$) obtained by all methods[‡] is now provided. Since this quantity is the coupling term used by the hydrodynamics solver, its accurate computation is mandatory to compute the correct final fire profile. The ray tracing code and the Monte Carlo code are used for the reference solutions[¶]. Both codes find similar solutions at all points in the facility. In Fig. 4 (left), the results are presented for points inside the fire. Good global agreement is found between all methods, though the DTM profile is slightly shifted from the ray tracing reference solution; DTM, M_1 , and DOM S_4 slightly overestimate the maximum value, and DOM LC_{11} slightly underestimates it. These small differences of less than 3% are sufficiently small to not have strong effects on the coupled energy equation. The accuracy and general agreement between these results is expected for this case where the radiation field inside the fire is mainly isotropic, $f < 0.2$, making it less sensitive to angular resolution.

For points outside, but still adjacent to, the fire, at $r = 1.15$ m (see Fig. 4 (right)), more discrepancies are seen among the methods^{||}. The DOM S_4 method is found to be less accurate, though still acceptable, compared to the DOM LC_{11} because the angular

[†] All results presented here with the DTM have been obtained with 350 angles.

[‡] when this term is positive (negative), net emission (absorption), is occurring.

[¶] The Monte Carlo code was primarily used to ensure that the solution given by the ray tracing was fully correct. It has been applied only at selected positions and not for all nodes of the domain.

^{||} a large error far outside the fire would not affect the dynamics of the fire and is hence not damaging.

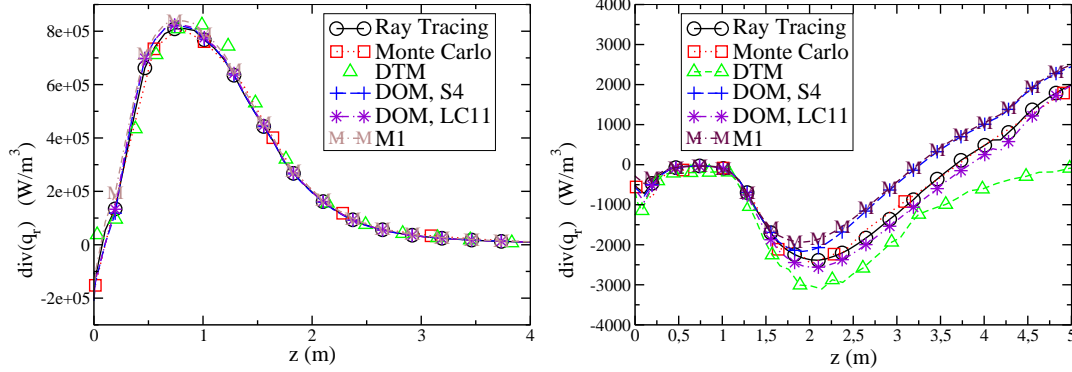


FIGURE 4. Radiative source term (W/m^3) as a function of elevation from the fuel pan. Left at $r = 0.29 \text{ m}$ and right at $r = 1.15 \text{ m}$ from the centerline of the fuel pan.

variation is not fully captured by S_4 and ray effects occur. The M_1 model gives results as accurate as those of the DOM S_4 , which is encouraging. These methods slightly underestimate absorption while the DTM method overestimates it. Despite the discrepancies, the magnitude of the source term is sufficiently small compared to that inside the fire that less accuracy is acceptable.

4.3. Radial heat flux

Since the Monte Carlo code, by its formulation, does not allow the computation of the radiative fluxes which are compared herein, the ray tracing results are used as the reference. In Figs. 5 and 6, net radial heat flux inside the fire are compared. All methods qualitatively agree and predict the same trends. Higher up, for $z > 1.5 \text{ m}$, all methods fully agree since strong temperature and opacity gradients are absent. The three methods, M_1 , S_4 and LC_{11} are in good agreement with the reference solution, but slightly underestimate the flux. The DTM method agrees globally with the other methods and the reference solution, but overestimates slightly, similar to LC_{11} , fluxes close to the outer edge of the fuel pan at $r = 1$ and $z = 0 \text{ m}$. Similarly to the source term computation, the M_1 and S_4 methods give comparable results. No noticeable difference is observed between S_4 and LC_{11} , whose results agree well with those of the ray tracing method.

The fact that S_4 computes both flux and source terms relatively well, when linked with the angular studies of section 4.1, implies that 24 angles should be enough inside the fire provided that the S_4 set of angles is chosen. This constitutes an improvement by a factor of two of the number of angle needed, compared to the use of uniformly distributed angles[†].

In Fig. 7, the fluxes outside the fire are compared. The DTM method gives results in agreement with the ray tracing solver. The DOM LC_{11} gives similar results, which suggest that approximately a hundred angles should be enough to compute radiation at 1 or 2 diameters away from the fire provided an accurate quadrature is chosen. This constitutes an improvement by a factor 3 compared to a uniformly spaced angular set which apparently needs 350 angles (see section 4.1). The DOM S_4 does not have enough angular

[†] It should be noted that the 24 angles of DTM used in the time evolution computation are uniformly distributed. This explains the inaccurate results of the time dependent problem for this angular resolution.

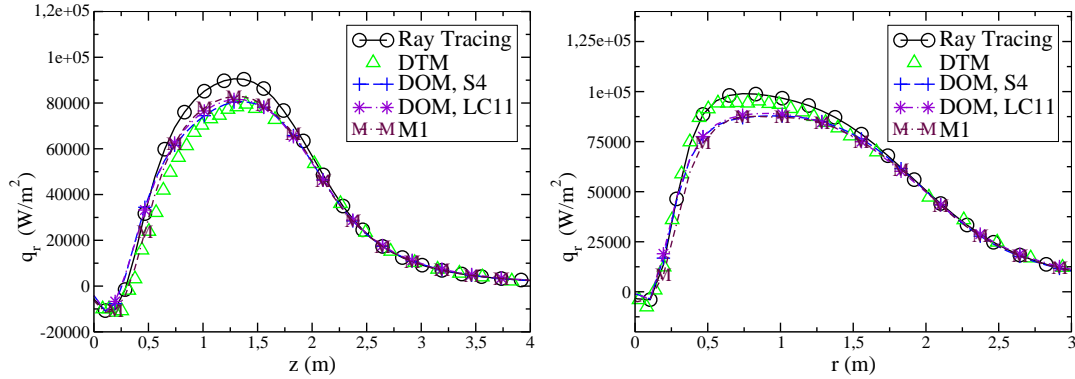


FIGURE 5. Radial component of the radiative flux (W/m^2) as a function of elevation from the fuel pan. Left at $r = 0.29$ m and right at $r = 0.42$ m from the centerline of the fuel pan.

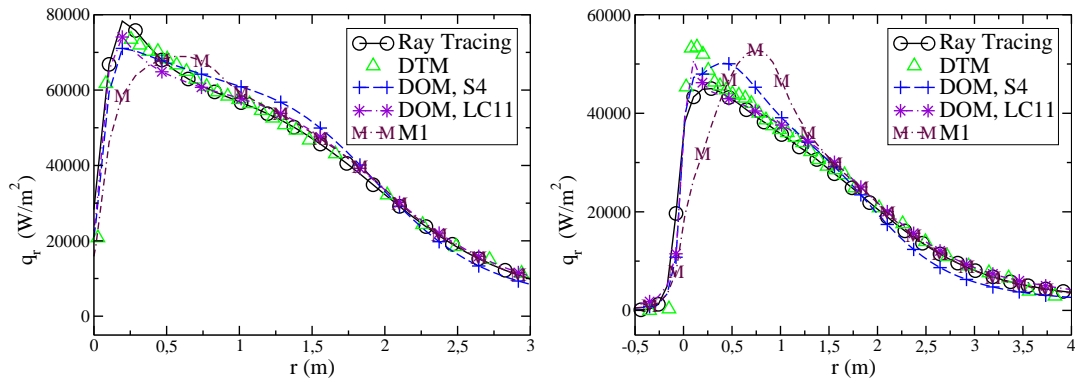


FIGURE 6. Radial component of the radiative flux (W/m^2) as a function of elevation from the fuel pan. Left at $r = 0.7$ m and right at $r = 1.03$ m from the centerline of the fuel pan.

resolution to provide accurate results at 1.42 m nor at 2 m away from the fire. LC_{11} thus constitutes an accuracy improvement compared to S_4 . Globally, this method is found to give the closest results to the ray tracing values for all positions shown here. The M_1 model is found here to not be accurate enough: results at 1.42 m could be admissible, but the fluxes are certainly overestimated 2 m away from this 2 m pool fire, by almost a factor of 2. There, the closure fails to model the anisotropy of the radiation. At 2 m, DOM S_4 computes the maximal values more accurately than M_1 , but does not find the correct overall shape[‡], whereas M_1 does.

5. Conclusions

Five different methods have been used to compute the radiative field of a synthetic 2-meter JP-8 pool fire: Monte Carlo, ray tracing, DOM S_4 and LC_{11} , DTM, and the M_1 moment model. Particular interest has been given to the M_1 method which is applied for the first time to a combustion problem occurring in a complex three-dimensional

[‡] a ray effect can be seen at $z = 0.1$ m due to the pan.

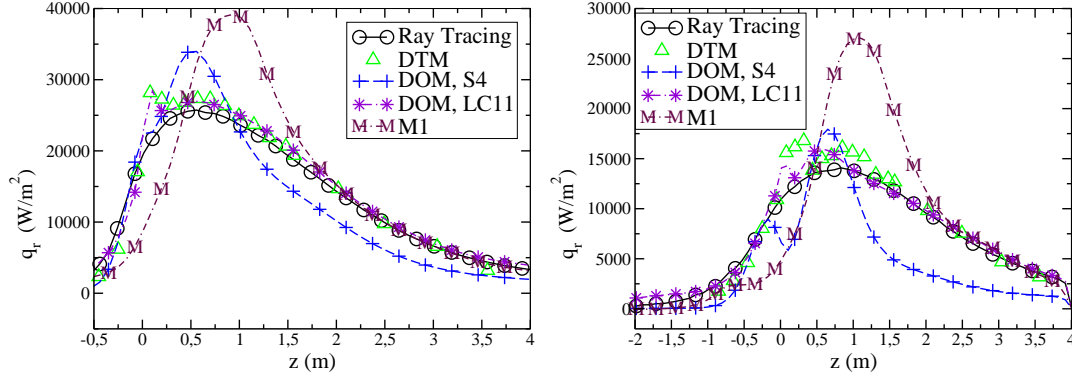


FIGURE 7. Radial component of the radiative flux (W/m^2) as a function of elevation from the fuel pan. Left at $r = 1.42$ m and right at $r = 2$ m from the centerline of the fuel pan.

geometry. Theoretically, this model should have the lowest computational cost of the five, since the directional integration has been modeled.

An angular resolution study has shown that roughly 50 angles inside and 350 outside the fire are needed to accurately compute radiation when a uniformly distributed set of angles is chosen. This choice of angles is not optimum, however, and the number of angles needed can be reduced to 24 inside and to roughly 100 outside when an optimum set is chosen, as is the case for both the S_4 and LC_{11} quadratures. Unfortunately, these numbers are still too high to guarantee a low cost computation. It has also been shown that if an insufficient angular distribution is used, then significant changes to the time dependent solution occur. It is thus not possible to accurately compute a time-evolving fire if the aforementioned angular requirements are not satisfied.

The ray tracing and Monte Carlo methods, which are the most accurate methods when their convergence is ensured, and the results of which were found to be consistent, were used to compute the reference solutions. Both of these methods, which need, respectively, a large number of angles or a large realization sample, are too costly to be used for a three-dimensional time dependent fire. The goal was then to quantify the accuracy of the four other methods, compared to the reference solutions, and to assess their usability.

The five methods were compared first through the computation of the radiative source term. It was found that, inside the fire, all methods correctly compute this term, which is needed for coupling with the hydrodynamics. Close to the fire, this term is underestimated by S_4 and M_1 and overestimated by DTM, but these deviations of less than 3% are quite admissible.

The computation of the radiative flux brought other conclusions. Inside the fire, all methods agree pretty well. Once again, M_1 gives a comparable solution to the DOM methods. However, outside the fire both S_4 and M_1 methods inaccurately compute the flux: S_4 suffers from ray effects and M_1 overestimates, by almost a factor two, the maximal value region. These two methods are thus not effective far away from the fire. On the other hand, LC_{11} and DTM give an accurate solution far away the fire, but deviate slightly close to the outer edge of the fuel pan.

Overall, it is found that M_1 gives results similar to DOM S_4 , in the sense that its results are accurate in regions where S_4 is accurate. The DTM and DOM LC_{11} methods were found to give results very close to the Monte-Carlo and ray tracing codes. The

comparison of the accuracy and speed of the five solution methods suggest that the M_1 model is a good alternative to S_4 when solving the RTE in complex cases such the large pool fire in this study. For the limited case where highly-accurate heat flux in the highly anisotropic area, e.g., the flux to an object a few diameters away from the fire, better accuracy is only achieved with higher angular resolution offered by DOM LC_{11} or a large number of angles using ray tracing or the DTM method.

Acknowledgments

The authors thank Dr. Sheldon Tieszen of Sandia National Laboratories for his extensive technical discussions and support. Kirk Jensen was supported by the Advanced Simulation and Computing Program of Sandia, a multi-program laboratory operated by Sandia Corporation, a Lockheed-Martin Company, for the United States Department of Energy's National Nuclear Safety Administration under Contract DE-AC04-94AL85000.

REFERENCES

- BROWN, A.L., & BLANCHAT, T.K. 2003 A validation quality heat flux dataset for large pool fires. *2003 ASME Summer Heat Transfer Conference, Las Vegas HT2003-40249*.
- CHERKAoui, M., DUFRESNE, J.L., FOURNIER, R., GRANDPEIX, J.Y. & LAHELLEC, A. 1996 Monte Carlo simulation of radiation in gases with a narrow-band model and a net-exchange formulation. *Jour. of Heat Transfer* **118**, 401-407.
- COELHO, P.J., PEREZ, P. & EL HAFI, M. 2003 Benchmark numerical solutions for radiative heat transfer in two-dimensional axisymmetric enclosures with non-grey sooting media. *Numerical Heat Transfer, Part B*, **43**, 425-444.
- DE LATAILLADE, A., DUFRESNE, J.L., EL HAFI, M., EYMET, V. & FOURNIER, R. 2002 A net exchange Monte Carlo approach to radiation in optically thick systems. *Jour. of Quant. Spectrosc. & Radiat. Transfer*, **74:5**, 563-584.
- EYMET, V., FOURNIER, R., BLANCO, S. & DUFRESNE, J.L. 2004 Boundary-based net exchange Monte-Carlo method for absorbing and scattering thick media. *Jour. of Quant. Spectrosc. & Radiat. Transfer*, in press.
- FARMER, J.T. & HOWELL J.R. 1994 Hybrid Monte Carlo/ diffusion method for enhanced solution of radiative transfer in optically thick non-gray media. *Radiative Transfer: Current Research*, Y. Bayazitoglu et al., eds. *ASME*, **276**, 203-212.
- FORT, J. 1997 Information-theoretical approach to radiative transfer. *Phys. A.*, **243**, 275-303.
- GRITZO, L.A., SIVATHANU, Y.R., & GILL, W. 1998 Transient measurements of radiative properties, soot volume fraction and soot temperature in a large pool fire. *Combustion Science and Technology* **84**, 113-136.
- HAMMERSLEY, J.M. & HANDSCOMB, D.S. 1967 *Monte Carlo Methods*. Dunod, Monographie.
- HOLEN, J., BROSTROM, M., & MAGNUSSEN, B.F. 1990 Finite difference calculation of pool fires. *Twenty-Third Symposium (International) on Combustion, The Combustion Institute*, 1677-1683.
- JOSEPH, D., COELHO, P.J., EL HAFI, M. & CUENOT, B. 2003 Application of the discrete ordinates method to grey media in complex geometries using unstructured meshes. *Proceedings of Eurotherm73 on Computational Thermal Radiation in participating media, Eurotherm Series* **11**, 97-106.

- KOCH, R. & BECKER, R. 2004 Evaluation of the quadrature schemes for the discrete ordinates method. *Jour. of Quant. Spectrosc. & Radiat. Transfer.*, **84**, 423-435.
- LEVERMORE, D. 1984 Relating Eddington factors to flux limiters. *Jour. of Quant. Spectrosc. & Radiat. Transfer*, **32(2)**, 149-160.
- MODEST, M.F. 2003 Radiative heat transfer. 3rd ed., McGraw-Hill.
- PEREZ, P., EL HAFI, M. COELHO, P.J. & FOURNIER R. 2004 Accurate solutions for radiative heat transfer in two-dimensional axisymmetric enclosures with gas radiation and reflective surfaces. Accepted in *Numerical Heat Transfer, Part B*.
- RIPOLL, J.-F. 2004 An average formulation of the M_1 radiation model with mean absorption coefficients and presumed probability functions for turbulent flows. *Jour. of Quant. Spectrosc. & Radiat. Transfer*, **83**, 493-517.
- RIPOLL, J.-F., DUBROCA, B., AUDIT, E. 2002 A factored operator method for solving coupled radiation-hydrodynamics models. *Trans. Theory and Stat. Phys.*, **31**(4-6), 531-557.
- SHAH, N.G. 1979 The computation of radiation heat transfer. *PhD thesis, University of London*.
- STRÖHLE, J., SCHNELL, U. & HEIN, K.R.G. 2001 A mean flux discrete ordinates interpolation scheme for general coordinates. *3rd International Conference on Heat Transfer, Antalya*.
- TIESZEN, S.R., NICOLETTE, V.F., GRITZO, L.A., HOLEN, J.K., MURRAY, D., & MOYA, J.L. 1996 Vortical structures in pool fires: observation, speculation, and simulation. *SAND Report No. SAND96-2607, Sandia National Laboratories*.

Temperature and pollution control in flames

By L. Debiene, B. Ivorra, B. Mohammadi & F. Nicoud †
A. Ern‡, T. Poinso¶ AND H. Pitsch

Controlling flame shapes and emissions is a major objective for all combustion engineers. Considering the complexity of reacting flows, novel optimization methods are required: this paper explores the application of control theory for partial differential equations to combustion. Both flame temperature and pollutant levels are optimized in a laminar Bunsen burner computed with complex chemistry schemes. The optimization procedure is coupled with mesh adaptation to provide grid-independent results. Finally, a recursive semi-deterministic global optimization approach is tested.

1. Introduction

Control of temperature and species in flames is an important challenge for industrial and environmental issues. Many studies exist on numerical simulation of pollutant formation in flames (Peters & Donnerhack 1981; Warnatz 1981; Williams 1985; Pitsch *et al.* 1996; Poinso & Veynante 2001; Pitsch 2002). This paper is to apply control theory for PDEs (Lions 2003) to flames.

We focus on a laminar bunsen H_2 -Air flame simulated with detailed chemistry and multicomponent transport (Burman *et al.* 2004). We concentrate on the reduction of the Zeldovich-NO, also called thermal NO. This is the major NO source in a bunsen H_2 -Air flame. We also study the control of temperature distribution in flames, which is of importance in combustion engine design. Finally, we pay attention to the control of flame length at given fuel rate in the flow. These formulations are alternative approaches to consider pollutant control in flame (Peters & Donnerhack 1981) and also have natural applications in the design of combustion chambers.

To keep the computational cost low we test here if it is possible to use approximate state and sensitivity evaluations (Mohammadi & Pironneau 2001) during optimization. Once the optimization is achieved, the final design is a posteriori validated by accurate calculation. In this sense, different discretizations are used for the computation of the state and gradient, and an unstructured mesh adaptation strategy is applied to adapt the mesh to the solution during optimization process (Frey 2001; Frey & George 2001; Debiene 2004).

As the functionals are not necessarily convex, we use a new recursive semi-deterministic global optimization approach. This algorithm permits to escape from local minima but has a lower cost than a genetic algorithm (Goldberg 1989; Ivorra 2005) because the nondeterministic features of the approach have been reduced. Randomness is introduced only when the deterministic part fails. In addition, in cases where the algorithm fails, the construction can be used together with a genetic algorithm to improve population selection and reduce the size of the sampling needed.

† University of Montpellier, France

‡ CERMICS, ENPC, France

¶ CERFACS, IMFT, CNRS and INPT, Toulouse, France

2. Semi-deterministic recursive optimization

Most deterministic minimization algorithms can be seen as discretizations of the following dynamical system (Attouch & Cominetti 1996; Mohammadi & Pironneau 2001; Mohammadi & Saiac 2002) where x denotes the vector of control parameters belonging to an admissible space Ω_{ad} . ζ is a fictitious parameter. M is a local metric transformation and d a direction in Ω_{ad} .

$$\begin{cases} M(\zeta)x_\zeta = -d(x(\zeta)) \\ x(\zeta = 0) = x_0 \end{cases} \quad (2.1)$$

For example if $d = \nabla J$, the gradient of the functional, and $M = Id$, the identity operator, we recover the classical steepest descent method while with $d = \nabla J$ and $M = \nabla^2 J$ the Hessian of J , we recover the Newton method. Quasi-Newton methods can also be recovered using approximate Hessian definition (Vanderplaats 1990).

In this work, the following assumptions for our optimization problem are made (Ivorra 2005):

- H1: $J \in C^1(\Omega_{ad}, \mathbb{R})$.
- H2: the infimum J_m is known. This is often the case in industrial applications.
- H3: the problem is admissible: the infimum is reached inside the admissible domain: $\exists x_m \in \Omega_{ad}, s.t. J(x_m) = J_m$.
- H4: J is coercive (i.e. $J(x) \rightarrow \infty$ when $|x| \rightarrow \infty$).

We consider that system (2.1) has a solution if for a given $x_0 \in \Omega_{ad}$, we can find a finite Z_{x_0} such that $J(x(Z_{x_0})) = J_m$:

$$\begin{cases} M(\zeta)x_\zeta = -d(x(\zeta)) \\ x(0) = x_0 \\ J(x(Z_{x_0})) = J_m \end{cases} \quad (2.2)$$

This is an over-determined boundary value problem which can be solved using classical techniques for BVPs (e.g. shooting, finite differences,...). Because we are interested in constrained global optimization we prefer to express the condition at Z_{x_0} on the functional instead of its gradient. Indeed, in our context a first order optimality condition is usually not satisfied at the infimum.

This over-determination is an explanation of why we should not solve global optimization problems with methods which are particular discretizations of first order differential systems. We could use variants of classical methods after adding second order derivatives (Attouch & Cominetti 1996):

$$\begin{cases} \eta x_{\zeta\zeta} + M(\zeta)x_\zeta = -d(x(\zeta)), \\ x(0) = x_0, \quad \dot{x}(0) = \dot{x}_0, \\ J(x(Z_{x_0})) = J_m \end{cases} \quad (2.3)$$

To avoid introducing too much perturbation in the method, we consider, in practice, $|\eta| \ll 1$.

The over determination can be removed, for instance, by considering $x_0 = v$ for (2.1) (resp. $\dot{x}(0) = v$ for (2.3)) as a new variable to be found by the minimization of $h(v) = J(x_v(Z_v)) - J_m$, where $x_v(Z_v)$ is the solution of (2.1) (resp. (2.3)) found at $\zeta = Z_v$ starting from v .

The algorithm $A_1(v_1, v_2)$ reads:

- (v_1, v_2) given,

- Find $v \in \operatorname{argmin}_{w \in \mathcal{O}(v_2)} h(w)$ where $h(w) = J(x_w(Z_w)) - J_m$, with $x_w(Z_w)$ solution of system (2.1) found at $\zeta = Z_w$ starting from w , and $\mathcal{O}(v_2) = \{t\overrightarrow{v_1 v_2}, t \in \mathbb{R}\} \cap \Omega_{ad}$.
- return v

The line search minimization might fail. For instance, a secant method degenerates on plateau and critical points. In this case, we add an external level to the algorithm A_1 , keeping v_1 unchanged, and looking for v_2 by minimizing a new functional h^2 defined by $h^2(v_2) = \min_{v_1} h(v_2)$ by algorithm $A_1(v_1, v_2)$.

This leads to the following two-level algorithm $A_2(v_1, v_2^2)$:

- (v_1, v_2^2) given,
- Find $v_2 \in \operatorname{argmin}_{w \in \mathcal{O}(v_2^2)} h^2(w)$ where $h^2(w) = h(A_1(v_1, w))$ and $\mathcal{O}(v_2^2) = \{t\overrightarrow{v_1 v_2^2}, t \in \mathbb{R}\} \cap \Omega_{ad}$.
- return v_2

The choice of initial conditions in this algorithm contains the non-deterministic feature of the algorithm. The construction can be pursued building recursively $h^i(v_2^i) = \min_{v_1} h^{i-1}(v_2^i)$ using $A_{i-1}(v_1, v_2^i)$, with $h^1(v) = h(v)$ where i denotes the external level. Mathematical background for this approach and validation on academic test cases and solution of nonlinear PDEs are available (Mohammadi & Saiac 2002; Ivorra & Mohammadi & Redont 2004; Ivorra 2005).

In practice, this algorithm succeeds if the trajectory passes close enough to the infimum (i.e. in $B_\varepsilon(x_m)$ where ε defines the accuracy in the capture of the infimum). This means that we should consider for h a functional of the form

$$h(v) = \int_{T_1}^T (J(x_v(\tau)) - J_m)^2 d\tau, \quad \text{for } 0 < T_1 < \tau < T$$

where $x_v(\tau)$ is the trajectory generated by (2.1) and $T_1 = T/2$ for instance. Also, in the algorithm above, $x_w(Z_w)$ is replaced by the best solution found over $[0, Z_w]$.

In cases where J_m is unknown, we set $J_m = -\infty$ and look for the best solution for a given complexity and computational effort. This is the approach adopted here where we predefine the effort we would like to make in each level of the algorithm.

3. Functionals and parameterizations

The symbols of this section are illustrated on figure (1), which shows the computational domain Ω . A section Γ , through which we would like to reduce the NO flux, is defined at $z = 1.5\text{cm}$.

Optimization control parameters are:

- the inflow velocity of the premixed mixture v_1 taken as

$$v_1(\overline{v_1}, p_1, p_2) = \overline{v_1} (1 - \exp(\frac{-|r_0 - r|}{r_1})) + S(p_1, p_2) \text{ with } r_0 = 0.2, r_1 = 0.05$$

with

$$S(p_1, p_2) = p_1 \left(\frac{r}{r_0}\right)^{1.2} \sin(p_2 r) \sin\left(\frac{r - r_0}{r_0}\right)$$

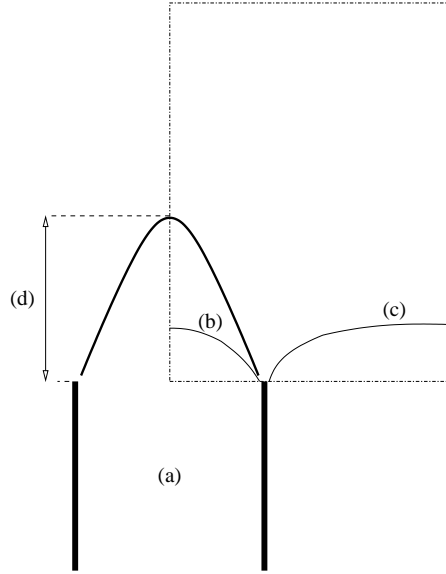


FIGURE 1. Computational domain for the bunsen flame and illustration of the parameterizations: (a) is the premixed mixture H_2 , O_2 , N_2 injected with velocity v_1 shown on (b), the coflow velocity v_2 (c) and the length of the flame (d).

- the coflow velocity v_2 of the form

$$v_2(\overline{v_2}) = \overline{v_2} \left(1 - \exp\left(\frac{-|r_0 + r_3 - r|}{r_1}\right) \right) \text{ with } r_3 = 0.05$$

Two of the following molar fraction quantities:

- the molar fraction of species H_2 in the premixed mixture χ_{H_2} ,
- the molar fraction of species O_2 in the premixed mixture χ_{O_2} ,
- the molar fraction of species N_2 in the premixed mixture χ_{N_2} ,

the third one being deduced from $\chi_{H_2} + \chi_{O_2} + \chi_{N_2} = 1$

The control space has therefore six degrees of freedom. We introduce two nondimensional numbers:

- ϕ , the equivalence ratio, defined by:

$$\phi = \frac{\chi_{H_2} / \chi_{O_2_{inj}}}{(\chi_{H_2} / \chi_{O_2})_{stoich}} = \frac{\chi_{H_2}}{2\chi_{O_2}}$$

where *inj* means injection and *stoich* means stoichiometric.

- $\alpha = \frac{\chi_{N_2}}{\chi_{O_2}}$, the dilution factor.

The vector of control parameters is $x = (\overline{v_1}, p_1, p_2, \overline{v_2}, \phi, \alpha) \in [50, 200] \times [-25, 25] \times [-10, 10] \times [50, 200] \times [4, 10] \times [0, 10]$. It should be noticed that a constraint on the fuel rate in the flow implies a compatibility relation between p_1, p_2 and $\overline{v_1}$.

The first cost function we consider aims to reduce the NO flux through Γ and at the same time achieve a target temperature profile:

$$J_1(x) = \gamma_1 \int_{\Gamma} \rho y_{NO} v \cdot n + \gamma_2 \int_{\Gamma} (T - T_{target})^2$$

where ρ is the density, y_{NO} the mass fraction of NO, v the flow velocity, T the temperature

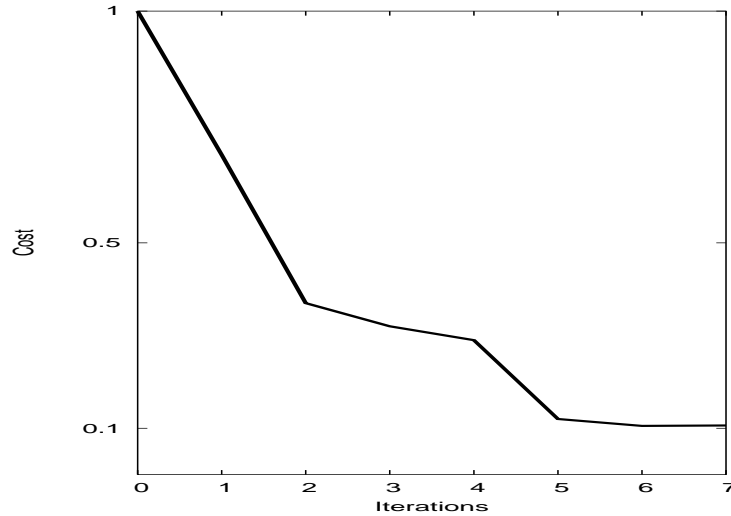


FIGURE 2. NO reduction functional J_1 evolution vs. accumulation of optimization iterations. The two-level algorithm permits to escape from local minima: a first plateau is reached in first level and the second level permits to reach a second plateau with a global reduction of 90 percent in the functional while the original algorithm alone (i.e. with only one level) only leads to 60 percent reduction in the functional.

and T_{target} a target temperature profile. γ_1 , γ_2 are given positive scalars and n the normal unit vector to Γ .

The second cost function aims to control the flame length at a given flow rate:

$$J_2(x) = \int_{r=0} y_{H_2} \quad \text{with} \quad \gamma_1 \int_{z=0} \rho y_{H_2} v \cdot n = \text{const.}$$

We observed that these functionals are not necessarily convex (Debiane 2004).

4. State equations

The hydrogen mechanism can be described using nineteen elementary reactions and nine species H_2 , O_2 , H , O , OH , HO_2 , H_2O , H_2O_2 , N_2 . The flame is simulated with an axisymmetric bunsen laminar flame code (Ern & Giovangigli 1994; Burman *et al.* 2004). Governing equations are discretized by a finite element method, which is an extension to chemically reacting flows of the streamline diffusion method, including least squares stabilization of the pressure gradient and the low-Mach continuity equation as well as a shock capturing term designed to control temperature and species mass fraction under-shoots near flame fronts. The species NO and N_2 are added to the mechanism in order to simulate the formation of the Zeldovich-NO (Williams 1985).

5. Numerical results

As combustion computations are quite expensive, we will analyze the feasibility of incomplete state and sensitivity evaluation during optimization with intermediate accurate validation of the optimal configurations. This means that during optimization we mostly achieve suboptimal search and analysis (Mohammadi & Pironneau 2001). This is possible because the semi-deterministic algorithm above requires less accuracy in sensitivity

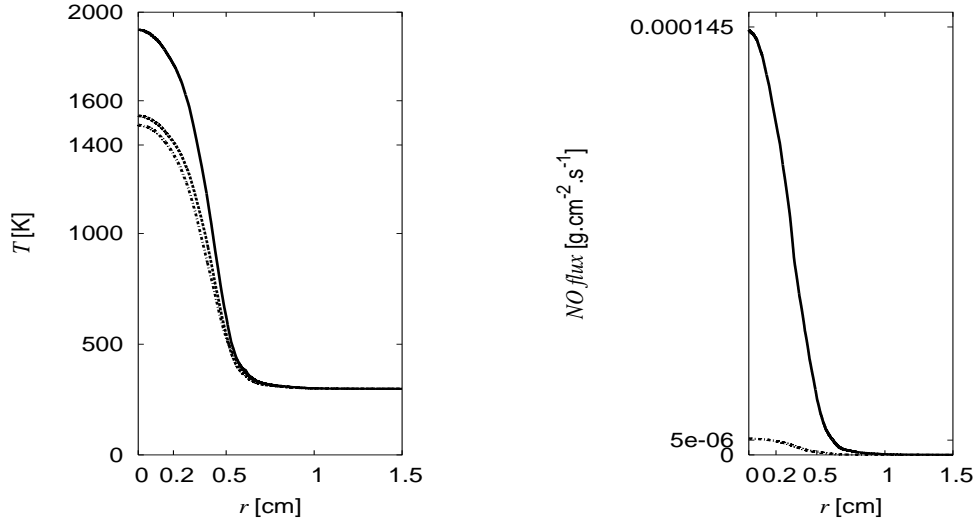


FIGURE 3. Left: initial (upper curve), target (lower) and optimized (middle) temperature profiles (K) along $z = 1.5\text{cm}$ (r -axis in cm). Right: NO flux ($\text{gcm}^{-2}\text{s}^{-1}$) through $z = 1.5\text{cm}$ before (upper curve) and after (lower) optimization. The NO flux has been drastically reduced and the temperature target almost achieved.

definitions. Also, during intermediate sensitivity and state analysis the previous states are used to define a suitable initialization for the solver. In addition, gradient computations are made on a coarser mesh than the one used for state evaluations. On the other hand, to monitor the accuracy of state calculations, and therefore the functional, at each iteration of optimization an unstructured solution-based mesh adaptation is performed (Frey & George 2001; Frey 2001; Debiante 2004). Using these ingredients, the cost for optimization is only 30 percent of the overall flame calculations.

The optimizations shown here have been performed with two levels of the algorithm presented above. The effect of each level can be seen in figure 2: a first plateau is reached and the algorithm permits to reach a second plateau with a global reduction of 90 percent in the functional.

Optimization results for functional J_1 are shown in figure 3. We can see that the target temperature is almost achieved and that the NO flux is drastically reduced. Initial and final temperature and NO mass fraction distributions are shown in figure 4.

Optimization results for functional J_2 are shown in figure 5. We show the maximum and minimum flame lengths which can be obtained with the current parameterization. There is a difference of 30 percent in flame length between the two configurations. Figure 6 shows a Delaunay type adapted mesh based on solution-based metric control which permits to monitor numerical errors during simulation and optimization. The injection profiles obtained from maximizing and minimizing the flame length at a given flow rate are quite counter-intuitive (see Figure 7) as the maximum injection along the symmetry line leads to a minimum flame length. The explanation of this phenomenon, which requires more investigations, is probably linked with the diffusion of the dihydrogen. This optimization clearly shows the correlation between flame length and pollutant production.

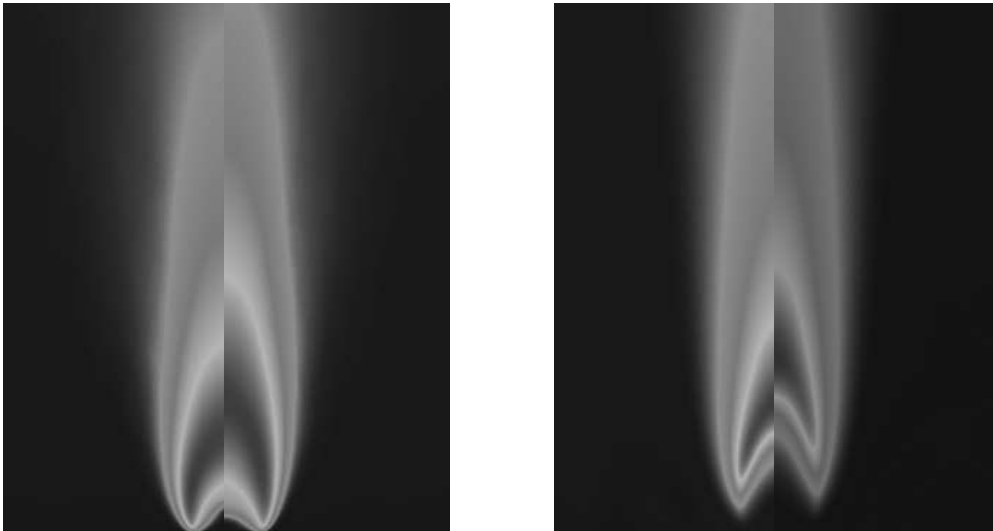


FIGURE 4. *Optimized and initial temperature (left) and NO mass fraction (right) distributions.*

6. Conclusions

A global optimization algorithm, based on the solution of boundary value instead of initial value problems, has been applied to the control of pollution, temperature and flame length in a bunsen flame simulated with complex chemistry making the problem stiff. It has been shown that controlling the fuel rate and the velocity profiles in both the premixed flow and the coflow is enough to achieve the targeted temperature, NO flux and flame shapes. Future investigations will concern shape optimization for such configurations in order to impact the design of combustion chambers.

Acknowledgements The authors would like to thank Professor P. Moin for his deep interest and helpful comments and orientations during this work at the Center for Turbulence Research at Stanford University. Authors are grateful to D. Cabale, M. Chethik and D. Michael for their assistance during the 2004 CTR summer program.

REFERENCES

- ATTOUCH, H. & COMINETTI, R. 1996 A dynamical approach to convex minimization coupling approximation with the steepest descent method. *J. Differential Equations* **128** (2), 519-540.
- BURMAN, E. & ERN, A. & V. GIOVANGIGLI 2004 Bunsen flame simulation by finite elements on adaptively refined, unstructured triangulations. *Combustion Theory Modelling* **8** (1), 65-84.
- DEBIANE, L. 2004 Application de l'adaptation de maillages en mécanique des fluides, combustion et traitement de l'image. *Ph.D. University of Montpellier*.
- ERN, A. & GIOVANGIGLI, V. 1994 Multicomponent Transport Algorithms. *Lecture Notes in Physics, New series Monographs in Physics, New Series Monographs, Springer-Verlag* **26**.
- FREY, P.J. 2001 Yams: A fully automatic adaptive isotropic surface remeshing procedure. *INRIA RT-0252*.

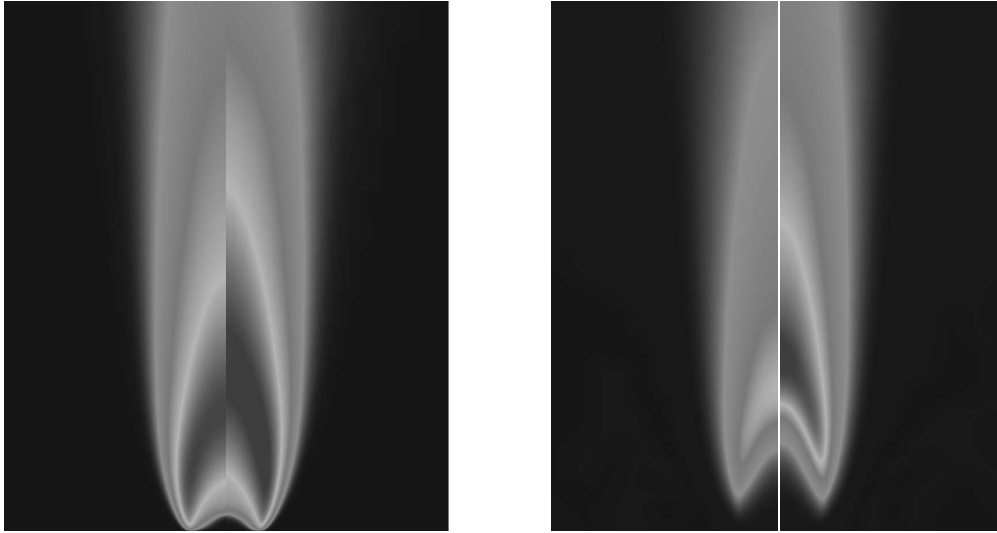


FIGURE 5. *Temperature contours (left) and NO mass fraction contours (right). There is a clear correlation between flame length and NO production.*

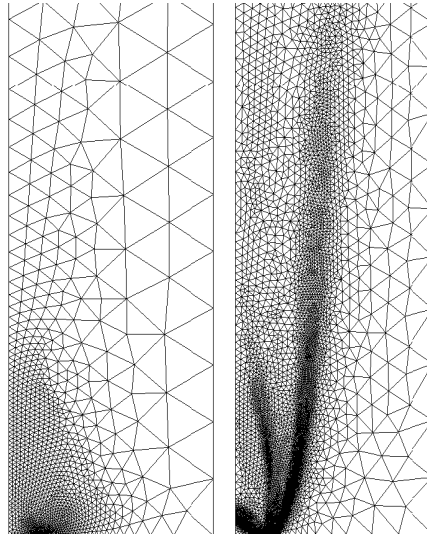


FIGURE 6. *Initial mesh (left) and adapted mesh (right). Solution-based adapted meshes permit to control numerical accuracy of the simulation and optimization.*

- FREY, P.J. & GEORGE, P.L. 2001 Mesh generation: application to finite elements. *Hermès Science Publisher*.
- GOLDBERG, D. 1989 Genetic algorithms in search, optimization and machine learning. *Addison Wesley*.
- IVORRA, B. 2005 Semi-Deterministic Global Optimization. *Ph.D. University of Montpellier*.
- IVORRA, B. MOHAMMADI, B. & REDONT, P. 2004 Low-Complexity Global Optimization by Solution of BVP. *Optimal Control: Applications and Methods* (to appear).

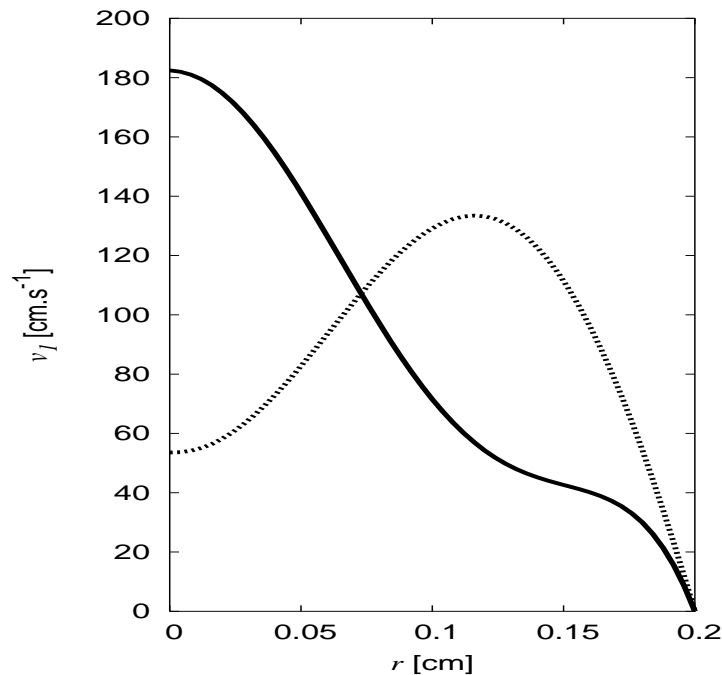


FIGURE 7. The injection velocity (cm.s^{-1}) profiles are quite counter-intuitive (r -axis in cm) as the maximum injection along the symmetry line leads to a minimum flame length. The continuous profile minimizes the length of the flame and the dash profile maximizes it.

- LIONS, J.L. 2003 Oeuvres choisies de Jacques-Louis Lions. Vol. II : Contrôle - Homogénéisation. *EDP Science*.
- MOHAMMADI, B. & PIRONNEAU, O. 2001 Applied shape optimization for fluids. *Oxford Univ. Press*.
- MOHAMMADI, B. & SAIAC, J. H. 2002 Pratique de la simulation numérique. *Dunod, Paris*.
- PETERS, N. & DONNERHACK, S. 1981 Structure and similarity of nitric oxide production in turbulent diffusion flames. *18th International Symposium on Combustion. The Combustion Institute*, 33-42.
- PITSCH, H. 2002 Improved Pollutant Predictions in Large-Eddy Simulation of Turbulent Non-Premixed Combustion by Considering Scalar Dissipation Rate Fluctuations. *Proc. Comb. Inst.* **29**, 1971-1978.
- PITSCH, H. & BARTHS, H. & PETERS, N. 1996 Three-Dimensional Modeling of NOx and Soot Formation in DI-Diesel Engines Using Detailed Chemistry Based on the Interactive Flamelet Approach. *SAE 962057*.
- POINSOT, T. & VEYNANTE, D. 2001 Theoretical and Numerical Combustion. *Edwards*.
- WARNATZ, J. 1981 Concentration, Pressure and Temperature dependence of the flame velocity in Hydrogen-Oxygen-Nitrogen Mixtures. *Combustion Science and Technology* **26**, 203-213.
- VANDERPLAATS, G.N. 1990 Numerical optimization techniques for engineering design. *Mc Graw-Hill*.
- WILLIAMS, F.A. 1985 Combustion Theory. *Addison-Welsey*.

Page intentionally left blank

Analysis of acoustic energy and modes in a turbulent swirled combustor

By C. Martin[†], L. Benoit[†], F. Nicoud[‡] AND T. Poinso[¶]

This paper presents the analysis of the self-excited combustion instability encountered in a lab-scale, swirl-stabilised combustion system. The instability, successfully captured by reactive Large Eddy Simulation (LES) is used to verify an acoustic energy equation. This energy equation shows how the source term due to combustion (equivalent to the Rayleigh criterion) is balanced by the acoustic fluxes at the boundaries when reaching the limit cycle. Additionally, an Helmholtz-equation solver including flame-acoustics interaction modelling is used to predict the stability characteristics of the system. Feeding the flame-transfer function from the LES into this solver allows to predict an amplification rate for each mode. The unstable mode encountered in the LES compares well with the mode of the highest amplification factor in the Helmholtz-equation solver, as well in terms of mode shape as in frequency.

1. Introduction

During the design phases of modern combustion chambers for gas turbines, a critical problem is often encountered: combustion oscillations (Candel 1992; Crighton *et al.* 1992; Poinso *et al.* 1987; Poinso & Veynante 2001). These oscillations cannot be predicted at the design stage and correcting actions can be extremely costly at later stages. Testing burners in simplified combustion chambers is a common method to verify their stability but is also an ambiguous approach because it is known that a given burner can produce unstable combustion in one chamber and not in another. Methods which could provide stability analysis before any tests are therefore requested. This paper demonstrates that Large Eddy Simulation, coupled to acoustic analysis, can provide such information. A proper framework to analyse combustion stability is the wave equation for reacting flows (Poinso & Veynante 2001). Such an equation is complex to derive because most assumptions used in classical acoustics must be revisited in a multi-species, non-isothermal, reacting gas. An approximate equation controlling the propagation of pressure perturbations in a reacting flow is:

$$\nabla \cdot (c_0^2 \nabla p_1) - \frac{\partial^2}{\partial t^2} p_1 = -(\gamma - 1) \frac{\partial \dot{\omega}_{T1}}{\partial t} - \gamma p_0 \nabla \vec{u}_1 : \nabla \vec{u}_1 \quad (1.1)$$

where the subscript 0 refers to mean quantities, and the subscript 1 to small perturbations. $\dot{\omega}_{T1}$ is the local perturbed heat release and c_0 is the sound speed, which can change locally because of changes in temperature and composition due to chemical reactions. These reactions are also the source of the additional RHS source term $(\gamma - 1) \partial \dot{\omega}_{T1} / \partial t$, which is responsible for combustion noise and instabilities. Equation (1.1) is difficult to use directly in practice. In the present work, it was solved or used in three different ways:

[†] CERFACS, CFD team, 42 Av. G. Coriolis, 31057 Toulouse Cedex

[‡] Université Montpellier II and CNRS

[¶] IMF Toulouse, INP de Toulouse and CNRS UMR 5149, 31400 Toulouse CEDEX, France

- First, a fully compressible LES of the reacting flow was performed, in which the pressure perturbations p_1 are explicitly solved for using the full Navier-Stokes equation (not the linearized form of Eq. 1.1). The code used for this LES is described in section 2.
- Second, Eq. 1.1 is solved in the frequency domain by assuming mono-harmonic fluctuations. This is done using a Helmholtz tool described in Section 3.
- Third, Eq. 1.1 is integrated to derive an equation for the fluctuating energy. The definition of such an energy in a reacting flow is discussed in Section 4.

The reasons for this combined strategy are the following. First, it is now clear that Large Eddy Simulation (LES) is a powerful tool to study the dynamics of turbulent flames (see special issue of *Flow Turbulence and Combustion* (65, 2000) on LES of reacting flows or recent books on turbulent combustion: Peters 2000; Poinso & Veynante 2001). Multiple recent papers have demonstrated the power of these methods (Angelberger, Egolfopoulos & Veynante 2000; Caraeni, Bergström & Fuchs 2000; Colin & Rudgyard 2000; Desjardins & Frankel 1999; Pierce & Moin 2004; Pitsch & Duchamp de la Geneste 2002; Selle *et al.* 2004). However, an important limitation of LES is its cost: the intrinsic nature of LES (full three-dimensional resolution of the unsteady Navier Stokes equations) makes it very expensive, even on today's computers. Faster tools are needed, for example for optimization and control of thermo-acoustic oscillations in chambers. Acoustic Helmholtz codes belong to this second category. These codes try to predict the global stability of a given combustion system by analyzing the amplification (or damping) of acoustic waves propagating through the entire combustion device. The most common versions of such codes describe combustion through very simplified linear formulations such as the n -tau model (Crocco 1969; Kaufmann, Nicoud & Poinso 2002; Poinso & Veynante 2001) or matrix formulations (Krueger *et al.* 2000; Paschereit, Flohr & Schuermans 2001; Polifke *et al.* 2001). In these formulations, the flame zone is viewed and modeled as a black box characterized only by its transfer function (or its matrix for matrix approaches), which essentially relates perturbations of heat release in the flame to perturbations of inlet velocity. LES and acoustic codes can be linked: LES is used to provide the mean fields, the unsteady fields and the flame transfer function. This flame transfer function can then be fed into acoustic codes to predict the overall stability of the combustion chamber when it is connected to upstream and downstream ducts.

2. Large Eddy Simulations for reacting flows in complex geometries

2.1. Numerical methods for compressible reacting LES

Most academic LES is often limited to fairly simple geometries for obvious reasons of cost and complexity reduction. In many cases, experiments are designed using simple two-dimensional shapes (Angelberger, Egolfopoulos & Veynante 2000; Duchamp de La Geneste & Pitsch 2001; Légier, Poinso & Veynante 2000) or axisymmetrical configurations (Kempf *et al.* 2000; Pitsch & Steiner 2000) and simple regimes (low speed flows, fully premixed or fully non-premixed flames) to allow research to focus on the physics of the LES (subgrid scale models, flame/turbulence interaction model), and more generally, to demonstrate the validity of the LES concept in academic cases. This approach is clearly adequate in terms of modelling development, but it can also be misleading in various aspects when it comes dealing with complex flames in complex geometries, especially in real gas turbines for which specific problems arise:

- Real geometries cannot be meshed easily or rapidly with structured or block-structured meshes: up to now, most LES of reacting flows have been performed in combustion cham-

bers where structured meshes were sufficient to describe the geometry. This is no longer the case in gas turbines and this brings additional difficulties. Indeed, on structured meshes, building high-order spatial schemes (typically 4th to 6th order in space) is easy and provides very precise numerical methods (Ducros, Comte & Lesieur 1996; Gamet *et al.* 1999; Lele 1992). For complex geometries such structured meshes must be replaced by unstructured grids, on which constructing high-order schemes is a more difficult task.

- Unstructured meshes also raise a variety of new problems in terms of subgrid scale filtering: defining filter sizes on a highly anisotropic irregular grid is another open research issue (Sagaut 2000; Scotti, Meneveau & Fatica 1997; Scotti, Meneveau & Lilly 1993; Vasilyev, Lund & Moin 1998). Many LES models, developed and tuned on regular hexahedral grids may, perform poorly on the low-quality unstructured grids required to mesh real combustion chambers. For example, the filtered structure model (Ducros, Comte & Lesieur 1996) is difficult to extend to non structured grids.

- LES validation is often performed in laboratory low-speed unconfined flames, in which acoustics do not play a role and the Mach number remains small so that acoustics and compressibility effects can be omitted from the equations (low-Mach number approximation: Kempf *et al.* 2000; Pierce & Moin 2004). In most real flames (for example in gas turbines), the Mach number can reach much higher values and acoustics are important so that taking compressibility effects into account becomes mandatory. This leads to a significantly heavier computational task: since, acoustic waves propagate faster than the flow, the time step becomes smaller and the boundary conditions must handle acoustic wave reflections (Poinsot & Veynante 2001). Being able to preserve computational speed on a large number of processors then also becomes an issue simply to obtain a result in a finite time.

- At the present time, it is impossible to perform a true LES everywhere in the flow and it will remain so for a long time. For example, the flow between vanes in swirled burners, inside the ducts feeding dilution jets or through multiperforated plates would require too many grid points. Compromises must be sought to offer (at least) robustness in places where the grid is not sufficient to resolve the unsteady flow.

In the present work, the full compressible Navier Stokes equations are solved on hybrid (structured and unstructured) grids. Subgrid stresses are described by the WALE model (Nicoud & Ducros 1999). The flame/turbulence interaction is modeled by the Thickened Flame (TF) model (Angelberger, Egolfopoulos & Veynante 2000; Colin *et al.* 2000). The numerical scheme is explicit in time and provides third-order spatial and third-order time accuracy (Colin *et al.* 2000).

2.2. Thickened Flame model and chemical scheme

For this study, the standard TF model developed by Colin *et al.* (2000) is used: in this model, preexponential constants and transport coefficients are both modified to offer thicker reaction zones that can be resolved on LES meshes. The fundamental property justifying this approach has been put forward by Butler & O'Rourke (1977) by considering the balance equation for the k-species mass fraction Y_k in a one-dimensional flame of thermal thickness δ_L^0 and speed s_L^0 :

$$\frac{\partial \rho Y_k}{\partial t} + \frac{\partial \rho u Y_k}{\partial x} = \frac{\partial}{\partial x} \left(\rho D_k \frac{\partial Y_k}{\partial x} \right) + \dot{\omega}_k(Y_j, T) \quad (2.1)$$

Modifying this equation to have:

$$\frac{\partial \rho Y_k^{th}}{\partial t} + \frac{\partial \rho u Y_k^{th}}{\partial x} = \frac{\partial}{\partial x} \left(\rho F D_k \frac{\partial Y_k^{th}}{\partial x} \right) + \frac{1}{F} \dot{\omega}_k \left(Y_j^{th}, T^{th} \right) \quad (2.2)$$

leads to a “thickened” flame equation where F is the thickening factor and superscript th stands for thickened quantities. Introducing the variable changes $X = x/F$; $\Theta = t/F$ leads to:

$$\frac{\partial \rho Y_k^{th}}{\partial \Theta} + \frac{\partial \rho u Y_k^{th}}{\partial X} = \frac{\partial}{\partial X} \left(\rho D_k \frac{\partial Y_k^{th}}{\partial X} \right) + \dot{\omega}_k \left(Y_j^{th}, T^{th} \right) \quad (2.3)$$

which has the same solution as Eq. (2.1) and propagates the flame front at the same speed s_L^0 . However, $Y_k^{th}(x, t) = Y_k(x/F, t/F)$ shows that the flame is thickened by a factor F . The thickened flame thickness is $\delta_L^1 = F \delta_L^0$. Choosing sufficiently large values of F allows to obtain a thickened flame which can be resolved on the LES mesh. Typically, if n is the number of mesh points within the flame front (n is of the order of 5 to 10) and Δx the mesh size, the resolved flame thickness δ_L^1 is $n \Delta x$ so that F must be $F = n \Delta x / s_L^0$. Note that F is not an additional parameter of the model but is imposed by the previous relation as soon as the mesh is created. In the framework of LES, this approach has multiple advantages: when the flame is a laminar premixed front, the TF model propagates it, in the limit of an infinitely thin front, at the laminar flame speed exactly like in a G equation approach. However, this flame propagation is due to the combination of diffusive and reactive terms which can also act independently so that quenching (near walls for example) or ignition may be simulated. Fully compressible equations may also be used as required to study combustion instabilities.

The thickening modification of the flame front also leads to a modified interaction between the turbulent flow and the flame: subgrid scale wrinkling must be reintroduced. This effect can be studied and parametrized using an efficiency function E derived from DNS results (Angelberger *et al.* 1998; Charlette, Veynante & Meneveau 2002; Colin *et al.* 2000). This efficiency function measures the subgrid scale wrinkling as a function of the local subgrid turbulent velocity u'_{Δ_e} and the filter width Δ_e . In practice, the diffusion coefficient D_k is replaced by $E F D_k$ and the preexponential constant A by $A E / F$ so that the conservation equation for species k is:

$$\frac{\partial \rho Y_k^{th}}{\partial t} + \frac{\partial \rho u Y_k^{th}}{\partial x} = \frac{\partial}{\partial x} \left(\rho E F D_k \frac{\partial Y_k^{th}}{\partial x} \right) + \frac{E}{F} \dot{\omega}_k \left(Y_j^{th}, T^{th} \right) \quad (2.4)$$

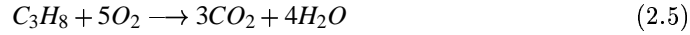
Such an equation propagates the turbulent flame at a turbulent speed $s_T = E s_L^0$, while keeping a thickness $\delta_L^1 = F \delta_L^0$. In laminar regions, E goes to unity, and Eq. 2.4 simply propagates the front at the laminar flame speed s_L^0 . The subgrid scale wrinkling function E was obtained from the initial model of Colin *et al.* (2000) as a function of the local filter size Δ_e , the local subgrid scale turbulent velocity u'_{Δ_e} , the laminar flame speed s_L^0 , the laminar and the flame thicknesses δ_L^0 and δ_L^1 .

The TF model uses finite rate chemistry: here the configuration corresponds to a lean fully premixed flame so that a one-step Arrhenius kinetics is sufficient. This one-step scheme (called 1sCM1) has been fitted with a genetic algorithm based tool on a laminar flame structure. The reference mechanism used to fit 1sCM1 is the Peters propane scheme (Peters & Rogg 1993). 1sCM1 takes into account five species (C_3H_8, O_2, CO_2, H_2O and

Chemical parameters					Schmidt numbers				
A	$n^{C_3H_8}$	n^{O_2}	E_a	C_3H_8	O_2	CO_2	H_2O	N_2	
3.29E10	0.856	0.503	31526	1.241	0.728	0.941	0.537	0.690	

TABLE 1. Rate constants and Schmidt numbers for the 1sCM1 scheme: the activation energy is in cal/moles and the preexponential constants in cgs units.

N_2):



The rate of the single step reaction is given by:

$$q = A \left(\frac{\rho Y_{C_3H_8}}{W_{C_3H_8}} \right)^{n^{C_3H_8}} \left(\frac{\rho Y_{O_2}}{W_{O_2}} \right)^{n^{O_2}} \exp \left(-\frac{E_a}{RT} \right) \quad (2.6)$$

where the parameters are provided in Table 1.

The diffusion coefficient D_k of species k is obtained as $D_k = \nu / S_c^k$ where ν is the viscosity and S_c^k the fixed Schmidt number of species k . The Schmidt number values used in the present simulations are given in Table 1, and correspond to the PREMIX values measured in the burnt gases. The Prandtl number is set to 0.68. With this parameter set, the agreement between flame profiles obtained using AVBP or PREMIX with the same chemical scheme is excellent. The agreement between the Peters scheme and the 1sCM1 in terms of laminar flame speed is excellent for the lean up to stoichiometric mixtures.

3. Acoustic solver for the Helmholtz equation

The acoustic tool used in this study (called AVSP) solves the eigenvalue problem associated to the wave equation (1.1). When dealing with thermo-acoustic instabilities, it is current practice to model the geometry of the combustor by a network of 1D or 2D axisymmetric acoustic elements where a simplified form of Eq (1.1) can be solved (Poinsot & Veynante 2001; Stow & Dowling 2001). Jump relations are used to connect all these elements and the amplitude of the forward and backward acoustic waves are determined so that the boundary conditions are satisfied. The main drawback of this approach is that the geometrical details of a combustor cannot be accounted for and only the first "equivalent" longitudinal or orthoradial modes are sought for. In AVSP, a finite element strategy is used to discretize the exact geometry of the combustor so that no assumption is made a priori regarding the shape of the modes. This feature gives AVSP the potential to test the effect of (small) geometrical changes on the stability of the whole system.

The wave equation (1.1) is solved in the frequency domain by assuming harmonic variations at frequency $f = \omega / (2\pi)$ for pressure, velocity and local heat release perturbations ($i^2 = -1$):

$$p_1 = \hat{P}(x, y, z) \exp(-i\omega t), \quad \vec{u}_1 = \hat{u}(x, y, z) \exp(-i\omega t) \quad \text{and} \quad \dot{\omega}_{T1} = \hat{\Omega}_T \exp(-i\omega t) \quad (3.1)$$

Introducing Eq. (3.1) into Eq. (1.1) and neglecting the turbulent noise $\gamma p_0 \nabla \tilde{u}_1 : \nabla \tilde{u}_1$ in front of the combustion term $(\gamma - 1) \partial \dot{\omega}_{T1} / \partial t$ leads to the Helmholtz equation:

$$\nabla \cdot (c_0^2 \nabla \hat{P}) + \omega^2 \hat{P} = i\omega(\gamma - 1) \hat{\Omega}_T \quad (3.2)$$

where the unknown quantities are the complex amplitude \hat{P} of the pressure oscillation at frequency f and pulsation ω . Note that $\hat{\Omega}_T$, the amplitude of the heat release perturbation is also unknown and must be modeled. This is obviously the difficult part of the modeling: it is done in AVSP through an extension of the $n - \tau$ model (Crocco 1969; Kaufmann, Nicoud & Poinso 2002; Poinso & Veynante 2001) where $\dot{\omega}_{T1} \propto nu_1(x_{\text{ref}}, t - \tau)$. In 1D approaches, the interaction index n and time delay τ are two parameters describing the acoustic behaviour of a compact flame located at the axial position x_{ref} . In AVSP, where the geometry of the combustor is fully described, the flame is distributed and the interaction index and time delay depend on space. These data can be extracted from LES results by post-processing either a self-excited or a forced oscillating regime. Once measured in LES, the fields $n(x)$ and $\tau(x)$ are used to model the unsteady heat release in Eq. (3.2) as $i\omega \hat{\Omega}_T = n(x) \exp(i\omega\tau(x)) \nabla \hat{P}(x_{\text{ref}}) \cdot \vec{n}_{\text{ref}} / \rho_{\text{ref}}$. Although they depend on ω in the most general case, n and τ have been obtained at the most energetic frequency observed in the LES ($f \simeq 380$ Hz) and considered constant over the frequency domain.

Three types of boundary conditions can be prescribed together with this equation (\vec{n} is the outward unit normal vector to the boundary):

- Dirichlet condition, viz. $\hat{P} = 0$, on fully reflecting outlets,
- Neumann condition, viz. $\nabla \hat{P} \cdot \vec{n} = 0$, on fully rigid walls or reflecting inlets,
- Robin condition, viz. $cZ \nabla \hat{P} \cdot \vec{n} = i\omega \hat{P}$, on general boundaries, where Z is the local reduced complex impedance $Z = \hat{P} / \rho_0 c_0 \vec{u} \cdot \vec{n}$

In this study, the reduced boundary impedance Z has been obtained by post-processing time series of the pressure and velocity on the boundary from the LES at $f \simeq 380$ Hz.

Knowing the boundary impedance (Z), the sound speed (c_0) distribution and the flame response $n(x); \tau(x)$, and assuming that Z does not depend on ω †, a Galerkin finite element method is used to transform Eq. (3.2) into a non-linear eigenvalue problem of size N (the number of nodes in the finite element grid used to discretize the geometry) of the form:

$$[A][\hat{P}] + \omega[B][\hat{P}] + \omega^2[C][\hat{P}] = [D(\omega)][\hat{P}] \quad (3.3)$$

where $[\hat{P}]$ stands for the column vector containing the eigenmode at pulsation ω , and $[A]$, $[B]$, $[C]$ are square matrices depending only on the discretized geometry of the combustor. $[D(\omega)]$ is the unsteady contribution of the flame and depends on the pulsation through the combustion term $n(x) \exp(i\omega\tau(x))$. No efficient numerical method exists to solve this non-linear eigenvalue problem. However, in the case where the unsteady flame response is neglected, viz. $[D(\omega)] = 0$, Eq. (3.3) simplifies into a quadratic eigenvalue problem depending only on ω and ω^2 . A change of variable can then be used (Chatelin 1993) to obtain an equivalent linear eigen value problem of size $2 \times N$. Several numerical methods can then be used to assess the eigenmodes. Direct methods (e.g. QR-based) are exact and have the advantage to provide all the eigenmodes. However, they can be expensive to solve for large problems ($N > 10^3$). Since only the first few frequencies are usually of interest from a physical point of view, it is more appropriate to use an iterative method which can be applied for large problems ($N > 10^5$) without difficulty. In AVSP, we are

† The same result holds if $1/Z = 1/Z_0 + C_1\omega + C_2/\omega$, where Z_0 , Z_1 and Z_2 are complex valued constants.

using a parallel implementation of the Arnoldi method (Lehoucq *et al.* 1996), which enables to solve complex problems of size $N \simeq 20000$ in a few minutes.

Setting $[D(\omega)] = 0$ is equivalent to finding the eigenmodes of the burner, taking into account the presence of the flame through the mean temperature field but neglecting the flame effect as an acoustically active element. The boundary conditions are also considered for and this approximation can provide relevant information about the shape and real frequency of the first few modes of the combustor. However, since there is no coupling between the acoustics and the flame, there is no hope to discriminate between stable and unstable modes, which is the ultimate objective of this study. Under the assumption that the unsteady flame response acts as a small perturbation of the modes without combustion, a linear expansion technique can be developed to assess the imaginary part of ω , hence the stability of the perturbed modes (Benoit & Nicoud 2004; Nicoud & Benoit 2003). Another path has been followed in this study in order to handle cases where the unsteady response of the flame changes the modes significantly and when the linear expansion is not justified. The non-linear eigenvalue problem Eq. (3.3) is then solved iteratively, the k^{th} iteration consisting in solving the quadratic eigenvalue problem in ω_k defined as:

$$([A] - [D(\omega_{k-1})])[\hat{P}] + \omega_k[B][\hat{P}] + \omega_k^2[C][\hat{P}] = 0 \quad (3.4)$$

A natural initialization is to set $[D(\omega_0)] = 0$ so that the computation of the modes without combustion is in fact the first step of the iteration loop. Usually, less than 5 iterations are enough to converge towards the complex pulsation and associated mode.

This linearized approach to describe the stability of the burner in terms of modes has drawbacks but remains one of the basic tools to study instabilities:

- The linearization is valid only for small amplitude perturbations, a condition which is obviously not true when limit cycles typical of combustion instabilities are observed in gas turbines. However, this assumption is valid when the instability grows (Poinsot *et al.* 1988) and helps to determine the unstable modes: such modes have to appear and grow before they reach a limit cycle and any analysis adapted to this early phase is of interest.
- Most acoustic tools work on linear regimes for which each oscillatory mode is independent of other modes. Many combustion instabilities exhibit non-linear coupling where high-frequency modes couple with low-frequency oscillations: classical papers from Rogers & Marble (1956) mention such coupling. These were also observed in the experiment of Poinsot *et al.* (1987) in which a 530 Hz mode (often called rumble) was systematically accompanied by a high-frequency mode (called screech) at 3750 Hz. The fact that combustion instabilities involve more than one mode of oscillation is one of the basis of theories by Yang & Culick (1986). The tool presented above treats each mode individually and cannot simulate such phenomena.
- The description of the coupling between acoustics and combustion in such models is extremely crude. The response of the flame excited by an acoustic wave depends on several physical phenomena such as chemical reactions, species diffusion, vortex shedding, vortex-flame interaction, etc All these phenomena are not neglected in the present study but their cumulative effect is modeled through the global time scale τ and index n .

Despite these limitations, such tools are useful because they provide relevant information about the modes triggered by the acoustic/flame coupling while running fast: for the configuration described in section 5, only 8000 grid points were necessary to describe the geometry and obtain the first 4 modes. For comparison, half a million nodes were used to perform the LES discussed in section 6. A typical run for solving the quadratic

eigenvalue problem of type Eq. (3.4) on this grid lasts 10 min by using 15 processors (R14000 500 MHz IP35) on an SGI O3800 parallel machine. Such tool can thus be used in the design process of new gas turbines to characterize their thermoacoustic modes. By describing the whole geometry between the compressor and the turbine, including all the injectors dispatched around the combustion chamber, such simulations would noticeably give unique information about the swirling modes that sometimes show up in large gas turbines. The difficult and computationally expensive task would be to compute the flame transfer function by performing a LES of the turbulent flame. Such simulation would be performed by considering an angular sector corresponding to only one injector, saving a huge amount of grid points and CPU resources.

4. Acoustic energy equation

The total acoustic energy equation is an integral form of the wave equation (1.1) which is quite useful to understand basic mechanisms of combustion instabilities. This equation cannot be used to predict unstable modes like the Helmholtz solver, but is a powerful method to analyze the results of an LES as done here. The conservation equation for the acoustic energy $e_1 = \frac{1}{2}\rho_0 u_1^2 + \frac{1}{2}p_1^2/(\rho_0 c_0^2)$ is derived in Poinso & Veynante (2001) and can be written:

$$\frac{\partial e_1}{\partial t} = s_1 - \nabla \cdot (p_1 \vec{u}_1) \quad \text{with} \quad s_1 = \frac{(\gamma - 1)}{\gamma p_0} p_1 \dot{\omega}_{T1} \quad (4.1)$$

If integrated over the whole volume V of the combustor bounded by the surface A , it yields:

$$\frac{d}{dt} \int_V e_1 dV = \int_V s_1 dV - \int_A p_1 \vec{u}_1 \cdot \vec{n} dA \quad \text{or} \quad \frac{d}{dt} \mathcal{E}_1 = \mathcal{S}_1 - \mathcal{F}_1 \quad (4.2)$$

where \vec{n} is the surface normal vector. This surface consists of walls or of inlet/outlet sections.

In Eq. (4.2), all terms are time dependent. The RHS source term \mathcal{S}_1 corresponds to the Rayleigh criterion (Rayleigh 1878): it measures the correlation between unsteady pressure p_1 and unsteady heat release $\dot{\omega}_{T1}$ averaged over the whole chamber. It can act as a source or a sink term for the acoustic energy. The other RHS term \mathcal{F}_1 is less studied because it is impossible to measure experimentally. It is an acoustic flux integrated on all the boundaries. Walls have zero contribution in this term because the velocity perturbations \vec{u}_1 vanish on walls. However, \mathcal{F}_1 may be large on inlets and outlets where it is usually a loss term. Eq. (4.1) is therefore a generalization of the Rayleigh criterion: the total acoustic energy in the chamber \mathcal{E}_1 will grow if the acoustic gain term \mathcal{S}_1 is larger than the acoustic losses \mathcal{F}_1 . The magnitudes and relative importance of the two terms \mathcal{S}_1 and \mathcal{F}_1 are controversial issues in the field of combustion instabilities. For example, one important question is to know whether acoustic losses are important or not in the determination of limit cycles. For these limit cycles, the acoustic energy \mathcal{E}_1 must remain constant over a period of oscillations and Eq. (4.1) shows that such a cycle can be reached for two situations:

- The limit cycle may be *combustion controlled*: if the acoustic losses are small ($\mathcal{F}_1 = 0$), the pressure and heat release signals may adjust to give $\mathcal{S}_1 \simeq 0$. The limit cycle is reached when this phase shift leads to a zero Rayleigh term \mathcal{S}_1 as observed in certain experiments. Physically, this is often obtained when the heat release oscillations saturate (because the minimum reaction rate reaches zero at some instant of the cycle) or when the phase

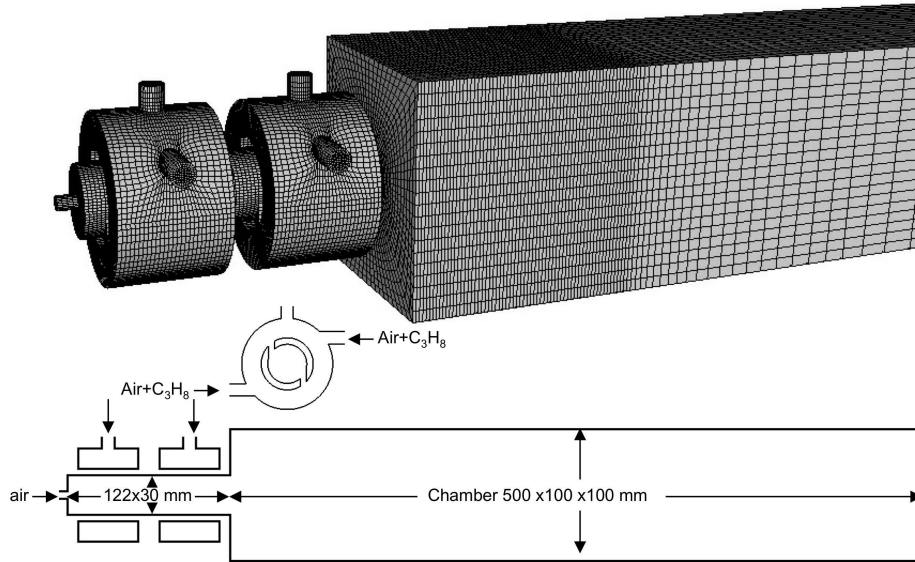


FIGURE 1. Configuration: a staged swirled combustor.

between pressure and heat release changes so that combustion itself controls the limit cycle amplitude.

- The limit cycle may be *acoustically controlled*: the source term S_1 may be large (pressure and heat release are oscillating in phase) but the acoustic losses are large too and compensate S_1 . In this case, the final amplitude of oscillation is controlled by the acoustic impedances of outlets and inlets.

Clearly, these two solutions lead to very different approaches of combustion instabilities: if the limit cycle is combustion controlled, the acoustic behavior of inlets and outlets have a limited effect on the stability; if it is acoustically controlled, acoustic impedances of inlets and outlets become essential elements of any method (experimental or numerical). In the present study, the LES results are post processed to measure all terms of Eq. (4.1) and determine whether the unstable mode is combustion or acoustically controlled (see Section 6.3).

5. Configuration

5.1. Geometry: a swirled premixed combustor

The methodologies described in the previous sections were tested for a swirled combustor displayed in Fig. 1. The configuration is typical of swirled combustion: premixed gases are introduced tangentially into a long cylindrical duct feeding the combustion chamber. The tangential injection creates the swirl required for stabilization. The fuel is propane. The two independent swirler elements allow fuel staging. The staging parameter α is defined as the ratio of fuel flow rate of the first to the second swirler. The regime studied here corresponds to the parameters given in Table 2. The staging of the burners corresponds to $\alpha = 0.3$.

Total flow rate (kg/s)	axial flow rate (kg/s)	Equivalence ratio	Reynolds number (burner mouth)
22.10 ⁻³	4.10 ⁻³	0.8	46700

TABLE 2. Flow parameters for combustion cases.

Case	Inlet σ	Outlet σ	Characteristic	Reduced impedance
LEAK	1000	1000	Non Reflecting outlet	$-0.85 + 0.35i$
REF	1000	10000	Reflecting outlet	$-0.04 + 0.21i$

TABLE 3. Acoustic inlet and outlet boundaries for the runs REF and LEAK. The last column comes from a post-processing of times series of velocity and pressure. The complex valued impedance was used as boundary condition in AVSP.

5.2. Boundary conditions

Specifying boundary conditions is a critical issue for compressible flows. Here, the NSCBC technique (Poinso & Lele 1992; Poinso & Veynante 2001) was used at the outlet. The level of reflection of this boundary can be controlled by changing the relaxation coefficient σ of the wave correction (Selle, Nicoud & Poinso 2004), which determines the amplitude of the incoming wave L_1 entering the computational domain:

$$L_1 = \sigma(p - p_t) \quad (5.1)$$

where p_t is the prescribed pressure value at infinity. Eq. 5.1 acts on the flow like a spring mechanism with a stiffness σ . The impedance of the boundary is a function of σ which can be obtained analytically for simple case (Selle, Nicoud & Poinso 2004). For more complex cases, this formula gives a good approximation of the actual impedance. For small values of σ , Eq. 5.1 keeps the pressure p close to its target value p_t while letting acoustic wave go out at the same time (Poinso & Veynante 2001): the outlet is non reflecting. When large values of σ are used, the outlet pressure remains strictly equal to p_t and the outlet becomes totally reflecting. Two sets of computation will be shown (Table 3). The first one (called LEAK) corresponds to a case where the spring stiffness σ is small so that the outlet is non reflecting and the acoustic waves are evacuated with very small reflection levels.

For the second set (REF), σ is large and the outlet is reflecting (the pressure oscillation is almost zero).

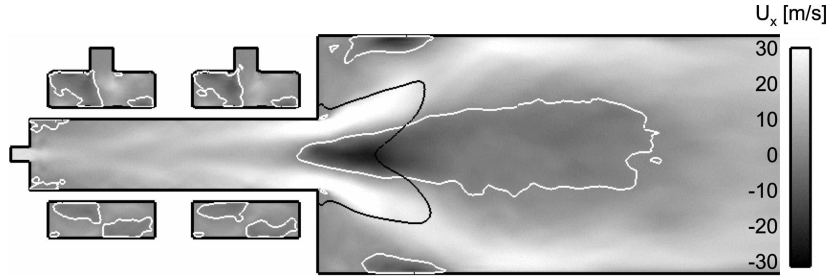


FIGURE 2. Mean axial velocity field, white line: $\text{iso-}u_x = 0$, black line: $\text{iso-T} = 1500 \text{ K}$ for stable combustion.

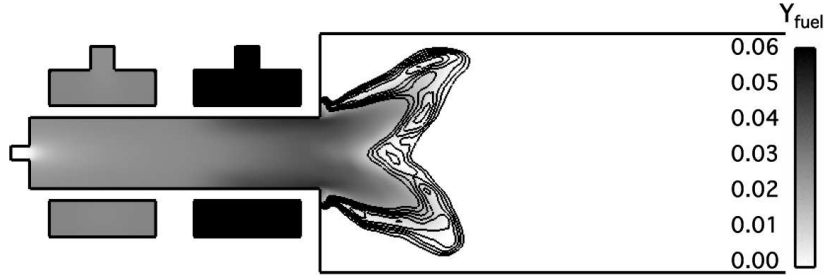


FIGURE 3. Mean fuel mass fraction field, black lines: iso-reaction rate for stable combustion.

6. Results

6.1. Stable flow

The first computation corresponds to the situation where the outlet section is non reflecting (case LEAK in Table 3). For this case, the acoustic feedback is minimized and the flame does not exhibit any strong unstable movement. The mean velocity and fuel mass fraction fields are displayed in Fig. 2 and Fig. 3. As expected, the downstream part of the central recirculation zone is filled by burnt gases and stabilize the turbulent flame.

6.2. Acoustic analysis

Using the mean temperature fields given by LES, the Helmholtz solver was used to obtain the thermoacoustic eigenmodes of the burner. For this analysis, the active effect of the flame is modelled using a transfer function ($n(x)$ and $\tau(x)$) obtained with LES, the mean sound speed is given by the average LES fields and the impedances of the REF run (Table 3) are used at the outlet and inlet of the combustor. When the outlet is set to a non reflecting condition similar to run LEAK, the acoustic solver predicts that all modes are damped. The frequency and decay/growth rate of the first four modes obtained with ($n(x)$ and $\tau(x)$ from LES) or without ($n(x)$ set to zero) acoustics/flame coupling in the REF case are displayed in Tab. 4. Note that the first four modes are mainly longitudinal. When the unsteady effect of the flame is not accounted for, all modes are damped (negative growth rate), because the mechanism which feeds the instability is not present and acoustic losses through the inlet/outlet boundary are not compensated. When the flame transfer function obtained from LES is used, the first mode is drastically damped by the acoustics/flame interaction, while the second mode is predicted to be the most unstable. The pressure node in the second mode vanishes when the acoustic/flame

Mode - no active flame	Frequency [Hz]	Growth rate [rd.s ⁻¹]	Mode - active flame	Frequency [Hz]	Growth rate [rd.s ⁻¹]
1	308	-42	1	304	-672
2	435	-23	2	432	653
3	833	-3.1	3	835	5
4	1184	-63	4	1136	232

TABLE 4. AVSP results: frequencies and growth rates of the first four modes predicted by the acoustic solver with and without acoustics/flame coupling.

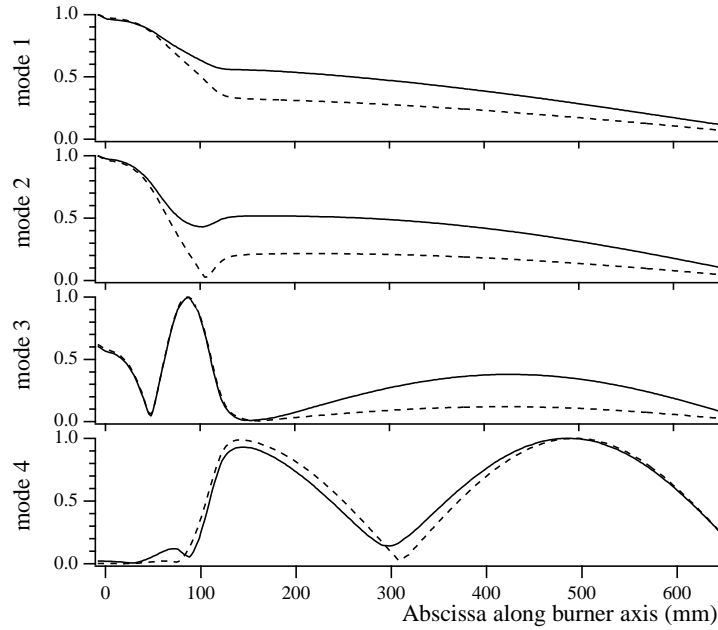


FIGURE 4. Longitudinal structure of the first four modes obtained with acoustic analysis: Normalized p_1^{rms} evolution along burner axis with acoustics/flame coupling (—) and without (----).

interaction is taken into account. The 3rd and 4th modes are only marginally triggered. Recall however that the flame transfer function has been assessed by post-processing the LES results in the 400 Hz range so that it is not clear whether the acoustics/flame interaction is properly accounted for as far as modes in the 1000 Hz range are concerned. Still, accounting for the flame transfer function allowed to discriminate between the first two modes of the burner although neither big difference in their shape can be found in Fig. 4 nor clear frequency discrimination can be stated compared to LES results (380 Hz).

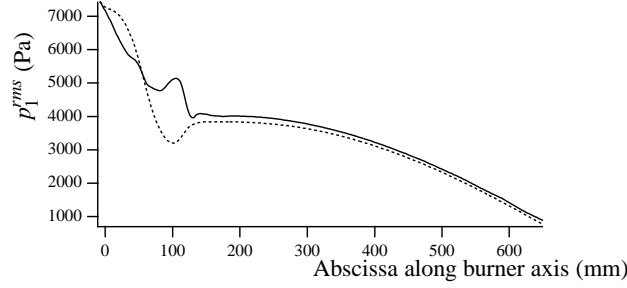


FIGURE 5. Comparison of LES (—) and acoustic (---) solvers: RMS pressure fluctuations p_1^{rms} along burner axis.

6.3. LES results

In addition to the average results of Section 6.1, LES also reveals that the combustor can exhibit a strong unstable mode when the outlet is acoustically closed (case REF). In this case, soon after ignition, the pressure and the global heat release start oscillating (Fig. 6 a) at 380 Hz which is very close to the mode predicted by AVSP in Section 6.2. To analyse the behavior of this instability, the following sequence is set up:

- Starting from a stable flame (LEAK), the outlet impedance is changed to become reflecting (case REF) at time $t = 0.127s$ (Fig. 6). The oscillation grows and reaches a limit cycle at a frequency of 380 Hz mode which is close to mode 2 predicted by the Helmholtz code (Section 6.2) at 432 Hz. Its mode structure is also very well predicted (Fig. 5): the pressure perturbation p_1^{rms} measured in the LES matches the acoustic structure of the 432 Hz mode predicted by AVSP.

- At time $t = 0.173s$, the outlet impedance is switched again to a non reflecting condition (case LEAK) so that the instability disappears.

This scenario provides three phases which are studied sequentially:

- A linear growth between times 0.127s and 0.150s (Section 6.4),
- A limit cycle between times 0.150s and 0.173s (Section 6.5),
- A decay phase starting at $t = 0.173s$ (Section 6.6)

For each phase, the instability is analyzed in terms of flame shape, flame oscillation and phase between heat release and pressure. Moreover, the acoustic energy equation budget is closed and all terms are analyzed.

6.4. Growth phase

Once the outlet boundary is acoustically closed ($t = 0.127 s$), the thermoacoustic instability starts. Fig. 6 displays the time variations of the combustion source term S_1 , the acoustic losses \mathcal{F}_1 (Fig. 6 b), the total acoustic energy in the chamber \mathcal{E}_1 (Fig. 6 d) and shows that the budget of Eq. 4.2 is very well closed by the LES data: the difference $S_1 - \mathcal{F}_1$ matches the time derivative of \mathcal{E}_1 (Fig. 6 c). This validates both the LES results and the wave equation 4.2. It is also the first example of such a treatment for a resonating combustor. Since the budget is closed, individual terms can then be analyzed.

The phase angle between pressure and heat release is displayed in Fig. 6a. During the growth phase, it is close to zero and slowly shifting towards $\pi/4$, leading to a strong coupling between pressure and heat release i.e. a positive S_1 term. During the growth phase, the source term S_1 is large and always positive (Fig. 6 b), because the phase angle stays in the $[-\pi/2; \pi/2]$ range. Fig. 6 b shows clearly that the acoustic losses balance the reacting term S_1 in the acoustic budget equation.

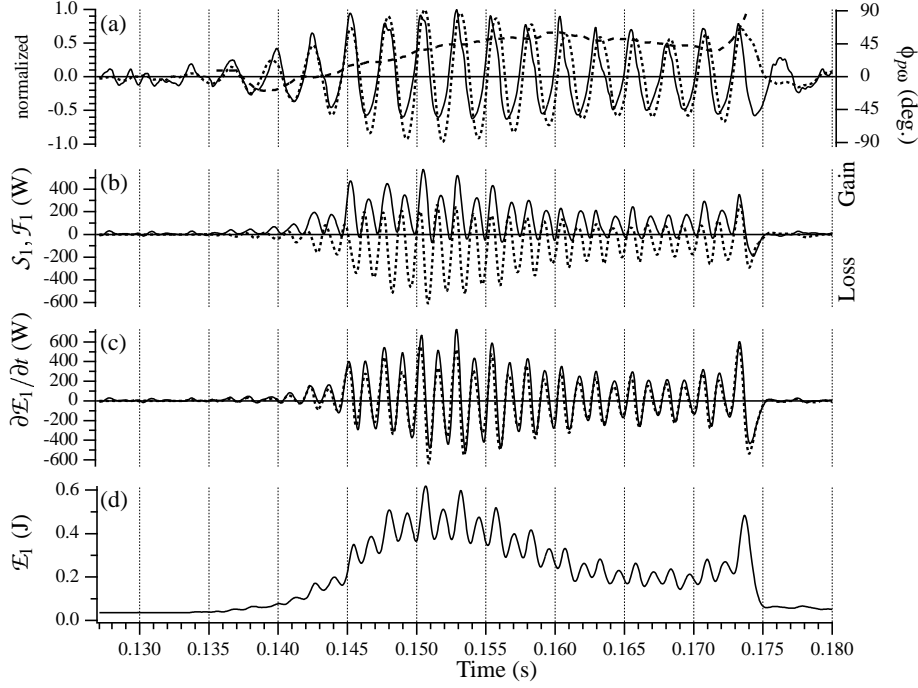


FIGURE 6. Closure of the acoustic energy equation: (a) mean normalized value of pressure (—), heat release (·····) and phase angle between these signals (---); (b) S_1 (—) and \mathcal{F}_1 (·····); (c) $S_1 - \mathcal{F}_1$ (—) and $\partial \mathcal{E}_1 / \partial t$ (·····); (d) \mathcal{E}_1 .

6.5. Limit cycle

At $t=0.150s$, the instability reaches a limit cycle at 380 Hz. Before reaching this limit cycle, a large overshoot of acoustic energy is observed: this is typical of combustion instabilities and it has been observed experimentally. Fig. 6 shows that reaching the non-linear zone, the phase difference between pressure and heat release increases from zero to $\pi/4$ in the limit cycle zone. The drift of this phase difference together with increasing acoustic losses lead to the saturation of the instability.

The coupling loop between p_1 and $\dot{\omega}_{T1}$ can be identified from LES as follows. The longitudinal mode induces the formation of a vortex ring at the dump plane. This vortex ring strongly interacts in phase with the flame. Fig. 7 illustrates the interaction between the acoustically induced vortex ring and the flame brush. Fig. 8 allows to locate LES snapshots in the acoustic period and displays the mean pressure fluctuation p_1 in the flame zone, the heat release fluctuation $\dot{\omega}_{T1}$, and the fluctuation of the mean velocity in the dump plane u_1^{dump} . At instant 1, a vortex ring appears at the dump plane when du_1^{dump}/dt is maximum. The ring structure detaches and is convected through the flame by the mean flow (instants 2, 3 and 4). During the period 1-3 the flow incoming from the injector pipe stretches the flame, increasing its area, whereas the flame wrinkling by the vortex ring remains weak. Consequently $\dot{\omega}_{T1}$ increases with a medium slope. Between points 3 and 5 the vortex ring is clearly wrinkling the flame and $\dot{\omega}_{T1}$ increases faster. Moreover, the vortex ring is gradually destroyed, and its global coherence disappears between instants 4 and 5, at a moment when du_1^{dump}/dt is minimum. At instant 5 some

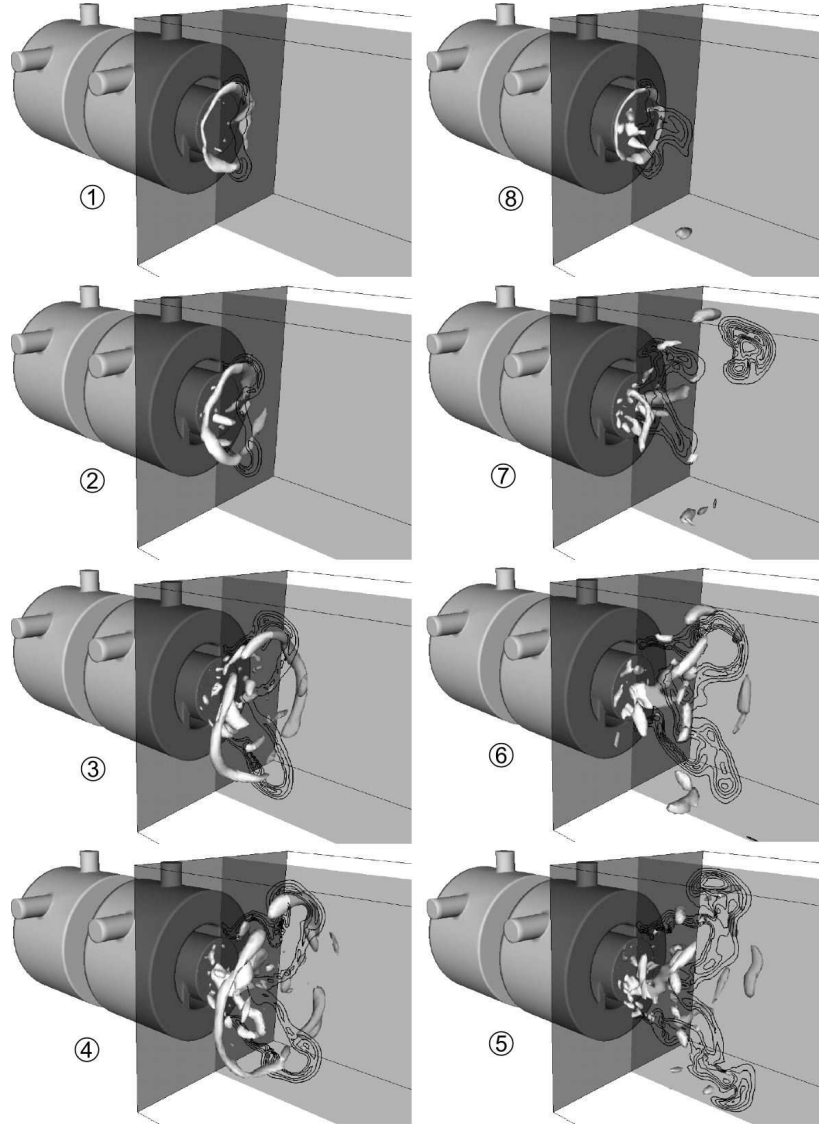


FIGURE 7. Vortex ring shedding for a period during the limit cycle, isosurface: Q vortex criterion; black lines: iso-reaction rate.

coherent structures are still interacting with the flame, producing (noisy) flame pockets and cusps. After 5, the flame burns out the fresh gases present in the chamber and propagates back to the injection pipe decreasing the overall flame surface and $\dot{\omega}_{T1}$.

6.6. Decay phase

The decay phase is triggered by the sudden change in the acoustic outlet boundary condition switching to non-reflecting (LEAK). The phase angle $\phi_{p\omega}$ increases by a large amount: $\phi_{p\omega} > \pi/2$ at $t = 0.174s$ i.e. $1.2ms$ after relaxing outlet pressure (Fig. 6). At this time S_1 becomes globally negative for the first time and the instability is rapidly damped. The acoustic losses actually become positive (gain term) during this last oscillation but

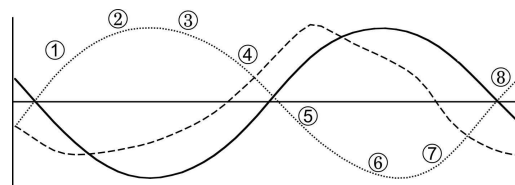


FIGURE 8. Time signals during the limit cycle and snapshots corresponding to the previous figure: pressure (—), inlet velocity (----) and total heat release (.....)

the instability *engine* is broken and the Rayleigh term S_1 becomes negative during a half cycle ($0.173 < t < 0.175\text{ms}$ on Fig. 6) leading to the immediate disappearance of all unstable activity.

7. Conclusions

Three complementary tools have been used to analyse the instability modes of a staged swirled combustor: full compressible LES, Helmholtz analysis and budget of acoustic energy. The two latter methods utilize LES results but provide essential new elements: the Helmholtz results allow the exact identification of modes appearing during the instability, while the budget of acoustic energy demonstrates that the Rayleigh criterion is not the only or even the largest term in the acoustic energy equation: acoustic losses at the outlet of the combustor contribute significantly to the budget of acoustic energy and determine the levels of oscillation amplitudes as well as their appearance.

Acknowledgments

Certain numerical simulations have been conducted on the computers of the CINES and IDRIS French national computing centers. Simulations have been supported partly by ALSTOM POWER and by the EC program (WP2) FUELCHIEF.

REFERENCES

- ANGELBERGER, C., EGOLFOPOULOS, F. & VEYNANTE, D. 2000 Large Eddy Simulations of chemical and acoustic effects on combustion instabilities *Flow Turb. and Combustion* **65**, 205-22.
- ANGELBERGER, D., VEYNANTE, D., EGOLFOPOULOS, F. & POINSOT, T. 1998 Large Eddy Simulations of combustion instabilities in premixed flames *Summer Program* 61-82.
- BENOIT, L. & NICLOUD, F. 2004 Numerical assessment of thermo-acoustic instabilities in gas turbines *ICFD Conference of numerical methods for fluid dynamics*.
- BUTLER, T.D. & O'ROURKE, P.J. 1977 A numerical method for two-dimensional unsteady reacting flows *16th Symp. (Int.) on Combustion* 1503 - 1515.
- CANDEL, S. 1992 Combustion instabilities coupled by pressure waves and their active control. *24th Symp. (Int.) on Combustion* 1277-1296.
- CARAENI, D., BERGSTRÖM, C. & FUCHS, L. 2000 Modeling of Liquid Fuel Injection, Evaporation and Mixing in a Gas Turbine Burner Using Large Eddy Simulation *Flow Turb. and Combustion* **65**, 223-244.
- CHARLETTE, F., VEYNANTE, D. & MENEVEAU, C. 2002 A power-law wrinkling model

- for LES of premixed turbulent combustion: Part I - non-dynamic formulation and initial tests *Combust. Flame* **131**, 159-180.
- CHATELIN, F. 1993 Eigenvalues of matrices, J. Wiley.
- COLIN, O. & RUDGYARD, M. 2000 Development of high-order Taylor-Galerkin schemes for unsteady calculations *J. Comput. Phys.* **162**, 338-371.
- COLIN, O., DUCROS, F., VEYNANTE, D. & POINSOT, T. 2000 A thickened flame model for large eddy simulations of turbulent premixed combustion *Phys. Fluids* **12**, 1843-1863.
- CRIGHTON, D.G., DOWLING, A., FLOWCS WILLIAMS, J.E., HECKL, M. & LEPPINGTON, F. 1992 Modern methods in analytical acoustics, Springer Verlag.
- CROCCO, L. 1969 Research on combustion instability in liquid propellant rockets. *12th Symp. (Int.) on Combustion* 85-99.
- DESJARDINS, P.E. & FRANKEL, S.H. 1999 Two dimensional Large Eddy Simulation of soot formation in the near field of a strongly radiating nonpremixed acetylene-air jet flame *Combust. Flame* **119**, 121-133.
- DUCHAMP DE LAGENESTE, L. & PITSCH, H. 2001 Progress in large eddy simulation of premixed and partially premixed turbulent combustion *Annual Research Briefs* 61-82.
- DUCROS, F., COMTE, P. & LESIEUR, M. 1996 Large-eddy simulation of transition to turbulence in a boundary layer developing spatially over a flat plate *J. Fluid Mech.* **326**, 1-36.
- GAMET, L., DUCROS, F., NICOUD, F. & POINSOT, T. 1999 Compact Finite Difference Schemes on Non-Uniform Meshes. Application to Direct Numerical Simulations of Compressible Flows. *Int. J. for Num. Meth. in Fluids* **29**, 159-191.
- KAUFMANN, A., NICOUD, F. & POINSOT, T. 2002 Flow forcing techniques for numerical simulation of combustion instabilities *Combust. Flame* **131**, 371-385.
- KELLER, J.O., VANEVELD, L., KORSCHOLT, D., HUBBARD, G.L., GHONIEM, A.F., DAILY, J.W. & OPPENHEIM, A.K. 1981 Mechanism of instabilities in turbulent combustion leading to flashback *AIAA Journal* **20**, 254-262.
- KEMPF, A., FORKEL, H., CHEN, J.-Y., SADIKI, A. & JANICKA, J. 2000 Large-eddy simulation of a counterflow configuration with and without combustion *Proc. of the Combustion Institute* **28**, 35-40.
- KRUEGER, U., HUEREN, J., HOFFMANN, S., KREBS, W., FLOHR, P. & BOHN, D. 2000 Prediction and measurements of thermoacoustic improvements in gas turbines with annular combustion systems *ASME TURBO EXPO 2000* 2000-GT-0095, ASME Paper,
- LEHOUCQ, R., MASCHOFF, K., SORENSEN, D. & YANG, C. 1996 ARPACK website, <http://www.caam.rice.edu/software/ARPACK>.
- LELE, S. 1992 Compact finite difference schemes with spectral like resolution *J. Comput. Phys.* **103**, 16-42.
- LÉGIER, J.-PH., POINSOT, T. & VEYNANTE, D. 2000 Dynamically thickened flame Large Eddy Simulation model for premixed and non-premixed turbulent combustion *Summer Program 2000* 157-168.
- NICOUD, F. & BENOIT, L. 2003 Global tools for thermo-acoustic instabilities in gas turbines *Bulletin of the American Physical Society* **48**, 240-241.
- NICOUD, F. & DUCROS, F. 1999 Subgrid-scale stress modelling based on the square of the velocity gradient *Flow Turb. and Combustion* **62**, 183-200.

- PASCHEREIT, C.O., FLOHR, P. & SCHUERMANS, B. 2001 Prediction of combustion oscillations in gas turbine combustors. *39th AIAA Aerospace Sciences Meeting and Exhibit*. 2001-0484, AIAA Paper, 484.
- PETERS, N. 2000 Turbulent combustion, Cambridge University Press.
- PETERS, N. & ROGG, B. 1993 Reduced Kinetic Mechanisms for Applications in Combustion Systems, Springer Verlag.
- PIERCE, C.D. & MOIN, P. 2004 Progress-variable approach for large eddy simulation of non-premixed turbulent combustion *J. Fluid Mech.* **504**, 73-97.
- PITSCH, H. & DUCHAMP DE LA GENESTE, L. 2002 Large Eddy Simulation of Premixed Turbulent Combustion using a level-set approach *Proc of the Comb. Institute* **29**, 2001-2008.
- PITSCH, H. & STEINER, H. 2000 Large Eddy Simulation of a Turbulent Piloted Methane/Air Diffusion Flame (Sandia Flame D) *Phys. Fluids* **12**, 2541-2554.
- POINSOT, T. & LELE, S. 1992 Boundary conditions for direct simulations of compressible viscous flows *J. Comput. Phys.* **101**, 104-129.
- POINSOT, T., TROUVE, A., VEYNANTE, D., CANDEL, S. & ESPOSITO, E. 1987 Vortex driven acoustically coupled combustion instabilities *J. Fluid Mech.* **177**, 265-292.
- POINSOT, T. & VEYNANTE, D. 2001 Theoretical and numerical combustion, R.T. Edwards.
- POINSOT, T., VEYNANTE, D., BOURIENNE, F., CANDEL, S., ESPOSITO, E. & SURJET, J. 1988 Initiation and suppression of combustion instabilities by active control *22nd Symp. (Int.) on Combustion* 1363-1370.
- POLIFKE, W., PONCET, A., PASCHEREIT, C.O. & DOEBBELING, K. 2001 Reconstruction of acoustic transfer matrices by instationnary computational fluid dynamics *J. Sound Vibration* **245**, 483-510.
- RAYLEIGH, L. 1878 The explanation of certain acoustic phenomena *Nature* July 18, 319-321.
- ROGERS, D.E. & MARBLE, F.E. 1956 A mechanism for high frequency oscillations in ramjet combustors and afterburners *Jet Propulsion* **26**, 456-462.
- SAGAUT, P. 2000 Large Eddy Simulation for incompressible flows, Springer-Verlag.
- SCOTTI, A., MENEVEAU, C. & FATICA, M. 1997 Generalized Smagorinski model for anisotropic grids *Phys. Fluids* **9**, 1856-1858.
- SCOTTI, A., MENEVEAU, C. & LILLY, D.K. 1993 Generalized Smagorinski model for anisotropic grids *Phys. Fluids* **5**, 2306-2308.
- SELLE, L., LARTIGUE, G., POINSOT, T., KOCH, R., SCHILDMACHER, K.U., KREBS, W., PRADE, B., KAUFMANN, P. & VEYNANTE, D. 2004 Compressible Large-Eddy Simulation of turbulent combustion in complex geometry on unstructured meshes *Combust. Flame* **137**, 489-505.
- SELLE, L., NICOD, F. & POINSOT, T. 2004 The actual impedance of non-reflecting boundary conditions: implications for the computation of resonators *AIAA Journal* **42**, 958-964.
- STOW, S.R. & DOWLING, A.P. 2001 Thermoacoustic oscillations in an annular combustor *ASME Paper*
- VASILYEV, O. V., LUND, T.S. & MOIN, P. 1998 A general class of commutative filters for LES in complex geometries *J. Comput. Phys.* **146**, 82-104.
- YANG, V. & CULICK, F.E.C 1986 Analysis of low-frequency combustion instabilities in a laboratory ramjet combustor *Combust. Sci. Tech.* **45**, 1-25.

Toward improved boundary conditions for the DNS and LES of turbulent subsonic flows

By R. Prosser[†] and J. Schlüter

A procedure is outlined for the specification of time dependent boundary conditions, suitable for viscous, conducting flows. The method is based on a low Mach number asymptotic expansion of the governing equations and the characteristics derived from them. By consistent matching of the terms in the expansions, it is possible to develop inflow and outflow conditions that are transparent to acoustic waves, yet retain the flexibility to allow for complex flow structures such as turbulence to enter or leave the computational domain. The boundary conditions developed here represent a midway point in the evolution of this approach, which was originally developed for Euler flows, and which is evolving toward treatment of fully reacting viscous simulations.

1. Introduction

The specification of appropriate boundary conditions for compressible, turbulent reacting flows is an open problem. Even for simplified flows, such as those without thermal conduction or chemical effects, the structure of a turbulent flow is complex. The specification of time dependent boundary conditions for such flows poses a challenge to many of the currently available methods, which themselves are essentially based on the linearized Euler equations.

Broadly speaking, boundary conditions fall into two categories: *global methods* and *local methods*. In the former category transforms are taken of the governing equations, and the boundary conditions are expressed in terms of a non-local asymptotic expression designed to admit the passage of wave-like phenomena (Tsynkov 1998). The family of global methods are difficult to implement in general flows however, and there are still significant uncertainties regarding their application to flows with chemical reactions and heat release. The second family of methods obtain boundary conditions by exploiting information derived from the local behaviour of the flow. A number of authors have used local methods to derive non-reflecting boundary conditions, such as the PML approach (Hu 1996; Hesthaven 1998) and the family of schemes based on the method of characteristics. This latter class is particularly popular, and although originally designed for the linearized Euler system (Thompson 1987; Vichnevetsky 1986; Hedstrom 1979; Rudy & Strikwerda 1981; Rudy & Strikwerda 1980), the methods have been developed considerably. The culmination of these efforts is found in the Navier-Stokes Characteristic Boundary Conditions (NSCBC) and the Local One Dimensional Inviscid (LODI) approaches developed by Poinso and Lele (Poinso & Lele 1992). This method has been demonstrated in a number of challenging flow cases, such as the free shear layer simulations of Grinstein (Grinstein 1994), for the short time integration of low Mach number flows. The NSCBC approach has been further modified for reacting flows by Baum,

[†] Dept. of Mechanical, Aerospace and Manufacturing Engineering UMIST, Manchester, UK

Poinsot and Thévenin (Baum *et al.* 1994; Thevenin *et al.* 1996), and more recently by Sutherland and Kennedy (Sutherland & Kennedy 2003). Recently, Nicoud (Nicoud 1999) has developed the LODI approach to provide a promising avenue toward the generation of acoustically transparent inflow conditions. In the LODI approach, the hyperbolic components of the governing equations are decomposed into characteristics at the computational boundary. If the required boundary specification is to be non-reflecting, then the amplitude time variation of the incoming characteristics are set to zero (Hedstrom 1979). The LODI mechanism provides a means of specifying Dirichlet or Neumann boundary conditions via the balancing of the incoming and outgoing characteristics. While elegant, the LODI/NSCBC approach has the drawback that (at this time), the scheme still prevents the specification of acoustically transparent, non-trivial inflow boundary conditions. Simultaneously, the method has some difficulty in representing the pressure field accurately when turbulence crosses the computational domain (Prosser 2004). The work described here builds on results obtained previously for inviscid flows (Prosser 2004), and aims to produce non-reflecting boundary conditions for non-reacting viscous, conducting flows. The extension of the method to the viscous reacting flow case will be described in a future paper.

2. The governing equations

In a domain $\Omega \subset \mathbf{R}^n$, the compressible Navier-Stokes equations can be written as

$$\partial_t (\tilde{\mathbf{U}}) + \sum_{i=1}^n \partial_{\tilde{x}_i} (\mathbf{F}_i) = \mathbf{C}, \quad (2.1)$$

where $\tilde{\mathbf{U}}$ is the $n+2$ dimensional vector of conserved variables, \mathbf{F}_i is the $n+2$ dimensional flux vector and \mathbf{C} is a vector containing diffusive fluxes, reaction rates and other algebraic terms.

For a boundary whose normal points in the x_α direction, the NSCBC approach decomposes the α -direction flux term into

$$\partial_t (\tilde{\mathbf{U}}) + \mathbf{P} \mathbf{S}_\alpha^{-1} \Lambda_\alpha \mathbf{S}_\alpha \partial_{\tilde{x}_\alpha} (\mathbf{U}) + \sum_{\substack{i=1 \\ i \neq \alpha}}^n \partial_{\tilde{x}_i} (\mathbf{F}_i) = \mathbf{C}. \quad (2.2)$$

In equation system 2.2, \mathbf{U} is a (non-unique) vector of primitive variables, $\mathbf{P} = \tilde{\mathbf{U}}_{\mathbf{U}}$, Λ_α is the diagonal matrix of eigenvalues of $\mathbf{P}^{-1} ((\mathbf{F}_\alpha)_{\mathbf{U}})$, and \mathbf{S}_α is the matrix of left eigenvalues of $\mathbf{P}^{-1} (\mathbf{F}_\alpha)_{\mathbf{U}}$. There is no summation over Greek indices. The equivalent primitive formulation to equation system 2.2 is

$$\partial_t (\mathbf{U}) + \mathbf{S}_\alpha^{-1} \Lambda_\alpha \mathbf{S}_\alpha \partial_{\tilde{x}_\alpha} (\mathbf{U}) + \sum_{\substack{i=1 \\ i \neq \alpha}}^n \mathbf{P}^{-1} (\mathbf{F}_i)_{\mathbf{U}} \partial_{\tilde{x}_i} (\mathbf{U}) = \mathbf{P}^{-1} \mathbf{C}. \quad (2.3)$$

In the literature on NSCBC boundary conditions the nomenclature $\mathbf{L}_\alpha = \Lambda_\alpha \mathbf{S}_\alpha$ is often used, with \mathbf{L}_α referred to as the vector of *characteristic wave amplitude variations* (or *amplitudes* hereafter). In the following, we extend the treatment developed by Prosser (Prosser 2004) for Euler flows, to include the effects of molecular transport on the specification of these amplitudes.

We begin by considering a two-dimensional problem ($n = 2$). We non-dimensionalise equation systems 2.2 and 2.3, and introduce a low Mach number expansion for each

of the dependent variables (McMurtry *et al.* 1986) i.e. the pressure is written as $p = p^{(0)} + Mp^{(1)} + M^2p^{(2)} + O(M^3)$. Bracketed, superscripted numbers are used to index the terms in a given expansion. The second step is to decompose the convective flux terms into motions defined on two length scales: inertial scales $\mathbf{x} = (x \ y)^T$ and acoustic scales $\eta = (\xi \ \theta)^T$, $\xi = Mx$, $\theta = My$. The convective derivatives appearing in the Navier-Stokes equations are consequently expressed as (in the case of the non-dimensionalised \tilde{x} derivative (Klein 1995))

$$\left. \frac{\partial}{\partial \tilde{x}} \right|_{M,t} = \frac{\partial}{\partial x} + M \frac{\partial}{\partial \xi}. \quad (2.4)$$

The expansions are inserted into the primitive equations and the associated characteristics. By appropriate matching of terms, revised treatments for time dependant boundary conditions can be derived that better satisfy the demands of mass, momentum and energy conservation.

For the choice of conservative vector $\tilde{\mathbf{U}} = (\rho \ \rho u \ \rho v \ \rho E)^T$, the dimensionless form of the equation system for a viscous, conducting, single species flow is written as

$$\begin{aligned} \frac{\partial \rho}{\partial t} + \frac{\partial}{\partial \tilde{x}_k} (\rho u_k) &= 0 \\ \frac{\partial (\rho u_i)}{\partial t} + \frac{\partial}{\partial \tilde{x}_k} (\rho u_i u_k) + \frac{1}{M^2} \frac{\partial p}{\partial \tilde{x}_k} &= \frac{1}{\text{Re}} \frac{\partial \tau_{ik}}{\partial \tilde{x}_k} \\ \frac{\partial (\rho E)}{\partial t} + \frac{\partial}{\partial \tilde{x}_k} ((\rho E + p) u_k) &= \frac{(\gamma - 1) M^2}{\text{Re}} \frac{\partial}{\partial \tilde{x}_k} (u_i \tau_{ik}) \\ &+ \frac{1}{\text{Re Pr}} \frac{\partial}{\partial \tilde{x}_k} \left(\lambda \frac{\partial T}{\partial \tilde{x}_k} \right). \end{aligned} \quad (2.5)$$

In the previous equations, \tilde{x}_i represents the dimensionless distance. Re is the flow Reynolds number. E is the stagnation internal energy, τ is the viscous stress tensor and M is a flow Mach number (defined below). Pr is the Prandtl number and λ is the thermal conductivity. The equations are closed by the thermal and caloric equations of state;

$$p = \rho RT \quad (2.6)$$

$$h = h^0 + \int c_p(T') dT'. \quad (2.7)$$

In equations 2.5a-c, the variables have been non-dimensionalised with respect to a length scale characterising the domain size l_0 , a density ρ_0 and a velocity u_0 , which is assumed to be small with respect to the local sound speed. Under these assumptions, the flow Mach number $u_0 (\gamma R_0 T_0)^{-\frac{1}{2}}$ appearing in equations 2.5b and 2.5c is small. The thermodynamic quantities c_p , c_v , and R , (which henceforth will be assumed to be constant) are non-dimensionalized with respect to $(c_p)_0 \equiv c_p$. The pressure is non-dimensionalized with respect to a thermodynamic pressure $\gamma \rho_0 R T_0$, where T_0 is an absolute temperature and γ is introduced to simplify the subsequent algebra. Using these variables, the local sound speed in dimensionless coordinates is $a = M^{-1} (\gamma p / \rho)^{\frac{1}{2}}$. Finally, we introduce a supplementary equation for the pressure as this will be useful in the later development;

$$\frac{\partial p}{\partial t} + u_k \frac{\partial p}{\partial \tilde{x}_k} + \gamma p \left(\frac{\partial u_k}{\partial \tilde{x}_k} \right) = \frac{(\gamma - 1) M^2}{\text{Re}} \tau_{ik} \frac{\partial u_i}{\partial \tilde{x}_k} + \frac{1}{\text{Re Pr}} \frac{\partial}{\partial \tilde{x}_k} \left(\lambda \frac{\partial T}{\partial \tilde{x}_k} \right). \quad (2.8)$$

equation 2.8 can be derived from equations 2.5a-c, 2.6 and 2.7, and can be used in place of equation 2.5c if desired (Majda & Sethian 1985).

For definiteness, we consider a two dimensional domain whose boundaries are aligned with the \tilde{x} and \tilde{y} axes. We assume that the left hand (inlet) boundary will be located at $\tilde{x} = 0$, the right hand (outlet) boundary will be located at $\tilde{x} = 1$. Using the methods outlined above, the governing equations are consequently replaced on the boundaries by

$$\begin{aligned}
 \frac{\partial \rho}{\partial t} &= - \left(\frac{\rho}{T} (L_1 + L_4) - \frac{\rho}{c_p} L_2 + v \frac{\partial \rho}{\partial \tilde{y}} + \rho \frac{\partial v}{\partial \tilde{y}} \right) \\
 \frac{\partial u}{\partial t} &= - \left(\frac{1}{MT} \sqrt{\frac{\gamma p}{\rho}} (L_4 - L_1) + v \frac{\partial u}{\partial \tilde{y}} \right) + \frac{1}{\text{Re}} \left(\frac{\partial \tau_{\tilde{x}\tilde{x}}}{\partial \tilde{x}} + \frac{\partial \tau_{\tilde{x}\tilde{y}}}{\partial \tilde{y}} \right) \\
 \frac{\partial v}{\partial t} &= - \left(L_3 + v \frac{\partial v}{\partial \tilde{y}} + \frac{1}{\rho M^2} \frac{\partial p}{\partial \tilde{y}} \right) + \frac{1}{\text{Re}} \left(\frac{\partial \tau_{\tilde{y}\tilde{x}}}{\partial \tilde{x}} + \frac{\partial \tau_{\tilde{y}\tilde{y}}}{\partial \tilde{y}} \right) \\
 \frac{\partial p}{\partial t} &= - \left(\rho c_p (L_4 + L_1) + \gamma p \frac{\partial v}{\partial \tilde{y}} + v \frac{\partial p}{\partial \tilde{y}} \right) \\
 &\quad + \frac{(\gamma - 1) M^2}{\text{Re}} \Phi + \frac{1}{\text{Re Pr}} \left(\frac{\partial}{\partial \tilde{x}} \left(\lambda \frac{\partial T}{\partial \tilde{x}} \right) + \frac{\partial}{\partial \tilde{y}} \left(\lambda \frac{\partial T}{\partial \tilde{y}} \right) \right)
 \end{aligned} \tag{2.9}$$

in which $\Phi \equiv \tau : \nabla u \geq 0$, and the dimensionless specific heats $c_p (\equiv 1)$ and $c_v (\equiv \gamma^{-1})$ are kept explicitly to help clarify the algebra when the equations are re-expressed in their dimensional form. The amplitudes are

$$\begin{aligned}
 L_1 &= \frac{1}{2\rho c_p} \left(u - \frac{1}{M} \sqrt{\frac{\gamma p}{\rho}} \right) \left(\frac{\partial p}{\partial \tilde{x}} - M \sqrt{\gamma \rho p} \frac{\partial u}{\partial \tilde{x}} \right) \\
 L_2 &= u \left(c_v \left(\frac{1}{p} \frac{\partial p}{\partial \tilde{x}} - \frac{\gamma}{\rho} \frac{\partial \rho}{\partial \tilde{x}} \right) \right) \\
 L_3 &= u \frac{\partial v}{\partial \tilde{x}} \\
 L_4 &= \frac{1}{2\rho c_p} \left(u + \frac{1}{M} \sqrt{\frac{\gamma p}{\rho}} \right) \left(\frac{\partial p}{\partial \tilde{x}} + M \sqrt{\gamma \rho p} \frac{\partial u}{\partial \tilde{x}} \right)
 \end{aligned} \tag{2.10}$$

At the inlet boundary, conditions must be specified for the unknown incoming amplitudes; L_2 , L_3 , L_4 . For the outlet boundary, the only incoming amplitude requiring specification is L_1 . Traditional non-reflecting boundary conditions (Hedstrom 1979; Thompson 1987) are obtained by setting all incoming amplitudes to zero. A range of other practical boundary conditions can be specified by appropriate matching of incoming or outgoing amplitudes (Poinsot & Lele 1992; Baum *et al.* 1994). It has been previously demonstrated (Prosser 2004) that these older boundary conditions produce spurious pressure oscillations that propagate into the computational domain at the local speed of sound. This is

because, for low Mach number flows, the non-linear amplitudes have the expansions

$$\begin{aligned} L_1 &= L_1^{(0)} + ML_1^{(1)} + \dots \\ &= \frac{1}{2\rho^{(0)}c_p} \left(\gamma p^{(0)} \frac{\partial u^{(0)}}{\partial x} + M \left(\gamma p^{(0)} \left(\frac{\partial u^{(0)}}{\partial \xi} + \frac{\partial u^{(1)}}{\partial x} + \frac{\partial u^{(0)}}{\partial x} \left(\frac{p^{(1)}}{p^{(0)}} - \frac{\rho^{(1)}}{\rho^{(0)}} \right) \right) \right. \right. \\ &\quad \left. \left. - \sqrt{\frac{\gamma p^{(0)}}{\rho^{(0)}}} \left\{ \frac{\partial p^{(1)}}{\partial \xi} + \frac{\partial p^{(2)}}{\partial x} + \rho^{(0)} u^{(0)} \frac{\partial u^{(0)}}{\partial x} \right\} \right) \right) + O(M^2) \end{aligned} \quad (2.11)$$

$$\begin{aligned} L_4 &= L_4^{(0)} + ML_4^{(1)} + \dots \\ &= \frac{1}{2\rho^{(0)}c_p} \left(\gamma p^{(0)} \frac{\partial u^{(0)}}{\partial x} + M \left(\gamma p^{(0)} \left(\frac{\partial u^{(0)}}{\partial \xi} + \frac{\partial u^{(1)}}{\partial x} + \frac{\partial u^{(0)}}{\partial x} \left(\frac{p^{(1)}}{p^{(0)}} - \frac{\rho^{(1)}}{\rho^{(0)}} \right) \right) \right. \right. \\ &\quad \left. \left. + \sqrt{\frac{\gamma p^{(0)}}{\rho^{(0)}}} \left\{ \frac{\partial p^{(1)}}{\partial \xi} + \frac{\partial p^{(2)}}{\partial x} + \rho^{(0)} u^{(0)} \frac{\partial u^{(0)}}{\partial x} \right\} \right) \right) + O(M^2). \end{aligned} \quad (2.12)$$

By comparing the leading order terms of L_1 and L_4 with the leading order expansion of equation 2.8, it can be seen that the amplitudes control the value of the global thermodynamic pressure (via the maintenance of a divergence free velocity field). Similarly, the momentum equation—which appears in the above equations as an $O(M)$ term—must also be retained for correct treatment of the momentum at the boundary. Consequently, we seek a new treatment for L_1 and/or L_4 that retains these essential features, but still keeps the non-reflecting behaviour.

3. Revised viscous outflow boundary conditions

A natural first step towards a revised outflow is to generalise the LODI/NSCBC boundary condition of Poinso *et al.* (Poinso & Lele 1992; Thevénin *et al.* 1996; Baum *et al.* 1994) to flows with transverse inertial structure and viscosity. We re-write equation 2.9b in terms of the leading orders of a low Mach number expansion and rearrange to obtain

$$L_1 = L_4 - MT^{(0)} \sqrt{\frac{\rho^{(0)}}{\gamma p^{(0)}}} \left(\frac{1}{\text{Re}} \left(\frac{\partial \tau_{yx}^{(0)}}{\partial x} + \frac{\partial \tau_{yy}^{(0)}}{\partial y} \right) - \frac{\partial u^{(0)}}{\partial t} - v \frac{\partial u^{(0)}}{\partial y} \right) + O(M^2). \quad (3.1)$$

There are two difficulties with equation 3.1: the specification of $\partial u^{(0)}/\partial t$, and the reflecting nature of the resulting boundary condition. There are a number of ways to deal with the temporal term. For the purposes of this paper, we use a simple frozen turbulence approximation:

$$\frac{\partial u^{(0)}}{\partial t} = -u_b \frac{\partial u^{(0)}}{\partial x}, \quad (3.2)$$

where u_b is the mean speed of the flow. To deal with the reflection, we realise that the boundary is reflective because L_1 should contain *only* left-going acoustic waves, while L_4 contains *only* right going waves (c.f. equations 2.11 and 2.12). Equating the two directly leads to L_1 inheriting a wave propagating in the wrong direction (Prosser 2004). The non-reflecting condition translates to the absence of incoming acoustic waves at the boundary and hence, equation 3.1 should have all acoustic behaviour removed from it.

This is achieved explicitly by subtracting the acoustic component of L_4 to obtain

$$\begin{aligned} L_1 = L_4 - MT^{(0)} & \sqrt{\frac{\rho^{(0)}}{\gamma p^{(0)}}} \left(\frac{1}{\text{Re}} \left(\frac{\partial \tau_{yx}^{(0)}}{\partial x} + \frac{\partial \tau_{yy}^{(0)}}{\partial y} \right) + u_b \frac{\partial u^{(0)}}{\partial x} - v \frac{\partial u^{(0)}}{\partial y} \right) \\ & - \frac{1}{2\rho^{(0)}c_p} \sqrt{\frac{\gamma p^{(0)}}{\rho^{(0)}}} \left(\sqrt{\gamma \rho^{(0)} p^{(0)}} \frac{\partial u^{(0)}}{\partial \xi} + \frac{\partial p^{(1)}}{\partial \xi} \right) + O(M^2). \end{aligned} \quad (3.3)$$

An alternative non-reflecting condition can then be written by applying the non-reflecting condition of Hedstrom (Hedstrom 1979) to the *acoustic components* of the characteristic amplitudes (Prosser 2004);

$$\left(\sqrt{\gamma \rho^{(0)} p^{(0)}} \frac{\partial u^{(0)}}{\partial \xi} - \frac{\partial p^{(1)}}{\partial \xi} \right) = 0. \quad (3.4)$$

Substituting this equation into equation 3.3, leads to

$$\begin{aligned} L_1 = L_4 - MT^{(0)} & \sqrt{\frac{\rho^{(0)}}{\gamma p^{(0)}}} \left(\frac{1}{\text{Re}} \left(\frac{\partial \tau_{yx}^{(0)}}{\partial x} + \frac{\partial \tau_{yy}^{(0)}}{\partial y} \right) + u_b \frac{\partial u^{(0)}}{\partial x} - v \frac{\partial u^{(0)}}{\partial y} \right) \\ & - (\gamma - 1) T^{(0)} \frac{\partial u^{(0)}}{\partial \xi}. \end{aligned} \quad (3.5)$$

Thus, the problem applying the non-reflecting condition devolves into one of calculating $\partial u^{(0)}/\partial \xi$; the flow divergence on the acoustic scales. This may be accomplished in practical terms by considering the leading order equation for pressure:

$$\frac{\partial p^{(0)}}{\partial t} + \gamma p^{(0)} \nabla_x \cdot \mathbf{u}^{(0)} = \frac{1}{\text{Re Pr}} \nabla_x \cdot \left(\lambda^{(0)} \nabla_x \cdot T^{(0)} \right). \quad (3.6)$$

$\partial u^{(0)}/\partial \xi$ can thus be calculated by a two step process. The first step is to calculate numerically $\nabla_{\tilde{x}} \cdot \mathbf{u}$, the *as-is* flow divergence. Then, from equation 3.6, the constancy of the thermodynamic pressure imposes $\nabla_x \cdot \mathbf{u}^{(0)} = \frac{1}{\text{Re Pr}} \nabla_x \cdot (\lambda^{(0)} \nabla_x \cdot T^{(0)})$. Hence the numerically calculated divergence satisfies

$$\nabla_{\tilde{x}} \cdot \mathbf{u} - \frac{1}{\text{Re Pr}} \nabla_x \cdot (\lambda^{(0)} \nabla_x \cdot T^{(0)}) = M \left(\frac{\partial u^{(0)}}{\partial \xi} + \frac{\partial v^{(0)}}{\partial \theta} \right) + O(M^2). \quad (3.7)$$

The second step is to assume that all acoustic waves incident on a boundary approach normally, implying $\partial v^{(0)}/\partial \theta = 0$. This step is consistent with the spirit of the original LODI/NSCBC and other characteristic approaches; future work will concentrate on generalising the treatment to include acoustic waves approaching the boundary obliquely. Recalling the definition $a = M^{-1}(\gamma p/\rho)^{\frac{1}{2}}$ —and with a slight abuse of notation—the required boundary conditions *in fully dimensional form* can be written as

$$\begin{aligned} L_1 = L_4 + \frac{(\gamma - 1) T}{a} & \left(v \frac{\partial u}{\partial y} - u_b \frac{\partial u}{\partial x} - \left(\frac{\partial \tau_{yx}}{\partial x} + \frac{\partial \tau_{yy}}{\partial y} \right) \right) \\ & - (\gamma - 1) T \frac{\partial u^{(0)}}{\partial \xi}, \end{aligned} \quad (3.8)$$

where

$$\frac{\partial u^{(0)}}{\partial \xi} = \left(\frac{\partial u}{\partial x} + \frac{\partial v}{\partial y} \right) - \left(\frac{\partial}{\partial x} \left(\lambda \frac{\partial T}{\partial x} \right) + \frac{\partial}{\partial y} \left(\lambda \frac{\partial T}{\partial y} \right) \right). \quad (3.9)$$

If the flow is cold, then it is straightforward to show that $T^{(0)} = \text{const.}$, and the thermal conduction term can be dropped from the preceding equation for $\partial u^{(0)}/\partial \xi$. We note that the molecular viscosity does not have an influence in calculating the $\partial u^{(0)}/\partial \xi$ term; this is due to viscosity only having a second order effect in the pressure transport equation.

4. Non reflecting viscous inflow conditions

The treatment of the inflow boundary conditions depends very much on the complexity of the field on the inlet plane. If the flow field is steady and has an analytic structure, the methods of the previous sections may be used to define non-reflecting conditions in a straightforward manner. If the incoming flow is turbulent, then a more sophisticated treatment is required.

For the turbulent inflow case, we have retained the method outlined in (Prosser 2004). We suppose that the simulation can be broken into two components: The *active* solution (for which we are seeking boundary conditions), and the precomputed *frozen* solution. The incoming characteristics required for the active solution are derived from the frozen solution, and convected across the inflow boundary.

In the precomputed solution, the periodic boundary conditions are usually employed, and these preclude the requirement for explicit conditions on the viscous fluxes (or indeed, any other terms). For open flow problems, we usually require the specification of some condition on the viscous fluxes. Hence, there is an inconsistency in the balancing of characteristics between the frozen solution and the active solution. We have as yet been unable to find a consistent way of matching the viscous effects between the two solutions. For a cold flow problem, the resulting pressure disturbances arising from this discrepancy should be small, as all momentum transport effects are of $O(M^2)$ in the pressure transport equation. If there are significant conduction effects—such as may be found when a flame approaches an inflow—then this error could grow to $O(1)$. Future work will concentrate on achieving a better consistency between frozen and active solutions, and will also examine methods of allowing evolving precomputed solutions to enter the active domain.

5. Results

5.1. The code

The boundary conditions described in this paper have been implemented in a code originally developed at UMIST. The code is parallel and is able to deal with any given chemical reaction mechanism. The code has been designed to work with a suite of numerical schemes, ranging from compact and explicit finite differences, to Chebyshev spectral methods and non-uniform high order discretisations. For this work, a uniform explicit fourth order approximation was used for spatial derivatives, and a minimal storage third order Runge-Kutta method developed by Wray (Wray 1990) was used for temporal integration. For all of the results that follow, the discretisation was based on a grid of 128×128 grid points, and ran on two processors on a SGI Origin 2000.

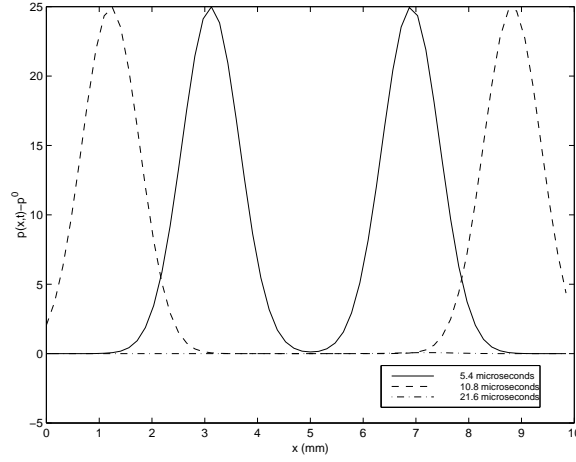


FIGURE 1. Sectional elevation of the flow field, showing the evolution of the acoustic pressure with time.

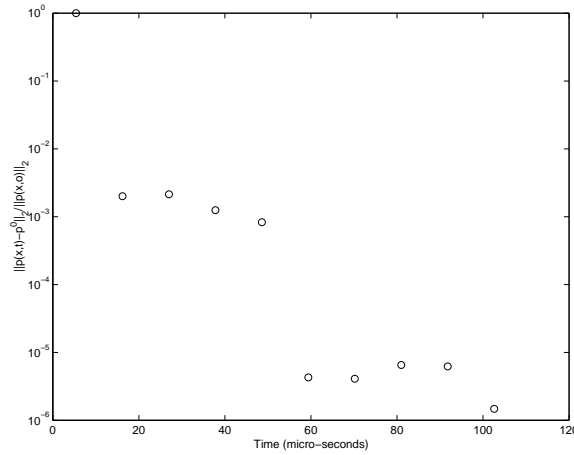


FIGURE 2. 2-norm of the evolving dynamic pressure field—laminar flow

5.2. Non-reflecting behaviour

Figure 1 shows the evolution of a pressure pulse in a domain 10mm square, comprising a steady flow of air with a uniform motion of 2m/s. The initial pressure field is given by

$$p'(\mathbf{x}, t) - p^{(0)} = 2 \exp \left(- \left(0.13 \left(x - \frac{1}{2} \right) \right)^2 \right) \quad -5 \times 10^{-3} \leq x, y \leq 5 \times 10^{-3}. \quad (5.1)$$

The simulation uses the boundary conditions developed above and incorporates the effects of viscosity and thermal conduction. This test is designed to demonstrate the non-reflective character of the boundary condition treatment. As can be seen, the pressure waves leave both the inflow and outflow boundaries smoothly. Figure 2 gives the time history of the 2-norm of the acoustic pressure: $\|p(\mathbf{x}, t) - p^{(0)}\|_2 / \|p(\mathbf{x}, 0)\|_2$. We note that after 1 acoustic transit time ($O(l_0/a_0) \simeq 30\mu s$, here), the magnitude of the acoustic mode has dropped to 0.1% of the initial condition. After subsequent multiples of the acoustic transit time, the magnitude of the acoustic mode drops to 0.001%, and 0.0001%,

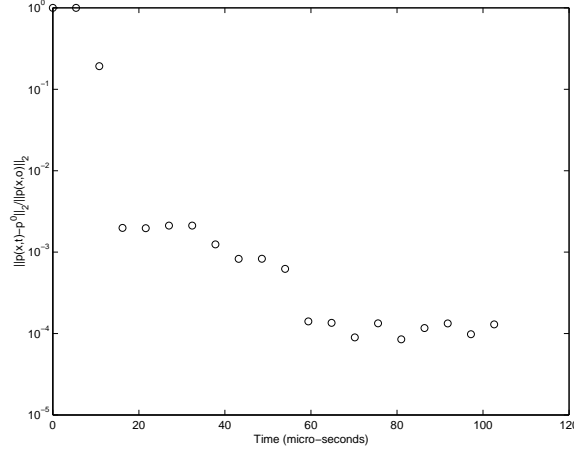


FIGURE 3. Evolution of the normalised pressure difference for the turbulent, acoustically perturbed solution.

respectively. The initial 0.1% reflection arises from the second order influence of the mean convection speed. The inclusion of a second order term in the non-reflecting criteria improves the performance of the boundary conditions further. This will be further explored in a future paper.

5.3. Cold turbulence

The second problem to be studied using the new boundary conditions is that of cold two-dimensional, viscous turbulence. The initial conditions for this flow were generated using the methods described by Rogallo (Rogallo 1981). The turbulent velocity fluctuations were calculated such that the resultant energy spectrum satisfied

$$E(k) = \begin{cases} \frac{72}{\pi} \frac{k}{k^4 + 6^4} & k \leq k_{\max} \\ 0 & k \geq k_{\max} \end{cases} \quad (5.2)$$

k_{\max} was set for this study at 12, a subsequent normalization of the energy spectrum produced a turbulence RMS intensity of 0.1m/s (5% of the mean flow speed for this case). The resultant flow field contains a range of length and time scales characteristic of turbulence, but one that is readily resolved using a low resolution grid of 128×128 grid points. This last comment is particularly aimed at the one sided schemes used at the inflow/outflow boundaries; these often have a lower formal order of accuracy, and a much poorer spectral resolution, than symmetric internal constructions. The mean velocity for this investigation was set at 2.0m/s and the physical size of the domain was set at 10mm \times 10mm.

The simulation was run twice. The first simulation evolved from the set of initial conditions *without* the pressure pulse, and provided the evolving benchmark pressure field $p_{ref}(\mathbf{x}, t)$. The second simulation shared the same inertial features as the benchmark solution, but also included the pressure perturbation given by equation 5.1. The idea is that the two simulations should share the same time dependent inertial behaviour, but the second simulation should have an additional acoustic component. If the non-reflecting boundary conditions work correctly, this component should leave the domain after half an acoustic transit time. The two solutions should thereafter evolve identically, and the

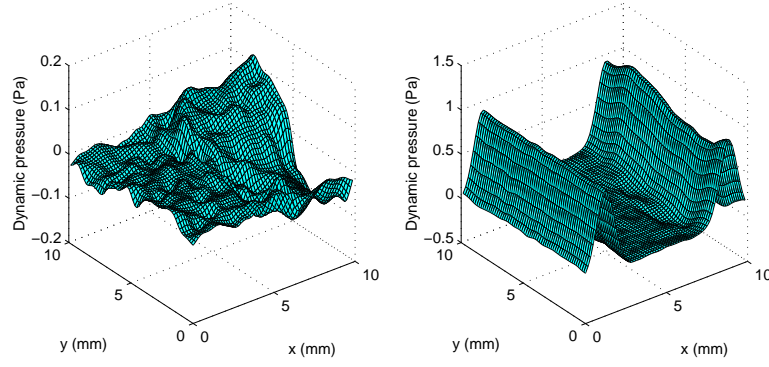


FIGURE 4. Comparison between dynamic pressure surfaces for the reference simulation and acoustically perturbed simulation after an elapsed simulation time of $16.2\mu s$

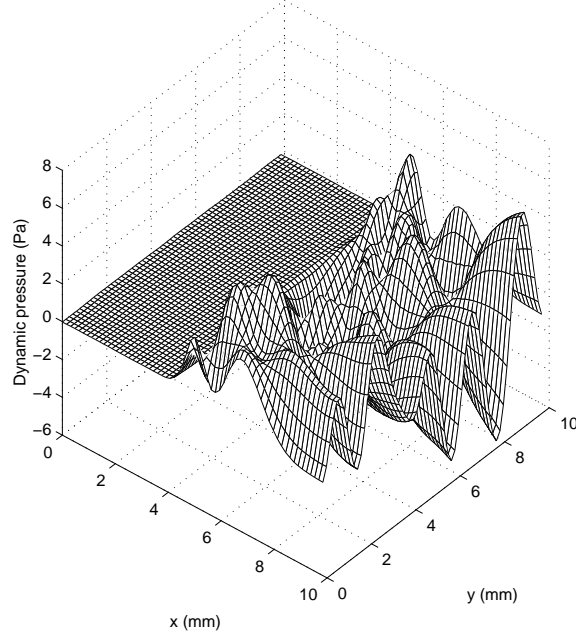


FIGURE 5. Propagation of spurious acoustic waves into the domain from the NSCBC outflow boundary. Elapsed simulation time = $16.2\mu s$.

difference between them, embodied by a normalised pressure difference

$$\frac{\|p(\mathbf{x}, t) - p_{ref}(\mathbf{x}, t)\|_2}{\|p(\mathbf{x}, 0)\|_2}, \quad (5.3)$$

should vanish.

Figure 3 shows a logarithmic plot of the time history of the normalised pressure difference (equation 5.3). Figures 4a and b show the dynamic pressure surfaces for the reference solution and the perturbed solution at an elapsed simulation time of $16.2\mu s$. In figure 4b, we can see the pressure pulses are just leaving the domain via the inlet and outlet boundaries. It is at this time that the large reduction in normalised pressure difference,

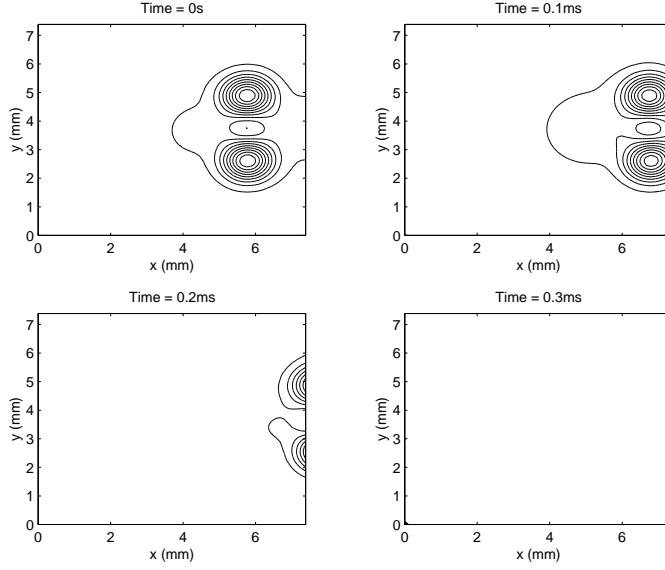


FIGURE 6. Pressure contour plots of twin co-rotating vortices approaching a revised non-reflecting outflow. Centres of vortices are heated to 600K.

visible in figure 3 takes place. Finally, figure 5 shows the pressure field obtained from a simulation also at an elapsed simulated time of $16.2\mu\text{s}$, but this time using NSCBC boundary conditions. As can be seen, spurious pressure oscillations from the outflow boundary conditions have begun to propagate upstream at the local sound speed, and are well on their way to swamping the pressure field induced by the dynamics alone.

The simulations using the new boundary conditions were allowed to continue to run for an additional 45×10^3 time steps, which corresponds to 1 flow transit time (defined as l_0/u_0). At the end of this extended run, no significant errors in the pressure field were observed, and the dynamic pressure variations remained bounded essentially by the kinetic energy of the turbulence.

5.4. Co-rotating hot vortices

Figures 6a-d show the pressure evolution for 2 co-rotating vortices leaving the computational domain. This configuration was chosen because there is an inertial evolution in the flow, as well as acoustic transients arising from the initial conditions. The mean flow speed is set to 10m/s, and the two vortices are initialised using a stream function

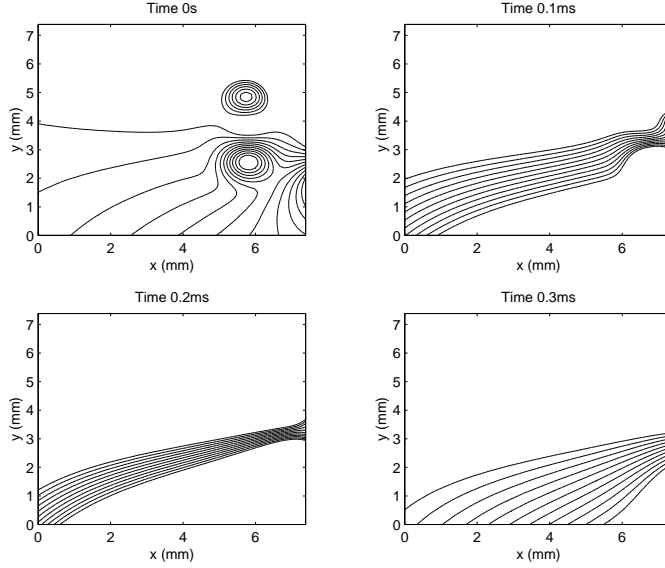


FIGURE 7. Pressure contour plots of twin co-rotating vortices approaching a standard non-reflecting outflow. Centres of vortices are heated to 600K.

approach defined initially on a domain $\tilde{\Omega} = \{\tilde{x}, \tilde{y} : 0 \leq \tilde{x} \leq 1, 0 \leq \tilde{y} \leq 1\}$,

$$\begin{aligned}
 \psi &= C \left(\exp \left(-\frac{r_a^2}{2r_v^2} \right) + \exp \left(-\frac{r_b^2}{2r_v^2} \right) \right) + u_b y \\
 r_a &= \left((\tilde{x} + 0.5)^2 + (\tilde{y} - 0.15)^2 \right)^{\frac{1}{2}} \\
 r_b &= \left((\tilde{x} + 0.5)^2 + (\tilde{y} + 0.15)^2 \right)^{\frac{1}{2}} \\
 u &= \frac{\partial \psi}{\partial \tilde{y}} \\
 v &= -\frac{\partial \psi}{\partial \tilde{x}} \\
 T &= 300 \left(1 + \exp \left(-\frac{r_a^2}{2r_v^2} \right) + \exp \left(-\frac{r_b^2}{2r_v^2} \right) \right). \tag{5.4}
 \end{aligned}$$

C is the vortex strength, u_b is the mean velocity and r_v is a characteristic radius. For this simulation, C was set at $0.5\text{m}^2/\text{s}^2$, r_v was set at 8% of the domain size and the mean velocity u_b was set at 10m/s. The physical flow domain is 7.5mm square, and a linear mapping was used to relate quantities in the physical domain to the initial conditions calculated by equations 5.4a-f. The pressure was assumed initially to be constant, and the density was calculated using the thermal equation of state. The thermal conductivity was calculated using (Echekki & Chen 1996)

$$\lambda = 2.58 \times 10^{-5} \times c_p \left(\frac{T}{300} \right)^{0.7} \tag{5.5}$$

As the flow field has a simple far field structure, the standard NSCBC treatment was used for the transverse directions. For the inlet a fixed velocity, non reflecting condition

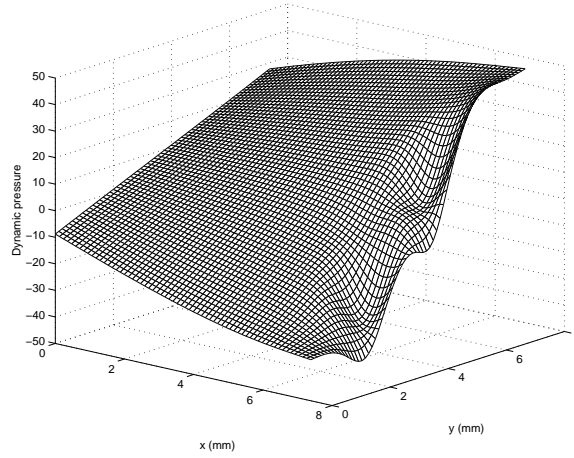


FIGURE 8. Dynamic pressure surface for hot vortices crossing NSCBC boundary conditions. Surface corresponds to contour plot 7c.

was imposed (Prosser 2004). As can be seen from figures 6a-d, there is no appreciable distortion arising from the boundary conditions. Figures 7a-d show the evolution of the pressure field for the problem when normal NSCBC boundary conditions are applied. In figure 7a-d, the contours have been restricted to the same range as those in figures 6a-d. Figure 8 shows the pressure surface corresponding to contour plot 7c. We note the significant transverse pressure variation across the entire domain, arising as a result of the pollution induced by the old boundary conditions.

6. Large-Eddy Simulations

In the next step, we want to apply the boundary condition to Large-Eddy Simulations (LES). In LES, the filtered Navier-Stokes equations are solved, which means in turbulent flows the large scale motions of turbulence are resolved in space and time on a given mesh, while the smaller scales are modeled using an eddy viscosity approach.

Here, we are using a structured compressible LES flow solver developed by Pierce (Pierce & Moin 1998) and Wall (Wall *et al.* 2002), which uses a second-order finite-volume scheme on a staggered grid (Akselvoll & Moin 1996). The sub-grid stresses are approximated by a dynamic procedure (Germano *et al.* 1991; Moin *et al.* 1991). The pressure and density field are determined by solving the Helmholtz equation and the time-step was set to satisfy the acoustic CFL condition.

Using the LES flow solver, the test-case described in section 5.4 was computed. The LES mesh size was $128 \times 128 \times 8$ nodes. The discretization in z -direction was intentionally left coarse in order to compute a quasi-2D flow. The mesh is concentrated near the path of the vortices. In transverse direction non-slip wall conditions were applied.

Fig. 9 shows the pressure distribution at the outlet cross section at the instant of maximum distortion. We note that the pressure distortion is much more attenuated using Eq. (3.8).

We performed additional LES computations without a subgrid model in order to assess the effect of the additional viscous terms of the subgrid model. The results of these computations were virtually indistinguishable from the previous results, which means that

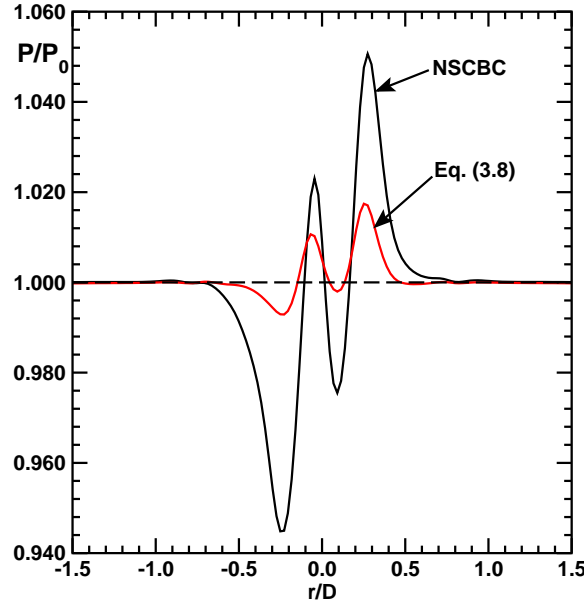


FIGURE 9. LES computation of co-rotating vortices passing outflow: cross-section pressure distribution at the instant of maximum pressure distortion.

for the chosen test case, the influence of the subgrid model on the boundary conditions is neglectable.

7. Conclusions

A procedure to improve the specification of time dependent boundary conditions for viscous flows has been described. The approach is based on a low Mach number expansion of the governing equations, and is an extension of a method originally developed for inviscid flows. The incorporation of thermal conduction and viscosity into the new boundary conditions are shown to have leading and second order effects, respectively. The new approach provides a significantly better treatment of the pressure field—both at inflow and outflow boundaries—than the previous characteristics based methods. The new treatment is able to deal with flows comprising inhomogeneous high temperature regions without inducing spurious effects. The scheme appears to be stable for long time integration periods.

A number of areas have emerged during the course of this investigation that require further analysis. Firstly, it can be shown that a modification to equation 3.3 to include second order effects provides a less reflective boundary condition. The effects on stability of this modification has yet to be established for long time scale integrations. Secondly, no viscous boundary conditions were imposed during the course of these simulations, other than the explicit coupling of the viscous fluxes to the inertial terms via the characteristics, as seen in equation 3.3. It is not clear at this stage whether the coupling can be interpreted as a type of viscous condition in the form recommended by Dutt (Dutt 1988), although the practical long term stability of the calculations presented here do provide grounds for cautious optimism. Thirdly, the extension of the asymptotic methods to reacting flows is straightforward and will be examined in a forthcoming paper.

Finally, the new approach still suffers from the thermodynamic pressure drift found in other characteristics based methods. This drift has been identified with the failure of the numerical schemes properly to enforce a leading order solenoidal constraint on the velocity field, when formally the flow should be divergence free. Future work will examine the improvement of numerical methods and/or boundary conditions to reduce the drift, without recourse to the pressure-at-infinity condition proposed by Strikwerda (Strikwerda 1977), which has a tendency to introduce Nyquist frequency oscillations into the flow field.

8. Acknowledgments

We thank Clifton Wall for providing the compressible LES flow solver.

REFERENCES

- AKSELVOLL, K., & MOIN, P. 1996 Large-eddy simulation of turbulent confined coannular jets. *J. of Fluid Mech.*, **315**, 387–411.
- BAUM, M., POINSOT, T.J. & THÉVENIN, D. 1994 Accurate Boundary Conditions for Multicomponent Reactive Flows. *J. Comp. Phys.*, **116**, 247–261.
- DUTT, P. 1988 Stable Boundary Conditions and Difference Schemes for Navier-Stokes Equations. *SIAM J. Num. Anal.*, **25**, 245–267.
- ECHEKKI, T. & CHEN, J.H. 1996 Unsteady Strain Rate and Curvature Effects in Turbulent Premixed Methane-Air Flames. *Combustion and Flame*, **106**, 184–202.
- GERMANO, M., PIOMELLI, U., MOIN, P. & CABOT, W. 1991 A dynamic subgrid-scale eddy viscosity model. *Phys. Fluids A* (**3**), 1760–1765.
- GRINSTEIN, F.F. 1994 Open Boundary Conditions in the Simulation of Subsonic Turbulent Shear Flows. *J. Comp. Phys.*, **115**, 43–55.
- HEDSTROM, G.W. 1979 Nonreflecting Boundary Conditions for Nonlinear Hyperbolic Systems. *J. Comp. Phys.*, **30**, 222–237.
- HESTHAVEN, J.S. 1998 On the Analysis and Construction of Perfectly Matched Layers for the Linearized Euler Equations. *J. Comp. Phys.*, **142**, 129–147.
- HU, F.Q. 1996 On Absorbing Boundary Conditions for Linearized Euler Equations by a Perfectly Matched Layer. *J. Comp. Phys.*, **129**, 201–219.
- KLEIN, R. 1995 Semi-Implicit Extension of a Godunov-Type Scheme Based on Low Mach Number Asymptotics I: One Dimensional Flow. *J. Comp. Phys.*, **121**, 213–237.
- MAJDA, A. AND SETHIAN, J. 1985 The derivation and Numerical Solution of the Equations for Zero Mach Number Combustion. *Combust. Sci. and Tech.*, **42**, 185–205.
- MCMURTRY, P.A., JOU, W.H., RILEY, J.J. & METCALFE, R.W. 1986 Direct Numerical Simulations of a Reacting Mixing Layer with Chemical Heat Release. *AIAA Journal*, **24**, 962–970.
- MOIN, P., SQUIRES, K., CABOT, W. & LEE, S. 1991 A dynamic subgrid-scale model for compressible turbulence and scalar transport. *Phys. Fluids, A* (**3**), 2746–2757.
- NICOUD, F. 1999 Defining Wave Amplitude in Characteristic Boundary Conditions. *J. Comp. Phys.*, **149**, 418–422.

- PIERCE, C. D. & MOIN, P. 1998 Large eddy simulation of a confined coaxial jet with swirl and heat release. *AIAA Paper* 98-2892.
- POINSOT, T.J. & LELE, S.K. 1992 Boundary Conditions for Direct Simulations of Compressible Viscous Flows. *J. Comp. Phys.*, **101**, 104–129.
- PROSSER, R. 2004 Improved Boundary Conditions for the Direct Numerical Simulation of Turbulent Subsonic Flows I: Inviscid Flows. *submitted to J. Comp. Phys.*
- ROGALLO, R. 1981 Numerical Experiments in Homogeneous Turbulence. *NASA Technical Report 81315*, NASA Ames.
- RUDY, D.H. AND STRIKWERDA, J.C. 1980 A Nonreflecting Outflow Boundary Condition for Subsonic Navier-Stokes Calculations. *J. Comp. Phys.*, **36**, 55–70.
- RUDY, D.H. AND STRIKWERDA, J.C. 1981 Boundary Conditions for Subsonic Compressible Navier-Stokes Calculations. *Comput. Fluids.*, **9**, 327–338.
- STRIKWERDA, J. C. 1996 Initial boundary value problems for incompletely parabolic systems. *Commun. Pure Appl. Math.*, **30**, 797–822.
- SUTHERLAND, J.C. & KENNEDY, C.A. 2003 Improved boundary conditions for viscous, reacting, compressible Flows. *J. Comp. Phys.*, **191**, 502–524.
- THEVÉNIN, D., BAUM, M. & POINSOT, T.J. 1996 Direct Numerical Simulation for Turbulent Reacting Flows. *Editions Technip, Paris*, 11–32.
- THOMPSON, K.W. 1987 Time Dependent Boundary Conditions for Hyperbolic Systems. *J. Comp. Phys.*, **68**, 1–24.
- TSYNKOV, S.V. 1998 Numerical solution of problems on unbounded domains. A review. *Appl. Numer. Math.*, **27**, 465–532.
- VICHNEVETSKY, R. 1986 Invariance Theorems Concerning Reflection at Numerical Boundaries. *J. Comp. Phys.*, **63**, 268–282.
- WALL, C., PIERCE, C.D. & MOIN, P. 2002 A Semi-implicit Method for Resolution of Acoustic Waves in Low Mach Number Flows. *J. Comp. Phys.*, **181**, 2, 545–563.
- WRAY A.A. 1990 Minimal Storage Time-Advancement Schemes for Spectral Methods. *unpublished*, NASA Ames Research Center.